Zweifach reduzierte 9,10-Dihydro-9,10-diboraanthracene: Von der Aktivierung kleiner Moleküle bis zum Einsatz als Katalysatoren

Dissertation

zur Erlangung des Doktorgrades

der Naturwissenschaften

vorgelegt dem Fachbereich Biochemie, Chemie und Pharmazie

der Johann Wolfgang Goethe-Universität

in Frankfurt am Main

von

Esther von Grotthuss

aus Koblenz

Frankfurt am Main 2019

D30

vom Fachbereich Biochemie, Chemie und Pharmazie der

Johann Wolfgang Goethe-Universität als Dissertation angenommen

Dekan:		Prof. Dr. Clemens Glaubitz
Gutachter:	(1)	Prof. Dr. Matthias Wagner
	(2)	Prof. Dr. Norbert Auner

Die vorliegende Arbeit wurde im Zeitraum von November 2015 bis Mai 2019 unter der Anleitung von Herrn Prof. Dr. Matthias Wagner am Institut für Anorganische und Analytische Chemie der Johann Wolfgang Goethe-Universität in Frankfurt am Main angefertigt.

Danksagung

Die Danksagung wurde aus der digitalen Version entfernt.

Inhaltsverzeichnis

Abkürzungsverzeichnis

A	neutrale 9,10-Dihydro-9,10-diboraanthracene
[**A**]$^{2-}$	zweifach reduzierte 9,10-Dihydro-9,10-diboraanthracene
[**A**-H_2]$^{2-}$	H_2-Aktivierungsprodukte von zweifach reduzierten 9,10-Dihydro-9,10-diboraanthracenen [**A**]$^{2-}$
Ar	Aryl
CAAC	cyclisches Alkylaminocarben (engl. cyclic alkyl amino carbene)
C≡C*t*Bu	*tert*-Butylacetylen
[Cp*]$^-$	[η^5-C_5Me_5]$^-$
Cy	Cyclohexyl
DBA	9,10-Dihydro-9,10-diboraanthracen
DFT	Dichtefunktionaltheorie
Dip	2,6-Di(*i*so-propyl)phenyl
DMF	Dimethylformamid
DMSO	Dimethylsulfoxid
DNA	Desoxyribonukleinsäure (engl. deoxyribonucleic acid)
E	beliebiges Element
Ed.	Editor(en)
Et	Ethyl
FLP	Frustriertes Lewis-Paar (engl. Frustrated Lewis Pair)
Fxyl	3,5-Bis(trifluormethyl)phenyl
H	Wasserstoff-Substituent
h	Stunde(n)
HBcat	Catecholboran
HBpin	Pinakolboran
HOMO	höchstes besetztes Molekülorbital (engl. highest occupied molecular orbital)
*i*Pr	*iso*-Propyl
L	Ligand
LUMO	niedrigstes unbesetztes Molekülorbital (engl. lowest unoccupied molecular orbital)
M	beliebiges Metallzentrum
Me	Methyl
Mes	Mesityl/1,3,5-Trimethylphenyl
min	Minute(n)
MO	Molekülorbital
n.a.	nicht aufgelöst
n.b.	nicht beobachtet
NHC	*N*-heterocyclisches Carben

NMR	kernmagnetische Resonanz (engl. nuclear magnetic resonance)
Ph	Phenyl
*p*Tol	*para*-Tolyl
R	beliebiger Rest
RT	Raumtemperatur
*t*Bu	*tert*-Butyl
Ter	Bis-(2,6-mesityl)-phenyl
THF	Tetrahydrofuran
TMP	2,2,6,6-Tetramethylpiperidin
TMS	Trimethylsilyl
TS	Übergangszustand (engl. transition state)
vgl.	vergleiche
X	beliebiges Halogenatom
Xyl	Xylyl/*meta*-Dimethylphenyl
z. B.	zum Beispiel

1. Einleitung

Die Photosynthese, die DNA-Replikation und die großtechnische Darstellung von Ammoniak entstammen gänzlich unterschiedlichen Kontexten, aber verfügen über zwei Gemeinsamkeiten: Diese chemischen Prozesse sind essentiell für das menschliche Dasein und benötigen Reaktionsbeschleuniger, um einen zügigen Stoffumsatz zu erzielen. Die Umwandlung von Kohlenstoffdioxid und Wasser zu Glucose und Sauerstoff wird durch den Farbstoff Chlorophyll ermöglicht.[1] Im menschlichen Körper sind Enzyme, sogenannte DNA-Polymerasen, für die Vervielfältigung unseres Erbguts verantwortlich.[2] Im Laufe der Historie hat der Mensch gelernt, dass nicht nur organische, sondern auch anorganische Stoffe zielgerichtete Synthesen erleichtern. Im Haber-Bosch-Verfahren hilft α-Eisen bei der industriellen Darstellung von Ammoniak aus den Elementen.[3] Die reaktionsfördernde Komponente wird als Katalysator bezeichnet, von dem kleinste Mengen für einen großen Stoffumsatz ausreichen. Zusammen mit einer hohen Selektivität und der Erschließung neuer Reaktionspfade bergen katalytische Prozesse nach wie vor ein großes Potential für unsere moderne Gesellschaft. Neben der ökonomischen gewinnt die ökologische Wertschöpfung immer mehr an Bedeutung, um Nebenprodukte auszuschließen, Abfallprodukte zu recyceln, Schadstoffe zu vermeiden oder neue Ressourcen zu nutzen.[4]

1.1. Grundlagen der Katalyse

Der Begriff der Katalyse wurde 1835 von Berzelius eingeführt, um die Fähigkeit eines Stoffes zu beschreiben, eine Reaktion zwischen zwei ansonsten unreaktiven Substanzen auszulösen. Über die Wirkungsweise eines Katalysators war damals noch nichts bekannt. Erst im Jahr 1894 lieferte Ostwald folgende Definition: „Katalyse ist die Beschleunigung eines langsam verlaufenden chemischen Vorgangs durch die Gegenwart eines fremden Stoffes“.[5] Etwas später ergänzte er, dass der Katalysator nicht im Endprodukt verbleibt, sondern immer wieder freigesetzt wird. Damit fungiert der Katalysator als Mediator einer thermodynamisch erlaubten Reaktion, indem er deren kinetische Reaktionsbarriere herabsetzt. Diese gedankliche Grundlage bildete das Fundament für eine zielgerichtete Katalysatorforschung.[5]

In Abhängigkeit von der Katalysatorbeschaffenheit und der Anzahl an Reaktionsphasen unterscheidet man zwischen einer heterogenen, homogenen und enzymatischen Katalyse. Die wirtschaftliche Relevanz katalytischer Prozesse ist enorm, da 70% aller industriellen Prozesse darauf aufbauen.[4] Mit einem Anteil von 80% sind heterogene Prozesse aktuell am bedeutendsten.[4] Ihren kommerziellen Anfang fanden diese im Döbereiner Feuerzeug: Mithilfe eines Kipp‘schen-Apparats wird Schwefelsäure in Kontakt mit einem Zinkstab gebracht, sodass chemisch H_2 entsteht, der sich an einem Platinschwamm durch Kontakt mit Luftsauerstoff entzündet.[5] Die Herausforderung bei der Nutzung von elementarem H_2 liegt in der Stärke und der schlechten Polarisierbarkeit der H–H-Bindung, womit eine hohe Reaktionsbarriere verbunden ist. Im Rahmen der vorliegenden Arbeit kommt dem Schritt der Wasserstoffaktivierung eine besondere Rolle zu, sodass dieses Element im Folgenden als Modellbeispiel für die Erläuterung grundlegender Katalyseprinzipien genutzt wird. In heterogenen Katalysen setzt man die Reaktionspartner häufig als Gase bei hohen Temperaturen und

Drücken ein. Beim Haber-Bosch-Verfahren dienen diese beiden Parameter zusätzlich dazu, das Gleichgewicht zwischen der Bildung von Ammoniak aus den Elementen und der Rückreaktion einzustellen.[3] Ebenfalls mit Eisen als Katalysator kann man H_2 mit CO zu Kohlenwasserstoffen umsetzen. Diese sogenannten Fischer-Tropsch-Synthesen haben die organische Rohstoffchemie katalytisch erschlossen, wenngleich damit Selektivitätsprobleme einhergehen, die mit einem heterogenen Katalysator schwierig zu beheben sind. Eine Optimierung der Reaktionsführung erlauben homogene Molekülkatalysatoren, deren definierte Strukturen ein tieferes Verständnis der Wirkungsweisen ermöglichen. Das Reaktionszentrum ist ein Metallatom, das von einer Ligandensphäre umgeben ist. Beide Komponenten können nach Maß gestaltet werden und gestatten oftmals eine Reaktionsführung unter milden Bedingungen. Einer der bekanntesten Hydrierkatalysatoren ist $Rh(PPh_3)_3Cl$, der nach seinem Erfinder Wilkinson benannt wird und mit dem erstmalig die homogen geführte Hydrierung von Olefinen realisiert wurde.[5] Am Beispiel dieser Reaktion sind in Schema 1 die Elementarschritte eines homogenen Katalysezyklus dargestellt, deren Aufklärung die vielfältige Entwicklung solcher Katalysatoren maßgeblich beeinflusst hat. Zu Beginn liegt der Katalysator nicht immer in seiner katalytisch aktiven Form vor, sondern erst die Dissoziation eines Liganden schafft eine freie Koordinationsstelle, die eine Wechselwirkung mit einem Reaktanden zulässt.

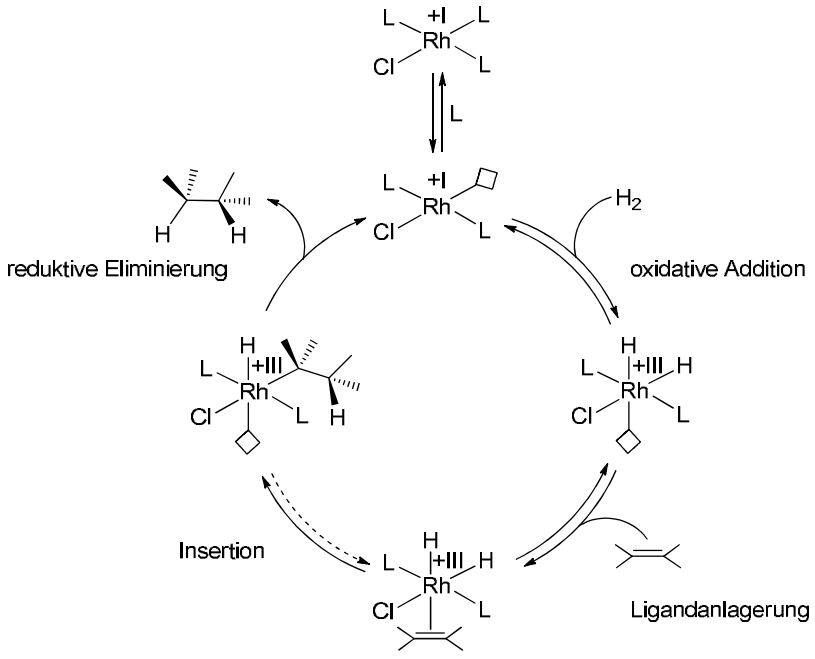

Schema 1. Elementarschritte der Olefinhydrierung mit dem Wilkinson-Katalysator. L = PPh_3.

Im ersten Schritt des Hydrierkatalyse-Zyklus addiert sich H_2 oxidativ an das Rhodiumzentrum. Dieser Vorgang ist ebenso reversibel wie die anschließende Anlagerung eines Olefin-Moleküls und die Insertion des Olefins in die *cis*-ständige Rh–H-Bindung. Die Labilität der intermediär gebildeten Komplexe garantiert das Durchlaufen des Katalysekreislaufes ohne dass ein thermodynamisches Minimum erreicht wird. Die abschließende reduktive Eliminierung des gesättigten Alkans ist hingegen irreversibel. Dadurch wird sichergestellt, dass der aktive Katalysatorkomplex für einen erneuten Durchgang bereitsteht.

1.2. Aktivierung kleiner Moleküle mit Übergangsmetallkomplexen

Sowohl heterogene als auch homogene Katalysen hängen häufig von der Reaktivität geeigneter Übergangsmetalle ab. Für enzymatische Katalysereaktionen greifen andere Wirkmechanismen, welche hier nicht diskutiert werden.[2] Betrachtet man die Elementarschritte der Hydrierung von Olefinen aus Schema 1, so offenbart sich die grundlegende Fähigkeit von Übergangsmetallen zwischen verschiedenen Oxidationsstufen und Koordinationsmodi zu wechseln. Beide Eigenschaften begründen die vielseitigen Einsatzmöglichkeiten von Übergangsmetallkomplexen als Katalysatoren.

Zentral für viele chemische Reaktionen ist die Energiedifferenz zwischen dem höchsten besetzten (HOMO) und dem niedrigsten unbesetzten Molekülorbital (LUMO) der einzelnen Reaktanden. Die geringen Energieunterschiede zwischen den d-Orbitalen in Metallkomplexen begünstigen eine Umverteilung von Elektronen mit geringen Aktivierungsenergien.[6] Eine Korrelation zwischen einem energetisch möglichen Elektronenübergang in einem Metallkomplex und der Aktivierungsbarriere für die Olefinpolymerisation wurde beispielsweise für einen $TiCl_3$-Aluminiumalkyl-Katalysator berechnet.[7] Gerade mit homogenen Katalysatoren lässt sich der HOMO-LUMO-Abstand durch geeignete Wahl des Metallzentrums und der Liganden leicht variieren und damit für eine spezifische Reaktion optimieren. Bei der Hydroformylierungsreaktion werden terminale Alkene mit CO und H_2 zumeist an einem Cobalt-Katalysator umgesetzt, was zur Bildung eines *n*- oder *iso*-Aldehyds führt. In der Reihe der Katalysatoren $CoH(CO)_3$, $CoH(CO)_2(PnBu_3)$ und $RhH(CO)(PPh_3)_2$ wurden durch geschickte Wahl von Metall und Ligand milde Reaktionsbedingungen ermöglicht, bei gleichzeitiger Erhöhung des *n/iso*-Verhältnisses.[5]

Das HOMO und das LUMO von Übergangsmetallkomplexen setzen sich größtenteils aus den d-Orbitalen des Metallatoms zusammen, die vielfältig in ihrer Symmetrie sind und damit die Grundlage für die Wechselwirkungen mit verschiedenen Substraten legen.[6] Passen die Symmetrien von HOMO und LUMO zweier Reaktionspartner zusammen, so ergibt sich eine positive Wechselwirkung. In Abbildung 1 ist gezeigt, dass die Interaktion des σ-MOs von H_2 mit einem leeren d-Orbital des Metallzentrums durch die Rückbindung eines gefüllten d-Orbitals in das σ*-MO von H_2 verstärkt wird, was zum H–H-Bindungsbruch führt.

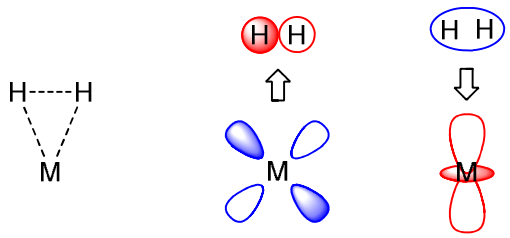

Abbildung 1. Struktur und Orbitalwechselwirkungen des Übergangszustands für die Aktivierung von H_2 mit Übergangsmetallzentren. HOMOs: blau; LUMOs: rot.

Aus diesen Betrachtungen lassen sich allgemein zwei Bedingungen formulieren, die für die katalytische Aktivität einer chemischen Verbindung notwendig sind:[6, 8]

1. kleiner HOMO-LUMO-Energieunterschied
2. günstige Symmetrien der Grenzorbitale

Diese Bedingungen werden von Übergangsmetallkomplexen in der Regel erfüllt und spiegeln sich nicht nur in deren Potential als Katalysatoren wider, sondern auch in Eigenschaften wie Farbigkeit und Magnetismus. Deshalb standen diese Charakteristika lange im starken Gegensatz zu Hauptgruppenverbindungen, denen gänzlich andere Attribute zugeordnet wurden, wie in Tabelle 1 gegenübergestellt.[9]

Tabelle 1. Gängige Sichtweisen auf Übergangsmetall- und Hauptgruppenverbindungen.

Übergangsmetallverbindungen	**Hauptgruppenverbindungen**
teilweise gefüllte d-Valenzorbitale, die oft energetisch ähnlich sind	s- oder p- Valenzorbitale, die entweder vollständig besetzt oder leer und energetisch weit voneinander entfernt sind
Donor- und Akzeptororbitale	stereochemisch aktive Elektronenpaare
oft farbig	oft farblos
paramagnetisch und diamagnetisch	meistens diamagnetisch

In den letzten zehn Jahren hat sich diese gegensätzliche Sichtweise massiv verändert, da über immer mehr Hauptgruppensysteme berichtet wurde, die die Reaktivität von Übergangsmetallen nachahmen.

1.3. Aktivierung kleiner Moleküle mit Hauptgruppenverbindungen

Die Beobachtung metallähnlicher Reaktivitäten von Hauptgruppenverbindungen führt zu dem Schluss, dass auch Vertreter aus dieser Verbindungsklasse die zuvor genannten Bedingungen erfüllen können. Im Folgenden werden die grundlegenden Wechselwirkungen von drei Substanzklassen am Beispiel von H_2 als Reaktionspartner vorgestellt.

1.3.1. Elektronische Strukturen von Hauptgruppenverbindungen

Frustrierte Lewis-Paare (FLPs). Die Kombination einer Lewis-Säure mit einer Lewis-Base, die aufgrund des sterischen Anspruchs ihrer Substituenten kein klassisches Addukt bilden können, wird als frustriertes Lewis-Paar bezeichnet. Im Jahr 2006 führte Stephan dieses Konzept mit einem Boran als Lewis-Säure und einem Phosphan als Lewis-Base ein.[10] Die Besonderheit dieses Systems liegt darin, dass die reaktiven Zentren sich nicht gegenseitig neutralisieren, sondern für kleine Moleküle weiterhin erreichbar sind. Wie genau diese Wechselwirkung aussieht, wurde lange diskutiert, da sich zwei unterschiedliche Konzepte entwickelten: Zum einen basierend auf den Grenzorbitalen und der Ausbildung eines nicht-linearen frustrierten Komplexes[11] und zum anderen durch ein entstehendes lineares elektrisches Feld zwischen den Lewis-Komponenten.[12] Letztendlich hat sich die MO-Betrachtung des frustrierten Komplexes durchgesetzt, weil die Struktur des Übergangszustandes und auch energetische Zusammenhänge durch den Ansatz des elektrischen Feldes nicht richtig erklärt werden können.[13] Ein nicht-linearer Übergangszustand ermöglicht die maximale Überlappung der involvierten Grenzorbitale wie in Abbildung 2 dargestellt. Das freie p_z-Orbital des Borans (Lewis-Säure) akzeptiert Elektronendichte des σ-MOs von H_2 und das freie Elektronenpaar des Phosphans (Lewis-Base) adressiert das σ^*-MO von H_2.

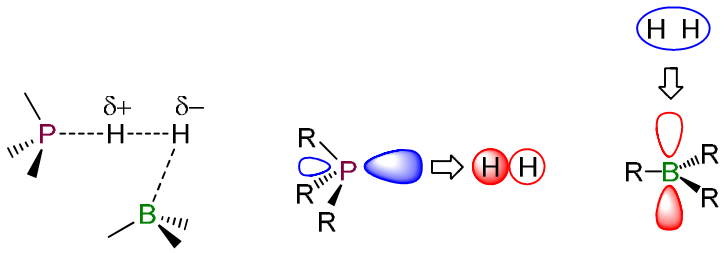

Abbildung 2. Struktur und Orbitalwechselwirkungen des Übergangszustands für die Aktivierung von H_2 mit FLPs. HOMOs: blau; LUMOs: rot.

Auf diese Weise wird das H_2-Molekül polarisiert und es kommt zum heterolytischen Bindungsbruch.[11] In einer theoretischen Studie formulierten Heine und Röschenthaler Kriterien, die für die Aktivierung von H_2 mit FLPs entscheidend sind.[14] Dazu betrachteten sie unter anderen die in Tabelle 2 gezeigten Lewis-Paare, für die experimentelle Vergleichsdaten vorlagen.

Tabelle 2. Untersuchung der Reaktivität verschiedener Lewis-Kombinationen gegenüber H_2 (Reaktionsbedingungen: 25 °C, 1 atm H_2, Toluol; Me = Methyl; Mes = Mesityl).

Eintrag	Lewis-Paar	Experimenteller Befund
1	Me_3P / $B(C_6F_5)_3$	klassische Adduktbildung, keine Reaktion mit H_2
2	Mes_3P / $B(C_6F_5)_3$	irreversible H_2-Aktivierung
3	(*o*-$MeH_4C_6)_3P$ / $B(p\text{-}C_6F_4H)_3$	reversible H_2-Aktivierung
4	$(F_5C_6)_3P$ / $B(C_6F_5)_3$	keine Reaktion

Eintrag 1 diente als Referenz, da diese Lewis-Kombination ein klassisches Addukt bildet, das keine weitere Reaktion eingeht. Gemäß der Definition eines FLPs ist der sterische Anspruch der Substituenten entscheidend für die Bildung eines frustrierten Komplexes (vgl. Eintrag 2), wobei der Abstand der reaktiven Zentren dennoch nicht zu groß sein darf. Eine thermodynamische Betrachtung der Aktivierung von H_2 durch Lewis-Kombinationen verdeutlicht, dass die Lewis-Azidität bzw. -Basizität sowie die Größe der Substituenten die Stabilität der resultierenden Salze $[R_3PH][HBR'_3]$ beeinflussen. Die Gibbs'sche Freie Energie der Reaktion korreliert mit der Reversibilität der H_2-Aktivierung (Eintrag 2 vs. 3; $\Delta G = -22$ *vs.* -1 kJ mol^{-1}). Wie bei den Übergangsmetallkomplexen dürfen die Grenzorbitale energetisch nicht zu weit separiert sein, da ansonsten keine Reaktion stattfindet (Eintrag 4, $\Delta G = 108$ kJ mol^{-1}). Außerdem müssen die Voraussetzungen für den nicht linearen Übergangszustand erfüllt sein, um die kinetischen Energiebarrieren herabzusetzen.

Carbene. Für diese Substanzklasse ist seit ihrer Entdeckung im späten 19. Jahrhundert bekannt, dass deren Vertreter als Elektronenmangelverbindungen über eine hohe Reaktivität verfügen. Carbene besitzen ein Kohlenstoffzentrum mit einem Elektronensextett, das zugleich zwei freie Valenzelektronen aufweist. Der favorisierte Singulett-Zustand wird im Folgenden ausschließlich diskutiert.[15] Arduengo bettete ein solches Kohlenstoffzentrum in ein Imidazol-Grundgerüst ein, um sogenannte *N*-heterocyclische Carbene (NHCs) als stabile Spezies darzustellen.[16] Später entwickelte Bertrand cyclische Alkyl-Amino-Carbene (CAACs), denen ein einziges benachbartes Stickstoffatom zur Stabilisierung der Struktur ausreicht.[17] Die Geometrien der Grenzorbitale sind für beide Verbindungen vergleichbar,

die HOMO-LUMO-Abstände unterscheiden sich jedoch merklich.[18, 19] Dies hat einen deutlichen Einfluss auf die Aktivierung von H_2, da nur CAACs dessen Bindung spalten können. Das Vorliegen von zwei elektronegativen und π-donierenden Stickstoffsubstituenten macht NHCs zu schwächeren σ-Donoren und π-Akzeptoren als CAACs, sodass NHCs energetisch deutlich stärker separierte Grenzorbitallagen haben.

Die Orbitalwechselwirkungen von Elektronensextett-Verbindungen mit H_2 bilden kein vergleichbar großes Überlappungsintegral wie im Fall von Übergangsmetallzentren (vgl. Abbildung 3). Dennoch läuft eine Aktivierung von H_2 mit CAACs bereits bei 35 °C ab.[19]

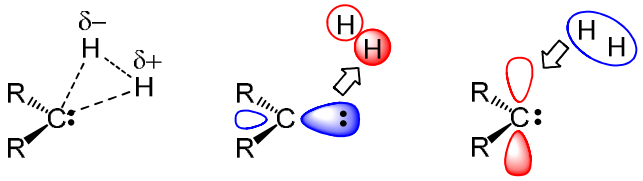

Abbildung 3. Struktur und Orbitalwechselwirkungen des Übergangszustands für die Aktivierung von H_2 mit Elektronensextett-Verbindungen am Beispiel von Carbenen. HOMOs: blau; LUMOs: rot.

Der Mechanismus gilt als Hybrid einer homogenen und heterogenen Bindungsspaltung von H_2.[19] Das H_2-Molekül wird durch die ausgeprägte Basizität des Carbens zunächst polarisiert, sodass formal ein Wasserstoffatom mit positiver Partialladung an das Kohlenstoffatom gebunden ist. Sukzessive wird die H–H-Bindung elongiert und der hydridische Charakter des bisher ungebundenen Wasserstoffatoms verstärkt. Eine stereochemische Inversion des Kohlenstoffzentrums bewirkt die Knüpfung der zweiten C–H-Bindung.

Dimere höherer Homologer der Hauptgruppenelemente. Das Periodensystem der Elemente gruppiert chemische Verwandtschaften und dient als Orientierung für Reaktivitätstrends. Einer dieser Trends ist die abnehmende Neigung von höheren Homologen der Hauptgruppenelemente, Mehrfachbindungen auszubilden.[3] Durch das Anbringen von großen Substituenten ist es Power 2005 allerdings trotzdem gelungen, eine formale Ge≡Ge-Dreifachbindung aufzubauen und deren Oligomerisierung zu unterbinden.[20] Die dargestellte Verbindung Ar'Ge≡GeAr' (Ar' = 2,6-(2,6-*i*Pr$_2$C$_6$H$_3$)$_2$C$_6$H$_3$) reagiert mit H_2 bereits bei Raumtemperatur und Normaldruck, ganz im Gegensatz zu Alkinen. Durch die zunehmende energetische Separierung der s- und p-Valenzorbitale wird es für höhere Homologe immer günstiger, kernnahe Elektronen mit hohem s-Charakter zu haben, die in erster Näherung als lokalisierte, nicht-bindende freie Elektronen vorliegen.[9] In Schema 2 ist die unvollständige Elektronendelokalisation über die Dreifachbindung mithilfe von mesomeren Grenzstrukturen verdeutlicht. Daraus ergeben sich partiell besetzte und unbesetzte Zustände, die im Mittel auch eine paramagnetische Elektronenkonfiguration aufweisen können.

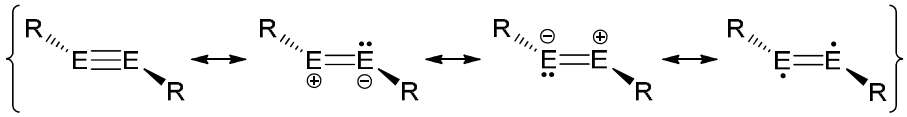

Schema 2. Mesomere Valenzstrukturen für höhere Alkin-Analoga der Gruppe 14.

Auf diese Weise liegen Akzeptor- und Donorzentren vor, die, zusammen mit einer moderaten HOMO-LUMO-Energieseparation, den Charakteristika eines Übergangsmetalls nahekommen. Der Mechanismus der H_2-Aktivierung durch solche Mehrfachbindungen wird durch eine konzertierte Interaktion des π-HOMOs der Mehrfachbindung mit dem σ*-MO von H_2 einerseits und des σ-MOs von H_2 mit dem LUMO der Mehrfachbindung andererseits beschrieben (Abbildung 4).[9] Die Struktur des Übergangszustandes ist vergleichbar mit der von Carbenen, sodass H_2 zunächst an nur eines der beiden Atome E addiert und die Reaktivität des Hauptgruppenelements über Folgereaktionen entscheidet (mehr dazu in Abschnitt 1.3.4.).

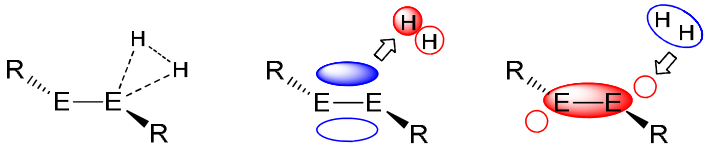

Abbildung 4. Struktur und Orbitalwechselwirkungen des Übergangszustands für die Aktivierung von H_2 durch Mehrfachbindungen höherer Hauptgruppenelemente. HOMOs: blau; LUMOs: rot.

Die vorgestellten Hauptgruppenverbindungen sind alle in der Lage, H_2 zu aktivieren, da ihre HOMO-LUMO-Abstände und Orbitalsymmetrien eine positive Wechselwirkung mit dem H_2-Molekül zulassen. Dabei zeigt sich, wie vielfältig auch Hauptgruppenverbindungen sein können, was die Natur der genutzten Grenzorbitale und die Strukturen der Übergangszustände betrifft.

In den folgenden Abschnitten wird auf diese Hauptgruppenverbindungen näher eingegangen, um bekannte Vertreter vorzustellen, deren Reaktivitätsspektrum aufzuzeigen und potentielle Anwendungsfelder darzulegen. Dabei besteht kein Anspruch auf Vollständigkeit, denn die ausgewählten Beispiele sollen ein allgemeines Verständnis vermitteln und als Vergleichssysteme für die in dieser Arbeit erzielten Ergebnisse dienen. Als Reaktionspartner stehen besonders H_2, E–E-Bindungen der Chalkogene, C–C-Mehrfachbindungen sowie CO_2 im Fokus.

1.3.2. Frustrierte Lewis-Paare (FLPs)

Klassische Lewis-Addukte werden zu FLPs, indem der sterische Anspruch ihrer Substituenten erhöht wird und das Lewis-saure nicht mehr mit dem Lewis-basischen Zentrum wechselwirken kann.[21] Eingeführt wurde dieses Konzept von Stephan mit dem in Schema 3 gezeigten System, das H_2 reversibel bindet.[10]

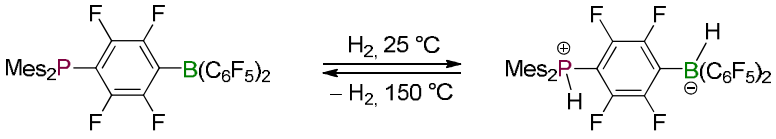

Schema 3. Reversible Bindung von H_2 durch das intramolekulare FLP Mes_2P-C_6F_4-$B(C_6F_5)_2$.

Mit dieser Reaktion eröffnete sich ein neues Forschungsfeld, das zwei Bedingungen an die Auswahl der Lewis-Zentren knüpft: die Anwesenheit eines Akzeptor- und eines Donororbitals, deren Reaktivität nicht durch die Bildung eines klassischen Addukts neutralisiert wird, unabhängig von der Atomsorte oder auftretenden Ladungen. Der Einbau eines Ab-

standhalters wie im Falle von Mes_2P-C_6F_4-$B(C_6F_5)_2$ erzeugt intramolekulare FLPs, ersetzt allerdings nicht die sterisch anspruchsvollen Substituenten um die Lewis-Zentren (Abbildung 5).[22, 23] Die Auswahl der gebundenen Reste stellt eine wichtige Stellschraube dar, um den Reaktionsverlauf bei späteren katalytischen Anwendungen zu beeinflussen.[14] Besonders hervorzuheben ist die Einführung von chiralen Zentren, die eine asymmetrische Katalyse erlauben.[24] Im Bereich der intermolekularen FLPs, deren Lewis-Zentren nicht durch ein Bindeglied verbunden sind, wurde eine Vielzahl an Möglichkeiten zum Aufbau von FLPs publiziert; eine Auswahl ist in Abbildung 5 zusammengefasst. Als Lewis-Säuren dienen neben Boranen auch Alane,[25, 26] Silylium-,[27] Borenium-[28, 29] sowie Phosphonium-Kationen[30] und Kumulene.[31] Neben Phosphanen als Lewis-Basen sind auch Stickstoff-Basen,[32] Borylanionen[30] und Carbene[33] etabliert. Da der Fokus dieser Einleitung auf Hauptgruppenverbindungen liegt, sei nur erwähnt, dass es auch Kombinationen mit Übergangsmetallzentren gibt.[34]

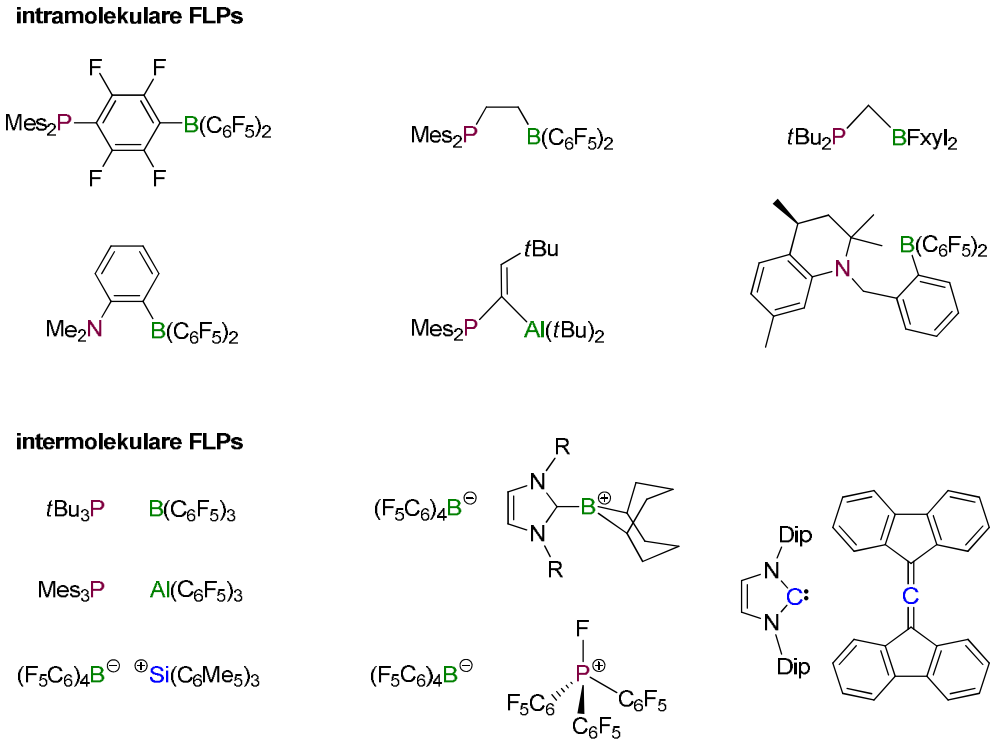

Abbildung 5. Ausgewählte Beispiele für intra- und intermolekulare FLPs; Mes = Mesityl, Fxyl = 3,5-Bis(trifluormethyl)phenyl, Dip = 2,6-Di(*iso*-propyl)phenyl.

Die Grenzen zwischen klassischen Addukten und FLPs wurden weiter aufgeweicht, als mit der Kombination von 2,6-Lutidin und $B(C_6F_5)_3$ die Aktivierung von H_2 gelang, obwohl die Lewis-Komponenten ein Addukt-Gleichgewicht eingehen.[35]

Die Zahl bekannter Reaktionspartner für FLP-Systeme ist bereits sehr groß, sodass nur eine Auswahl an Substraten in Abbildung 6 dargestellt ist, zusammen mit den entsprechenden Additionsprodukten an Mes_2P-C_2H_4-$B(C_6F_5)_2$, das Erker und Mitarbeiter ausgiebig untersucht haben.[22] Die Reaktion mit H_2O unterstützt den postulierten Mechanismus der heterolytischen Bindungsspaltung für H_2, weil ein Proton an das Phosphan und ein Hydroxid-Ion ans Boran gebunden ist. Terminale Alkine konnten ebenfalls deprotoniert und in ähnlicher Weise addiert werden, wohingegen das gezeigte Carbodiimid nur die Lewis-Säure adressierte. Mit Carbonyl-Verbindungen bildete sich immer dasselbe Strukturmotiv einer verbrückenden

CO-Einheit, wobei das Sauerstoffatom mit dem Boran verknüpft ist. C=C-Doppelbindungen binden ebenfalls in einem verbrückenden Modus an das FLP.

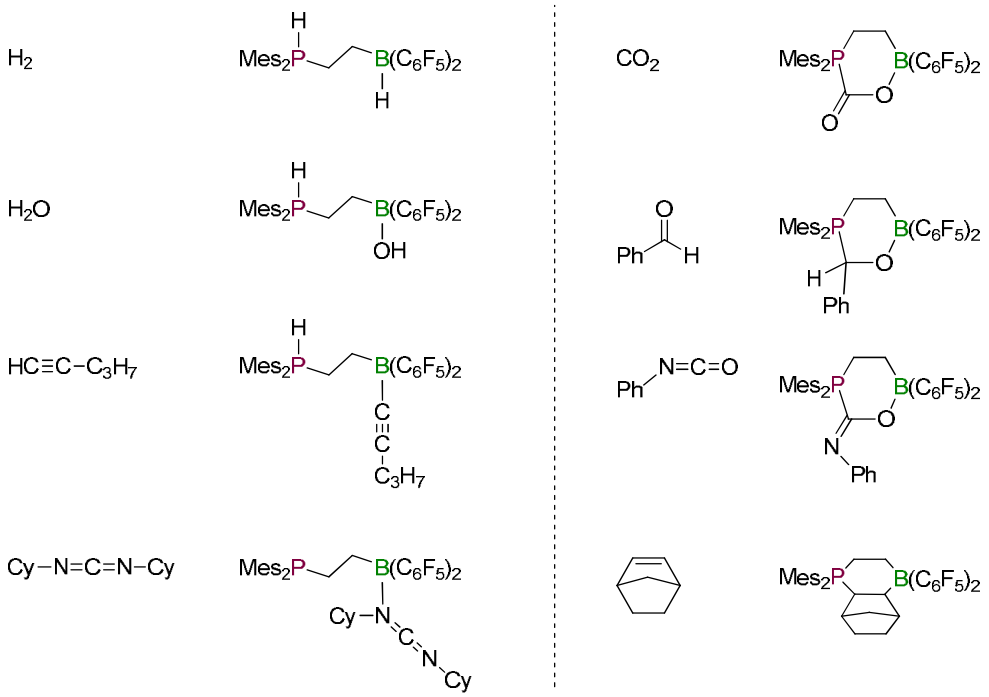

Abbildung 6. Ausgewählte Beispiele für die Reaktivität von Mes_2P-C_2H_4-$B(C_6F_5)_2$; Cy = Cyclohexyl.

Die Addition eines Substrats an ein FLP ist gleichzusetzen mit der Aktivierung einer Bindung dieses Substrats, die dadurch bereitwilliger für Folgereaktionen nutzbar sein kann. Dies trifft jedoch nur zu, wenn diese Form der Adduktbildung in ein reversibles Gleichgewicht involviert ist, so wie bei den Teilschritten homogener Katalysezyklen mit Übergangsmetallkomplexen. In der Tat gibt es viele Anwendungsfelder für FLPs als Katalysatoren, von denen im Folgenden der Einsatz in Hydrierungsreaktionen, die Umwandlung von CO_2 und die Reaktionen mit Mehrfachbindungen ausgeführt werden. Neueste Entwicklungen zur Aktivierung von E–H- (E = Si[22], N[24, 36]) und C–H-Bindungen sind nicht erläutert,[37] da sie für die vorliegende Arbeit keine Relevanz haben.

Hydrierungsreaktionen. Nach dem Initialschritt der H_2-Aktivierung dauerte es nicht lange, bis die ersten Versuche unternommen wurden, das aufgenommene H_2-Äquivalent auf ein geeignetes Substrat zu übertragen.[38, 39] Es stellte sich heraus, dass Imine besonders bereitwillige Reaktionspartner sind, da der erste Schritt des zugrundeliegenden Mechanismus in deren Protonierung besteht. In Schema 4 ist die Hydrierung von Ph(H)C=N*t*Bu mit Stephans FLP gezeigt, wobei intermediär ein Iminium-Ion und ein Hydridoborat vorliegen. Im nächsten Schritt erfolgt ein Hydrid-Transfer und das FLP steht nach erfolgreicher Freigabe des resultierenden Amins für einen erneuten Katalysezyklus zur Verfügung.[39]

Polare Substrate können die Rolle von Lewis-Basen in FLPs übernehmen, sodass die Zugabe von $B(C_6F_5)_3$ als vielseitig einsetzbare Lewis-Säure in vielen Fällen ausreicht, um bei vergleichbaren Reaktionsbedingungen hohe Ausbeuten zu erzielen (Tabelle 3).[22] Da der

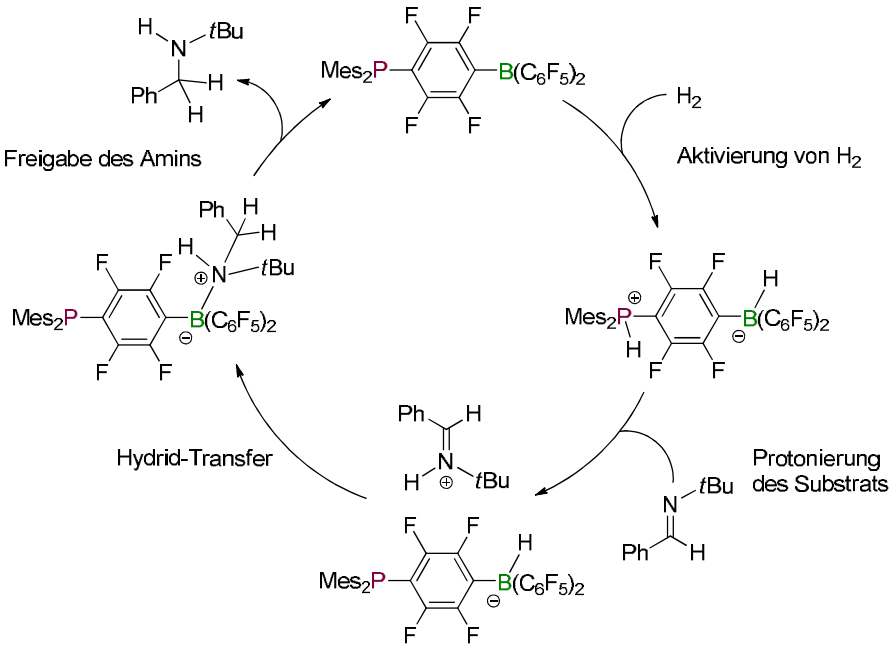

Schema 4. Mechanismus der Hydrierungsreaktionen mit FLPs am Beispiel eines Imins.

geschwindigkeitsbestimmende Schritt die Protonierung des Imins ist, werden elektronenreiche Imine unter milderen Bedingungen hydriert als elektronenarme, was Tabelle 3 zu entnehmen ist.[39] Limitierungen dieses Hydrierungsprozesses treten auf, wenn das resultierende Amin zu stark an das Boratom bindet und das aktive Zentrum nicht wieder frei gibt, sodass das FLP nur als stöchiometrisches Hydrierungsreagenz wirkt.[22, 40] Das Problem kann umgangen werden, indem man entweder den sterischen Anspruch des Substrats oder des FLPs erhöht, um eine Produkthemmung zu vermeiden. Alternativ kann die stöchiometrische Zugabe einer stärkeren Lewis-Säure[22] oder die Wahl drastischerer Reaktionsbedingungen[39] für die Regeneration des FLPs sorgen. Die Variation der Substituenten des FLPs wurde sowohl für asymmetrische Hydrierungen[24] als auch für eine erhöhte Gruppentoleranz ausgenutzt.[41] Neben elementarem H_2 eignen sich auch ausgewählte Amine wie *i*Pr_2NH dazu, ein H_2-Äquivalent zu übertragen, weil $B(C_6F_5)_3$ ein Hydrid-Ion vom α-Kohlenstoffatom abstrahiert, sodass sich ein Iminium-Ion und eine Hydridoboratspezies bilden (vgl. Schema 4).[42]

Im Allgemeinen verläuft die Hydrierung von Stickstoff-Verbindungen unter milden Bedingungen, wobei die Gegenwart einer Lewis-Säure ausreicht, da das Substrat selbst als Lewis-Base fungiert.[38] Sollen unpolare Verbindungen wie Olefine oder Aromaten hydriert werden, muss eine Lewis-basische Komponente zugegen sein, deren protonierte Form hinreichend sauer ist, um ein Proton auf das Substrat zu übertragen, wie es der Mechanismus in Schema 4 vorsieht.[43, 44] In diesem Kontext wurden schwächer basische Phosphane wie $Ph_2P(C_6F_5)$ als Donorkomponenten untersucht, die ebenfalls H_2 in Kombination mit $B(C_6F_5)_3$ aktivieren können. Dieser Prozess unterliegt einem schnellen Gleichgewicht, sodass die H_2-Aktivierungsprodukte nur bei tiefen Temperaturen mittels NMR-Spektroskopie sichtbar werden.[45] In Gegenwart eines Substrats wird das kurzlebige Aktivierungsprodukt abgefangen, was eine katalytische Reaktionsführung ermöglicht. Dabei finden oftmals hohe Wasserstoffdrücke oder erhöhte Katalysatorladungen Anwendung, um sehr gute Ausbeuten zu erzielen (vgl. Tabelle 3).

Tabelle 3. Ausgewählte Beispiele für Hydrierungsreaktionen mithilfe des FLP-Konzepts.

Substrat	Katalysator	Reaktionsbedingungen				Ausbeute	hydriertes Produkt
		n	*p*(H_2)	*T*	*t*		
		mol%	bar	°C	h	%	
	Mes_2P-C_6F_4-$B(C_6F_5)_2$	5	1	80	1	79[38]	
	$B(C_6F_5)_3$	5	1	80	2	89[38]	
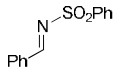	$B(C_6F_5)_3$	5	5	120	41	94[38]	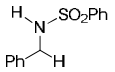
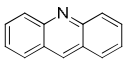	$B(C_6F_5)_3$	5	4	25	2	80[38]	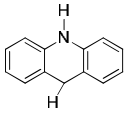
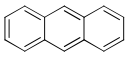	$Ph_2P(C_6F_5)/B(C_6F_5)_3$	10	102	80	10	97[43]	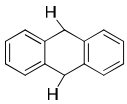
	$Ph_2P(C_6F_5)/B(C_6F_5)_3$	20	5	RT	24	99[45]	
	$Et_2O/B(C_6F_5)_3$	5	60	70	12	90[46]	

Für elektronenarme Olefine kann eine erfolgreiche Protonierung im ersten Schritt nicht immer erreicht werden, sodass zunächst eine Hydroborierung des Substrats erfolgt und mit der resultierenden Spezies eine H_2-Aktivierung analog zu Borolen (vgl. Abschnitt 1.3.5.) gelingt, wie Schema 5 verdeutlicht.[44]

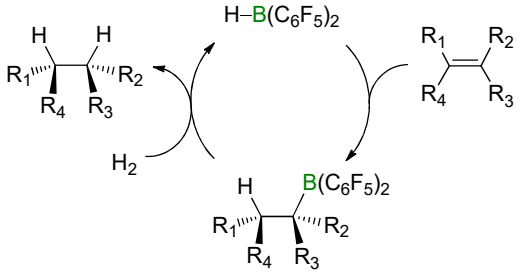

Schema 5. Möglichkeit zur metallfreien Hydrierung elektronenarmer Olefine.

Ähnlich wie die unpolaren, schwer zu aktivierenden Aromaten oder Olefine sind Carbonylverbindungen wie Ketone anspruchsvolle Substrate für FLP-Hydrierkatalysatoren. Wie bei den Stickstoff-Derivaten übernimmt auch hier die funktionelle Gruppe die Aufgabe der Lewis-Base. Das nach der H_2-Aktivierung erhaltene protonierte Keton ist in der Lage, einen B–C-Bindungsbruch in $[HB(C_6F_5)_3]^-$ zu bewirken, sodass ein Borinsäureester und C_6F_5H entstehen (Schema 6). Ein Wechsel des Lösungsmittels ermöglicht die gewünschte Umwandlung des Ketons zum Alkohol, da das protonierte Keton in polaren Lösungsmitteln stabilisiert ist und ein üblicher Hydrid-Transfer stattfinden kann.[42, 46]

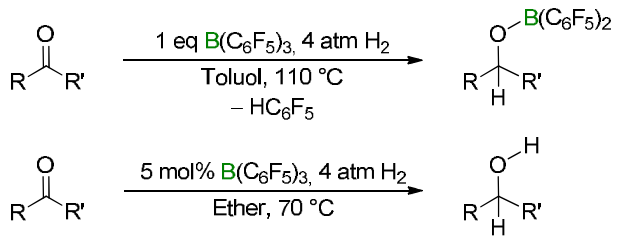

Schema 6. Reduktion von Ketonen in verschiedenen Lösungsmitteln.

Umwandlungen von CO_2. Die Nutzung von FLPs als Katalysatoren für die Reduktion von CO_2 scheiterte lange an der zu starken Azidität der verwendeten Lewis-Säuren, sodass eine Vielzahl stöchiometrischer Additionsprodukte bekannt ist.[34] Ashley und O'Hare nutzten das H_2-Aktivierungsprodukt des bekannten TMP/$B(C_6F_5)_3$-FLP-Systems (TMP = 2,2,6,6-Tetramethylpiperidin; Schema 7 links),[32] wobei das zwischenzeitlich gebildete Hydridoborat-Anion [**1**]$^-$ als Hydrid-Quelle dient, um das Formiat-Borat [**2**]$^-$ zu erhalten.[47] Nach Destillation im Vakuum bei 100 °C konnte mit bis zu 25% Ausbeute Methanol isoliert werden, das vermutlich aus der Reaktion beider FLP-Salze [TMPH][**1**] und [TMPH][**2**] entsteht. Mithilfe eines P/Al-FLPs und NH_3BH_3 als Reduktionsmittel erzielten Stephan und Mitarbeiter ebenso die Reduktion von CO_2 zu Methanol, nachdem ein intermediär gebildetes Methoxidsalz hydrolysiert wurde.[48] Den bisher überzeugendsten Ansatz zur katalytischen Reduktion von CO_2 lieferte die Gruppe von Fontaine, die 1,2-Ph_2P-C_6H_4-$B(O_2C_6H_4)$ (**3**) mit einem Überschuss an Catecholboran [Bcat] kombinierten (Schema 7 rechts).[49-51] Bemerkenswert ist, dass CO_2

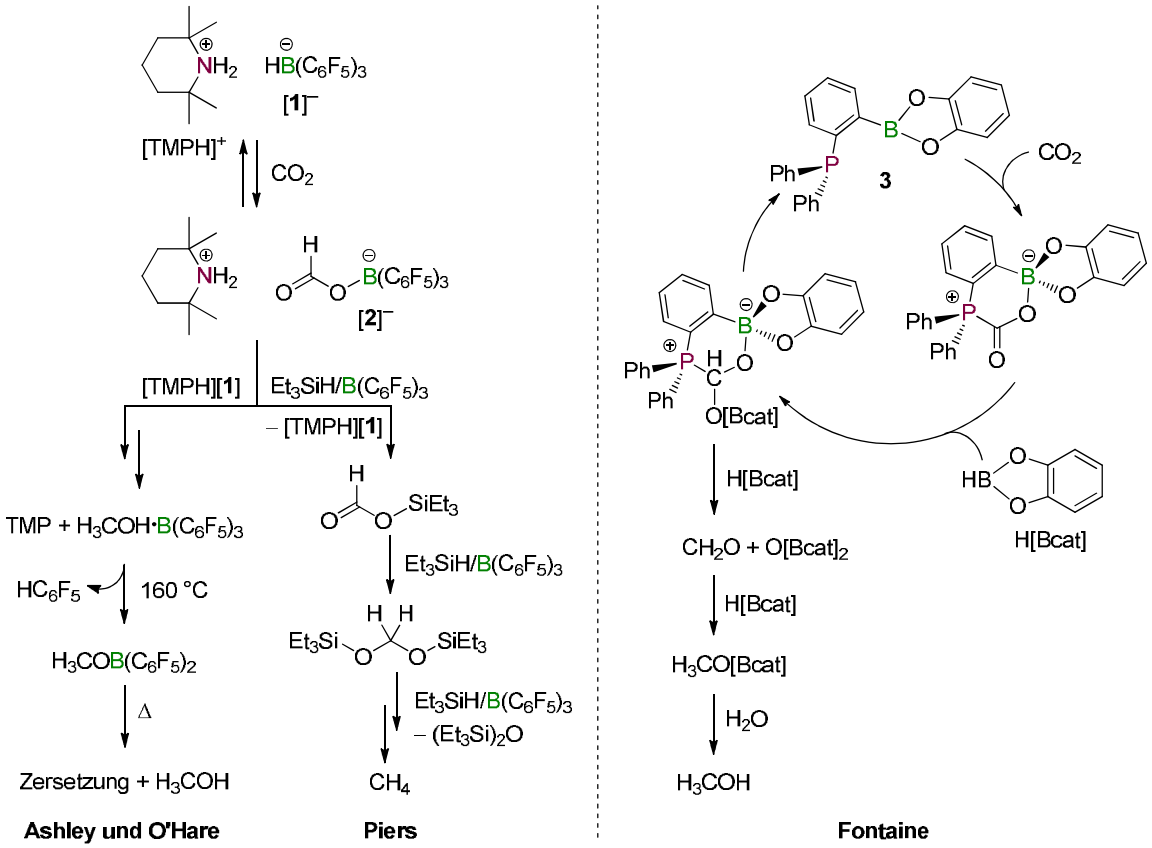

Schema 7. Reduktion von CO_2 mithilfe von FLP-Systemen.

nur schwache Wechselwirkungen mit den einzelnen Verbindungen eingeht, aber dennoch bei Mischung aller Komponenten schrittweise hydroboriert wird. Am Ende einer Reaktionskaskade entstehen O[Bcat]$_2$ und H_3CO[Bcat]. Letzteres wird durch Hydrolyse in Methanol überführt. Anstelle eines Hydroborans als Reduktionsmittel setzte Piers Et_3SiH ein, welches zusammen mit $B(C_6F_5)_3$ und dem bereits von Ashley und O'Hare benutzten Formiat-Borat [**2**]$^-$ ein Silyl-Formiat bildet. Nach mehrfacher Hydrosilylierung des gebildeten Silyl-Formiats entsteht selektiv Methan (Schema 7 Mitte).[52]

Reaktionen mit Mehrfachbindungen. Während die meisten internen Mehrfachbindungen einfache Additionsprodukte mit FLPs liefern, wie bspw. in Abbildung 6 dargestellt, eröffnen terminale Olefine oder Alkine zahlreiche strukturelle Möglichkeiten.

Intramolekulare FLPs ermöglichen den Aufbau von cyclischen Strukturen durch die Anlagerung von Olefinen wie z. B. *n*-Hexen (Schema 8).[53] Als Substrate für intramolekulare Cyclisierungen eignen sich Anilin-Derivate mit *ortho*-Alkenyl-Substituenten, die mithilfe von $B(C_6F_5)_3$ zwitterionische *N*-Heterocyclen bilden (Schema 8).[24]

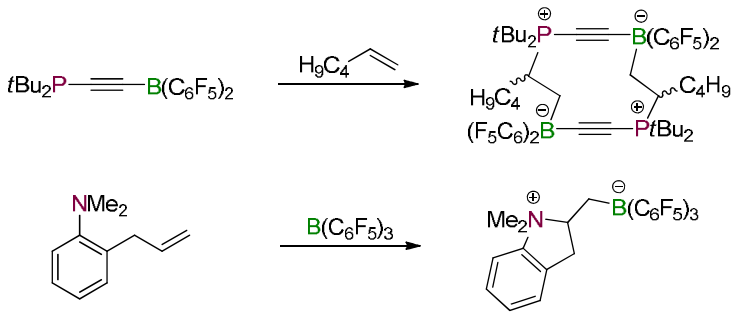

Schema 8. Inter- (oben) und intramolekulare (unten) Cyclisierungsreaktionen mit FLPs und Olefinen.

Terminale Alkine können über zwei unterschiedliche Pfade mit FLPs reagieren (Schema 9 oben): i) Mit starken Lewis-Basen erfolgt eine Deprotonierung des Alkins unter Bildung eines Phosphoniumboratsalzes. ii) Mit schwächeren Lewis-Basen wird ein zwitterionisches Additionsprodukt gebildet, analog zu den in Schema 8 gezeigten Olefinstrukturen.[54] Diese bereits bekannten Additionsmuster wurden sowohl zum Aufbau von inter- als auch intramolekularen Cyclisierungsprodukten genutzt.[55, 56] Ähnlich wie Olefine ermöglichen

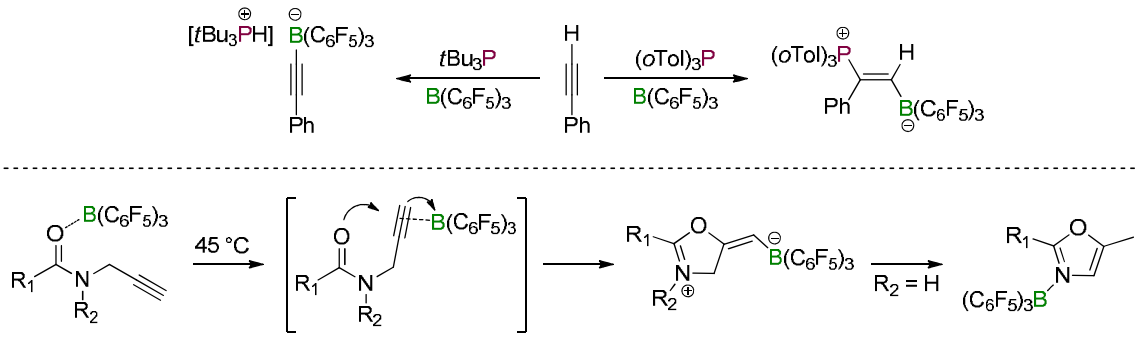

Schema 9. Die Basizität des Phosphans entscheidet über die Reaktivität von FLPs gegenüber terminalen Alkinen (oben). Ausnutzung der Lewis-Säure $B(C_6F_5)_3$ für Cyclisierungsreaktionen mit Propargylamiden (unten).

Alkin-Derivate, die Stickstoffatome beinhalten, Ringschlussreaktionen, die für Naturstoffsynthesen relevante Heterocyclen aufbauen. Geeignet sind auch Propargylamide, bei denen $B(C_6F_5)_3$ bei Raumtemperatur zwar an die basische Amidgruppe koordiniert, bei erhöhten Temperaturen aber eine B···C≡C-Wechselwirkung ausbildet.[57] Die hierdurch erhöhte Elektrophilie der Dreifachbindung ermöglicht einen Ringschluss über den Angriff des Carbonyl-Sauerstoffatoms, sodass ein intramolekulares Salz gebildet wird (Schema 9 unten). Für den Fall R_2 = H isomerisiert dieses Salz zu einem neutralen Oxazol, wobei die nur schwach ausgeprägte Koordination von $B(C_6F_5)_3$ an das Stickstoffatom eine katalytische Reaktionsführung erlaubt.

1.3.3. Carbene und isoelektronische Verbindungen

Das Strukturmotiv eines Elektronensextetts an einem Hauptgruppenelement wurde nicht nur in Form der bereits vorgestellten Carbene (Abschnitt 2.1) stabilisiert,[58] sondern findet Analoga in den Gruppen 13 und 14.[59] Schema 10 fasst typische Grundgerüste zusammen, wobei Elemente der Gruppe 13 mithilfe von starken mono- oder bidentaten Liganden komplexiert werden und Homologe von Kohlenstoff oftmals von zwei sterisch anspruchsvollen Substituenten umgeben sind.

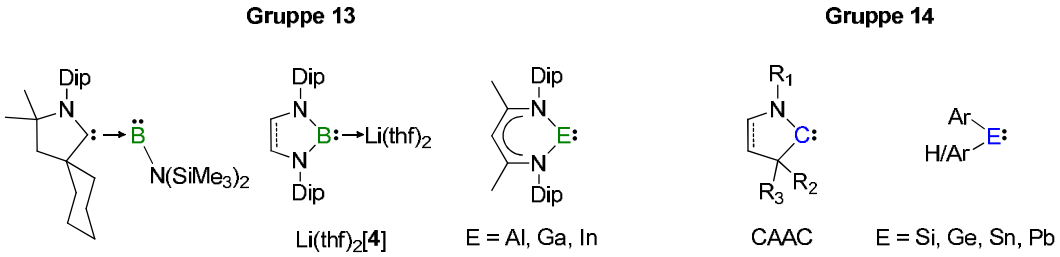

Schema 10. Strukturmotive von Hauptgruppenverbindungen mit Elektronensextetten; Dip = 2,6-Di(*iso*-propyl)phenyl.

Aktivierung kleiner Moleküle. Die Umsetzung mit H_2 liefert überwiegend Produkte, in denen das H_2-Äquivalent an das reaktive Zentrum addiert ist, so wie es der in Abschnitt 1.3. erläuterte Mechanismus erklärt.[59] Wie die Anwesenheit von Kationen die entscheidenden Wechselwirkungen beeinflusst, verdeutlicht die Reaktion des Borans Li(thf)$_2$[**4**] mit H_2 (Schema 10). Zwar spendet weiterhin das gefüllte sp^2-Orbital am Borzentrum Ladungsdichte in das σ^*-Orbital von H_2, aber die Rückbindung des H_2 erfolgt zum Li^+-Kation anstatt zum leeren p_z-Orbital des Borzentrums. Infolgedessen findet eine heterolytische H_2-Bindungsspaltung statt, im Zuge derer Lithiumhydrid eliminiert wird.[60] Sonstige Abweichungen zum gängigen Additionsmotiv aus 1.3. ergeben sich für höhere Homologe der Tetrele (E = Ge, Sn), weil die Stärken der resultierenden E–H-Bindungen abnehmen und die Stabilität von nichtbindenden Elektronen zunimmt (vgl. Schema 11).[61] Germylene ergeben entweder tetra-valente H_2-Additionsprodukte des Typs $Ar^{\#}_2GeH_2$ oder durch einen anschließenden Ge–C-Bindungsbruch hervorgerufene Spezies der Form Ar*GeH_3. Bei Stannylenen entscheiden die Substituenten über eine erfolgreiche H_2-Aktivierung, die dann zu H-verbrückten Ar*Sn-(μ-H_2)-SnAr* Dimeren führt, was wiederum die Abspaltung eines Substituenten erfordert.

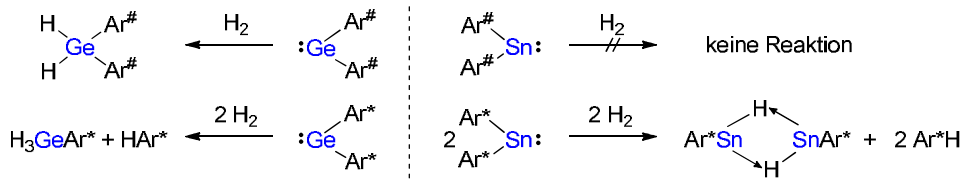

Schema 11. Abhängigkeit der H_2-Aktivierungsprodukte von Germylenen und Stannylenen vom sterischen Anspruch der gewählten Substituenten. $Ar^{\#}$ = 2,6-Di(mesityl)phenyl; Ar* = 2,6-Di(2‘,6‘-di-*iso*-propylphenyl)phenyl.

Jutzi postulierte für die Anlagerung von CO_2 an Cp^*_2Si, dass diese vergleichbar zur Anlagerung von H_2 verläuft (vgl. **5** in Schema 12), was mit der Eliminierung von CO nach der Addition von weiterem CO_2 im Einklang ist (Cp*H = Decamethylcyclopentadien).[62] Intermediär entsteht vermutlich die κ^2-gebundene Carbonat-Spezies **6**, aus der die Spiroverbindung **7** nach dem Angriff von [Cp^*_2Si=O] (Intermediat entsteht nach der Eliminierung von CO aus **5**) hervorgeht. Bei der Reaktion von CO_2 mit NHCs hingegen bestimmt die Basizität des freien Elektronenpaares allein über die gebildeten Strukturmotive. Es entstehen Zwitterionen, in denen das Carbonylkohlenstoffatom von CO_2 an die Carbeneinheit gebunden ist (Schema 12).[63]

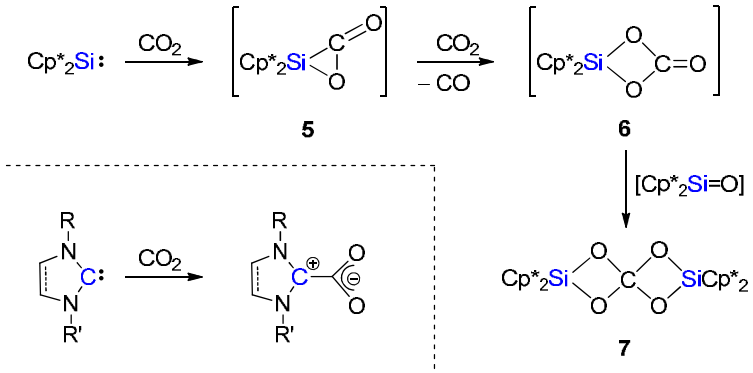

Schema 12. Unterschiedliche Koordinationsmodi von CO_2 an NHCs und Cp^*_2Si, welches durch sukzessive Reaktion mit CO_2 die Spiroverbindung **7** bildet; Cp*H = Decamethylcyclopentadien.

Neben der Aktivierung dieser gasförmigen Reaktionspartner sind Umsetzungen mit C–H-,[64, 65] C–X-[59, 66] sowie E–E-Bindungen[67, 68] am häufigsten im Zusammenhang mit Carbenen und isoelektronischen Verbindungen dokumentiert. In der Mehrzahl der Fälle erfolgt eine 1,1-Addition der entsprechenden Bindung, ähnlich zur Aktivierung von H_2 (vgl. Abbildung 3). In der Literatur lässt sich eine Vielzahl derartiger Additionsprodukte finden, jedoch gibt es nur vereinzelte Beispiele für Folgereaktionen.[69, 70]

Einsatz als Katalysatoren. Aldridge und Mitarbeiter nutzten das H_2-Additionsprodukt **8** als Hydrid-Quelle, das nach Übertragung des Hydrid-Ions auf CO_2 einen Formiat-Liganden im Komplex **9** liefert (Schema 13).[71] Analog zu den FLP-Varianten (vgl. Schema 7) ermöglicht die Zugabe von Hydroboranen, hier HBpin, die Regeneration des Katalysators **8**. Das Eliminierungsprodukt **10** reagiert mit einem Überschuss HBpin unter katalytischen Bedingungen weiter zu MeOBpin und $O(Bpin)_2$.[72]

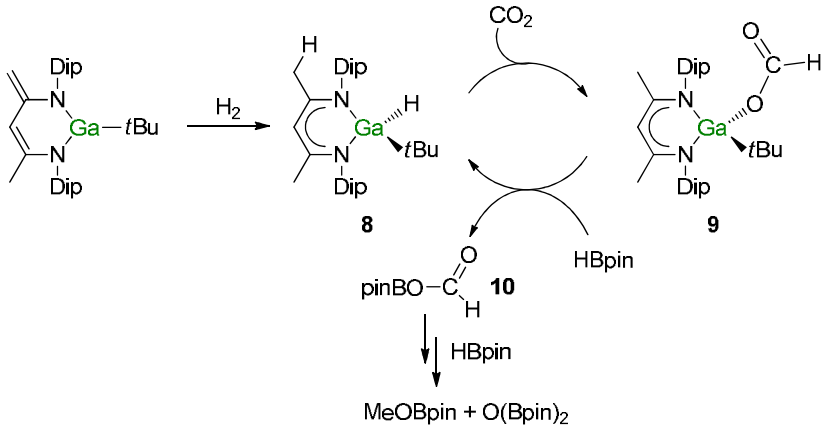

Schema 13. Reduktion von CO_2 zu MeOBpin durch HBpin mit **8** als Katalysator; Dip = 2,6-Di(*iso*-propyl)phenyl.

Basierend auf den theoretischen Vorarbeiten von Sakaki et al.[73] belegte die Gruppe von Jones mithilfe von Germylenen das in Schema 14 dargestellte allgemeine Reaktionsschema einer Metathese.[74] Im ersten Schritt addiert ein Aldehyd oder ein Keton an das Tetrelzentrum und bildet nach erfolgtem Hydridtransfer einen Alkoxysubstituenten. Im zweiten Schritt dient erneut HBpin als Reduktionsmittel, sodass die ursprüngliche Carbonylverbindung formal hydroboriert und der Tetrel-Katalysator regeneriert wird.

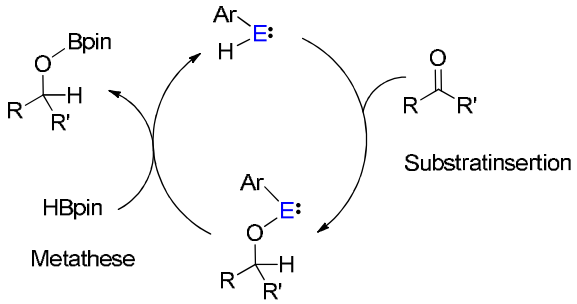

Schema 14. Katalytische Hydrierung von Carbonylverbindungen mit Hydrido-Tetrelen. E = Si-Pb; Ar = monoanionischer Ligand.

Ausgehend von dem Dihydridoaluminat **11**, das durch H_2-Aktivierung entstehen könnte,[75] und einem terminalen Alkin erzeugten Roesky und Mitarbeiter den Hydrido-Alkinyl-Komplex **12** (Schema 15).[76] Die Dreifachbindung wurde mit HBpin hydroboriert, wobei ein Alkin-Überschuss zur Protolyse der Al–C-Bindung und zur Abspaltung des erhaltenen *trans*-

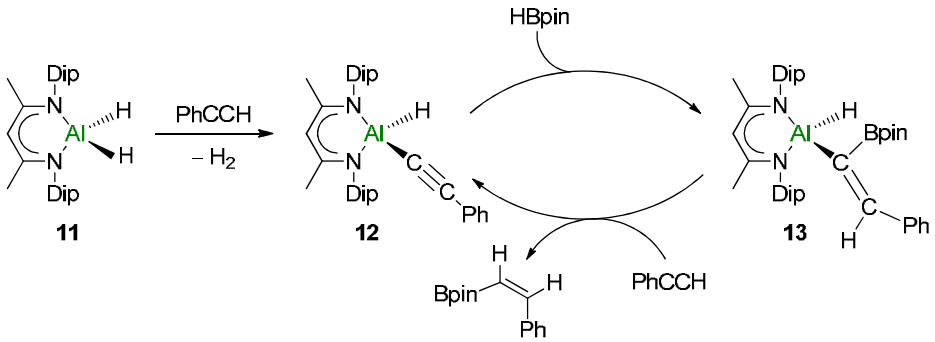

Schema 15. Reaktionsmechanismus der Hydroborierung von Phenylacetylen mithilfe von **12**; Dip = 2,6-Di(*iso*-propyl)phenyl.

Alkens im Komplex **13** unter Regenerierung der aktiven Tetrel-Spezies **12** führt.

Die bisher besprochenen Katalysatoren enthielten alle ein gebundenes Hydrid-Ion, das für die Reduktion des eingesetzten Substrats sorgte. Dabei diente der H_2-Aktivierungsschritt meist nur zur Darstellung des Präkatalysators, wohingegen die stöchiometrische Zugabe eines Hydroborans für die Regeneration des aktiven Katalysators sorgte.

Für Folgereaktionen mit Carbenen wird nur die Donorfähigkeit des gefüllten sp^2-Orbitals genutzt, aber nicht der Akzeptorcharakter des leeren p_z-Orbitals, sodass eine Diskussion entsprechender Reaktionen im Rahmen dieser Arbeit entfällt. Es sei nur darauf hingewiesen, dass Carbene als Liganden von Übergangsmetallkomplexen, als Lewis-Basen in organischen Reaktionen[77] und für Polymerisationsreaktionen Einsatz finden.[18, 78, 79] Darüber hinaus ist bekannt, dass CO_2 durch Carbene und R_2SiH_2 zu verschiedenen Methoxyprodukten reduziert werden kann.[80]

1.3.4. Verbindungen mit E–E-Bindungen

Die Darstellung von niedervalenten Hauptgruppenverbindungen erlebte einen Durchbruch mit dem Einsatz von Carbenen als stabilisierende Substituenten. Gerade dimere Hauptgruppenverbindungen der höheren Homologen waren lange nicht greifbar, weil der sterische Anspruch der Substituenten nicht ausreichte, um eine Polymerisierung zu unterdrücken. Das Zusammenspiel des reaktiven Zentrums und der gebundenen Reste führt zu unterschiedlichen Bindungssituationen, wobei die Stabilisierung von freien Elektronenpaaren die Bindungsordnung mitbestimmt.[9] Die Aktivierung kleiner Moleküle mithilfe dieser niedervalenten Hauptgruppenverbindungen bereichert die Grundlagenforschung zur Erfassung neuer Verknüpfungsmuster. Eine erweiterte Untersuchung zum Einsatz der neuen Aktivierungsprodukte für Folgereaktionen steht bisher aus.

1.3.4.1. Verbindungen mit E–E-Einfachbindungen

Yamashita und Mitarbeiter untersuchen die Diboran(4)-Verbindung **14** als besonders vielseitigen Reaktionspartner: Unter B–B-Bindungsspaltung wurde sowohl H_2 als auch ein aromatisches System mit N=N-Einheit aktiviert.[81, 82] Mit H_2 bildet sich das Diboran(6)-Derivat **15** (Schema 16 links), das durch Lewis-Basen wie THF oder Pyridin in die Monomere überführt wird. Ebenso gelang es der Gruppe von Yamaguchi, H_2 mit dem Diboran(4) **16** zu spalten, begleitet von einem Farbwechsel von grün (**16**) zu gelb (**17**), was eine Verwendung von **16** als optischen Indikator für die Gegenwart von H_2 möglich macht (Schema 16 rechts).[83]

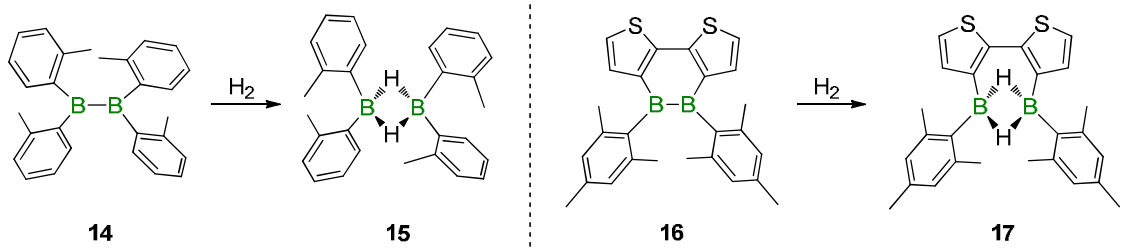

14 **15** **16** **17**

Schema 16. Als Folge der H_2-Aktivierung ersetzen H-Brücken die B–B-Bindungen.

Das Digermin **18** mit einer Ge–Ge-Einfachbindung addiert H_2 nur an eines der beiden Germanium-Zentren, sodass das Reaktionsprodukt **19** dem einer analogen Germylen-Verbindung ähnelt (vgl. Schema 11 und 17).[84] Entsprechend legen die Autoren einen vergleichbaren Bildungsmechanismus nahe. Die Analogie zu carbenartigen Strukturen spiegelt sich auch in der Interaktion von **18** mit CO_2 wider, da die Struktur **20** als Zwischenstufe auf dem Reaktionspfad zu **21** berechnet wurde (Schema 17).[85] Die final gebildete Ge–O–Ge-Einheit erwies sich als stabiles Strukturmotiv im Produkt **21**. Eine zusätzliche Triebkraft der Reaktion ist die Eliminierung von CO.

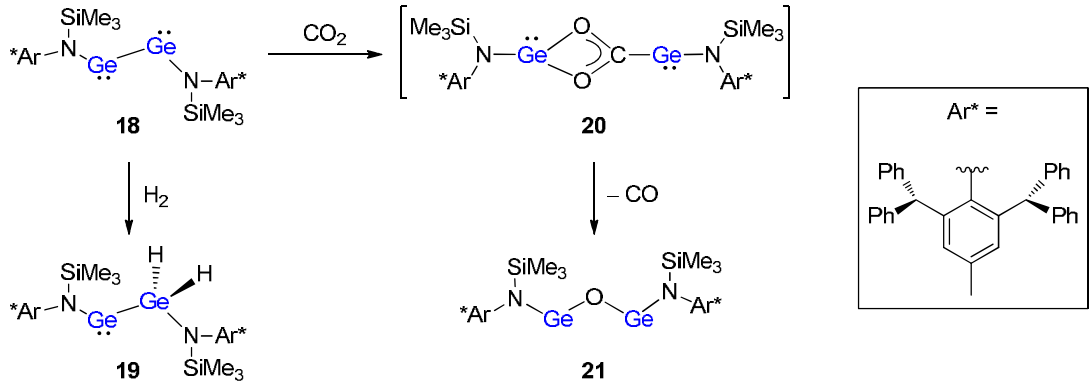

Schema 17. Das Digermin **18** reagiert sowohl mit H_2 als auch mit CO_2.

Das bekannte Strukturmotiv einer Sn–(μ-H_2)–Sn-Einheit aus Schema 11 tritt ebenso auf, wenn das Distannin **22** mit H_2 zu **23** reagiert (Schema 18).[86] Trotz des vergleichbaren Reaktionsausgangs liegen vermutlich unterschiedliche Mechanismen zugrunde. Mit Pinzerliganden an den Zinnatomen wurde die Sn–Sn-Bindung in **24** durch die Zugabe von Diphenyldichalkogenen gespalten, sodass der hochvalente Zinn-Komplex **25** gebildet wurde.[87]

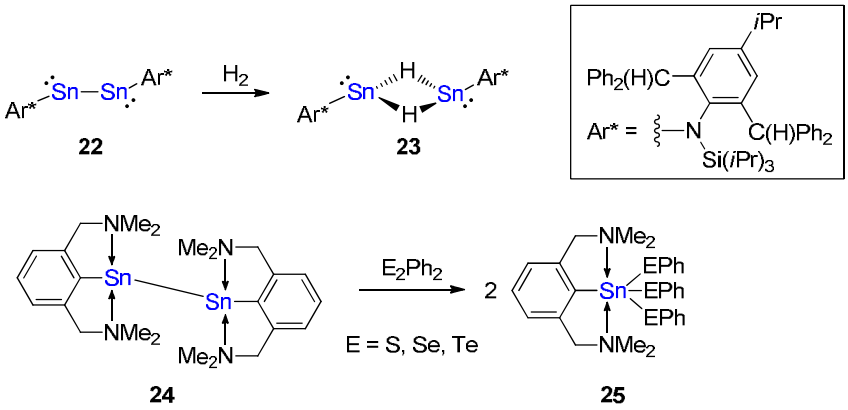

Schema 18. Spaltung der Sn–Sn-Bindung in **22** zugunsten zweier Sn–(μ-H)–Sn-Einheiten in **23** (oben) und in **24** zugunsten der koordinativen Absättigung der Sn-Zentren durch Arylchalkogenide in **25** (unten).

1.3.4.2. Verbindungen mit E=E-Doppelbindungen

Die Gruppe von Braunschweig nutzte Diboracumulene wie **26**, um 1,2-Dihydrodiborene wie **27** darzustellen (Schema 19 oben).[88] Theoretische Rechnungen legen einen zweistufigen Aktivierungsmechanismus nahe, wobei nur ein Borzentrum in den ersten Schritt involviert

ist. Eine nochmalige Addition von H_2 findet nicht statt. Zusammen mit Acetylen konnte Diboracumulen **26** zur Synthese des Borheterocyclus 1,4-Diborabenzol **28** genutzt werden (Schema 19 Mitte).[89] **28** verfügt über dieselben Grenzorbitale wie Benzol, das sich ausgehend von Acetylen nur in Anwesenheit eines Katalysators herstellen lässt. Einen Einfluss des Carbenliganden auf die Reaktivität der Borverbindungen beobachtete dieselbe Gruppe bei Umsatz von Diborenen **29** mit CO_2, da nur ein NHC mit ungesättigtem Rückgrat zur Fixierung von CO_2 führte.[90] Als Zwischenstufe konnte **30** als formales [2+2]-Cycloadditionsprodukt isoliert werden, das nach mehrtägiger Lagerung bei Raumtemperatur zu **31** umlagerte (Schema 19 unten).

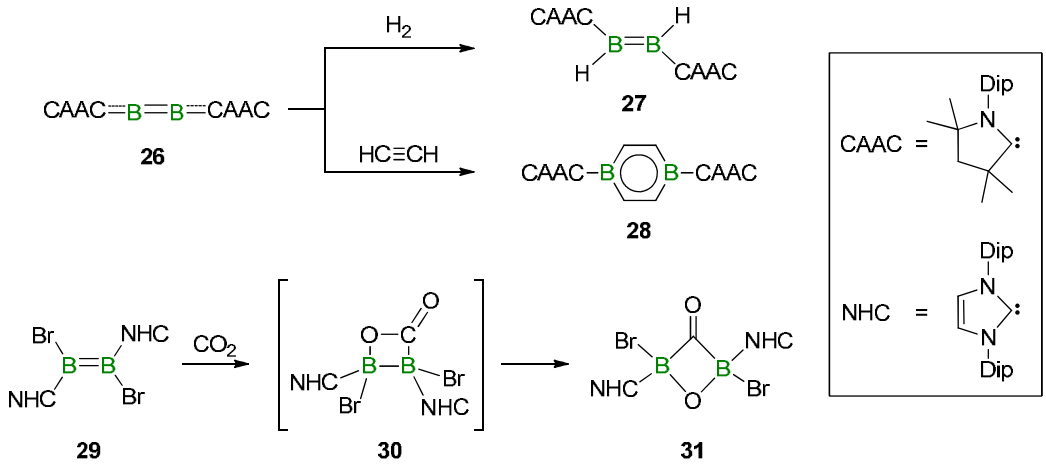

Schema 19. Reaktivitäten von B-μ-B-Mehrfachbindungen gegenüber H_2 (oben), Acetylen (Mitte) und CO_2 (unten); Dip = 2,6-Di(*iso*-propyl)phenyl.

Ein weiteres Reaktivitätsmuster von B=B-Doppelbindungen beobachtete die Arbeitsgruppe Wagner anhand des zweifach bordotierten Dibenzo[*g,p*]chrysen-Derivats Li_2[**32**]. Der Elektronenreichtum des Dianions verleiht den Borzentren in Li_2[**32**] nukleophile Eigenschaften, sodass eine Reaktion mit α,ω-Dihalogenalkanen bereitwillig abläuft.[91] Begleitet von Gerüstumlagerungen erfolgt eine zweifache Substitutionsreaktion an kurzkettigen Halogenalkanen zu Verbindungen **33**^{Cn}, wohingegen sich bei langkettigen Halogenderivaten eine CH-Aktivierung einer ersten C–X-Substitution anschließt, sodass das in Schema 20 gezeigte

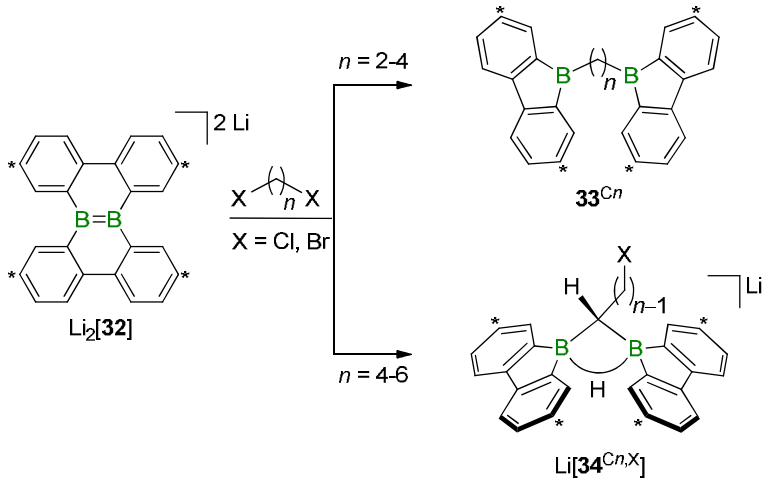

Schema 20. Das Diboran(4)-Dianion Li_2[**32**] zeigt nukleophile Eigenschaften und aktiviert C–H-Bindungen. Kohlenstoffatome, die mit * gekennzeichnet sind, tragen *t*Bu-Gruppen.

Strukturmotiv Li[**34**^{Cn,X}] entsteht. Auf diese Weise erweitert sich das Reaktionsspektrum von Organoboranen grundlegend, weil sie herkömmlich nur als Elektrophile Einsatz fanden.[92]

Höhere Homologe der Triele mit Doppelbindungen reagieren mit H_2 unter Ausbildung von E–(μH)–E-verbrückten Strukturmotiven. Dabei dient das Dialuman **35** als Präkursor für das Dialumen **36**, das bereitwillig mit zwei Äquivalenten H_2 das Strukturmotiv **37** liefert (Schema 21 oben). Die Zwischenstufe des Dialumens **36** gilt durch ein Abfangexperiment als gesichert, da die Umsetzung mit Bis(trimethylsilyl)acetylen ein entsprechendes Cycloadditionsprodukt liefert.[93] Schema 21 veranschaulicht die Analogie zwischen **36** und dem Digallen **38**, das mit H_2 die verbrückte Verbindung **39** bildet.[94] DFT-Rechnungen halfen, den Mechanismus zu verstehen, da experimentell nicht klar nachweisbar war, ob die dimere oder monomere Form von **38** ausschlaggebend für die H_2-Addition ist. Thermodynamisch am günstigsten ist die Bildung von 1,2-Dihydridogallan ausgehend vom Dimer **38** mit anschließender Spaltung der Ga–Ga-Bindung und Bildung von zwei Äquivalenten $ArGaH_2$. Durch eine abschließende Dimerisierung wird **39** erhalten. In Verbindung mit terminalen Alkinen können mit **38** ähnlich wie mit Diboracumulenen Heterocyclen aufgebaut werden, die leicht reduzierbar sind.[95]

Während bei den Trielen eine Doppelbindung als reaktives Zentrum vorherrscht, verfügt das Disilen **40** über eine sehr lange Si=Si-Doppelbindung, die vielmehr als Kombination zweier Silylenfragmente gilt. Die gewinkelte Struktur ermöglicht nur eine *anti*-Addition von H_2, sodass die 1,2-Dihydrostruktur **41** entsteht (Schema 21 unten).[96]

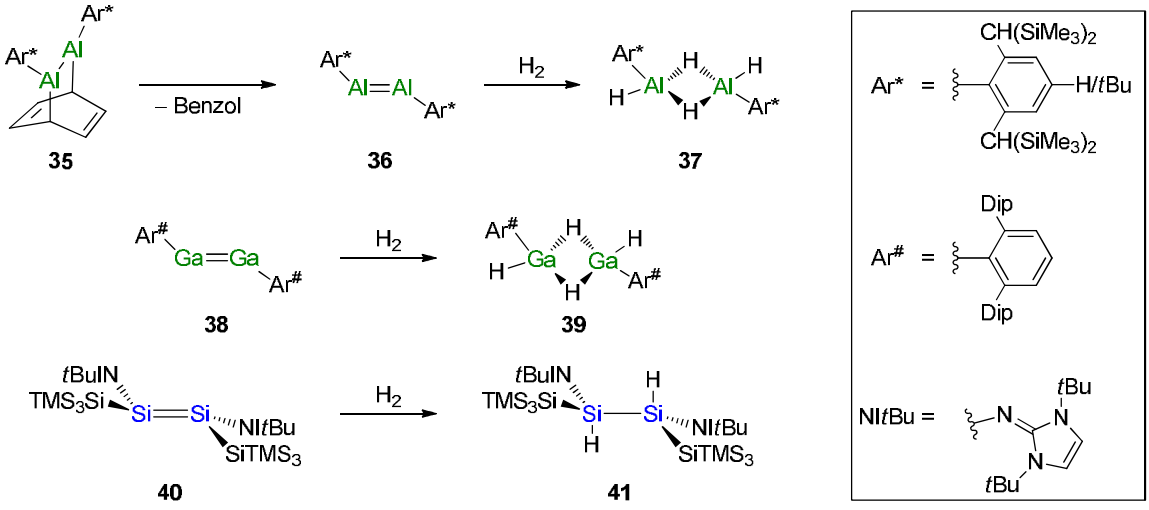

Schema 21. Reaktionen von H_2 mit E=E-Doppelbindungen (E = Al, Ga, Si; Dip = 2,6-Di(*iso*-propyl)phenyl).

Das NHC-stabilisierte Disilen **42** erwies sich als besonders reaktiv gegenüber CO_2, da nicht nur eine Doppelbindung, sondern auch freie Elektronenpaare für eine Wechselwirkung zur Verfügung stehen. Das Reaktionsprodukt **43** (Schema 22), in dem die Si-Atome durch ein Sauerstoffatom und eine Carbonateinheit verbrückt sind, zeugt von einer Si=Si-Bindungsspaltung. Neben der Oxidation der Si-Zentren wurde CO als Nebenprodukt freigesetzt.[97]

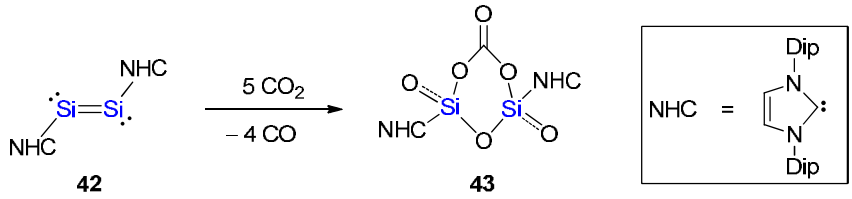

Schema 22. Drei verschiedene O-haltige Liganden in **43** entstehen durch Reaktion von **42** mit CO_2; Dip = 2,6-Di(*iso*-propyl)phenyl.

1.3.4.3. Verbindungen mit E≡E-Dreifachbindungen

Die höheren Homologen der Alkine mit E = Ge, Sn zeichnen sich durch eine besondere Strukturvielfalt aus, wenn es zur Reaktion mit H_2 kommt, wie in Schema 23 zusammengefasst ist.[61, 98] Die erste Annäherung erfolgt sowohl für das Distannin **44** als auch für das Digermin **47** in Übergangsmetall-ähnlicher Weise (vgl. Abschnitt 1.2.), sodass zwei Hydrid-Ionen an ein Tetrelzentrum gebunden sind. Für die Stannanverbindungen ist das resultierende Strukturmotiv **45** nur mit sterisch anspruchsvollen Substituenten isolierbar, da ansonsten die H-Atome in verbrückende Positionen (**46**) verschoben werden. Das Verbindung **45** entsprechende Germaniumderivat **48** geht bereitwillig Folgereaktionen ein, ausgelöst durch eine Isomerisierung zu **49**, welches entweder ein weiteres Äquivalent H_2 aufnimmt (**50**) oder wiederum im Gleichgewicht mit dem dazugehörigem Germylen **51** steht, das nach Aufnahme von einem weiteren Äquivalent H_2 zum monomeren Trihydridogerman **52** weiterreagiert. Auf diese Weise entscheidet die verfügbare Menge an H_2 über den Reaktionsausgang bei Digerminen. Die Distannine bleiben hingegen unberührt von der Stöchiometrie des Reaktionspartners, weil deren Reaktivität durch die ausgeprägtere Inertheit der freien Elektronenpaare herabgesetzt ist.

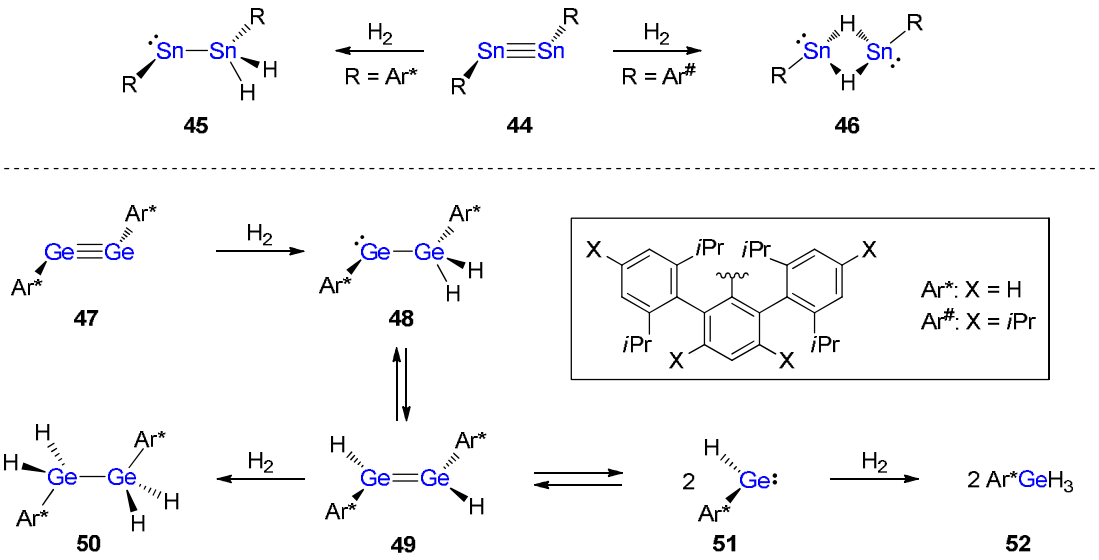

Schema 23. Strukturelle Vielfalt bei der Reaktion von H_2 mit dem Distannin **44** und dem Digermin **47**.

1.3.5. Cyclische Verbindungen

Für das Pentaphenylborol **53** gelten die vorliegende Ringspannung und die Aufhebung der Antiaromatizität als Triebkräfte, um mit H_2 das Boracyclopent-3-en **54** zu bilden (Schema 24).[99] Das Borzentrum wirkt als Elektronenakzeptor und ein benachbartes endocyclisches Kohlenstoffatom als Elektronendonor, um in einem ersten Schritt nicht nur das H_2-Molekül, sondern auch eine B–C-Bindung zu spalten. Anschließend erfolgt eine schnelle Recyclisierung, die zum Isomerengemisch *cis*/*trans*-**54** führt.[100]

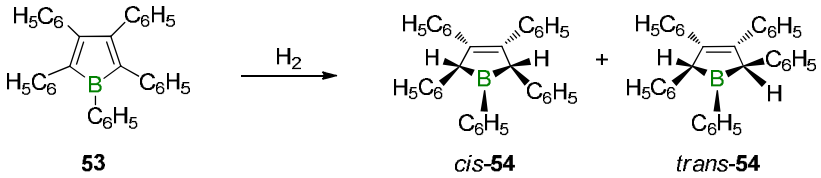

Schema 24. Die H_2-Aktivierung mit dem Borol **53** liefert die Isomere *cis*/*trans*-**54**.

Kinjo und Mitarbeiter untersuchten die Substanzklasse der Diazadiborinine, bei der zwei Borzentren in den 1,4-Positionen als reaktive Zentren fungieren.[101, 102] Wie aus den in Schema 25 (oben) gezeigten mesomeren Grenzstrukturen hervorgeht, besitzen die Boratome einen ambiphilen Charakter. Im Experiment bestätigte sich die besondere Reaktivität von **55**, das bereitwillig formale [4+2]-Cycloadditionsprodukte mit Alkinen oder auch CO_2 eingeht. Die Aktivierung von H_2 war hingegen schwerer zu verwirklichen, weil der HOMO-LUMO-Abstand von **55** recht groß ist, was eine Veränderung der elektronischen Struktur des Heterocyclus nötig machte.[103] Mit dem 1,4,2,5-Diazadiborinin **56** gelang letztlich die Spaltung der H_2-Bindung bei erhöhten Temperaturen, sodass zwei borgebundene Hydrid-Ionen auf derselben Seite des Heterocyclus platziert sind. Die *cis*-Form (**57**-*cis*) kann durch die Zugabe der Lewis-Säure BH_3 zum entsprechenden *trans*-Derivat (**57**-*trans*) isomerisiert werden (Schema 25 unten).[104] Mit Kinjos Diazadiborininen vergleichbar ist das strukturell verwandte 1,4-Digermabenzol von Sasamori und Tokitoh, das ebenso die H_2-Bindung aktiviert und [4+2]-Cycloadditionsprodukte mit Acetylen und CO_2 bildet.[105]

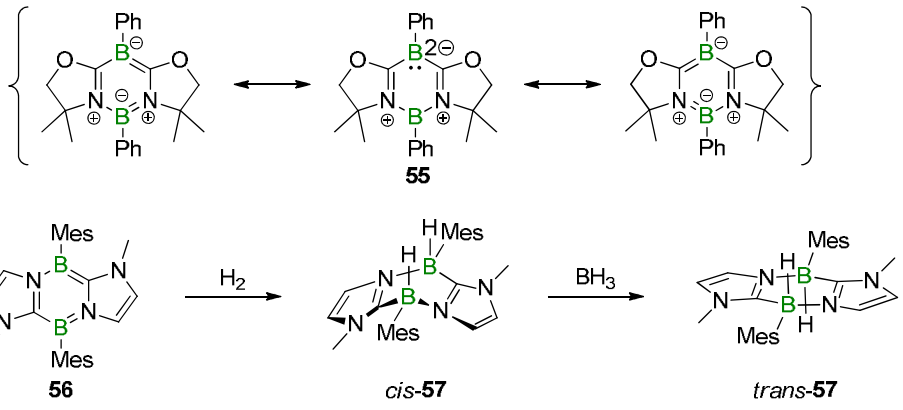

Schema 25. Mesomere Grenzstrukturen des Diazadiborinins **55** (oben). H_2-Addition an Derivat **56** mit anschließender Lewis-Säure-induzierter Isomerisierung (unten).

Das neutrale 1,3,2,5-Diazadiborinin **55** erlangt durch die stöchiometrische Addition von Aryllithium-Verbindungen an ein Borzentrum als Monoanion Li[**58**] nukleophilen Charakter, sodass eine bereitwillige Reaktion mit Elektrophilen wie Iodmethan eintritt (**59**; Schema 26).[106] Die elektronische Struktur der Diazadiborinine wurde von Kinjo folglich durch die

Verteilung der Heteroatome im zentralen Ring und die Wahl der borgebundenen Substituenten beeinflusst, um unterschiedliche Substrate zu aktivieren.

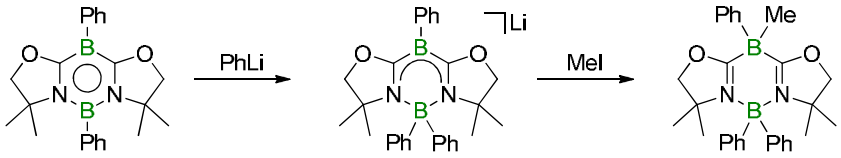

Schema 26. Erzeugung eines nukleophilen Zentrums im 1,3,2,5-Diazadiborinin **55** durch Zugabe von Phenyllithium.

Neben Boratomen hat sich der Einbau von Phosphoratomen in cyclische Systeme als vorteilhaft für die Aktivierung kleiner Moleküle erwiesen. Hinz et al. verfolgten dabei den Ansatz mit dem Singulett-Biradikaloid **60** die elektronische Struktur und das Reaktivitätsmuster von Hauptgruppenstrukturen mit Mehrfachbindungen nachzuahmen.[107] Wie Schema 27 zeigt, reagiert **60** bereitwillig mit H_2 und CO_2: Das H_2-Additionsprodukt **61** verliert das aufgenommene H_2 wieder bei erhöhten Temperaturen, wohingegen mit CO_2 eine irreversible Redoxreaktion eintritt, bei der neben **62** auch CO entsteht.

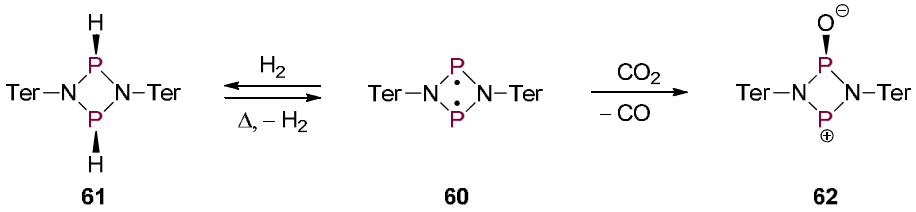

Schema 27. Reaktion von [P(μNTer)]$_2$ **60** mit H_2 und CO_2. Ter = Bis-(2,6-mesityl)-phenyl.

Die Gruppen von Nyulászi und Streubel haben untersucht, ob das 1,4-Diphosphinin **63** Dichalkogene nur an ein Phosphorzentrum in Analogie zu Elektronensextett-Verbindungen bindet.[108] Entgegen den Erwartungen wurde das 1,4-Additionsprodukt **64** isoliert, in dem die Chalkogenreste *trans* zueinander orientiert sind (Schema 28). Mit elektronenarmen Doppelbindungen geht **63** [4+2]-Cycloadditionen ein, sodass verbrückende Strukturmotive gebildet werden.

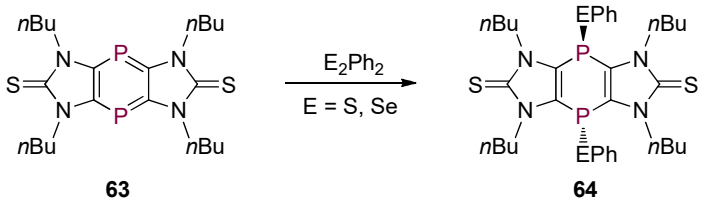

Schema 28. 1,4-Addition von Dichalkogenen an das 1,4-Diphosphinin **63**.

1.4. Die Verbindungsklasse der 9,10-Dihydro-9,10-diboraanthracene

Im Arbeitskreis Wagner sind 9,10-Dihydro-9,10-diboraanthracene (DBA, **A**) als heterocyclische Hauptgruppenverbindungen etabliert (Schema 29).[109, 110] Die freien p_z-Orbitale der Boratome ermöglichen einerseits die Delokalisierung der π-Elektronendichte der angrenzenden Arylringe und dienen andererseits als elektrophile Zentren. Ersteres macht bordotierte polycyclische aromatische Systeme häufig zu Emittern sichtbaren Lichts. Letzteres gestattet die Koordination von Lewis-Basen, worauf katalytische Anwendungen aufbauen. Die vielfältigen Ansätze zur Beeinflussung der Emittereigenschaften von **A** durch die Erweiterung des π-Grundgerüstes oder die Auswahl verschiedener borgebundener Substituenten werden im Rahmen der vorliegenden Arbeit nicht diskutiert. Vielmehr soll der Einsatz von **A** als Katalysator im Fokus stehen.

Zur Synthese des 9,10-Dihydro-9,10-diboraanthracen-Grundgerüsts **A** ausgehend von *ortho*-Dibrombenzol **65** benötigt man drei Stufen (Schema 29).[111] Im ersten Schritt findet eine Grignardreaktion statt, die Bis(trimethylsilyl)benzol **66** liefert, welches anschließend in einer Cyclokondensationsreaktion mit BBr_3 zum 9,10-Dibrom-DBA **67** führt. Die B–Br-Bindung in **67** eignet sich gut, um mithilfe von Grignardverbindungen verschiedene Substituenten an die Borzentren anzubringen.[112]

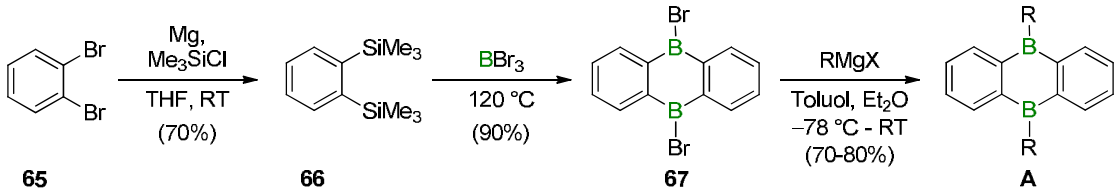

Schema 29. Synthese von 9,10-Dihydro-9,10-diboraanthracen-Derivaten **A**. Ausbeuten für jeden Schritt in Klammern; R = Alkyl, Aryl.

Im Zuge der Derivatisierung von DBAs entdeckte Andreas Lorbach aus dem Arbeitskreis Wagner, dass ditope Lewis-Basen wie Phthalazin verbrückend an die beiden Borzentren des DBAs binden, wodurch sich dessen Hydrolyseempfindlichkeit verringert.[113] Die Gruppe von Wegner nutzte das Phthalazin-Addukt von 9,10-Dimethyl-DBA (**68**) später als Edukt für Diels-Alder-Reaktionen mit inversem Elektronenbedarf (Schema 30). Durch sein herabgesetztes LUMO-Energielevel ist DBA-koordiniertes Phthalazin **69** empfänglicher für elektronenreiche Dienophile.[114, 115] Eine zusätzliche Triebkraft für die Bildung des Naphthalin-

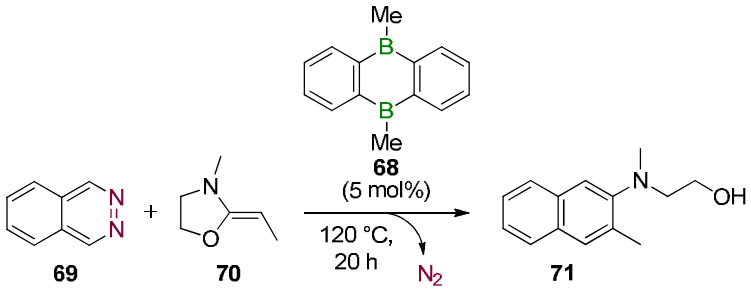

Schema 30. Diels-Alder-Reaktion mit inversem Elektronenbedarf zwischen Phthalazin (**69**) und dem Dienophil **70** mit 9,10-Dimethyl-DBA (**68**) als Katalysator.

Derivats **71** durch Zugabe des Oxazolidins **70** stellt die Eliminierung von N_2 dar. Die finale Produktbildung benötigt oftmals einen zusätzlichen Schritt, wie etwa die Verschiebung eines H-Atoms zur Rearomatisierung. Die DBA-Komponente wird regeneriert und übernimmt damit die Rolle eines Katalysators.

Wegners Gruppe setzte 9,10-Dichlor-DBA auch zur Freisetzung von H_2 aus Amminboran (NH_3BH_3) ein, welches als potentieller Wasserstoffspeicher gilt. Aus einem Äquivalent NH_3BH_3 konnten bis zu 2.5 Äquivalente H_2 gewonnen werden, wobei die DBA-Komponente (5 mol%, THF/Diglyme, 60 °C, 7 h) bis zu 15 Zyklen ohne nennenswerte Reaktivitätseinbußen überstand und als Begleitprodukte Borazin sowie dessen Oligomere auftraten.[116]

Unter Ausnutzung der guten koordinierenden Fähigkeiten der DBA-Derivate wählten mehrere Gruppen diese auch als Liganden in Übergangsmetallkomplexen aus. Marks und Mitarbeiter setzten auf deren Lewis-Azidität, um die Olefinpolymerisation mit Zirconocen-Komplexen zu verbessern.[117] Die Arbeiten von Siebert zeigten, dass DBAs über vielseitige Ligandeneigenschaften verfügen, die zur Darstellung unterschiedlichster Übergangsmetallkomplexe dienten.[118] Dafür erwies sich das Redoxverhalten von DBAs als hilfreich, da nicht nur dessen neutrale, sondern auch radikalische und dianionische Form genutzt wurden. Die Arbeitsgruppe von Wagner untersuchte ausführlich die zweifach reversible Reduzierbarkeit verschiedener DBA-Derivate mittels Cyclovoltammetrie:[110, 111, 119-121] Deren Elektronenaffinität war besonders hoch, wenn diese über elektronenziehende Substituenten oder ein vergrößertes π-System verfügten. Zuletzt verwendete die Gruppe von Harman Biphosphane mit einem DBA-Rückgrat, weil redoxaktive Liganden als vielversprechend zur Beeinflussung der Chemie von Übergangsmetallzentren in Molekülkatalysatoren gelten.[122]

Im Arbeitskreis Wagner wurde die Reaktivität von DBA-Dianionen gegenüber organischen Substraten erstmalig von Andreas Lorbach durchgeführt.[123] Die Darstellung der zweifach reduzierten Spezies Li_2[**72**] erfolgte aus (**72**)$_n$ in THF-Lösung mit einem Überschuss an elementarem Lithium. Wie in Schema 31 zu sehen, entsteht durch die Kombination von Li_2[**72**] mit einem Benzophenon-Derivat das [4+2]-Cycloadditionsprodukt Li_2[**73**]. Im Gegensatz zu neutralen Hydroboranen geht Li_2[**72**] keine Hydroborierungsreaktion mit terminalen Alkinen ein, sondern spaltet die C–H-Bindung, sodass Li_2[**74**] entsteht. Liegt ein Überschuss des Alkins vor, so wird unter Freisetzung von H_2 und Bildung von Li_2[**75**-H_2] in einer Säure-Base-Reaktion eine zweite C–H-Bindung aktiviert.

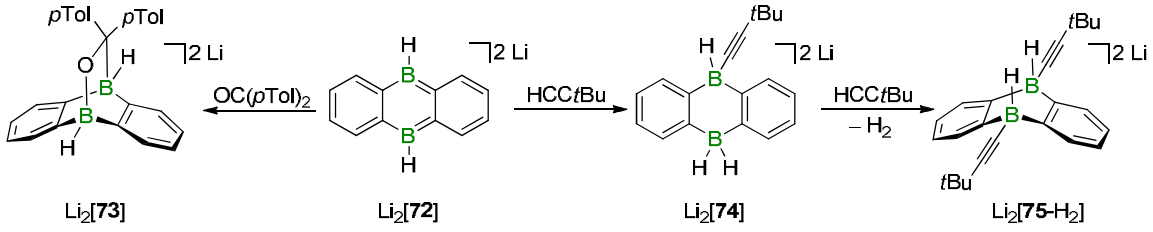

Schema 31. Li_2[**72**] geht [4+2]-Cycloadditionen (links) und C–H-Aktivierungen (rechts) ein.

Harman und Mitarbeiter synthetisierten ein zu Li_2[**72**] isoelektronisches, neutrales DBA-Derivat, welches durch borständige NHC-Liganden stabilisiert wird (NHC = 1,3-bis(2,6-di-*iso*-propylphenyl)imidazol-2-ylidene). Mit diesem DBA konnten zu Li_2[**73**] vergleichbare [4+2]-Cycloadditionsprodukte mit CO_2, O_2 und Ethen realisiert werden.[124]

1.5. Zielsetzung

Im Kontext der Aktivierung kleiner Moleküle mit Hauptgruppenverbindungen in niedrigen Oxidationsstufen sollte die Reaktivität zweifach reduzierter 9,10-Dihydro-9,10-diboraanthracene ([**A**]$^{2-}$) eingehender untersucht werden. Als Grundlage dienten die Untersuchungen von Andreas Lorbach zur Reduktion von 9,10-Dihydro-9,10-diboraanthracen (**72**)$_n$ und die Umsetzungen des erhaltenen Li_2[**72**] mit 4,4'-Dimethylbenzophenon sowie *tert*-Butylacteylen (vgl. Schema 31). Sowohl die NMR- als auch Röntgenstrukturdaten von Li_2[**72**] legen eine vollständige Delokalisierung der π-Elektronendichte über das gesamte Grundgerüst nahe.[123] In Analogie zur FLP-Chemie entstand dennoch das Bild einer mesomeren Grenzstruktur von [**72**]$^{2-}$ (Schema 32 rechts), in der ein Elektronenpaar einem Boratom zugewiesen wird, das damit isolobal zu einem Stickstoff- oder Phosphoratom wird.

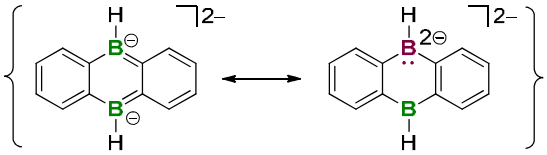

Schema 32. Kann die rechte mesomere Grenzstruktur von [**72**]$^{2-}$ dessen Reaktivität im Sinne eines intramolekularen FLPs erklären?

Die Polarisierbarkeit der Elektronendichte in Li_2[**72**] lässt ein Reaktionsverhalten im Sinne eines maskierten FLP-Systems erwarten. Motiviert durch diese Analogiebetrachtung sollte in der vorliegenden Arbeit untersucht werden, ob die Salze M_2[**A**] (M^+ = Li^+, Na^+, K^+) die Bindung des H_2-Moleküls spalten können. Aufbauend auf diesem Initialschritt sind zwei Anwendungsfelder für die H_2-Additionsprodukte M_2[**A**-H_2] denkbar: i) die Übertragung des aufgenommenen H_2-Äquivalents auf ungesättigte Verbindungen oder ii) die Bereitstellung von zwei H^--Ionen für nukleophile Substitutionsreaktionen (Schema 33).

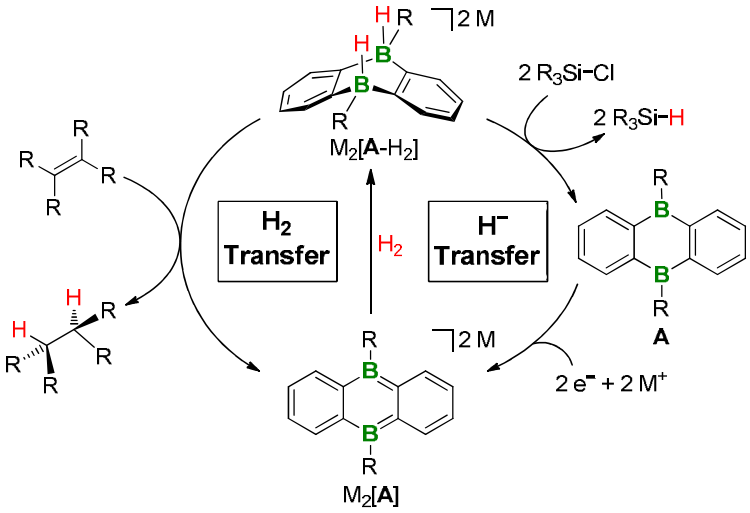

Schema 33. Können die Salze M_2[**A**] H_2 aktivieren und als H_2- sowie als H^--Transferkatalysatoren eingesetzt werden?

Es galt zu überprüfen, ob M_2[**A**] als Katalysatoren in beiden Anwendungsbereichen eingesetzt werden können. Im ersten Fall ermöglicht die Abgabe von H_2 intrinsisch einen Katalysezyklus. Im zweiten Fall der Hydrid-Übertragung entsteht zunächst das neutrale DBA **A**, das erst mithilfe eines zusätzlichen Reduktionsschritts wieder in die reaktive Spezies [**A**]$^{2-}$ über-

führt werden müsste. Für diesen Regenerationsschritt war geplant, die Umsetzbarkeit einer elektrochemischen Darstellung von [**A**]$^{2-}$ zu bewerten.

Die Reaktivitätsstudien mit M_2[**A**] sollten nicht auf H_2 als Reaktionspartner beschränkt bleiben, sondern Mehrfachbindungen, CO_2 und Elektrophile einschließen.

2. Übersicht der Ergebnisse

2.1. Aktivierung von H_2 mit M_2[**A**]

Die Eignung von zweifach reduzierten 9,10-Dihydro-9,10-diboraanthracenen [**A**]$^{2-}$ als Hydrierungskatalysatoren setzt voraus, dass deren HOMO-LUMO-Energieunterschiede klein und die Symmetrien der Grenzorbitale mit denen des H_2-Moleküls kompatibel sind (vgl. Abschnitt 1.2.). In einer Kooperation mit der Gruppe Holthausen fertigte Martin Diefenbach quantenchemische Rechnungen zur Aktivierung von H_2 mit [**A**]$^{2-}$ an {[**A**]$^{2-}$ = [**72**]$^{2-}$ mit R = H; [**75**]$^{2-}$ mit R = C≡C*t*Bu (vgl. Abbildung 7); Theorielevel: B2GP-PLYP-D/CBS(T,Q)//SMD-PBE0D/6-31+G(d,p)}. Das HOMO und das LUMO von [**A**]$^{2-}$ verfügen über dieselben Symmetrien an den Boratomen wie die Grenzorbitale, die im Falle einer Übergangsmetall-vermittelten Spaltung der H_2-Bindung am Katalysator involviert sind (Abbildung 7). Die Struktur des Übergangszustands ist ideal präorganisiert für eine konzertierte Addition unter homolytischem H–H-Bindungsbruch. In einer theoretischen Betrachtung ähnelt das System [**A**]$^{2-}$ in dessen Fähigkeit zur H_2-Aktivierung folglich mehr einem Übergangsmetallkomplex als einem FLP hinsichtlich der Orbitalwechselwirkungen im Übergangszustand (vgl. 1.2. und 1.3.1.).

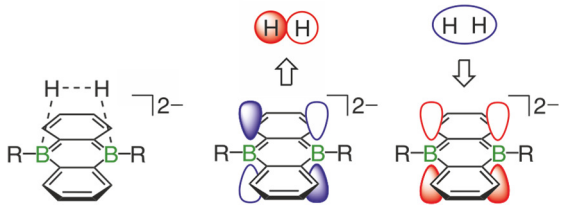

Abbildung 7. Struktur und Orbitalwechselwirkungen des Übergangszustands für die Aktivierung von H_2 mit [**A**]$^{2-}$. HOMOs: blau; LUMOs: rot.

Für eine konzertierte Addition von H_2 an das native [**72**]$^{2-}$ liegt die berechnete Aktivierungsbarriere bei 88 kJ mol^{-1} und kann durch Wärmezufuhr überwunden werden. Insgesamt verläuft die Reaktion von [**72**]$^{2-}$ mit H_2 exergonisch ($\Delta_r G$ = –67 kJ mol^{-1}). Beim isoelektronischen Anthracen, das über die gleichen Grenzorbitale wie [**72**]$^{2-}$ verfügt, findet eine unkatalysierte Bildung von 9,10-Dihydroanthracen durch direkte Hydrierung unter moderaten Reaktionsbedingungen nicht statt.[125] In Übereinstimmung dazu liegt für Anthracen eine mehr als doppelt so hohe berechnete Aktivierungsbarriere vor ($\Delta G^{\ddagger}$ = 191 kJ mol^{-1}) und die Gibbs'sche Freie Reaktionsenthalpie der H_2-Addition sinkt auf $\Delta_r G$ = –33 kJ mol^{-1}.

Die quantenchemischen Rechnungen stehen im Einklang mit den experimentellen Ergebnissen, dass die Salze M_2[**72**] (M^+ = Li^+, K^+) die Bindung des H_2-Moleküls bereits unter milden Bedingungen (50 - 100 °C, ca. 1 atm H_2) spalten können (Schema 34). Wurde Li_2[**72**], das Deuterium- anstelle von H-Substituenten an den Boratomen trug, mit H_2 umgesetzt, zeigte das ^{1}H-NMR-Spektrum der Reaktionslösung im Vergleich zur Startverbindung eine neue Protonenresonanz mit einem Integral von exakt zwei. Die Hydrid-Ionen im Produkt Li_2[**72**-H_2] stammen demnach vom H_2-Molekül.

Die erfolgreiche Aktivierung von H_2 mit M_2[**72**] ermutigte zur Nutzung anderer Derivate M_2[**A**], die synthetisch leicht zugänglich sind (Schema 34). Ausgehend von einer THF-Lösung eines neutralen 9,10-Dihydro-9,10-diboraanthracen-Derivats **A** erzeugt die Zugabe eines Alkalimetalls in Form von elementarem Li bzw. Na oder KC_8 die entsprechenden reduzierten Spezies M_2[**A**], die tiefrote (M^+ = Li^+) oder -grüne (M^+ = Na^+, K^+) Lösungen bilden.[123, 126]

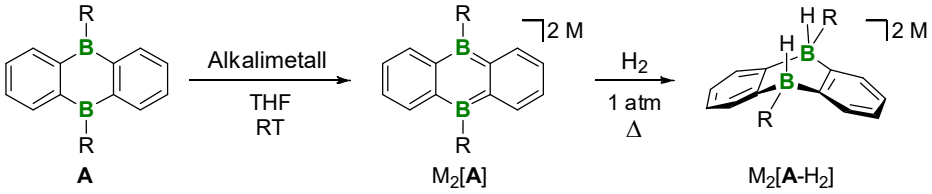

Schema 34. Darstellung der Salze M_2[**A**] und deren Reaktivität gegenüber H_2. R = H, Alkinyl, Alkyl, Aryl; $M^+ = Li^+, Na^+, K^+$.

Im Zuge der Reduktion lässt sich somit das Gegenkation variieren und das Grundgerüst 9,10-Dibrom-DBA (**67**) ermöglicht das Einführen verschiedenster borgebundener Substituenten (vgl. Schema 29).[110] Der Einfluss dieser beiden Parameter auf den Schritt der H_2-Aktivierung mit M_2[**A**] wird in den beiden folgenden Abschnitten ausgeführt. Zu den gewonnen Erkenntnissen trugen die Ergebnisse aus der Bachelorarbeit von Sven E. Prey bei, die von mir betreut wurde.[127]

2.1.1. Einfluss des borgebundenen Substituenten

Die Auswahl der DBA-Derivate **A** stützte sich teilweise auf bereits bekannte Vertreter dieser Substanzklasse, die ausgehend von **67** durch (a) Hydrid-Transfer mit Et_3SiH (**72**),[128] (b) nukleophile Substitution mit LiC≡C*t*Bu (**75**),[129] (c) Hydrid-Transfer mit anschließender Hydroborierung von HC≡C*t*Bu (**76**)[128] und (d) nukleophile Substitution mit BrMgR (**68**, **77**-**81**; Schema 35) darstellbar sind.[119, 126, 130, 131]

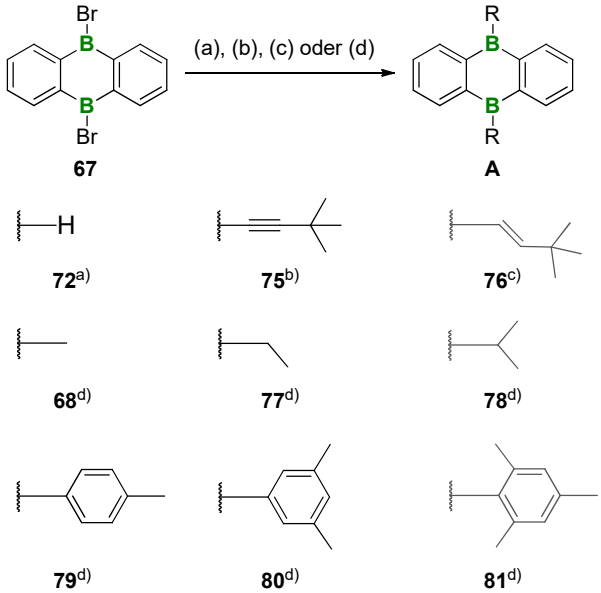

Schema 35. Darstellung von symmetrisch B-substituierten DBA-Derivaten **A**: (a) Et_3SiH,[128] (b) LiC≡C*t*Bu,[129] (c) 1. Et_3SiH, 2. HC≡C*t*Bu[128] und (d) RMgBr.

Das etablierte Syntheseprotokoll zur Darstellung von **81** mit Mesitylmagnesiumbromid und **67** wurde modifiziert, um es auf die anderen luftempfindlichen Derivate zu übertragen, die bisher nur mithilfe von weniger selektiven lithiumorganischen oder toxischen zinnorganischen Verbindungen zugänglich waren.[126, 130, 131] Die in Schema 35 zusammengefassten Derivate, die sich im sterischen Anspruch der borgebundenen Substituenten sowie in deren

elektronischen Eigenschaften unterscheiden, werden in guten Ausbeuten (60-80%) erhalten.

Zur Bestimmung relativer Kinetiken der H_2-Addition an $[\mathbf{A}]^{2-}$ in Abhängigkeit von den Substituenten wurden folgende Punkte berücksichtigt: (i) die Verbindungen müssen hinreichend temperaturstabil sein, da für die Überwindung der Aktivierungsbarriere Normalbedingungen nicht ausreichen, (ii) die Umsatzgeschwindigkeit sollte auf der NMR-Zeitskala verfolgbar sein und (iii) der H_2-Aktivierungsschritt sollte keine Nebenreaktionen hervorrufen. Diese Anforderungen führten zum Ausschluss des temperaturinstabilen Derivats **78** sowie von Li_2[**76**] und Li_2[**81**], weil Ersteres nicht selektiv reagierte und Letzteres aufgrund der sterischen Abschirmung der Boratome inert gegenüber H_2 blieb. Die Durchführung der H_2-Additionen erfolgte in abgeschmolzenen NMR-Rohren bei 100 °C und einem initialen H_2-Druck von 1 atm. Li_2[**A**] wiesen die längsten Reaktionszeiten auf, die somit eine Verfolgung der Umsatzraten mittels NMR-Spektroskopie erlaubten. Li_2[**A**] und Li_2[**A**-H_2] unterscheiden sich markant in den chemischen Verschiebungen der aromatischen Multipletts ihrer DBA-Gerüste, sodass über eine Integration der entsprechenden Protonensignale der Stoffumsatz bestimmt werden konnte. Die Unterbrechung der Wärmebehandlung der Probe für die Zeit der NMR-Messung war in Anbetracht der langsamen Additionsgeschwindigkeit und einer ausbleibenden Rück- bzw. Weiterreaktion bei Raumtemperatur vernachlässigbar. Der Anteil an Li_2[**A**-H_2] wurde in regelmäßigen Abständen erfasst und im abgebildeten Umsatz-Zeit-Diagramm aufgetragen (Abbildung 8).

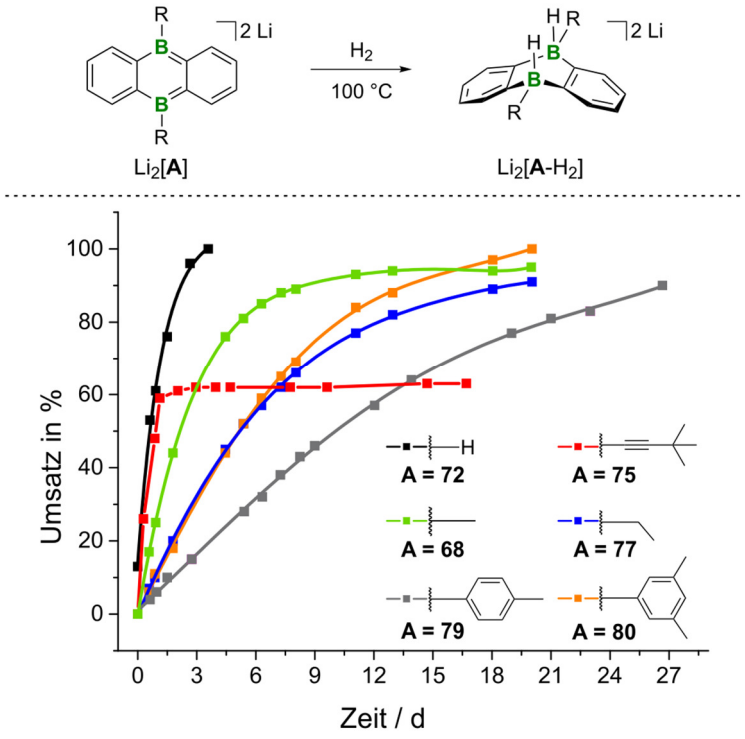

Abbildung 8. Umsatz-Zeit-Diagramm für die Reaktion von Li_2[**A**] mit H_2 zu Li_2[**A**-H_2] (bestimmt durch ^{1}H-NMR-Spektroskopie).

Der Kurvenverlauf von Li_2[**75**]/H_2 sticht hervor, da die Bildung von Li_2[**75**-H_2] nicht quantitativ ist, sondern bei einem Umsatz von 60% in ein Gleichgewicht mündet. Dieses Gleichgewicht wird ebenfalls erreicht, wenn man von reinem Li_2[**75**-H_2] ausgeht, das über eine dop-

pelte Hydroborierung von HC≡C*t*Bu mit Li_2[**72**] synthetisiert wurde (vgl. Schema 31). Später postulierten Wegner und Mitarbeiter passend dazu eine Freisetzung von H_2 aus der strukturell verwandten Verbindung **82**, wobei der Vorläufer eines stabilen Biradikaloids entsteht (Schema 36).[132]

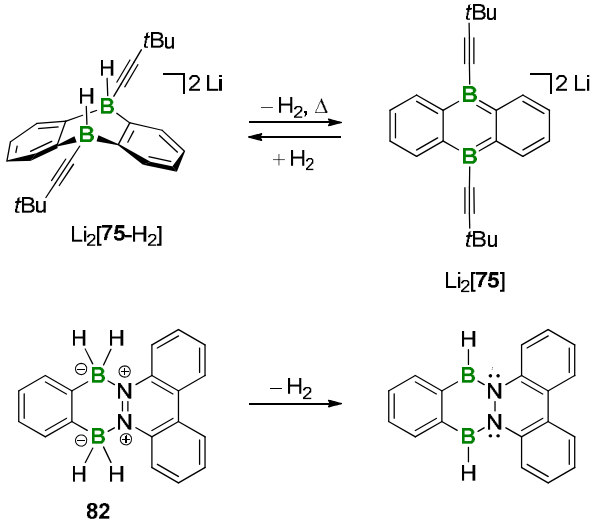

Schema 36. Gegenüberstellung einer reversiblen (oben) und einer irreversiblen (unten) Eliminierung von H_2 aus ditopen, tetrakoordinierten Borverbindungen.

Im Gegensatz zu Li_2[**75**], das in ein H_2-Additions-/Eliminierungs-Gleichgewicht mündet, addiert Li_2[**72**] das H_2-Molekül schnell und quantitativ. In Übereinstimmung mit den abweichenden Kurvenverläufen in Abbildung 8 berechnete Martin Diefenbach unterschiedlich ausgeprägte Triebkräfte für die Bildung von [**A**-H_2]$^{2-}$: die Freie Gibbs'sche Reaktionsenthalpie ist für [**72**-H_2]$^{2-}$ um 34 kJ mol^{-1} exergonischer als für [**75**-H_2]$^{2-}$ ($\Delta_r G$ = –67 *vs.* –33 kJ mol^{-1}), was eine Rückreaktion, also die Freisetzung von H_2, für [**75**-H_2]$^{2-}$ wahrscheinlicher macht.

Als genereller Trend lässt sich aus dem Umsatz-Zeit-Diagramm (Abbildung 8) ableiten, dass Anionen [**A**]$^{2-}$ mit kleinen borgebundenen Substituenten bereitwilliger H_2 aufnehmen als sterisch belastetere (vgl. R = H, Me *vs.* Xyl, *p*Tol). Die Sterik der borgebundenen Reste kann jedoch nicht als Erklärung für das divergierende Reaktionsverhalten von Li_2[**79**] und Li_2[**80**] gegenüber H_2 herangezogen werden. Hier müssen die Ursachen elektronischer Natur sein. Vor diesem Hintergrund wurden die neutralen DBAs **A** mithilfe von cyclovoltammetrischen Messungen untersucht, um ein Maß für die Stabilitäten der Dianionen [**A**]$^{2-}$ in Abhängigkeit von den elektronischen Einflüssen der Substituenten zu erhalten (THF, RT, [^{n}Bu$_4$N][PF_6], referenziert gegen FcH/FcH$^+$). Mit einem ersten Redoxhalbstufenpotential von $E_{1/2}^{Red1}$ = –1.66 V ist [**75**]$^{2-}$ das stabilste Dianion. Darauf folgen [**79**]$^{2-}$ ($E_{1/2}^{Red1}$ = –1.80 V) und mit etwas Abstand [**80**]$^{2-}$ ($E_{1/2}^{Red1}$ = –1.90 V). Unter der Annahme, dass das stabilere Dianion die geringe Affinität zu H_2 haben sollte, erklären die Redoxpotentiale die unterschiedlichen Reaktionsgeschwindigkeiten von [**79**]$^{2-}$ und [**80**]$^{2-}$ in Bezug auf die H_2-Aktivierung. Gleichzeitig wird auch die Reversibilität der H_2-Addition an Li_2[**75**] noch verständlicher.

2.1.2. Einfluss des Kations

Das gemeinsame Strukturmotiv aller Salze M_2[**A**] im Festkörper ist ein inverser Sandwich-Komplex, der immer dunkelrot gefärbt ist und in dem die Gegenkationen den zentralen B_2C_4-Ring von beiden Seiten komplexieren. Die Natur des Alkalimetallkations M^+ entscheidet dann über die Verknüpfung der M_2[**A**]-Einheiten: Li_2[**A**] bilden isolierte Komplexe, wohingegen Na_2[**A**] als lineare und K_2[**A**] als Fischgräten-artige Koordinationspolymere vorliegen, wie Abbildung 9 am Beispiel des dianionischen Grundgerüsts [**72**]$^{2-}$ zeigt. Die gemittelten $M^+\cdots$COG Abstände betragen in [**72**]$^{2-}$ für Li^+ = 1.960 Å,[123] Na^+ = 2.239 Å und K^+ = 2.755 Å (COG = Schwerpunkt des jeweiligen B_2C_4-Rings). Mit steigendem Ionenradius vergrößert sich also der Abstand zwischen Kation und Schwerpunkt des B_2C_4-Rings.

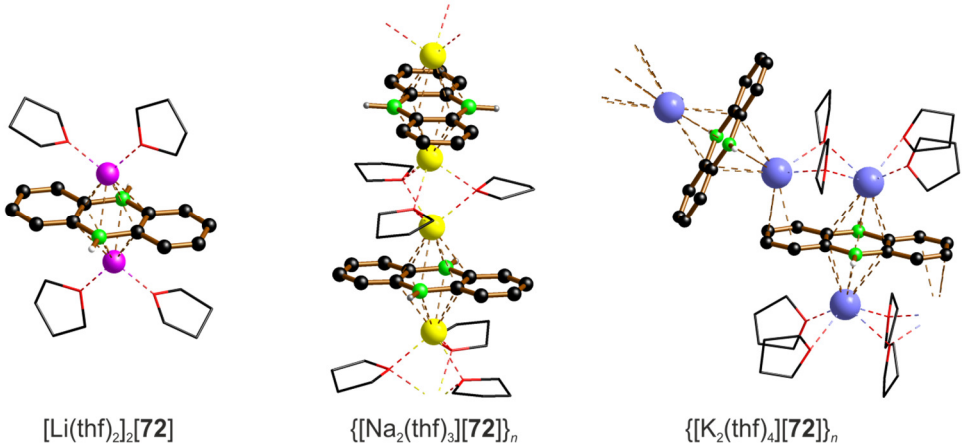

Abbildung 9. Festkörperstrukturen des inversen Sandwich-Komplexes [Li(thf)$_2$]$_2$[**72**][123] sowie der Koordinationspolymere {[Na$_2$(thf)$_3$][**72**]}$_n$ und {[K$_2$(thf)$_4$][**72**]}$_n$. Kohlenstoffgebundene H-Atome sind nicht dargestellt.

Kontaktionenpaare bestehen für Li_2[**72**] nicht nur im Festkörper, sondern auch in Lösung, wie die chemische Verschiebung von –9.0 ppm des ^{7}Li-NMR-Signals bestätigt.[133] Die Natrium- und Kaliumsalze bilden vermutlich deutlich schwächere Komplexe in THF-Lösung, da in diesen Fällen eine tiefgrüne Farbe beobachtet wird, anstelle einer roten Färbung wie bei den Lithiumsalzen.

Bei der Untersuchung der Reaktion von M_2[**A**] mit H_2 in Abhängigkeit vom Kation hat sich gezeigt, dass dieser Parameter erhebliche Auswirkungen auf die Reaktionskinetik hat. Aus der vorangegangenen Studie mit Li_2[**A**] wurden die Dianionen [**72**]$^{2-}$ und [**68**]$^{2-}$ als beste H_2-Akzeptoren und [**79**]$^{2-}$ als langsamster Vertreter ausgewählt, um den Einfluss von M^+ = Li^+, Na^+ und K^+ auf den Schritt der H_2-Addition zu messen (Abbildung 10). Unabhängig vom borgebundenen Substituenten reagieren die Natriumsalze bei 100 °C wesentlich schneller mit H_2 als die Lithiumsalze. Eine Verringerung der Temperatur auf 50 °C verlangsamt die Reaktionszeiten für Na_2[**A**], jedoch nicht signifikant für K_2[**A**], die immer noch sehr hohe Umsatzraten vorweisen. Während die Bildung von Li_2[**A**-H_2] mehrere Tage in Anspruch nimmt, kann K_2[**A**-H_2] innerhalb einiger Stunden quantitativ gebildet werden. Mit zunehmender Größe des Kations ist der Einfluss des borgebundenen Substituenten weniger ausgeprägt.

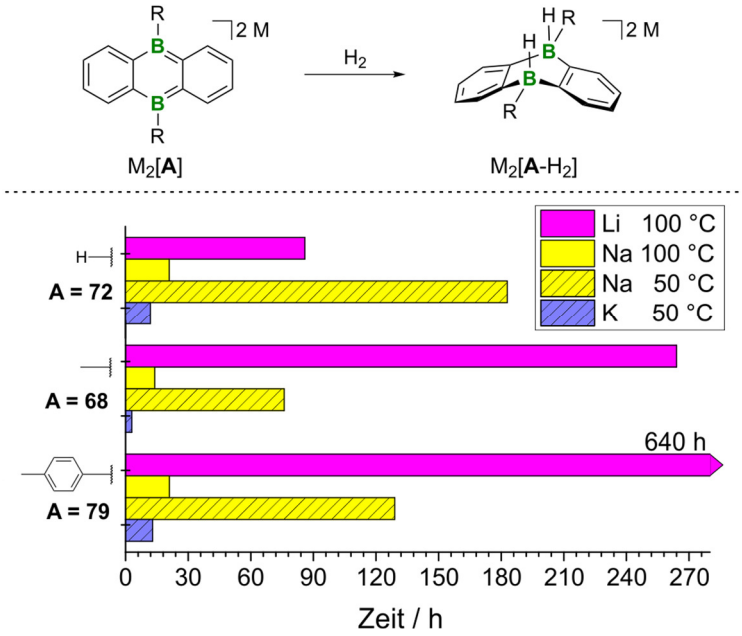

Abbildung 10. Geschwindigkeit der H_2-Aktivierung mit M_2[**A**] in Abhängigkeit vom Kation und vom borgebundenen Substituenten.

Die Bereitschaft zur H_2-Aufnahme steigt demnach mit zunehmendem $M^+\cdots$COG-Abstand selbst bei gleichzeitiger Herabsetzung der Temperatur. Dieser Befund legt die Vermutung nahe, dass K^+- bereitwilliger als Li^+-Ionen ihre Positionen verlassen, um Platz für das ankommende H_2-Molekül zu schaffen. Quantenchemische Rechnungen von Martin Diefenbach zum Reaktionspfad der H_2-Aktivierung für $[M(thf)_2]_2$[**72**] ($M^+ = Li^+, K^+$) bestätigten Unterschiede in den Aktivierungsbarrieren für $M^+ = Li^+$ bzw. K^+: Das größere K^+-Ion behindert die Addition von H_2 weniger. Die Reaktionspfade zeigen, dass insbesondere das K^+-Ion seine Koordinationssphäre auf einen angrenzenden *ortho*-Phenylenring des DBA-Gerüsts ausweiten kann (Abbildung 11).

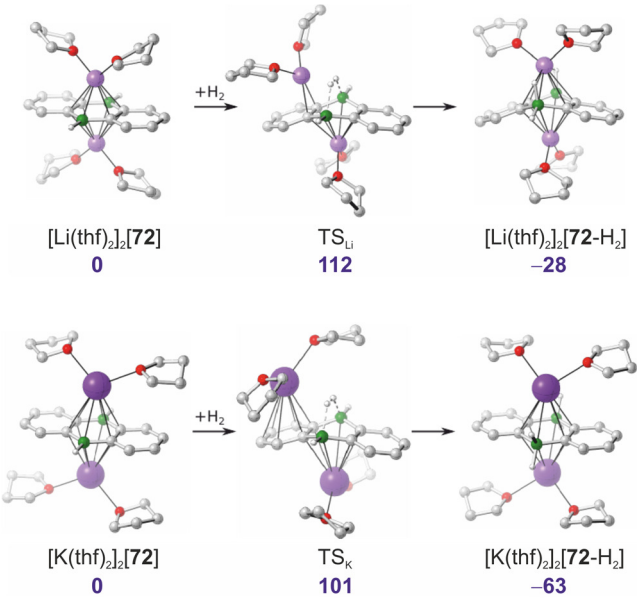

Abbildung 11. Berechneter Reaktionspfad für die H_2-Addition an $[M(thf)_2]_2$[**72**] [$M^+ = Li^+, K^+$; ΔG^{298} in kJ mol^{-1}, Theorielevel: B2GP-PLYP-D/CBS(T,Q)//SMD-PBE0D/6-31+G-(d,p)].

Aufgrund der größeren Freien Gibbs'schen Reaktionsenthalpie ist die Bildung von $[K(thf)_2]_2$[**72**-H_2] zudem begünstigt, da diese mit einer erhöhten Produktstabilität des Kaliumsalzes einhergeht.

2.1.3. Strukturmotive der H_2-Aktivierungsprodukte M_2[**A**-H_2]

Die in Abbildung 11 gezeigten berechneten Strukturen von $[M(thf)_2]_2$[**72**-H_2] (M^+ = Li^+, K^+) unterscheiden sich in der Konformation des jeweiligen DBA-Grundgerüsts, das für M^+ = Li^+ abgewinkelt und für M^+ = K^+ planar ist. Einkristallröntgenstrukturanalysen der entsprechenden Salze im Festkörper bestätigten diese Unterschiede (Abbildung 12).

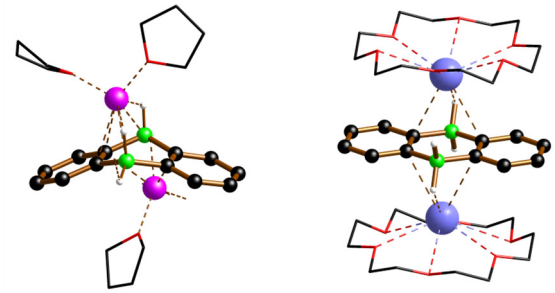

$[Li(thf)_2][Li(thf)]$[**72**-H_2] $[K(18\text{-c-}6)]_2$[**72**-H_2]

Abbildung 12. Festkörperstrukturen von $[Li(thf)_2][Li(thf)]$[**72**-H_2] und $[K(18\text{-c-}6)]_2$[**72**-H_2]. Kohlenstoffgebundene H-Atome sind nicht dargestellt.

Aus dem vorgeschlagenen konzertierten H_2-Additionsmechanismus folgt, dass die H-Atome, die aus dem H_2-Molekül stammen, auf derselben Seite des B_2C_4-Rings positioniert sein müssen. Tragen die Boratome in M_2[**A**-H_2] nicht nur H-Substituenten, so sollten die C-Substituenten die stereochemisch günstigeren äquatorialen und die H-Atome die axialen Positionen einnehmen. Für $[Li(12\text{-c-}4)_2]_2$[**79**-H_2](THF) konnte eine Einkristallröntgenstruktur erhalten werden, deren Qualität ausreicht, um dieses Verknüpfungsmuster zu bestätigen (Abbildung 13). Nach Koordination sperriger NHC-Substituenten an das von mir bereitgestellte 9,10-Dihydro-9,10-diboraanthracen **72** wiesen Bettinger und Mitarbeiter dasselbe Strukturmotiv für Verbindung **83** nach.[134] Die Gruppe um Kinjo zeigte mit einem strukturell verwandten Diazadiborinin-Gerüst, dass diese Spezies ebenfalls H_2 aktiviert, wobei die H-Atome in **84** zwar *cis*-ständig sind, aber in äquatorialen Positionen zu liegen kommen.[103]

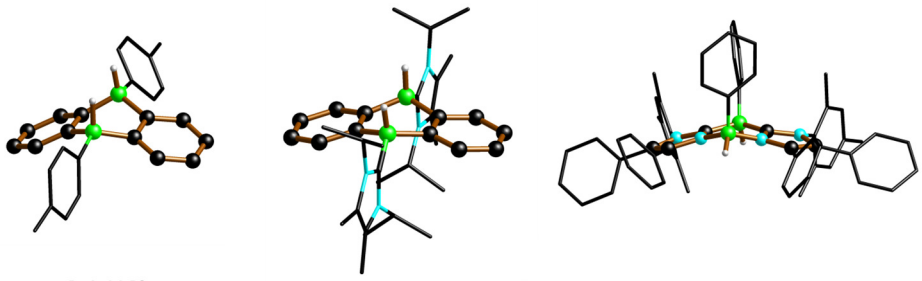

[**79**-H_2]$^{2-}$ **83** **84**

Abbildung 13. Festkörperstrukturen des Dianions aus $[Li(12\text{-c-}4)_2]_2$[**79**-H_2](THF) und der neutralen Verbindungen **83** sowie **84**. Kohlenstoffgebundene H-Atome sind nicht dargestellt.

Im Rahmen der Bestimmung der H_2-Additionsgeschwindigkeit in Abhängigkeit vom Kation wurde gelegentlich eine besondere Flexibilität des dianionischen Grundgerüstes beobachtet: Während für Li_2[**A**-H_2] (R ≠ H) jeweils nur ein Signalsatz in den NMR-Spektren der Reaktionslösungen auftrat, zeigten die von M_2[**A**-H_2] mit M^+ = Na^+, K^+ und R ≠ H zwei verschiedene, wenn auch ähnliche Sätze von Resonanzen für jedes Salz. Betrachtet man beispielsweise den Reaktionsverlauf von K_2[**79**] mit H_2 (THF-d_8, 50 °C), so bildet sich zunächst ein Hauptprodukt. Dazu kommt wenig später ein zweites, dessen Anteil stetig zunimmt, selbst wenn K_2[**79**] bereits vollständig verbraucht ist (Abbildung 14). Die erhöhte Reaktionstemperatur löst offenbar eine Umlagerung der ursprünglichen Struktur zu einer anderen aus. Beide NMR-Signalsätze sind mit zweifachen Hydrid-Addukten an 9,10-(*p*Tol)$_2$-DBA (**79**) vereinbar, sodass der Unterschied durch deren *cis*- bzw. *trans*-Konfigurationen verursacht wird.

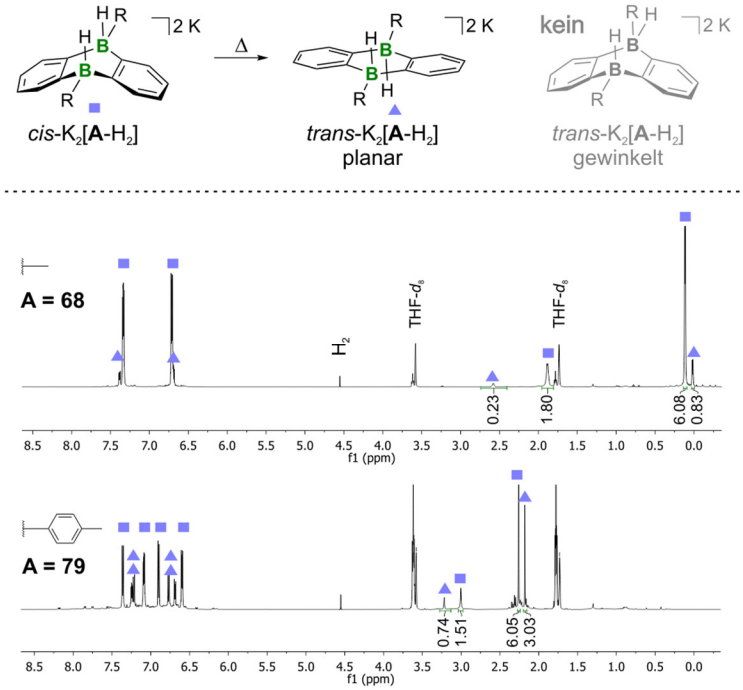

Abbildung 14. Thermisch induzierte Isomerisierung der H_2-Aktivierungsprodukte K_2[**A**-H_2] (R = Me, *p*Tol). ^{1}H-NMR-Spektren (500.2 MHz, THF-d_8) der Reaktionsmischungen K_2[**68**]/H_2 (oben) und K_2[**79**]/H_2 (unten) nach 13 h bei 50 °C. Das Verhältnis zwischen *cis*- (■) und *trans*- (▲) Konfiguration ist vom borgebundenen Substituenten abhängig.

Mithilfe einer THF-d_8-Lösung manuell selektierter Einkristalle von *cis*-[Na][Na(thf)$_2$(18-c-6)]-[Na(thf)$_2$]$_2$[**79**-H_2]$_2$(*n*-Hexan) konnte die thermisch induzierte Umlagerung des ursprünglichen *cis*-Addukts zur *trans*-Konfiguration in Abwesenheit von Na_2[**79**] und H_2 belegt werden, was den konzertierten Mechanismus der H_2-Addition weiter untermauert. Die Dianionen von *trans*-K_2[**79**-H_2] müssen entweder planar sein oder schnell auf der NMR-Zeitskala invertieren, um die hohe mittlere Symmetrie des Systems zu erklären, die sich aus dem beobachteten Signalsatz ergibt. Arbeiten von Kinjo und Mitarbeitern ergänzen diese Befunde: Das H_2-Aktivierungsprodukt des Diazadiborinins **56** (vgl. Schema 25) zeigt nicht nur eine verwandte, Lewis-Säure induzierte *cis*/*trans*-Isomerie,[104] sondern Einkristallröntgenstrukturen belegen zudem, dass das ursprüngliche *cis*-H_2-Addukt ein gewinkeltes Grundgerüst besitzt, das in der *trans*-Form planarisiert vorliegt. Wie Abbildung 14 veranschaulicht, hängt das Ausmaß der *cis*/*trans*-Isomerisierung vom borgebundenen Substituenten ab: der Effekt

ist für K_2[**79**-H_2] wesentlich ausgeprägter als für das Vergleichssystem K_2[**68**-H_2]. Berücksichtigt man die abnehmende Aktivität von Alkalimetallhydriden als Isomerisierungskatalysatoren in der Reihe KH >> NaH > LiH wird zudem verständlich, warum Li_2[**A**-H_2] (R ≠ H) nur in den primär entstandenen *cis*-Konfigurationen vorliegen.[135]

2.2. M_2[**A**] als H_2-Transferkatalysatoren

Die Bereitschaft von Li_2[**75**-H_2], das aufgenommene H_2-Äquivalent auch in Abwesenheit eines geeigneten Akzeptormoleküls wieder freizugeben, bildete die Grundlage für den Einsatz von M_2[**A**] als Katalysatoren in Hydrierungsreaktionen. Um zu bestimmen, welches M_2[**A**]-Derivat als besonders leistungsfähiger Katalysator fungiert, wurde das Imin Ph(H)C=N*t*Bu als Testsubstrat gewählt, das sich bei FLP-vermittelten Hydrierungen bewährt hat. An den experimentellen Arbeiten im Kontext der Hydrierungsreaktionen wirkte Sven E. Prey im Rahmen einer von mir betreuten Bachelorarbeit mit.[127] Tabelle 4 fasst die verwendeten Katalysatoren zusammen, die Kombinationen aus den borgebundenen Substituenten H, Me und *p*Tol mit den Kationen Li^+, Na^+ und K^+ boten. Die Durchführung der Testhydrierungen erfolgte in THF-d_8-Lösungen mit 37 mol% des jeweiligen M_2[**A**]-Derivats in abgeschmolzenen NMR-Rohren (1 atm H_2-Initialdruck, 100 °C, 16 h). Unter den in Tabelle 4 aufgeführten Umsatzraten für die Hydrierung von Ph(H)C=N*t*Bu sticht eine nahezu quantitative Bildung von $Ph(H)_2C$–N(H)*t*Bu mit Li_2[**68**] als Katalysator heraus.

Tabelle 4. Umsatzraten in % des Imins Ph(H)C=N*t*Bu zum hydrierten Produkt $Ph(H)_2C$–N(H)*t*Bu bei Verwendung von neun verschiedenen M_2[**A**]-Salzen (Katalysatorladung: 37 mol%, 1 atm H_2, THF-d_8, 100 °C, 16 h).

M_2[**A**]	$M^+ = Li^+$	$M^+ = Na^+$	$M^+ = K^+$
M_2[**72**]	11	1	1
M_2[**68**]	97	27	1
M_2[**79**]	3	0	0

Insgesamt zeigte sich ein zur Geschwindigkeit der H_2-Addition gegenläufiger Trend, da gerade die Li^+-Salze höhere Umsatzraten als ihre schwereren Homologen lieferten. Zum einen werden die H_2-Additionsprodukte in der Reihe der Alkalimetalle von oben nach unten thermodynamisch immer günstiger (vgl. Abbildung 11), verbunden mit einer abnehmenden Triebkraft, in ein H_2-Additions-/Eliminierungs-Gleichgewicht einzutreten. Zum anderen heißt das auch, dass gerade die Li_2[**A**]-Salze stabile Strukturen darstellen, deren Regeneration durch H_2-Transfere energetisch bevorzugt ist.

Der deutliche Unterschied in der Aktivität von Li_2[**72**] gegenüber Li_2[**68**] wird durch eine Nebenreaktion verursacht, weil diese Salze mit Ph(H)C=N*t*Bu die [4+2]-Cycloadditionsprodukte Li_2[**85**] bzw. Li_2[**86**] bilden (Abbildung 15). Diese erinnern an die Umsetzung von Li_2[**72**] mit 4,4‘-Dimethylbenzophenon zu Li_2[**73**] (vgl. Schema 31), das einen ähnlichen NMR-Signalsatz erzeugt.[123] Im Festkörper konnte die *N*-protonierte Form von Li_2[**86**], [Li(12-c-4)$_2$][**86**-H], isoliert werden. Vermutlich steigerte die Zugabe des Kronenethers zum Kristallisationsansatz die Basizität des Stickstoffatoms, das damit sehr sensitiv gegenüber Restfeuchtigkeit wurde. Li_2[**68**] verfügt im Vergleich zu Li_2[**72**] über eine gesteigerte Kataly-

satoraktivität, weil bei den erhöhten Temperaturen der Hydrierungsreaktionen von 100 °C Li_2[**86**] stärker als Li_2[**85**] im Gleichgewicht mit den jeweiligen Edukten steht (Abbildung 15). Der große *p*Tol-Substituent in Li_2[**79**] verhindert zwar die Bildung eines [4+2]-Cycloadditionsprodukts der Form Li_2[**B**], scheint aber die Annäherung von Ph(H)C=N*t*Bu an Li_2[**79**-H_2] nicht hinreichend gut zu gewährleisten, damit überhaupt eine Hydrierung stattfinden kann.

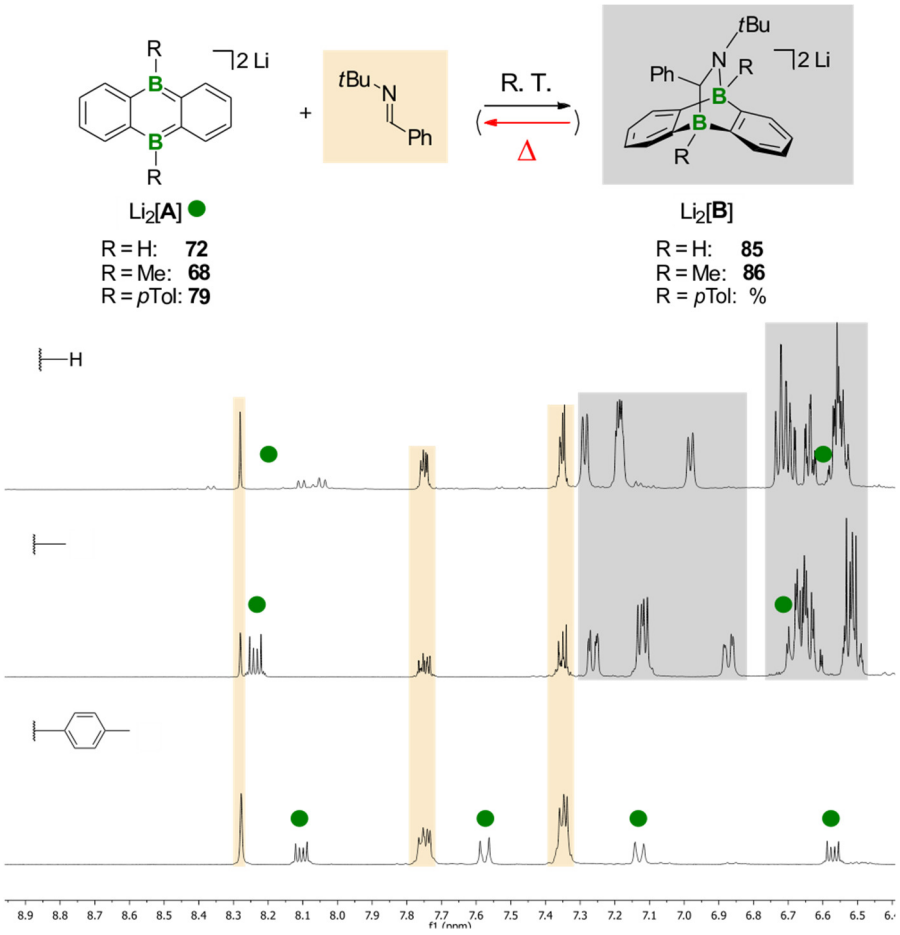

Abbildung 15. Vergleich der Wechselwirkungen von Li_2[**A**] und Ph(H)C=N*t*Bu in Abhängigkeit vom borgebundenen Substituenten (R = H, Me, *p*Tol). ^{1}H-NMR-Spektren (500.2 MHz, THF-d_8) der jeweiligen 1:1 Mischungen wurden unmittelbar nach der Probenpräparation bei Raumtemperatur aufgenommen.

Mit nur 10 mol% Li_2[**68**] als Katalysator gelang die erfolgreiche Darstellung von $Ph(H)_2C$–N(H)*t*Bu im 100 mL Reaktionsautoklaven (7 bar H_2, THF, 100 °C, 18 h), was die generelle Übertragbarkeit dieses Systems auf einen präparativen Maßstab veranschaulicht. Um die Substratpalette auszuloten, dienten die in Abbildung 16 gezeigten Vertreter verschiedenster Substanzklassen als Reaktionspartner für Li_2[**68**]/H_2. Neben dem Imin Ph(H)C=N*t*Bu konnten das terminale Alken $Ph_2C{=}CH_2$ und der Aromat Anthracen hydriert werden. Die anderen Substrate wurden nicht hydriert, da sie entweder inert gegenüber Li_2[**68**]/H_2 blieben oder stabile [4+2]-Cycloadditionsprodukte mit Li_2[**68**] bildeten (weitere Informationen dazu in Abschnitt 2.3.1.). Die Abstimmung des sterischen Anspruchs der borgebundenen Substituenten und der Substrate ist folglich entscheidend, um eine erfolgreiche Hydrierung mit H_2 und katalytischen Mengen von Li_2[**A**] zu erzielen. Neben dem Raumanspruch der beteiligten Komponenten können auch elektronische Faktoren von Bedeutung sein: Im Fall des etablierten H_2-Donors 9,10-Dihydroanthracen, dem neutralen Analogon von [**A**]$^{2-}$ ist

generell akzeptiert, dass die Abgabe von H_2 in zwei Stufen abläuft, initiiert durch einen $H^{\bullet}$-Atom- oder H^--Ion-Transfer.[136, 137] Für [**A**-H_2]$^{2-}$ sollte aufgrund der polaren B–H-Bindung ein ionischer Mechanismus favorisiert sein. Die Annahme eines H^--Ion-Transfers im ersten Schritt würde auch erklären, warum 1-(1-Piperidinyl)cyclohexen von [**68**-H_2]$^{2-}$ nicht hydriert wird, da die resultierende negative Ladung nicht hinreichend stabilisiert wäre. Für FLPs hingegen bereitet dieses Substrat keine Schwierigkeiten, da diese zuerst ein H^+-Ion übertragen.[39]

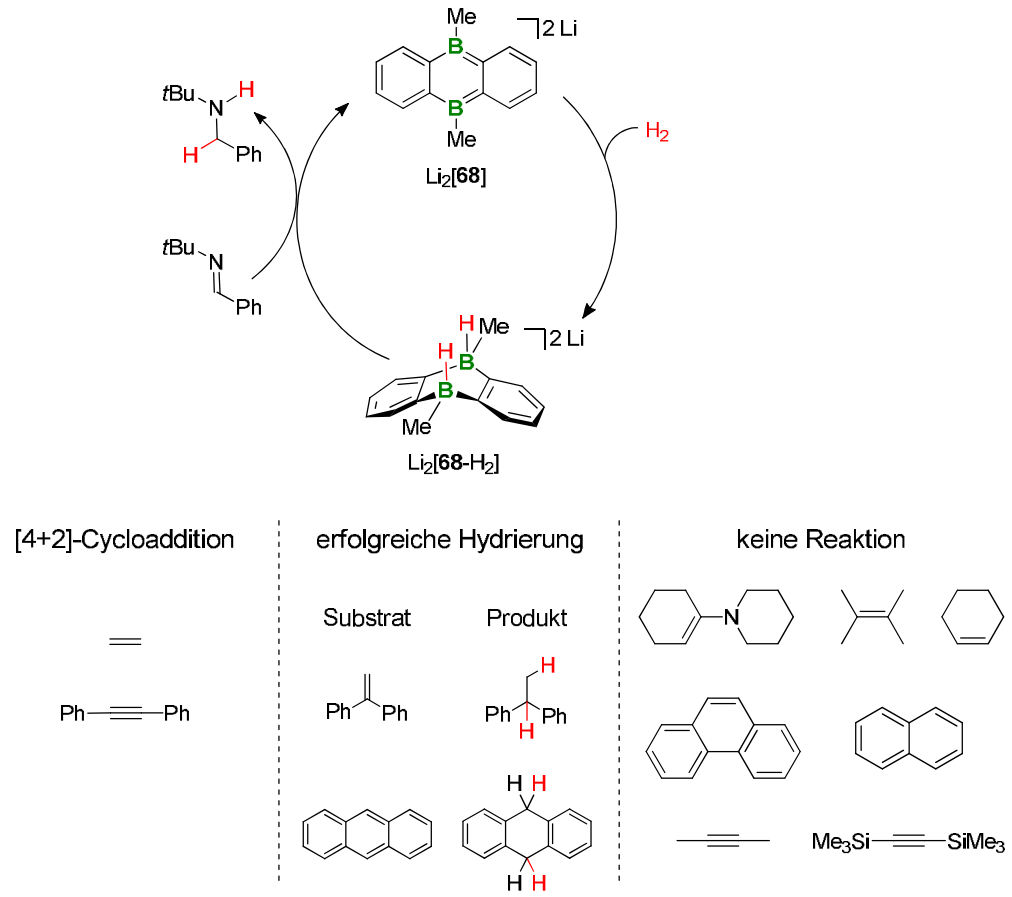

Abbildung 16. Katalytischer Kreislauf für Li_2[**68**] als Hydrierungskatalysator (oben). Die ausgewählten Substrate bildeten entweder [4+2]-Cycloadditionsprodukte (links), konnten erfolgreich hydriert werden (Mitte) oder zeigten keine Reaktion (rechts).

2.3. Aktivierung von Mehrfachbindungen mit M_2[**68**]

2.3.1. [4+2]-Cycloadditionsprodukte von M_2[**68**]

Die Salze M_2[**68**] verhalten sich wie Diene in einer klassischen Diels-Alder-Reaktion, wenn sie in Kontakt mit Mehrfachbindungen kommen, sodass [4+2]-Cycloadditionsprodukte des Typs Li_2[**B**] (vgl. Abbildung 15) gebildet werden. Die folgenden Ergebnisse berücksichtigen jeweils THF-d_8-Lösungen mit 1:1-Mischungen von M_2[**68**] mit dem genannten Substrat, wenn dieses eine Flüssigkeit oder ein Feststoff war. Gasförmige Dienophile wurden stets im Überschuss eingesetzt. An den praktischen Arbeiten waren unter meiner Anleitung die Studenten Sven E. Prey, Maximiliane Horz und Felix Nawa beteiligt.

Unter den getesteten Substraten mit **Doppelbindungen** lieferte eine Umsetzung von Li_2[**68**] mit Ethen das Bicyclo[2.2.2]-Addukt Li_2[**87**], dessen Strukturbeleg mittels Röntgendiffraktometrie am Einkristall erfolgte (Abbildung 17). Versuche zur Nutzung von Li_2[**87**] als Reagenz in einer Hydroaminierung von Ethen mit $Ph(H)_2C–N(H)tBu$ oder einer Hydrosilylierung mit Et_3SiH waren nicht zielführend. Bei der Variation der Reaktionsbedingungen wurde jedoch eine Freisetzung von Ethen aus Li_2[**87**] durch Bestrahlung mit einer Hg-Dampflampe beobachtet. Wird Butadien als Reaktionspartner von Li_2[**68**] eingesetzt, sind die NMR-Daten der Reaktionslösung im Einklang mit dem Strukturmotiv von Li_2[**88**] in Abbildung 17. Mit der gewählten 1:1 Stöchiometrie blieb die terminale Doppelbindung unberührt, was sich beim Einsatz von Li_2[**68**] im Überschuss ändern könnte.

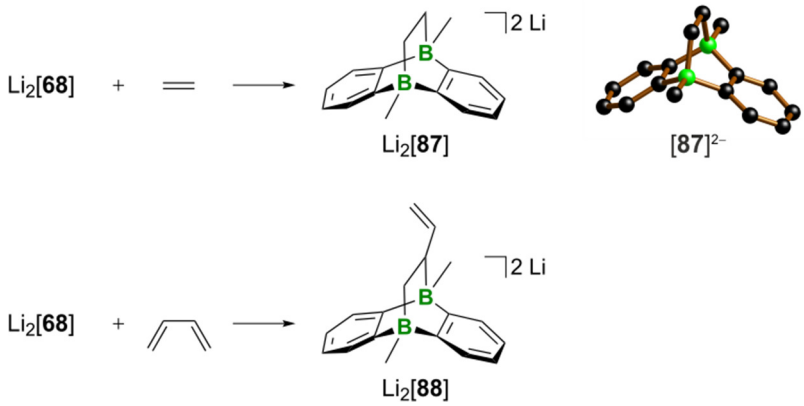

Abbildung 17. Reaktivität von Li_2[**68**] gegenüber Alkenen, sowie die Festkörperstruktur des Dianions von [Li(12-c-4)(thf)][Li(12-c-4)][**87**]. H-Atome sind nicht dargestellt.

Mit Li_2[**72**] anstelle von Li_2[**68**] war die Addition von Ethen ebenfalls möglich. Allerdings war die Reaktionsgeschwindigkeit bei Raumtemperatur niedriger, sodass erst eine Lagerung der Probe bei 50 °C über Nacht zur vollständigen Bildung von Li_2[**89**] führte (Schema 37). Durch die Zugabe von Me_3SiCl zu Li_2[**89**] konnten die H-Atome an den tetrakoordinierten Boratomen entfernt werden. Aufgrund der Durchführung der Reaktion in THF-Lösung lag das Produkt **90** vermutlich als THF-Addukt vor ($\delta(^{11}B)$ = 11.0 ppm; Schema 37). Bemühungen, Li_2[**89**] im nicht-koordinierenden Lösungsmittel Benzol darzustellen, scheiterten an der erfolglosen Reduktion von (**72**)$_n$ unter diesen Bedingungen. Die Reduktion von **90**·(2 THF) mit elementarem Lithium in THF-Lösung zerstörte das DBA-Grundgerüst. Von einer Untersuchung der Lewis-Azidität von **90**·(2 THF) wurde abgesehen, weil dessen Reinheit durch die Gegenwart von 9,10-Diethyl-DBA (**77**) als Nebenkomponente (ca. 10%) beeinträchtigt war. Um die Bildung dieses Nebenprodukts zu verstehen, muss man berücksichtigen (Schema 37),

dass das Edukt Li_2[**72**] auf dem gewählten Syntheseweg nicht frei von Li_2[**72**-H_2] hergestellt werden kann, was mit der Ausbildung von Koordinationspolymeren (**72**)$_n$ in Zusammenhang steht,[128, 129] jedoch beim Einsatz von Li_2[**72**] als Hydrierungskatalysator nicht stört. Im weiteren Reaktionsverlauf ist Li_2[**72**-H_2] zwar inert gegenüber Ethen, aber nicht gegenüber einer H^--Abstraktion durch Me_3SiCl, sodass überschüssig vorliegendes Ethen durch das entstehende **72**·(2 THF) hydroboriert wird.

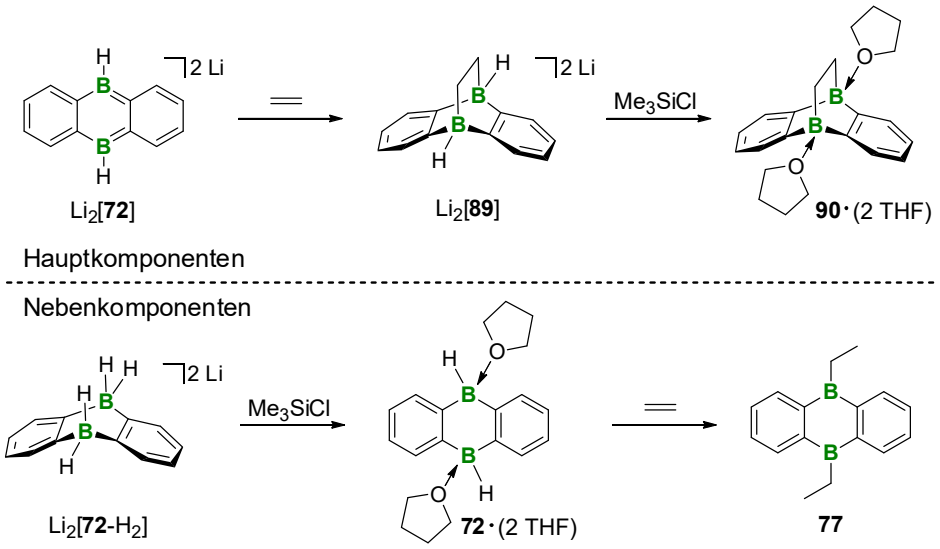

Schema 37. Die Darstellung von **90**·(2 THF) in Reinform, ausgehend von Li_2[**72**] durch 1. Ethen und 2. Me_3SiCl, ist aufgrund der Nebenkomponente Li_2[**72**-H_2] erschwert.

Die Umsetzung der **Alkine** PhC≡CPh und pinBC≡CBpin mit Li_2[**68**] ermöglichte die Darstellung der [4+2]-Cycloadditionsprodukte Li_2[**91**] bzw. Li_2[**92**] (Abbildung 18).

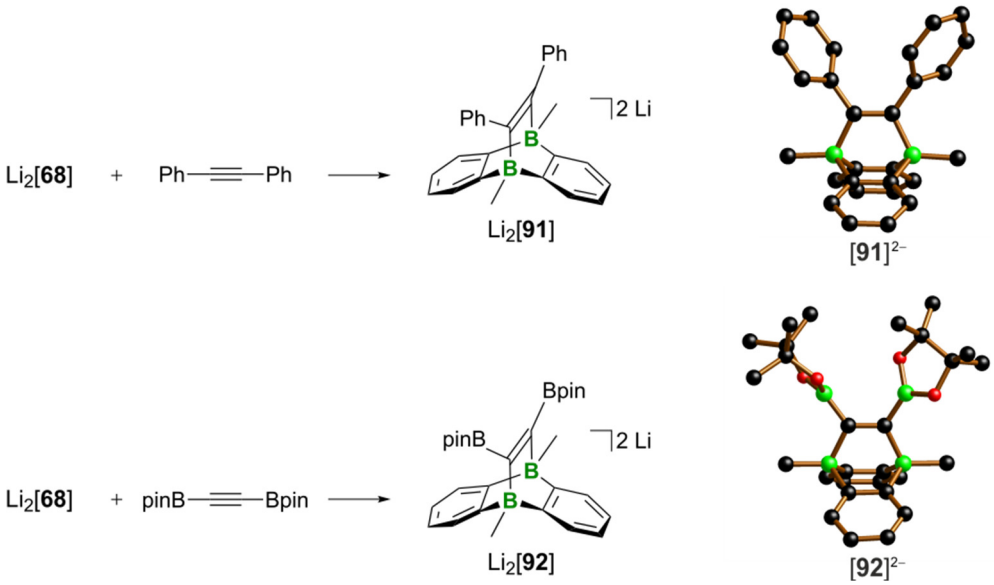

Abbildung 18. Reaktionsprodukte von Li_2[**68**] mit Alkinen sowie dazugehörige Festkörperstrukturen der Dianionen von [Li(12-c-4)(thf)]$_2$[**91**] und [Li(12-c-4)(thf)]$_2$[**92**](THF). H-Atome sind nicht dargestellt.

Eine Verknüpfung der Phenylringe in Li_2[**91**] durch Anwendung gängiger Cyclisierungsprotokolle (Luftsauerstoff, I_2/Propylenoxid)[138] führte nicht zum Aufbau eines Trypticen-Analogons.

Die Reaktivität von **polaren Doppelbindungen** mit M_2[**68**] (M^+ = Li^+, Na^+) wurde untersucht, um einen Strukturbeleg für die von Andreas Lorbach veröffentlichte Verbindung Li_2[**73**] (vgl. Schema 31) zu erhalten. Mischungen der Carbonylverbindungen Benzophenon bzw. Aceton mit M_2[**68**] lieferten die Strukturmotive M_2[**93**] bzw. M_2[**94**] (Abbildung 19), die das auf Basis von NMR-Daten postulierte Verknüpfungsmuster von Li_2[**73**] bestätigten. Die Reihe ergänzen die [4+2]-Cycloadditionsprodukte M_2[**95**] des Carbodiimids *i*PrN=C=N*i*Pr mit M_2[**68**]. Die Einkristallröntgenstruktur des Natriumsalzes [Na][Na(18-c-6)(thf)$_2$][**95**] zeigte, dass die Überbrückung der Boratome über eine N–C-Einheit erfolgt.

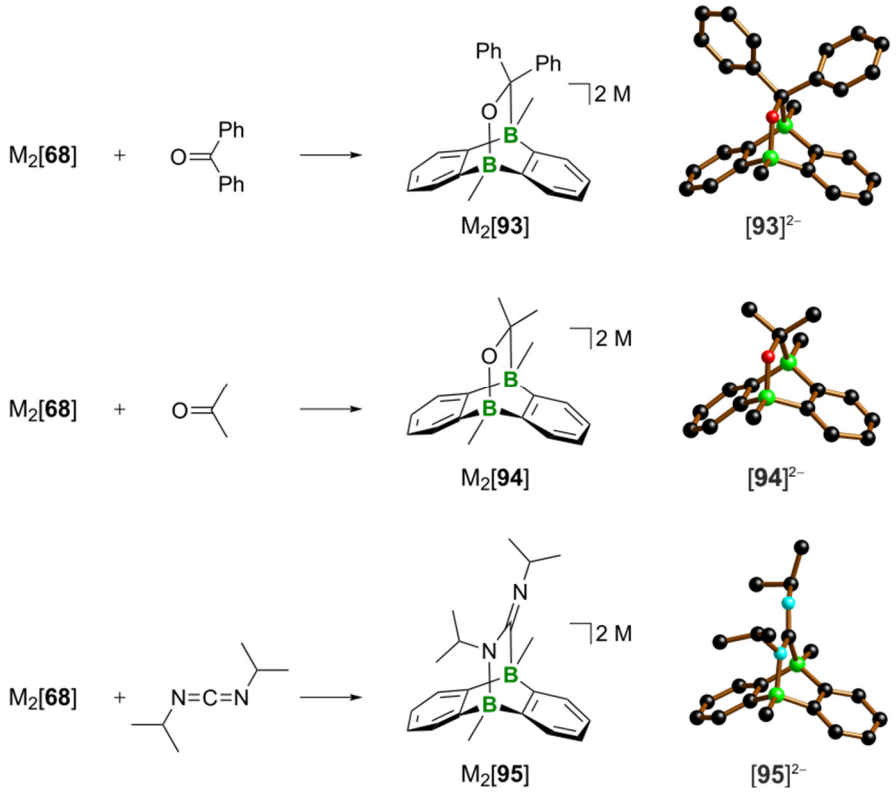

Abbildung 19. Reaktionsprodukte von M_2[**68**] mit Carbonylverbindungen und einem Carbodiimid sowie die dazugehörigen Festkörperstrukturen der Dianionen von [Li(12-c-4)(thf)][Li(thf)$_2$][**93**](THF), [Na(thf)$_2$][Na(thf)][**94**] und [Na][Na(18-c-6)(thf)$_2$][**95**]. H-Atome sind nicht dargestellt; M^+ = Li^+, Na^+.

Keine Diels-Alder-Produkte wurden bei Umsetzungen von Li_2[**68**] mit Anthron bzw. Dimethylsulfoxid erhalten. In einer Säure-Base-Reaktion deprotoniert Li_2[**68**] das Anthron, wie die erhaltene Festkörperstruktur von Lithiumanthrolat Li[**96**] belegte (Abbildung 20). Passend dazu konnten die Resonanzen für Li[**68**-H], der monoprotonierten Form von Li_2[**68**], in den ^{1}H- und ^{11}B-NMR-Spektren zugeordnet werden. Unklar bleibt, wie Dimethylsulfoxid mit Li_2[**68**] das Bicyclo[2.2.2.]-Produkt Li[**97**] bildet (Abbildung 20). In Anlehnung an die vorhergehende Umsetzung wäre ein Deprotonierungs-Protonierungs-Mechanismus vorstellbar, der durch Li_2[**68**] unterstützt wird. Formal könnte dadurch ein „$[MeS{=}CH_2]^+$“-Äquivalent freigesetzt werden, das eine [4+2]-Cycloadditionsreaktion mit Li_2[**68**] nach üblichem Muster einginge. Um die Stoffbilanz der Reaktion auszugleichen, sollte zudem LiOH entstehen.

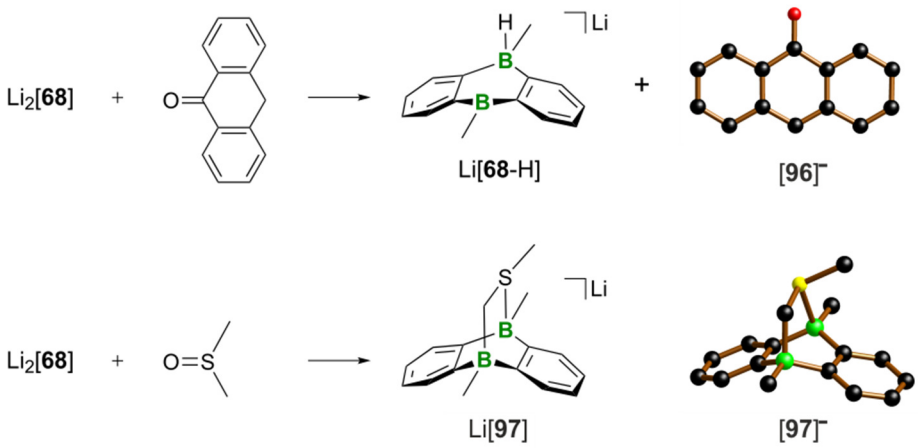

Abbildung 20. Reaktionsprodukte von Li_2[**68**] mit Anthron und Dimethylsulfoxid sowie die dazugehörigen Festkörperstrukturen der Anionen von [Li(thf)$_2$][**96**] und [Li(12-c-4)$_2$][**97**](12-c-4). H-Atome sind nicht dargestellt.

2.3.2. Reaktionen von M_2[**68**] mit CO_2

Die Umsetzung von Li_2[**68**] mit einem Überschuss an CO_2 blieb nicht auf der Stufe eines Bicyclo[2.2.2]-Additionsprodukts stehen, sondern lieferte **68**, CO und Li_2CO_3 (Schema 38). Die selektive Reaktion fand zügig bei Raumtemperatur statt und die entstandenen Produkte konnten mithilfe der NMR-Spektroskopie und Röntgenpulverdiffraktometrie im Masterpraktikum von Sven E. Prey unter meiner Anleitung eindeutig nachgewiesen werden. Im NMR-Maßstab war der Umsatz von Li_2[**68**] immer quantitativ und auch bei der Durchführung im Young-Hahn-Gefäß gelang Maximiliane Horz die Isolierung von Li_2CO_3 in 83% der theoretischen Ausbeute. Der Erhalt des DBA-Grundgerüsts ermöglichte über eine anschließende Reduktion der Neutralverbindung **68** eine pseudo-katalytische Reaktionsführung.

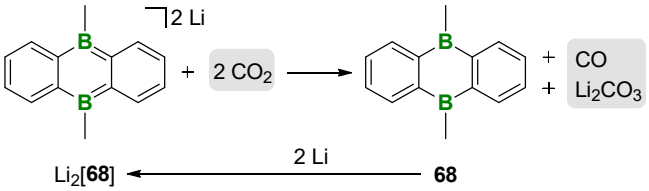

Schema 38. Selektive Umwandlung von CO_2 durch Li_2[**68**] in CO und Li_2CO_3 (1 atm CO_2, THF, Raumtemperatur). Das neutrale **68** kann erneut reduziert werden und damit als pseudo-Katalysator fungieren.

Da die Wahl des Kations bei der Aktivierung von H_2 besonders entscheidend war (vgl. Abschnitt 2.1.2.), wurde auch Na_2[**68**] mit CO_2 versetzt. Wie zuvor trat eine CO-Gasentwicklung ein, wohingegen die Bildung von **68** ausblieb. Stattdessen entstand der mit einem $[CO_3]^{2-}$-Ion überbrückte Komplex Na_2[**100**], wie eine Röntgenstrukturanalyse von entsprechenden, unmittelbar aus der Reaktionslösung gewonnen, Einkristallen bestätigte (Abbildung 21). Offensichtlich beeinflusst die höhere Gitterenergie von Li_2CO_3 im Vergleich zu Na_2CO_3 (ΔU_{POT} = 2523 *vs.* 2301 kJ mol^{-1})[139] die Thermodynamik der Reaktion, sodass Ersteres ausfällt und Letzteres an **68** koordiniert.

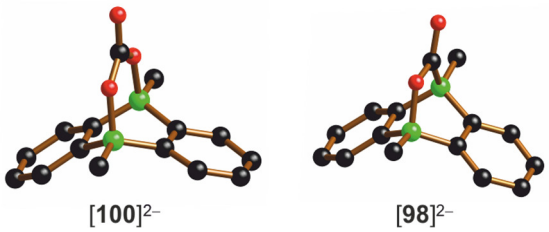

Abbildung 21. Festkörperstrukturen der Anionen von $[Na_8(thf)_{14}][\mathbf{100}]_4$ und $[Na][Na_3(thf)_6][\mathbf{98}]_2$. H-Atome sind nicht dargestellt.

Um den zugrundeliegenden Mechanismus zu verstehen, wurde $M_2[\mathbf{68}]$ mit nur einem Äquivalent CO_2 umgesetzt. Die NMR-Spektren der Reaktionslösungen zeigten Signalsätze, die zu [4+2]-Cycloadditionsprodukten des Typs $M_2[\mathbf{98}]$ passen. Der Strukturvorschlag wurde durch eine Einkristallröntgenstrukturanalyse von $[Na][Na_3(thf)_6][\mathbf{98}]_2$ bestätigt (Abbildung 21). Generell sei an dieser Stelle angemerkt, dass nicht nur das Konzept einer Diels-Alder-Reaktion, sondern auch die mesomere Grenzstruktur $M_2[\mathbf{68}^*]$ mit ambiphilen Boratomen als Erklärung für die Bildung solcher Strukturmotive nützlich sein kann (Schema 39). In $M_2[\mathbf{68}^*]$ agiert ein Boratom als Nukleophil und das andere als Elektrophil, die jeweils eine entsprechende Akzeptor- bzw. Donorstelle im CO_2-Molekül finden, was zur Entstehung von $M_2[\mathbf{98}]$ führt. Bringt man $M_2[\mathbf{98}]$ mit einem Überschuss an CO_2 in Kontakt, so werden die zuvor beschriebenen Produkte erhalten. Dies ist als Nachweis für die Rolle von $M_2[\mathbf{98}]$ als Intermediate bei der Umsetzung von $M_2[\mathbf{68}]$ und CO_2 zu werten.

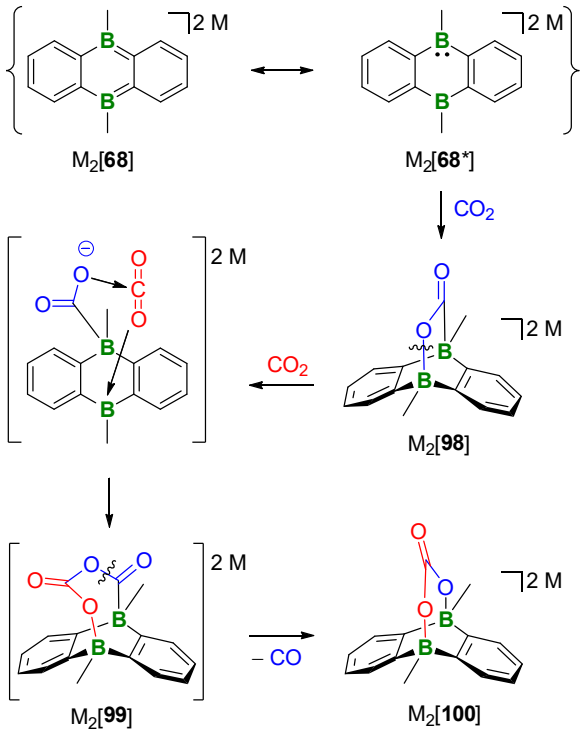

Schema 39. Vorgeschlagener Mechanismus für die Reaktion von $M_2[\mathbf{68}]$ ($M^+ = Li^+, Na^+$) mit CO_2.

Eine schwache B–O-Bindung in $M_2[\mathbf{98}]$ bietet sich dabei als Angriffspunkt für ein zweites CO_2-Molekül an: Nach heterolytischem B–O-Bindungsbruch könnte das resultierende, kurzlebige B/O-FLP CO_2 in bekannter Weise aktivieren und Verbindung $M_2[\mathbf{99}]$ hervorbringen. Das enthaltene $[R_3B–O–C(O)–O–C(O)–BR_3]^{2–}$-Fragment findet seine Entsprechung in gemischten Kohlensäure-Carbonsäure-Anhydriden $R_3C–O–C(O)–O–C(O)–CR_3$, die oft sehr in-

stabil sind.[140] Die schnelle Zersetzung von [**99**]$^{2-}$ erlaubte keine NMR-spektroskopische Charakterisierung der Verbindung, sodass quantenchemische Rechnungen durchgeführt wurden, um die Struktur von [**99**]$^{2-}$ als lokales Minimum zu validieren. Angesichts der Freisetzung von CO aus [**99**]$^{2-}$ sind unterschiedliche C(sp^2)–O-Bindungslängen in der zentralen C–O–C-Einheit der berechneten Struktur mit der beobachteten Bruchstelle im Einklang. Das verbleibende $[CO_3]^{2-}$-Ion nimmt im Falle von M^+ = Na^+ eine B···B-verbrückende Position ein oder wird für M^+ = Li^+ in Form von Li_2CO_3 gefällt.

Limberg und Mitarbeiter beschriebenen einen vergleichbaren Reaktionspfad für einen Mangankomplex, der CO_2 nukleophil angreift, sodass ein [Mn(I)-CO_2]$^-$-Anion entsteht.[141] Die Aufnahme eines zweiten CO_2-Moleküls erweitert die Carboxylateinheit in diesem Komplex, wie in Schema 40 zu sehen ist. Die erhaltene [O–C(O)–O–C(O)–Mn]$^-$-Kette zerfällt in $[CO_3]^{2-}$ und [Mn(I)-CO]$^+$.

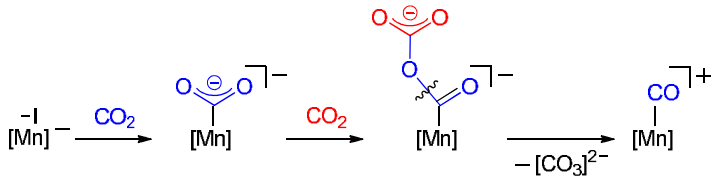

Schema 40. Umwandlung von CO_2 mit einem anionischen Mangankomplex.

Als weiterer Hinweis für das Intermediat [**99**]$^{2-}$ wurde ein Derivatisierungsansatz gewählt, bei dem das zu M_2[**98**] verwandte, Aceton-überbrückte DBA-Salz Na_2[**94**] als Ausgangsverbindung diente (vgl. Abbildung 19). Na_2[**94**] reagierte mit einem Äquivalent CO_2 zu einer stabilen Verbindung, deren NMR-Daten im Einklang mit dem Strukturvorschlag Na_2[**101**] sind (Schema 41). Der formale Austausch der borgebundenen CO-Einheit in [**99**]$^{2-}$ durch „CMe_2“ begründet die Beständigkeit von [**101**]$^{2-}$, da die bei [**99**]$^{2-}$ beobachtete Extrusion von CO nicht mehr möglich ist.

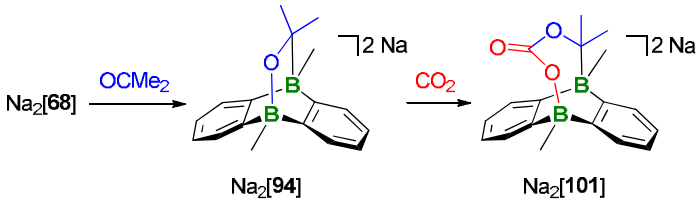

Schema 41. Synthese der Modellverbindung Na_2[**101**] über die Reaktion von Na_2[**68**] mit Aceton und CO_2.

2.4. M_2[**A**] als H^--Transferkatalysatoren

Die reversible Aufnahme von H_2 durch M_2[**A**] ermöglicht deren Einsatz als Hydrierungskatalysatoren, wie in Abschnitt 2.2. erläutert. Eine klassische Betrachtung der H_2-Aktivierungsprodukte M_2[**A**-H_2] ordnet diese als Hydridoborate ein, womit der hydridische Charakter der borgebundenen H-Substituenten unterstrichen wird. In der organischen Synthese dienen vergleichbare Hydridoborate wie $Na[BH_4]$ oder $Li[B(H)Et_3]$ als gängige H^--Quellen, um geeignete Abgangsgruppen zu ersetzen.[142] Die genannten Reagenzien sind selektiv, jedoch nicht besonders atomökonomisch, da sie nur stöchiometrisch eingesetzt werden können. Unter diesem Aspekt bietet das System M_2[**A**-H_2] den Vorzug, dass die neutralen DBA-Grundgerüste **A** nach der Abgabe von zwei H^--Ionen erhalten bleiben und damit die Grundlage für deren erneute Verwertung legen. Die Reduktion von **A** regeneriert die Salze M_2[**A**] (a), die wiederum H_2 aufnehmen (b) und in der hydrierten Form [**A**-H_2]$^{2-}$ als H^--Donoren zur Verfügung stehen (c; Abbildung 22). Geeignete Substrate in H^--Transferreaktionen sind allgemein Elektrophile, wobei vor allem Verbindungen mit E–X-Bindungen in der vorliegenden Arbeit verwendet wurden (X = Halogen).

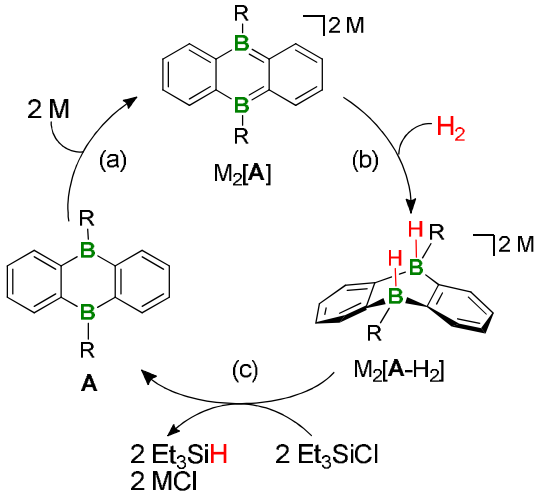

Substrat	EtBr	Me_3SiCl	Ph_2SiCl_2	ECl_4	PCl_3	CO_2
Produkt	EtH	Me_3SiH	Ph_2SiH_2	EH_4	PH_3	HCO_2Na
				E = Si, Ge		

Abbildung 22. Kreisprozess für die Umwandlung von Et_3SiCl zu Et_3SiH mit M_2[**A**-H_2] als H^--Donoren (oben). Mit Na_2[**68**] konnten die aufgelisteten Substrate in gezeigter Weise hydriert werden (unten).

Die Reaktivität von M_2[**A**] gegenüber den Edukten und Produkten ist maßgebend für eine schrittweise Durchführung der Reaktionssequenz, die in Abbildung 22 mit Et_3SiCl als Substrat dargestellt ist: Parallel können die einzelnen Reaktionsschritte (a) – (c) nicht geführt werden, weil ansonsten unerwünschte Wechselwirkungen zwischen den Komponenten auftreten würden. Mit Elektrophilen wie Et_3SiCl reagieren M_2[**A**] als Nukleophile, sodass ein Boratom tetrakoordiniert wird (vgl. Abschnitt 2.6.3.) und M_2[**A**] als Katalysator vergiftet ist. Eine stöchiometrische Zugabe des Elektrophils zu M_2[**A**-H_2] garantiert, dass kein überschüssiges Substrat (z. B. Et_3SiCl) bei der anschließenden Reduktion von **A** vorliegt, welches die Regeneration von M_2[**A**] behindert. Auf diese Weise kann die Reaktionsabfolge (a) – (c) aus Abbildung 22 als Kreisprozess realisiert werden, sofern das hydrierte Produkt (z. B. Et_3SiH)

keine Wechselwirkungen mit M_2[**A**] oder **A** eingeht. Eine derartige Trennung von Reaktionsschritten wird auch beim industriellen Anthrachinon-Prozess eingehalten, da zuerst reduktive und dann oxidative Bedingungen bei der Darstellung von H_2O_2 notwendig sind (1. Hydrierung von Anthrachinon; 2. Oxidation von Anthrahydrochinon).[143]

Die sequentielle Reaktionsabfolge ist besonders effizient, wenn alle Teilschritte selektiv, schnell und quantitativ verlaufen. Die Reduktion von **A** (a) und der H^--Transfer mit M_2[**A**-H_2] (c) entsprechen diesen Kriterien unabhängig vom borgebundenen Substituenten und dem verwendeten Kation. Kleine borgebundene Substituenten und große Kationen begünstigen eine zügige Addition von H_2 an M_2[**A**] (b; vgl. Abschnitte 2.1.1. und 2.1.2.). Aufgrund der einfachen Synthese von Na_2[**68**-H_2] bot sich dieses Derivat als H^--Donor in besonderer Weise an: CO_2 konnte durch H^--Aufnahme zu Natriumformiat reduziert und verschiedene Tetrelhalogenide sowie PCl_3 als Vertreter der Pniktogenhalogenide konnten durch einen H/Halogen-Austausch hydriert werden (Abbildung 22). Eine Anreicherung der hydrierten Produkte über mehrere Katalysezyklen ist für Ethan als Kohlenwasserstoffverbindung, die untersuchten Silane und GeH_4 möglich. Das Formiat-Ion überbrückt das neutrale DBA **68** und auch PH_3 interagiert mit dessen Lewis-sauren Boratomen, was in diesen Fällen die Regeneration von Na_2[**68**] einschränkt. Ein Vorteil des Natriumsalzes Na_2[**68**-H_2] ist zudem, dass die Lewis-basischen Halogenid-Abgangsgruppen der Elektrophile dem Reaktionsgemisch durch Niederschlagsbildung (NaCl) entzogen werden.

Unabhängig von der Anzahl der zu ersetzenden Halogenfunktionen war eine hohe Selektivität des H^--Transfers mit Na_2[**68**-H_2] zu beobachten, da alle Halogenid-Substituenten der jeweiligen Substrate durch Hydride ausgetauscht wurden. Die Umsetzung von Na_2[**68**-H_2] mit einem Äquivalent Et_3SiCl legt einen schrittweisen ionischen Mechanismus für die H^--Übertragung nahe, da das unsymmetrische DBA-Derivat Na[**68**-H] mit nur einem verbleibenden H^--Substituenten isolierbar war. Mechanistisch könnte intermediär die fünffach koordinierte Silicium-Spezies Na[$Et_3Si(H)Cl$] vorliegen, aus der NaCl anschließend eliminiert wird.

Bei Verwendung einer 1:2 Stöchiometrie bei der Umsetzung von Na_2[**68**-H_2] mit Me_2SiCl_2 wird zunächst ein Äquivalent vollständig zu Me_2SiH_2 hydriert (Schema 42). Zusammen mit dem verbleibenden Me_2SiCl_2 tritt dann jedoch eine Komproportionierungsreaktion ein, die $Me_2Si(H)Cl$ hervorbringt, einen wichtigen Baustein für den Aufbau von vernetzten Silikonen.[144] Es ist bekannt, dass Lewis-Säuren solche Umwandlungen katalysieren;[145] im vorliegenden Fall dürfte dem neutralen DBA **68** diese Rolle zukommen.

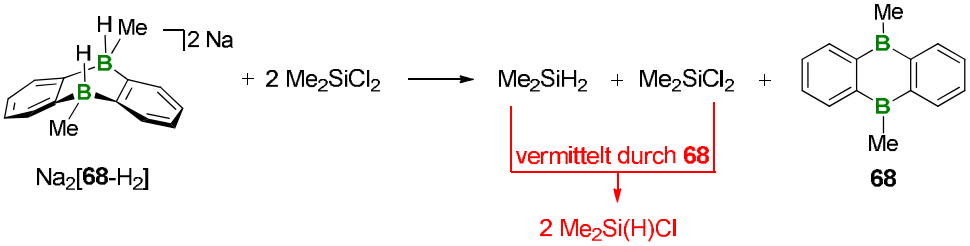

Schema 42. Na_2[**68**-H_2] wird nach H^--Abgabe an Me_2SiCl_2 in der neutralen Form **68** zum Komproportionierungs-Katalysator für Me_2SiH_2 und verbliebenes Me_2SiCl_2, sodass $Me_2Si(H)Cl$ entsteht.

2.5. Elektrochemische Reduktion von **68**

Beim Einsatz von Na_2[**68**-H_2] als H^--Quelle bildet sich das neutrale **68** nach Abgabe beider H^--Ionen. Eine Reduktion von **68** ermöglicht die erneute Nutzung des DBA-Gerüsts für eine H_2-Aufnahme, sodass Na_2[**68**-H_2] regeneriert wird. In diesem Abschnitt soll geklärt werden, ob allein Alkalimetalle für diesen Reduktionsschritt in Frage kommen oder ob eine Elektrode in einem Elektrolyseexperiment ebenso als Elektronenquelle dienen kann. Eine elektrochemische Realisierung würde den H^--Transfer-Kreislauf in einer sicherheitstechnischen Betrachtung des Prozesses attraktiver machen.

Erste Hinweise auf eine elektrochemische Reduzierbarkeit von **68** liefert dessen Cyclovoltammogramm, das zwei Reduktionsereignisse beinhaltet, wobei der zweite Redoxprozess irreversibel ist (Abbildung 23; referenziert gegen FcH/FcH^+, THF, 0.1 M [^{n}Bu_4N][PF_6]). Das erste Elektrodenhalbstufenpotential $E_{1/2}^{Red1}$ beträgt –2.02 V und das Peakpotential der zweiten Reduktion –2.77 V.

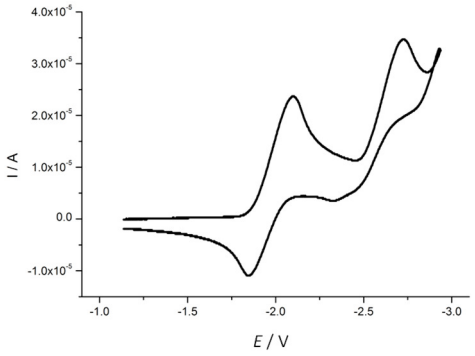

Abbildung 23. Cyclovoltammogramm von **68** in THF (*vs.* FcH/FcH^+, Raumtemperatur, Leitsalz: 0.1 M [^{n}Bu_4N][PF_6], Vorschubgeschwindigkeit: 200 mV s^{-1}).

Im Zuge der Elektrolyseexperimente wurde zunächst überprüft, welche Lösungsmittel verwendbar sind, um die Leitfähigkeit des Systems zu erhöhen. Ein Ersatz von THF war nicht möglich, da [**68**]$^{2-}$ mit Acetonitril, DMF und DMSO reagiert (vgl. Abschnitt 2.3.1.). Die Leitfähigkeit von aprotischen Lösungsmitteln wird durch die Zugabe von Leitsalzen erreicht. Deren Auswahl ist zum einen durch ihre Löslichkeit in THF und zum anderen durch die Kompatibilität mit dem reaktiven Dianion [**68**]$^{2-}$ begrenzt. Bei der Wahl des Leitsalz-Anions erwies sich nur $[BPh_4]^-$ als geeignet, da andere gängige Anionen,[146] wie $[ClO_4]^-$ oder $[NO_3]^-$, aufgrund ihrer oxidierenden Wirkung ausschieden. Die Verwendung von $[PF_6]^-$ oder $[BF_4]^-$ führte zur Polymerisation von THF an der Anode, weil die Zersetzungsgrenze des Lösungsmittels früher als die des Leitsalz-Anions erreicht wurde.[147] Die THF-Polymerisation konnte zwar durch den Zusatz von löslichen Ammoniumhalogeniden wie [^{n}Bu_4N]Br unterdrückt werden,[148] die bereitwilliger oxidieren; die entstehenden Oxidationsprodukte reagierten aber mit der reduzierten DBA-Spezies. Über Li[PF_6] ist außerdem bekannt, dass dieses Salz selbst bei Raumtemperatur im Gleichgewicht mit LiF und PF_5 vorliegt, das durch die Freisetzung des gasförmigen PF_5 begünstigt wird.[149, 150] Um die Auswirkungen dieses Gleichgewichts auf die Inertheit von $[PF_6]^-$-Ionen gegenüber Na_2[**68**] zu testen, wurden die beiden Komponenten in einer THF-Lösung vereint. Die resultierende Entfärbung der zuvor grünen Na_2[**68**]-Lösung belegt die Unverträglichkeit von $[PF_6]^-$-Ionen mit dem Dianion [**68**]$^{2-}$. Als Leitsalz-Kationen sind Alkalimetall- oder Tetraalkylammonium-Ionen geläufig.[146] Bei der Reduktion von [**68**]$^{2-}$ dienen diese Kationen auch dazu, dessen negative Ladung als Gegenkationen zu

stabilisieren. Das dominante Strukturmotiv eines inversen Sandwich-Komplexes für M_2[**A**] (vgl. Abbildung 9) besteht in Lösung für M^+ = Li^+, Na^+ und K^+, wohingegen das schwachkoordinierende [^{n}Bu$_4$N]$^+$-Kation nicht zur Stabilisierung von [**68**]$^{2-}$ fähig war. Ein korrespondierender Versuch, Li_2[**68**] mit [^{n}Bu$_4$N]F umzusalzen, blieb erfolglos. Da sich Na_2[**68**] bei den H^--Transferreaktionen bewährt hatte, wurden Na^+-Ionen als Leitsalz-Kationen ausgesucht. Das Leitsalz Na[BPh_4] brachte eine weitere vorteilhafte Eigenschaft mit, da dessen sehr schlechte Löslichkeit in Et_2O eine Isolierung der elektrochemisch erzeugten [**68**]$^{2-}$-Spezies durch Extraktion ermöglichte. Die Abtrennung des Leitsalzes ist zwingend notwendig für eine NMR-spektroskopische Charakterisierung des Reduktionsprodukts. Eine Aufarbeitung der Elektrolyselösung wurde durchgeführt, sobald eine für Na_2[**68**]-Lösungen charakteristische, tiefgrüne Farbe vorlag.

Wie bei der Cyclovoltammetrie war ein Drei-Elektroden-Aufbau in den Elektrolysen hilfreich, um das Potential an der Kathode festzulegen, das eine Reduktion von **68** ermöglicht. Als Gegenelektrode diente ein Platindraht und als Arbeitselektrode ein Platinnetz, in dessen Mitte eine Ag/Ag^+-Referenzelektrode positioniert wurde. Die Anordnung der Elektroden zeigt Abbildung 24, in der die geteilte Elektrolysezelle schematisch dargestellt ist. Die Trennung der Elektrodenhalbräume soll das gebildete [**68**]$^{2-}$-Dianion vor einer Re-Oxidation an der Anode schützen. Verschiedene Materialien kamen als Separatoren in einer geteilten Zelle zum Einsatz: eine Glasfritte (G4) konnte die Durchmischung der Zellhalbräume nicht effektiv genug verhindern. Der zusätzliche Einbau eines Wattebauschs verschaffte eine geringere Durchlässigkeit, sodass erstmals eine grünliche Färbung der Reaktionslösung durch Elektrolyse beobachtet wurde. Die verbesserte Trennung von Anoden- und Kathodenraum ging allerdings mit einer Abnahme der Leitfähigkeit einher, da der Widerstand des Systems zunahm. In diesem Zusammenhang stellte eine Kationenaustauschermembran, die nur Kationen durchlässt, eine Alternative dar, um den Ladungsausgleich in der Elektrolysezelle zu gewährleisten.

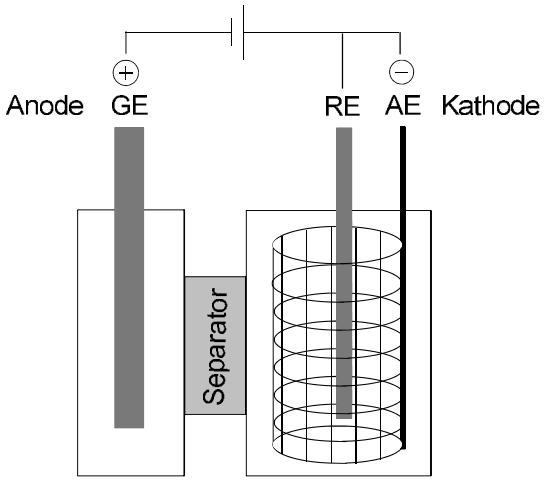

Abbildung 24. Schematische Darstellung der geteilten Elektrolysezelle. Gegen- und Arbeitselektrode (GE und AE) aus Platin kombiniert mit einer Ag/Ag^+-Referenzelektrode (RE). Als Separatoren dienten Glasfritten, teilweise in Kombination mit einem Wattebausch, oder eine Kationenaustauschermembran.

Bisher zielten alle Überlegungen darauf ab, die Reduktion von **68** an der Kathode optimal zu gestalten. Dabei entscheidet das Zusammenspiel von einer Reduktions- und einer Oxidati-

onsreaktion über den Elektronenfluss in der Elektrolysezelle. Für Synthesen, die sich auf das Geschehen an der Kathode konzentrieren, ist in aprotischen Lösungsmitteln etabliert, eine Metallelektrode zu verwenden, die lösliche Ionen durch Oxidation generiert.[151] Dieser Ansatz soll unerwünschte Folgereaktionen vermeiden und wurde im Rahmen der vorliegenden Arbeit als Machbarkeitsstudie verfolgt, wenngleich die ursprüngliche Motivation, auf Alkalimetalle zu verzichten, dadurch verloren geht. Der Vorteil einer Natrium-Opferelektrode liegt darin, dass stetig Na^+-Ionen entstehen, die als Kationen für die [**68**]$^{2-}$-Dianionen dienen und damit die Ladungsneutralität der Elektrolysezelle sicherstellen.

In Abbildung 25 ist der optimierte Elektrolyseaufbau zu sehen, mit der eine erfolgreiche elektrochemische Reduktion von **68** prinzipiell gelang, wie die tiefgrüne Färbung der Lösung andeutet. Die Elektrolysehalbräume sind mit einer 0.1 M $Na[BPh_4]$-THF-Lösung befüllt und die Kationenaustauschermembran wird mithilfe von Glasflanschen fixiert. Das Anlegen einer Spannung von –2.2 V an der Kathode für 20 Minuten ermöglichte die Umsetzung von 20 mg **68**.

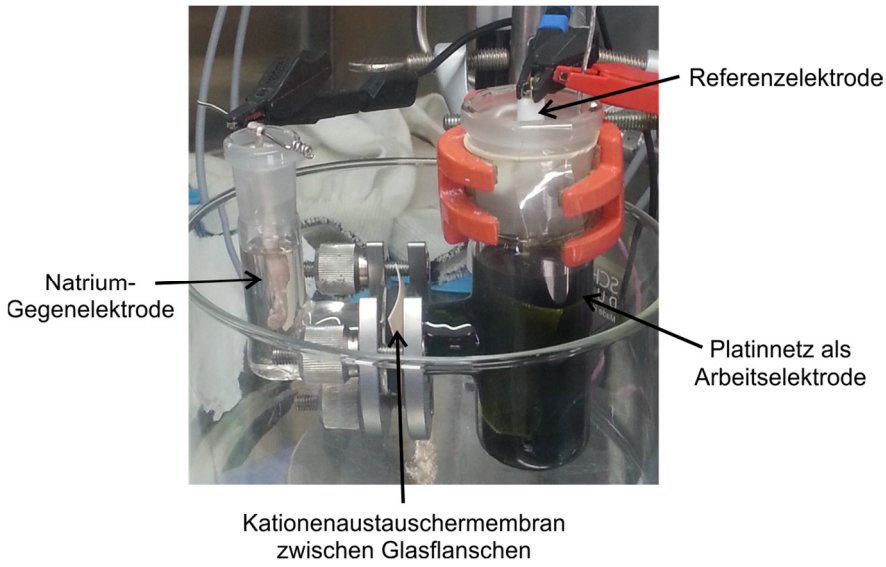

Abbildung 25. Foto der optimierten Elektrolysezelle, die sich in einem Handschuhkasten befindet. Die tiefgrüne Farbe der Elektrolytlösung im Kathodenraum ist charakteristisch für THF-Lösungen von Na_2[**68**].

Allerdings liegen mit den durchgeführten Experimenten nur dann Belege für ein erfolgreiches Reaktionsprinzip vor, wenn auch die Reinheit des erhaltenen Na_2[**68**] gewährleistet ist. Abbildung 26 stellt das ^{1}H-NMR-Spektrum einer aufgearbeiteten Elektrolysereaktion dem einer herkömmlichen Reduktionsmischung gegenüber. Die zu Na_2[**68**] gehörigen Resonanzen stimmen in beiden ^{1}H-NMR-Spektren gut überein. Allerdings bringt die Elektrolyse mehrere undefinierbare Nebenprodukte hervor. Je schlechter der Separator die Elektrolysehalbräume voneinander trennen konnte, desto höher war der Anteil der unerwünschten NMR-Signale. Dieser Befund weist auf einen systematischen Fehler hin, dessen Ursache vermutlich auf die anodische Zersetzung von $[BPh_4]^-$ zurückzuführen ist: Wenn ausschließlich die anodische Oxidation von $Na \rightarrow Na^+ + e^-$ wie angestrebt abliefe, sollten nur Na^+-Kationen entstehen, die [**68**]$^{2-}$ stabilisieren. Da aber die bewusste Zugabe der Elektrolyselösung aus dem Anodenraum zu der des Kathodenraumes das Verschwinden der grünen Farbe bewirkte, liegt es nahe, dass andere elektrochemisch generierte Spezies als Na^+-Ionen aus dem

Anodenraum für die Zersetzung des grünen Na_2[**68**] verantwortlich sind. Geske und Mitarbeiter berichteten über eine Elektrooxidation von $[BPh_4]^-$, das durch eine irreversible zwei-Elektronen-Abgabe zerfällt, u. a. zu $[BPh_2]^+$ und Biphenyl.[152, 153] Entsprechende oxidierte Spezies konnten alle verwendeten Separatoren durchdringen und mit $[\mathbf{68}]^{2-}$ reagieren. In den Elektrolyseexperimenten konnte Na_2[**68**] nur isoliert werden, wenn mehr **68** elektrochemisch reduziert wurde als störende Oxidationsprodukte den Separator passierten. Unter den gewählten Bedingungen kamen die Vorteile der Natrium-Elektrode offenbar nicht wesentlich zum Tragen.

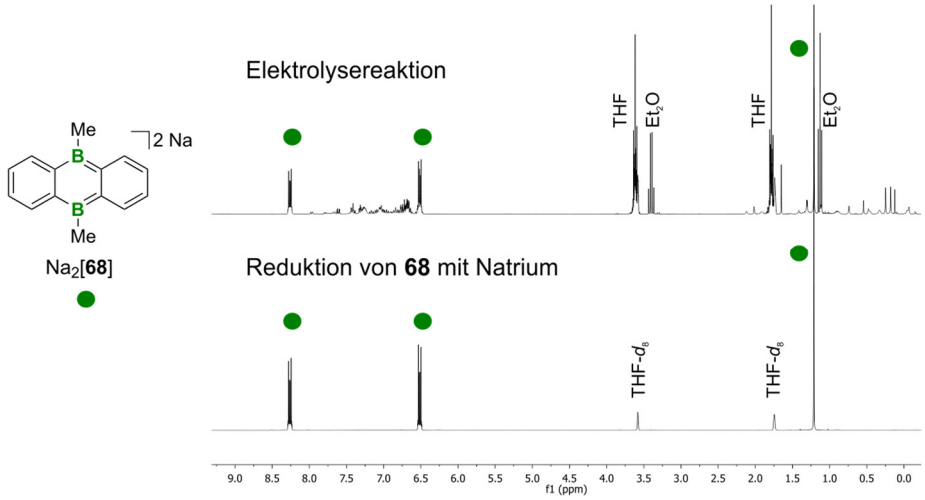

Abbildung 26. Vergleich der ^{1}H-NMR-Spektren der Elektrolysemischung nach Aufarbeitung (oben) und der Reduktion von **68** mit elementarem Natrium (unten).

Als Alternative erschien die Nutzung von zwei verschiedenen Leitsalz-Anionen in den jeweiligen Elektrolysehalbräumen sinnvoll, da das oxidationsstabile $Na[PF_6]$-Salz eine Auflösung von Natrium an der Anode zulassen sollte. Im Kathodenraum diente weiterhin $Na[BPh_4]$ als Leitsalz aufgrund dessen Inertheit gegenüber $[\mathbf{68}]^{2-}$. Experimentell konnte die verwendete Kationenaustauschermembran die Anionen aber nicht effektiv in ihren Elektrolysehalbräumen zurückhalten, sodass eine Zersetzung von $[BPh_4]^-$ weiterhin stattfand. Laut Hersteller liegt eine Permselektivität der Membran von 94%* vor, die für das empfindliche $[\mathbf{68}]^{2-}$-Dianion offenbar nicht hoch genug ist (*gemessen für zwei Halbräume mit einer 0.1 M und einer 0.5 M wässrigen KCl-Lösung gelangten 6% der Cl^--Anionen durch die Membran).[154]

Zusammengefasst verbleiben zwei Probleme bei der Elektrolyse von **68**: 1. Die Zersetzung des Leitsalzes $Na[BPh_4]$ generiert oxidierte Spezies, die mit $[\mathbf{68}]^{2-}$ reagieren. 2. Die eingesetzte Kationenaustauschermembran erlaubte nicht den Einsatz von zwei verschiedenen Leitsalzen in den Elektrolysehalbräumen wegen einer unzureichenden Permselektivität. Zu 1.: Andere gängige Leitsalze kamen nicht in Frage und ionische Flüssigkeiten dürften auch problematisch sein, da deren schwach koordinierende Kationen die negative Ladung von $[\mathbf{68}]^{2-}$ nicht stabilisieren (vgl. Einsatz von $[^n Bu_4N]^+$-Ionen). Zu 2.: Die Permselektivität von Kationenaustauschermembranen, wie sie für die Alkalisalzelektrolyse entwickelt werden, variiert konzentrationsabhängig im Bereich von 60% bis 98% und garantiert damit nie den quantitativen Verbleib der Anionen in ihren jeweiligen Halbräumen.[155] In beiden Fällen verhindert damit die Reaktivität bzw. die Empfindlichkeit des Dianions $[\mathbf{68}]^{2-}$ die Durchführung einer effizienten Elektrolyse.

2.6. M_2[**A**] in Reaktionen mit Elektrophilen

In der mesomeren Grenzstruktur von [**A**]$^{2-}$ in Schema 43 besitzt nur eines der beiden Boratome ein Elektronenpaar, sodass formal betrachtet parallel ein Boran-Dianion und ein Lewis-saures Boratom vorliegen.

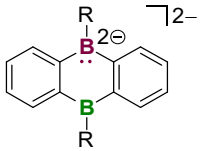

Schema 43. Mesomere Grenzstruktur von [**A**]$^{2-}$, die einer Boran-Dianion/Lewis-Säure-Kombination entspricht.

Die Umpolung der Reaktivität von klassischen Boranen durch den Einsatz von Boran-Anionen ist noch nicht lange etabliert, bietet allerdings neuartige Nukleophile für organische Synthesen an.[92, 156] In der Arbeitsgruppe Wagner zeigten Thomas Kaese und Timo Trageser, dass die reduzierte Organoborverbindung Li_2[**32**] mit α,ω-Dihalogenalkanen reagiert, wobei ein Boryl-Anion als Intermediat postuliert wurde (vgl. Schema 20).[91] Die erhaltenen ditopen Lewis-Säuren **33**^{Cn} könnten als Organokatalysatoren oder Elektronenspeicher Einsatz finden.

Zur Bewertung der nukleophilen Eigenschaften von [**A**]$^{2-}$ dienten Dichalkogene, Halogenalkane und Halogensilane als Reaktionspartner. Die in den folgenden Abschnitten zusammengefassten Ergebnisse sind im Rahmen der von mir betreuten Bachelorarbeit von Felix Nawa entstanden.[157]

2.6.1. Reaktionen mit Chalkogen–Chalkogen-Einfachbindungen

Li_2[**68**] reagiert mit den Dichalkogenen O_2(*t*Bu)$_2$, S_2Me_2, S_2(*p*Tol)$_2$, Se_2Ph_2 und Te_2Ph_2 bei Raumtemperatur unter reduktiver Spaltung der Chalkogen–Chalkogen-Bindungen (Schema 44). Betrachtet man Li_2[**68**] in dieser Reaktion als Nukleophil, so bewirkt es einen heterolytischen Bindungsbruch. Die unterschiedlichen Donoreigenschaften der resultierenden Lithiumchalkogenide erklären die verschiedenen Verknüpfungsmotive der Chalkogenid-Anionen mit dem DBA-Grundgerüst **68** (Schema 44). Röntgenstrukturanalysen von Einkristallen, die aus den Reaktionsmischungen erhalten wurden, offenbarten die atomaren Verknüpfungen der Produkte im Festkörper (Abbildung 27). Die beiden Äquivalente Li[O*t*Bu] koordinieren

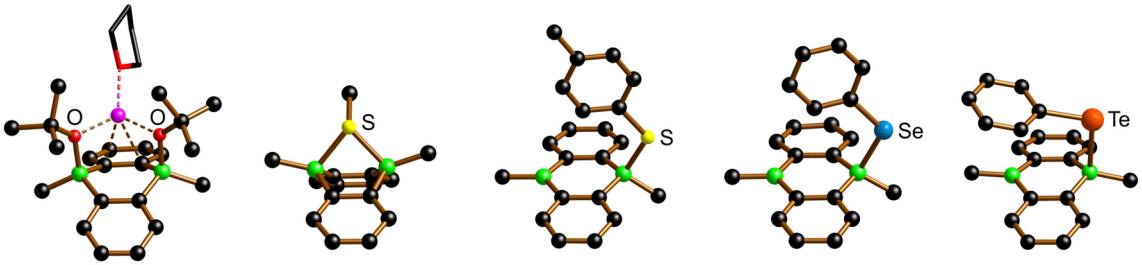

[Li(thf)][**102**]$^-$ [**103**]$^-$ [**104**]$^-$ [**105**]$^-$ [**106**]$^-$

Abbildung 27. Festkörperstrukturen der Salze [Li(thf)][Li(12-c-4)$_2$][**102**], [Li(12-c-4)$_2$][**103**], [Li(12-c-4)$_2$][**104**], [Li(12-c-4)$_2$][**105**] und [Li(12-c-4)$_2$][**106**]. Alle [Li(12-c-4)$_2$]$^+$-Kationen und H-Atome sind nicht abgebildet.

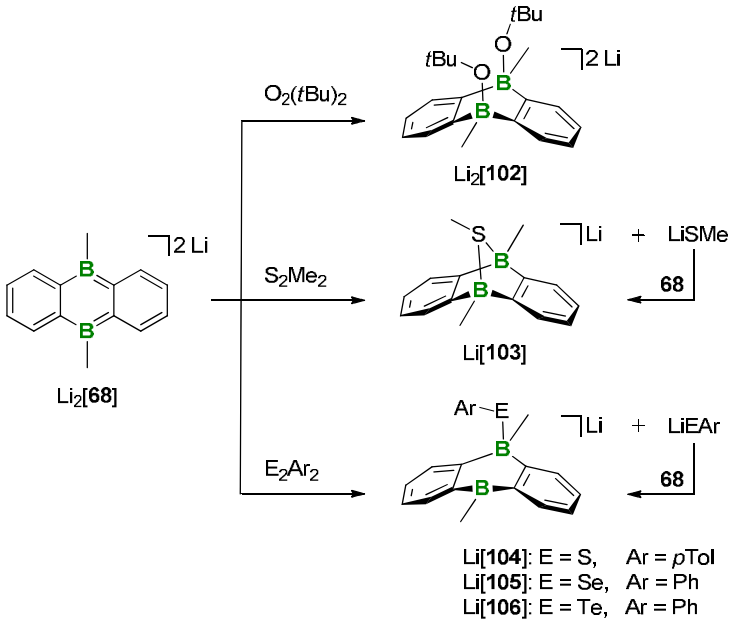

Schema 44. Reduktive Spaltungen von Chalkogen–Chalkogen-Einfachbindungen mit Li_2[**68**], durch die das symmetrische Diaddukt Li_2[**102**], das verbrückende Monoaddukt Li[**103**] und die terminalen Monoaddukte Li[**104**]-Li[**106**] erzeugt wurden.

an die beiden Boratome und besetzen die zwei axialen Positionen in Li_2[**102**]. Die höheren Homologen bilden 1:1 Addukte aus: Der kleine $[SMe]^-$-Ligand nimmt in Li[**103**] eine verbrückende Position zwischen den Boratomen ein, wohingegen die größeren Chalkogenide in Li[**104**]-Li[**106**] nur an jeweils ein Boratom gebunden sind. Die B–E–C-Winkel nehmen in der Reihe [**104**]$^-$, [**105**]$^-$ und [**106**]$^-$ ab (112.4°, 111.2° und 99.1°), in Übereinstimmung mit einer geringeren Bereitschaft zur Hybridisierung der schweren Donoratome.

Die Vermessung der Einkristalle in THF-d_8-Lösung lieferte ^{1}H-, ^{11}B- und ^{13}C{^{1}H}-NMR-Spektren, die auf eine gemittelte C_{2v}-Symmetrie der Verbindungen in Lösung hinweisen. Dies entspricht der Erwartung für [**102**]$^-$, setzt aber für [**103**]$^-$ voraus, dass das verbrückende Schwefelatom formal schnell invertieren kann – vermutlich über ein Dissoziations-/Assoziations-Gleichgewicht. Für [**104**]$^-$ muss ein solches Gleichgewicht noch ausgeprägter sein, indem der Thiolat-Ligand zwischen den Boratomen wechselt. Die ^{11}B-NMR-Verschiebungen für [Li(12-c-4)$_2$][**103**] und [Li(12-c-4)$_2$][**104**] sind 2.3 bzw. 22.0 ppm und deuten auf einen höheren Anteil der freien Lewis-Säure **68** für [**104**]$^-$ hin.

Untersucht man die ursprünglichen Reaktionsmischungen mittels NMR-Spektroskopie, so lassen die Integralverhältnisse der Protonen eine 2:1 Stöchiometrie des Chalkogenids und des DBAs **68** erkennen, anders als die entsprechenden THF-d_8-Lösungen der Einkristalle für [**103**]$^-$ - [**106**]$^-$. Exemplarisch ist das ^{1}H-NMR-Spektrum von Li_2[**68**] nach der Zugabe von einem Äquivalent S_2(*p*Tol)$_2$ in Abbildung 28 oben gezeigt. Offenbar ist es nicht möglich, zwischen dem freien und dem koordinierten Thiolatliganden zu unterscheiden, was den oben beschriebenen intramolekularen dynamischen Prozess um einen intermolekularen Ligandenaustausch erweitert. Der Anteil des freien Thiolats konnte durch Zugabe von einem Äquivalent des Akzeptormoleküls **68** abgefangen werden (Schema 44), sodass die bekannten NMR-Resonanzen der gelösten Einkristalle erhalten wurden (Abbildung 28).

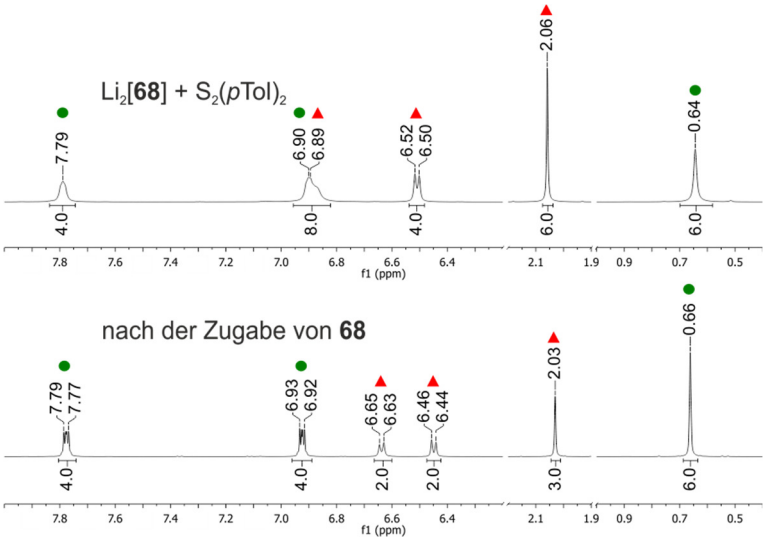

Abbildung 28. ^{1}H-NMR-Spektren (500.2 MHz, THF-d_8) von 1:1 Reaktionsmischungen Li_2[**68**]/S_2(*p*Tol)$_2$ vor (oben) und nach (unten) der Zugabe von einem Äquivalent **68** (● DBA-, ▲ [S(*p*Tol)]$^-$-Resonanzen).

2.6.2. Reaktionen mit Halogenalkanen

Als geeignetes Modellreagenz für nukleophile Substitutionen mit M_2[**A**] erwies sich Bromethan, das mit M_2[**68**] und M_2[**72**] (M^+ = Li^+, Na^+) jeweils in einer 1:1 Stöchiometrie umgesetzt wurde. In beiden Fällen bildete sich ein tetrakoordiniertes Boratom, weil der Ethylrest wie gewünscht eingeführt wurde (M[**107**] bzw. M[**108**] in Schema 45). Das Natriumsalz Na[**107**] kristallisierte als [Na(18-c-6)(thf)$_2$][**107**], dessen Einkristallröntgenstruktur das vermutete Verknüpfungsmotiv belegte (Schema 45). Die Zwischenstufe M[**108**] lässt sich nur postulieren, da eine Hydrid-Verschiebung im unmittelbaren Anschluss M[**109**] lieferte, das als stabiles Reaktionsprodukt mittels NMR-Spektroskopie charakterisierbar war.

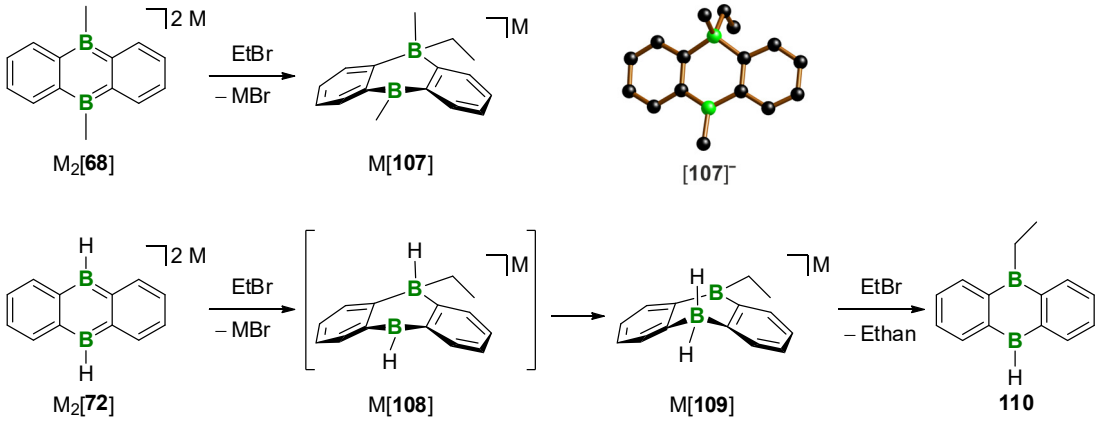

Schema 45. Übersicht der Reaktivität von M_2[**68**] (oben) und M_2[**72**] (unten) mit Bromethan. Festkörperstruktur des Anions von [Na(18-c-6)(thf)$_2$][**107**] (oben rechts); H-Atome sind nicht abgebildet.

Eine Verdopplung der Menge an Bromethan hatte keinen Einfluss auf die Reaktion mit M_2[**68**], führte aber für das H-Derivat zu einer Folgereaktion: Das primär gebildete Hydridoborat [**109**]$^-$ kann, wie in Abschnitt 2.4. für Na_2[**68**-H_2] beschrieben, als H^--Donor für Brom-

ethan fungieren. Das entsprechende Hydrierungsprodukt Ethan ließ sich mittels NMR-Spektroskopie neben der DBA-Verbindung **110** nachweisen (Schema 45). Auf diese Weise wurde ausgehend von M_2[**72**] eine neue Syntheseroute für unsymmetrisch B-substituierte DBA-Grundgerüste gefunden.[112, 158]

Li_2[**68**] und die Dihalogenalkane 1,2-Dibromethan oder 1,2-Dibrombenzol reagierten zu **68** und Ethen (selektiv) bzw. Benzol (unselektiv). Dies verdeutlicht, dass eine formale nukleophile Reaktion von M_2[**A**] immer auch mit einer Redoxreaktion konkurriert.

Zur Unterscheidung eines nukleophilen von einem radikalischen Mechanismus wird in der organischen Chemie eine sogenannte Radikaluhr verwendet, mit der auch die Geschwindigkeit für eine vorliegende radikalische Reaktion bestimmt werden kann.[159] Eine schnelle Radikalreaktion mit bekannter Geschwindigkeitskonstante k_R dient dabei als interner Standard. Die Ringöffnung des Cyclopropylmethyl-Radikals verläuft besonders schnell (k_R = $1.2 \cdot 10^8\ s^{-1}$) und kann daher mit den meisten organischen Reaktionen konkurrieren.[160] Setzt man Brommethylcyclopropan mit M_2[**68**] ($M^+ = Li^+, Na^+$) um, so entstehen die zwei Produkte M[**111**] und M[**112**] zu unterschiedlichen Anteilen in Abhängigkeit vom Kation (Schema 46). Bei der Umsetzung mit M_2[**68**] liegt mit hoher Wahrscheinlichkeit ein radikalischer Mechanismus vor, da M[**112**] als Reaktionsprodukt gefunden wurde. Die Berechnung der Geschwindigkeitskonstanten für die Reaktionen aus dem Verhältnis von M[**111**] zu M[**112**] wurde im vorliegenden Fall nicht vorgenommen, weil die Gegenwart von Metallkationen M^+ die Geschwindigkeit der Reaktionen von Radikaluhren beeinflusst und eine entsprechend angepasste Geschwindigkeitskonstante für das Cyclopropylmethyl-Radikal nicht literaturbekannt ist.[161, 162]

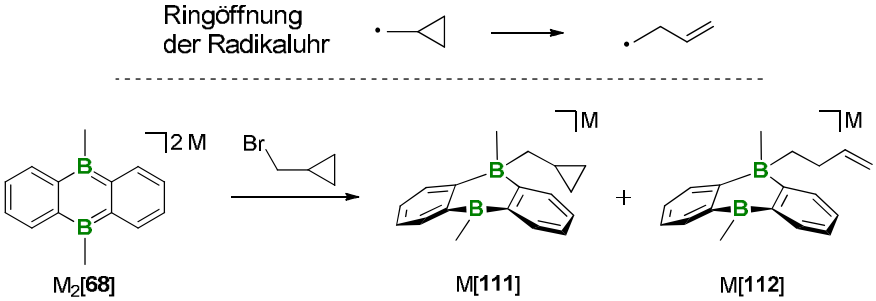

Schema 46. Die Nutzung des Cyclopropylmethyl-Radikals als Radikaluhr legte nahe, dass bei der Reaktion von M_2[**68**] mit Elektrophilen ein radikalischer Pfad nicht ausgeschlossen werden kann.

2.6.3. Reaktionen mit dem Halogensilan Et_3SiBr

Mit einem Äquivalent Et_3SiBr als Reaktionspartner trat, wie bei Bromethan, eine Addition an M_2[**68**] bzw. M_2[**72**] (M^+ = Li^+, Na^+) ein, sodass die monoanionischen Borate M[**113**] bzw. M[**114**] mit einem trigonal planaren und einem tetrakoordinierten Boratom entstanden (Schema 47). Im Gegensatz zum Ethyl-Derivat M[**108**] fand in M[**113**] kein Hydridaustausch statt. In Kombination mit einem Überschuss an Et_3SiBr zersetzte sich M[**113**] jedoch und Et_3SiH konnte nur in geringen Mengen nachgewiesen werden.

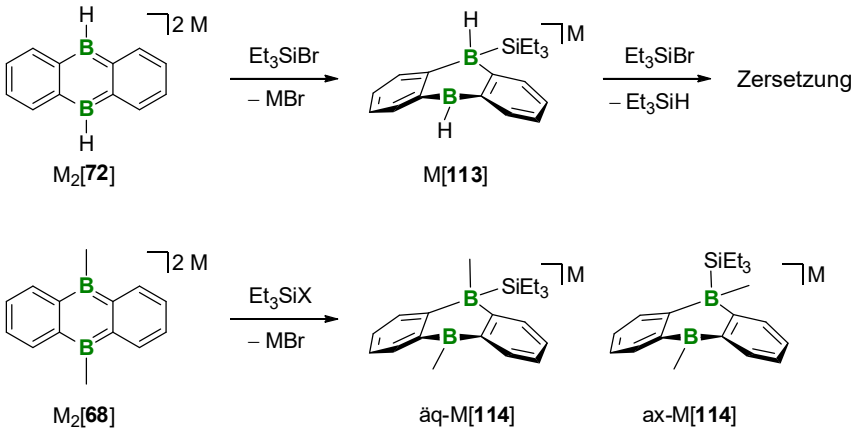

$M^+ = Li^+$, X = Cl, Br	80%	20%
$M^+ = Na^+$, X = Cl	70%	30%
$M^+ = Na^+$, X = Br	100%	0

Schema 47. Übersicht der Reaktionen von M_2[**72**] (oben) und M_2[**68**] (unten) mit Et_3SiBr. Die Additionsprodukte M[**113**] zersetzten sich bei Zugabe von mehr als einem Äquivalent Et_3SiBr. M[**114**] können als Isomerengemische vorliegen.

Für die Reaktion von Na_2[**68**] mit Et_3SiBr wurde äq-Na[**114**] erhalten, das vermutlich in einer vergleichbaren Konfiguration wie Na[**107**] vorliegt, was man aus dem Vergleich der jeweiligen NMR-Signalsätze schließen kann (Schema 47, Abbildung 29). Demnach müsste das DBA-Rückgrat in äq-Na[**114**] wie in Na[**107**] leicht abgewinkelt sein und der Et_3Si-Substituent eine

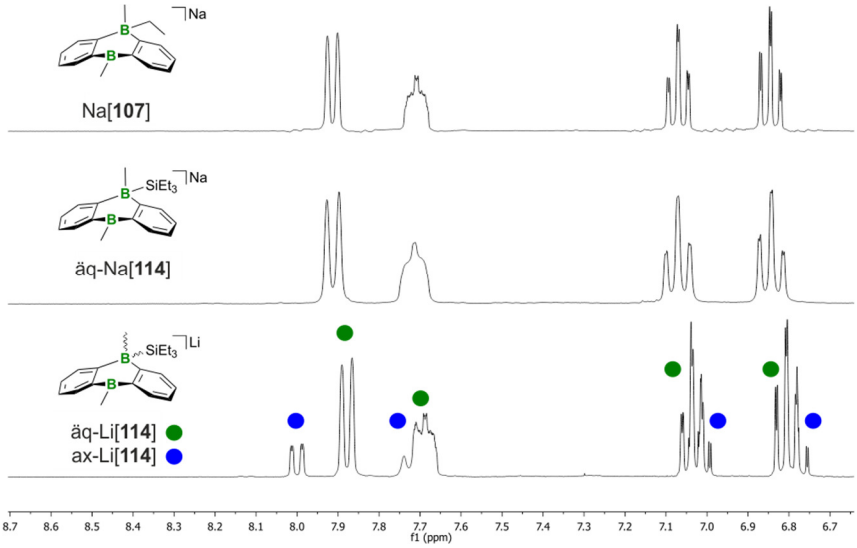

Abbildung 29. Ausschnitte der ^{1}H-NMR-Spektren (300.0 MHz) der THF-d_8-Lösungen von Na[**107**] (oben), äq-Na[**114**] (Mitte) und dem Isomerengemisch Li[**114**] (unten).

äquatoriale Position besetzen. Li_2[**68**] liefert bei der Umsetzung mit Et_3SiBr zwei Spezies, die laut NMR-Spektroskopie Isomere darstellen (Verhältnis 4:1; Schema 47, Abbildung 29). Die gegenseitige Umwandlung der beiden Isomere war durch eine thermische Behandlung bei 100 °C für 16 h nicht möglich: entweder liegen Konformationsisomere vor, die durch eine sehr hohe Inversionsbarriere getrennt sind, oder Konfigurationsisomere, die prinzipiell nicht ineinander überführbar sind. Für die Entstehung der verschiedenen Isomere könnten unterschiedliche Wechselwirkungen in den jeweiligen Übergangszuständen verantwortlich sein. Beispielsweise neigen nukleophile Substitutionsreaktionen am Silicium häufig zur Isomerenbildung, da fünffach koordinierte Zwischenprodukte oftmals mit niedriger Barriere umlagern.[133] Verwendet man für die Substitution mit M_2[**68**] ein Elektrophil mit einer schlechteren Abgangsgruppe, wie Et_3SiCl, nimmt die Reaktionsgeschwindigkeit ab und es bildeten sich unabhängig vom Kation zwei Spezies aus. Im vorliegenden Fall bietet sich die Arbeitshypothese an, dass für den Et_3Si-Substituenten nicht ausschließlich die äquatoriale Position (äq-Li[**114**]) begünstigt ist, sondern auch eine axiale Position (ax-Li[**114**]) möglich ist. Das Strukturmotiv von ax-Li[**114**] ist vergleichbar mit dem der Chalkogenid-Addukte Li[**104**] - Li[**106**] in Schema 44, deren sterisch anspruchsvolle Substituenten ebenfalls axial orientiert sind.

3. Zusammenfassung

Die in der vorliegenden Arbeit gewonnenen Erkenntnisse zur Reaktivität zweifach reduzierter 9,10-Dihydro-9,10-diboraanthracene $[\mathbf{A}]^{2-}$ erweitern das Einsatzspektrum von Hauptgruppenverbindungen im Hinblick auf die Aktivierung kleiner Moleküle. Komplementär zu Übergangsmetallkomplexen und FLPs ermöglichen die Dianionen $[\mathbf{A}]^{2-}$ die Entwicklung neuartiger Synthesestrategien. Als besondere Herausforderung gilt die Aktivierung des stabilen H_2-Moleküls, dessen Bindung die Dianionen $[\mathbf{A}]^{2-}$ homolytisch in einer konzertierten Reaktion spalten. In Abbildung 30 lässt der Vergleich der Übergangszustände bei der H_2-Addition deutlich die Verwandtschaft zwischen $[\mathbf{A}]^{2-}$ und Übergangsmetallkomplexen erkennen, wohingegen FLPs nicht-lineare Strukturen ausbilden, die zu einem heterolytischen H_2-Bindungsbruch führen. Dennoch kann man die Spezies $[\mathbf{A}]^{2-}$ formal als maskierte FLPs betrachten (vgl. die mesomere Grenzstruktur $[\mathbf{A}^*]^{2-}$), um die Reaktivitäten der Dianionen abzuschätzen.

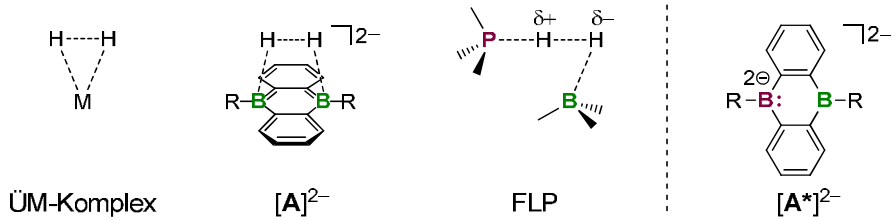

Abbildung 30. Vergleich der Übergangszustände der H_2-Aktivierung durch Übergangsmetall-Komplexe, zweifach reduzierte 9,10-Dihydro-9,10-diboraanthracene $[\mathbf{A}]^{2-}$ und FLPs. $[\mathbf{A}^*]^{2-}$ ist eine mesomere Grenzstruktur von $[\mathbf{A}]^{2-}$, die eine formale Analogie zu FLPs erkennen lässt.

Untersuchungen zur Kinetik der H_2-Addition an $M_2[\mathbf{A}]$ stellten die Abhängigkeit dieses Reaktionsschritts vom borgebundenen Substituenten und vom Kation heraus (Abbildung 31). Eine geringe sterische Abschirmung der Boratome durch kleine borgebundene Substituen-

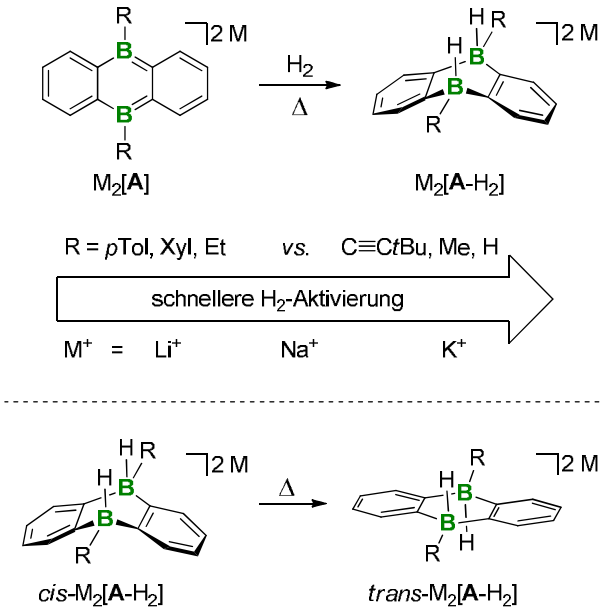

Abbildung 31. Abhängigkeit der Kinetik des H_2-Additionsschritts vom borgebundenen Substituenten und vom Gegenkation (oben). Thermisch induzierte Isomerisierung von *cis*-$M_2[\mathbf{A}\text{-}H_2]$ zu *trans*-$M_2[\mathbf{A}\text{-}H_2]$ für $M^+ = Na^+$ oder K^+ (unten).

ten (C≡C*t*Bu, Me, H) begünstigt die H_2-Aufnahme gegenüber großen Substituenten (*p*Tol, Xyl, Et). Der Zugang zu den Boratomen wird ebenso durch die Wahl des Kations beeinflusst, da M_2[**A**] als inverse Sandwich-Komplexe vorliegen, in denen der zentrale B_2C_4-Ring von beiden Seiten durch die Kationen komplexiert wird. Mit zunehmendem Kationenradius (M^+ = Li^+, Na^+, K^+) nimmt die Ionenseparation zu, was vorteilhaft für die H_2-Aktivierung ist: Die maximale Ausbeute an Li_2[**A**-H_2] wird erst nach mehreren Tagen bei 100 °C erhalten, während einige Stunden bei nur 50 °C für die quantitative Bildung von K_2[**A**-H_2] ausreichen. In Übereinstimmung mit dem berechneten konzertierten Mechanismus der H_2-Addition befinden sich die H-Substituenten auf derselben Seite des B_2C_4-Rings, wie Einkristallröntgenstrukturanalysen belegten. In diesen *cis*-Konfigurationen sind die dianionischen Grundgerüste abgewinkelt, können aber infolge thermisch induzierter *cis*/*trans*-Isomerisierungen für M^+ = Na^+ bzw. K^+ zu den Salzen *trans*-M_2[**A**-H_2] planarisieren (Abbildung 31).

Unter den Salzen M_2[**A**] eignet sich Li_2[**68**] mit borgebundenen Me-Substituenten besonders gut zum Einsatz als Hydrierungskatalysator. Die H_2-Aktivierungsprodukte Na_2[**A**-H_2] und K_2[**A**-H_2] sind für einen effizienten H_2-Transfer jedoch thermodynamisch zu stabil. Mit Li_2[**68**] konnten das Imin Ph(H)C=N*t*Bu, das terminale Alken $Ph_2C=CH_2$ und Anthracen erfolgreich im NMR-Maßstab hydriert werden (Katalysatorladung 37 mol%, THF-d_8, 1 atm H_2-Initialdruck, 100 °C, 16 h; Abbildung 32). Im Reaktionsautoklaven war für die Hydrierung von Ph(H)C=N*t*Bu eine Verringerung der Katalysatorladung auf 10 mol% Li_2[**68**] möglich (THF, 7 atm H_2-Initialdruck, 100 °C, 18 h). Konkurrenzreaktionen begründen Einschränkungen in Bezug auf die Substratpalette, da Li_2[**68**] mit elektronenarmen ungesättigten Verbindungen, die C=C-, C≡C-, C=O- oder C=N-Bindungen enthalten, [4+2]-Cycloadditionsprodukte des Typs

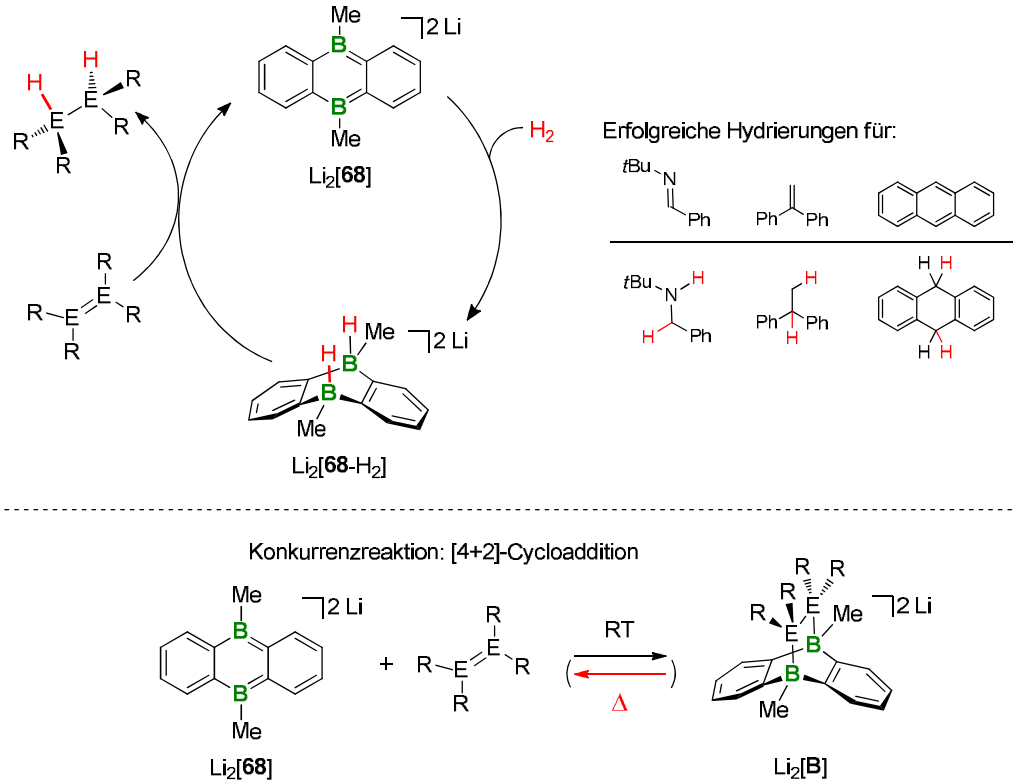

Abbildung 32. Einsatz von Li_2[**68**] als Hydrierungskatalysator (oben). Einschränkung der Substratpalette aufgrund konkurrierender [4+2]-Cycloadditionsreaktionen zwischen Li_2[**68**] und Substraten mit ungesättigten Bindungen (unten). E = C, N, O.

Li_2[**B**] bilden kann (Abbildung 32). Die Reversibilität dieser Reaktion entscheidet, ob Li_2[**68**] als Katalysator fungiert oder irreversibel in den Strukturen Li_2[**B**] gebunden bleibt. An dieser Stelle wird die Bedeutung einer geschickten Wahl des borgebundenen Substituenten deutlich, da ein kleiner Substituent, wie z. B. ein H-Atom, die Ausbildung irreversibler [4+2]-Cycloadditionsprodukte begünstigt, aber ein Rest, wie z. B. ein *p*Tol-Ring, die H_2-Aufnahme von Li_2[**A**] ebenso wie die Annäherung des Substrats an Li_2[**A**-H_2] erschwert.

Die Reaktionen zwischen M_2[**68**] (M^+ = Li^+, Na^+) und CO_2 bleiben nicht auf der Stufe der Bicyclo[2.2.2.]-Produkte M_2[**98**] stehen, sondern laufen unter Aufnahme eines weiteren CO_2-Äquivalents weiter (Schema 48). Mechanistische Betrachtungen konnten die Bildung von CO und der $[CO_3]^{2-}$-überbrückten Komplexe M_2[**100**] erklären. Für M^+ = Na^+ wurde Na_2[**100**] isoliert, wohingegen mit M^+ = Li^+ lediglich Folgeprodukte des postulierten Li_2[**100**], nämlich das neutrale **68** und Li_2CO_3, nachweisbar waren.

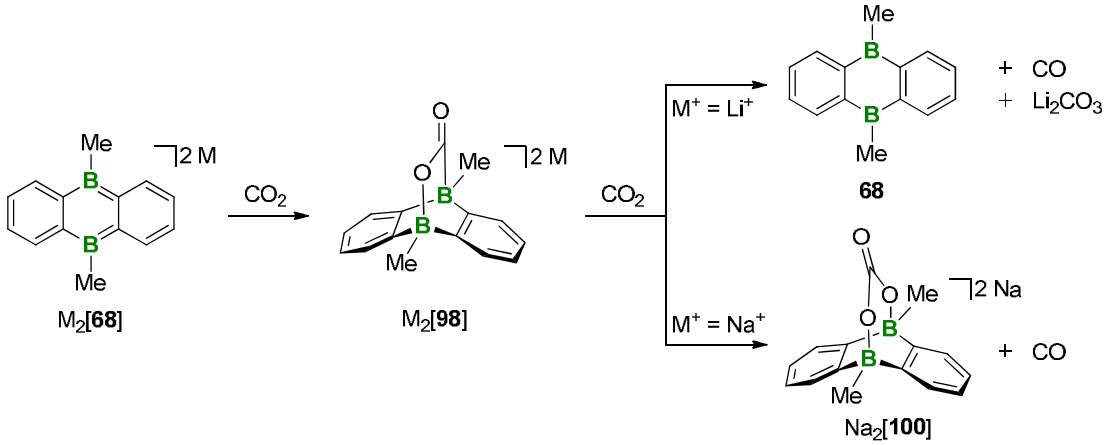

Schema 48. Die Reaktion von M_2[**68**] (M^+ = Li^+, Na^+) mit CO_2 führt zur Bildung von CO und $[CO_3]^{2-}$. In Abhängigkeit vom Kation verbleibt Letzteres als verbrückender Ligand in Na_2[**100**] oder wird in Form von Li_2CO_3 gebunden.

Die Bildung von [4+2]-Cycloadditionsprodukten schränkt die Verwendung von M_2[**A**-H_2] als Hydrierungskatalysatoren ein. Vielseitiger sind die H_2-Aktivierungsprodukte M_2[**A**-H_2] als H^--Donoren geeignet (Abbildung 33): Na_2[**68**-H_2] ersetzt Halogenid- durch H^--Substituenten in Bromethan, sowie in Chlorsilanen und PCl_3; CO_2 wird in Natriumformiat überführt. Unabhängig von der Anzahl der Chlorliganden waren die Produkte immer vollständig hydriert. Im Zuge der H^--Abgabe bildet sich stets die Neutralverbindung **68**, die nach der partiellen Umsetzung von Me_2SiCl_2 zu Me_2SiH_2 als Komproportionierungskatalysator zur Darstellung des gemischten Chlorsilans $Me_2Si(H)Cl$ diente. Im Gegensatz zu stöchiometrisch verwendeten H^--Reagenzien wie $Na[BH_4]$ ermöglicht die Wiederverwendung von **68** den Aufbau eines pseudo-katalytischen Kreisprozesses: Eine Reduktion von **68** kann wieder Na_2[**68**] bereitstellen (a), das erneut H_2 aufnimmt und Na_2[**68**-H_2] regeneriert (b), das für neue H^--Abgaben zur Verfügung steht (c; Abbildung 33). Die Verwendung von Alkalimetallen für diesen Reduktionsschritt war einer Elektrolyse überlegen, da deren experimenteller Aufbau trotz zahlreicher Optimierungen der Empfindlichkeit von $[$**68**$]^{2-}$ nicht gerecht wurde. Die Reaktionen (a) und (c) verlaufen zügig und quantitativ bei Raumtemperatur, sodass die H_2-Addition (b) der geschwindigkeitsbestimmende Schritt des Kreisprozesses ist. Das synthetisch leicht zugängliche Derivat Na_2[**68**] fand oft Verwendung, da es schnell und quantitativ mit H_2 reagiert. Bei der Ausführung des Kreislaufs ist wichtig, die Reaktionssequenzen (a) – (c) nacheinander auszuführen und jeweils nur stöchiometrische Mengen des Elektrophils zuzugeben.

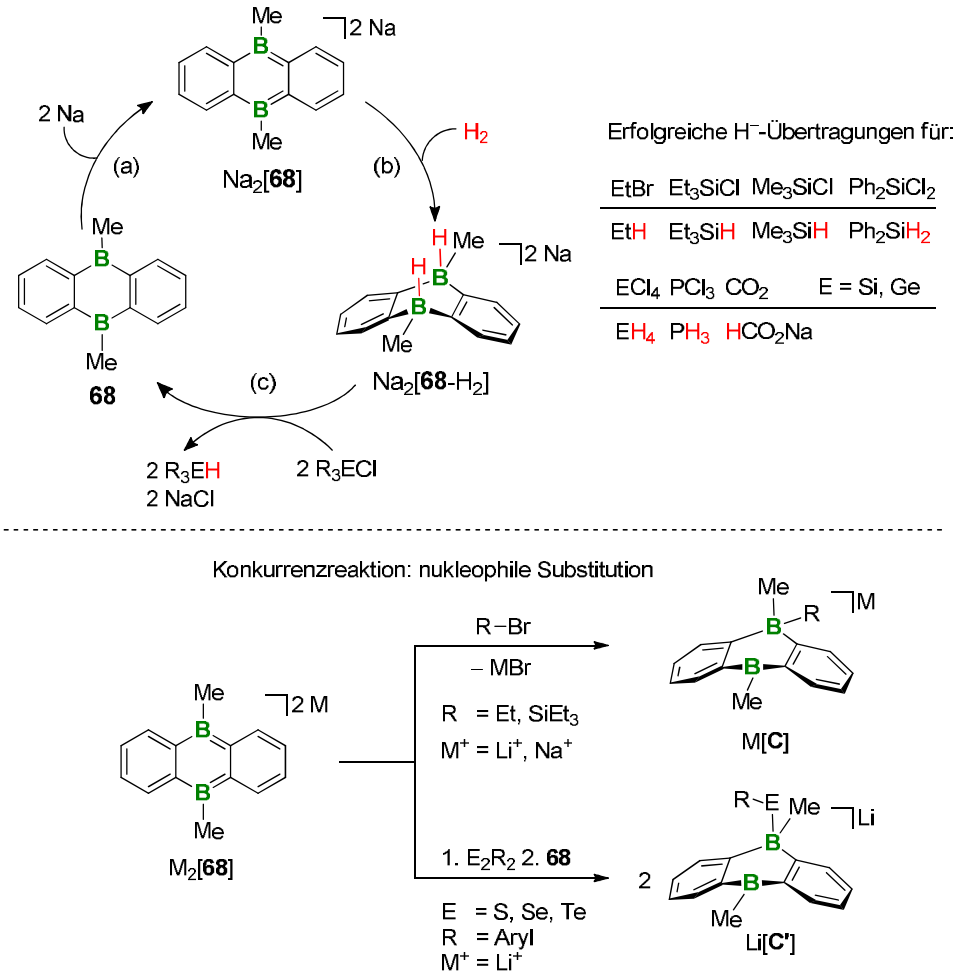

Abbildung 33. Einsatz von Na_2[**68**-H_2] als regenerierbarer H^--Donor (oben). Ein schrittweiser Kreisprozess mit stöchiometrischer Zugabe des Elektrophils stellt sicher, dass nukleophile Substitutionsreaktionen vermieden werden und Na_2[**68**] regenerierbar bleibt (unten).

Bei Abweichungen vom schrittweisen Syntheseprotokoll finden formale nukleophile Substitutionen mit M_2[**68**] statt und monoanionische Spezies des Typs M[**C**] entstehen, z. B. wenn Bromethan oder das Bromsilan Et_3SiBr als Elektrophile anwesend sind (Abbildung 33). Vergleichbare Strukturmotive Li[**C'**] wurden auch durch die Reaktion von M_2[**68**] mit ausgewählten Dichalkogenen (S_2(*p*Tol)$_2$, Se_2Ph_2, Te_2Ph_2) und anschließender Zugabe von **68** erhalten (Abbildung 33). Die Arbeiten zum Einsatz von [**A**]$^{2-}$ als Nukleophile eignen sich als Grundlage, um das Potenzial zweifach reduzierter 9,10-Dihydro-9,10-diboraanthracene auch zukünftig für katalytische Anwendungsfelder auszuschöpfen.

Die Dianionen [**A**]$^{2-}$ stechen unter anderen cyclischen Borverbindungen in niedrigen Oxidationsstufen heraus, da mit [**A**]$^{2-}$ nicht nur die Aktivierung von H_2 oder CO_2 gelang, sondern erstmalig über die Einbindung der Additionsprodukte in zum Teil katalytische Folgereaktionen berichtet werden konnte.

4. Experimentelle Daten nicht publizierter Verbindungen

4.1. Allgemeine Arbeitstechniken

Die Handhabung luftempfindlicher Verbindungen erfolgte unter Verwendung von gängigen Schlenk-Arbeitstechniken in einer Inertgasatmosphäre (Argon oder Stickstoff) oder in einer mit Argon (5.0) gefüllten Glovebox. THF und THF-d_8 wurden mithilfe von Na/K-Legierungen getrocknet, durch vier Einfrieren-Pumpen-Auftauen-Zyklen entgast und anschließend über aktiviertem Molekularsieb (3.0 Å) gelagert.

4.1.1. NMR-Spektroskopie

Alle NMR-spektroskopischen Messungen erfolgten bei 298 K an NMR-Spektrometern der Firma *Bruker* mit den hier angegebenen Messfrequenzen:
DPX-250 (^{1}H: 250.1 MHz)
Avance-300 (^{1}H: 300.0 MHz, ^{11}B: 96.3 MHz, ^{13}C: 75.4 MHz),
Avance-500 (^{1}H: 500.2 MHz, ^{11}B: 160.5 MHz, ^{13}C: 125.8 MHz).

Die durch Kopplungen entstehenden Multiplizitäten werden mit (s) für Singulett, (d) für Dublett, (t) für Triplett, sept (Septett) und (m) für Multiplett angegeben. Nicht aufgelöste Kopplungen oder nicht beobachtete Resonanzen sind mit (n.a.) bzw. (n.b.) gekennzeichnet; vebreiterete Signal mit (br). Als interner Standard bei den ^{1}H-NMR-Spektren dienten die Restprotonen des verwendeten Lösungsmittels bezogen auf Tetramethylsilan (δ = 0 ppm): THF-d_8: 3.58 ppm.[163] Als interner Standard bei den ^{13}C-NMR-Spektren dienten die ^{13}C-Signale des deuterierten Lösungsmittels wiederum bezogen auf Tetramethylsilan (δ = 0 ppm): THF-d_8: 67.21 ppm.[163] Alle ^{13}C{^{1}H}-NMR-Experimente sind ^{1}H-breitbandentkoppelt.

Allgemeines Nummerierungsschema für symmetrisch und unsymmetrisch B-substituierte DBA-Derivate:

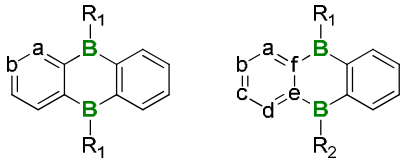

4.1.2. Einkristall-Röntgendiffraktometrie

Sämtliche Daten der Röntgenbeugungsexperimente an Einkristallen wurden an einem *STOE IPDS II* Zweikreisdiffraktometer mit einer Genix Mikrofokusröhre, Spiegeloptiken und MoK_α-Strahlung (λ = 0.71073 Å) aufgenommen. Die Skalierung der Daten erfolgte mit der *frame-scaling Prozedur* des *X-AREA* Programms.[164] Die Strukturen wurden über direkte Methoden unter Verwendung des Programms *SHELXS* gelöst und gegen F^2 mit *full-matrix least-square* Techniken mithilfe des Programms *SHELXL* verfeinert.[165]

4.1.3. Cyclovoltammetrie

Alle cyclovoltammetrischen Messungen wurden unter Argonatmosphäre bei RT und mit einer Platin-Scheibenelektrode (ø = 2 mm) als Arbeitselektrode und einem Platindraht als Gegenelektrode an einem *EG&G Princeton Applied Research 263A*-Potentiostat durchgeführt. Die Proben (ca. 2 mg) wurden in THF zusammen mit [^{n}Bu$_4$N][PF_6] (0.1 M) gelöst. Als Referenzelektrode diente ein Silberdraht, der mit Silberchlorid durch Eintauchen in Königs-

wasser beschichtet wurde. Als interner Standard wurde Ferrocen jeweils nach einer Messreihe zur Analytlösung gegeben und einige Messzyklen wiederholt. Als Vorschubgeschwindigkeiten wurden 100, 200 und 500 mV s^{-1} gewählt.

4.1.4. Elektrolyse

Die Elektrolyseexperimente wurden unter Argonatmosphäre bei RT mithilfe eines *EG&G Princeton Applied Research 263A*-Potentiostat durchgeführt. Über die Programmfunktion *Chronoamperiometrie* konnte das Sollpotential an der Arbeitselektrode in Höhe von –2.1 V eingestellt werden. Der optimierte Elektrolyseaufbau war folgendermaßen zusammengesetzt:

- Arbeitselektrode: Platin-Netz (Höhe: 4 cm; Umfang: 10.5 cm; Maschenweite 1 mm)

- Referenzelektrode: nicht-wässrige Ag/Ag^+-Referenzelektrode RE-7 von *ALS* (Vertrieb durch C3 Prozess- und Analysentechnik GmbH); 0.01 M $AgNO_3$ in 0.1 M $[^nBu_4N][ClO_4]$-Acetonitril-Lösung

- Gegenelektrode: Natriummetall über Platin-Draht kontaktiert

- Kationenaustauschermembran: CMI-7000 von *Membranes International Inc.* (Nafion-Membran, die als Natriumsalz ausgeliefert wird); die Präkonditionierung erfolgte über Nacht in einer 0.2 M $Na[BPh_4]$-THF-Lösung

- Elektrolytlösung: 0.2 M $Na[BPh_4]$-THF-Lösung (Anodenraum: 9 mL; Kathodenraum: 35 mL)

Nach der Zugabe von **68** (20 mg) in den Kathodenraum wurde das Elektrolyseexperiment gestartet, das meistens ca. 30 min dauerte. Dann lag eine tiefgrüne Lösung im Kathodenraum vor, die abgetrennt wurde. Für deren Aufarbeitung musste THF unter vermindertem Druck entfernt, der Rückstand mit Et_2O extrahiert und anschließend Schlenk-filtriert (G4) werden. Nach dem erneuten Entfernen des Lösungsmittels unter vermindertem Druck, wurde der Rückstand mit THF-d_8 (0.5 mL) aufgenommen und in ein NMR-Rohr für die Analytik mittels NMR-Spektroskopie abgefüllt.

4.2. Synthese und NMR-Daten nicht publizierter Verbindungen

4.2.1. [4+2]-Cycloadditionsprodukte

Li_2[88]

Eine frisch hergestellte Lösung von Li_2[**68**] (59 µmol) in THF-d_8 (0.5 mL),[166] die sich in einem NMR-Rohr befand, wurde mit flüssigem Stickstoff eingefroren, das System evakuiert und Butadien (1 atm) einströmen gelassen. Beim Erwärmen der Lösung auf RT entwich der Gasüberdruck durch eine Hg-Wanne. Nach 10 min wurde die Reaktionsmischung wieder eingefroren und das NMR-Rohr vorm Abschmelzen evakuiert. Die NMR-Spektroskopie zeigte eine vollständige Umsetzung von Li_2[**68**] zu Li_2[**88**] an.

^{1}H NMR (500.2 MHz, THF-d_8): δ = 7.32–7.30 (n.a., 3H; C_6H_4), 7.23–7.22 (m, 1H; C_6H_4), 6.64–6.59 (m, 4H; C_6H_4), 5.07–5.04 (m, 1H; BCHC*H*CH_2), 3.95 (dd, ^3J(H,H) = 16.8 Hz, ^2J(H,H) = 4.2 Hz, 1H; BCHCHC*H*$_2$), 3.82 (dd, ^3J(H,H) = 9.7 Hz, ^2J(H,H) = 4.2 Hz, 1H; BCHCHC*H*$_2$), 0.75 (n.a., 1H; BC*H*$CHCH_2$), 0.14 (m, 3H; H_2CBCH_3 + 1H; BC*H*$_2$), 0.09 (br, 3H; HCBC*H*$_3$), –0.41 (m, 1H; BC*H*$_2$).
^{11}B NMR (160.5 MHz, THF-d_8): δ = –14.3 (s), –15.6 (s).
^{13}C{^{1}H} NMR (125.8 MHz, THF-d_8): δ = 169.9 (m; *C*BCH_2), 166.9 (q, ^1J(B,C) = 46.8 Hz; *C*BCH), 161.1 (BCH*C*HCH_2), 129.0 (C_6H_4), 127.4 (C_6H_4), 126.9 (C_6H_4), 120.7 (C_6H_4), 97.1 (BCHCH*C*H_2), 44.5 (m; B*C*$HCHCH_2$), 33.9 (q, ^1J(B,C) = 36.7 Hz; B*C*H_2), 4.6 (q ^1J(B,C) = 44.9 Hz; H_2CBCH_3), 3.2 (q, ^1J(B,C) = 44.3 Hz; HCB*C*H_3).

Li_2[89] und 90·(2 THF)

Eine frisch hergestellte Lösung von Li_2[**72**] (55 µmol) in THF-d_8 (0.5 mL),[129] die sich in einem NMR-Rohr befand, wurde mit flüssigem Stickstoff eingefroren, das System evakuiert und Ethen (1 atm) einströmen gelassen. Beim Erwärmen der Lösung auf RT entwich der Gasüberdruck durch eine Hg-Wanne. Nach 10 min wurde die Reaktionsmischung wieder eingefroren und das NMR-Rohr vorm Abschmelzen evakuiert. Nach einer Lagerung der Probe bei 50 °C für 18 h zeigte die NMR-Spektroskopie eine vollständige Umsetzung von Li_2[**72**] zu Li_2[**89**] an.

^{1}H{^{11}B} NMR (500.2 MHz, THF-d_8): δ = 7.20–7.18 (m, 4H; H-a), 6.61–6.60 (m, 4H; H-b), 2.22 (s, 2H; BH), –0.05 (s, 4H; CH_2).
^{11}B NMR (160.5 MHz, THF-d_8): δ = –13.2 (d, ^1J(B,H) = 73.2 Hz).
^{13}C{^{1}H} NMR (125.8 MHz, THF-d_8): δ = 167.3 (br; BC), 128.4 (C-a), 121.8 (C-b), 14.5 (br; CH_2).

Nach der Überführung der THF-d_8-Lösung von Li_2[**89**] in ein neues NMR-Rohr wurde Me_3SiCl (7.0 µL, 6.0 mg, 55 µmol, 1.00 eq) hinzugefügt. Alle flüchtigen Bestandteile wurden unter vermindertem Druck entfernt und die Probe erneut in THF-d_8 (0.5 mL) gelöst. Die Analyse mittels NMR-Spektroskopie bestätigte die Bildung von **90**·(2 THF) neben ca. 10% **77**.[167]

^{1}H NMR (500.2 MHz, THF-d_8): δ = 7.13–7.11 (m, 4H; H-a), 6.77–6.75 (m, 4H; H-b), 0.26 (s, 4H; CH_2).
^{11}B NMR (160.5 MHz, THF-d_8): δ = 10.6 (br).
^{13}C{^{1}H} NMR (125.8 MHz, THF-d_8): δ = 155.2 (br; BC), 124.2 (C-a), 122.1 (C-b), 15.6 (br; CH_2).

Li_2[92]

Bei Raumtemperatur wurde pinBC≡CBpin (19 mg, 70 µmol, 0.95 eq) zu einer frisch hergestellten Lösung von Li_2[**68**] (74 µmol, 1.00 eq)[166] in THF-d_8 (0.5 mL) gegeben. Die NMR-Spektroskopie zeigte die quantitative Darstellung von Li_2[**92**] an. Durch Gasphasendiffusion von *n*-Hexan in die Reaktionslösung von Li_2[**92**], der 12-Krone-4 (12-c-4) zugesetzt war, konnten Einkristalle der Form [Li(12-c-4)(thf)]$_2$[**92**](THF) gewonnen werden.

^{1}H NMR (500.2 MHz, THF-d_8): δ = 7.14–7.13 (m, 4H; H-a), 6.47–6.45 (m, 4H; H-b), 1.26 (s, 24H; Bpin), 0.59 (s, 6H; BCH_3).
^{11}B NMR (160.5 MHz, THF-d_8): δ = –11.2 (s); Bpin (n.b.).
^{13}C{^{1}H} NMR (125.8 MHz, THF-d_8): δ = 182.2 (br; C=C), 167.4 (br; BC), 125.6 (C-a), 120.1 (C-b), 82.8 ($C(CH_3)_2$), 25.5 ($C(CH_3)_2$), 1.7 (br; BCH_3).

M_2[95] (M^+ = Li^+, Na^+)

Bei Raumtemperatur wurde *i*PrN=C=N*i*Pr (11 µL, 9 mg, 71 µmol, 0.97 eq) zu einer frisch hergestellten Lösung von M_2[**68**] (74 µmol, 1.00 eq)[166] in THF-d_8 (0.5 mL) gegeben. Die NMR-Spektroskopie zeigte die quantitative Darstellung von M_2[**95**] an. Durch Gasphasendiffusion von *n*-Hexan in die Reaktionslösung von Na_2[**95**], der 18-Krone-6 (18-c-6) zugesetzt war, konnten Einkristalle der Form [Na][Na(18-c-6)(thf)$_2$][**95**] gewonnen werden.

Li_2[**95**]

^{1}H NMR (500.2 MHz, THF-d_8): δ = 7.17–7.15 (m, 4H; C_6H_4), 6.52–6.50 (m, 4H; C_6H_4), 4.64 (n.a., 1H; $CH(CH_3)_2$), 4.36 (n.a., 1H; $CH(CH_3)_2$), 0.91 (d, ^3J(H,H) = 6.3 Hz, 6H; $CH(CH_3)_2$), 0.86 (d, ^3J(H,H) = 6.3 Hz, 6H; $CH(CH_3)_2$), 0.63 (s, 3H; $NBCH_3$), 0.55 (m, 3H; $CBCH_3$).
^{11}B NMR (96.3 MHz, THF-d_8): δ = –8.4 (br; BC), –13.6 (s; BN).
^{13}C{^{1}H} NMR (125.8 MHz, THF-d_8): δ = 203.7 (br; NCN), 167.9 (br; BC), 126.6 (C_6H_4), 125.6 (C_6H_4), 120.8 (C_6H_4), 120.4 (C_6H_4), 49.6 ($CH(CH_3)_2$), 46.9 ($CH(CH_3)_2$), 28.1 ($CH(CH_3)_2$), 24.2 ($CH(CH_3)_2$), 6.0 (br; $NBCH_3$), 5.4 (br; $CBCH_3$).

Na_2[**95**]

^{1}H NMR (500.2 MHz, THF-d_8): δ = 7.26–7.25 (m, 4H; C_6H_4), 6.64–6.62 (m, 4H; C_6H_4), 4.88 (sept, ^3J(H,H) = 6.2 Hz, 1H; $CH(CH_3)_2$), 4.60 (sept, ^3J(H,H) = 6.2 Hz, 1H; $CH(CH_3)_2$), 0.91 (d, ^3J(H,H) = 6.2 Hz, 6H; $CH(CH_3)_2$), 0.89 (d, ^3J(H,H) = 6.2 Hz, 6H; $CH(CH_3)_2$), 0.69 (s, 3H; $NBCH_3$), 0.58 (m, 3H; $CBCH_3$).
^{11}B NMR (96.3 MHz, THF-d_8): δ = –8.7 (br, BC), –13.6 (s, BN).
^{13}C{^{1}H} NMR (125.8 MHz, THF-d_8): δ = 198.5 (q, ^1J(B,C) = 47.7 Hz; NCN), 169.2 (br; BC), 126.3 (C_6H_4), 125.4 (C_6H_4), 121.5 (C_6H_4), 121.3 (C_6H_4), 48.1 ($CH(CH_3)_2$), 47.2 ($CH(CH_3)_2$), 28.7 ($CH(CH_3)_2$), 23.4 ($CH(CH_3)_2$), 6.3 (q, ^1J(B,C) = 45.6 Hz; $NBCH_3$), 5.4 (br; $CBCH_3$).

Li_2[68] in der Reaktion mit Anthron

Bei Raumtemperatur wurde Anthron (10 mg, 49 µmol, 1.00 eq) zu einer frisch hergestellten Lösung von Li_2[**68**] (49 µmol, 1.00 eq)[166] in THF-d_8 (0.5 mL) gegeben. Die NMR-Spektroskopie zeigte unter anderem die Reaktionsprodukte Li[**68**-H] und Lithiumanthrolat (Li[**96**]) an. Durch langsames Abdampfen der Reaktionslösung konnten Einkristalle der Form [Li(thf)$_2$][**96**] gewonnen werden.

Li[**68**-H] im Reaktionsgemisch

^{1}H NMR (500.2 MHz, THF-d_8): δ = 7.40–7.39 (m, 2H; C_6H_4), 6.74–6.72 (m, 2H; C_6H_4), 6.39–6.36 (m, 2H; C_6H_4), 6.28–6.26 (m, 2H; C_6H_4), 0.48 (s, 3H; BCH_3), –0.20 (s, 3H; BCH_3); n.b. (BH).
^{11}B NMR (160.5 MHz, THF-d_8): δ = 22.8 (br), –17.5 (d, ^1J(B,H) = 62.1 Hz).
Kommentar: Die Verschiebungen sind nicht mit isoliertem Li[**68**-H] in THF-d_8 vergleichbar, da die NMR-Daten aus einer Reaktionsmischung bestimmt wurden, die noch Lithiumanthrolat (Li[**96**]) und Anthron enthielt.

Li[**96**] im Reaktionsgemisch

^{1}H NMR (500.2 MHz, THF-d_8): δ = 8.82–8.80 (m, 2H; C_6H_4), 7.72–7.71 (m, 2H; C_6H_4), 7.28 (s, 1H; CH), 7.25–7.22 (m, 2H; C_6H_4), 7.11–7.08 (m, 2H; C_6H_4).

Li[97]

Bei Raumtemperatur wurde DMSO (5.1 µL, 5.6 mg, 71 µmol, 0.97 eq) zu einer frisch hergestellten Lösung von Li_2[**68**] (74 µmol, 1.00 eq)[166] in THF-d_8 (0.5 mL) gegeben. Die NMR-Spektroskopie zeigte die quantitative Darstellung von Li[**97**] an. Durch Gasphasendiffusion von *n*-Hexan in die Reaktionslösung, der 12-Krone-4 (12-c-4) zugesetzt war, konnten Einkristalle der Form [Li(12-c-4)$_2$][**97**] gewonnen werden.

^{1}H NMR (500.2 MHz, THF-d_8): δ = 7.27–7.26 (m, 2H; H-d), 7.22–7.21 (m, 2H; H-a), 6.71–6.68 (m, 2H; H-c), 6.67–6.64 (m, 2H; H-b), 1.20 (s, 3H; SCH_3), 1.04 (s, 2H; SCH_2), 0.57 (s, 3H; $SBCH_3$), 0.21 (s, 3H; H_2CBCH_3).
^{11}B NMR (160.5 MHz, THF-d_8): δ = –1.8 (s; BS), –16.9 (s; BC).
^{13}C{^{1}H} NMR (125.8 MHz, THF-d_8): δ = 169.1 (br; C-e), 154.2 (br; C-f), 127.9 (C-a), 127.2 (C-d), 123.0 (C-c), 120.9 (C-b), 38.6 (br; SCH_2), 21.2 (SCH_3), 4.2 (br; $CBCH_3$), 0.2 ($SBCH_3$).

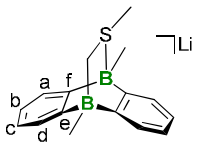

Li[97]

Übersicht der Substrate, die nach der Reaktion mit Li_2[**68**] Multi-Komponenten-Spektren lieferten:

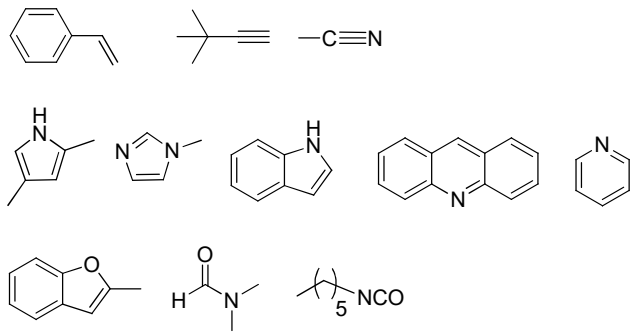

4.2.2. M_2[**A**] in Reaktionen mit Elektrophilen

M[107]

Bei Raumtemperatur wurde EtBr (5.5 µL, 8.0 mg, 74 µmol, 1.00 eq) zu einer frisch hergestellten Lösung von M_2[**68**] (M^+ = Li^+, Na^+) (74 µmol, 1.00 eq)[166] in THF-d_8 (0.5 mL) gegeben. Die NMR-Spektroskopie zeigte die quantitative Darstellung von M[**107**] an. Durch Gasphasendiffusion von *n*-Hexan in die Reaktionslösung von Na[**107**], der 18-Krone-6 (18-c-6) zugesetzt war, konnten Einkristalle der Form [Na(18-c-6)(thf)$_2$][**107**] gewonnen werden.

Li[**107**]

^{1}H NMR (500.2 MHz, THF-d_8): δ = 7.89–7.88 (m, 2H; H-d), 7.70–7.67 (m, 2H; H-a), 7.06–7.02 (m, 2H; H-b), 6.83–6.80 (m, 2H; H-c), 1.25 (s, 3H; BCH_3), 0.42–0.35 (m, 2H; CH_2CH_3), 0.13–0.08 (m, 3H; CH_2CH_3), –0.10–(–0.13) (m, 3H; $EtBCH_3$).
^{11}B NMR (160.5 MHz, THF-d_8): δ = 62.0 (br), –14.8 (s).
^{13}C{^{1}H} NMR (125.8 MHz, THF-d_8): δ = 183.0 (q, ^1J(B,C) = 48.5 Hz; C-f), 145.3 (C-e), 133.9 (C-d), 132.7 (C-a), 128.5 (C-b), 120.4 (C-c), 26.8 (q, ^1J(B,C) = 38.3 Hz; CH_2CH_3), 13.8 (q, ^1J(B,C) = 41.0 Hz; $EtBCH_3$), 12.4 (CH_2CH_3), 4.8 (BCH_3).

Na[**107**]

^{1}H NMR (500.2 MHz, THF-d_8): δ = 7.92–7.90 (m, 2H; H-d), 7.72–7.69 (m, 2H; H-a), 7.08–7.05 (m, 2H; H-b), 6.86–6.83 (m, 2H; H-c), 1.27 (s, 3H; BCH_3), 0.42–0.35 (m, 2H; CH_2CH_3), 0.12–0.07 (m, 3H; CH_2CH_3), –0.08–(–0.11) (m, 3H; $EtBCH_3$).
^{11}B NMR (160.5 MHz, THF-d_8): δ = 65.4 (br), –14.8 (s).
^{13}C{^{1}H} NMR (125.8 MHz, THF-d_8): δ = 182.4 (q, ^1J(B,C) = 48.2 Hz; C-f), 145.3 (C-e), 134.0 (C-d), 132.8 (C-a), 128.7 (C-b), 120.7 (C-c), 27.0 (q, ^1J(B,C) = 38.3 Hz; CH_2CH_3), 13.4 (q, ^1J(B,C) = 40.8 Hz; $EtBCH_3$), 12.3 (CH_2CH_3), 4.9 (BCH_3).

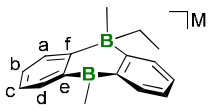

M[**107**]

M[109] und 110

Bei Raumtemperatur wurde EtBr (5.5 µL, 8.0 mg, 74 µmol, 1.00 eq) zu einer frisch hergestellten Lösung von M_2[**72**] (74 µmol, 1.00 eq; $M^+ = Li^+$, Na^+)[166] in THF-d_8 (0.5 mL) gegeben. Die NMR-Spektroskopie zeigte die quantitative Darstellung von M[**109**] an. Nach der Zugabe eines weiteren Äquivalents EtBr entstanden Ethan und **110**.

Li[**109**]

^{1}H NMR (500.2 MHz, THF-d_8): δ = 7.98–7.97 (m, 2H; H-d), 7.58 (n.a., 2H; H-a), 7.05–7.02 (m, 2H; H-b), 6.91–6.88 (m, 2H; H-c), 2.56 (q, ^1J(B,H) = 76.2 Hz, 2H; BH_2), 1.91 (q, ^3J(H,H) = 8.1 Hz, 2H; CH_2CH$_3$), 1.13 (t, ^3J(H,H) = 8.1 Hz, 3H; CH$_2$CH_3).
^{11}B NMR (160.5 MHz, THF-d_8): δ = 67.6 (br; BC), –18.9 (t, ^1J(B,H) = 76.2 Hz; BH_2).
^{13}C{^{1}H} NMR (125.8 MHz, THF-d_8): δ = 177.0 (q, ^1J(B,C) = 49.9 Hz; C-f), 144.1 (C-e), 135.1 (C-a), 134.7 (C-d), 127.9 (C-b), 121.1 (C-c), 11.7 (*C*H$_2$*C*H$_3$).

Na[**109**]

^{1}H NMR (250.1 MHz, THF-d_8): δ = 8.29–8.26 (m, 2H; C_6H_4), 7.62 (n.a.-m, 2H; C_6H_4), 7.17–7.09 (m, 2H; C_6H_4), 7.04–6.96 (m, 2H; C_6H_4), 2.56 (q, ^1J(B,H) = 76.2 Hz, 2H; BH_2), 1.95 (q, ^3J(H,H) = 7.9 Hz, 2H; CH_2CH$_3$), 1.13 (t, ^3J(H,H) = 8.1 Hz, 3H; CH$_2$CH_3).
^{11}B NMR (96.3 MHz, THF-d_8): δ = 65.4 (br; BC), –19.4 (t, ^1J(B,H) = 77.2 Hz; BH_2).

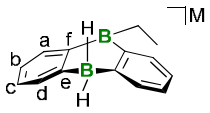

M[**109**]

110

^{1}H NMR (500.2 MHz, THF-d_8): δ = 8.01–7.99 (m, 2H; H-a), 7.66–7.64 (m, 2H; H-d), 7.35–7.32 (m, 2H; H-c), 7.26–7.23 (m, 2H; H-b), 4.10 (br, 1H; BH), 1.91 (q, ^3J(H,H) = 8.1 Hz, 2H; CH_2CH$_3$), 1.05 (t, ^3J(H,H) = 7.3 Hz, 3H; CH$_2$CH_3).
^{11}B NMR (160.5 MHz, THF-d_8): δ = 62.5 (br; BC), 9.3 (br; BH).
^{13}C{^{1}H} NMR (125.8 MHz, THF-d_8): δ = 156.9 (C-e), 145.7 (C-f), 136.0 (C-d), 135.5 (C-a), 131.4 (C-c), 127.1 (C-b), 12.0 (br; *C*H$_2$CH$_3$), 10.3 (CH$_2$*C*H$_3$).

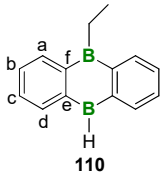

110

M[111] und M[112]

Bei Raumtemperatur wurde (Brommethyl)cyclopropan (5.7 µL, 8.0 mg, 59 µmol, 1.00 eq) zu einer frisch hergestellten Lösung von M_2[**72**] (M^+ = Li^+, Na^+) (59 µmol, 1.00 eq)[166] in THF-d_8 (0.5 mL) gegeben. Die NMR-Spektroskopie zeigte die Bildung von M[**111**] und M[**112**] im Verhältnis 10:1 für M^+ = Li^+ bzw. 1.6:1 für M^+ = Na^+ an. Kommentar: Die NMR-Verschiebungen der beiden Verbindungen sind zusammen aufgeführt, da deren Signale stark überlappen (schwarze Farbe). War eine eindeutige Zuordnung möglich, ist dies farblich hervorgehoben.

Li[**111**] und Li[**112**]

^{1}H NMR (250.1 MHz, THF-d_8): δ = 7.90–7.87 (m, 2H + 2H; H-d), 7.72 (n.a., 2H + 2H; H-a), 7.09–7.00 (m, 2H + 2H; H-b), 6.85–6.79 (m, 2H + 2H; H-c), 5.66–5.50 (m, 1H; $CH_2CH_2CHCH_2$), 4.46 (d, ^3J(H,H) = 17.1 Hz, 1H; $CH_2CH_2CHCH_2$), 4.33 (d, ^3J(H,H) = 10.4 Hz, 1H; $CH_2CH_2CHCH_2$), 1.26 (s, 3H; BCH_3), 1.25 (s, 3H; BCH_3), 1.20–1.14 (m, 2H; $CH_2CH_2CHCH_2$), 0.57–0.44 (m, 2H; $CH_2CH_2CHCH_2$), 0.36–0.28 (m, 2H; $CH_2CHCH_2CH_2$), –0.03–(–0.07) (m, 3H; H_2CBCH_3), –0.09–(–0.13) (m, 1H + 3H; $CH_2CHCH_2CH_2$ + H_2CBCH_3), –0.34–(–0.41) (m, 2H; $CH_2CHCH_2CH_2$), –0.72–(–0.78) (m, 2H; $CH_2CHCH_2CH_2$).
^{11}B NMR (96.3 MHz, THF-d_8): δ = 62.2 (br), –16.8 (s), –17.0 (s).
^{13}C{^{1}H} NMR (125.8 MHz, THF-d_8): δ = 183.1 (q, ^1J(B,C) = 48.7 Hz; C-f), 148.4 ($CH_2CH_2CHCH_2$), 145.2 (C-e), 134.0 (C-d), 133.8 (C-d), 132.9 (C-a), 132.8 (C-a), 128.7 (C-b), 128.3 (C-b), 120.6 (C-c), 120.6 (C-c), 108.0 ($CH_2CH_2CHCH_2$), 42.9 (q, ^1J(B,C) = 37.2 Hz; $CH_2CHCH_2CH_2$), 35.0 (q, ^1J(B,C) = 38.2 Hz; $CH_2CH_2CHCH_2$), 33.9 ($CH_2CH_2CHCH_2$), 14.2 (q, ^1J(B,C) = 40.7 Hz; H_2CBCH_3), 12.8 (q, ^1J(B,C) = 41.5 Hz; H_2CBCH_3), 11.4 ($CH_2CHCH_2CH_2$), 6.6 (2x$CH_2CHCH_2CH_2$), 4.9 (BCH_3).

Na[**111**] und Na[**112**]

^{1}H NMR (500.2 MHz, THF-d_8): δ = 7.92–7.91 (m, 2H + 2H; H-d), 7.75 (n.a., 2H; H-a), 7.71 (n.a., 2H; H-a), 7.08–7.05 (m, 2H + 2H; H-b), 6.87–6.83 (m, 2H + 2H; H-c), 5.63–5.55 (m, 1H; $CH_2CH_2CHCH_2$), 4.46 (d, ^3J(H,H) = 17.1 Hz, 1H; $CH_2CH_2CHCH_2$), 4.33 (d, ^3J(H,H) = 10.2 Hz, 1H; $CH_2CH_2CHCH_2$), 1.27 (s, 3H + 3H; BCH_3), 1.20–1.15 (m, 2H; $CH_2CH_2CHCH_2$), 0.53–0.49 (m, 2H; $CH_2CH_2CHCH_2$), 0.35–0.31 (m, 2H; $CH_2CHCH_2CH_2$), –0.01–(–0.04) (m, 3H; H_2CBCH_3), –0.08–(–0.10) (m, 1H + 3H; $CH_2CHCH_2CH_2$ + H_2CBCH_3), –0.36–(–0.40) (m, 2H; $CH_2CHCH_2CH_2$), –0.75–(–0.78) (m, 2H; $CH_2CHCH_2CH_2$).
^{11}B NMR (96.3 MHz, THF-d_8): δ = 63.5 (br), –15.0 (s), –15.2 (s).
^{13}C{^{1}H} NMR (125.8 MHz, THF-d_8): δ = 182.3 (q, ^1J(B,C) = 48.5 Hz; C-f), 148.4 ($CH_2CH_2CHCH_2$), 145.1 (C-e), 134.1 (C-d), 134.0 (C-d), 133.0 (C-a), 132.8 (C-a), 128.8 (C-b), 128.5 (C-b), 120.8 (2xC-c), 108.1 ($CH_2CH_2CHCH_2$), 43.1 (q, ^1J(B,C) = 37.7 Hz; $CH_2CHCH_2CH_2$), 35.1 (q, ^1J(B,C) = 40.0 Hz; $CH_2CH_2CHCH_2$), 33.9 ($CH_2CH_2CHCH_2$), 14.1 (q, ^1J(B,C) = 40.6 Hz; H_2CBCH_3), 12.4 (q, ^1J(B,C) = 41.3 Hz; H_2CBCH_3), 11.3 ($CH_2CHCH_2CH_2$), 6.5 (2x$CH_2CHCH_2CH_2$), 5.0 (BCH_3).

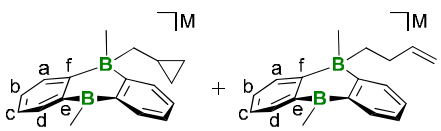

M[**111**] M[**112**]

M[113]

Bei Raumtemperatur wurde Et_3SiBr (12.7 µL, 14.0 mg, 74 µmol, 1.00 eq) zu einer frisch hergestellten Lösung von M_2[**72**] (M^+ = Li^+, Na^+) (74 µmol, 1.00 eq)[166] in THF-d_8 (0.5 mL) gegeben. Die NMR-Spektroskopie zeigte die quantitative Darstellung von M[**113**] an.

Li[**113**]

^{1}H NMR (500.2 MHz, THF-d_8): δ = 7.86–7.84 (m, 2H; H-d), 7.64–7.63 (m, 2H; H-a), 7.00–6.96 (m, 2H; H-b), 6.81–6.78 (m, 2H; H-c), 5.53 (br, 1H; BH), 3.19 (q, ^1J(B,H) = 86.8 Hz, 1H; BH), 0.56 (t, ^3J(H,H) = 7.9 Hz, 9H; CH_2CH_3), –0.03 (q, ^3J(H,H) = 7.9 Hz, 6H; CH_2CH_3).
^{11}B NMR (96.3 MHz, THF-d_8): δ = 22.7 (br; BH), –17.0 (d, ^1J(B,H) = 85.9 Hz; B(H)$SiEt_3$).
^{13}C{^{1}H} NMR (125.8 MHz, THF-d_8): δ = 179.8 (br; C-f), 146.9 (C-e), 140.8 (C-d), 133.8 (C-a), 126.7 (C-b), 118.9 (C-c), 8.9 (CH_2CH_3), 4.0 (CH_2CH_3).
^{29}Si NMR (99.4 MHz, THF-d_8): δ = 0.2.

Na[**113**]

^{1}H NMR (500.2 MHz, THF-d_8): δ = 7.98–7.96 (m, 2H; C_6H_4), 7.70–7.69 (m, 2H; C_6H_4), 7.14–7.12 (m, 2H; C_6H_4), 6.96–6.93 (m, 2H; C_6H_4), 5.48 (br-s, 1H; BH), 3.04 (q, ^1J(B,H) = 82.1 Hz, 1H; BH), 0.58 (t, ^3J(H,H) = 7.9 Hz, 9H; CH_2CH_3), 0.01 (q, ^3J(H,H) = 7.9 Hz, 6H; CH_2CH_3).
^{11}B NMR (96.3 MHz, THF-d_8): δ = 24.1 (br; BH), –18.0 (d, ^1J(B,H) = 82.1 Hz; B(H)$SiEt_3$).
^{29}Si NMR (99.4 MHz, THF-d_8): δ = 0.9.

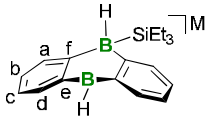

M[**113**]

M[114]

Bei Raumtemperatur wurde Et_3SiBr (12.7 µL, 14.0 mg, 74 µmol, 1.00 eq) zu einer frisch hergestellten Lösung von M_2[**68**] (M^+ = Li^+, Na^+) (74 µmol, 1.00 eq)[166] in THF-d_8 (0.5 mL) gegeben. Die NMR-Spektroskopie zeigte den vollständigen Verbrauch von M_2[**68**] an.

Li[**114**]

äq:ax = 2.5:1; Kommentar: Bei nicht eingefärbten Resonanzen überlagern sich die Signale der beiden Spezies.

^{1}H NMR (500.2 MHz, THF-d_8): δ = 8.01–8.00 (m, 2H; H-d), 7.89–7.88 (m, 2H; H-d), 7.74–7.72 (m, 2H; H-a), 7.69 (n.a., 2H; H-a), 7.06–7.01 (m, 4H; H-b), 6.83–6.77 (m, 4H; H-c), 1.30 (s, 3H; BCH_3), 1.25 (s, 3H; BCH_3), 0.87 (t, ^3J(H,H) = 7.9 Hz, 9H; CH_2CH_3), 0.48–0.43 (m, 18H; CH_2CH_3 + CH_2CH_3 + Et_3SiBCH_3), –0.08–(–0.14) (m, 9H; CH_2CH_3 + Et_3SiBCH_3).
^{11}B NMR (96.3 MHz, THF-d_8): δ = 66.1 (br), 23.7 (br), –15.2 (s), –16.6 (s).
^{13}C{^{1}H} NMR (125.8 MHz, THF-d_8): δ = 183.2 (q, ^1J(B,C) = 48.5 Hz; C-f), 178.2 (C-f), 144.9 (C-e), 144.3 (C-e), 134.5 (C-d), 133.9 (C-d), 132.7 (C-a), 132.0 (C-a), 128.4 (C-b), 126.9 (C-b), 120.3 (C-c), 118.8 (C-c), 14.2 (q, ^1J(B,C) = 40.6 Hz; Et_3SiBCH_3), 9.0 (CH_2CH_3), 6.9 (CH_2CH_3), 6.8 (br; Et_3SiBCH_3), 4.9 (CH_2CH_3), 4.7 (BCH_3), 3.8 (BCH_3), 3.3 (CH_2CH_3).
^{29}Si NMR (99.4 MHz, THF-d_8): δ = 14.7, –3.4.

äq-Na[**114**]

^{1}H NMR (500.2 MHz, THF-d_8): δ = 7.92–7.90 (m, 2H; H-d), 7.71 (n.a., 2H; H-a), 7.08–7.05 (m, 2H; H-b), 6.86–6.82 (m, 2H; H-c), 1.27 (s, 3H; BCH_3), 0.87 (t, ^3J(H,H) = 8.0 Hz, 9H; CH_2CH_3), 0.46 (q, ^3J(H,H) = 7.9 Hz, 6H; CH_2CH_3), –0.11 (m, 3H; Et_3SiBCH_3).
^{11}B NMR (96.3 MHz, THF-d_8): δ = 66.8 (br), –17.1 (s).
^{13}C{^{1}H} NMR (125.8 MHz, THF-d_8): δ = 182.4 (q, ^1J(B,C) = 48.2 Hz; C-f), 144.9 (C-e), 134.0 (C-d), 132.8 (C-a), 128.6 (C-b), 120.6 (C-c), 13.8 (q, ^1J(B,C) = 40.6 Hz; Et_3SiBCH_3), 6.9 (CH_2CH_3), 5.0 (CH_2CH_3), 4.8 (BCH_3).
^{29}Si NMR (99.4 MHz, THF-d_8): δ = 14.8.

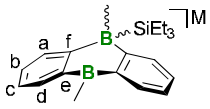

M[**114**]

4.3. Kristallographische Daten nicht publizierter Verbindungen

Tabelle 5. Kristallographische Daten von $[Li(12\text{-}c\text{-}4)_2]_2$[**79**-$H_2$](THF), $[Li(12\text{-}c\text{-}4)(thf)]_2$[**92**](THF) und [Na][Na(18-c-6)$(thf)_2$][**95**].

	[Li(12-c-4)$_2$]$_2$[**79**-H_2](THF)	[Li(12-c-4)(thf)]$_2$[**92**](THF)	[Na][Na(18-c-6)$(thf)_2$][**95**]
Interner Code	wa2611	wa2628	wa2700
Summenformel	$C_{62}H_{96}B_2Li_2O_{17}$	$C_{56}H_{94}B_4Li_2O_{15}$	$C_{82}H_{136}B_4N_4Na_4O_{16}$
M_r [g mol^{-1}]	1148.88	1064.43	1569.14
Farbe, Morphologie	farblos, Block	farblos, Block	farblos, Block
T [K]	173(2)	173(2)	173(2)
Strahlung, λ [Å]	MoK_α, 0.71073	MoK_α, 0.71073	MoK_α, 0.71073
Kristallsystem	triklin	monoklin	triklin
Raumgruppe	P–1	$P2_1/n$	P–1
a [Å]	12.1304(6)	16.5042(9)	10.2466(4)
b [Å]	13.8522(8)	21.4033(8)	14.7968(6)
c [Å]	39.674(2)	17.2449(9)	15.6728(6)
α [°]	91.267(5)	90	108.371(3)
β [°]	91.500(4)	97.538(4)	95.677(3)
γ [°]	108.934(4)	90	90.320(3)
V [Å^3]	6300.4(6)	6039.0(5)	2242.39(16)
Z	4	4	1
$D_{berechnet}$ [g cm^{-3}]	1.211	1.171	1.162
μ [mm^{-1}]	0.085	0.081	0.094
F(000)	2480	2304	848
Kristallgröße [mm^3]	0.23 x 0.19 x 0.17	0.24 x 0.22 x 0.19	0.24 x 0.19 x 0.13
Gesammelte Reflexe	50998	63558	44204
Unabhängige Reflexe (R_{int})	50998	10641 (0.0589)	8385 (0.0329)
Daten/Restraints/ Parameter	50998 / 936 / 1516	10641 / 59 / 832	8385 / 60 / 543
GOF on F^2	1.545	1.266	1.071
R_1, wR_2 [$I > 2\sigma(I)$]	0.1618, 0.3935	0.0728, 0.1818	0.0571, 0.1515
R_1, wR_2 (alle Daten)	0.2481, 0.2495	0.1035, 0.1956	0.0647, 0.1570
Restelektronendichte (peak and hole) [e Å^{-3}]	1.383, –1.140	0.770, –0.525	0.668, –0.263

Tabelle 6. Kristallographische Daten von $[Li(thf)_2][\mathbf{96}]$, $[Li(12\text{-}c\text{-}4)_2][\mathbf{97}](12\text{-}c\text{-}4)$ und $[Na(18\text{-}c\text{-}6)(thf)_2][\mathbf{107}]$.

	$[Li(thf)_2][\mathbf{96}]$	$[Li(12\text{-}c\text{-}4)_2][\mathbf{97}](12\text{-}c\text{-}4)$	$[Na(18\text{-}c\text{-}6)(thf)_2][\mathbf{107}]$
Interner Code	wa2587	wa2675	wa2709
Summenformel	$C_{44}H_{50}Li_2O_6$	$C_{36}H_{59}B_2LiO_{10}S$	$C_{36}H_{59}B_2NaO_8$
M_r [g mol^{-1}]	688.72	712.45	664.44
Farbe, Morphologie	gelb-braun, Nadel	farblos, Block	farblos, Block
T [K]	173(2)	173(2)	173(2)
Strahlung, λ [Å]	MoK_α, 0.71073	MoK_α, 0.71073	MoK_α, 0.71073
Kristallsystem	monoklin	monoklin	triklin
Raumgruppe	$P2_1/c$	$C2/c$	$P\bar{1}$
a [Å]	8.527(3)	24.4353(10)	8.9650(5)
b [Å]	21.342(5)	14.7369(6)	9.1162(5)
c [Å]	20.925(7)	24.0705(10)	23.7647(14)
α [°]	90	90	85.367(5)
β [°]	99.01(3)	119.476(3)	89.681(5)
γ [°]	90	90	83.363(5)
V [Å^3]	3761(2)	7545.9(6)	1922.88(19)
Z	4	8	2
$D_{berechnet}$ [g cm^{-3}]	1.216	1.254	1.148
μ [mm^{-1}]	0.078	0.140	0.087
F(000)	1472	3072	720
Kristallgröße [mm^3]	0.18 x 0.04 x 0.02	0.22 x 0.18 x 0.16	0.24 x 0.14 x 0.13
Gesammelte Reflexe	25586	32328	28333
Unabhängige Reflexe (R_{int})	6643 (0.2376)	6647 (0.0421)	7195 (0.0327)
Daten/Restraints/ Parameter	6643 / 0 / 469	6647 / 72 / 452	7195 / 72 / 483
GOF on F^2	0.862	1.057	1.065
R_1, wR_2 [$I > 2\sigma(I)$]	0.0987, 0.1724	0.1115, 0.2985	0.0780, 0.1987
R_1, wR_2 (alle Daten)	0.3055, 0.2569	0.1248, 0.3099	0.1025, 0.2155
Restelektronendichte (peak and hole) [e Å^{-3}]	0.210, –0.283	1.162, –0.805	0.774, –0.461

5. Referenzen

[1] P. K. Stumpf and E. E. Conn, *The Biochemistry of Plants*, in *Photosynthesis*, Ed. M. D. Hatch und N. K. Boardman, Academic Press, *8*, New York, London, **1981**.

[2] J. M. Berg, J. L. Tymoczko, G. J. Gatto und L. Stryer, *Stryer Biochemie*, *8*, Springer Spektrum, Berlin, **2017**.

[3] A. F. Holleman, E. Wiberg und N. Wiberg, *Lehrbuch der Anorganischen Chemie*, *102*, De Gruyter, Berlin, New York, **2007**.

[4] J. Hagen, *Economic Importance of Catalysts*, in *Industrial Catalysis*, Ed. J. Hagen, Wiley-VCH, Weinheim, **2015**.

[5] D. Steinborn, *Grundlagen der metallorganischen Komplexkatalyse*, *2., überarbeitete und erweiterte Aufl.*, Vieweg+Teubner, Wiesbaden, **2010**.

[6] K. Fukui, *Introductory Remarks on the Quantum Theory of Catalysis and Related Surface Phenomena*, in *The New World of Quantum Chemistry*, Ed. B. Pullman und R. Parr, Springer, *2*, Dordrecht, **1976**.

[7] J. W. Begley und F. Pennella, *J. Catal.* **1967**, *8*, 203-211.

[8] D. G. Musaev and K. Morokuma, *Transition Metal Catalyzed σ-Bond Activation and Formation Reactions*, in *Theoretical Aspects of Transition Metal Catalysis*, Ed. G. Frenking, Springer, Berlin, Heidelberg, **2005**.

[9] P. P. Power, *Nature* **2010**, *463*, 171-177.

[10] G. C. Welch, R. R. San Juan, J. D. Masuda und D. W. Stephan, *Science* **2006**, *314*, 1124-1126.

[11] A. Hamza, A. Stirling, T. A. Rokob und I. Pápai, *Int. J. Quantum Chem.* **2009**, *109*, 2416-2425.

[12] S. Grimme, H. Kruse, L. Goerigk und G. Erker, *Angew. Chem. Int. Ed.* **2010**, *49*, 1402-1405.

[13] T. A. Rokob, I. Bakó, A. Stirling, A. Hamza und I. Pápai, *J. Am. Chem. Soc.* **2013**, *135*, 4425-4437.

[14] L. L. Zeonjuk, N. Vankova, A. Mavrandonakis, T. Heine, G.-V. Röschenthaler und J. Eicher, *Chem. Eur. J.* **2013**, *19*, 17413-17424.

[15] W. Kirmse, *Angew. Chem. Int. Ed.* **2004**, *43*, 1767-1769.

[16] A. J. Arduengo, R. L. Harlow und M. Kline, *J. Am. Chem. Soc.* **1991**, *113*, 361-363.

[17] V. Lavallo, Y. Canac, C. Präsang, B. Donnadieu und G. Bertrand, *Angew. Chem. Int. Ed.* **2005**, *44*, 5705-5709.

[18] M. Melaimi, R. Jazzar, M. Soleilhavoup und G. Bertrand, *Angew. Chem. Int. Ed.* **2017**, *56*, 10046-10068.

[19] G. D. Frey, V. Lavallo, B. Donnadieu, W. W. Schoeller und G. Bertrand, *Science* **2007**, *316*, 439-441.

[20] G. H. Spikes, J. C. Fettinger und P. P. Power, *J. Am. Chem. Soc.* **2005**, *127*, 12232-12233.

[21] G. Erker und D. W. Stephan, *Frustrated Lewis Pairs I & II*, Springer, Heidelberg, **2013**.

[22] D. W. Stephan und G. Erker, *Angew. Chem. Int. Ed.* **2010**, *49*, 46-76.

[23] K. Samigullin, I. Georg, M. Bolte, H.-W. Lerner und M. Wagner, *Chem. Eur. J.* **2016**, *22*, 3478-3484.

[24] D. W. Stephan, *J. Am. Chem. Soc.* **2015**, *137*, 10018-10032.

[25] G. Ménard, J. A. Hatnean, H. J. Cowley, A. J. Lough, J. M. Rawson und D. W. Stephan, *J. Am. Chem. Soc.* **2013**, *135*, 6446-6449.

[26] W. Uhl, C. Appelt, J. Backs, H. Westenberg, A. Wollschläger und J. Tannert, *Organometallics* **2014**, *33*, 1212-1217.

[27] A. Schäfer, M. Reißmann, A. Schäfer, W. Saak, D. Haase und T. Müller, *Angew. Chem. Int. Ed.* **2011**, *50*, 12636-12638.

[28] P. Eisenberger, A. M. Bailey und C. M. Crudden, *J. Am. Chem. Soc.* **2012**, *134*, 17384-17387.

[29] J. Lam, B. A. Günther, J. M. Farrell, P. Eisenberger, B. P. Bestvater, P. D. Newman, R. L. Melen, C. M. Crudden und D. W. Stephan, *Dalton Trans.* **2016**, *45*, 15303-15316.
[30] C. B. Caputo, L. J. Hounjet, R. Dobrovetsky und D. W. Stephan, *Science* **2013**, *341*, 1374-1377.
[31] B. Inés, D. Palomas, S. Holle, S. Steinberg, J. A. Nicasio und M. Alcarazo, *Angew. Chem. Int. Ed.* **2012**, *51*, 12367-12369.
[32] V. Sumerin, F. Schulz, M. Atsumi, C. Wang, M. Nieger, M. Leskelä, T. Repo, P. Pyykkö und B. Rieger, *J. Am. Chem. Soc.* **2008**, *130*, 14117-14119.
[33] E. L. Kolychev, T. Bannenberg, M. Freytag, C. G. Daniliuc, P. G. Jones und M. Tamm, *Chem. Eur. J.* **2012**, *18*, 16938-16946.
[34] D. W. Stephan und G. Erker, *Angew. Chem. Int. Ed.* **2015**, *54*, 6400-6441.
[35] S. J. Geier und D. W. Stephan, *J. Am. Chem. Soc.* **2009**, *131*, 3476-3477.
[36] T. Mahdi und D. W. Stephan, *Angew. Chem. Int. Ed.* **2013**, *52*, 12418-12421.
[37] M. A. Légaré, M. A. Courtemanche, E. Rochette und F.-G. Fontaine, *Science* **2015**, *349*, 513-516.
[38] D. W. Stephan, S. Greenberg, T. W. Graham, P. Chase, J. J. Hastie, S. J. Geier, J. M. Farrell, C. C. Brown, Z. M. Heiden, G. C. Welch und M. Ullrich, *Inorg. Chem.* **2011**, *50*, 12338-12348.
[39] D. W. Stephan, *Org. Biomol. Chem.* **2012**, *10*, 5740-5746.
[40] P. A. Chase, G. C. Welch, T. Jurca und D. W. Stephan, *Angew. Chem. Int. Ed.* **2007**, *46*, 8050-8053.
[41] G. Erős, K. Nagy, H. Mehdi, I. Pápai, P. Nagy, P. Király, G. Tárkányi und T. Soós, *Chem. Eur. J.* **2012**, *18*, 574-585.
[42] D. W. Stephan, *Acc. Chem. Res.* **2015**, *48*, 306-316.
[43] Y. Segawa und D. W. Stephan, *Chem. Commun.* **2012**, *48*, 11963-11965.
[44] J. Paradies, *Angew. Chem. Int. Ed.* **2014**, *53*, 3552-3557.
[45] L. Greb, P. Oña-Burgos, B. Schirmer, S. Grimme, D. W. Stephan und J. Paradies, *Angew. Chem. Int. Ed.* **2012**, *51*, 10164-10168.
[46] T. Mahdi und D. W. Stephan, *J. Am. Chem. Soc.* **2014**, *136*, 15809-15812.
[47] A. E. Ashley, A. L. Thompson und D. O'Hare, *Angew. Chem. Int. Ed.* **2009**, *48*, 9839-9843.
[48] G. Ménard und D. W. Stephan, *J. Am. Chem. Soc.* **2010**, *132*, 1796-1797.
[49] F.-G. Fontaine und D. W. Stephan, *Curr. Op. Green Sus. Chem.* **2017**, *3*, 28-32.
[50] M.-A. Courtemanche, M. A. Légaré, L. Maron und F.-G. Fontaine, *J. Am. Chem. Soc.* **2014**, *136*, 10708-10717.
[51] R. Declercq, G. Bouhadir, D. Bourissou, M.-A. Légaré, M.-A. Courtemanche, K. S. Nahi, N. Bouchard, F.-G. Fontaine und L. Maron, *ACS Catal.* **2015**, *5*, 2513-2520.
[52] A. Berkefeld, W. E. Piers und M. Parvez, *J. Am. Chem. Soc.* **2010**, *132*, 10660-10661.
[53] X. Zhao, A. J. Lough und D. W. Stephan, *Chem. Eur. J.* **2011**, *17*, 6731-6743.
[54] M. A. Dureen und D. W. Stephan, *J. Am. Chem. Soc.* **2009**, *131*, 8396-8397.
[55] M. A. Dureen, C. C. Brown und D. W. Stephan, *Organometallics* **2010**, *29*, 6594-6607.
[56] A. Fukazawa, H. Yamada und S. Yamaguchi, *Angew. Chem. Int. Ed.* **2008**, *47*, 5582-5585.
[57] R. L. Melen, M. M. Hansmann, A. J. Lough, A. S. Hashmi und D. W. Stephan, *Chem. Eur. J.* **2013**, *19*, 11928-11938.
[58] D. Martin, M. Soleilhavoup und G. Bertrand, *Chem. Sci.* **2011**, *2*, 389-399.
[59] T. Chu und G. I. Nikonov, *Chem. Rev.* **2018**, *118*, 3608-3680.
[60] N. Dettenrieder, Y. Aramaki, B. M. Wolf, C. Maichle-Mössmer, X. Zhao, M. Yamashita, K. Nozaki und R. Anwander, *Angew. Chem. Int. Ed.* **2014**, *53*, 6259-6262.
[61] P. P. Power, *Acc. Chem. Res.* **2011**, *44*, 627-637.
[62] P. Jutzi und A. Möhrke, *Angew. Chem. Int. Ed.* **1989**, *28*, 762-763.
[63] L. Yang und H. Wang, *Chem. Sus. Chem.* **2014**, *7*, 962-998.
[64] T. W. Hudnall und C. W. Bielawski, *J. Am. Chem. Soc.* **2009**, *131*, 16039-16041.
[65] Z. R. Turner, *Chem. Eur. J.* **2016**, *22*, 11461-11468.

[66] M. S. Hill, P. B. Hitchcock und R. Pongtavornpinyo, *Inorg. Chem.* **2007**, *46*, 3783-3788.
[67] C. Ganesamoorthy, G. Bendt, D. Bläser, C. Wölper und S. Schulz, *Dalton Trans.* **2015**, *44*, 5153-5159.
[68] T. Chu, Y. Boyko, I. Korobkov, L. G. Kuzmina, J. A. Howard und G. I. Nikonov, *Inorg. Chem.* **2016**, *55*, 9099-9104.
[69] S. Dagorne und R. Wehmschulte, *Chem. Cat. Chem.* **2018**, *10*, 2509-2520.
[70] C. Weetman und S. Inoue, *Chem. Cat. Chem.* **2018**, *10*, 4213-4228.
[71] J. A. Abdalla, I. M. Riddlestone, R. Tirfoin und S. Aldridge, *Angew. Chem. Int. Ed.* **2015**, *54*, 5098-5102.
[72] M. D. Anker, M. Arrowsmith, P. Bellham, M. S. Hill, G. Kociok-Köhn, D. J. Liptrot, M. F. Mahon und C. Weetman, *Chem. Sci.* **2014**, *5*, 2826-2830.
[73] N. Takagi und S. Sakaki, *J. Am. Chem. Soc.* **2013**, *135*, 8955-8965.
[74] T. J. Hadlington, M. Driess und C. Jones, *Chem. Soc. Rev.* **2018**, *47*, 4176-4197.
[75] T. Chu, I. Korobkov und G. I. Nikonov, *J. Am. Chem. Soc.* **2014**, *136*, 9195-9202.
[76] Z. Yang, M. Zhong, X. Ma, K. Nijesh, S. De, P. Parameswaran und H. W. Roesky, *J. Am. Chem. Soc.* **2016**, *138*, 2548-2551.
[77] N. Marion, S. Díez-González und S. P. Nolan, *Angew. Chem. Int. Ed.* **2007**, *46*, 2988-3000.
[78] J. L. Moore und T. Rovis, *Top. Curr. Chem.* **2010**, *291*, 77-144.
[79] A. Katharina Reitz, Q. Sun, R. Wilhelm und D. Kuckling, *J. Polym. Sci., Part A: Polym. Chem.* **2017**, *55*, 820-829.
[80] S. N. Riduan, Y. Zhang und J. Y. Ying, *Angew. Chem. Int. Ed.* **2009**, *48*, 3322-3325.
[81] N. Tsukahara, H. Asakawa, K. H. Lee, Z. Lin und M. Yamashita, *J. Am. Chem. Soc.* **2017**, *139*, 2593-2596.
[82] Y. Katsuma, L. Wu, Z. Lin, S. Akiyama und M. Yamashita, *Angew. Chem. Int. Ed.* **2019**, *58*, 317-321.
[83] T. Araki, M. Hirai, A. Wakamiya, W. E. Piers und S. Yamaguchi, *Chem. Lett.* **2017**, *46*, 1714-1717.
[84] J. Li, C. Schenk, C. Goedecke, G. Frenking und C. Jones, *J. Am. Chem. Soc.* **2011**, *133*, 18622-18625.
[85] J. Li, M. Hermann, G. Frenking und C. Jones, *Angew. Chem. Int. Ed.* **2012**, *51*, 8611-8614.
[86] T. J. Hadlington und C. Jones, *Chem. Commun.* **2014**, *50*, 2321-2323.
[87] M. Wagner, C. Dietz, M. Bouška, L. Dostál, Z. Padělková, R. Jambor und K. Jurkschat, *Organometallics* **2013**, *32*, 4973-4984.
[88] M. Arrowsmith, J. Böhnke, H. Braunschweig, M. A. Celik, T. Dellermann und K. Hammond, *Chem. Eur. J.* **2016**, *22*, 17169-17172.
[89] M. Arrowsmith, J. Böhnke, H. Braunschweig, M. A. Celik, C. Claes, W. C. Ewing, I. Krummenacher, K. Lubitz und C. Schneider, *Angew. Chem. Int. Ed.* **2016**, *55*, 11271-11275.
[90] A. Stoy, J. Böhnke, J. O. C. Jiménez-Halla, R. D. Dewhurst, T. Thiess und H. Braunschweig, *Angew. Chem. Int. Ed.* **2018**, *57*, 5947-5951.
[91] T. Kaese, T. Trageser, H. Budy, M. Bolte, H.-W. Lerner und M. Wagner, *Chem. Sci.* **2018**, *9*, 3881-3891.
[92] H.-J. Himmel, *Eur. J. Inorg. Chem.* **2018**, *2018*, 2139-2154.
[93] K. Nagata, T. Murosaki, T. Agou, T. Sasamori, T. Matsuo und N. Tokitoh, *Angew. Chem. Int. Ed.* **2016**, *55*, 12877-12880.
[94] C. A. Caputo, J. Koivistoinen, J. Moilanen, J. N. Boynton, H. M. Tuononen und P. P. Power, *J. Am. Chem. Soc.* **2013**, *135*, 1952-1960.
[95] Z. Zhu, X. Wang, M. M. Olmstead und P. P. Power, *Angew. Chem. Int. Ed.* **2009**, *48*, 2027-2030.
[96] D. Wendel, T. Szilvási, C. Jandl, S. Inoue und B. Rieger, *J. Am. Chem. Soc.* **2017**, *139*, 9156-9159.

[97] Y. Wang, M. Chen, Y. Xie, P. Wei, H. F. Schaefer, III und G. H. Robinson, *J. Am. Chem. Soc.* **2015**, *137*, 8396-8399.
[98] L. Zhao, F. Huang, G. Lu, Z.-X. Wang und P. Schleyer, *J. Am. Chem. Soc.* **2012**, *134*, 8856-8868.
[99] C. Fan, L. G. Mercier, W. E. Piers, H. M. Tuononen und M. Parvez, *J. Am. Chem. Soc.* **2010**, *132*, 9604-9606.
[100] Z.-W. Qu und H. Zhu, *J. Phys. Chem. C* **2013**, *117*, 11989-11993.
[101] B. Wang, Y. Li, R. Ganguly, H. Hirao und R. Kinjo, *Nat. Commun.* **2016**, *7*, 11871.
[102] D. Wu, L. Kong, Y. Li, R. Ganguly und R. Kinjo, *Nat. Commun.* **2015**, *6*, 7340.
[103] Y. Su, Y. Li, R. Ganguly und R. Kinjo, *Angew. Chem. Int. Ed.* **2018**, *57*, 7846-7849.
[104] B. Wang und R. Kinjo, *Tetrahedron* **2018**, *74*, 7273-7276.
[105] T. Sugahara, J.-D. Guo, D. Hashizume, T. Sasamori und N. Tokitoh, *J. Am. Chem. Soc.* **2019**, *141*, 2263-2267.
[106] D. Wu, Y. Li, R. Ganguly und R. Kinjo, *Chem. Commun.* **2017**, *53*, 12734-12737.
[107] A. Hinz, A. Schulz und A. Villinger, *Angew. Chem. Int. Ed.* **2016**, *55*, 12214-12218.
[108] A. Koner, Z. Kelemen, G. Schnakenburg, L. Nyulászi und R. Streubel, *Chem. Commun.* **2018**, *54*, 1182-1184.
[109] A. Lorbach, A. Hübner und M. Wagner, *Dalton Trans.* **2012**, *41*, 6048-6063.
[110] E. von Grotthuss, A. John, T. Kaese und M. Wagner, *Asian J. Org. Chem.* **2018**, *7*, 37-53.
[111] C. Reus, S. Weidlich, M. Bolte, H.-W. Lerner und M. Wagner, *J. Am. Chem. Soc.* **2013**, *135*, 12892-12907.
[112] E. von Grotthuss, Masterarbeit, Goethe-Universität Frankfurt, Frankfurt am Main, **2015**.
[113] A. Lorbach, M. Bolte, H.-W. Lerner und M. Wagner, *Chem. Commun.* **2010**, *46*, 3592-3594.
[114] L. Schweighauser und H. A. Wegner, *Chem. Eur. J.* **2016**, *22*, 14094-14103.
[115] L. Hong, S. Ahles, M. A. Strauss, C. Logemann und H. A. Wegner, *Org. Chem. Front.* **2017**, *4*, 871-875.
[116] Z. Lu, L. Schweighauser, H. Hausmann und H. A. Wegner, *Angew. Chem. Int. Ed.* **2015**, *54*, 15556-15559.
[117] M. V. Metz, D. J. Schwartz, C. L. Stern, P. N. Nickias und T. J. Marks, *Angew. Chem. Int. Ed.* **2000**, *39*, 1312-1316.
[118] P. Müller, H. Pritzkow und W. Siebert, *J. Organomet. Chem.* **1996**, *524*, 41-47.
[119] C. Hoffend, M. Diefenbach, E. Januszewski, M. Bolte, H.-W. Lerner, M. C. Holthausen und M. Wagner, *Dalton Trans.* **2013**, *42*, 13826-13837.
[120] A. John, M. Bolte, H.-W. Lerner und M. Wagner, *Angew. Chem. Int. Ed.* **2017**, *56*, 5588-5592.
[121] S. Brend'amour, J. Gilmer, M. Bolte, H.-W. Lerner und M. Wagner, *Chem. Eur. J.* **2018**, *24*, 16910-16918.
[122] J. W. Taylor, A. McSkimming, M. E. Moret und W. H. Harman, *Inorg. Chem.* **2018**, *57*, 15406-15413.
[123] A. Lorbach, M. Bolte, H.-W. Lerner und M. Wagner, *Organometallics* **2010**, *29*, 5762-5765.
[124] J. W. Taylor, A. McSkimming, C. F. Guzman und W. H. Harman, *J. Am. Chem. Soc.* **2017**, *139*, 11032-11035.
[125] H. Wieland, *Ber. Dtsch. Chem. Ges.* **1912**, *45*, 484-493.
[126] M. P., S. Huck, H. Köppel, H. Pritzkow und W. Siebert, *Z. Naturforsch.* **1995**, *50b*, 1476-1484.
[127] S. E. Prey, Bachelorarbeit, Goethe-Universität Frankfurt, Frankfurt am Main, **2017**.
[128] A. Lorbach, M. Bolte, H. Li, H.-W. Lerner, M. C. Holthausen, F. Jäkle und M. Wagner, *Angew. Chem. Int. Ed.* **2009**, *48*, 4584-4588.
[129] E. von Grotthuss, M. Diefenbach, M. Bolte, H.-W. Lerner, M. C. Holthausen und M. Wagner, *Angew. Chem. Int. Ed.* **2016**, *55*, 14067-14071.

[130] J. Chai, C. Wang, L. Jia, Y. Pang, M. Graham und S. Z. D. Cheng, *Synth. Met.* **2009**, *159*, 1443-1449.

[131] S. N. Kessler und H. A. Wegner, *Org. Lett.* **2010**, *12*, 4062-4065.

[132] Z. Lu, H. Quanz, O. Burghaus, J. Hofmann, C. Logemann, S. Beeck, P. R. Schreiner und H. A. Wegner, *J. Am. Chem. Soc.* **2017**, *139*, 18488-18491.

[133] C. Elschenbroich, *Organometallics*, Wiley-VCH, Wiesbaden, **2005**.

[134] J. Hahn, C. Keck, C. Maichle-Mössmer, E. von Grotthuss, P. N. Ruth, A. Paesch, D. Stalke und H. F. Bettinger, *Chem. Eur. J.* **2018**, *24*, 18634-18637.

[135] L. H. Slaugh, *J. Org. Chem.* **1967**, *32*, 108-113.

[136] C. Rüchardt, M. Gerst und J. Ebenhoch, *Angew. Chem.* **1997**, *109*, 1474-1498.

[137] E. A. Braude, L. M. Jackman und R. P. Linstead, *J. Chem. Soc. Res.* **1954**, 3548-3563.

[138] F. Mallory and C. W. Mallory, *Photocyclization of Stilbenes and Related Molecules*, in *Organic Reactions*, Ed. S. E. Denmark, Wiley-VCH, *30*, Weinheim, **2005**.

[139] L. Glasser und H. D. B. Jenkins, *J. Am. Chem. Soc.* **2000**, *122*, 632-638.

[140] D. S. Tarbell und N. A. Leister, *J. Org. Chem.* **1958**, *23*, 1149-1152.

[141] P. Zimmermann, S. Hoof, B. Braun-Cula, C. Herwig und C. Limberg, *Angew. Chem. Int. Ed.* **2018**, *57*, 7230-7233.

[142] R. Brückner, *Organic Mechanisms*, Springer Verlag, Berlin, Heidelberg, **2001**.

[143] M. Bertau, A. Müller, P. Fröhlich und M. Katzberg, *Industrielle Anorganische Chemie*, *4*, Wiley-VCH, Weinheim, **2013**.

[144] F. A. Bernd Pachaly, Christian Herzig, Konrad Mautner, *Silicone*, Wiley-VCH, Weinheim, **2005**.

[145] A. Gilbert, G. Cooper und R. Shade, *Ind. Eng. Chem.* **1959**, *51*, 665-668.

[146] D. T. Sawyer, A. Sobkowiak und J. L. Roberts, *Electrochemistry for chemists*, *2*, Wiley, New York, **1995**.

[147] R. Hoene und K.-H. W. Reichert, *Die Makromolekulare Chemie* **1976**, *177*, 3545-3570.

[148] C. F. Heins, *J. Polym. Sci., Part B: Polym. Lett.* **1969**, *7*, 625-626.

[149] K. Xu, *Chem. Rev.* **2004**, *104*, 4303-4418.

[150] J. Kalhoff, G. G. Eshetu, D. Bresser und S. Passerini, *Chem. Sus. Chem.* **2015**, *8*, 2154-2175.

[151] D. Pletcher, R. A. Green und R. C. D. Brown, *Chem. Rev.* **2018**, *118*, 4573-4591.

[152] D. H. Geske, *J. Phys. Chem.* **1959**, *63*, 1062-1070.

[153] P. K. Pal, S. Chowdhury, M. G. B. Drew und D. Datta, *New J. Chem.* **2002**, *26*, 367-371.

[154] https://membranesinternational.com/cmi-7000-cation-exchange-membranes-technical-specifications/, 17.03.19 16:35.

[155] F. Wolf und H. Wyszomirski, *Materials and Corrosion/Werkstoffe und Korrosion* **1967**, *18*, 898-901.

[156] Q. Zhao, R. D. Dewhurst, H. Braunschweig und X. Chen, *Angew. Chem. Int. Ed.* **2019**, *58*, 3268-3278.

[157] F. Nawa, Bachelorarbeit, Goethe-Universität Frankfurt, Frankfurt am Main, **2018**.

[158] E. Januszewski, A. Lorbach, R. Grewal, M. Bolte, J. W. Bats, H.-W. Lerner und M. Wagner, *Chem. Eur. J.* **2011**, *17*, 12696-12705.

[159] D. Griller und K. U. Ingold, *Acc. Chem. Res.* **2002**, *13*, 317-323.

[160] D. C. Nonhebel, *Chem. Soc. Rev.* **1993**, *22*, 347-359.

[161] A. H. Horn und T. Clark, *J. Am. Chem. Soc.* **2003**, *125*, 2809-2816.

[162] C. M. Jäger, M. Hennemann und T. Clark, *Chem. Eur. J.* **2009**, *15*, 2425-2433.

[163] G. R. Fulmer, A. J. M. Miller, N. H. Sherden, H. E. Gottlieb, A. Nudelman, B. M. Stoltz, J. E. Bercaw und K. I. Goldberg, *Organometallics* **2010**, *29*, 2176-2179.

[164] X.-A. Stoe & Cie, *Diffractometer control program system*, Stoe & Cie, Darmstadt, Germany, **2002**.

[165] G. M. Sheldrick, *Acta Crystallogr. Sect. A* **2008**, *64*, 112-122.

[166] E. von Grotthuss, S. E. Prey, M. Bolte, H.-W. Lerner und M. Wagner, *Angew. Chem. Int. Ed.* **2018**, *57*, 16491-16495.

[167] E. von Grotthuss, S. E. Prey, M. Bolte, H.-W. Lerner und M. Wagner, *J. Am. Chem. Soc.* **2019**, *141*, 6082-6091.

6. Anhang

6.1. Publikationsliste mit Angabe des eigenen Anteils

Allgemeine Anmerkungen:

- Die folgenden Nummerierungen der Verbindungen beziehen sich auf die jeweiligen Veröffentlichungen in den Fachjournalen und unterscheiden sich daher von denen in den Kapiteln 1–4.
- Das Lösen der Röntgenstrukturen von mir gezüchteter Einkristalle erfolgte in allen Fällen von Dr. Michael Bolte.

I) *Dual Role of Doubly Reduced Arylboranes as Dihydrogen- and Hydride-Transfer Catalysts*
von E. von Grotthuss, S. E. Prey, M. Bolte, H.-W. Lerner und M. Wagner
J. Am. Chem. Soc. **2019**, *141*, 6082-6091.

a. Sämtliche präparative Arbeiten und Analytik. Ausnahmen: Unter meiner Betreuung stellte S. E. Prey die Natrium-Derivate Na_2[**A**] und Na_2[**A**-H_2] her. Außerdem testete er mehrere M_2[**A**]-Derivate als Hydrierungskatalysatoren (auch im Druckautoklaven), versuchte Li_2[**4**] zur Hydrierung weiterer Substrate einzusetzen und führte den Hydrid-Transfer-Prozess in Gegenwart eines internen Standards durch.
b. Quantenchemische Rechnungen.

II) *Chalcogen–Chalcogen-Bond Activation by an Ambiphilic, Doubly Reduced Organoborane*
von E. von Grotthuss, F. Nawa, M. Bolte, H.-W. Lerner und M. Wagner
Tetrahedron **2019**, *75*, 26-30.

a. Die von mir betreute Bachelorarbeit von F. Nawa stellte die Grundlage für diese Veröffentlichung dar. Von mir wurden die Ergebnisse präparativ reproduziert und das Syntheseprotokoll erweitert (Zugabe eines zweiten Äquivalents von **1**). Außerdem vervollständigte ich die Analytik.

III) *Selective CO_2 Splitting by Doubly Reduced Aryl Boranes to Give CO and $[CO_3]^{2-}$*
von E. von Grotthuss, S. E. Prey, M. Bolte, H.-W. Lerner und M. Wagner
Angew. Chem. Int. Ed. **2018**, *57*, 16491-16495.

a. Präparative Arbeiten und Analytik von Na_2[**2**] und Na_2[**4**]. Versuchsplanung und Betreuung der praktischen Arbeiten von S. E. Prey zu der Thematik.
b. Quantenchemische Rechnungen.

IV) *Synthesis and Ring Strain of a Benzoborirene-N-Heterocyclic Carbene Adduct*
von J. Hahn, C. Keck, C. Maichle-Mössmer, E. von Grotthuss, P. N. Ruth, A. Paesch, D. Stalke und H. Bettinger
Chem. Eur. J. **2018**, *24*, 18634-18637.

a. Synthese von Verbindung **11**.

V) *Doping Polycyclic Aromatics with Boron for Superior Performance in Materials Science and Catalysis*
von E. von Grotthuss,[a] A. John,[a] T. Kaese[a] und M. Wagner
([a] Diese Autoren haben zu gleichen Teilen an der Arbeit beigetragen)
Asian J. Org. Chem. **2018**, *7*, 37-53.

VI) *Reversible Dihydrogen Activation by Reduced Aryl Boranes as Main-Group Ambiphiles*
von E. von Grotthuss, M. Diefenbach, M. Bolte, H.-W. Lerner, M. C. Holthausen und M. Wagner
Angew. Chem. Int. Ed. **2016**, *55*, 14067-14071.

a. Sämtliche präparative Arbeiten und Analytik.

VII) *10,9-Oxaboraphenanthrenes as Luminescent Fluorophores*
von A. Budanow, E. von Grotthuss, M. Bolte, M. Wagner und H.-W. Lerner
Tetrahedron **2016**, *72*, 1477-1484.

a. Reproduktion der Synthesen zur Derivatisierung von **1** mithilfe verschiedener Grignard-Reagenzien. Untersuchung der Fluoreszenzeigenschaften der Verbindungen **5**-**9**.

6.2. Eigene Publikationen in Fachjournalen

6.2.1. Dual Role of Doubly Reduced Arylboranes as Dihydrogen- and Hydride-Transfer Catalysts

JACS
JOURNAL OF THE AMERICAN CHEMICAL SOCIETY
Article
Cite This: J. Am. Chem. Soc. 2019, 141, 6082−6091
pubs.acs.org/JACS

Dual Role of Doubly Reduced Arylboranes as Dihydrogen- and Hydride-Transfer Catalysts

Esther von Grotthuss, Sven E. Prey, Michael Bolte, Hans-Wolfram Lerner, and Matthias Wagner*

Institut für Anorganische und Analytische Chemie, Goethe-Universität Frankfurt, Max-von-Laue-Straße 7, Frankfurt am Main D-60438, Germany

Supporting Information

ABSTRACT: Doubly reduced 9,10-dihydro-9,10-diboraanthracenes (DBAs) are introduced as catalysts for hydrogenation as well as hydride-transfer reactions. The required alkali metal salts M_2[DBA] are readily accessible from the respective neutral DBAs and Li metal, Na metal, or KC_8. In the first step, the ambiphilic M_2[DBA] activate H_2 in a concerted, metal-like fashion. The rates of H_2 activation strongly depend on the B-bonded substituents and the counter cations. Smaller substituents (e.g., H, Me) are superior to bulkier groups (e.g., Et, *p*Tol), and a Mes substituent is even prohibitively large. Li^+ ions, which form persistent contact ion pairs with $[DBA]^{2-}$, slow the H_2-addition rate to a higher extent than more weakly coordinating Na^+/K^+ ions. For the hydrogenation of unsaturated compounds, we identified Li_2[**4**] (Me substituents at boron) as the best performing catalyst; its substrate scope encompasses Ph(H)C═N*t*Bu, Ph_2C═CH_2, and anthracene. The conversion of E−Cl to E−H bonds (E = C, Si, Ge, P) was best achieved by using Na_2[**4**]. The latter protocol provides facile access also to $Me_2Si(H)Cl$, a most important silicone building block. Whereas the H_2-transfer reaction regenerates the dianion $[\mathbf{4}]^{2-}$ and is thus immediately catalytic, the H^--transfer process releases the neutral **4**, which has to be recharged by Na metal before it can enter the cycle again. To avoid Wurtz-type coupling of the substrate, the reduction of **4** must be performed in the absence of the element halide, which demands an alternating process management (similar to the industrial anthraquinone process).

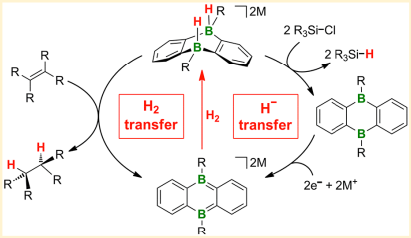

■ INTRODUCTION

In addition to transition metal complexes and Frustrated Lewis Pairs (FLPs),[1] main group species in low oxidation states are emerging as a third class of compounds capable of H_2 activation.[2] Three subclasses can be distinguished: (1) Single-site activators possess a coordinatively unsaturated atom bearing a lone pair of electrons together with an orthogonally positioned vacant orbital. Examples include borylenes, carbenes, and silylenes (cf., Bertrand's borylene[3] in Scheme 1). In all of these cases, the result is an oxidative addition of H_2, but the actual reaction mechanisms differ between electrophilic (B, Si) and nucleophilic (C) activation.[4] (2) Compounds containing two mutually connected active sites are known with single as well as multiple bonds (cf., Yamashita's diborane(4)[5] in Scheme 1). As a general motif, the initial reaction step involves donation of charge from the σ orbital of H_2 to only one of the active sites. In a synergic electron flow, σ- or π-electron density from between the main group centers accepts a proton and thereby splits the H_2 molecule.[6] (3) Compounds containing two spatially separated active sites can nevertheless achieve a cooperative action of the latter on the H_2 substrate.[7] For the dianion salt Li_2[**1**] (Scheme 1),[8] quantum-chemical calculations revealed that the HOMO and the LUMO of $[\mathbf{1}]^{2-}$ have the same local symmetries as the σ^* and σ orbitals, respectively, of the H−H bond. The spatial disposition of the frontier orbitals of $[\mathbf{1}]^{2-}$ is also ideally suited for interaction with H_2, which suggests a concerted, homolytic addition across both boron atoms.

The discovery of main group compounds rivaling transition metal complexes for the cleavage of the thermodynamically stable H−H bond represented a paradigm shift in fundamental research.[9] In terms of synthetic applications, however, the H_2-addition products should not be inert thermodynamic sinks, but rather have the potential to hand over the received hydrogen atoms to an added substrate molecule. For FLPs, such reactivity has been amply demonstrated and led to the development of entire catalytic cycles.[10] In contrast, hydrogenation reactions mediated by main group species in low oxidation states are essentially unknown,[11] and even reversible H_2 activation has rarely been reported. One of the few examples is the singlet biradicaloid $[P(\mu NTer)]_2$ (Ter = 2,6-bis(mesityl)phenyl), which adds H_2 at room temperature across its phosphorus atoms and releases it again at 60 °C.[12] Our group recently observed a dynamic addition/elimination

Received: February 21, 2019
Published: March 15, 2019

DOI: 10.1021/jacs.9b01998
J. Am. Chem. Soc. 2019, 141, 6082−6091

Scheme 1. Examples of H_2 Activation with Boron Species in Low Oxidation States: Single-Site Activator (Top), Compound Containing Two Mutually Connected Active Sites (Middle), and Compound Containing Two Spatially Separated Active Sites (Bottom)[a]

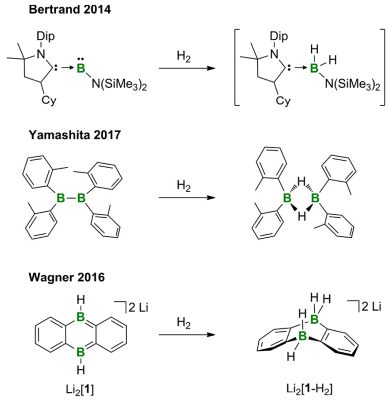

[a]Dip = 2,6-diisopropylphenyl; Cy = spiro-cyclohexyl.

equilibrium between H_2 and a derivative of Li_2[**1**] bearing two alkynyl instead of hydrogen substituents at its boron atoms (cf., Li_2[**2**] in Scheme 2).[8]

Herein, we use the parent Li_2[**1**] as a platform for the development of versatile hydrogenation catalysts. Our main group ambiphiles stand out for their ability to transfer not only one H_2 molecule to unsaturated compounds, but also two H^- ions to element halides. As key factors governing the catalyst performance, the B-bonded substituents and the counter cations have been identified. Mechanistic studies helped to confirm a concerted H_2 activation, explain the substrate scopes, and arrive at workable reaction conditions.

■ RESULTS AND DISCUSSION

The 9,10-dihydro-9,10-diboraanthracene (DBA) derivatives employed in this Article will be denoted as "**A**" whenever we refer to the general structure. Arabic numerals are assigned to species carrying specific B-bonded substituents (cf., Scheme 2). Aromatic dianion salts and their corresponding H_2-activation products are named M_2[**A**] and M_2[**A**-H_2], respectively (M^+ = Li^+, Na^+, K^+). The B-bonded substituents were chosen such that they cover a broad range of sizes (e.g., H < Me < aryl) and group electronegativities (e.g., alkyl < aryl < alkynyl).

Synthesis of DBAs A, Their Dianion Salts M_2[A], and Their H_2-Activation Products M_2[A-H_2]. The B-substituted DBAs **1**−**9** are accessible from 9,10-dibromo-DBA through (a) hydride transfer using Et_3SiH (**1**),[13] (b) nucleophilic substitution with LiC≡C*t*Bu (**2**),[8] (c) hydride transfer and subsequent hydroboration of HC≡C*t*Bu (**3**),[13] and (d) nucleophilic substitution with BrMgR (**4**−**9**; Scheme 2, top and the Supporting Information).[14−16] The *i*Pr derivative **6** underwent partial dehydroboration already during efforts at its purification by vacuum sublimation (110 °C, 10^{-3} mbar). Given that the H_2-activation reaction with Li_2[**1**] required temperatures of 100 °C,[8] compound **6** was regarded as too

Scheme 2. Top: Synthesis of Symmetrically Substituted DBA Derivatives: (a) Et_3SiH,[13] (b) LiC≡C*t*Bu,[8] (c) (1**) Et_3SiH, (2) HC≡C*t*Bu,[13] (d) RMgBr, Toluene/Et_2O, −78 °C to Room Temperature; Bottom: Reduction of the DBA Derivatives with Alkali Metals; Reduction Successful (√), Unsuccessful (×), and Not Investigated (−)**

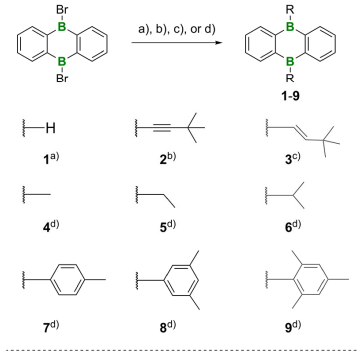

M_2[A]	A = 1	2	3	4	5	7	8	9
M = Li	✓	✓	✓	✓	✓	✓	✓	✓
Na	✓	✓	–	✓	–	✓	–	–
K	✓	×	–	✓	✓	✓	✓	–

temperature sensitive to be considered further. All attempted reductions of **1**−**5** and **7**−**9** using Li metal, Na metal, or KC_8 in THF quantitatively furnished the corresponding dianion salts M_2[**1**]−M_2[**5**] and M_2[**7**]−M_2[**9**] with the only exception of the KC_8/**2** system (Scheme 2, bottom). H_2-activation reactions were successfully performed with all alkali metal salts compiled in Scheme 2 (bottom), apart from Li_2[**3**], which decomposed at the applied temperature of 100 °C, and Li_2[**9**], which showed no reaction due to steric hindrance.

In THF-d_8 solution, compound **9** possesses an ^{11}B NMR shift of 72 ppm,[15] as is typical of three-coordinate triarylboranes.[15] The sterically less shielded derivatives are characterized by ^{11}B signals in the ranges 43−40 ppm (**4**, **5**) and 38−36 ppm (**7**, **8**), at 33 ppm (**2**),[18] and 22 ppm (**1**), testifying to the presence of (weak) solvent adducts. Upon reduction, all resonances shift to higher field strengths (28−14 ppm). A successful H_2 addition is evidenced by doublet multiplicities of the ^{11}B signals and further upfield shifts to the region between −10 and −24 ppm. ^{1}H and ^{13}C{^{1}H} NMR spectra were recorded and assigned for all three substance classes **A**, M_2[**A**], and M_2[**A**-H_2]. The signal patterns are in agreement with the proposed structural motifs, which were also confirmed by X-ray analysis (cf., the Supporting Information for full details).

Key Parameters Determining the H_2 Activation with M_2[A]. *Influence of the B-Bonded Substituents.* The conversion of M_2[**A**] to M_2[**A**-H_2] leads to qualitatively similar

DOI: 10.1021/jacs.9b01998
J. Am. Chem. Soc. 2019, 141, 6082−6091

changes in the ^{1}H NMR spectra of all derivatives **A** = **1**, **2**, **4**, **5**, **7**, **8**, which allowed us to monitor the reaction progress in dependence of the B-bonded substituents. We selected the Li_2[**A**] salts for this purpose to maximize the time resolution, knowing that Li_2[**1**] activates H_2 at a much slower rate than K_2[**1**].[8] All samples were prepared in flame-sealed NMR tubes and stored at 100 °C for several days (0.050 mmol Li_2[**A**], $p(H_2)$ < 1 atm at room temperature, THF-d_8). NMR spectra were recorded in regular intervals at room temperature with short measurement times and thus under conditions at which the reaction comes to a halt. The conversion-time diagram obtained reveals two important effects (Figure 1): (1) H_2

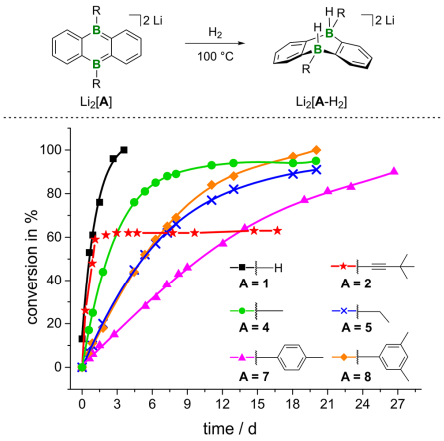

Figure 1. Conversion-time diagram for the reactions between Li_2[**A**] and H_2 to give Li_2[**A**-H_2] (obtained from ^{1}H NMR spectroscopy).

activation by the alkynyl derivative Li_2[**2**] cannot be driven to completion, but reaches a dynamic addition/elimination equilibrium.[8,19] (2) Smaller substituents result in faster H_2 addition (cf., H, C≡C*t*Bu, Me vs Et, *m*Xyl, *p*Tol). The latter finding can be rationalized by the fact that rapid H_2 addition requires unhindered access of the substrate molecule to the reactive boron sites. Barriers along the trajectory are the $[Li(thf)_n]^+$ ions, which form contact ion pairs with the negatively charged B_2C_4 heterocycles, not only in the solid state but also in THF solution.[8] By the same token, an increasing bulk of the substituent has a negative impact on the H_2 approach (kinetic control). One might argue that this effect could be compensated by a concomitant sterically induced weakening of the $Li^+\cdots[A]^{2-}$ interaction, but this assumption is not supported by X-ray crystallography: the average distances between Li^+ and the respective DBA centroids decrease rather than increase along the series $[Li(thf)_2]_2$[**1**] > $[Li(thf)_2]_2$[**4**] > $[Li(thf)_2]_2$[**7**] (1.960,[20] 1.911,[16] 1.891 Å, respectively).

Two questions are still remaining: (1) Why does the alkynyl species Li_2[**2**] show such a peculiar behavior? (2) Why is the performance of the sterically similar *p*Tol (Li_2[**7**]) and *m*Xyl (Li_2[**8**]) derivatives so different? We suggest the following answers based on the different stabilities of the $[A]^{2-}$ ions (a justification will be given below):[21] (1) Of all species Li_2[**A**], Li_2[**2**] contains the most stable dianion, which decreases the exoergicity of the H_2-addition reaction. At the same time, the high reaction velocity indicates an energetically low-lying transition state. Taken together, both factors render the forward as well as reverse reaction thermodynamically and kinetically feasible. (2) The stability of $[7]^{2-}$ is higher than that of $[8]^{2-}$. If we assume a closely similar steric contribution of the *p*Tol and *m*Xyl substituents to the kinetic shielding of the boron centers, the dianion $[8]^{2-}$ should be more reactive.

To a first approximation, the relative stabilities of the $[A]^{2-}$ ions are determined by the LUMO-energy levels of the neutral species **A** and, in turn, mirrored by the half-wave potentials $E_{1/2}$ of the **A**/$[A]^-$ redox couples (Figure 2). Because of its

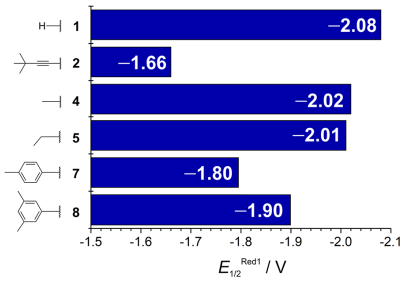

Figure 2. $E_{1/2}^{Red1}$ values of the compounds **1**, **2**, **4**, **5**, **7**, and **8** (THF, room temperature, supporting electrolyte $[nBu_4N][PF_6]$, referenced against internal FcH/FcH^+).

electronegative C(sp) substituents, compound **2** indeed possesses the least cathodic redox potential, followed by **7** and then **8** with less electronegative C(sp^2) aryl groups. Even harder to reduce are the C(sp^3) alkyl derivatives **4** and **5**. The reduction of the parent DBA **1** requires the most cathodic electrode potential, even though an H atom should be less electron releasing than, for example, an alkyl substituent. Yet, as evidenced by the ^{11}B NMR shifts mentioned above, **1** forms a strong THF adduct, which needs to be cleaved in the course of the reduction process and therefore hampers electron injection.[18] To further substantiate this interpretation, we also computed the LUMO energy levels of the DBAs (B3LYP/6-31G*). Now that THF ligation is not an issue, all LUMO energies, including that of **1**, follow the trend expected on the basis of electronic substituent effects (see the Supporting Information for more details).

Influence of the Counter Cations. As mentioned above, the formation of contact ion pairs in M_2[**A**] could impede the access of H_2 to the boron centers. It is generally accepted that the affinity of an alkali metal ion M^+ to the π face of an aryl ring follows an electrostatic trend and consequently decreases with an increasing ionic radius of M^+.[22] This is strictly true for the gas phase, but also applies for THF solutions of M_2[**A**]: ^{7}Li NMR spectroscopy on Li_2[**1**] provided evidence for the existence of contact ion pairs in THF-d_8 solution.[8] Corresponding information regarding the ion aggregation of Na_2[**1**] and K_2[**1**] was gained through $^{13}C\{^1H\}$ NMR spectroscopy. The peripheral *o*-phenylene carbon atom C-b is sensitive to changes in the π-electron structure of the B_2C_4 ring; a higher charge density leads to a higher magnetic shielding.[15] For Li_2[**1**], Na_2[**1**], and K_2[**1**], δ(C-b) equals 118.3, 115.9, and 115.1 ppm, respectively. An M^+ cation

DOI: 10.1021/jacs.9b01998
J. Am. Chem. Soc. 2019, 141, 6082−6091

located above the B_2C_4 plane should pull away charge density from the dianion and concomitantly cause a more downfield-shifted C-b signal. We therefore conclude that $Na_2[\mathbf{1}]$ and $K_2[\mathbf{1}]$ establish less strongly bound ion pairs than $Li_2[\mathbf{1}]$. In line with that, THF solutions of $Na_2[\mathbf{1}]$ and $K_2[\mathbf{1}]$ possess a deep green color, whereas those of $Li_2[\mathbf{1}]$ are deep red. In the solid state, all three salts show the same structural motif of an inverse sandwich complex (Figure 3) and, in turn, exhibit the

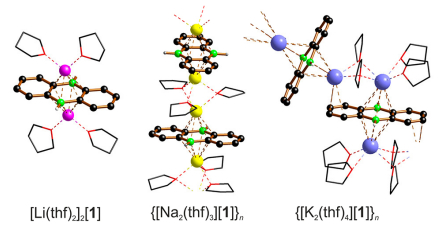

Figure 3. Solid-state structures of the discrete inverse-sandwich complex $[Li(thf)_2]_2[\mathbf{1}]$ and the coordination polymers $\{[Na_2(thf)_3][\mathbf{1}]\}_n$ and $\{[K_2(thf)_4][\mathbf{1}]\}_n$. C-bonded H atoms are omitted for clarity. Averaged $M^+\cdots$COG distances [Å]: Li^+ = 1.960, Na^+ = 2.239, K^+ = 2.755; COG = centroid of the planar B_2C_4 ring. A description of the crystal structures is provided in the Supporting Information.

same dark red color. Given this background, the choice of M^+ could provide a similar powerful set-screw for tuning the reactivity of $M_2[\mathbf{A}]$ toward H_2 as the selection of the B-bonded substituent.

To test this conclusion, we studied next the relative velocities of the H_2-activation reactions using M^+ = Li^+, Na^+, and K^+ in combination with the best performing dianions $[\mathbf{1}]^{2-}$, $[\mathbf{4}]^{2-}$, and the lowest performer $[\mathbf{7}]^{2-}$ (Figure 4). At a temperature of 100 °C, the Na^+ species react significantly faster than the Li^+ salts. A temperature decrease to 50 °C slows the reaction rate of $Na_2[\mathbf{A}]$, whereas that of $K_2[\mathbf{A}]$ is still high, even in the case of the *p*Tol derivative $K_2[\mathbf{7}]$. All in all, a switch

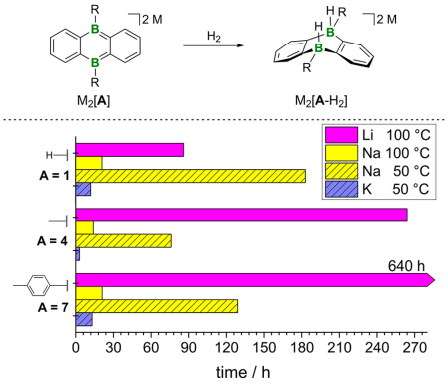

Figure 4. Velocity of the H_2 activation by $M_2[\mathbf{A}]$ as a function of the nature of the counter cation and the B-bonded substituent.

from $Li_2[\mathbf{A}]$ to $K_2[\mathbf{A}]$ cuts down the required reaction time from multiple days to a few hours.

The H_2-activation products $Li_2[\mathbf{1}\text{-}H_2]$, $Na_2[\mathbf{7}\text{-}H_2]$, $K_2[\mathbf{1}\text{-}H_2]$, $K_2[\mathbf{4}\text{-}H_2]$, and $K_2[\mathbf{7}\text{-}H_2]$ have been investigated by X-ray analysis.[23] As a further counterion effect we note that $Li_2[\mathbf{1}\text{-}H_2]$ contains bent anions,[8] whereas the anion in $K_2[\mathbf{1}\text{-}H_2]$ is perfectly planar (Figure 5, left). Moreover, the inverse

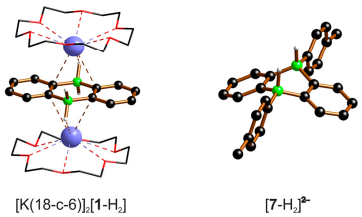

Figure 5. Solid-state structures of the discrete inverse-sandwich complex $[K(18\text{-c-}6)]_2[\mathbf{1}\text{-}H_2]$ (left) and a dianion of the dimeric $[Na][Na(thf)_2(18\text{-c-}6)][Na(thf)_2]_2(n\text{-hexane})[\mathbf{7}\text{-}H_2]_2$ (right). C-Bonded H atoms are omitted for clarity.

sandwich structure is retained, thereby allowing a direct comparison of the $K^+\cdots$COG distances before and after H_2 addition, which reveals a remarkably small increase of less than 6% (av values: 2.755 vs 2.917 Å; COG = centroid of the planar B_2C_4 ring). The other structurally characterized ions $[\mathbf{A}\text{-}H_2]^{2-}$ show bent frameworks. In agreement with a concerted, metal-like H_2-addition mechanism,[8] the B-bonded hydrogen atoms occupy axial positions of the boat-shaped B_2C_4 rings (*cis* configuration; cf., the structure of $[\mathbf{7}\text{-}H_2]^{2-}$ in Figure 5, right).

Each of the lithium salts $Li_2[\mathbf{A}\text{-}H_2]$ shows one set of ^1H, ^{11}B, and $^{13}C\{^1H\}$ NMR signals. The same is true for $Na_2[\mathbf{1}\text{-}H_2]$ and $K_2[\mathbf{1}\text{-}H_2]$. In contrast, resonances assignable to two different, albeit closely related, products were observable after the quantitative conversion of $Na_2[\mathbf{4}]$, $Na_2[\mathbf{7}]$, $K_2[\mathbf{4}]$, or $K_2[\mathbf{7}]$ with H_2.

A subsequent ^1H NMR monitoring of the $K_2[\mathbf{7}]/H_2$ mixture revealed one strongly predominant product in the early stages of the reaction (THF-d_8, 50 °C). Signals of a second product appeared as the reaction progressed and continuously gained intensity, even after full consumption of $K_2[\mathbf{7}]$ (Figure 6). The primary reaction product thus rearranges to the second product at the elevated temperature applied. Because the NMR characteristics of the first as well as the second product point toward hydride diadducts of 9,10-(*p*Tol)$_2$-DBA (**7**), the difference must lie in their *cis* vs *trans* configurations.[24] Indeed, the THF-d_8 solution of manually selected single crystals of *cis*-$Na_2[\mathbf{7}\text{-}H_2]$ (confirmed by X-ray analysis; Figure 5, right) gave only one set of resonances (corresponding to those of the first product of the $K_2[\mathbf{7}]/H_2$ reaction). During storage of the sample at 50 °C, a second signal set evolved (corresponding to that of the second product of the $K_2[\mathbf{7}]/H_2$ reaction).

The nature of the primary hydrogenation products as *cis*-$M_2[\mathbf{A}\text{-}H_2]$ confirms the mechanistic picture of a concerted, metal-like H_2-addition reaction.[8] The single diastereomer observed for $Li_2[\mathbf{A}\text{-}H_2]$ is therefore the result of a completely kinetically controlled process where subsequent isomerization to the *trans* isomer is not taking place (in contrast to the Na^+ and K^+ counterparts). In this context, we also treated the DBA derivative **4** in THF-d_8 with 2 equiv of $K[HBEt_3]$, which

DOI: 10.1021/jacs.9b01998
J. Am. Chem. Soc. 2019, 141, 6082−6091

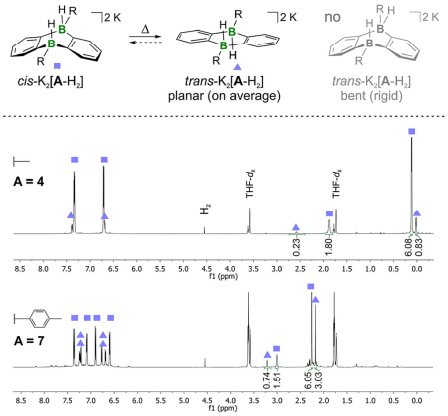

Figure 6. Thermally induced isomerization of the H_2-addition products K_2[**A**-H_2] (R = Me, *p*Tol). $^1H\{^{11}B\}$ NMR spectra (500.2 MHz, THF-d_8) of the reaction mixtures K_2[**4**]/H_2 (top) and K_2[**7**]/H_2 (bottom) after 13 h at 50 °C. The ratios between the *cis* (■) configuration (primary product of the H_2 addition) and the *trans* (▲) configuration (secondary product) depend on the B-bonded substituent.

should react in a nonconcerted fashion (LiH, NaH, and KH react only slowly due to solubility issues). This time, an equimolar mixture of *cis*/*trans*-K_2[**4**-H_2] was obtained (cf., the Supporting Information for more details).

The dianions *trans*-[**A**-H_2]$^{2-}$ must either be planar or invert rapidly on the NMR time scale, because otherwise they could not give rise to the highly symmetrical signal patterns observed (Figure 6).[25] In THF, the activities of alkali metal hydrides as rearrangement catalysts follow the order KH ≫ NaH > LiH,[26] which correlates with our observation that *cis*/*trans* isomerization is particularly pronounced for K_2[**7**-H_2], but not observed for Li_2[**7**-H_2]. We consequently propose dissociation/reassociation of KH (or NaH) as the key isomerization step. Apart from the counter cation, also the B-bonded substituent influences the *cis*/*trans* isomerization as evidenced by the fact that *cis*-K_2[**7**-H_2] rearranges to a larger extent than does *cis*-K_2[**4**-H_2] (Figure 6).

Dual Role of M_2[A-H_2] as H_2- and H^--Transfer Catalysts. FLPs are nowadays established hydrogenation catalysts, because they are capable not only of activating H_2 but also of transferring it onto a plethora of substrates. The observation that Li_2[**2**-H_2] liberates the added H_2 even in the absence of an acceptor molecule suggests similarly useful applications for main group ambiphiles M_2[**A**], too. Alternatively, M_2[**A**-H_2] could supply two H^- ions, which decidedly distinguishes them from classical FLPs, because the latter heterolytically cleave H_2 to furnish only one H ion together with a proton. On the basis of these considerations, we propose a dual role of the M_2[**A**]/M_2[**A**-H_2] system both for the conversion of unsaturated into saturated compounds (Figure 7, left) and for the transformation of element−halogen into element−hydrogen bonds (Figure 7, right). After successful H_2 transfer, M_2[**A**] is regenerated in an inherently catalytic process. The transfer of two H^- ions, however, leaves the neutral DBA behind, which needs to be recharged with two electrons before it can activate a new H_2 molecule and enter the cycle again.

H_2 Transfer. To start, we discuss the scope and limitations of selected M_2[**A**] derivatives as hydrogenation catalysts. The system was optimized with regard to the counter cation (M^+ = Li^+, Na^+, or K^+) and the B-bonded substituent (H, Me, or *p*Tol) by using the imine Ph(H)C=N*t*Bu as the model substrate (catalyst loading: 37 mol%, 1 atm H_2, THF-d_8, 100 °C, 16 h; Table 1).

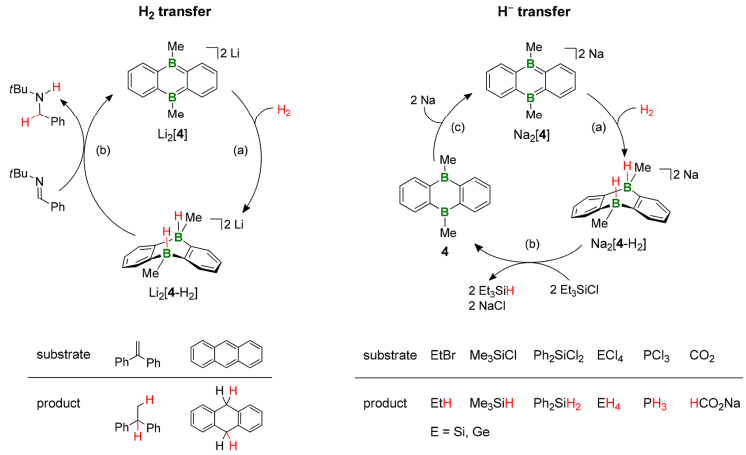

Figure 7. Left: Catalytic cycle for Li_2[**4**] as the hydrogenation catalyst. Right: Cyclic process for the transformation of Et_3SiCl into Et_3SiH with Na_2[**4**-H_2] as the hydride donor. (a) H_2 activation; (b) H_2/2H^- transfer; (c) DBA reduction.

DOI: 10.1021/jacs.9b01998
J. Am. Chem. Soc. 2019, 141, 6082−6091

Table 1. Percent Conversion of the Imine Ph(H)C═N*t*Bu to Its Hydrogenation Product Ph(H)$_2$C−N(H)*t*Bu Using Nine Different M$_2$[A] Combinations[a]

[A]$^{2-}$ derivative	M$^+$ = Li$^+$	M$^+$ = Na$^+$	M$^+$ = K$^+$
M$_2$[**1**]	11	1	1
M$_2$[**4**]	97	27	1
M$_2$[**7**]	3	0	0

[a]Catalyst load: 37 mol%, 1 atm H$_2$, THF-d_8, 100 °C, 16 h.

Irrespective of the choice of [**A**]$^{2-}$, Li$^+$ performed much better than its higher homologues. The cation trend observed for the overall catalytic process (cf., entry 2) is in fact inverse to that observed for the H$_2$-activation step alone (see above). Even though strong contact ion pair formation has an adverse effect on the H$_2$ addition, it provides the necessary thrust for the H$_2$ transfer from Li$_2$[**A**-H$_2$] by thermodynamically stabilizing the liberated Li$_2$[**A**] (cf., the H$_2$ addition/elimination equilibrium observed for the particularly stable Li$_2$[**2**]). Apparently, the beneficial influence of Li$^+$ coordination on the second step outweighs its negative impact on the first step.

Of the three B-bonded substituents studied, *p*Tol turned out to be least suitable, likely because it exerts a high steric hindrance not only on H$_2$ addition, but also on its transfer. The smaller Me substituent gave excellent results, but a further decrease in substituent size from Me to H led to a less active catalyst again. We assumed the origin behind this puzzling finding was a [4+2]-cycloaddition reaction between Ph(H)C═N*t*Bu and Li$_2$[**1**], which competes with H$_2$ activation and poisons the catalyst. Such reactivity has its precedence in cycloadditions between Li$_2$[**1**] or Li$_2$[**4**] and carbonyl compounds.[16,20] NMR spectra recorded on equimolar mixtures of Ph(H)C═N*t*Bu and Li$_2$[**1**] or Li$_2$[**4**] showed signals assignable to the expected tricyclic skeletons, that is, ^{1}H-, ^{11}B-, and ^{13}C-signal patterns indicative of C_1-symmetric DBA fragments, proton-integral ratios in line with 1:1 cycloadducts, and ^{11}B resonances typical of four-coordinate boron centers (cf., Figure 8). Moreover, the cycloadduct Li$_2$[**10**] of Li$_2$[**4**] was structurally characterized by X-ray diffraction, albeit only in its *N*-protonated form [Li(12-c-4)$_2$]H[**10**] (Figure 9). We speculate that the crown ether-induced ion separation led to a significantly enhanced basicity of the N atoms, which therefore abstracted protons from adventitious traces of water during the prolonged crystallization process (cf., the Supporting Information for more details). In the case of Li$_2$[**1**], cycloadduct formation is fast and quantitative already at room temperature; Li$_2$[**4**] reacts at a much slower rate such that the NMR resonances of the two starting materials and the product Li$_2$[**10**] are detectable at the same time (Figure 8). At 100 °C, the temperature required for imine hydrogenation, Li$_2$[**10**] reverts back to a much higher degree than the corresponding Li$_2$[**1**] cycloadduct, which straightforwardly explains the observed differences in the catalytic activities of Li$_2$[**4**] vs Li$_2$[**1**]. We finally note that the *p*Tol derivative Li$_2$[**7**] shows no interaction with Ph(H)C═N*t*Bu (Figure 8).

Having identified Li$_2$[**4**] as the best performing catalyst, we next confirmed that its loading can be cut down from the previously employed 37 mol% to 10 mol% without detrimental consequences on product yield and conversion time. As a proof-of-principle, the reaction was also conducted in a 100 mL stainless steel autoclave to prepare 150 mg of Ph(H)$_2$C−N(H)*t*Bu (catalyst loading: 10 mol%, 7 bar H$_2$, THF, 100 °C, 18 h). To obtain a first impression of the substrate scope, we selected the 10 unsaturated compounds compiled in Figures 7 and 8. Of these species, which contain either C═C double or C≡C triple bonds and differ in their steric and electronic properties, Ph$_2$C═CH$_2$ and anthracene underwent quantitative hydrogenation. The remaining substrates that failed to be hydrogenated can be categorized into two groups: Members of the first group behave entirely inert toward Li$_2$[**4**]/H$_2$, whereas those of the second group form stable [4+2]-cycloadducts with the [**4**]$^{2-}$ ion (for a crystallographic proof of the formation of the ethylene cycloadduct Li$_2$[**11**], see Figure 9).[27] For a

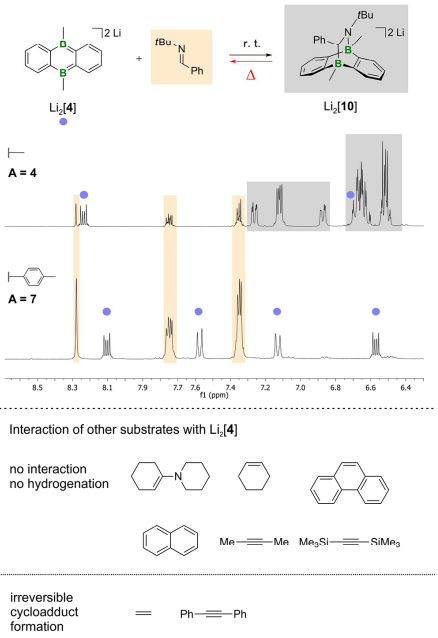

Figure 8. Top: Comparison of the interaction between Li$_2$[**A**] and Ph(H)C═N*t*Bu in dependence of the B-bonded substituents R = Me or *p*Tol. The ^{1}H NMR spectra of respective 1:1 mixtures were recorded immediately after sample preparation (500.2 MHz, THF-d_8). Bottom: Some substrates form irreversible [4+2]-cycloaddition products with Li$_2$[**4**], whereas others show no interaction.

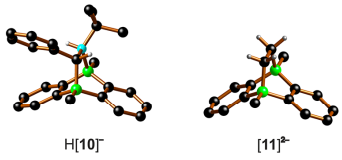

Figure 9. Solid-state structures of the anions of [Li(12-c-4)$_2$]H[**10**]·THF (left) and [Li(12-c-4)(thf)][Li(12-c-4)][**11**] (right). Most C-bonded H atoms are omitted for clarity.

DOI: 10.1021/jacs.9b01998
J. Am. Chem. Soc. 2019, 141, 6082−6091

successful hydrogenation, one has therefore to maintain a delicate balance between the steric demands of the catalyst and the substrate molecules.

Apart from steric influences, also electronic factors likely govern the substrate scope. The Woodward-Hoffmann rules predict that the metal-like addition of an unpolar H–H bond across the boron atoms of M_2[**A**] proceeds via a thermally allowed transition state (6 e^-; Figure 10).[8] The concerted H_2

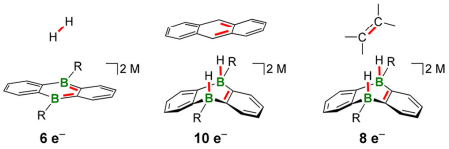

Figure 10. Illustration of the concerted H_2 activation with M_2[**A**] (allowed; left) and the H_2 transfers from M_2[**A**-H_2] to either anthracene (allowed; middle) or an olefin (forbidden; right).

transfer from M_2[**A**-H_2] to anthracene is also allowed (10 e^-), but forbidden for olefins and alkynes (8 e^-).[28] Related issues have already been discussed for the established H_2-donor reagent 9,10-dihydroanthracene, an isoelectronic neutral analogue of [**A**]$^{2-}$.[29] Here, it is generally accepted that the reactions follow two-step mechanisms, involving either initial H^--ion or $H^•$-atom transfer.[30] The lower electronegativity of boron as compared to carbon results in a more negative partial charge on the bridgehead hydrogen atoms of [**A**-H_2]$^{2-}$ than on those of 9,10-dihydroanthracene. An ionic pathway should therefore be favored in our case, also considering that we never observed indications for the presence of paramagnetic intermediates or byproducts during in situ NMR experiments (e.g., deuterium abstraction from THF-d_8, unusual signal broadening).[31] The assumption of an initial H^--ion transfer straightforwardly explains why [**4**-H_2]$^{2-}$ failed to hydrogenate the enamine 1-(1-piperidinyl)cyclohexene, an archetypal substrate in FLP-reduction chemistry: Classical FLPs usually transfer an H^+ ion first and after an H^- ion and consequently prefer electron-rich reaction partners,[10] whereas the opposite should be true for [**4**-H_2]$^{2-}$. To further substantiate this interpretation, we treated Na_2[**4**-H_2] with 1 equiv of Et_3SiCl and quantitatively obtained Et_3SiH together with Na[**4**-H], a monoanion salt with only one remaining bridgehead hydrogen (cf., the Supporting Information and ref 32). This experiment also lays the conceptual foundation for the use of [**A**-H_2]$^{2-}$ as a source of two H^- nucleophiles, which is discussed in the next paragraph.

H^- Transfer. The transformation of element halides into element hydrides was optimized with the help of Et_3SiCl as the model substrate. Contrary to the case of the hydrogenation reaction, a 2-fold H^- transfer from [**A**-H_2]$^{2-}$ liberates the catalyst molecule in its spent neutral state **A**. A circular process thus requires the rereduction of **A** to [**A**]$^{2-}$ in the absence of Et_3SiCl to avoid unwanted Wurtz-type coupling of the chlorosilane.[33] The resulting necessity for a temporal separation of the alkali metal reduction and H_2-activation steps from the H/Cl-exchange step demands an alternating addition of the three components to the catalyst system. Before the stoichiometric amount of Et_3SiCl is allowed into the reaction vessel, the formation of [**A**-H_2]$^{2-}$ has to be quantitative and should therefore proceed as fast as possible, which renders Na metal or KC_8 the reducing agents of choice. Considering safety hazards and the higher lattice energy of NaCl as compared to KCl,[34] we identified Na_2[**4**] as the best-suited catalyst system for the given purpose. It has to be emphasized that an alternating process management is not uncommon even on an industrial scale, a famous example being the anthraquinone process for the production of H_2O_2.[35]

Figure 11 shows ^{1}H NMR spectra recorded after each of the three reaction steps required to complete a full cycle. The

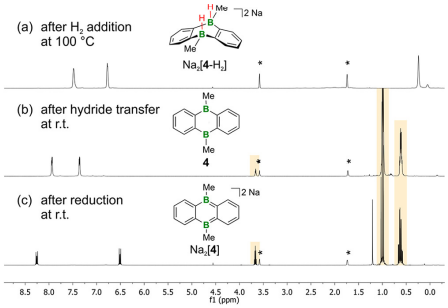

Figure 11. ^{1}H NMR spectra (400.0, 500.2 MHz; THF-d_8) recorded after each step of the catalytic cycle shown in Figure 7, right; the reaction product Et_3SiH is highlighted in beige; residual solvent resonances are marked with "*".

individual conversions, carried out at 100 °C (H_2 activation) or room temperature (H/Cl exchange; rereduction of **4**), are quantitative and perfectly selective with no detectable formation of side products. The product Et_3SiH does not interfere with any of the subsequent steps and can therefore be accumulated over multiple cycles (a corresponding proof-of-principle experiment is outlined in the Supporting Information). As discussed above, the alternating process management is enforced by the fact that the reduction of **4** has to be carried out separately from the H^--transfer reaction to circumvent wasting starting materials through unwanted Si–Si coupling. Yet, in the course of our studies, we discovered an even more pressing reason that directly affects the integrity of the catalyst: The electron-rich [**4**]$^{2-}$ acts as a remarkable boron-centered nucleophile[36] toward Et_3SiCl and furnishes the monoanionic silylborate [MeB-(oC_6H_4)$_2$-B(Me)$SiEt_3$]$^-$ containing one four-coordinate boron atom with a B–Si bond (cf., the Supporting Information for more details).

The H/halogen-exchange reaction works faithfully not only for other tetrel halides, but also for PCl_3 as an example of the pnictogen halides (Figure 7, right). A mere I^- addition to give sodium formate was achieved for CO_2.[37] So far, we encountered no substrate limitations for Na_2[**4**-H_2] as a H^- source; however, investigations are still ongoing. With the help of Me_2SiCl_2, we next addressed the question: Are partially hydrogenated products available if the number of halide substituents in the substrate molecules exceeds the number of provided H^- ions? ^{1}H and ^{29}Si NMR spectroscopy on a 1:2 mixture of Na_2[**4**-H_2] and Me_2SiCl_2 revealed equimolar amounts of unreacted starting material (Me_2SiCl_2) and dimethylsilane (Me_2SiH_2) immediately after sample preparation. Over time, new resonances slowly grew in that were

DOI: 10.1021/jacs.9b01998
J. Am. Chem. Soc. 2019, 141, 6082–6091

assignable to dimethylchlorosilane ($Me_2Si(H)Cl$; Scheme 3). The comproportionation reaction becomes significantly faster

Scheme 3. 1 Equiv of Me_2SiCl_2 Quantitatively Converted to 1 Equiv of Me_2SiH_2 upon Treatment with 1 Equiv of Na_2[4-H_2][a]

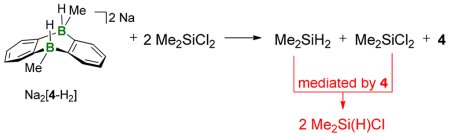

[a]If an excess of Me_2SiCl_2 is present, the Lewis acid **4** catalyzes a subsequent dismutation reaction furnishing 2 equiv of $Me_2Si(H)Cl$.

with increasing temperature (120 °C) and is mediated by the Lewis acidic borane **4**.[38] Thus, the DBA$^\Lambda$ serves two purposes in the overall process, first to accomplish H_2 activation/H^- transfer and second to catalyze the silane comproportionation. The obtained $Me_2Si(H)Cl$ is a most important building block for the silicone industry, because it possesses two orthogonal reactive sites and can extensively be derivatized via hydrosilylation protocols.[39]

It has been proposed that the reduction of chlorosilanes with aluminum hydrides involves four-membered Al-H-Si-Cl rings in the transition state.[40] A similar scenario is also conceivable for [**4**-H_2]$^{2-}$ as the reducing agent. Alternatively, a chlorosilane R_3SiCl could abstract one H^- ion from Na_2[**4**-H_2] (or Na[**4**-H]) to afford Na[$R_3Si(H)Cl$] and Na[**4**-H] (or **4**). The subsequent elimination of NaCl from the five-coordinate Na[$R_3Si(H)Cl$] should be facile. The comproportionation reaction $Me_2SiH_2 + Me_2SiCl_2 \rightarrow 2Me_2Si(H)Cl$ catalyzed by **4** likely starts with the formation of an adduct $R_3B\cdots H{-}Si(H)Me_2$. Such intermediates, which have already been described in the context of triorganylborane-mediated hydrosilylation and Piers-Rubinsztajn reactions,[41] are prone to nucleophilic attack at the silicon atom. If the incoming nucleophile is a chlorine substituent of Me_2SiCl_2, the formation of a disilyl chloronium salt [R_3BH][$Me_2(H)Si{-}Cl{-}Si(Cl)Me_2$] can be envisaged.[42] H^- migration from boron to silicon finally affords 2 equiv of $Me_2Si(H)Cl$.

CONCLUSION

The ambiphilic doubly reduced 9,10-dihydro-9,10-diboraanthracenes [DBA]$^{2-}$ described in this Article have taken the next step in mimicking transition metal complexes, because they not only activate H_2 but can subsequently use both hydrogen atoms for further syntheses. Depending on the specific substrate, the transfer of the H_2 equivalent results either in the hydrogenation of unsaturated bonds (formal delivery of an H^+ and H^- ion) or in the nucleophilic substitution at E–X bonds (delivery of two H^- ions). If in the latter case the released neutral DBA is rereduced, it can run through the process again and thereby act as a rechargeable analogue of $NaBH_4$.

For the H_2-activation step alone, it is advantageous to select a weakly coordinating counter cation and a small B-bonded substituent to minimize steric hindrance to the approaching H_2 molecule. An opposite counter cation effect is operative for the H_2-transfer step, because cation coordination stabilizes the regenerated [DBA]$^{2-}$ dianion. Moreover, the B-bonded substituent must not be too small to avoid catalyst poisoning through the formation of persistent substrate-[DBA]$^{2-}$ cycloadducts. H^- transfer proved less sensitive to the choices of the B-bonded substituents and the cations, such that the focus can be placed on maximizing the efficiency of the H_2-activation step. We finally came to the result that Li_2[**4**] and Na_2[**4**] carrying Me groups at boron are best suited to mediate H_2- and double H^--transfer reactions, respectively.

We have shown in the past that a derivatization of the DBA scaffold is also facile at the *o*-phenylene rings.[43] Almost any substitution pattern can be installed, which allows the preparation of custom-tailored catalysts. Yet, the largest potential for further improvement arguably lies in the replacement of the alkali metal reductants by an electric current to close the catalytic H^--transfer cycle.

ASSOCIATED CONTENT

Supporting Information

The Supporting Information is available free of charge on the ACS Publications website at DOI: 10.1021/jacs.9b01998.

Experimental details and characterization data (PDF)
X-ray crystallographic data (CIF)
Cartesian coordinates of calculated structures (XYZ)

AUTHOR INFORMATION

Corresponding Author

*matthias.wagner@chemie.uni-frankfurt.de

ORCID

Michael Bolte: 0000-0001-5296-6251
Hans-Wolfram Lerner: 0000-0003-1803-7947
Matthias Wagner: 0000-0001-5806-8276

Notes

The authors declare no competing financial interest.

ACKNOWLEDGMENTS

We gratefully acknowledge Dr. Thomas Kaese and Marc Zeplichal (M.Sc.) for their assistance with quantum chemical calculations and autoclave experiments, respectively.

REFERENCES

(1) (a) Erker, G., Stephan, D. W., Eds. *Frustrated Lewis Pairs I & II*; Springer: Heidelberg, 2013. (b) Stephan, D. W.; Erker, G. Frustrated Lewis Pair Chemistry of Carbon, Nitrogen and Sulfur Oxides. *Chem. Sci.* **2014**, *5*, 2625. (c) Stephan, D. W. Frustrated Lewis Pairs. *J. Am. Chem. Soc.* **2015**, *137*, 10018.

(2) (a) Chu, T.; Nikonov, G. I. Oxidative Addition and Reductive Elimination at Main-Group Element Centers. *Chem. Rev.* **2018**, *118*, 3608. (b) Weetman, C.; Inoue, S. The Road Travelled: After Main-Group Elements as Transition Metals. *ChemCatChem* **2018**, *10*, 4213. (c) Hadlington, T. J.; Driess, M.; Jones, C. Low-Valent Group 14 Element Hydride Chemistry: Towards Catalysis. *Chem. Soc. Rev.* **2018**, *47*, 4176. (d) Dagorne, S.; Wehmschulte, R. Recent Developments on the Use of Group 13 Metal Complexes in Catalysis. *ChemCatChem* **2018**, *10*, 2509. (e) Légaré, M.-A.; Pranckevicius, C.; Braunschweig, H. Metallomimetic Chemistry of Boron. *Chem. Rev.* **2019**, DOI: 10.1021/acs.chemrev.8b00561.

(3) Dahcheh, F.; Martin, D.; Stephan, D. W.; Bertrand, G. Synthesis and Reactivity of a CAAC-Aminoborylene Adduct: A Hetero-Allene or an Organoboron Isoelectronic with Singlet Carbenes. *Angew. Chem., Int. Ed.* **2014**, *53*, 13159.

(4) (a) Peng, Y.; Guo, J. D.; Ellis, B. D.; Zhu, Z.; Fettinger, J. C.; Nagase, S.; Power, P. P. Reaction of Hydrogen or Ammonia with Unsaturated Germanium or Tin Molecules under Ambient Con-

DOI: 10.1021/jacs.9b01998
J. Am. Chem. Soc. 2019, 141, 6082–6091

ditions: Oxidative Addition versus Arene Elimination. *J. Am. Chem. Soc.* **2009**, *131*, 16272. (b) Seifert, A.; Scheid, D.; Linti, G.; Zessin, T. Oxidative Addition Reactions of Element−Hydrogen Bonds with Different Polarities to a Gallium(I) Compound. *Chem. - Eur. J.* **2009**, *15*, 12114. (c) Martin, D.; Soleilhavoup, M.; Bertrand, G. Stable Singlet Carbenes as Mimics for Transition Metal Centers. *Chem. Sci.* **2011**, *2*, 389. (d) Protchenko, A. V.; Birjkumar, K. H.; Dange, D.; Schwarz, A. D.; Vidovic, D.; Jones, C.; Kaltsoyannis, N.; Mountford, P.; Aldridge, S. A Stable Two-Coordinate Acyclic Silylene. *J. Am. Chem. Soc.* **2012**, *134*, 6500. (e) Chu, T.; Korobkov, I.; Nikonov, G. I. Oxidative Addition of Sigma Bonds to an Al(I) Center. *J. Am. Chem. Soc.* **2014**, *136*, 9195. (f) Protchenko, A. V.; Bates, J. I.; Saleh, L. M.; Blake, M. P.; Schwarz, A. D.; Kolychev, E. L.; Thompson, A. L.; Jones, C.; Mountford, P.; Aldridge, S. Enabling and Probing Oxidative Addition and Reductive Elimination at a Group 14 Metal Center: Cleavage and Functionalization of E−H Bonds by a Bis(boryl)-stannylene. *J. Am. Chem. Soc.* **2016**, *138*, 4555.

(5) Tsukahara, N.; Asakawa, H.; Lee, K. H.; Lin, Z.; Yamashita, M. Cleaving Dihydrogen with Tetra(*o*-tolyl)diborane(4). *J. Am. Chem. Soc.* **2017**, *139*, 2593.

(6) (a) Zhu, Z.; Wang, X.; Peng, Y.; Lei, H.; Fettinger, J. C.; Rivard, E.; Power, P. P. Addition of Hydrogen or Ammonia to a Low-Valent Group 13 Metal Species at 25 °C and 1 atm. *Angew. Chem., Int. Ed.* **2009**, *48*, 2031. (b) Fan, C.; Mercier, L. G.; Piers, W. E.; Tuononen, H. M.; Parvez, M. Dihydrogen Activation by Antiaromatic Pentaarylboroles. *J. Am. Chem. Soc.* **2010**, *132*, 9604. (c) Li, J.; Schenk, C.; Goedecke, C.; Frenking, G.; Jones, C. A Digermyne with a Ge−Ge Single Bond That Activates Dihydrogen in the Solid State. *J. Am. Chem. Soc.* **2011**, *133*, 18622. (d) Hermann, M.; Goedecke, C.; Jones, C.; Frenking, G. Reaction Pathways for Addition of H_2 to Amido-Ditetrylynes $R_2N{-}EE{-}NR_2$ (E = Si, Ge, Sn). A Theoretical Study. *Organometallics* **2013**, *32*, 6666. (e) Hadlington, T. J.; Jones, C. A Singly Bonded Amido-Distannyne: H_2 Activation and Isocyanide Coordination. *Chem. Commun.* **2014**, *50*, 2321. (f) Arrowsmith, M.; Böhnke, J.; Braunschweig, H.; Celik, M. A.; Dellermann, T.; Hammond, K. Uncatalyzed Hydrogenation of First-Row Main Group Multiple Bonds. *Chem. - Eur. J.* **2016**, *22*, 17169. (g) Nagata, K.; Murosaki, T.; Agou, T.; Sasamori, T.; Matsuo, T.; Tokitoh, N. Activation of Dihydrogen by Masked Doubly Bonded Aluminum Species. *Angew. Chem., Int. Ed.* **2016**, *55*, 12877. (h) Araki, T.; Hirai, M.; Wakamiya, A.; Piers, W. E.; Yamaguchi, S. Antiaromatic Dithieno-1,2-dihydro-1,2-diborin Splits Diatomic Hydrogen. *Chem. Lett.* **2017**, *46*, 1714. (i) Wendel, D.; Szilvási, T.; Jandl, C.; Inoue, S.; Rieger, B. Twist of a Silicon−Silicon Double Bond: Selective *Anti*-Addition of Hydrogen to an Iminodisilene. *J. Am. Chem. Soc.* **2017**, *139*, 9156.

(7) (a) Taylor, J. W.; McSkimming, A.; Guzman, C. F.; Harman, W. H. N-Heterocyclic Carbene-Stabilized Boranthrene as a Metal-Free Platform for the Activation of Small Molecules. *J. Am. Chem. Soc.* **2017**, *139*, 11032. (b) Su, Y.; Li, Y.; Ganguly, R.; Kinjo, R. Engineering the Frontier Orbitals of a Diazadiborinine for Facile Activation of H_2, NH_3, and an Isonitrile. *Angew. Chem., Int. Ed.* **2018**, *57*, 7846.

(8) von Grotthuss, E.; Diefenbach, M.; Bolte, M.; Lerner, H.-W.; Holthausen, M. C.; Wagner, M. Reversible Dihydrogen Activation by Reduced Aryl Boranes as Main-Group Ambiphiles. *Angew. Chem., Int. Ed.* **2016**, *55*, 14067.

(9) (a) Welch, G. C.; San Juan, R. R.; Masuda, J. D.; Stephan, D. W. Reversible, Metal-Free Hydrogen Activation. *Science* **2006**, *314*, 1124. (b) Frey, G. D.; Lavallo, V.; Donnadieu, B.; Schoeller, W. W.; Bertrand, G. Facile Splitting of Hydrogen and Ammonia by Nucleophilic Activation at a Single Carbon Center. *Science* **2007**, *316*, 439. (c) Power, P. P. Main-Group Elements as Transition Metals. *Nature* **2010**, *463*, 171. (d) Zhao, L.; Huang, F.; Lu, G.; Wang, Z.-X.; Schleyer, P. Why the Mechanisms of Digermyne and Distannyne Reactions with H_2 Differ So Greatly. *J. Am. Chem. Soc.* **2012**, *134*, 8856.

(10) Stephan, D. W. "Frustrated Lewis Pair" Hydrogenations. *Org. Biomol. Chem.* **2012**, *10*, 5740.

(11) For a remote example, see: Abdalla, J. A.; Riddlestone, I. M.; Tirfoin, R.; Aldridge, S. Cooperative Bond Activation and Catalytic Reduction of Carbon Dioxide at a Group 13 Metal Center. *Angew. Chem., Int. Ed.* **2015**, *54*, 5098.

(12) Hinz, A.; Schulz, A.; Villinger, A. Metal-Free Activation of Hydrogen, Carbon Dioxide, and Ammonia by the Open-Shell Singlet Biradicaloid $[P(\mu\text{-NTer})]_2$. *Angew. Chem., Int. Ed.* **2016**, *55*, 12214. Reversible H_2 activation by a triphosphabenzene has also been published: Longobardi, L. E.; Russell, C. A.; Green, M.; Townsend, N. S.; Wang, K.; Holmes, A. J.; Duckett, S. B.; McGrady, J. E.; Stephan, D. W. Hydrogen Activation by an Aromatic Triphosphabenzene. *J. Am. Chem. Soc.* **2014**, *136*, 13453.

(13) Lorbach, A.; Bolte, M.; Li, H.; Lerner, H.-W.; Holthausen, M. C.; Jäkle, F.; Wagner, M. 9,10-Dihydro-9,10-diboraanthracene: Supramolecular Structure and Use as a Building Block for Luminescent Conjugated Polymers. *Angew. Chem., Int. Ed.* **2009**, *48*, 4584.

(14) (a) Eisch, J. J.; Kotowicz, B. W. Novel Organoborane Lewis Acids via Selective Boron-Tin Exchange Processes Steric Constraints to Electrophilic Initiation by the Boron Halide. *Eur. J. Inorg. Chem.* **1998**, *1998*, 761. (b) Kessler, S. N.; Neuburger, M.; Wegner, H. A. Bidentate Lewis Acids for the Activation of 1,2-Diazines - a New Mode of Catalysis. *Eur. J. Org. Chem.* **2011**, *2011*, 3238.

(15) Hoffend, C.; Diefenbach, M.; Januszewski, E.; Bolte, M.; Lerner, H.-W.; Holthausen, M. C.; Wagner, M. Effects of Boron Doping on the Structural and Optoelectronic Properties of 9,10-Diarylanthracenes. *Dalton Trans.* **2013**, *42*, 13826.

(16) von Grotthuss, E.; Prey, S. E.; Bolte, M.; Lerner, H.-W.; Wagner, M. Selective CO_2 Splitting by Doubly Reduced Aryl Boranes to Give CO and $[CO_3]^{2-}$. *Angew. Chem., Int. Ed.* **2018**, *57*, 16491.

(17) Nöth, H.; Wrackmeyer, B. *Nuclear Magnetic Resonance Spectroscopy of Boron Compounds*. In *NMR Basic Principles and Progress*; Diehl, P., Fluck, E., Kosfeld, R., Eds.; Springer: Berlin, 1978.

(18) In **2**, the boron atoms are located in the shielding cone of the C≡C triple bond (cf., $\delta(^{11}B)$ in C_6D_6: **2** = 53 ppm, **9** = 73 ppm). Care must be taken not to overestimate the extent of THF ligation in **2** on the basis of the $\delta(^{11}B)$ value recorded for this compound in THF-d_8. We therefore believe that THF ligation is mainly relevant for **1** (and here for its redox potential).

(19) Also, for the Me derivative **4**, a dynamic equilibrium close to 90% conversion cannot be excluded, but the size of the effect is likely already beyond the limits of measurement error.

(20) Lorbach, A.; Bolte, M.; Lerner, H.-W.; Wagner, M. Dilithio 9,10-diborataanthracene: Molecular Structure and 1,4-Addition Reactions. *Organometallics* **2010**, *29*, 5762.

(21) The conversion of the sodium salt $Na_2[\mathbf{2}]$ to $Na_2[\mathbf{2}\text{-}H_2]$ is quantitative after 93 h at 100 °C. Thus, not only the stability of the $[\mathbf{2}]^{2-}$ ion but also the nature of the counter cation is an important factor.

(22) (a) Kumpf, R. A.; Dougherty, D. A. A Mechanism for Ion Selectivity in Potassium Channels: Computational Studies of Cation-π Interactions. *Science* **1993**, *261*, 1708. (b) Ma, J. C.; Dougherty, D. The Cation−π Interaction. *Chem. Rev.* **1997**, *97*, 1303. (c) Gokel, G. W.; De Wall, S. L.; Meadows, E. S. Experimental Evidence for Alkali Metal Cation−π Interactions. *Eur. J. Org. Chem.* **2000**, *2000*, 2967. (d) Ilkhechi, A. H.; Mercero, J. M.; Silanes, I.; Bolte, M.; Scheibitz, M.; Lerner, H.-W.; Ugalde, J. M.; Wagner, M. A Joint Experimental and Theoretical Study of Cation-π Interactions: Multiple-Decker Sandwich Complexes of Ferrocene with Alkali Metal Ions (Li^+, Na^+, K^+, Rb^+, Cs^+). *J. Am. Chem. Soc.* **2005**, *127*, 10656. (e) Kaufmann, L.; Vitze, H.; Bolte, M.; Lerner, H.-W.; Wagner, M. Experimental Assessment of the Relative Affinities of Benzene and Ferrocene toward the Li^+ Cation. *Organometallics* **2007**, *26*, 1771.

(23) The compounds crystallize as (dimeric) solvates $[Li(thf)_2][Li(thf)][\mathbf{1}\text{-}H_2]$, $[Na][Na(thf)_2(18\text{-c-}6)][Na(thf)_2]_2(n\text{-hexane})[\mathbf{7}\text{-}H_2]_2$, $[K(18\text{-c-}6)]_2[\mathbf{1}\text{-}H_2]$, $[K][K(thf)]_3[\mathbf{4}\text{-}H_2]_2$, and $[K]_2[K(18\text{-c-}6)][K(18\text{-c-}6)(thf)_2][\mathbf{7}\text{-}H_2]_2$. A discussion of the crystal structures is provided in the Supporting Information.

DOI: 10.1021/jacs.9b01998
J. Am. Chem. Soc. 2019, 141, 6082−6091

(24) For a related, $BH_3{\cdot}SMe_2$-mediated *cis/trans* isomerization of a hydrogenated 1,4,2,5-diazadiborinine, see: Wang, B.; Kinjo, R. Activation of Dihydrogen by 1,4,2,5-Diazadiborinine. *Tetrahedron* **2018**, *74*, 7273.
(25) A planar configuration was also observed for the pyridine diadduct of the parent DBA **1**; see ref 13.
(26) Slaugh, L. H. Metal Hydrides. Hydrogenation and Isomerization Catalysts. *J. Org. Chem.* **1967**, *32*, 108.
(27) For a related ethylene cycloaddition product of 1,3,2,5-diazadiborinine, see: Wu, D.; Ganguly, R.; Li, Y.; Hoo, S. N.; Hirao, H.; Kinjo, R. Reversible [4+2] Cycloaddition Reaction of 1,3,2,5-Diazadiborinine with Ethylene. *Chem. Sci.* **2015**, *6*, 7150.
(28) In principle, a thermally allowed 6 e^- transition state would be achievable also for olefins and alkynes if we assume that a Dewar benzene-like valence isomer of $[\mathbf{A}]^{2-}$ with a transannular B−B bond is released. However, the associated activation energies should be high and the corresponding structures have so far not been reported; the closest known relatives are 1,4-disila(Dewar-benzene)s: Kabe, Y.; Ohkubo, K.; Ishikawa, H.; Ando, W. 1,4-Disila(Dewar-benzene) and 1,4-Disilabenzene: Valence Isomerization of Bis(alkylsilacyclopropenyl)s. *J. Am. Chem. Soc.* **2000**, *122*, 3775.
(29) Rüchardt, C.; Gerst, M.; Ebenhoch, J. Uncatalyzed Transfer Hydrogenation and Transfer Hydrogenolysis: Two Novel Types of Hydrogen-Transfer Reactions. *Angew. Chem., Int. Ed. Engl.* **1997**, *36*, 1406.
(30) Braude, E. A.; Jackman, L. M.; Linstead, R. P. Hydrogen Transfer. Part II. The Dehydrogenation of 1:4-Dihydronaphthalene by Quinones. Kinetics and Mechanism. *J. Chem. Soc.* **1954**, *0*, 3548.
(31) As a caveat, we note that B−H bond-dissociation energies similar to those of frequently used H$^\bullet$-atom donors have been obtained for BH_3 adducts with neutral Lewis bases (especially *N*-heterocyclic carbenes). Yet, a competing H^--ion transfer scenario would require an energetically unfavorable charge separation as opposed to the case of $[\mathbf{A}\text{-}H_2]^{2-}$: (a) Ueng, S.-H.; Solovyev, A.; Yuan, X.; Geib, S. J.; Fensterbank, L.; Lacôte, E.; Malacria, M.; Newcomb, M.; Walton, J. C.; Curran, D. P. N-Heterocyclic Carbene Boryl Radicals: A New Class of Boron-Centered Radical. *J. Am. Chem. Soc.* **2009**, *131*, 11256. (b) Hioe, J.; Karton, A.; Martin, J. M.; Zipse, H. Borane-Lewis Base Complexes as Homolytic Hydrogen Atom Donors. *Chem. - Eur. J.* **2010**, *16*, 6861. (c) Ueng, S.-H.; Fensterbank, L.; Lacôte, E.; Malacria, M.; Curran, D. P. Radical Reductions of Alkyl Halides Bearing Electron Withdrawing Groups with N-Heterocyclic Carbene Boranes. *Org. Biomol. Chem.* **2011**, *9*, 3415. (d) Curran, D. P.; Solovyev, A.; Makhlouf Brahmi, M.; Fensterbank, L.; Malacria, M.; Lacôte, E. Synthesis and Reactions of N-Heterocyclic Carbene Boranes. *Angew. Chem., Int. Ed.* **2011**, *50*, 10294.
(32) von Grotthuss, E.; Nawa, F.; Bolte, M.; Lerner, H.-W.; Wagner, M. Chalcogen−Chalcogen-Bond Activation by an Ambiphilic, Doubly Reduced Organoborane. *Tetrahedron* **2019**, *75*, 26.
(33) Jedliński, Z. J.; Kurcok, P.; Nozirow, F. Synthesis of Polysilanes by Reductive Coupling of Dichlorosilanes Mediated with Alkali Metal/Crown Ether Supramolecular Complexes in a Homogeneous System. *Macromol. Rapid Commun.* **1997**, *18*, 483.
(34) Morris, D. F. C. The Lattice Energies of the Alkali Halides. *Acta Crystallogr.* **1956**, *9*, 197.
(35) Deberitz, J.; Boche, G. *Industrielle Anorganische Chemie*, 4th ed.; Wiley-VCH: Weinheim, 2013.
(36) For further examples of boron-centered nucleophiles, see: (a) Hübner, A.; Bolte, M.; Lerner, H.-W.; Wagner, M. Extensive Structural Rearrangements Upon Reduction of 9H-9-Borafluorene. *Angew. Chem., Int. Ed.* **2014**, *53*, 10408. (b) Hübner, A.; Kaese, T.; Diefenbach, M.; Endeward, B.; Bolte, M.; Lerner, H.-W.; Holthausen, M. C.; Wagner, M. A Preorganized Ditopic Borane as Highly Efficient One- or Two-Electron Trap. *J. Am. Chem. Soc.* **2015**, *137*, 3705. (c) Kaese, T.; Budy, H.; Bolte, M.; Lerner, H.-W.; Wagner, M. Deprotonation of a Seemingly Hydridic Diborane(6) to Build a B−B Bond. *Angew. Chem., Int. Ed.* **2017**, *56*, 7546. (d) Wu, D.; Li, Y.; Ganguly, R.; Kinjo, R. A Snapshot of Inorganic Janovsky Complex Analogues Featuring a Nucleophilic Boron Center. *Chem. Commun.* **2017**, *53*, 12734. (e) Kaese, T.; Trageser, T.; Budy, H.; Bolte, M.; Lerner, H.-W.; Wagner, M. A Redox-Active Diborane Platform Performs C(sp^3)-H Activation and Nucleophilic Substitution Reactions. *Chem. Sci.* **2018**, *9*, 3881. (f) Himmel, H.-J. Nucleophilic Neutral Diborane(4) Compounds with sp^3-sp^3-Hybridized Boron Atoms. *Eur. J. Inorg. Chem.* **2018**, *2018*, 2139. (g) Zhao, Q.; Dewhurst, R. D.; Braunschweig, H.; Chen, X. A New Perspective on Borane Chemistry: The Nucleophilicity of the B−H Bonding Pair Electrons. *Angew. Chem., Int. Ed.* **2019**, *58*, 3268.
(37) CO_2 reduction by $NaBH_4$ has already been reported: Knopf, I.; Cummins, C. C. Revisiting CO_2 Reduction with $NaBH_4$ under Aprotic Conditions: Synthesis and Characterization of Sodium Triformatoborohydride. *Organometallics* **2015**, *34*, 1601.
(38) Gilbert, A.; Cooper, G.; Shade, R. Alkylchlorosilanes. Reduction of Alkylchlorosilenes by Sodium Hydride and Hydrogen-Chlorine Interchange in Chlorosilanes. *Ind. Eng. Chem.* **1959**, *51*, 665.
(39) Pachaly, B.; Achenbach, F.; Herzig, C.; Mautner, K. *Silicone*; Wiley-VCH: Weinheim, 2005.
(40) Sommer, L. H.; Golino, C. M.; Roark, D. N.; Bush, R. D. Reduction of Silicon Halides and Alkoxides with Diisobutylaluminum Hydride. Stereochemistry-Rate Law Correlations for the S_Ni−Si and S_N2−Si Mechanisms. *J. Organomet. Chem.* **1973**, *49*, C3.
(41) (a) Houghton, A. Y.; Hurmalainen, J.; Mansikkamaki, A.; Piers, W. E.; Tuononen, H. M. Direct Observation of a Borane-Silane Complex Involved in Frustrated Lewis-Pair-Mediated Hydrosilylations. *Nat. Chem.* **2014**, *6*, 983. (b) Brook, M. A. New Control over Silicone Synthesis Using SiH Chemistry: The Piers-Rubinsztajn Reaction. *Chem. - Eur. J.* **2018**, *24*, 8458.
(42) (a) Budanow, A.; Sinke, T.; Tillmann, J.; Bolte, M.; Wagner, M.; Lerner, H.-W. Two-Coordinate Gallium Ion $[t\mathrm{Bu_3Si{-}Ga{-}SitBu_3}]^+$ and the Halonium Ions $[t\mathrm{Bu_3Si{-}X{-}SitBu_3}]^+$ (X = Br, I): Sources of the Supersilyl Cation $[t\mathrm{Bu_3Si}]^+$. *Organometallics* **2012**, *31*, 7298. (b) Budanow, A.; Bolte, M.; Wagner, M.; Lerner, H.-W. The Ion-Like Supersilylium Compound $t\mathrm{Bu_3Si{-}F{-}Al[OC(CF_3)_3]_3}$. *Eur. J. Inorg. Chem.* **2015**, *2015*, 2524.
(43) (a) Reus, C.; Weidlich, S.; Bolte, M.; Lerner, H.-W.; Wagner, M. C-Functionalized, Air- and Water-Stable 9,10-Dihydro-9,10-diboraanthracenes: Efficient Blue to Red Emitting Luminophores. *J. Am. Chem. Soc.* **2013**, *135*, 12892. (b) John, A.; Bolte, M.; Lerner, H.-W.; Wagner, M. A Vicinal Electrophilic Diborylation Reaction Furnishes Doubly Boron-Doped Polycyclic Aromatic Hydrocarbons. *Angew. Chem., Int. Ed.* **2017**, *56*, 5588. (c) Kirschner, S.; Mewes, J. M.; Bolte, M.; Lerner, H.-W.; Dreuw, A.; Wagner, M. How Boron Doping Shapes the Optoelectronic Properties of Canonical and Phenylene-Containing Oligoacenes: A Combined Experimental and Theoretical Investigation. *Chem. - Eur. J.* **2017**, *23*, 5104. (d) Brend'amour, S.; Gilmer, J.; Bolte, M.; Lerner, H.-W.; Wagner, M. C-Halogenated 9,10-Diboraanthracenes: How the Halogen Load and Distribution Influences Key Optoelectronic Properties. *Chem. - Eur. J.* **2018**, *24*, 16910. (e) John, A.; Kirschner, S.; Fengel, M. K.; Bolte, M.; Lerner, H.-W.; Wagner, M. Simultaneous Expansion of 9,10 Boron-Doped Anthracene in Longitudinal and Lateral Directions. *Dalton Trans.* **2019**, *48*, 1871.

DOI: 10.1021/jacs.9b01998
J. Am. Chem. Soc. 2019, 141, 6082−6091

Supporting Information

Dual Role of Doubly Reduced Arylboranes as Dihydrogen- and Hydride-Transfer Catalysts

Esther von Grotthuss, Sven E. Prey, Michael Bolte, Hans-Wolfram Lerner, and Matthias Wagner*

Table of contents:

1. Experimental details and characterization data

General considerations. All reactions, manipulations, and analyses were carried out in an argon-filled glovebox or by applying standard Schlenk techniques under a nitrogen atmosphere. Toluene, Et_2O, and THF were dried over Na/benzophenone; THF-d_8 was dried over Na-K alloy without benzophenone. Prior to use, the solvents were distilled from the drying agent; THF and THF-d_8 were degassed by applying three freeze-pump-thaw cycles.

NMR spectra were recorded at 298 K using the following spectrometers: Bruker DPX-250, Avance-300, Avance-400, or Avance-500.

Chemical shifts are referenced to (residual) solvent signals ($^1H/^{13}C\{^1H\}$; THF-d_8: δ = 3.58/67.21 ppm[1]) or external $BF_3{\cdot}Et_2O$ (^{11}B; $^{11}B\{^1H\}$). Abbreviations: s = singlet, d = doublet, t = triplet, q = quartet, sept = septet, m = multiplet, br = broad, n.o. = not observed, n.r. = not resolved.

Numbering schemes for symmetrically substituted (left) and unsymmetrically substituted (right) DBA cores are as follows:

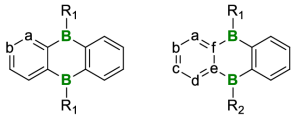

The compounds 9,10-dibromo-DBA,[2] **1**,[3] **2**,[4] **3**,[3] **4**,[6,7] **9**,[5] Li_2[**1**],[4,8] Li_2[**2**],[4] K_2[**1**],[4] Li_2[**4**],[7] Na_2[**4**],[7] Li_2[**1**-H_2],[4] Li_2[**2**-H_2],[4] and K_2[**1**-H_2][4] were synthesized according to literature procedures.

Cyclic voltammetry (CV) measurements were performed in a glovebox at room temperature in a one-chamber, three-electrode cell using an EG&G Princeton Applied Research 263A potentiostat. A platinum disk electrode (2.00 mm diameter) was used as the working electrode with a platinum wire counter electrode and a silver wire reference electrode, which was coated with AgCl by immersion into HCl/HNO_3 (3:1). Prior to measurements, the solvent THF was dried with Na-K alloy. [nBu$_4$N][PF_6] was employed as the supporting electrolyte (0.1 mol L^{-1}). All potential values were referenced against the FcH/FcH^+ redox couple (FcH = ferrocene; $E_{1/2}$ = 0 V). Scan rates were varied between 100 and 400 mV s^{-1}.

High-resolution mass spectra were measured in positive mode using a Thermo Fisher Scientific MALDI LTQ Orbitrap XL and α-cyano-4-hydroxycinnamic acid or 4-chloro-α-cyanocinnamic acid as the matrix. Exact masses were calculated based on the predominant combination of natural isotopes.

1.1 Synthesis of the DBA derivatives

General procedure for the synthesis of symmetrically substituted DBA-derivatives:

The freshly prepared Grignard reagent aryl-MgBr or alkyl-MgBr (1.888 mmol, 2.1 equiv) in Et_2O (15 mL) was added dropwise with stirring over 15 min to a cooled (−78 °C) solution of 9,10-dibromo-DBA (300 mg, 0.899 mmol, 1.0 equiv) in toluene (25 mL). The reaction mixture was slowly allowed to warm to room temperature and stirred overnight. All volatiles were removed under reduced pressure, the residue was extracted with toluene (3 × 10 mL) and the combined extracts were filtered over a glass frit (G4) covered with Celite (1 cm; pre-dried at 120 °C for several days). After the removal of all volatiles in a dynamic vacuum, the symmetrically substituted DBA derivatives were obtained as pale yellow to ocher solids. See Table S1 for the obtained yields.

The ethyl derivative **5** was sufficiently volatile to grow X-ray quality crystals by sublimation (110 °C/10^{-3} mbar). X-ray quality crystals of **8** were obtained by gas-phase diffusion of *n*-hexane into its toluene solution.

Table S1. Overview of the DBA derivatives obtained via the described method. (*) Yield not determined because compound was not pure.

DBA derivative	reagent		yield	
		mL	mg	%
5	1-bromoethane	0.14	150	72
6	2-bromopropane	0.18	–	(*)
7	4-bromotoluene	0.22	246	77
8	5-bromo-*m*-xylene	0.26	224	65

General procedure for DBA reduction with lithium granules:

In a glovebox, lithium granules (10 mg, 1.44 mmol) were added at room temperature to a stirred solution of the respective neutral DBA (**1**-**5** and **7**-**9**; 0.050 mmol) in THF-d_8 (0.5 mL), whereupon the reaction mixture immediately adopted a red color. After 30 min, the solution was separated from residual lithium metal with a syringe and used without further treatment. NMR analysis revealed a quantitative conversion to the respective dianion in all cases.

X-ray quality crystals of $[Li(thf)_2]_2$[**7**] were grown by slow evaporation of its THF-d_8 solution.

General procedure for DBA reduction with elemental sodium:

In a glovebox, sodium metal (10 mg, 0.435 mmol) was added at room temperature to a stirred solution of the respective neutral DBA (**1**, **2**, **4**, and **7**; 0.050 mmol) in THF-d_8 (0.5 mL), whereupon the reaction mixture immediately adopted a pink color and turned dark green within 30 min. After 60 min, the solution was separated from residual sodium metal with a syringe and used without further treatment. NMR analysis revealed a quantitative conversion to the respective dianion in all cases.

X-ray quality crystals of $[Na_2(thf)_3]$[**1**] were grown by slow evaporation of its THF-d_8 solution.

General procedure for DBA reduction with KC_8:

In a glovebox, KC_8 (27 mg, 0.200 mmol) was added at room temperature to a stirred solution of the respective neutral DBA (**1** and **4**-**8**; 0.050 mmol) in THF (1 mL), whereupon the reaction mixture immediately adopted a pink color and turned dark green within 30 min. After 60 min, the solution was separated from residual KC_8 and graphite by filtration (G4 glass frit), the solvent was removed from the filtrate under reduced pressure, and the residue dissolved in THF-d_8. NMR analysis showed exclusively the resonances of the respective dianion in all cases.

Red X-ray quality crystals of $[K_2(thf)_4][\mathbf{1}]$ and $[K(thf)]_2[\mathbf{7}]$ were grown by slow evaporation of their THF solutions.

Note: The compound $K_2[\mathbf{4}]$ was previously prepared by Siebert et al., who observed a red color, both for the solid material and its THF solutions. However, they also mentioned broad and purely resolved NMR spectra containing more resonances than expected.[9]

General procedure for the measurement of H_2-addition kinetics:

H_2 activation reactions were carried out in flame-sealed NMR tubes. The experimental setup was as follows: An NMR tube connected to a Schlenk line was charged with a THF-d_8 solution (0.5 mL) of the respective doubly reduced 9,10-dihydro-9,10-diboraanthracene (approx. 0.050 mmol $[\mathbf{A}]^{2-}$; preparation as described above). The solution was frozen with liquid nitrogen, the system was evacuated, and then H_2 (purity grade 5.0) was filled in through a condensation trap cooled with liquid nitrogen (to remove traces of H_2O). The content of the NMR tube was allowed to unfreeze whereby H_2 dissolved in the THF-d_8.[10] During the entire process, the system remained connected to the H_2 cylinder and a mercury bubbler to release the overpressure.

The mixture was frozen again, the partial pressure of H_2 was adjusted such that it remained slightly below 1 atm, and the NMR tube was flame-sealed. CAUTION: Care must be taken not to generate a leak in the glass wall. However, given the small amount of H_2 present in the NMR tube, we found that the hazard of an oxyhydrogen explosion was low even in the event of a leakage.

The sealed NMR samples were kept at either 50 or 100 °C (*cf.* Table S2) and the progress of the H_2-activation reaction was monitored by ^{1}H NMR spectroscopy in regular steps (*cf.* Figure 1). The spectra were recorded at ambient temperature, at which the activation reaction does not proceed further.[4] The conversion rates of H_2-addition in dependence of the boron-bonded substituent and the counter cation are summarized in Table S2 and Figures 1 and 4.

Table S2. Time (in hours) required until the individual H_2-addition reactions reached a dynamic equilibrium or were completed (see also Figures 1 and 4).

$[\mathbf{A}]^{2-}$ derivative	M = Li T = 100 °C	M = Na T = 100 °C	M = Na T = 50 °C	M = K T = 50 °C
$[\mathbf{1}]^{2-}$	86	21	183	12
$[\mathbf{2}]^{2-}$	48	93	-	-
$[\mathbf{4}]^{2-}$	264	14	76	3
$[\mathbf{5}]^{2-}$	480	-	-	8
$[\mathbf{7}]^{2-}$	640	21	129	13
$[\mathbf{8}]^{2-}$	480	-	-	11

X-ray quality crystals of [Na][Na(thf)$_2$(18-c-6)][Na(thf)$_2$]$_2$(*n*-hexane)[**7**-H_2]$_2$, [K(18-c-6)]$_2$[**1**-H_2], and [K]$_2$[K(18-c-6)][K(18-c-6)(thf)$_2$][**7**-H_2]$_2$ were obtained by gas-phase diffusion of *n*-hexane into their THF-d_8/18-crown-6 (18-c-6) solutions.

X-ray quality crystals of [K][K(thf)]$_3$[**4**-H_2]$_2$ were obtained by gas-phase diffusion of *n*-hexane into its THF-d_8 solution.

1.2 Spectroscopic data for the DBA derivatives

NMR data in THF-d_8 for the neutral DBA derivatives:

5

^{1}H NMR (500.2 MHz, THF-d_8): δ = 7.88–7.86 (m, 4H; H-a), 7.33–7.31 (m, 4H; H-b), 1.54 (q, ^3J(H,H) = 7.7 Hz, 4H; CH_2CH$_3$), 0.69 (t, ^3J(H,H) = 7.7 Hz, 6H; CH$_2$CH_3).

^{11}B NMR (160.5 MHz, THF-d_8): δ = 40.3 ($h_{1/2}$ = 500 Hz).

^{13}C{^{1}H} NMR (125.8 MHz, THF-d_8): δ = 151.4 (BC), 133.5 (C-a), 129.0 (C-b), 14.3 (*C*H$_2$CH$_3$), 10.3 (CH$_2$*C*H$_3$).

^{1}H NMR data in C_6D_6 are in accordance with the literature.[11]

^{1}H NMR (500.2 MHz, C_6D_6): δ = 8.04–8.02 (m, 4H; C_6H_4), 7.36–7.34 (m, 4H; C_6H_4), 1.92 (q, ^3J(H,H) = 8.3 Hz, 4H; CH_2CH$_3$), 1.10 (t, ^3J(H,H) = 8.3 Hz, 6H; CH$_2$CH_3).

6

^{1}H NMR (250.1 MHz, C_6D_6): δ = 8.02–7.99 (m, 4H; C_6H_4), 7.31–7.27 (m, 4H; C_6H_4), 2.46 (sept, ^3J(H,H) = 7.4 Hz, 2H; C*H*(CH$_3$)$_2$), 1.33 (t, ^3J(H,H) = 7.4 Hz, 12H; CH(C$_3$)$_2$).

Note: The compound could not be purified. Further NMR data were therefore not recorded.

7

^{1}H NMR (500.2 MHz, THF-d_8): δ = 7.65–7.63 (m, 4H; H-a), 7.35 (d, ^3J(H,H) = 7.7 Hz, 4H; Tol-H-*o*), 7.25–7.23 (m, 4H; H-b), 7.13 (d, ^3J(H,H) = 7.7 Hz, 4H; Tol-H-*m*), 2.34 (s, 6H; Tol-CH$_3$-*p*).

^{11}B NMR (160.5 MHz, THF-d_8): δ = 36.3 ($h_{1/2}$ = 670 Hz).

^{13}C{^{1}H} NMR (125.8 MHz, THF-d_8): δ = 152.4 (BC), 145.4 (Tol-C-*i*), 137.3 (C-a), 136.5 (Tol-C-*p*), 134.0 (Tol-C-*o*), 129.3 (C-b), 128.6 (Tol-C-*m*), 21.0 (Tol-CH$_3$-*p*).

8

^{1}H NMR (500.2 MHz, THF-d_8): δ = 7.64–7.62 (m, 4H; H-a), 7.25–7.23 (m, 4H; H-b), 7.07 (s, 4H; Xyl-H-*o*), 6.90 (s, 2H; Xyl-H-*p*), 2.30 (s, 12H; Xyl-CH$_3$-*m*).

^{11}B NMR (160.5 MHz, THF-d_8): δ = 38.1 ($h_{1/2}$ = 830 Hz).

^{13}C{^{1}H} NMR (125.8 MHz, THF-d_8): δ = 151.7 (BC), 148.3 (Xyl-C-*i*), 137.2 (C-a), 136.2 (Xyl-C-*m*), 131.0 (Xyl-C-*o*), 129.1 (C-b), 128.5 (Xyl-C-*p*), 21.6 (Xyl-CH$_3$-*m*).

NMR data in THF-d_8 for Li_2[A] salts:

Li_2[3]

^{1}H NMR (500.2 MHz, THF-d_8): δ = 8.45–8.43 (m, 4H; H-a), 7.10–7.07 (d, ^3J(H,H) = 18.1 Hz, 2H; CH=CH), 6.66–6.64 (m, 4H; H-b), 6.11–6.08 (d, ^3J(H,H) = 18.1 Hz, 2H; CH=CH), 1.24 (s, 18H; CH_3)

^{11}B NMR (160.5 MHz, THF-d_8): δ = 21.6 ($h_{1/2}$ = 390 Hz).

^{13}C{^{1}H} NMR (125.8 MHz, THF-d_8): δ = 148.4 (CH=CH), 136.4 (C-a), 131.9 (br; CH=CH), 118.4 (C-b), 34.9 ($C(CH_3)_3$), 30.6 ($C(CH_3)_3$); n.o. (BC).

Li_2[5]

^{1}H NMR (500.2 MHz, THF-d_8): δ = 8.29–8.27 (m, 4H; H-a), 6.67–6.65 (m, 4H; H-b), 1.98 (q, ^3J(H,H) = 7.9 Hz, 4H; CH_2CH_3), 1.32 (t, ^3J(H,H) = 7.9 Hz, 6H; CH_2CH_3).

^{11}B NMR (160.5 MHz, THF-d_8): δ = 25.7 ($h_{1/2}$ = 420 Hz).

^{13}C{^{1}H} NMR (125.8 MHz, THF-d_8): δ = 135.3 (C-a), 134.1 (BC), 117.8 (C-b), 16.9 (CH_2CH_3), 8.7 (CH_2CH_3).

Li_2[7]

^{1}H NMR (500.2 MHz, THF-d_8): δ = 8.12–8.10 (m, 4H; H-a), 7.58 (d, ^3J(H,H) = 7.6 Hz, 4H; Tol-H-*o*), 7.14 (d, ^3J(H,H) = 7.6 Hz, 4H; Tol-H-*m*), 6.59–6.57 (m, 4H; H-b), 2.40 (s, 6H; Tol-CH_3-*p*).

^{11}B NMR (160.5 MHz, THF-d_8): δ = 26.8 ($h_{1/2}$ = 570 Hz).

^{13}C{^{1}H} NMR (125.8 MHz, THF-d_8): δ = 149.8 (Tol-C-*i*), 137.2 (Tol-C-*o*), 136.9 (C-a), 134.8 (BC), 132.7 (Tol-C-*p*), 128.3 (Tol-C-*m*), 118.8 (C-b), 21.1 (Tol-CH_3-*p*).

Li_2[8]

^{1}H NMR (500.2 MHz, THF-d_8): δ = 8.10–8.08 (m, 4H; H-a), 7.30 (s, 4H; Xyl-H-*o*), 6.79 (s, 2H; Xyl-H-*p*), 6.58–6.56 (m, 4H; H-b), 2.35 (s, 12H; Xyl-CH_3-*m*).

^{11}B NMR (160.5 MHz, THF-d_8): δ = 26.0 ($h_{1/2}$ = 540 Hz).

^{13}C{^{1}H} NMR (125.8 MHz, THF-d_8): δ = 153.4 (Xyl-C-*i*), 137.0 (C-a), 135.6 (Xyl-C-*m*), 135.2 (Xyl-C-*o*), 134.7 (BC), 125.9 (Xyl-C-*p*), 118.7 (C-b), 21.6 (Xyl-CH_3-*m*).

NMR data in THF-d_8 for Na_2[A] salts:

Na_2[1]

$^1H\{^{11}B\}$ NMR (300.0 MHz, THF-d_8): δ = 8.07–8.04 (m, 4H; H-a), 6.47–6.44 (m, 4H; H-b), 5.47 (br, 2H; BH).

^{11}B NMR (96.3 MHz, THF-d_8): δ = 20.3 ($h_{1/2}$ = 510 Hz).

$^{13}C\{^1H\}$ NMR (75.4 MHz, THF-d_8): δ = 143.0 (BC), 139.8 (C-a), 115.9 (C-b).

Na_2[2]

^1H NMR (500.2 MHz, THF-d_8): δ = 8.50–8.48 (m, 4H; H-a), 6.60–6.58 (m, 4H; H-b), 1.40 (s, 18H; CH_3).

^{11}B NMR (160.5 MHz, THF-d_8): δ = 16.6 ($h_{1/2}$ = 410 Hz).

$^{13}C\{^1H\}$ NMR (125.8 MHz, THF-d_8): δ = 141.2 (BC), 137.1 (C-a), 116.5 (C-b), 114.4 (C≡*C*C(CH_3)$_3$), 95.8 (*C*≡CC(CH_3)$_3$), 33.1 (C(*C*H_3)$_3$), 29.5 (*C*(CH_3)$_3$).

Na_2[7]

^1H NMR (500.2 MHz, THF-d_8): δ = 8.29–8.27 (m, 4H; H-a), 7.62 (d, ^3J(H,H) = 7.6 Hz, 4H; Tol-H-*o*), 7.05 (d, ^3J(H,H) = 7.6 Hz, 4H; Tol-H-*m*), 6.49–6.47 (m, 4H; H-b), 2.36 (s, 6H; Tol-CH_3-*p*).

^{11}B NMR (160.5 MHz, THF-d_8): δ = 27.8 ($h_{1/2}$ = 620 Hz).

$^{13}C\{^1H\}$ NMR (125.8 MHz, THF-d_8): δ = 151.7 (Tol-C-*i*), 137.4 (Tol-C-*o*), 136.6 (C-a), 136.2 (BC), 130.7 (Tol-C-*p*), 127.2 (Tol-C-*m*), 116.2 (C-b), 21.4 (Tol-CH_3-*p*).

NMR data in THF-d_8 for K_2[A] salts:

K_2[4]

^{1}H NMR (300.0 MHz, THF-d_8): δ = 8.22–8.19 (m, 4H; H-a), 6.47–6.44 (m, 4H; H-b), 1.22 (s, 6H; CH_3).

^{11}B NMR (96.3 MHz, THF-d_8): δ = 23.6 ($h_{1/2}$ = 550 Hz).

^{13}C{^{1}H} NMR (75.4 MHz, THF-d_8): δ = 139.2 (BC), 135.1 (C-a), 113.9 (C-b), –0.1 (CH_3).

K_2[5]

^{1}H NMR (500.2 MHz, THF-d_8): δ = 8.28–8.26 (m, 4H; H-a), 6.47–6.45 (m, 4H; H-b), 1.96 (q, ^3J(H,H) = 7.7 Hz, 4H; CH_2CH$_3$), 1.22 (t, ^3J(H,H) = 7.7 Hz, 6H; CH$_2$CH_3).

^{11}B NMR (160.5 MHz, THF-d_8): δ = 27.0 ($h_{1/2}$ = 450 Hz).

^{13}C{^{1}H} NMR (125.8 MHz, THF-d_8): δ = 138.8 (BC), 135.2 (C-a), 114.6 (C-b), 16.2 (CH$_2$CH_3), 9.5 (CH_2CH$_3$).

K_2[7]

^{1}H NMR (500.2 MHz, THF-d_8): δ = 8.20–8.18 (m, 4H; H-a), 7.56 (d, ^3J(H,H) = 7.6 Hz, 4H; Tol-H-*o*), 7.04 (d, ^3J(H,H) = 7.6 Hz, 4H; Tol-H-*m*), 6.43–6.41 (m, 4H; H-b), 2.35 (s, 6H; Tol-CH$_3$-*p*).

^{11}B NMR (160.5 MHz, THF-d_8): δ = 27.7 ($h_{1/2}$ = 400 Hz).

^{13}C{^{1}H} NMR (125.8 MHz, THF-d_8): δ = 153.3 (Tol-C-*i*), 139.0 (BC), 137.4 (Tol-C-*o*), 136.5 (C-a), 130.8 (Tol-C-*p*), 127.6 (Tol-C-*m*), 115.8 (C-b), 21.2 (Tol-CH$_3$-*p*).

K_2[8]

^{1}H NMR (400.1 MHz, THF-d_8): δ = 8.19–8.17 (m, 4H; H-a), 7.30 (s, 4H; Xyl-H-*o*), 6.66 (s, 2H; Xyl-H-*p*), 6.43–6.40 (m, 4H; H-b), 2.32 (s, 12H; Xyl-CH$_3$-*m*).

^{11}B NMR (128.4 MHz, THF-d_8): δ = 28.8 ($h_{1/2}$ = 630 Hz).

^{13}C{^{1}H} NMR (100.6 MHz, THF-d_8): δ = 156.2* (Xyl-C-*i*), 138.5* (BC), 136.2 (C-a), 135.0 (Xyl-C-*o*), 134.2 (Xyl-C-*m*), 124.0 (Xyl-C-*p*), 115.4 (C-b), 22.0 (Xyl-CH$_3$-*m*). *detectable only in the ^{13}C/^{1}H HMBC spectrum

NMR data in THF-d_8 for Li_2[A-H_2] salts:

Li_2[4-H_2]

^{1}H NMR (300.0 MHz, THF-d_8): δ = 7.36–7.33 (m, 4H; H-a), 6.64–6.61 (m, 4H; H-b), 1.74 (n.r., 2H; BH), 0.21 (m, 6H; CH_3).

^{11}B NMR (96.3 MHz, THF-d_8): δ = –20.0 (d, ^1J(B,H) = 59.1 Hz).

^{13}C{^{1}H} NMR (125.8 MHz, THF-d_8): δ = 164.6 (BC), 130.0 (C-a), 121.4 (C-b), 5.1 (CH_3).

Li_2[5-H_2]

^{1}H{^{11}B} NMR (300.0 MHz, THF-d_8): δ = 7.39–7.36 (m, 4H; H-a), 6.63–6.60 (m, 4H; H-b), 1.61 (s, 2H; BH), 1.04–0.94 (m, 10H; CH_2CH_3).

^{11}B NMR (96.3 MHz, THF-d_8): δ = –17.9 (d, ^1J(B,H) = 57.1 Hz).

^{13}C{^{1}H} NMR (75.4 MHz, THF-d_8): δ = 163.9* (BC), 130.8 (C-a), 121.5 (C-b), 14.1 (CH_2*C*H_3), 11.7** (*C*H_2CH$_3$). *detectable only in the ^{13}C/^{1}H HMBC spectrum, **detectable only in the ^{13}C/^{1}H HSQC spectrum

Li_2[7-H_2]

^{1}H NMR (400.1 MHz, THF-d_8): δ = 7.33 (d, ^3J(H,H) = 7.5 Hz, 4H; Tol-H-*o*), 6.87–6.84 (m, 8H; Tol-H-*m*, H-a), 6.46–6.44 (m, 4H; H-b), 2.61 (n.r., 2H; BH), 2.28 (s, 6H; Tol-CH_3-*p*).

^{11}B NMR (128.4 MHz, THF-d_8): δ = –9.9 (d, ^1J(B,H) = 60.1 Hz).

^{13}C{^{1}H} NMR (100.6 MHz, THF-d_8): δ = 138.3 (Tol-C-*o*), 133.3 (C-a), 130.1 (Tol-C-*p*), 127.2 (Tol-C-*m*), 121.7 (C-b), 21.2 (Tol-CH_3-*p*); n.o. (BC, Tol-C-*i*).

Li_2[8-H_2]

^{1}H NMR (500.2 MHz, THF-d_8): δ = 7.08 (s, 4H; Xyl-H-*o*), 6.88–6.86 (m, 4H; H-a), 6.52 (s, 2H; Xyl-H-*p*), 6.46–6.44 (m, 4H; H-b), 2.61 (n.r., 2H; BH), 2.21 (s, 12H; Xyl-CH_3-*m*).

^{11}B NMR (160.5 MHz, THF-d_8): δ = –12.3 (d, ^1J(B,H) = 58.8 Hz).

^{13}C{^{1}H} NMR (125.8 MHz, THF-d_8): δ = 165.8 (Xyl-C-*i*), 162.6 (BC), 136.4 (Xyl-C-*o*), 133.8 (Xyl-C-*m*), 133.6 (C-a), 124.1 (Xyl-C-*p*), 121.6 (C-b), 21.7 (Xyl-CH_3-*m*).

NMR data in THF-d_8 for Na_2[A-H_2] salts:

A color code is used in order to distinguish the NMR resonances of the *cis* (red) and *trans* (blue) stereoisomers of the respective H_2 addition product. A black color is used if *cis*/*trans*-signals are overlapping.

Na_2[1-H_2]

^{1}H NMR (500.2 MHz, THF-d_8): δ = 7.35 (n.r., 4H; H-a), 6.68–6.66 (m, 4H; H-b), 2.5 (q, ^1J(B,H) = 77.3 Hz, 4H; BH).

^{11}B NMR (160.5 MHz, THF-d_8): δ = –19.8 (t, ^1J(B,H) = 77.3 Hz).

^{13}C{^{1}H} NMR (125.8 MHz, THF-d_8): δ = 161.5 (BC), 135.1 (C-a), 122.6 (C-b).

Na_2[2-H_2]

^{1}H NMR (500.2 MHz, THF-d_8): δ = 7.82–7.80 (m, 4H; H-a), 6.79–6.77 (m, 4H; H-b), 2.17 (q, ^1J(B,H) = 72.4 Hz, 2H; BH), 1.33 (s, 18H; CH_3).

^{11}B NMR (96.3 MHz, THF-d_8): δ = –23.6 (d, ^1J(B,H) = 72.4 Hz).

^{13}C{^{1}H} NMR (125.8 MHz, THF-d_8): δ = 159.9 (BC), 131.1 (C-a), 122.6 (C-b), 33.3 (C(CH$_3$)$_3$), 28.9 (C(CH$_3$)$_3$); n.o. $C{\equiv}C$.

Na_2[4-H_2]

^{1}H{^{11}B} NMR (500.2 MHz, THF-d_8): δ = 7.49–7.47 (m, 4H; H-a), 7.45–7.43 (m, 4H; H-a), 6.78–6.75 (m, 4H; H-b/4H; H-b), 2.52 (br, 2H; BH), 1.91 (br, 2H; B), 0.24 (br, 6H; CH_3), 0.05 (m, 6H; CH_3).

^{11}B NMR (160.5 MHz, THF-d_8): δ = –18.5 (d, ^1J(B,H) = 70.8 Hz), –19.8 (d, ^1J(B,H) = 69.0 Hz).

^{13}C{^{1}H} NMR (125.8 MHz, THF-d_8): δ = 165.6 (BC), 163.0* (BC), 135.1 (C-a), 130.9 (C-a), 123.2 (C-b), 122.7 (C-b), 11.5 (CH_3), 4.8 (CH_3). *detectable only in the ^{13}C/^{1}H HMBC spectrum

Note: The *cis*:*trans* integral ratio was approx. 4:1.

Na_2[7-H_2]

^{1}H{^{11}B} NMR (500.2 MHz, THF-d_8): δ = 7.36–7.35 (m, 4H; Tol-H-*o*), 7.31–7.29 (m, 4H; H-a), 7.23–7.21 (m, 4H; Tol-H-*o*), 7.03–7.01 (m, 4H; H-a), 6.94–6.93 (m, 4H; Tol-H-*m*), 6.80–6.78 (m, 4H; Tol-H-*m*), 6.75–6.73 (m, 4H; H-b), 6.61–6.59 (m, 4H; H-b), 3.09 (s, 1.5H; BH), 2.69 (s, 2H; BH), 2.30 (s, 6H; Tol-CH_3-*p*), 2.19 (s, 4.5H; Tol-CH_3-*p*).

^{11}B NMR (160.5 MHz, THF-d_8): δ = –11.2 (d, ^1J(B,H) = 67.4 Hz), –11.6 (d, ^1J(B,H) = 69.1 Hz).

^{13}C{^{1}H} NMR (125.8 MHz, THF-d_8): δ = 164.4 (BC), 162.9 (BC), 161.4 (Tol-C-*i*), 138.0 (Tol-C-*o*), 136.2 (Tol-C-*o*), 135.2 (C-a), 133.2 (C-a), 131.0 (Tol-C-*p*), 130.8 (Tol-C-*p*), 127.8 (Tol-C-*m*), 123.2 (C-b), 122.2 (C-b), 21.1 (Tol-CH_3-*p*), 20.9 (Tol-CH_3-*p*).

Note: The *cis*:*trans* integral ratio was approx. 4:3.

NMR data in THF-d_8 for Na_2[A-H_2] salts:

A color code is used in order to distinguish the NMR resonances of the *cis* (red) and *trans* (blue) stereoisomers of the respective H_2 addition product. A black color is used if *cis*/*trans*-signals are overlapping.

K_2[4-H_2]

$^1H\{^{11}B\}$ NMR (500.2 MHz, THF-d_8): δ = 7.39–7.38 (m, 4H; H-a), 7.35–7.33 (m, 4H; H-a), 6.72–6.68 (m, 4H; H-b/ 4H; H-b), 2.57 (s, 2H; BH), 1.88 (s, 2H; BH), 0.12 (m, 6H; CH_3), 0.02 (m, 6H; CH_3).

^{11}B NMR (160.5 MHz, THF-d_8): δ = –16.4 (d, ^1J(B,H) = 71.3 Hz), –17.9 (d, ^1J(B,H) = 69.0 Hz).

$^{13}C\{^1H\}$ NMR (125.8 MHz, THF-d_8): δ = 167.0 (BC), 165.1 (BC), 133.8 (C-a), 129.8 (C-a), 122.3 (C-b), 122.2 (C-b), 10.2 (CH_3), 4.8 (CH_3).

Note: The *cis*:*trans* integral ratio was approx. 8:1.

K_2[5-H_2]

$^1H\{^{11}B\}$ NMR (500.2 MHz, THF-d_8): δ = 7.41–7.38 (m, 4H; H-a/4H; H-a), 6.74–6.72 (m, 4H; H-b), 6.71–6.69 (m, 4H; H-b), 2.32 (br, 2H; BH), 1.82 (br, 2H; B), 1.05 (t, ^3J(H,H) = 7.4 Hz, 6H; CH_2CH_3), 0.92–0.85 (m, 4H; CH_2CH_3/6H; CH_2CH_3), 0.60–0.54 (m, 4H; CH_2CH_3).

^{11}B NMR (160.5 MHz, THF-d_8): δ = –12.7 (d, ^1J(B,H) = 71.1 Hz), –14.5 (d, ^1J(B,H) = 66.7 Hz).

$^{13}C\{^1H\}$ NMR (125.8 MHz, THF-d_8): δ = 167.5 (BC), 133.1 (C-a), 130.8 (C-a), 122.4 (C-b), 122.3 (C-b), 16.9*(CH_2CH), 14.4 (CH_2CH_3), 14.3 (CH_2CH_3), 12.8* (CH_2CH_3); n.o. (BC). *detectable only in the $^{13}C/^1H$ HSQC spectrum

Note: The *cis*:*trans* integral ratio was approx. 2:1.

K_2[7-H_2]

$^1H\{^{11}B\}$ NMR (500.2 MHz, THF-d_8): δ = 7.37–7.35 (m, 4H; Tol-H-*o*), 7.25–7.24 (m, 4H; H-a), 7.23–7.21 (m, 4H; Tol-H-*o*), 7.10–7.08 (m, 4H; H-a), 6.91–6.89 (m, 4H; Tol-H-*m*), 6.78–6.76 (m, 4H; Tol-H-*m*), 6.70–6.68 (m, 4H; H-b), 6.61–6.59 (m, 4H; H-b), 3.22 (br, 2H; BH), 3.00 (br, 2H; BH), 2.26 (s, 6H; Tol-CH_3-*p*), 2.18 (s, 6H; Tol-CH_3-*p*).

^{11}B NMR (160.5 MHz, THF-d_8): δ = –11.5 (d, ^1J(B,H) = 81.2 Hz), –12.0 (d, ^1J(B,H) = 77.9 Hz).

$^{13}C\{^1H\}$ NMR (125.8 MHz, THF-d_8): δ = 162.8* (Ph-C-*i*), 162.6* (Ph-C-*i*), 165.9* (BC), 165.2* (BC), 137.5 (Tol-C-*o*), 136.7 (Tol-C-*o*), 134.1 (C-a), 133.6 (C-a), 130.7 (Tol-C-*p*), 130.4 (Tol-C-*p*), 127.9 (Tol-C-*m*), 127.6 (Tol-C-*m*), 122.8 (C-b), 122.5 (C-b), 21.1 (Tol-CH_3-*p*), 20.9 (Tol-CH_3-*p*). *detectable only in the $^{13}C/^1H$ HMBC spectrum

Note: The *cis*:*trans* integral ratio was approx. 2:1.

K_2[8-H_2]

$^{1}H\{^{11}B\}$ NMR (500.2 MHz, THF-d_8): δ = 7.26–7.25 (m, 4H; H-a), 7.18–7.16 (m, 4H; H-a), 7.10 (s, 4H; Xyl-H-*o*), 6.97 (s, 4H; Xyl-H-*o*), 6.71–6.69 (m, 4H; H-b), 6.65–6.63 (m, 4H; H-b), 6.51 (s, 2H; Xyl-H-*p*), 6.44 (s, 2H; Xyl-H-*p*), 3.20 (br, 2H; BH), 3.01 (br, 2H; BH), 2.19 (s, 12H; Xyl-CH_3-*m*), 2.13 (s, 12H; Xyl-CH_3-*m*).

^{11}B NMR (160.5 MHz, THF-d_8): δ = –10.1 (d, ^{1}J(B,H) = 73.2 Hz), –10.6 (d, ^{1}J(B,H) = 68.9 Hz).

$^{13}C\{^{1}H\}$ NMR (125.8 MHz, THF-d_8): δ = 165.6* (Xyl-C-*i*), 165.3* (BC), 164.8* (BC), 135.0 (Xyl-C-*o*), 134.4 (Xyl-C-*o*), 134.3 (Xyl-C-*m*), 133.7 (C-a), 133.3 (C-a), 124.1 (Xyl-C-*p*), 123.9 (Xyl-C-*p*), 122.4 (C-b), 122.2 (C-b), 21.9 (Xyl-CH_3-*m*), 21.8 (Xyl-CH_3-*m*). *detectable only in the $^{13}C/^{1}H$ HMBC spectrum

Note: The *cis*:*trans* integral ratio was approx. 1:1.

2. Additional data regarding the isomerization of DBA derivatives of the type M_2[A-H_2]

In line with the ^{1}H NMR spectra (Figure 6) of K_2[**4**-H_2] and K_2[**7**-H_2], the ^{11}B NMR spectra in Figure S1 show different ratios of the respective *cis* (■) and *trans* (▲) isomers.

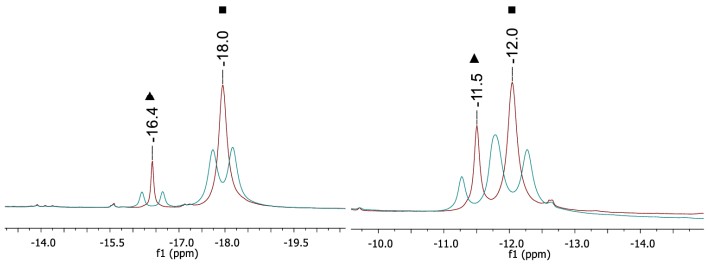

Figure S1. Comparison of the ^{11}B NMR (blue) and ^{11}B{^{1}H} NMR (red) spectra (160.5 MHz, THF-d_8) of K_2[**4**-H_2] (left) and K_2[**7**-H_2] (right); resonances of the *cis* (■) and the *trans* isomer (▲).

During H_2 activation experiments, the appearance of two compounds (*cis* and *trans* isomer of M_2[**A**-H_2]; M = Na, K; only exception: R = C≡C*t*Bu) was observed. According to the postulated concerted mechanism of the H_2 addition, H_2 approaches the DBA core from one side so that initially the *cis* isomer is formed.[4] At the elevated temperatures applied, a subsequent isomerization takes place and the *trans* isomer is generated. In the case of Na_2[**7**-H_2], we succeeded in the selective crystallization of *cis*-[Na][Na(thf)$_2$(18-c-6)][Na(thf)$_2$]$_2$(*n*-hexane)[**7**-H_2]$_2$ (confirmed by X-ray analysis). NMR spectra recorded on these single crystals allowed us to unequivocally confirm the chemical shift values of the *cis* isomer (Figure S2a). With time, also this sample showed the slow formation of a second species – the *trans* isomer – even at room temperature (Figure S2b). The isomerization is accelerated at elevated temperatures (Figure S2c).

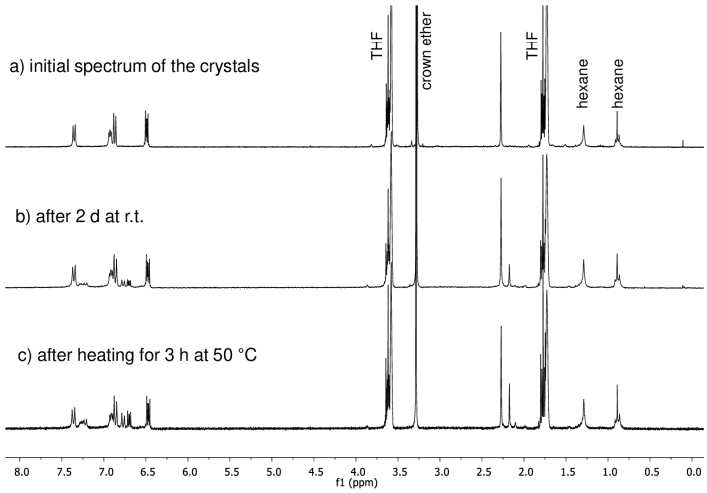

Figure S2. ^{1}H NMR spectra (THF-d_8) of re-dissolved single crystals of *cis*-[Na][Na(thf)$_2$(18-c-6)][Na(thf)$_2$]$_2$(*n*-hexane)[**7**-H$_2$]$_2$: a) spectrum recorded immediately after sample preparation (300.0 MHz), b) spectrum recorded after storage of the sample at room temperature for 2 d (250.1 MHz; resonances of the *trans* isomer start to appear), c) spectrum recorded after storage of the sample at 50 °C for 3 h (250.1 MHz; the amount of the *trans* isomer has almost doubled. Note: after storage of the NMR tube at room temperature for several months, the amount of *cis* isomer increased again at the expense of the *trans* isomer. This points toward a temperature-dependent dynamic isomerization equilibrium).

In order to further proof the existence of *cis*/*trans* isomers, K$_2$[**7**-H$_2$] was also synthesized via a non-concerted route by using a 1M THF solution of K[HBEt$_3$] instead of H$_2$. K[HBEt$_3$] readily reacts with **7** (0.050 mmol) in a 2:1 stoichiometry (THF-d_8, 0.5 mL). In Figure S3, the ^{1}H NMR spectra of both reaction mixtures are shown for comparison. In each case, two isomers are formed. However, the *cis*/*trans* ratios differ significantly depending on the hydride source, which is in line with the assumption of a concerted *vs*. non-concerted mechanism.

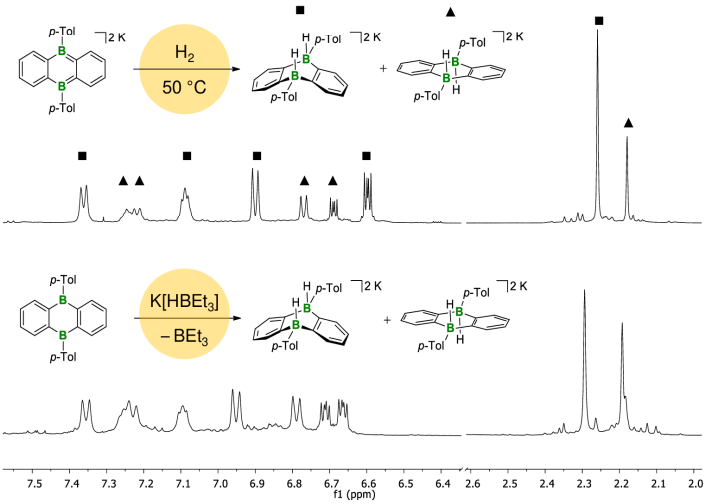

Figure S3. Comparison of the ^{1}H NMR spectra of the reaction mixtures of K_2[**7**] with H_2 (top: 500.2 MHz, THF-d_8) and **7** with K[$HBEt_3$] (bottom: 400.1 MHz, THF-d_8).

3. Hydrogenation reactions using $[A]^{2-}$ derivatives

3.1 General procedures and characterization data

General procedure for the hydrogenation of Ph(H)C=N*t*Bu with 37 mol% of the respective M_2[A] in an NMR tube:

Neat, dry *N*-benzylidene-*tert*-butylamine (10 µL, 9.1 mg, 56.2 µmol) was added to the respective freshly reduced M_2[**A**] derivative (20.8 µmol) in THF-d_8 (0.5 mL) and the solution was transferred to an NMR tube. After the addition of H_2 following the procedure described in 1.1, the NMR tube was flame-sealed, and warmed to 100 °C. The progress of the reaction was monitored by ^{1}H NMR spectroscopy. The percent conversion to the hydrogenation product after 16 h is summarized in Table 1.

^{1}H NMR (300.0 MHz, THF-d_8): δ = 7.35–7.32 (m, 2H; C_6H_5), 7.25–7.20 (m, 2H; C_6H_5), 7.16–7.11 (m, 1H; C_6H_5), 3.72 (d, ^3J(H,H) = 7.6 Hz, 2H; CH_2), 1.14 (s, 9H; CH_3); n.o. (NH).

The NMR data are in accordance with those of a commercial sample of the amine $Ph(H)_2C$–N(H)*t*Bu measured in THF-d_8, except for the doublet multiplicity of the CH_2 resonance. Given that an independently prepared mixture of Li_2[**4**] and the commercial amine showed the same effect, the doublet for the CH_2 protons likely results from Li^+ coordination (this was also observed for the corresponding Na^+ salt).

Hydrogenation of Ph(H)C=N*t*Bu with 10 mol% of Li_2[4] in a steel autoclave:

In a glovebox, the glass inlet of a steel autoclave (100 mL/100 bar steel autoclave from *Roth*, model I) was charged with a solution of freshly prepared Li_2[**4**] (0.124 mmol) in THF (10 mL). Neat, dry *N*-benzylidene-*tert*-butylamine (200 mg, 1.24 mmol) was added, the autoclave was closed inside the glovebox, and an H_2 pressure of approx. 7 bar was applied under inert conditions outside the glovebox. The reaction mixture was stirred at 100 °C for 18 h, the cooled autoclave was opened under ambient atmosphere, and the conversion to $Ph(H)_2C$–N(H)*t*Bu determined to be quantitative by ^{1}H NMR spectroscopy. The amine was isolated after aqueous work-up: THF was removed under reduced pressure, the residue extracted with Et_2O, the extract washed with NaOH solution (0.1 M), and dried over $MgSO_4$. After evaporation of all volatiles *in vacuo*, a colorless oil of $Ph(H)_2C$–N(H)*t*Bu remained. Yield: 153 mg, 0.94 mmol, 76%.

^{1}H NMR (500.2 MHz, C_6D_6): δ = 7.38–7.37 (m, 2H; C_6H_5), 7.23–7.20 (m, 2H; C_6H_5), 7.14–7.11 (m, 1H; C_6H_5), 3.59 (s, 2H; CH_2), 1.01 (s, 9H; CH_3); n.o. (N*H*).

^{13}C{^{1}H} NMR (125.8 MHz, C_6D_6): δ = 142.4 (C_6H_5), 128.6 (C_6H_5), 128.5 (C_6H_5), 126.9 (C_6H_5), 50.4 (C(CH_3)$_3$), 47.4 (CH_2), 29.2 (C(CH_3)$_3$).

The NMR data in C_6D_6 are in accordance with the literature.[12]

HRMS: 164.14355 (found); 164.14338 (calc. as $[C_{11}H_{17}N_1+H]^+$).

General procedure for hydrogenation reactions using 37 mol% of Li_2[4] in an NMR tube:
The respective substrate (53.0 µmol) was added to freshly prepared Li_2[**4**] (19.6 µmol) in THF-d_8 (0.5 mL) and the resulting mixture was transferred to an NMR tube. After the addition of H_2 following the procedure described in 1.1, the NMR tube was flame-sealed and kept at 100 °C. The progress of the reaction was monitored by ^{1}H NMR spectroscopy.

1,1-Diphenylethylene → 1,1-diphenylethane
1,1-Diphenylethylene (9.6 mg, 9.4 µL) was quantitatively hydrogenated after 35 h.
^{1}H NMR (500.2 MHz, THF-d_8): δ = 7.24–7.10 (m, 10H; C_6H_5), 4.14 (q, ^3J(H,H) = 7.3 Hz, 1H; CH), 1.61 (d, ^3J(H,H) = 7.3 Hz, 3H; CH_3).
^{13}C{^{1}H} NMR (125.8 MHz, THF-d_8): δ = 147.7 (C_6H_5), 129.2 (C_6H_5), 128.5 (C_6H_5), 126.8 (C_6H_5), 45.4 (CH), 21.7 (CH_3).
HRMS: 221.08007 (found); 221.07271 (calc. as $[C_{14}H_{14}+K]^+$).

Anthracene → 9,10-dihydroanthracene
Anthracene (9.4 mg) was quantitatively hydrogenated after 35 h. Note: A solvent mixture of THF-d_8 (0.5 mL) and C_6D_6 (0.1 mL) was used in order to improve the solubility of anthracene.
^{1}H NMR (500.2 MHz, THF-d_8/C_6D_6): δ = 7.24–7.22 (m, 4H; CH), 7.14–7.12 (m, 4H; CH), 3.85 (s, 4H; CH_2).
^{13}C{^{1}H} NMR (125.8 MHz, THF-d_8/C_6D_6): δ = 137.9 (C), 128.2 (CH), 126.9 (CH), 36.3 (CH_2).
HRMS: 180.08830 (found); 180.09335 (calc. as $C_{14}H_{12}$).

The following substrates showed no reaction with Li_2[**4**]/H_2: 1-(1-piperidinyl)cyclohexene, 2,3-dimethyl-2-butene, cyclohexene, phenanthrene, naphthalene, 2-butyne, and bis-(trimethylsilyl)-acetylene.

3.2 Additional experimental data regarding the hydrogenation reactions

[4+2]-Cycloaddition reaction between Ph(H)C=N*t*Bu and Li_2[4]: In order to investigate the interaction between Ph(H)C=N*t*Bu and Li_2[**4**], a ^{1}H NMR temperature study was undertaken using an approx. equimolar mixture of both substrates in THF-d_8 (0.5 mL). Figure S4a shows that the [4+2]-cycloaddition product Li[**10**] forms to some extent already within 0.5 h at room temperature. After 2 d at room temperature, the conversion was almost complete as evidenced by NMR spectroscopy (Figure S4b) and a color change of the solution from deep red to pale red. A temperature rise, however, promotes the retro-Diels-Alder reaction and shifts the dynamic cycloaddition equilibrium back toward the starting materials (Figure S4c); in agreement with that the red color became more intense again.

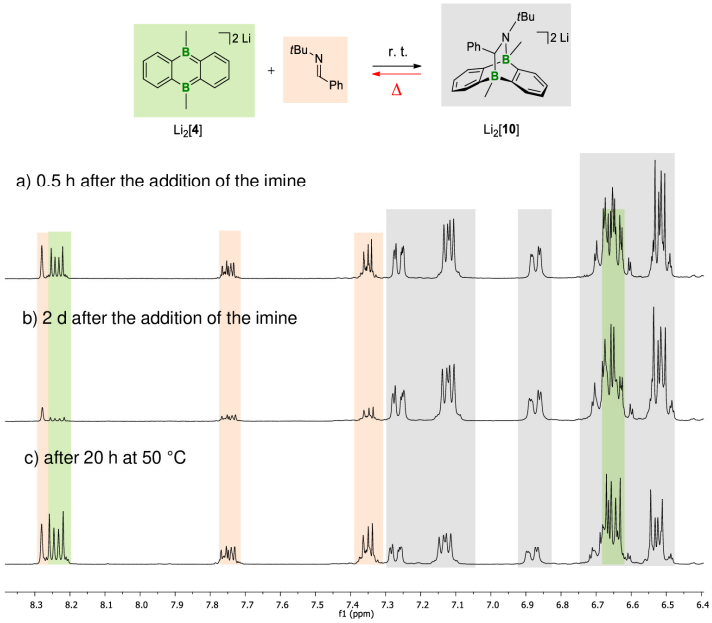

Figure S4. Comparison of the ^{1}H NMR spectra (250.1 MHz, THF-d_8) of the same sample of Li_2[**4**] a) 0.5 h after the addition of the imine Ph(H)C=N*t*Bu, b) 2 d after the addition of the imine Ph(H)C=N*t*Bu, and c) after 20 h at 50 °C (the spectrum was recorded immediately after the sample had been cooled to room temperature).

Li_2[10]

^{1}H NMR (500.2 MHz, THF-d_8): δ = 7.27–7.25 (m, 1H; C_6H_4), 7.12–7.10 (m, 2H; C_6H_4), 6.87–6.86 (m, 1H; C_6H_4), 6.70–6.64 (m, 3H; 1×C_6H_4 and 2×Ph), 6.65–6.61 (m, 1H; C_6H_4), 6.54–6.49 (m, 3H; 1×Ph and 2×C_6H_4), 6.00 (very br, 2H; Ph), 2.71 (s, 1H; CH), 0.80 (s, 9H; $C(CH_3)_3$), 0.63 (s, 3H; $NBCH_3$), −0.41 (s, 3H; $CBCH_3$).

^{11}B NMR (160.5 MHz, THF-d_8): δ = −10.5 (br; BN), −15.0 (s; BC).

^{13}C{^{1}H} NMR (125.8 MHz, THF-d_8): δ = 176.5 (very br; CB*C*), 171.3 (very br; CB*C*), 164.5 (br; NBC), 164.1 (Ph-*i*), 163.7 (br; NBC), 130.0 (C_6H_4), 126.4 (2×Ph), 126.3 (C_6H_4), 125.6 (C_6H_4), 124.2 (C_6H_4), 123.5 (C_6H_4), 120.7, 120.6, 120.4 (1×C_6H_4 and 2×C_6H_4), 120.1 (Ph), 69.8 (n.r.; CH), 58.9 (*C*$(CH_3)_3$), 32.8 (C(*C*$H_3)_3$), 8.7 ($NBCH_3$), 2.9 (n.r.; $CBCH_3$); n.o. (2×Ph).

Note: Resonances marked with a blue/red color belong to the same C_6H_4 spin system.

The attempt to grow single crystals of the addition product Li_2[**10**] from THF in the presence of 12-crown-4 resulted in the crystallization of the *N*-protonated salt [Li(12-c-4)$_2$]H[**10**](THF). The origin of the proton is not clear. We speculate that Li^+ coordination by the crown ether drastically increases the basicity of the tricyclic amine; the crown ether might also have contained traces of water as proton source.

[Li(12-c-4)$_2$]H[10](THF)

^{1}H NMR (500.2 MHz, THF-d_8): δ = 7.39–7.38 (m, 1H; C_6H_4), 7.33–7.30 (m, 2H; C_6H_4), 6.91 (br, 1H; Ph), 6.82–6.81 (m, 2H; C_6H_4 and Ph), 6.79–6.76 (m, 2H; C_6H_4), 6.73–6.72 (m, 1H; C_6H_4), 6.70–6.67 (m, 2H; C_6H_4 and Ph), 6.63 (br, 1H; Ph), 5.21 (br, 1H; Ph), 2.86 (d, ^3J(H,H) = 7.00 Hz, 1H; CH), 2.73 (d, ^3J(H,H) = 7.00 Hz, 1H; NH), 0.89 (s, 9H; $C(CH_3)_3$), 0.79 (s, 3H; $NBCH_3$), −0.29 (s, 3H; $CBCH_3$).

^{11}B NMR (160.5 MHz, THF-d_8): δ = −2.0 (br, BN), −14.7 (s, BC).

^{13}C{^{1}H} NMR (125.8 MHz, THF-d_8): δ = 170.5 (very br; CB*C*), 167.7 (very br; CB*C*), 160.5 (br; NBC), 159.0 (br; NBC), 153.3 (Ph-*i*), 129.5 (C_6H_4), 128.7 (br; Ph), 128.1 (C_6H_4), 127.2 (br; Ph), 126.5 (C_6H_4 and Ph), 126.4 (C_6H_4), 123.3 (C_6H_4), 123.1 (C_6H_4), 122.3 (2×Ph), 121.6 (C_6H_4), 121.5 (C_6H_4), 68.0 (CH), 61.5 (*C*$(CH_3)_3$), 30.4 (C(*C*$H_3)_3$), 7.6 (br; $NBCH_3$), 2.4 (very br; $CBCH_3$).

[4+2]-Cycloaddition products of other substrates

The imine Ph(H)C=N*t*Bu is not the only substrate that undergoes a formal [4+2] cycloaddtion with Li_2[**4**].

1,1'-Diphenylethylene and Li_2[4]

Neat 1,1'-diphenylethylene (13 µL, 13 mg, 74 µmol) was added at room temperature to Li_2[**4**], freshly prepared from **4** (15 mg, 74 µmol) and excess lithium granules, in THF-d_8 (0.5 mL; see 1.1). The mixture was transferred to an NMR tube and the tube was flame-sealed. NMR spectroscopy revealed the immediate and quantitative consumption of the starting materials and the selective formation of a cycloadduct.

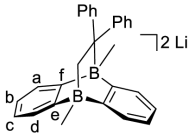

^{1}H NMR (500.2 MHz, THF-d_8): δ = 7.30 (n.r., 2H; H-d), 7.14–7.13 (m, 2H; H-a), 6.75–6.73 (m, 4H; Ph-H-*o*), 6.61–6.58 (m, 2H; H-c), 6.53–6.50 (m, 6H; Ph-H-*m* and H-b), 6.38–6.35 (m, 2H; Ph-H-*p*), 0.81–0.80 (n.r., 2H; CH_2), 0.19 (s, 3H; $CBCH_3$), 0.18 (n.r., 3H; CH_2BCH_3).

^{11}B NMR (160.5 MHz, THF-d_8): δ = −11.7 (s; BC), −15.4 (s; BCH_2).

^{13}C{^{1}H} NMR (125.8 MHz, THF-d_8): δ = 171.7 (q, ^1J(B,C) = 44 Hz; C-e), 169.5 (n.r.; C-f), 165.0 (Ph-C-*i*), 131.6 (Ph-C-*o*), 129.7 (C-a), 126.8 (C-d), 124.6 (Ph-C-*m*), 120.9 (C-b), 120.8 (C-c), 118.9 (Ph-C-*p*), 51.5 (q, ^1J(B,C) = 37 Hz; CH_2), 4.6 (q, ^1J(B,C) = 45 Hz; CH_2BCH_3), 2.1 (n.r.; $CBCH_3$); n.o. (CPh_2).

Ethylene and Li_2[4]

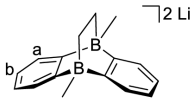

Li_2[**11**]

An NMR tube, charged with a solution of freshly prepared Li_2[**4**] (74 µmol) in THF-d_8 (0.5 mL; see 1.1), was connected to a Schlenk line. The solution was frozen with liquid nitrogen, the system evacuated, and ethylene (1 atm; quality grade > 99.95% GC) was filled in. The content of the NMR tube was allowed to warm to room temperature and the excess pressure released through a Hg bubbler. After 10 min, the reaction mixture was frozen again, the NMR tube was evacuated and flame-sealed. After storage of the sample at room temperature for 3 h, NMR spectroscopy revealed the immediate and quantitative consumption of Li_2[**4**] and the selective formation of the cycloadduct Li_2[**11**]. X-ray-

quality crystals of [Li(12-c-4)(thf)][Li(12-c-4)][**11**] were obtained by gas-phase diffusion of *n*-hexane into a THF/12-crown-4 solution of Li_2[**11**].

^{1}H NMR (500.2 MHz, THF-d_8): δ = 7.28 (n.r., 4H; H-a), 6.60–6.59 (m, 4H; H-b), 0.15 (n.r., 6H; BCH_3), –0.30 (n.r., 4H; CH_2).

^{11}B NMR (160.5 MHz, THF-d_8): δ = –15.2.

^{13}C{^{1}H} NMR (125.8 MHz, THF-d_8): δ = 170.8–169.6 (m; BC), 127.2 (C-a), 120.6 (C-b), 25.2–24.4 (m; CH_2), 5.5–4.3 (m; BCH_3).

1,2-Diphenylacetylene and Li_2[4]

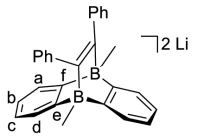

Neat 1,2-diphenylacetylene (13 mg, 74 µmol) was added at room temperature to Li_2[**4**], freshly prepared from **4** (15 mg, 74 µmol) and excess lithium granules in THF-d_8 (0.5 mL; see 1.1). The mixture was transferred to an NMR tube and the tube was flame-sealed. NMR spectroscopy revealed the immediate and quantitative consumption of 1,2-diphenylacetylene and the selective formation of an cycloadduct. X-ray-quality crystals of this cycloadduct were obtained by gas-phase diffusion of *n*-hexane into its THF/12-crown-4 solution. The structure is deposited with the CCDC and can be accessed via the following code: 1888739.

^{1}H NMR (500.2 MHz, THF-d_8): δ = 7.31–7.30 (m, 4H; H-a), 6.67–6.64 (m, 4H; Ph-H-*m*), 6.56–6.54 (m, 4H; Ph-H-*o*), 6.55–6.51 (m, 4H; H-b), 6.49–6.46 (m, 2H; Ph-H-*p*), 0.26 (s, 6H; BCH_3).

^{11}B NMR (160.5 MHz, THF-d_8): δ = –13.3 (s).

^{13}C{^{1}H} NMR (125.8 MHz, THF-d_8): δ = 170.9 (n.r.; BC), 168.5 (n.r.; C=C), 154.9 (Ph-C-*i*), 130.2 (Ph-C-*o*), 126.9 (C-a), 125.7 (Ph-C-*m*), 120.4 (Ph-C-*p*), 120.0 (C-b), 2.1 (n.r.; BCH_3).

Influence of the counter cation on the hydrogenation step

A comparison of Li_2[**4**] and Na_2[**4**] as catalysts for the hydrogenation of Ph(H)C=N*t*Bu reveals four distinct differences (Figure S5):

1. The cycloaddition product [**10**]$^{2-}$ of [**4**]$^{2-}$ and Ph(H)C=N*t*Bu is only observable with Li^+ as the counter cation (*cf.* Figures S5a *vs.* S5c). The strong Lewis acid Li^+ is likely required to promote cycloaddition by means of imine coordination.

2. Due to the reversibility of the cycloaddition process, the reaction mixture – after storage at 100 °C for 16 h – contains no Li_2[**10**] but exclusively Li_2[**4**] and amine Ph(H)$_2$C–N(H)*t*Bu (*cf.* Figure S5b).

3. Given that H_2 activation is much slower with Li_2[**4**] than with Na_2[**4**], the former reaction mixture contains mainly M_2[**4**] and only little M_2[**4**-H_2], whereas the opposite is true for the latter (after 16 h at 100 °C; *cf.* Figures S5b *vs.* S5d).

4. Hydrogenation of Ph(H)C=N*t*Bu occurs much faster using Li_2[**4**] than Na_2[**4**], even though the H_2-activation step is slower with the Li^+ than with the Na^+ salt.

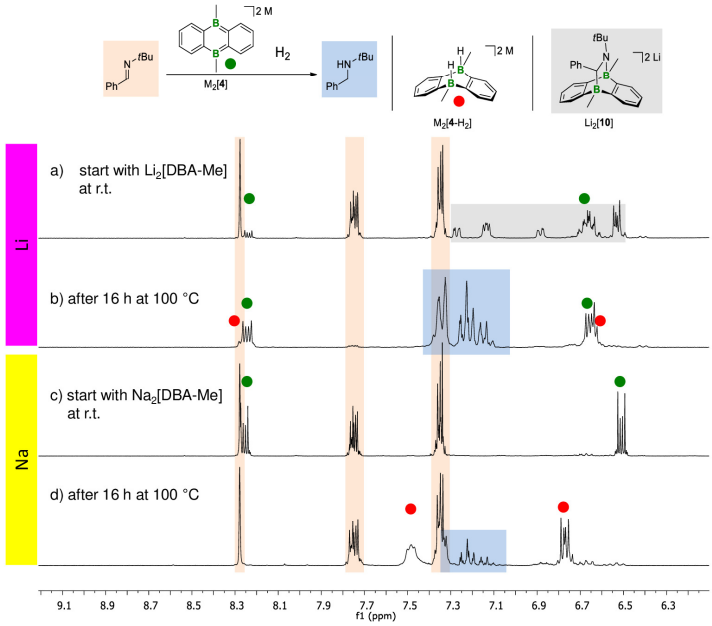

Figure S5. Comparison of the hydrogenation of Ph(H)C=N*t*Bu with Li_2[**4**] (a+b) or Na_2[**4**] (c+d) as the catalyst (THF-d_8). ^{1}H NMR spectra recorded on a mixture of Ph(H)C=N*t*Bu, Li_2[**4**], and excess H_2 immediately after sample preparation (a, 300.0 MHz) and after 16 h at 100 °C (b, 250.1 MHz). ^{1}H NMR spectra recorded on a mixture of Ph(H)C=N*t*Bu, Na_2[**4**], and excess H_2 immediately after sample preparation (a, 300.0 MHz) and after 16 h at 100 °C (b, 250.1 MHz).

4. Hydride-transfer reactions with $Na_2[4\text{-}H_2]$

It is conceivable that the hydride transfer from $Na_2[\mathbf{4}\text{-}H_2]$ to substrates R_nECl proceeds in a stepwise manner *via* an intermediate hydride monoadduct $Na[\mathbf{4}\text{-}H]$. We therefore treated $Na_2[\mathbf{4}\text{-}H_2]$ with either 1 or 2 equiv Et_3SiCl.

4.1 Reaction of $Na_2[4\text{-}H_2]$ with 1 equiv of Et_3SiCl

The reaction was performed at room temperature in THF-d_8 solution in an NMR tube: $Na_2[\mathbf{4}\text{-}H_2]$ (0.060 mmol), Et_3SiCl (10 µL, 9.0 mg, 0.060 mmol).

^{1}H NMR (500.2 MHz, THF-d_8): δ = 8.05 (n.r., 2H; C_6H_4), 7.75 (n.r., 2H; C_6H_4), 7.19 (n.r., 2H; C_6H_4), 7.01 (n.r., 2H; C_6H_4), 2.32 (q, ^1J(B,H) = 69.8 Hz, 1H; BH), 1.32 (s, 3H; Me), 0.01 (s, 3H; Me).
^{11}B NMR (160.5 MHz, THF-d_8): δ = 62.5 ($h_{1/2}$ = 820 Hz), −17.6 (d, ^1J(B,H) = 69.8 Hz).

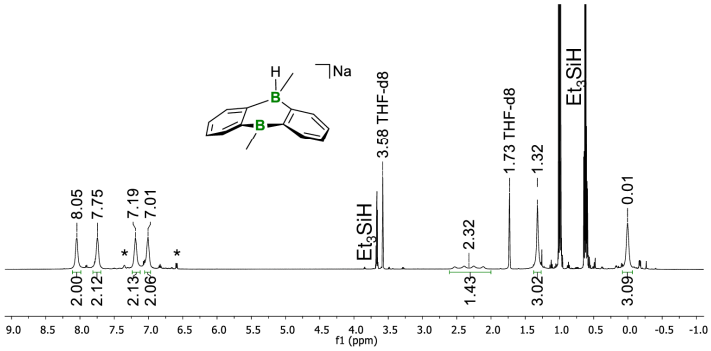

Figure S6. ^{1}H NMR spectrum of the reaction mixture $Na_2[\mathbf{4}\text{-}H_2]$/1 Et_3SiCl (500.2 MHz, THF-d_8). Asterisks mark resonances of the starting material $Na_2[\mathbf{4}\text{-}H_2]$.

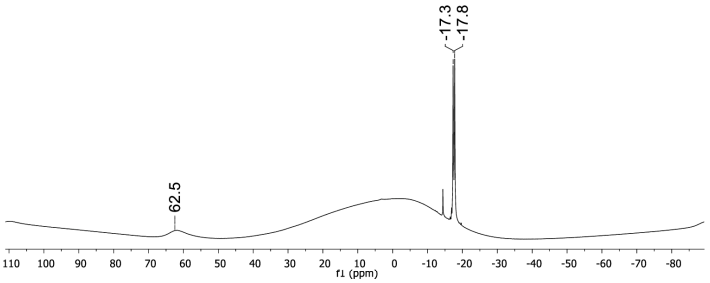

Figure S7. ^{11}B NMR spectrum of the reaction mixture $Na_2[\mathbf{4}\text{-}H_2]$/1 Et_3SiCl (160.5 MHz, THF-d_8).

The structural motif of $Na[\mathbf{4}\text{-}H]$ with one tetracoordinated and one trigonal-planar boron atom is already known for other DBA derivatives (compare crystal structures with the following CSD codes: IBUTAC, IBUTEG, IBUTOQ, IBUVAE, XITREA, XITRIE, XITROK, XITRUQ, XITSAX, XUQHAS).

4.2 Reaction of Na_2[4**-H_2] with 2 equiv of Et_3SiCl; perspectives for a catalytic cycle**

The aimed-for accumulation of Et_3SiH over multiple catalytic cycles as described in the main text requires a stepwise procedure in order to avoid side reactions between Et_3SiCl and Na_2[**4**] or sodium metal.

1) Twofold reduction of **4** (as described in 1.1) using elemental sodium in THF-d_8.

Comment: The use of NMR tubes as reaction vessels limited the amount of Na_2[**4**] to 0.074 mmol because otherwise the available volume of H_2 is not sufficient to convert all of the starting material to Na_2[**4**-H_2].

2) Transfer of the THF-d_8 solution of Na_2[**4**] to an NMR tube and addition of H_2 following the procedure described in 1.1. Heating of the reaction mixture to 100 °C for 18 h so that no unreacted Na_2[**4**] remained.

3) Transfer of the resulting THF-d_8 solution of Na_2[**4**-H_2] to a new NMR tube and addition of 2 equiv of Et_3SiCl (24 µL, 22 mg, 0.143 mmol). The hydride-transfer reaction is completed within minutes and accompanied by the precipitation of NaCl (*cf.* Figure S10 for an X-ray powder diffractogram of the precipitate).

4) Repetition of the steps 1) − 3) in the presence of Et_3SiH, which has no effect on the reaction cascade. *Comment:* As a proof of concept, we have successfully repeated this protocol three times.

$Et_3SiCl \rightarrow Et_3SiH$

^{1}H NMR (500.2 MHz, THF-d_8): δ = 3.66 (n.r., 1H; Et_3SiH), 0.99 (t, ^3J(H,H) = 7.9 Hz, 9H; ($H_3CH_2C)_3SiH$), 0.62 (dq, ^3J(H,H) = 7.9 Hz, ^3J(H,H) = 3.0 Hz, 6H; ($H_3CH_2C)_3SiH$).

^{29}Si NMR (99.4 MHz, THF-d_8): δ = 0.3 (d, ^1J(Si,H) = 178 Hz; Et_3SiH).

The ^{29}Si NMR shift is in accordance with the literature: δ = 0.2 (^1J(Si,H) = 179 Hz).[13]

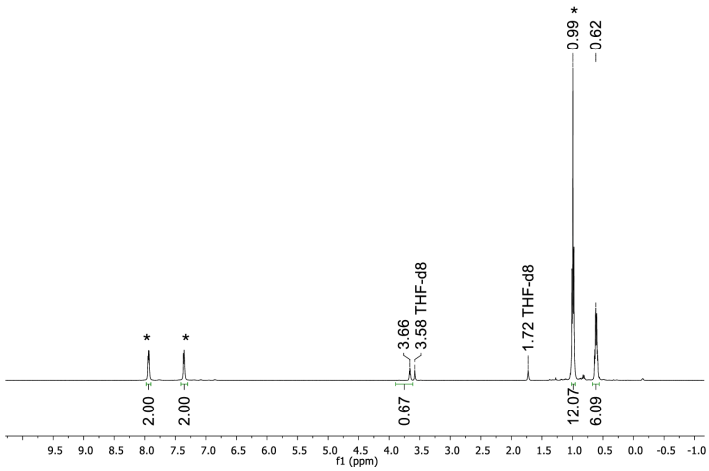

Figure S8. ^{1}H NMR spectrum (500.2 MHz, THF-d_8) recorded after the reaction between Na_2[**4**-H_2] and Et_3SiCl to give Et_3SiH and **4** (*).

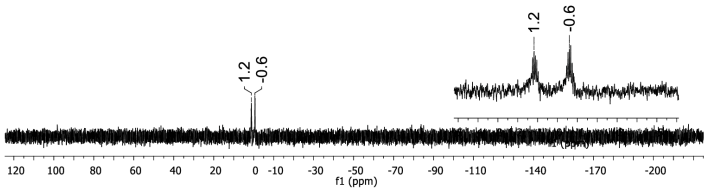

Figure S9. ^{29}Si NMR spectrum (99.4 MHz, THF-d_8) recorded after the reaction between Na_2[**4**-H_2] and Et_3SiCl to give Et_3SiH and **4**.

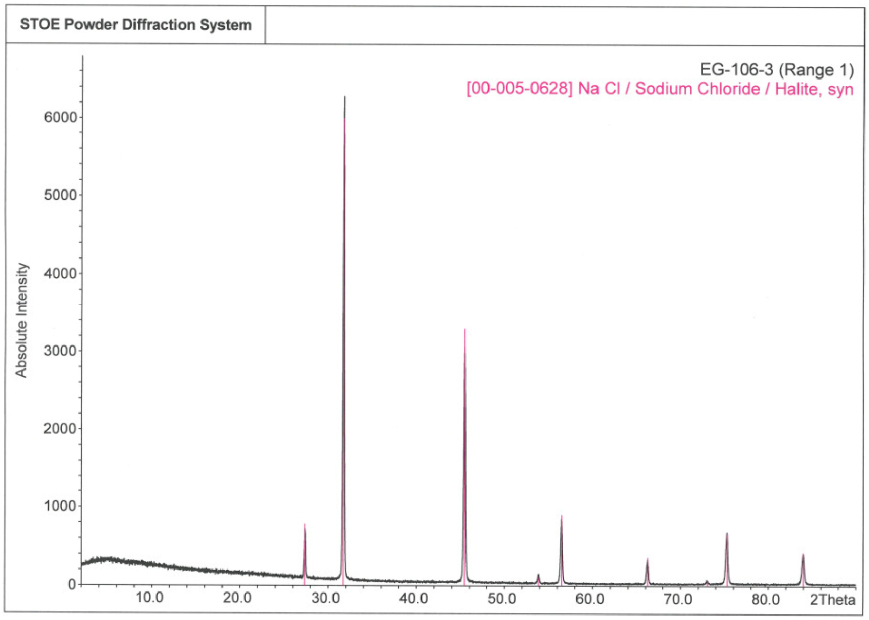

Figure S10. X-ray powder diffraction pattern of the NaCl precipitate from the reaction between Na_2[**4**-H_2] and Et_3SiCl (black: experiment, red: simulation).

In a second experiment, two cycles 1)-4) (see above) were conducted. A sealed glass capillary containing Me_4Si and THF-d_8 served as an internal reference in order to determine the yield of Et_3SiH. In Figure S11, the proton-integral value of the CH_2 groups of Et_3SiH are compared to the normalized integral value of the internal standard. As expected, the amount of Et_3SiH doubled from the first to the second cycle. The amount of the catalyst **4** remained unchanged, as proven by the integral ratios.
Comment: A perfectly equimolar stoichiometry between Na_2[**4**-H_2] and Et_3SiCl was not achieved in the 2nd cycle; the black square in Figure S11 indicates small amounts of still unreacted Et_3SiCl.

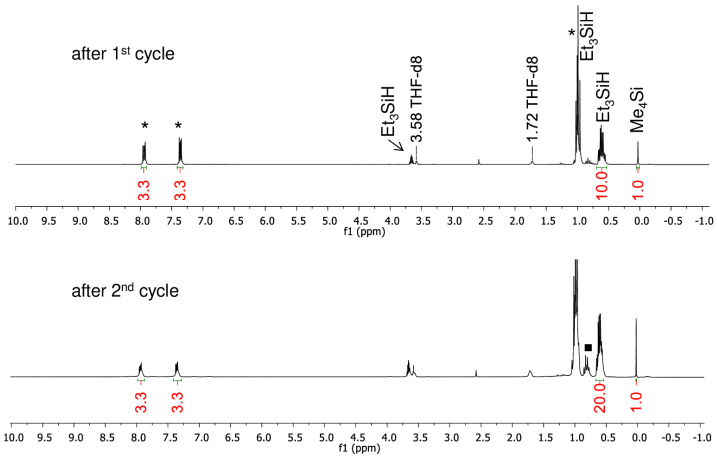

Figure S11. ^{1}H NMR spectra recorded on the reaction mixture Na_2[**4**-H_2]/Et_3SiCl (top: 250.1 MHz, bottom: 300.0 MHz; THF-d_8). Asterisks mark resonances of Na_2[**4**] and the black square indicates remaining Et_3SiCl.

4.3 Reaction between Et_3SiCl and Na_2[4]

As discussed in the main article, Et_3SiCl should not directly encounter the dianion Na_2[**4**] in order to avoid unwanted side reactions. In the following, this issue is assessed in more detail.

As shown in Figure S12, the cathodic peak potential for the reduction of Et_3SiCl amounts to $E^{pc} = -1.3$ V (*vs.* FcH/FcH^+) and is thus more anodic than $E_{1/2}$ of **4** (*cf.* Table S4). Na_2[**4**] should therefore be capable of reducing Et_3SiCl.

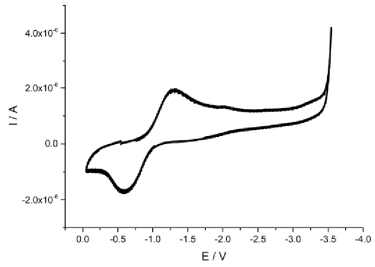

Figure S12. Cyclic voltammogram of Et_3SiCl in THF (*vs.* FcH/FcH^+, room temperature, supporting electrolyte: [*n*-Bu_4N][PF_6] (0.1 M), scan rate 200 mV s^{-1}).

An ^1H NMR spectrum recorded on a stoichiometric mixture of Na_2[**4**] and Et_3SiCl 15 min after sample preparation showed substantially broadened Na_2[**4**] resonances (Figure S13). This indicates an interaction between both components, but at this point no new resonances had emerged.

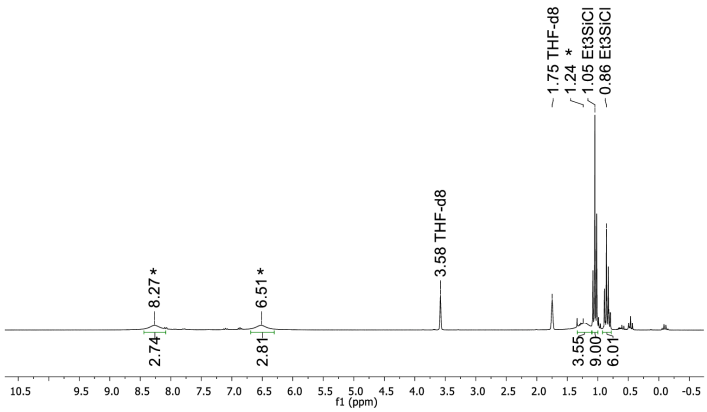

Figure S13. ^1H NMR spectrum (250.1 MHz, THF-d_8) recorded 15 min after the addition of Et_3SiCl to the solution of Na_2[**4**] (1:1). Asterisks mark the broadened resonances of Na_2[**4**].

After storage of the sample for 2 d at room temperature, a colorless precipitate had formed and NMR signals assignable to the silylborate $[MeB\text{-}(oC_6H_4)_2\text{-}B(Me)SiEt_3]^-$ had appeared (two stereoisomers with Et_3Si in axial or equatorial positions).

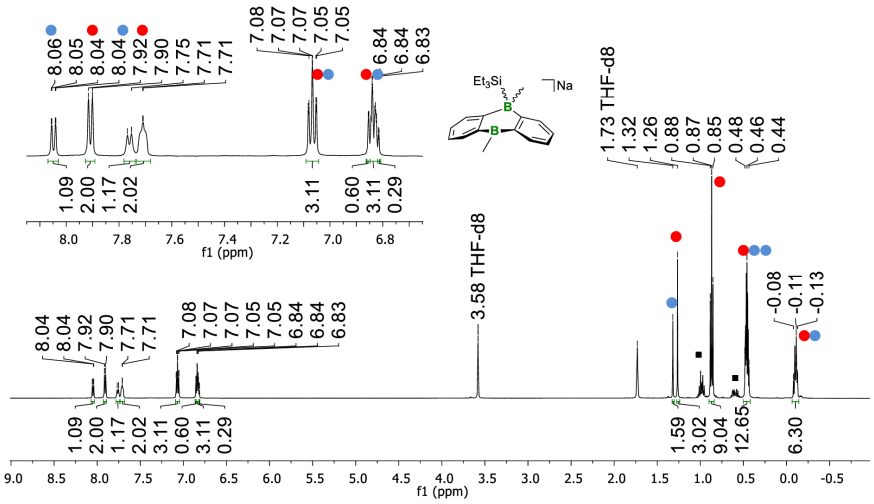

Figure S14. ^{1}H NMR spectrum (500.2 MHz, THF-d_8) recorded 2 d after the addition of Et_3SiCl to the solution of Na_2[**4**] (1:1). Red and blue dots indicate the resonances of the two stereoisomers of $[MeB\text{-}(oC_6H_4)_2\text{-}B(Me)SiEt_3]^-$; squares mark resonances of residual Et_3SiCl.

The NMR data below referring to the major component are colored in red, the one of the minor component in blue. Note: The major:minor integral ratio was approx. 2:1.

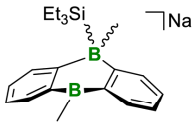

^{1}H NMR (500.2 MHz, THF-d_8): δ = 8.06–8.04 (m, 2H; H-d), 7.92–7.90 (m, 2H; H-d), 7.77–7.75 (m, 2H; H-a), 7.71 (n.r., 2H; H-a), 7.08–7.05 (m, 2H; H-b/2H; H-b), 6.85–6.83 (m, 2H; H-c), 6.84–6.81 (m, 2H; H-c), 1.32 (s, 3H; BCH_3), 1.26 (s, 3H; BCH_3), 0.87 (t, ^3J(H,H) = 7.9 Hz, 9H; CH_2CH_3), 0.48–0.44 (m, 6H+12H; CH_2CH_3, CH_2CH_3, $SiBCH_3$), −0.08–(−0.13) (m, 3H+6H; CH_2CH_3, $SiBCH_3$).

^{11}B NMR (96.3 MHz, THF-d_8): δ = 59.0 (br), –15.3, –16.6.

^{13}C{^{1}H} NMR (125.8 MHz, THF-d_8): δ = 182.8 (q, ^1J(C,B) = 48 Hz; C-f), 177.5 (q, ^1J(C,B) = 48 Hz; C-f), 145.0 (C-e), 144.2 (C-e), 134.8 (C-d), 134.1 (C-d), 132.8 (C-a), 132.2 (C-a), 128.7 (C-b), 127.3 (C-b), 120.7 (C-c), 119.3 (C-c), 14.1 (q, ^1J(C,B) = 41 Hz, $SiBCH_3$), 9.0 (CH_2CH_3), 7.0 (CH_2CH_3), 5.0 (CH_2CH_3), 4.9 (BCH_3), 4.9 (q, ^1J(C,B) = 43 Hz; $SiBCH_3$), 4.0 (BCH_3), 3.3 (CH_2CH_3).

^{29}Si NMR (99.4 MHz, THF-d_8): δ = 14.8, –2.6.

4.4 Reaction between Na_2[4-H_2] and Me_2SiCl_2

The reaction between Na_2[**4**-H_2] and Me_2SiCl_2 (1:1; THF-d_8) resulted in the clean formation of **4** and Me_2SiH_2 (Figure S16a). If 2 equiv of Me_2SiCl_2 were employed, the primary product was not $Me_2Si(H)Cl$, but an equimolar mixture of Me_2SiH_2 and Me_2SiCl_2. Over several days, however, the free Lewis acid **4** catalyzes a comproportionation reaction furnishing $Me_2Si(H)Cl$ as the final product.

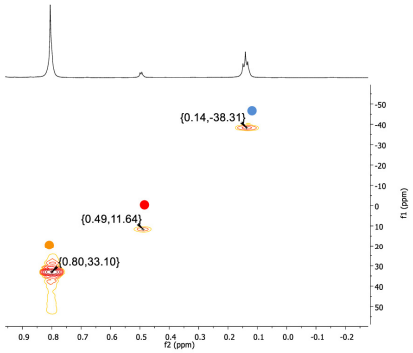

Figure S15. $^{29}Si/^{1}H$ HMBC-NMR spectrum of the reaction mixture Na_2[**4**-H_2]/Me_2SiCl_2, recorded after the sample had been kept at room temperature for 5 h (500.2 MHz, THF-d_8). Orange: Me_2SiCl_2, red: $Me_2Si(H)Cl$, blue: Me_2SiH_2.

The conversion Me_2SiCl_2 + Me_2SiH_2 → 2 $Me_2Si(H)Cl$ can be accelerated by heating the sample to 120 °C and is almost quantitative after 16 h at this temperature (Figure S16b).

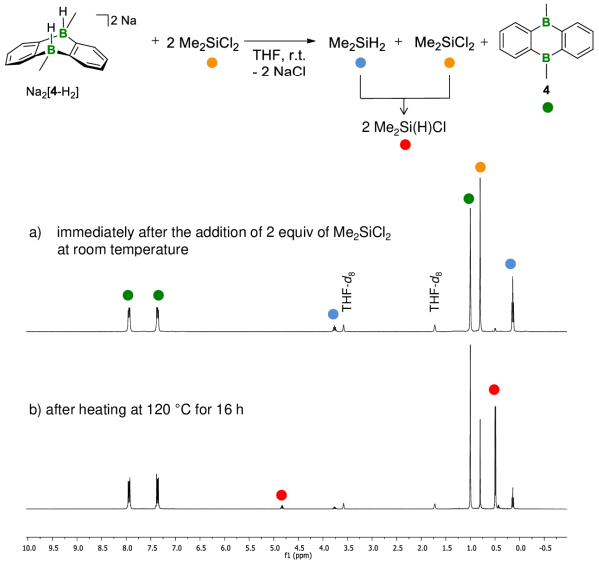

Figure S16. ^{1}H NMR spectra (250.1 MHz, THF-d_8) (a) of the reaction mixture Na_2[**4**-H_2]/2 Me_2SiCl_2 immediately after sample preparation and (b) after the sample had been kept at 120 °C for 16 h.

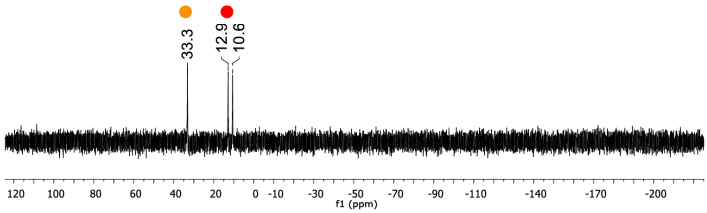

Figure S17. ^{29}Si NMR spectrum (99.4 MHz, THF-d_8) corresponding to sample (b) in Figure S16.

Published ^{29}Si NMR shifts for comparison:[13]
Me_2SiCl_2 $\delta = 32.0$
$Me_2Si(H)Cl$ $\delta = 11.1$
Me_2SiH_2 $\delta = -37.7$ (^1J(Si,H) = 179 Hz)

4.5 Substrate scope of the hydride-transfer reaction

General procedure

The respective substrate was added to an NMR tube containing M_2[**A**-H_2] (preparation described in 1.1) in THF-d_8 (0.5 mL). After mixing the components by shaking the NMR tube, the sample was flame-sealed. Table S3 summarizes the stoichiometries used in this screening process. Each reaction was accompanied by the formation of a colorless precipitate and complete within minutes (according to ^{1}H NMR spectroscopy). *Note*: Similar to the case of Me_2SiCl_2 (see above), we always observed the exclusive formation of exhaustively hydrogenated products, even if an excess of the halogenated substrate was used.

Table S3. [**A**]$^{2-}$ derivatives and substrates investigated for the hydride-transfer reaction.

DBA derivative			**substrate**				**product**
compound	*n* / mmol	equiv	compound	*n* / mmol	equiv	*V* / µL	
Li_2[**1**-H_2]	0.028	1	Me_3SiCl	0.056	2	7.1	Me_3SiH
K_2[**1**-H_2]	0.015	1	Me_3SiCl	0.030	2	3.8	Me_3SiH
Na_2[**4**-H_2]	0.050	1	Ph_2SiCl_2	0.050	1	10.5	Ph_2SiH_2
Na_2[**4**-H_2]	0.050	1	$SiCl_4$	0.025	0.5	2.9	SiH_4
Na_2[**4**-H_2]	0.050	1	$GeCl_4$	0.025	0.5	2.9	GeH_4
Na_2[**4**-H_2]	0.058	3	PCl_3	0.039	2	3.4	PH_3
Na_2[**4**-H_2]	0.050	1	EtBr	0.100	2	7.5	EtH

Me_3SiCl → Me_3SiH

^{1}H NMR (500.2 MHz, THF-d_8): δ = 3.95 (m, 1H; Me_3SiH), 0.08 (d, ^3J(H,H) = 3.6 Hz, 9H; Me_3SiH).

^{29}Si-INEPT NMR (99.4 MHz, THF-d_8): δ = –17.1 (Me_3SiH).

The ^{29}Si NMR shift is in accordance with the literature: δ = −16.3.[13]

Ph_2SiCl_2 → Ph_2SiH_2

^{1}H NMR (500.2 MHz, THF-d_8): δ = 7.41–7.33 (m, 10H; Ph_2SiH_2), 4.90 (s, 2H; Ph_2SiH_2).

^{29}Si NMR (99.4 MHz, THF-d_8): δ = –33.9 (t, ^1J(Si,H) = 199 Hz; Ph_2SiH_2).

The ^{29}Si NMR shift is in accordance with the literature: δ = −33.8 (^1J(Si,H) = 200 Hz).[13]

$SiCl_4$ → SiH_4

^{1}H NMR (400.1 MHz, THF-d_8): δ = 3.18 (s; SiH_4).

The ^{1}H NMR shift is in accordance with the literature (THF-d_8): δ = 3.14.[14]

^{29}Si NMR (99.4 MHz, THF-d_8): δ = –96.3 (q, ^1J(Si,H) = 200 Hz; SiH_4).

The ^{29}Si NMR shift is in accordance with the literature: δ = –93.1 (^1J(Si,H) = 202 Hz).[13]

$GeCl_4$ → GeH_4

^{1}H NMR (400.1 MHz, THF-d_8): δ = 3.14 (s; GeH_4).

The ^{1}H NMR shift is in accordance with the literature (CCl_4): δ = 3.27.[15]

PCl_3 → PH_3

^{1}H NMR (400.1 MHz, THF-d_8): δ = 1.76 (d, ^1J(P,H) = 186 Hz; PH_3).

The ^{1}H NMR shift is in accordance with the literature (acetonitrile): τ = 8.21 (≙ δ = 1.79, ^1J(P,H) = 189 Hz).[16]

^{31}P{^{1}H} NMR (121.5 MHz, THF-d_8): δ = –247.4 (q, ^1J(P,H) = 186 Hz; PH_3).

The ^{31}P NMR shift is in accordance with the literature (THF): δ = –245.4.[17]

EtBr → C_2H_6

^{1}H NMR (500.2 MHz, THF-d_8): δ = 0.85 (s; C_2H_6).

^{13}C{^{1}H} NMR (125.8 MHz, THF-d_8): δ = 6.4 (C_2H_6).

The ^{1}H and ^{13}C{^{1}H} NMR shifts are in accordance with the literature.[1]

Procedure for the reduction of CO_2

An NMR tube, charged with a solution of Na_2[**4**-H_2] (0.059 mmol) in THF-d_8 (0.5 mL), was connected to a Schlenk line. The solution was frozen with liquid nitrogen, the system evacuated, and CO_2 (1 atm; quality grade 4.5) was filled in. The content of the NMR tube was allowed to warm to room temperature and the excess pressure released through a Hg bubbler. After 10 min, a precipitate had formed. The reaction mixture was frozen again, the NMR tube was evacuated, flame-sealed, and investigated by NMR spectroscopy. Afterwards, the liquid phase was discarded and the precipitate characterized by IR and NMR spectroscopy (in D_2O).

The mother liquor showed NMR signals assignable to a weak formate adduct.

^{1}H NMR (500.2 MHz, THF-d_8): δ = 8.00 (s, 1H; HCOO), 7.79–7.77 (m, 4H; H-a), 7.17–7.15 (m, 4H; H-b), 0.72 (s, 6H; CH_3).

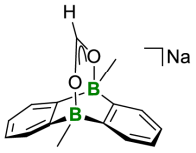

^{11}B NMR (160.5 MHz, THF-d_8): δ = 34.7 ($h_{1/2}$ = 750 Hz).

^{13}C{^{1}H} NMR (125.8 MHz, THF-d_8): δ = 171.6 (HCOO), 155.7 (BC), 133.5 (C-a), 127.6 (C-b), 9.4 (CH_3).

Note: Attempts at the crystallization of the formate adduct gave crystals of the free Lewis acid **4**.

NMR data of the precipitated sodium formate (*Note*: 1 equiv of Na_2[**4**-H_2] is sufficient to produce 2 equiv of sodium formate):

^{1}H NMR (500.2 MHz, D_2O): δ = 8.44 (HCOO).

^{13}C{^{1}H} NMR (125.8 MHz, D_2O): δ = 171.0 (HCOO).

The ^{13}C NMR shift is in accordance with the literature: 171.0 ppm.[18]

ATR-IR data of the precipitated sodium formate: 2830, 1587, 1363, 775 cm^{-1}.

Literature data (KBr): 2831, 1611, 1362, 775 cm^{-1}.[19]

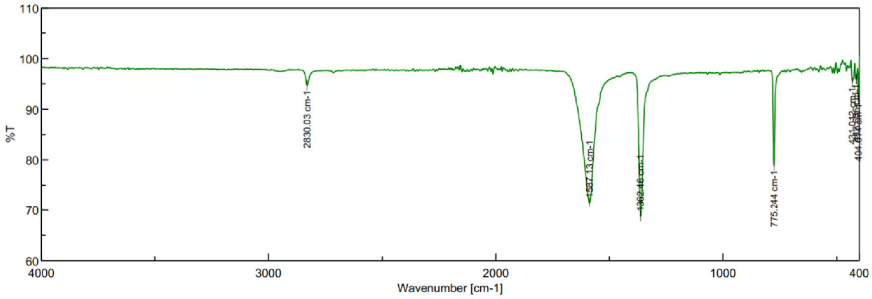

Figure S18. ATR-IR spectrum of the sodium formate obtained from the reaction between Na_2[**4**-H_2] and CO_2.

5. Cyclic voltammetry measurements

Table S4. Electrochemical data obtained by cyclic voltammetry (*vs.* FcH/FcH$^+$; red1 = first reduction event, red2 = second reduction event, pc = peak current).

DBA derivative	$E_{1/2}$, red1 (V)	$E_{1/2}$, red2 (V)	E^{pc}, red2 (V)
1	−2.08	–	−2.75
2	−1.66	−2.32	–
4	−2.02	–	−2.77
5	−2.01	–	−2.74
7	−1.80	–	−2.48
8	−1.90	–	−2.71

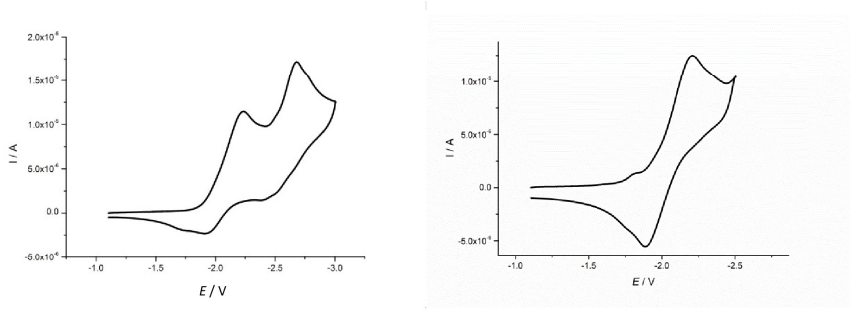

Figure S19. Cyclic voltammograms of **1** in THF (*vs.* FcH/FcH$^+$, room temperature, supporting electrolyte: [*n*-Bu$_4$N][PF$_6$] (0.1 M), scan rate 200 mV s^{-1}). Left: Full voltammogram; right: first redox event only.

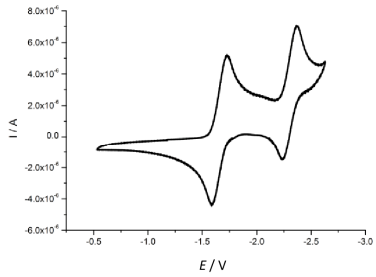

Figure S20. Cyclic voltammogram of **2** in THF (*vs.* FcH/FcH$^+$, room temperature, supporting electrolyte: [*n*-Bu$_4$N][PF$_6$] (0.1 M), scan rate 200 mV s^{-1}).

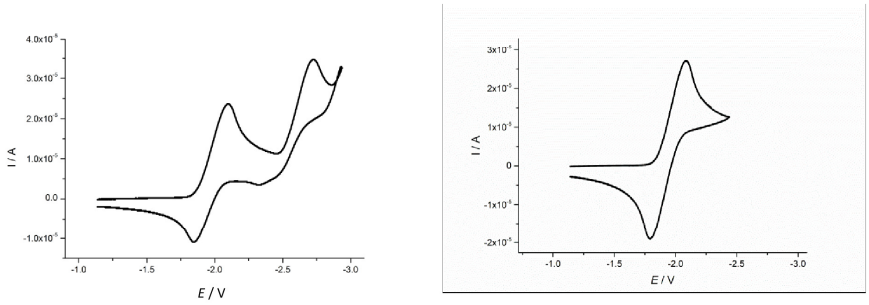

Figure S21. Cyclic voltammograms of **4** in THF (*vs.* FcH/FcH^+, room temperature, supporting electrolyte: [*n*-Bu_4N][PF_6] (0.1 M), scan rate 200 mV s^{-1}). Left: Full voltammogram; right: first redox event only.

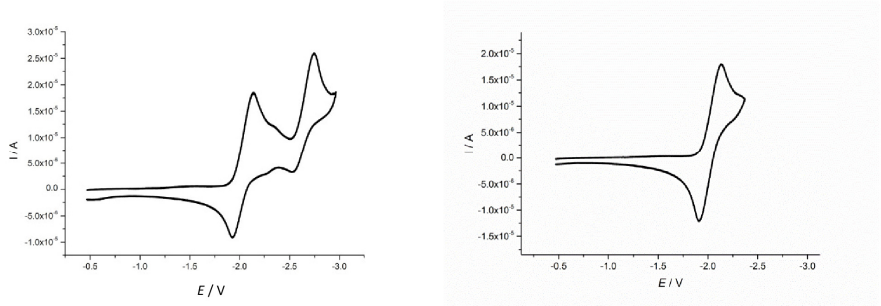

Figure S22. Cyclic voltammograms of **5** in THF (*vs.* FcH/FcH^+, room temperature, supporting electrolyte: [*n*-Bu_4N][PF_6] (0.1 M), scan rate 200 mV s^{-1}). Left: Full voltammogram; right: first redox event only.

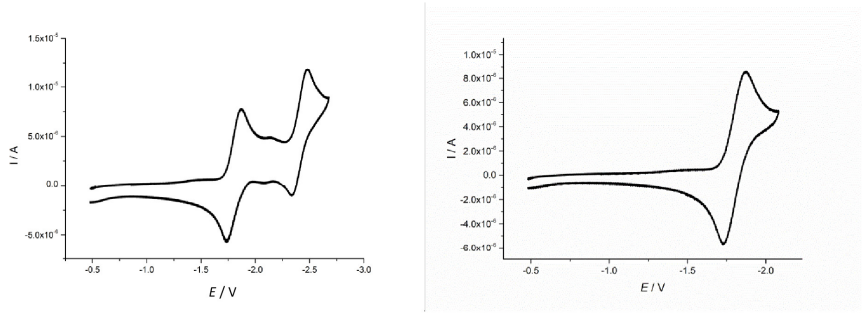

Figure S23. Cyclic voltammograms of **7** in THF (*vs.* FcH/FcH^+, room temperature, supporting electrolyte: [*n*-Bu_4N][PF_6] (0.1 M), scan rate 200 mV s^{-1}). Left: Full voltammogram; right: first redox event only.

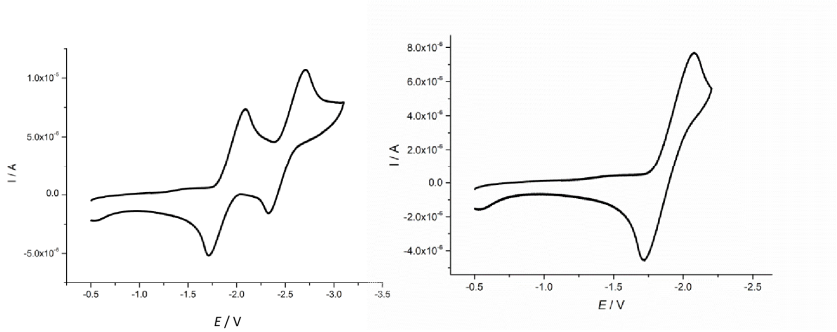

Figure S24. Cyclic voltammograms of **8** in THF (*vs.* FcH/FcH^+, room temperature, supporting electrolyte: [*n*-Bu_4N][PF_6] (0.1 M), scan rate 200 mV s^{-1}).

6. Computational details

Geometry optimizations and frequency calculations were carried out with the Gaussian 09 software package[20] using the B3LYP functional and the 6-31G* basis set in combination with the SMD solvation model[21] (to account for effects of the THF solvent). The stationary points were characterized as minima (no imaginary frequencies in the vibrational analysis).

Table S5. LUMO-energy values of **1**, **2**, **4**, **5**, **7**, **8**, and **9**, as estimated from cyclic voltammetry (E_{LUMO}^{CV}) or computed by DFT (E'_{LUMO}^{DFT}).

Cmpd	E_{LUMO}^{CV} / eV[a]	E'_{LUMO}^{DFT} / eV	E_{LUMO}^{DFT} / eV[b]
1	–2.72	–2.59	–3.12
2	–3.14	–2.59	–3.12
4	–2.78	–2.17	–2.70
5	–2.79	–2.26	–2.79
8	–2.90	–2.42	–2.95
7	–3.00	–2.43	–2.96
9	–2.96[c]	–2.43	–2.96

[a] $E_{LUMO}^{CV} = -4.8\ eV - E_{1/2}^{Red1}$ ($FcH/FcH^+ = -4.8$ eV *vs.* vacuum level).[22]
[b] For better comparability with the E_{LUMO}^{CV} values, the computed LUMO energies (E'_{LUMO}^{DFT}) were scaled by addition of a constant value of –0.53 eV, which corresponds to the difference E_{LUMO}^{CV}(**9**) – E'_{LUMO}^{DFT}(**9**). Compound **9** was selected, because it does not coordinate THF ligands.
[c] Ref.[5].

The electrochemical and computed LUMO-energy levels are directly juxtaposed in Figure S25 for better comparison. We note a pleasingly good correlation, except for the case of **1**. THF ligation is an important perturbative factor only to the least hindered parent DBA, but negligible for its derivatives. In conclusion, cyclic voltammetry is a proper tool to evaluate electronic substituent effects provided that THF ligation is not an issue.

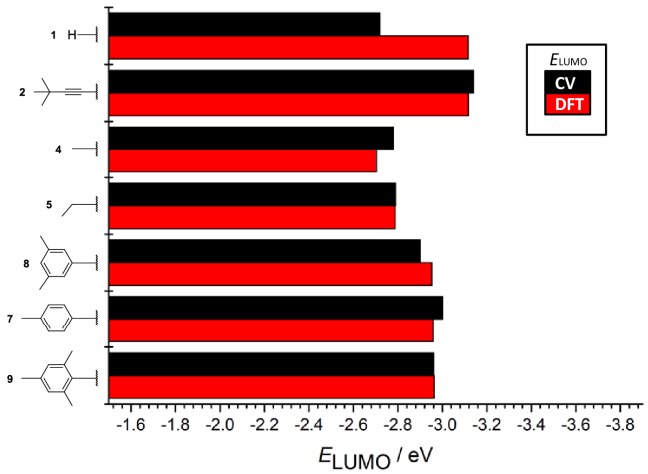

Figure S25. Comparison of the E_{LUMO}^{CV} and E_{LUMO}^{DFT} values of the compounds **1**, **2**, **4**, **5**, **7**, **8**, and **9** (data from Table S5).

1

B	0.000000	-1.482377	0.000291
C	-1.350470	-0.714609	0.000130
C	-2.578127	-1.394479	-0.000022
H	-2.587756	-2.482479	-0.000027
C	-3.792753	-0.697621	-0.000176
H	-4.734007	-1.241607	-0.000295
C	1.350470	-0.714609	0.000130
C	2.578127	-1.394478	-0.000022
H	2.587756	-2.482479	-0.000027
C	3.792753	-0.697621	-0.000176
B	0.000000	1.482377	0.000291
C	1.350470	0.714609	0.000131
H	4.734007	-1.241608	-0.000295
C	2.578127	1.394478	-0.000022
H	2.587756	2.482479	-0.000028
C	3.792753	0.697621	-0.000176
H	4.734007	1.241608	-0.000295
C	-1.350470	0.714609	0.000131
C	-2.578127	1.394479	-0.000022
H	-2.587756	2.482479	-0.000028
C	-3.792753	0.697621	-0.000176
H	-4.734007	1.241607	-0.000295
H	0.000000	2.683826	0.000005
H	0.000000	-2.683826	0.000000

2

B	1.496402	0.002296	-0.000736	B	-1.496401	-0.002293	0.000565
C	0.715583	-1.353161	-0.000545	C	-0.715581	1.353163	0.000339
C	-0.711417	-1.355375	0.000448	C	0.711419	1.355377	-0.000648
C	-1.386444	-2.587850	0.001024	C	1.386446	2.587852	-0.001239
H	-2.473677	-2.597848	0.001817	H	2.473679	2.597850	-0.002021
C	-0.691944	-3.800316	0.000576	C	0.691946	3.800318	-0.000821
H	-1.236861	-4.741167	0.001050	H	1.236863	4.741170	-0.001310
C	0.703923	-3.798127	-0.000551	C	-0.703920	3.798130	0.000300
H	1.251765	-4.737281	-0.000958	H	-1.251762	4.737284	0.000690
C	1.394532	-2.583458	-0.001108	C	-1.394530	2.583460	0.000881
H	2.481794	-2.589629	-0.002018	H	-2.481791	2.589632	0.001796
C	3.019298	0.004476	-0.000235	C	-3.019297	-0.004474	0.000204
C	4.241800	0.006545	0.001422	C	-4.241798	-0.006551	-0.001304
C	5.714036	0.005043	0.001595	C	-5.714037	-0.005044	-0.001362
C	6.212572	-0.561386	-1.349964	C	-6.212440	0.561086	1.350366
H	7.308927	-0.571539	-1.361204	H	-7.308794	0.571151	1.361739
H	5.856849	-1.585686	-1.504907	H	-5.856778	1.585386	1.505451
H	5.866036	0.052021	-2.188782	H	-5.865753	-0.052459	2.189018
C	6.238958	1.446874	0.189615	C	-6.238991	-1.446832	-0.189622
H	7.335563	1.448358	0.189418	H	-7.335596	-1.448296	-0.189326
H	5.895359	2.100474	-0.619695	H	-5.895327	-2.100604	0.619522
H	5.896763	1.870070	1.140405	H	-5.896893	-1.869842	-1.140530
C	6.218862	-0.890418	1.157954	H	-6.218971	0.890669	-1.157479
H	7.315274	-0.900795	1.164296	H	-7.315386	0.900989	-1.163766
H	5.874370	-0.515322	2.127870	H	-5.874506	0.515824	-2.127501
H	5.864910	-1.920780	1.044425	H	-5.865071	1.921022	-1.043715

4

B	-0.00000	-1.50656	-0.19526	C	-2.57172	1.38874	0.10268
C	1.34766	-0.71365	-0.04611	H	-2.59205	2.47587	0.09654
C	2.57167	-1.38875	0.10271	C	-3.77411	0.69751	0.27540
H	2.59203	-2.47587	0.09665	H	-4.70513	1.24442	0.40410
C	3.77408	-0.69750	0.27534	C	0.00001	3.07009	-0.43447
H	4.70511	-1.24441	0.40392	C	1.34765	0.71367	-0.04616
C	0.00014	-3.07008	-0.43445	C	2.57166	1.38879	0.10266
C	-1.34770	-0.71369	-0.04625	H	2.59199	2.47592	0.09656
C	-2.57172	-1.38879	0.10257	C	3.77407	0.69756	0.27531
H	-2.59211	-2.47590	0.09639	H	4.70510	1.24449	0.40386
C	-3.77411	-0.69756	0.27534	H	0.88463	3.43276	-0.97092
H	-4.70513	-1.24448	0.40396	H	0.00050	3.58513	0.54116
H	-0.88489	-3.43325	-0.96987	H	-0.88489	3.43301	-0.97028
B	-0.00004	1.50656	-0.19522	H	0.88462	-3.43269	-0.97118
C	-1.34771	0.71364	-0.04620	H	0.00117	-3.58495	0.54128

5

B	0.000178	-1.485283	0.312034	B	-0.000190	1.485289	-0.312048
C	-1.352272	-0.698977	0.149948	C	1.352261	0.698981	-0.149968
C	-1.352436	0.698602	-0.149954	C	1.352424	-0.698597	0.149938
C	-2.588209	1.355184	-0.290088	C	2.588197	-1.355179	0.290071
H	-2.612389	2.416721	-0.519827	H	2.612377	-2.416716	0.519812
C	-3.804015	0.681173	-0.144743	C	3.804003	-0.681170	0.144721
H	-4.742880	1.217862	-0.258286	H	4.742868	-1.217859	0.258264
C	-3.803857	-0.682183	0.144683	C	3.803845	0.682186	-0.144707
H	-4.742597	-1.219102	0.258165	H	4.742586	1.219104	-0.258191
C	-2.587880	-1.355887	0.290021	C	2.587869	1.355890	-0.290043
H	-2.611787	-2.417451	0.519691	H	2.611776	2.417454	-0.519713
C	0.000399	-3.053379	0.564144	C	-0.000412	3.053392	-0.564108
H	0.874594	-3.369033	1.148276	H	-0.874635	3.369074	-1.148183
H	-0.873943	-3.369380	1.147859	H	0.873902	3.369405	-1.147860
C	0.000819	-3.834727	-0.773958	C	-0.000750	3.834696	0.774019
H	0.000779	-4.918379	-0.600953	H	-0.000701	4.918354	0.601050
H	-0.881979	-3.597075	-1.379896	H	0.882076	3.597010	1.379903
H	0.883933	-3.597048	-1.379416	H	-0.883836	3.597012	1.379516

7

B	1.511976	-0.007032	-0.043171
B	-1.512000	-0.007115	-0.043285
C	0.715377	-1.359070	0.000295
C	-0.715308	-1.359118	0.000321
C	-1.386899	-2.589516	0.112805
H	-2.472212	-2.605771	0.143173
C	-0.696425	-3.802360	0.197928
H	-1.245387	-4.737518	0.277684
C	0.696730	-3.802307	0.197898
H	1.245768	-4.737421	0.277633
C	1.387089	-2.589402	0.112749
H	2.472408	-2.605531	0.143067
C	3.084852	-0.001261	-0.001491
C	3.861499	-0.671337	-0.967499
H	3.367444	-1.208921	-1.773939
C	5.257382	-0.654018	-0.930015
H	5.820857	-1.171214	-1.704090
C	5.945812	0.008714	0.094167
C	-3.084866	-0.001391	-0.001691
C	-3.861617	-0.671765	-0.967395
H	-3.367647	-1.209593	-1.773724
C	-5.257499	-0.654412	-0.929791
H	-5.821046	-1.171854	-1.703647
C	-5.945830	0.008727	0.094187
C	-7.454539	0.024184	0.147777
C	0.715027	1.342749	-0.120071
C	-0.715117	1.342701	-0.120211
C	-1.387385	2.569929	-0.259868
H	-2.472982	2.585483	-0.284596
C	-0.696718	3.779789	-0.380008
H	-1.245533	4.712627	-0.484243
C	0.696524	3.779839	-0.379855
H	1.245290	4.712721	-0.483954
C	1.387245	2.570021	-0.259603
H	2.472844	2.585632	-0.284129
C	3.792275	0.677274	1.014523
H	3.240742	1.210480	1.785955
C	5.184818	0.668516	1.071609
H	5.692003	1.188027	1.882713
C	-3.792211	0.677639	1.014079
H	-3.240594	1.211208	1.785199
C	-5.184739	0.668956	1.071276
H	-5.691859	1.188865	1.882167
H	-7.889395	-0.624682	-0.619434
H	-7.849697	1.036601	-0.009236
C	7.454530	0.024356	0.147440
H	7.849618	1.036280	-0.012986
H	7.889255	-0.626942	-0.617787
H	7.824386	-0.309507	1.124889
H	-7.824194	-0.312879	1.124224

8

B	1.511246	0.012423	0.018691	C	1.387800	2.515366	-0.633568
C	0.714043	-1.299098	0.346008	H	2.473211	2.524525	-0.661957
C	-0.716034	-1.298551	0.346144	C	0.697571	3.689210	-0.951391
C	-1.388814	-2.478899	0.708880	H	1.247039	4.592079	-1.206809
H	-2.474334	-2.488414	0.735536	C	-0.695649	3.689441	-0.952568
C	-0.698358	-3.646826	1.047459	H	-1.244385	4.592481	-1.208953
H	-1.247707	-4.545164	1.318607	C	-1.386774	2.515857	-0.635750
C	0.694892	-3.647430	1.047010	H	-2.472134	2.525272	-0.665916
H	1.243636	-4.546260	1.317753	C	-3.086568	0.005652	-0.003423
C	1.386093	-2.480006	0.708244	C	-3.800097	-0.843487	-0.875847
H	2.471628	-2.490222	0.734487	H	-3.251485	-1.503592	-1.545211
C	3.085510	0.003391	-0.002015	C	-5.197524	-0.856839	-0.921731
C	3.836748	0.836081	0.848903	C	-5.902067	-0.020760	-0.042012
H	3.320404	1.504282	1.535839	H	-6.991083	-0.031050	-0.056916
C	5.238580	0.825734	0.853094	C	-5.239920	0.824291	0.854096
C	5.901321	-0.015278	-0.048436	C	-3.836835	0.838208	0.846422
H	6.990585	-0.020393	-0.068878	H	-3.320235	1.506942	1.533083
C	5.196982	-0.851620	-0.926054	C	-5.938604	-1.743739	-1.895131
C	3.798497	-0.841433	-0.877096	H	-5.270053	-2.480046	-2.353495
H	3.250563	-1.499282	-1.549166	H	-6.754433	-2.287537	-1.403422
C	6.017146	1.688649	1.818960	H	-6.389975	-1.157223	-2.706679
H	5.439346	2.565940	2.129720	C	-6.011368	1.696575	1.817615
H	6.957521	2.038803	1.378304	H	5.246123	-2.335008	-2.503129
H	6.276492	1.131469	2.729857	H	6.598499	-2.446924	-1.364645
C	5.938394	-1.746339	-1.892257	H	6.572598	-1.163727	-2.572768
B	-1.512212	0.013394	0.017896	H	-7.077610	1.722987	1.569185
C	-0.715150	1.329867	-0.290001	H	-5.637510	2.727591	1.815052
C	0.715204	1.329576	-0.289013	H	-5.922005	1.327834	2.848327

9

B	-1.512270	0.001484	0.000339
B	1.512273	0.001508	-0.000283
C	-0.714362	1.351991	0.000195
C	0.714343	1.352002	-0.000142
C	1.389259	2.584729	-0.000384
H	2.476160	2.597570	-0.000751
C	0.697001	3.800182	-0.000236
H	1.244555	4.739469	-0.000433
C	-0.697058	3.800172	0.000167
H	-1.244626	4.739450	0.000305
C	-1.389296	2.584708	0.000376
H	-2.476198	2.597532	0.000747
C	-3.094965	0.001028	0.001134
C	-3.819759	-0.000668	-1.215310
C	-5.218599	-0.005332	-1.197271
H	-5.758206	-0.008401	-2.143522
C	-5.940486	-0.006864	0.002374
C	-7.451064	0.009044	-0.001405
C	3.094966	0.001078	-0.001135
C	3.817139	-0.001910	-1.216338
C	5.218239	-0.006653	-1.199150
H	5.757294	-0.011193	-2.145349
C	5.940486	-0.006864	-0.002433
C	7.451065	0.009032	0.001282
C	-0.714326	-1.349027	0.000207
C	0.714347	-1.349015	-0.000112
C	1.389286	-2.581746	-0.000290
H	2.476179	-2.594591	-0.000638
C	0.697064	-3.797209	-0.000101
H	1.244648	-4.736477	-0.000243
C	-0.696996	-3.797221	0.000270
H	-1.244563	-4.736498	0.000441
C	-1.389241	-2.581771	0.000411
H	-2.476134	-2.594642	0.000748
C	-3.817157	-0.001856	1.216314
C	-5.218268	-0.006583	1.199096
H	-5.757331	-0.011052	2.145290
C	3.819780	-0.000536	1.215288
C	5.218629	-0.005242	1.197216
H	5.758248	-0.008278	2.143460
C	-3.089312	-0.000566	-2.542044
H	-2.443447	0.880905	-2.647716
H	-3.790405	-0.000735	-3.383252
H	-2.442842	-0.881591	-2.647843
C	-3.087504	-0.003040	2.543549
H	-2.441386	-0.884323	2.649330
H	-3.789222	-0.003719	3.384244
H	-2.441572	0.878212	2.650640
C	3.089364	-0.000394	2.542032
H	2.443408	0.881015	2.647646
H	3.790472	-0.000428	3.383229
H	2.442978	-0.881474	2.647914
C	3.087434	-0.003135	-2.543545
H	3.789118	-0.003837	-3.384269
H	2.441495	0.878113	-2.650636
H	2.441314	-0.884423	-2.649273

H	-7.855848	-0.214470	0.991398	H	7.855816	-0.215630	-0.991277
H	-7.860973	-0.724484	-0.706421	H	7.860966	-0.723705	0.707120
H	-7.840807	0.991200	-0.302164	H	7.840836	0.991523	0.300903

7. Plots of the NMR spectra

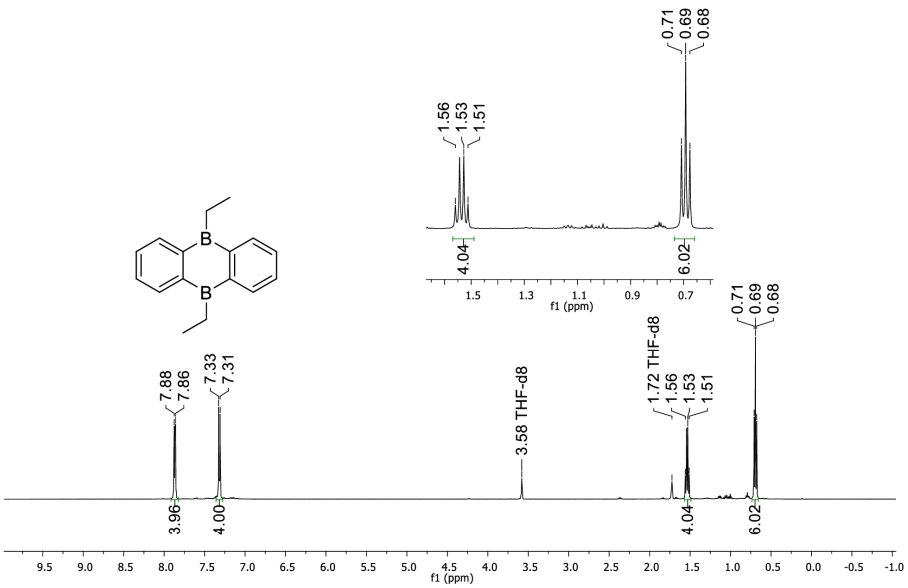

Figure S26. ^{1}H NMR spectrum of **5** (500.2 MHz, THF-d_8).

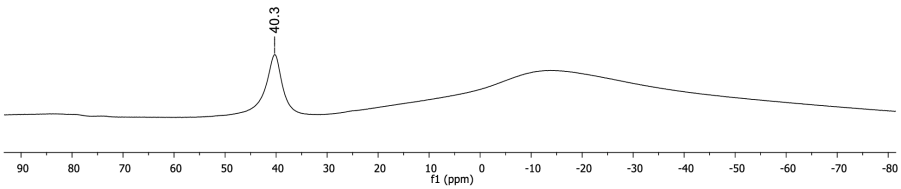

Figure S27. ^{11}B NMR spectrum of **5** (160.5 MHz, THF-d_8).

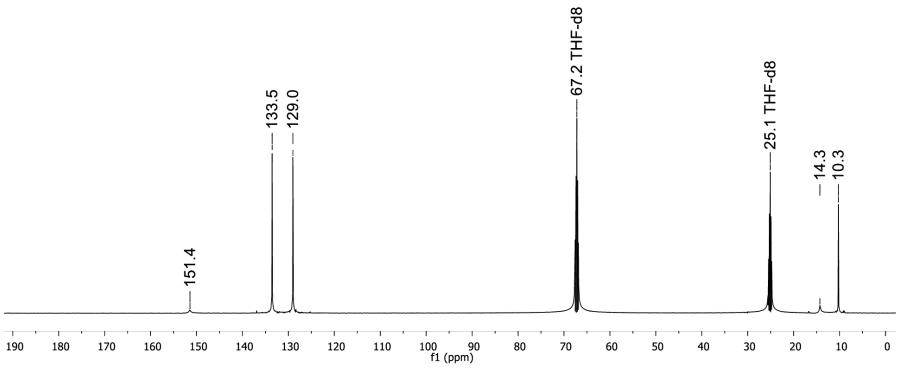

Figure S28. ^{13}C{^{1}H} NMR spectrum of **5** (125.8 MHz, THF-d_8).

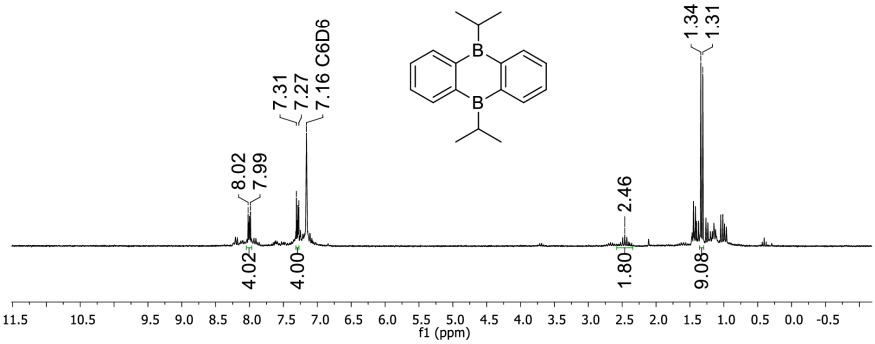

Figure S29. ^{1}H NMR spectrum of **6** (250.1 MHz, C_6D_6).

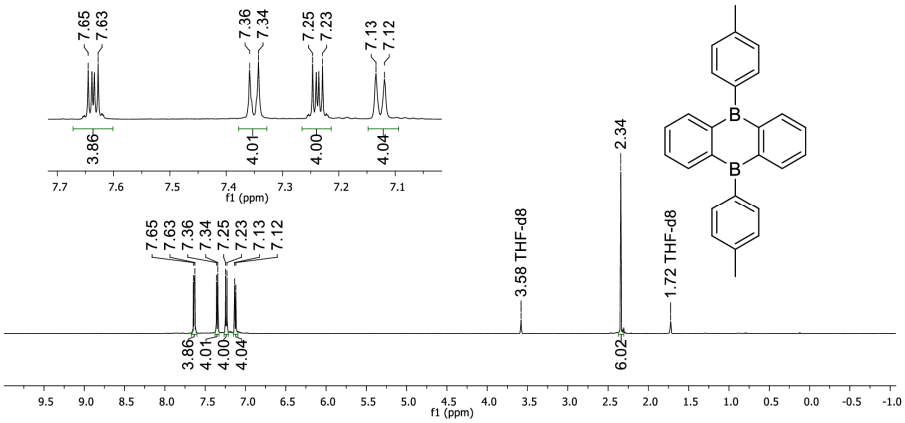

Figure S30. ^{1}H NMR spectrum of **7** (500.2 MHz, THF-d_8).

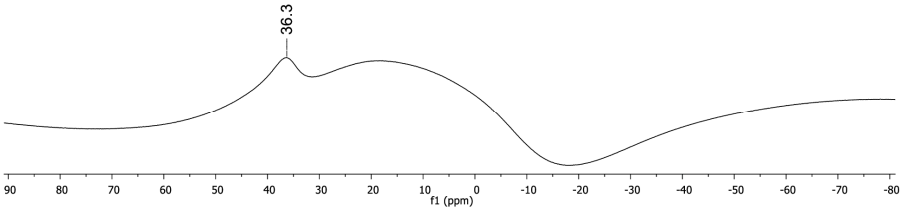

Figure S31. ^{11}B NMR spectrum of **7** (160.5 MHz, THF-d_8).

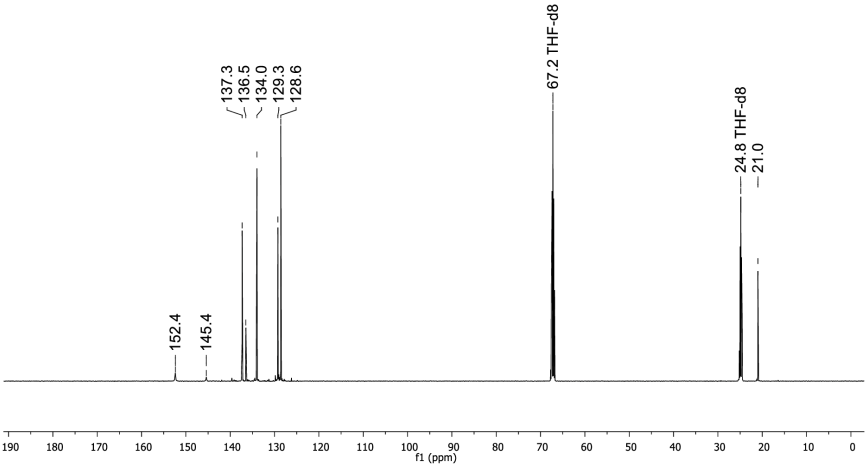

Figure S32. ^{13}C{^{1}H} NMR spectrum of **7** (125.8 MHz, THF-d_8).

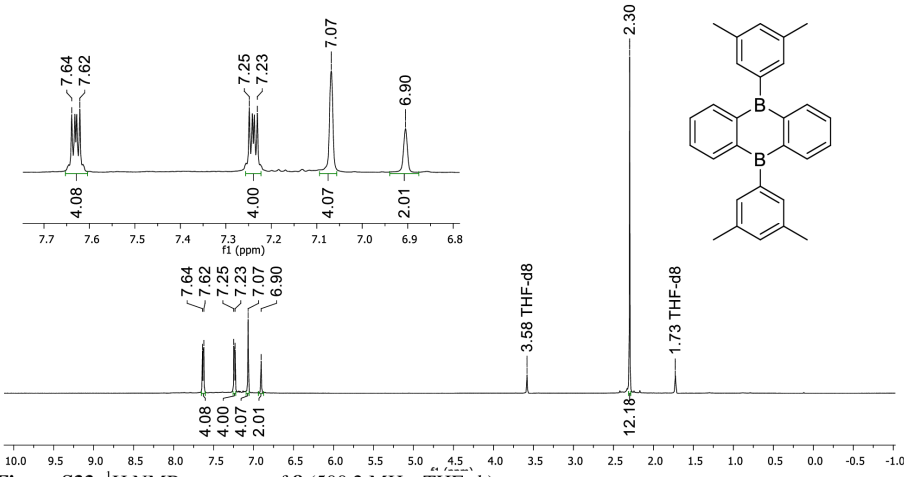

Figure S33. ^{1}H NMR spectrum of **8** (500.2 MHz, THF-d_8).

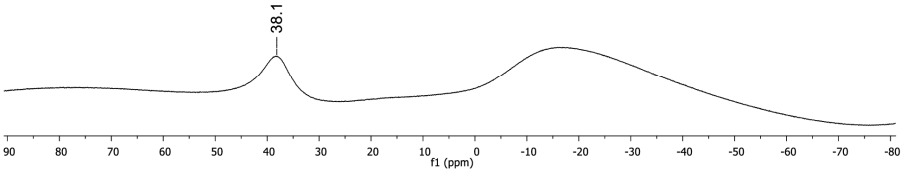

Figure S34. ^{11}B NMR spectrum of **8** (160.5 MHz, THF-d_8).

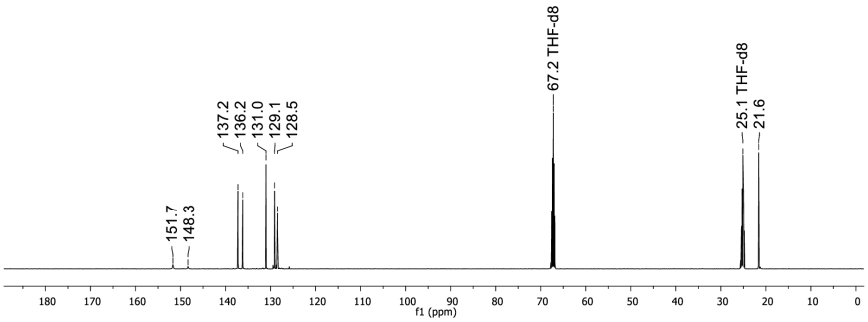

Figure S35. ^{13}C{^{1}H} NMR spectrum of **8** (125.8 MHz, THF-d_8).

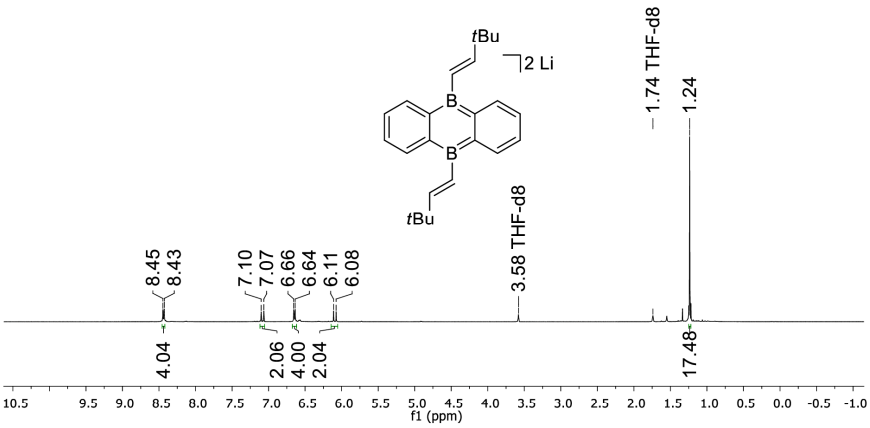

Figure S36. ^{1}H NMR spectrum of Li_2[**3**] (500.2 MHz, THF-d_8).

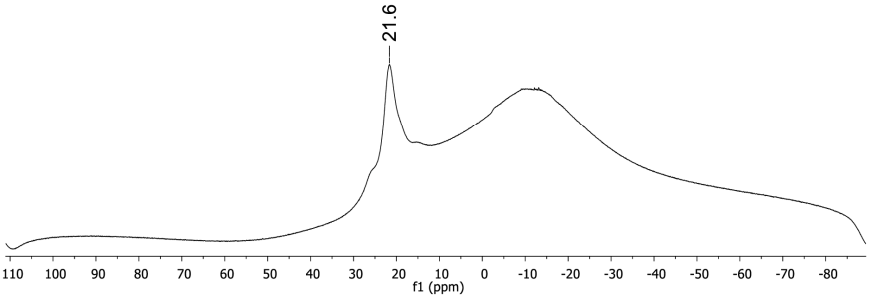

Figure S37. ^{11}B NMR spectrum of Li_2[**3**] (160.5 MHz, THF-d_8).

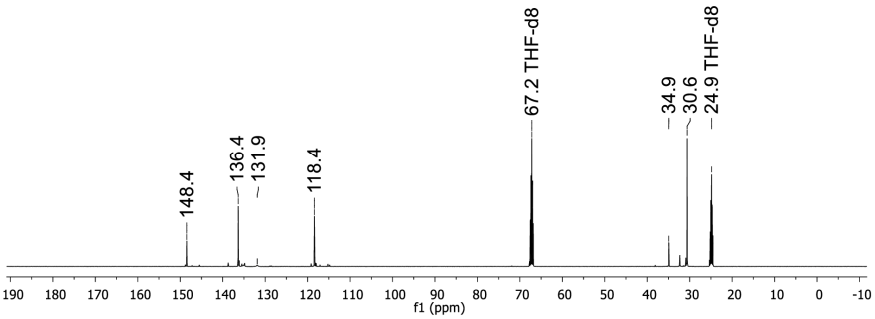

Figure S38. ^{13}C{^{1}H} NMR spectrum of Li_2[**3**] (125.8 MHz, THF-d_8).

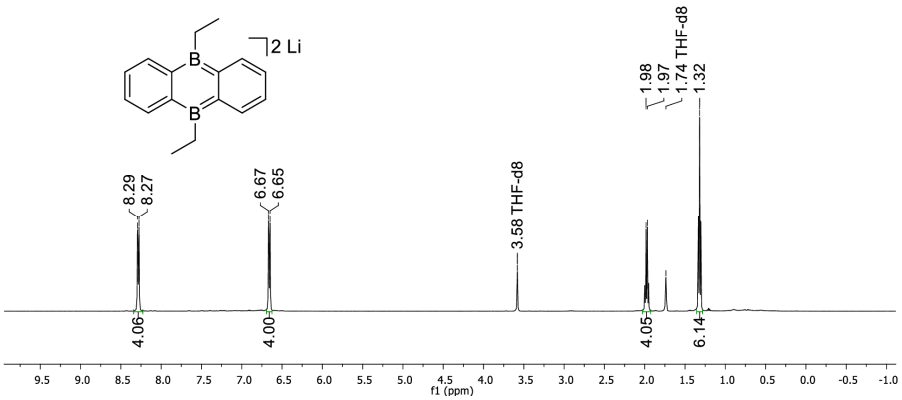

Figure S39. ^{1}H NMR spectrum of Li_2[**5**] (500.2 MHz, THF-d_8).

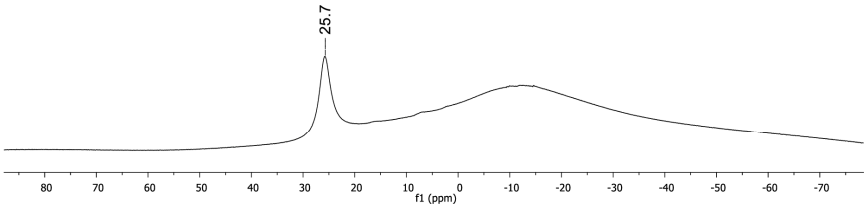

Figure S40. ^{11}B NMR spectrum of Li_2[**5**] (160.5 MHz, THF-d_8).

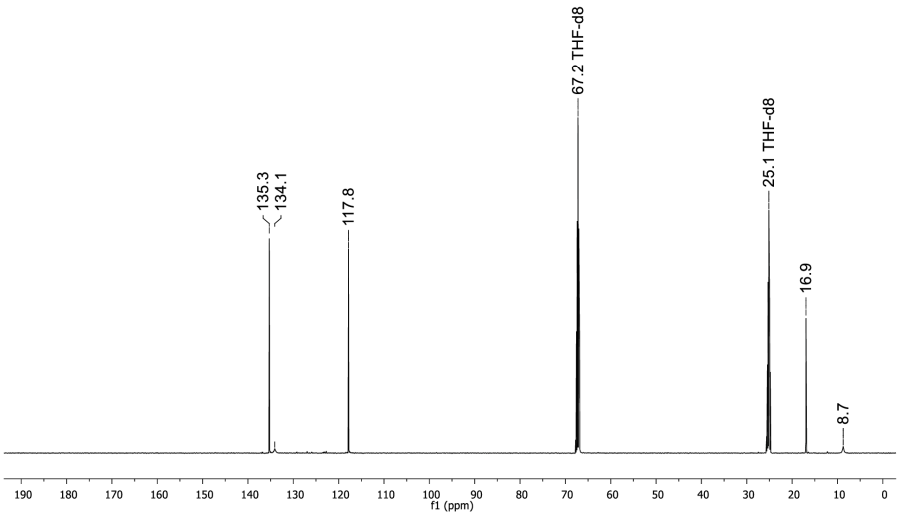

Figure S41. ^{13}C{^{1}H} NMR spectrum of Li_2[**5**] (125.8 MHz, THF-d_8).

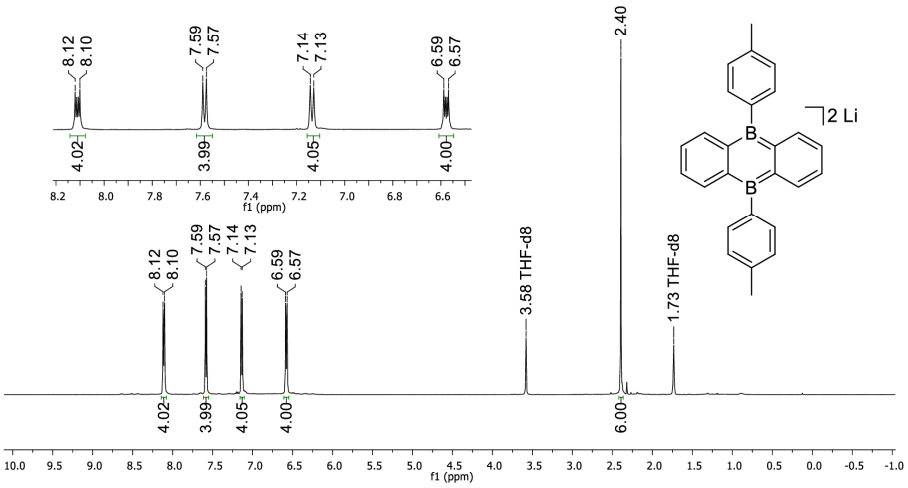

Figure S42. ^{1}H NMR spectrum of Li_2[**7**] (500.2 MHz, THF-d_8).

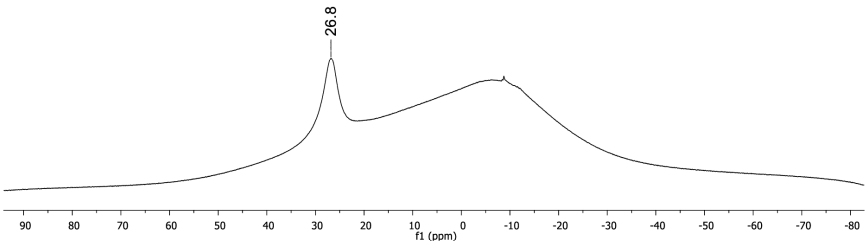

Figure S43. ^{11}B NMR spectrum of Li_2[**7**] (160.5 MHz, THF-d_8).

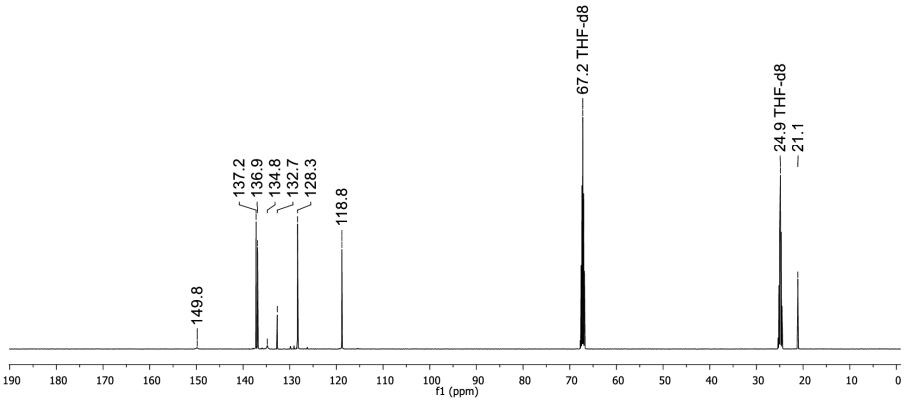

Figure S44. ^{13}C{^{1}H} NMR spectrum of Li_2[**7**] (125.8 MHz, THF-d_8).

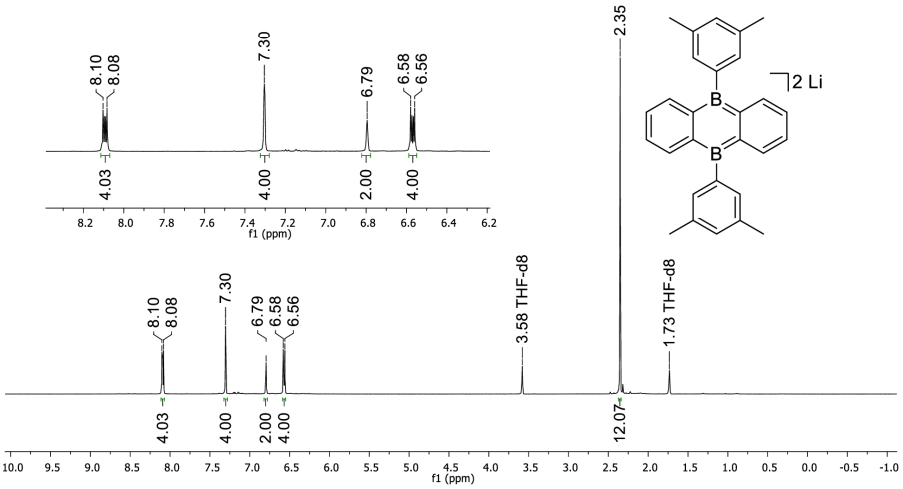

Figure S45. ^{1}H NMR spectrum of Li_2[**8**] (500.2 MHz, THF-d_8).

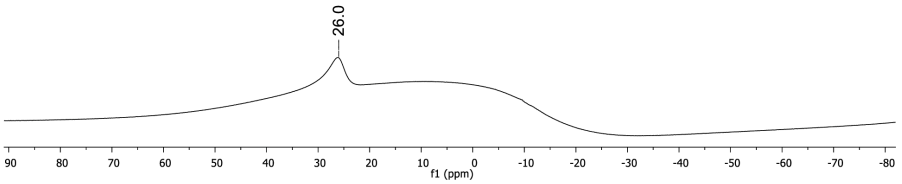

Figure S46. ^{11}B NMR spectrum of Li_2[**8**] (160.5 MHz, THF-d_8).

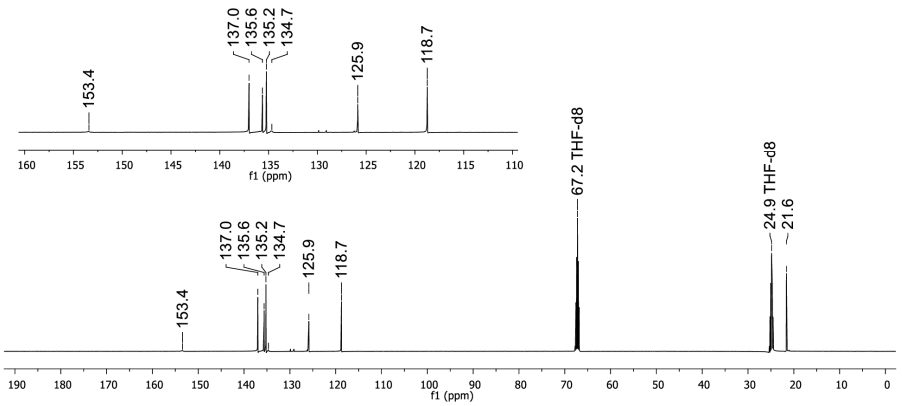

Figure S47. ^{13}C{^{1}H} NMR spectrum of Li_2[**8**] (125.8 MHz, THF-d_8).

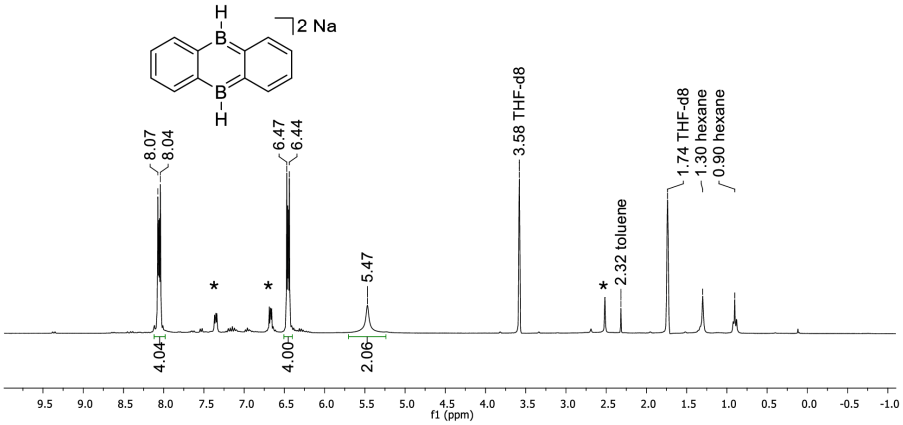

Figure S48. $^{1}H\{^{11}B\}$ NMR spectrum of Na_2[**1**] (300.0 MHz, THF-d_8). Asterisks mark resonances of Na_2[**1**-H_2] as a minor component; explanation of its derivation is provided in the SI of Ref. [4].

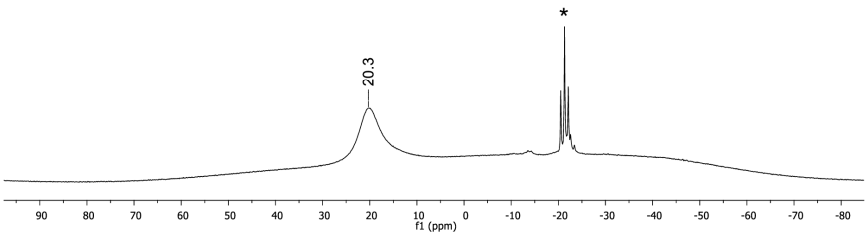

Figure S49. ^{11}B NMR spectrum of Na_2[**1**] (96.3 MHz, THF-d_8).

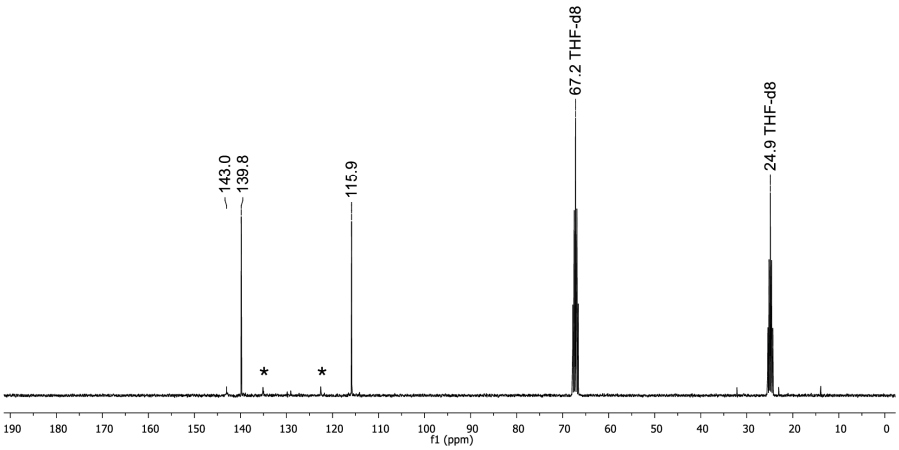

Figure S50. $^{13}C\{^{1}H\}$ NMR spectrum of Na_2[**1**] (75.4 MHz, THF-d_8).

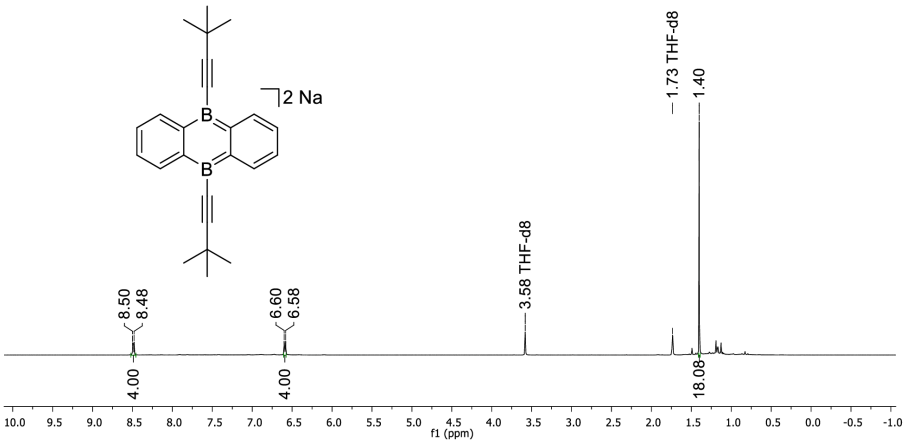

Figure S51. ^{1}H NMR spectrum of Na_2[**2**] (500.2 MHz, THF-d_8).

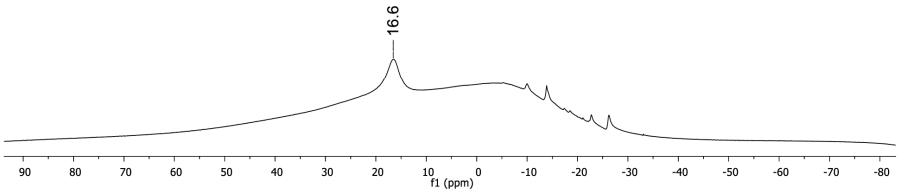

Figure S52. ^{11}B NMR spectrum of Na_2[**2**] (160.5 MHz, THF-d_8).

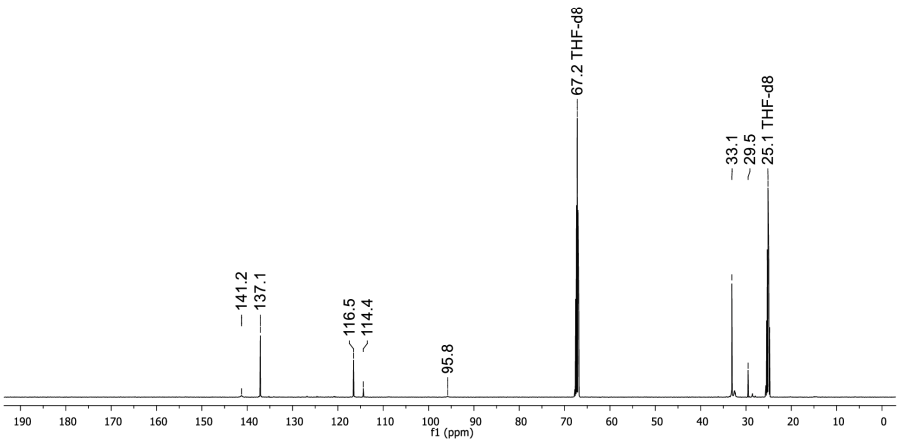

Figure S53. ^{13}C{^{1}H} NMR spectrum of Na_2[**2**] (125.8 MHz, THF-d_8).

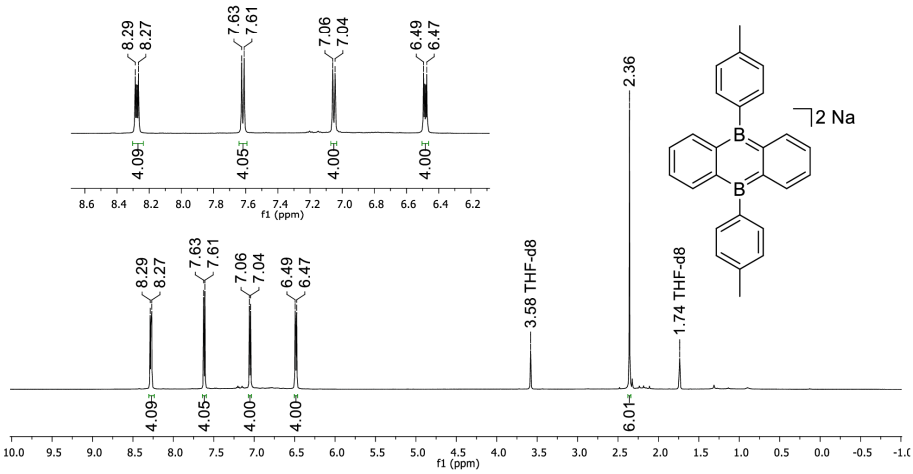

Figure S54. ^{1}H NMR spectrum of Na_2[**7**] (500.2 MHz, THF-d_8).

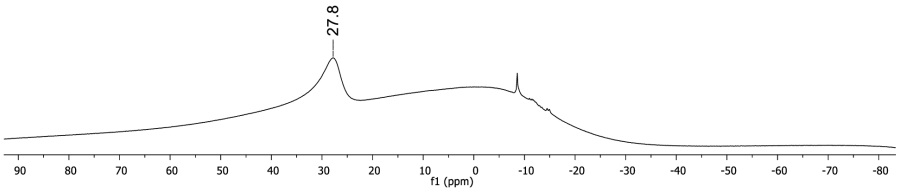

Figure S55. ^{11}B NMR spectrum of Na_2[**7**] (160.5 MHz, THF-d_8).

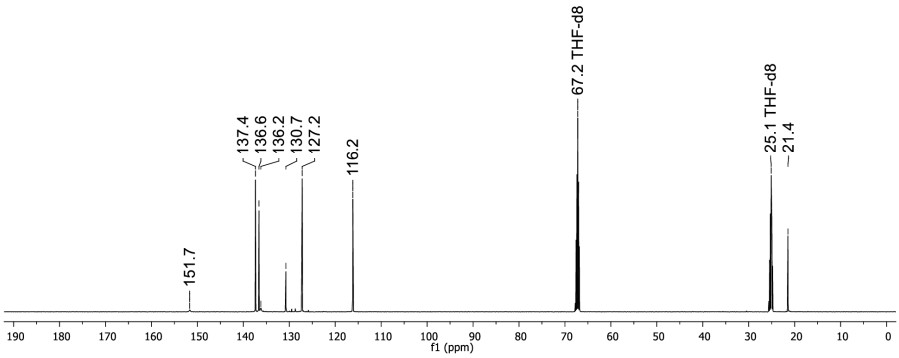

Figure S56. ^{13}C{^{1}H} NMR spectrum of Na_2[**7**] (125.8 MHz, THF-d_8).

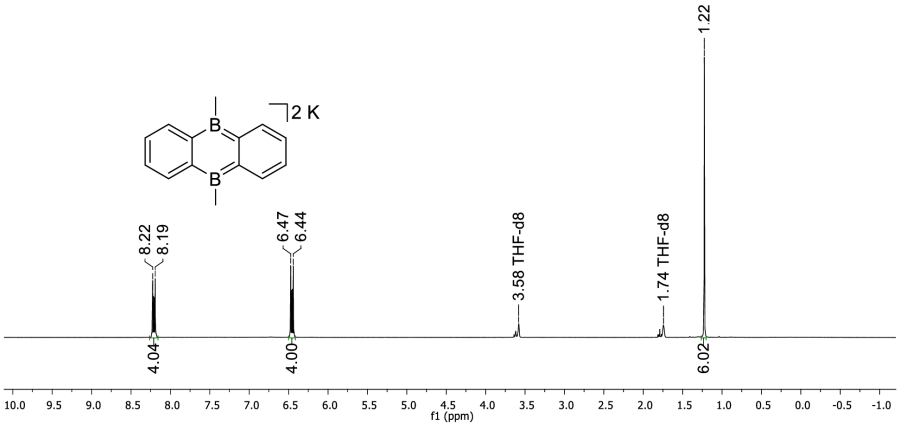

Figure S57. ^{1}H NMR spectrum of K_2[**4**] (300.0 MHz, THF-d_8).

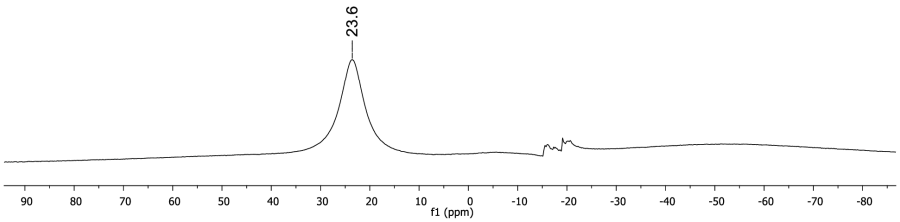

Figure S58. ^{11}B NMR spectrum of K_2[**4**] (96.3 MHz, THF-d_8).

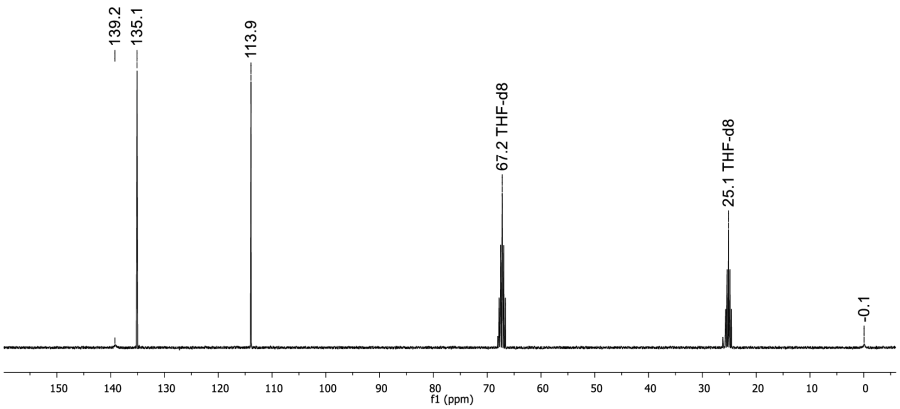

Figure S59. ^{13}C{^{1}H} NMR spectrum of K_2[**4**] (75.4 MHz, THF-d_8).

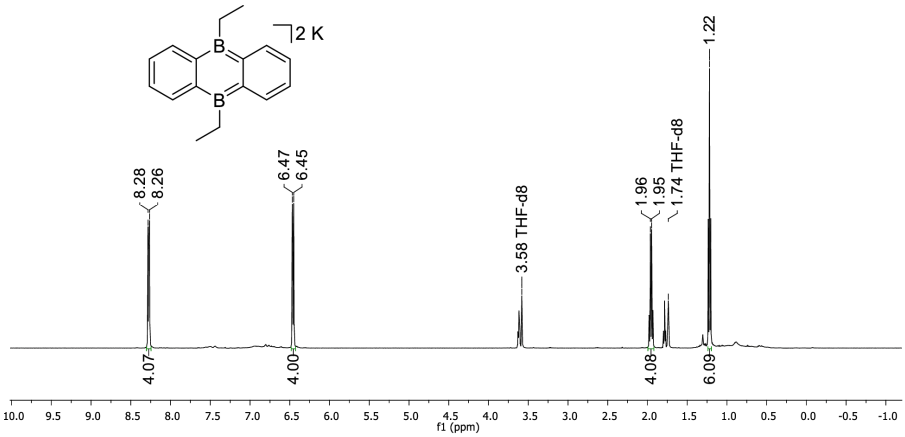

Figure S60. ^{1}H NMR spectrum of K_2[**5**] (500.2 MHz, THF-d_8).

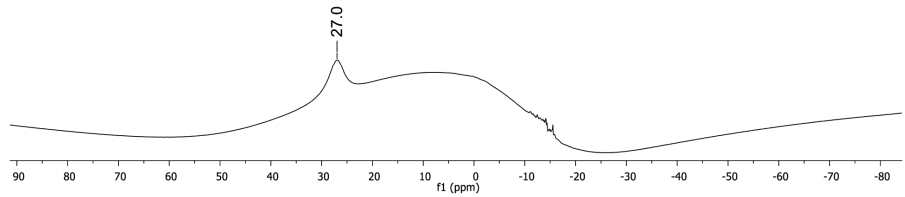

Figure S61. ^{11}B NMR spectrum of K_2[**5**] (160.5 MHz, THF-d_8).

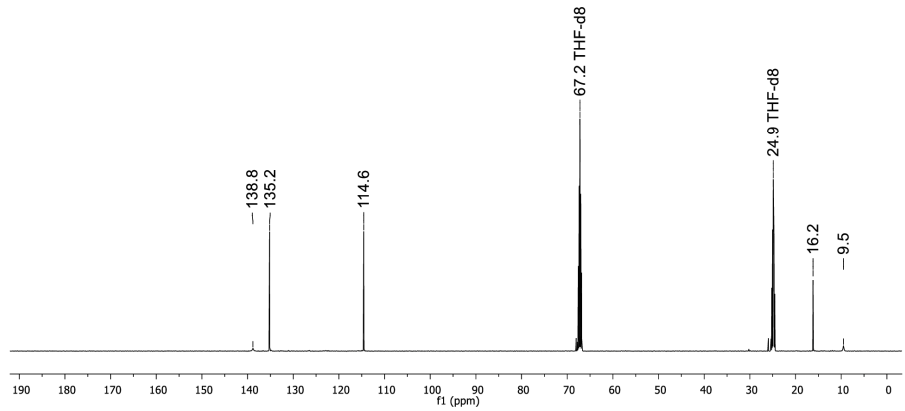

Figure S62. ^{13}C{^{1}H} NMR spectrum of K_2[**5**] (125.8 MHz, THF-d_8).

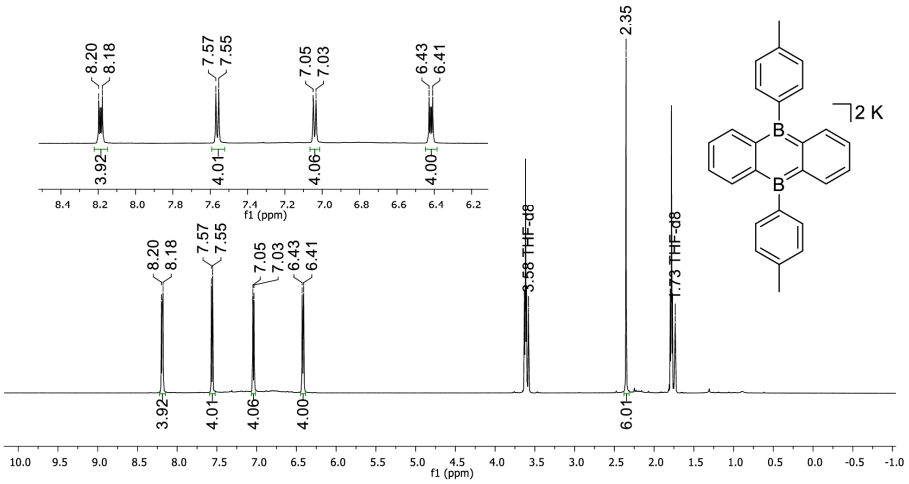

Figure S63. ^{1}H NMR spectrum of K_2[**7**] (500.2 MHz, THF-d_8).

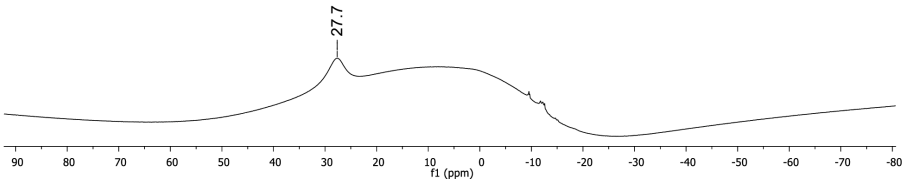

Figure S64. ^{11}B NMR spectrum of K_2[**7**] (160.5 MHz, THF-d_8).

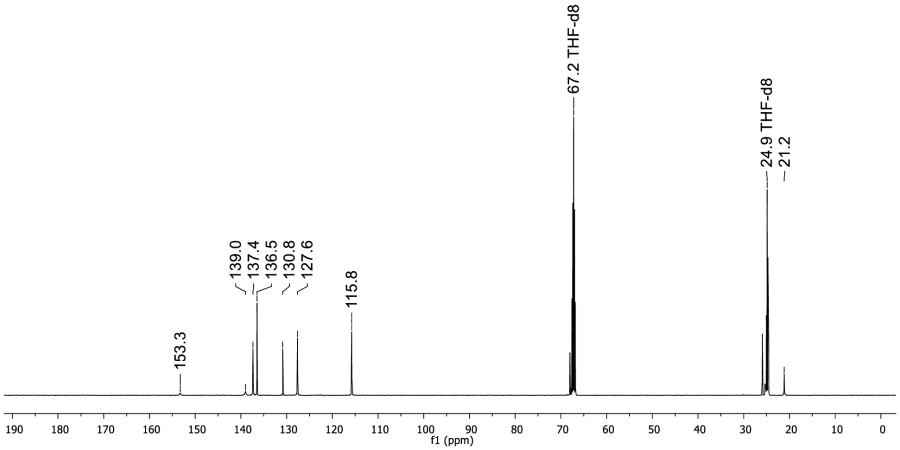

Figure S65. ^{13}C{^{1}H} NMR spectrum of K_2[**7**] (125.8 MHz, THF-d_8).

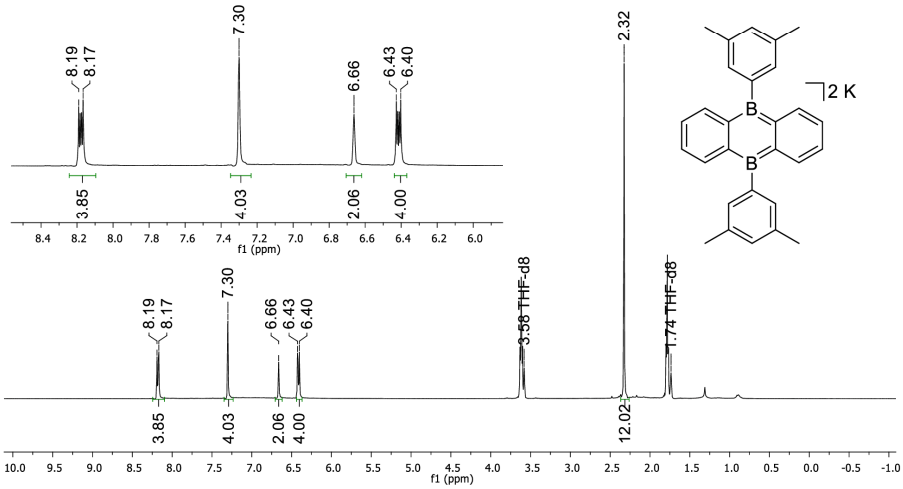

Figure S66. ^{1}H NMR spectrum of K_2[**8**] (400.1 MHz, THF-d_8).

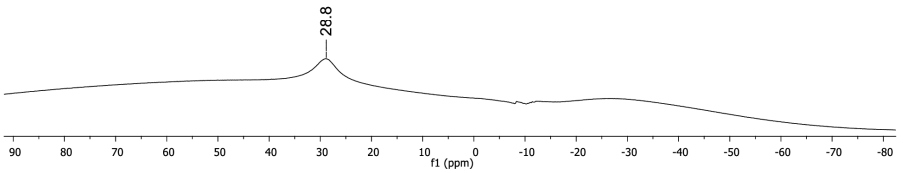

Figure S67. ^{11}B NMR spectrum of K_2[**8**] (128.4 MHz, THF-d_8).

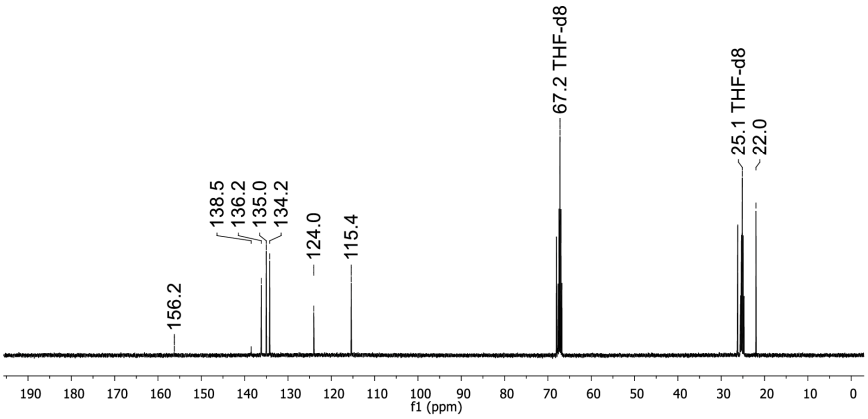

Figure S68. ^{13}C{^{1}H} NMR spectrum of K_2[**8**] (100.6 MHz, THF-d_8).

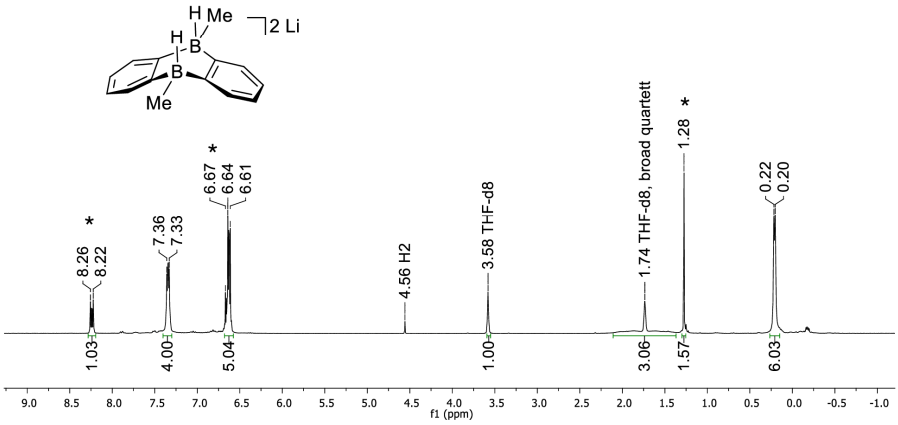

Figure S69. ^{1}H NMR spectrum of Li_2[**4**-H_2] (300.0 MHz, THF-d_8). Asterisks mark resonances of the starting material.

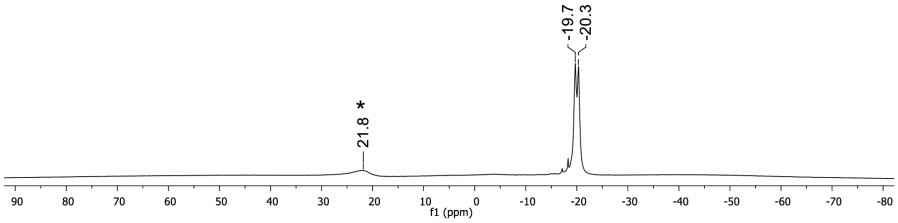

Figure S70. ^{11}B NMR spectrum of Li_2[**4**-H_2] (96.3 MHz, THF-d_8). Asterisk marks resonance of the starting material.

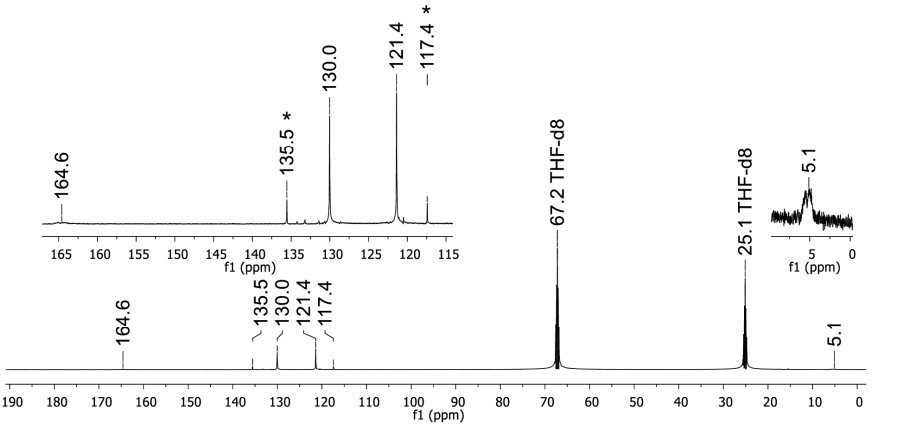

Figure S71. ^{13}C{^{1}H} NMR spectrum of Li_2[**4**-H_2] (125.8 MHz, THF-d_8). Asterisks mark resonances of the starting material.

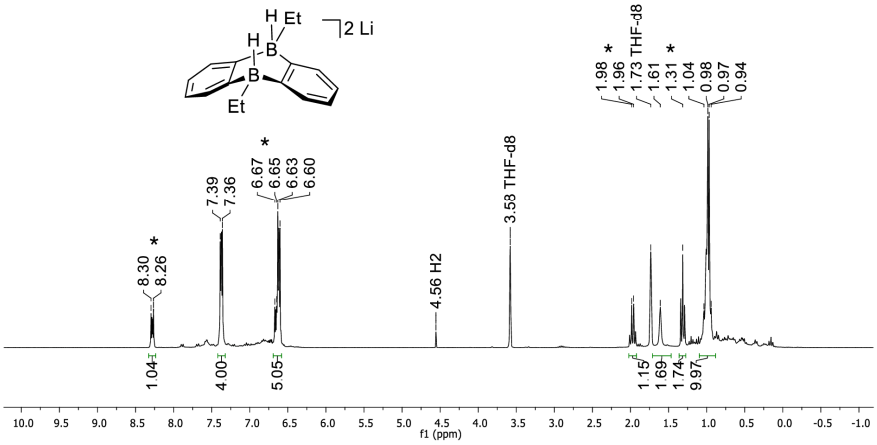

Figure S72. $^{1}H\{^{11}B\}$ NMR spectrum of Li_2[**5**-H_2] (300.0 MHz, THF-d_8). Asterisks mark resonances of the starting material.

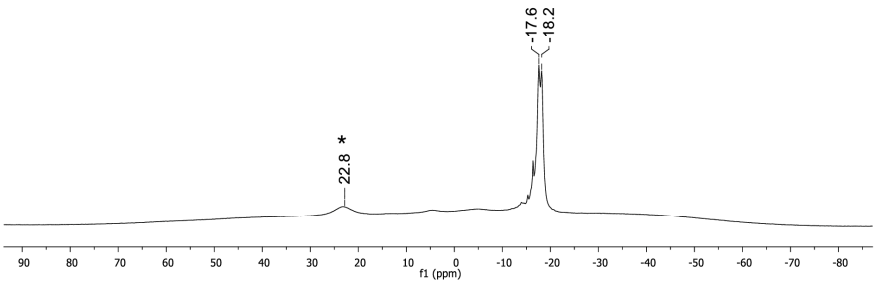

Figure S73. ^{11}B NMR spectrum of Li_2[**5**-H_2] (96.3 MHz, THF-d_8). Asterisk marks resonance of the starting material.

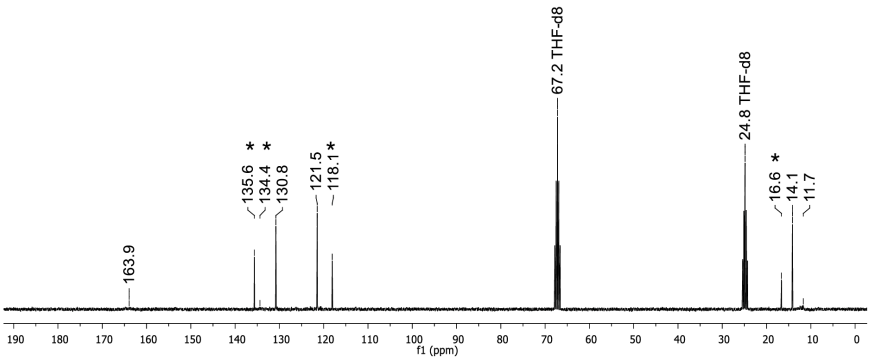

Figure S74. $^{13}C\{^{1}H\}$ NMR spectrum of Li_2[**5**-H_2] (75.4 MHz, THF-d_8). Asterisks mark resonances of the starting material.

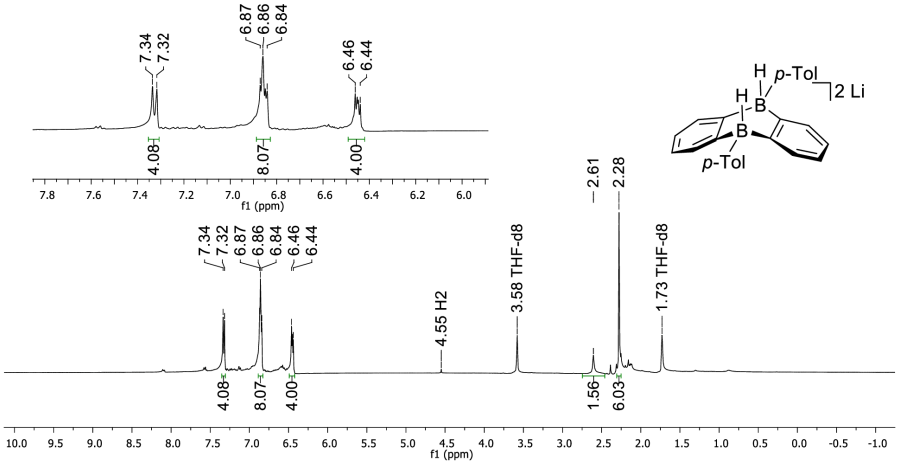

Figure S75. $^{1}H\{^{11}B\}$ NMR spectrum of Li_2[**7**-H_2] (400.1 MHz, THF-d_8).

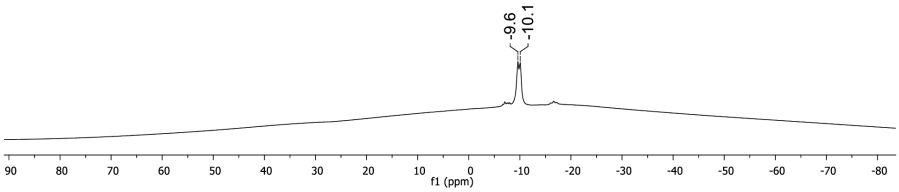

Figure S76. ^{11}B NMR spectrum of Li_2[**7**-H_2] (128.4 MHz, THF-d_8).

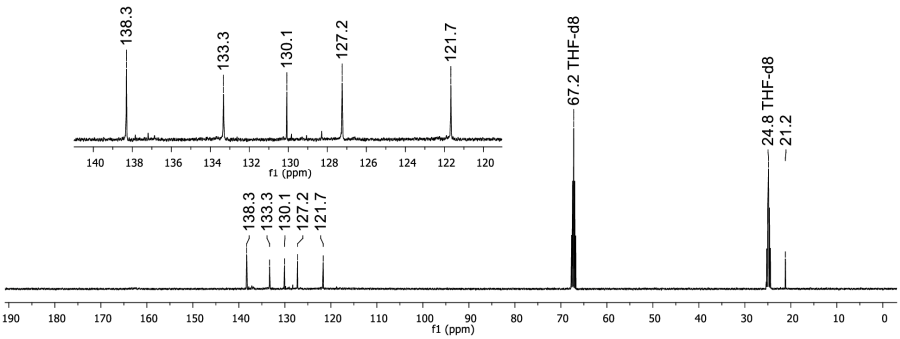

Figure S77. $^{13}C\{^{1}H\}$ NMR spectrum of Li_2[**7**-H_2] (100.6 MHz, THF-d_8).

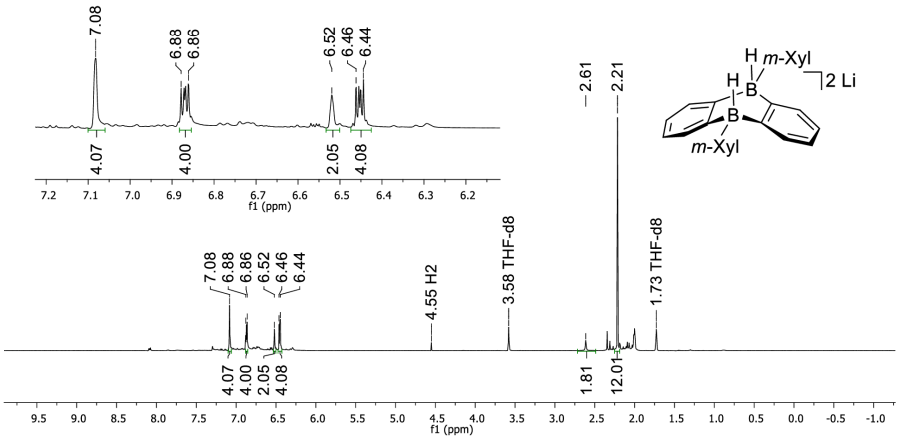

Figure S78. $^{1}H\{^{11}B\}$ NMR spectrum of $Li_2[\mathbf{8}\text{-}H_2]$ (500.2 MHz, THF-d_8).

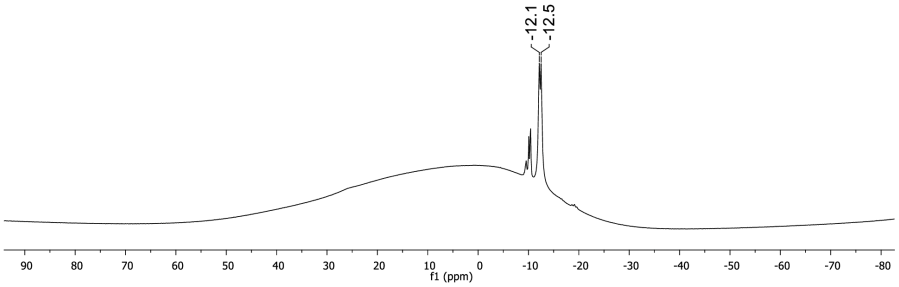

Figure S79. ^{11}B NMR spectrum of $Li_2[\mathbf{8}\text{-}H_2]$ (160.5 MHz, THF-d_8).

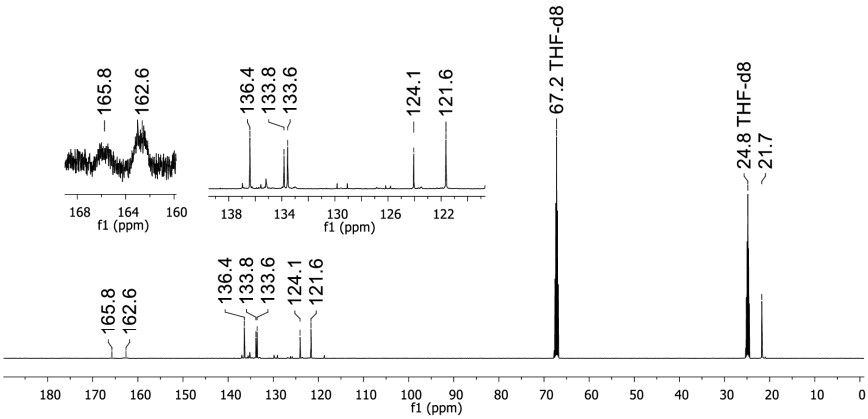

Figure S80. $^{13}C\{^{1}H\}$ NMR spectrum of $Li_2[\mathbf{8}\text{-}H_2]$ (125.8 MHz, THF-d_8).

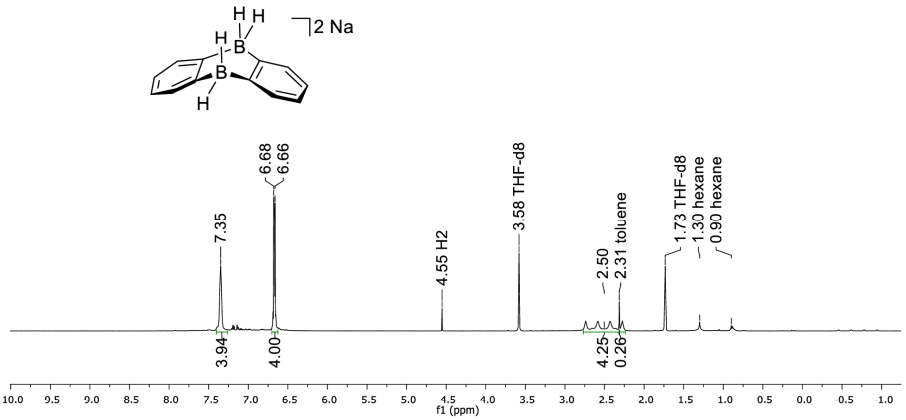

Figure S81. $^{1}H\{^{11}B\}$ NMR spectrum of $Na_2[\mathbf{1}\text{-}H_2]$ (500.2 MHz, THF-d_8).

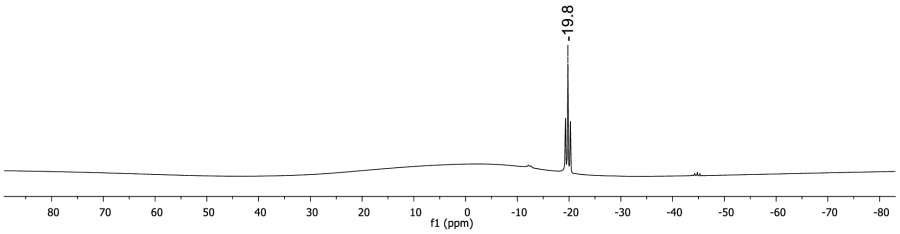

Figure S82. ^{11}B NMR spectrum of $Na_2[\mathbf{1}\text{-}H_2]$ (160.5 MHz, THF-d_8).

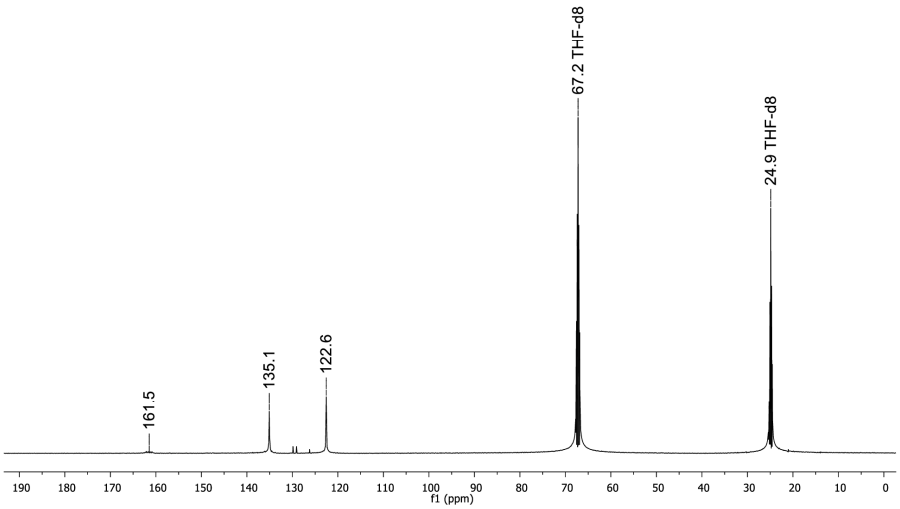

Figure S83. $^{13}C\{^{1}H\}$ NMR spectrum of $Na_2[\mathbf{1}\text{-}H_2]$ (125.8 MHz, THF-d_8).

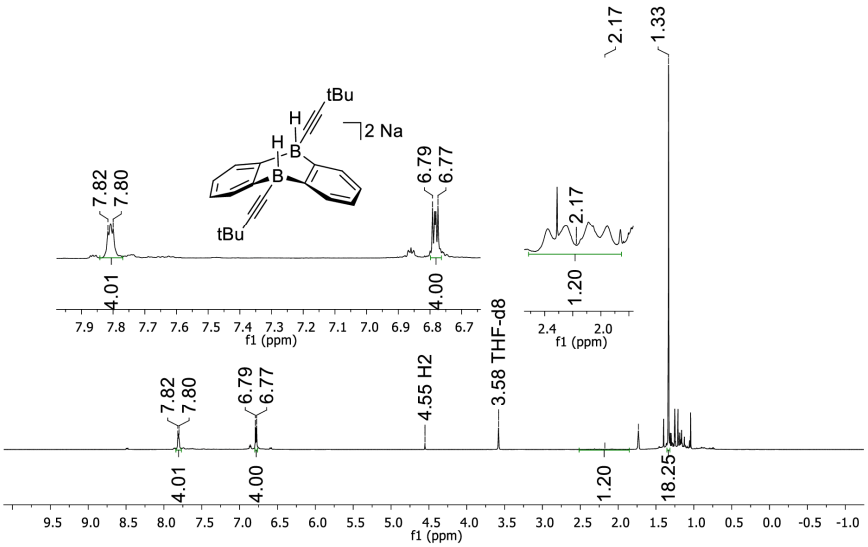

Figure S84. ^{1}H NMR spectrum of Na_2[**2**-H_2] (500.2 MHz, THF-d_8). Unpicked peaks are not specified decomposition products.

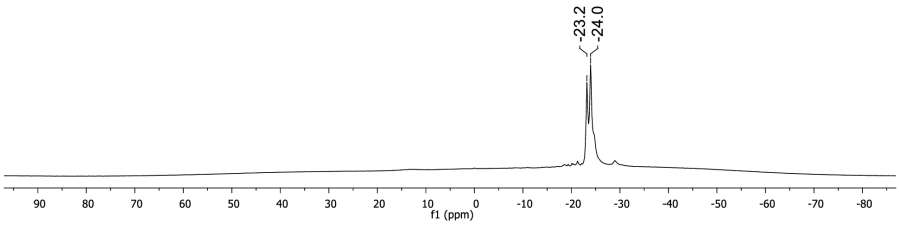

Figure S85. ^{11}B NMR spectrum of Na_2[**2**-H_2] (96.3 MHz, THF-d_8).

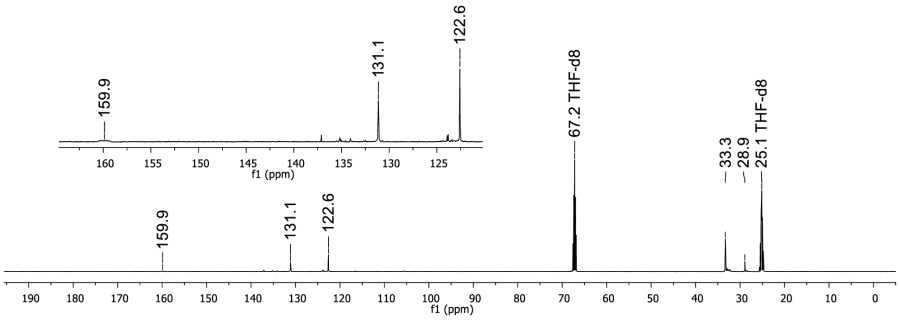

Figure S86. ^{13}C{^{1}H} NMR spectrum of Na_2[**2**-H_2] (125.8 MHz, THF-d_8).

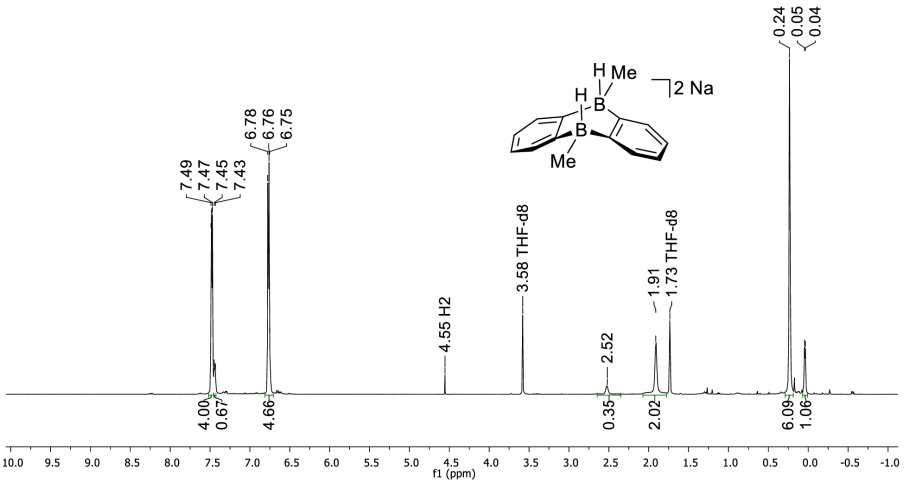

Figure S87. $^{1}H\{^{11}B\}$ NMR spectrum of $Na_2[\mathbf{4}\text{-}H_2]$ (500.2 MHz, THF-d_8).

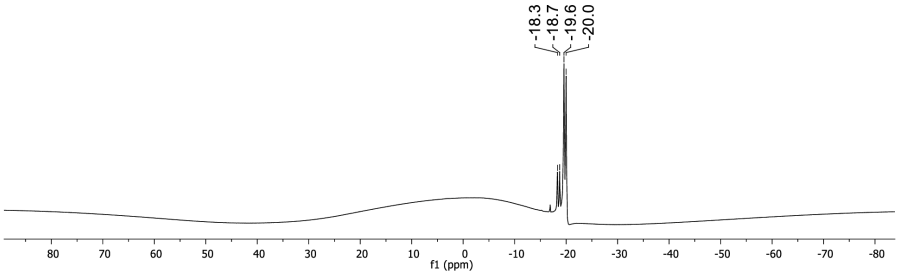

Figure S88. ^{11}B NMR spectrum of $Na_2[\mathbf{4}\text{-}H_2]$ (160.5 MHz, THF-d_8).

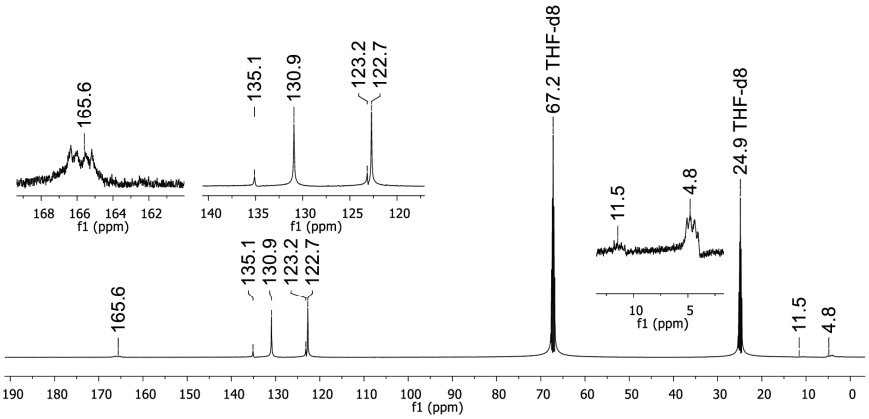

Figure S89. $^{13}C\{^{1}H\}$ NMR spectrum of $Na_2[\mathbf{4}\text{-}H_2]$ (125.8 MHz, THF-d_8).

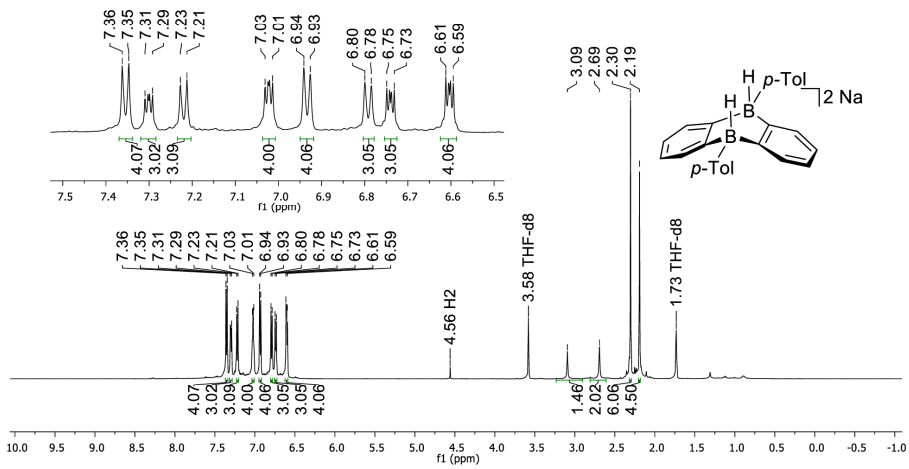

Figure S90. $^{1}H\{^{11}B\}$ NMR spectrum of $Na_2[\mathbf{7}\text{-}H_2]$ (500.2 MHz, THF-d_8).

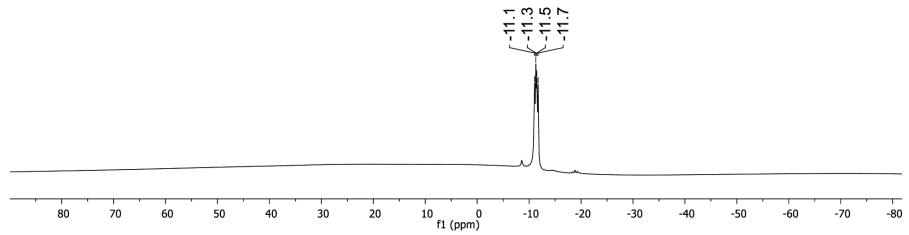

Figure S91. ^{11}B NMR spectrum of $Na_2[\mathbf{7}\text{-}H_2]$ (160.5 MHz, THF-d_8).

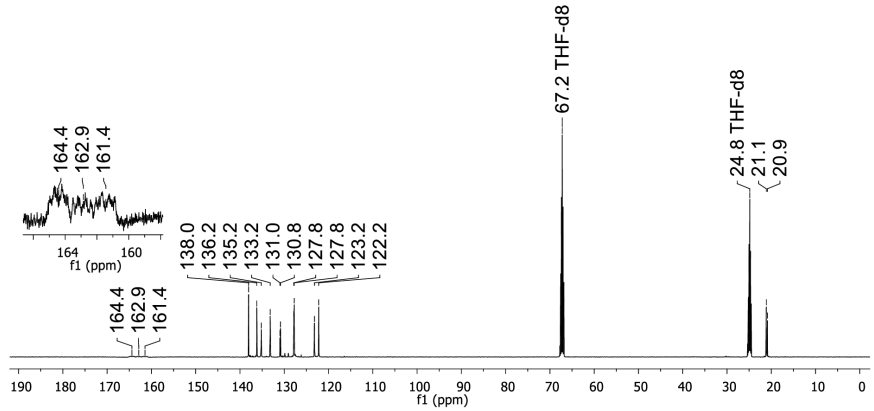

Figure S92. $^{13}C\{^{1}H\}$ NMR spectrum of $Na_2[\mathbf{7}\text{-}H_2]$ (125.8 MHz, THF-d_8).

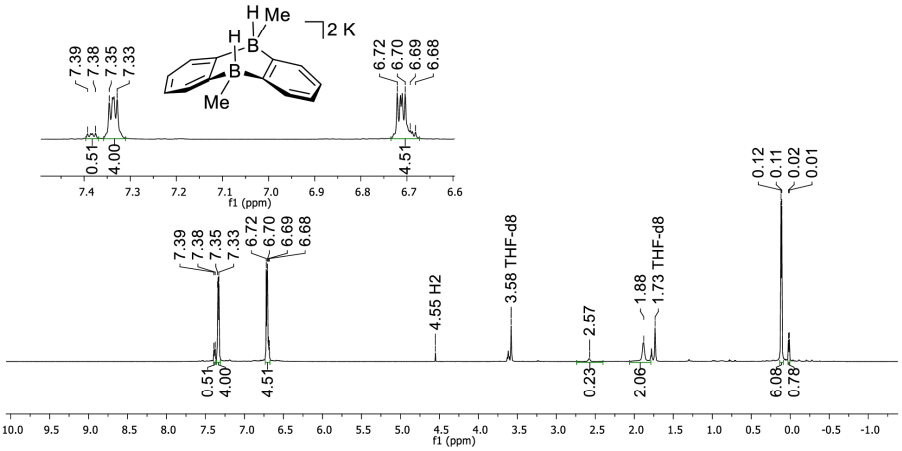

Figure S93. $^{1}H\{^{11}B\}$ NMR spectrum of K_2[**4**-H_2] (500.2 MHz, THF-d_8).

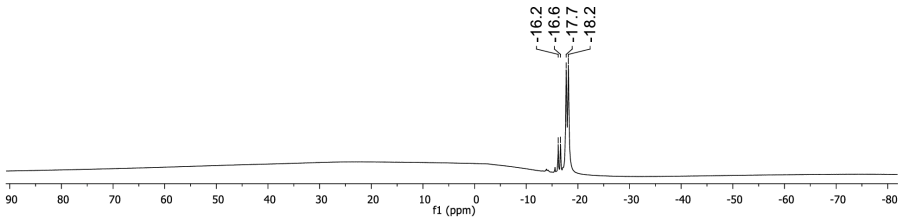

Figure S94. ^{11}B NMR spectrum of K_2[**4**-H_2] (160.5 MHz, THF-d_8).

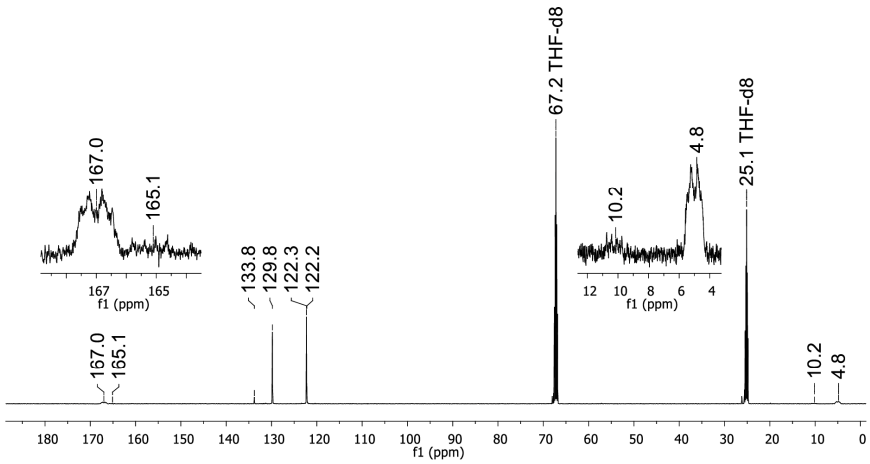

Figure S95. $^{13}C\{^{1}H\}$ NMR spectrum of K_2[**4**-H_2] (125.8 MHz, THF-d_8).

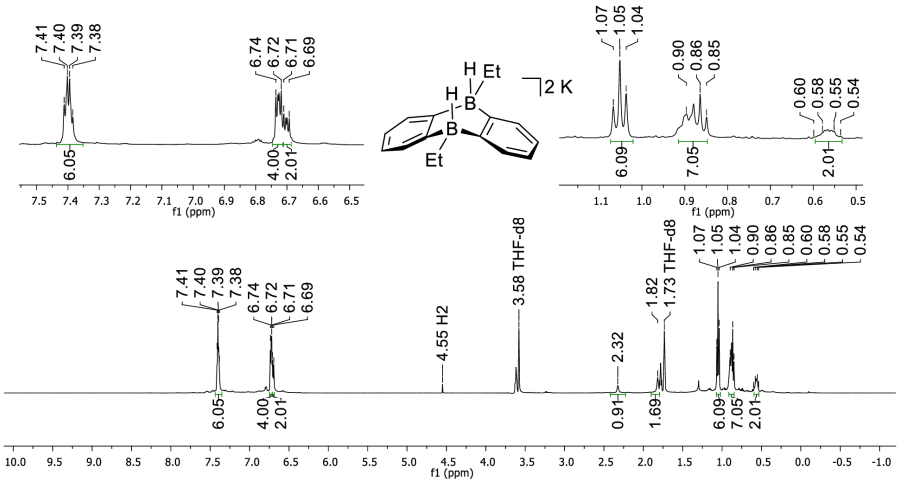

Figure S96. $^{1}H\{^{11}B\}$ NMR spectrum of K_2[**5**-H_2] (500.2 MHz, THF-d_8).

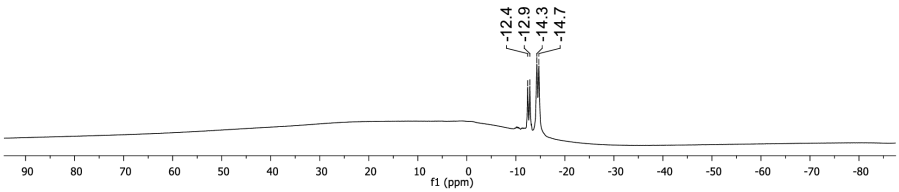

Figure S97. ^{11}B NMR spectrum of K_2[**5**-H_2] (160.5 MHz, THF-d_8).

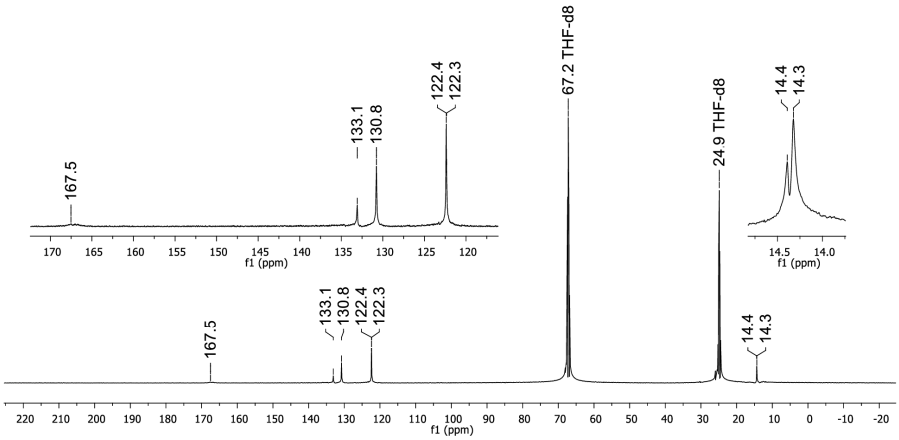

Figure S98. $^{13}C\{^{1}H\}$ NMR spectrum of K_2[**5**-H_2] (125.8 MHz, THF-d_8).

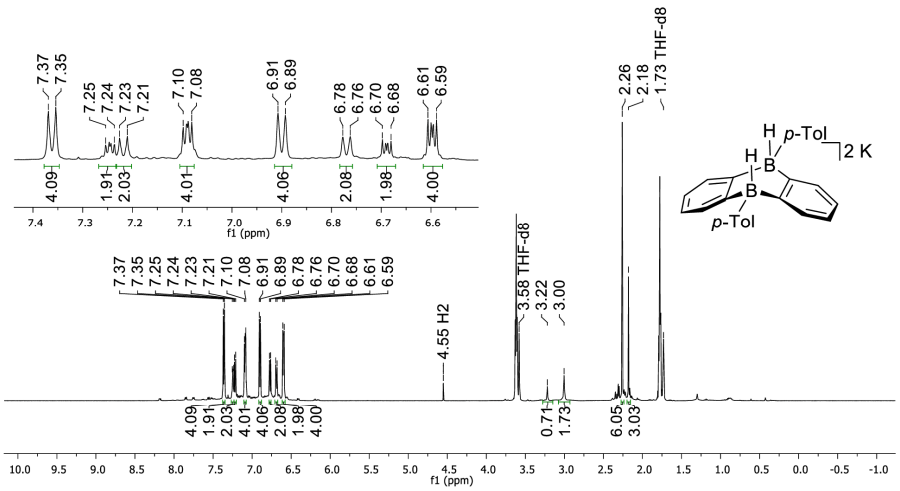

Figure S99. $^{1}H\{^{11}B\}$ NMR spectrum of K_2[**7**-H_2] (500.2 MHz, THF-d_8).

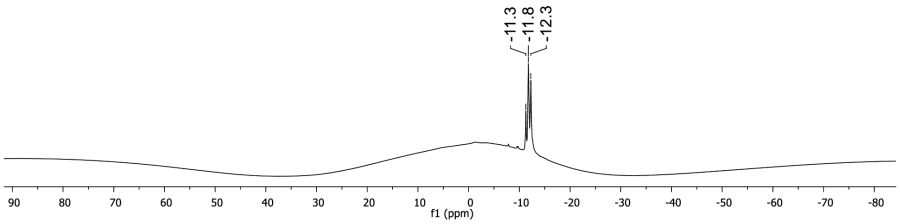

Figure S100. ^{11}B NMR spectrum of K_2[**7**-H_2] (160.5 MHz, THF-d_8).

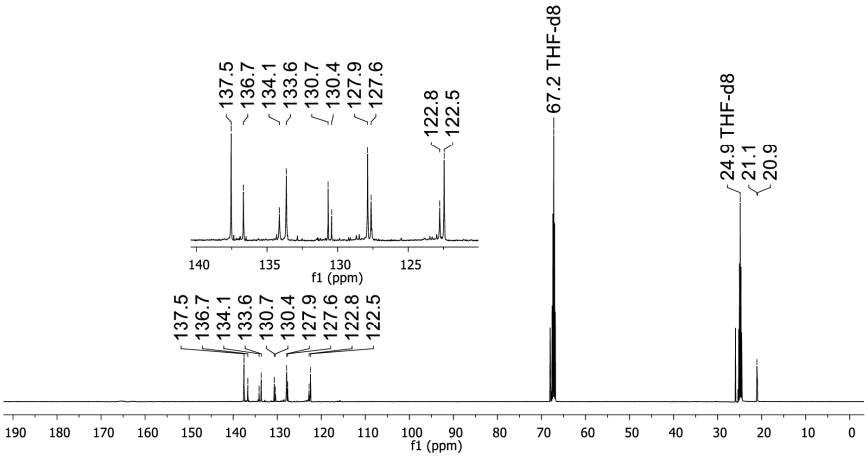

Figure S101. $^{13}C\{^{1}H\}$ NMR spectrum of K_2[**7**-H_2] (125.8 MHz, THF-d_8).

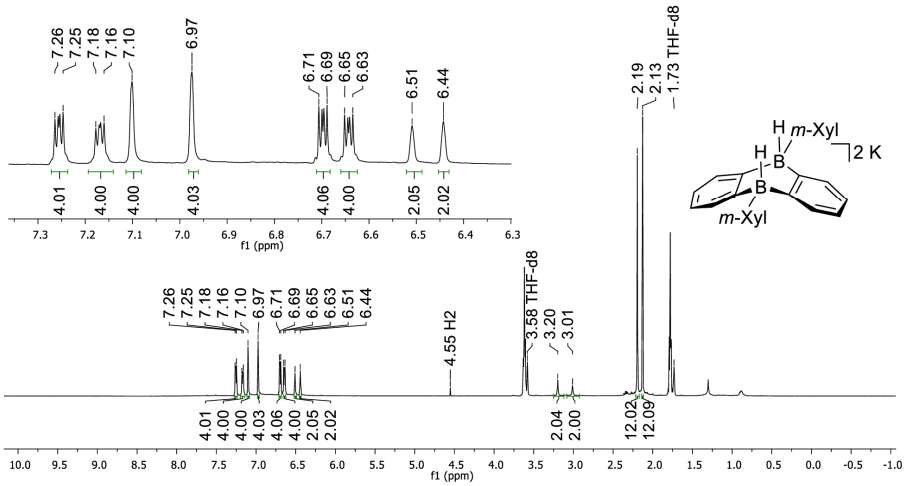

Figure S102. $^{1}H\{^{11}B\}$ NMR spectrum of K_2[**8**-H_2] (500.2 MHz, THF-d_8).

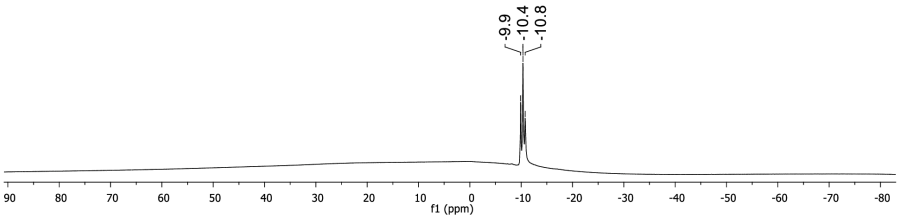

Figure S103. ^{11}B NMR spectrum of K_2[**8**-H_2] (160.5 MHz, THF-d_8).

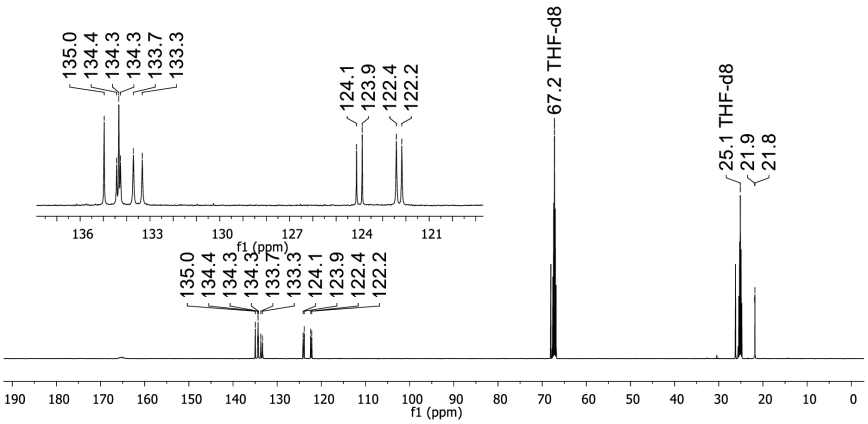

Figure S104. $^{13}C\{^{1}H\}$ NMR spectrum of K_2[**8**-H_2] (125.8 MHz, THF-d_8).

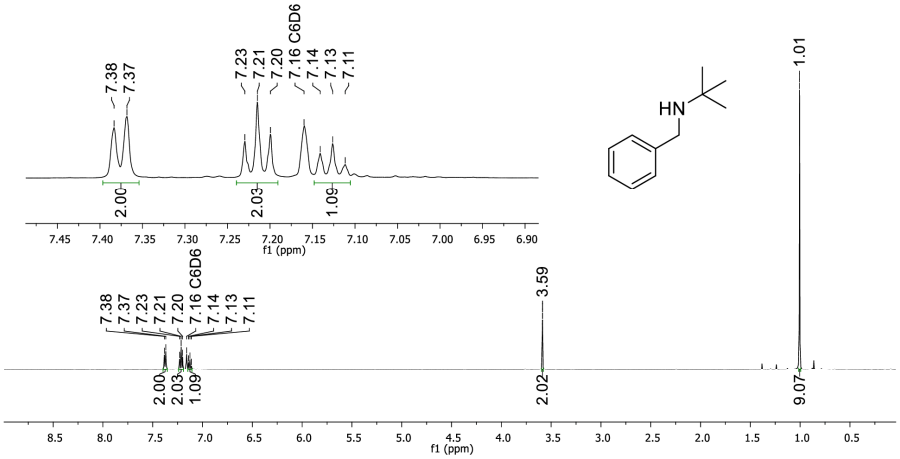

Figure S105. ^{1}H NMR spectrum of the amine Ph(H)$_2$C–N(H)*t*Bu from the autoclave reaction (500.2 MHz, C_6D_6).

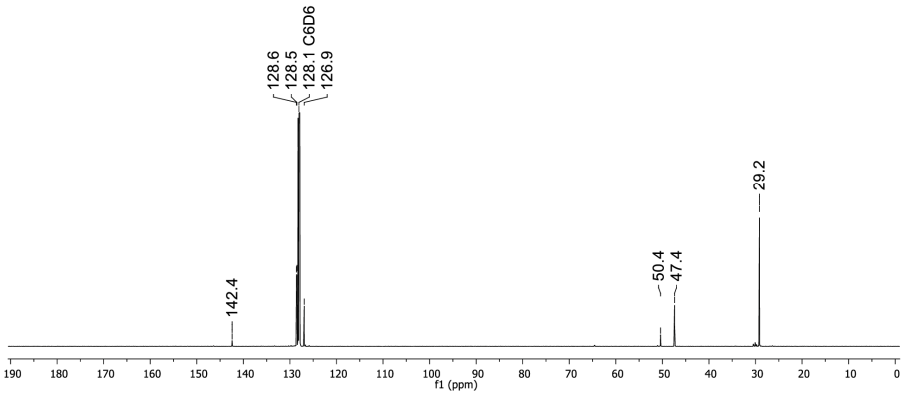

Figure S106. ^{13}C{^{1}H} NMR spectrum of the amine Ph(H)$_2$C–N(H)*t*Bu from the autoclave reaction (125.8 MHz, C_6D_6).

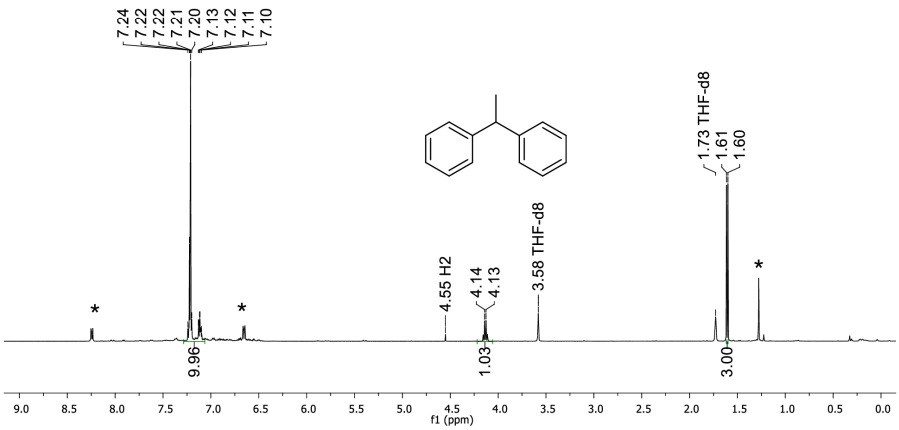

Figure S107. ^{1}H NMR spectrum of 1,1'-diphenylethane (500.2 MHz, THF-d_8). Asterisks mark resonances of the catalyst Li_2[**4**].

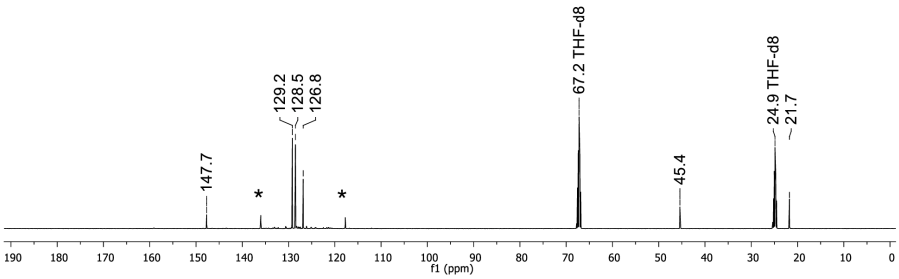

Figure S108. ^{13}C{^{1}H} NMR spectrum of 1,1'-diphenylethane (125.8 MHz, THF-d_8). Asterisks mark resonances of the catalyst Li_2[**4**].

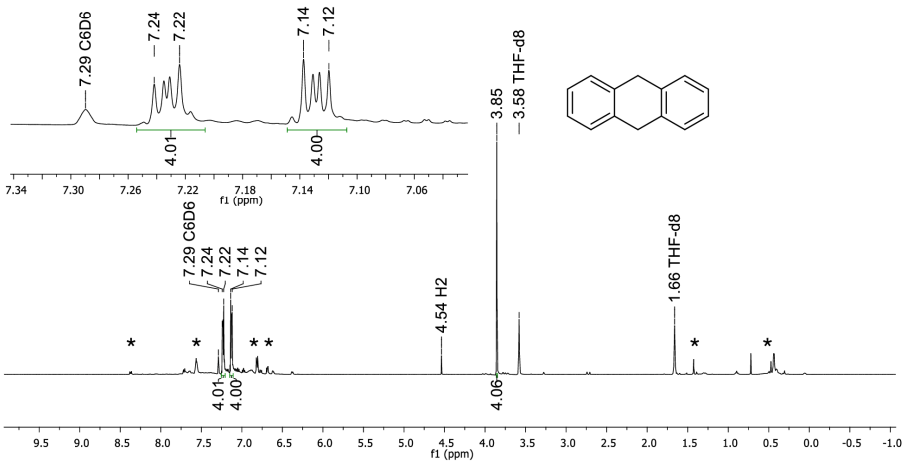

Figure S109. ^{1}H NMR spectrum of 9,10-dihydroanthracene (500.2 MHz, THF-d_8). Asterisks mark resonances of the catalyst Li_2[**4**] and its H_2 addition product.

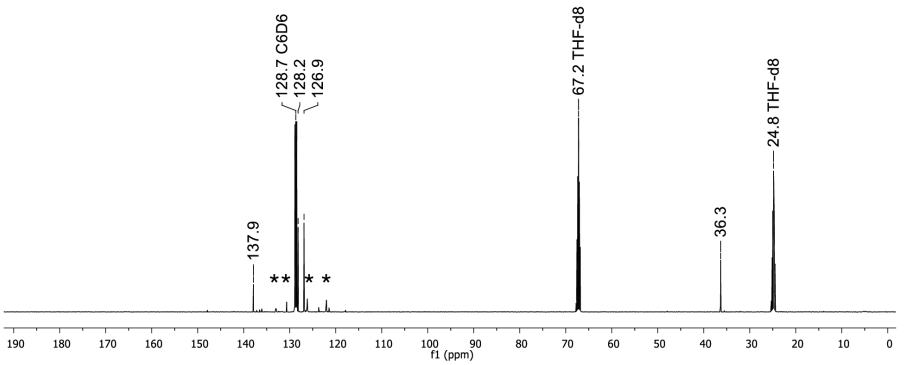

Figure S110. ^{13}C{^{1}H} NMR spectrum of 9,10-dihydroanthracene (125.8 MHz, THF-d_8). Asterisks mark resonances of the catalyst Li_2[**4**] and its H_2 addition product.

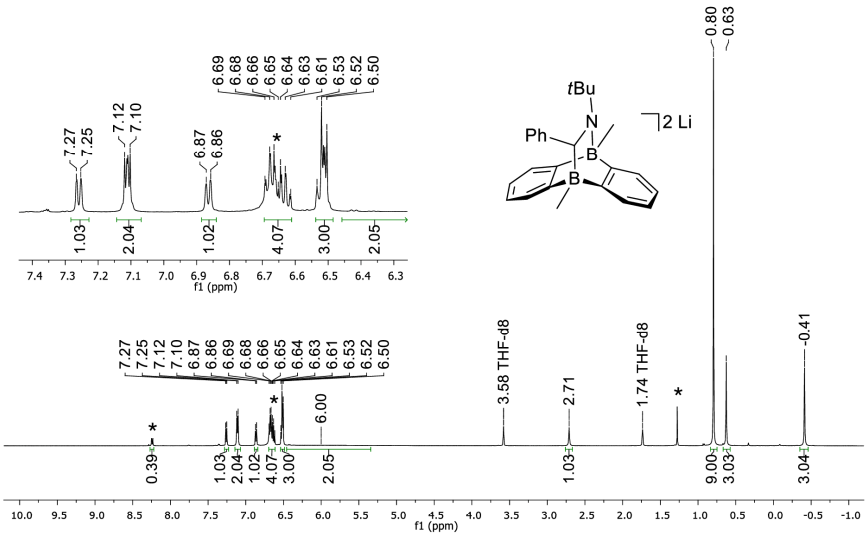

Figure S111. ^{1}H NMR spectrum of Li[**10**] (500.2 MHz, THF-d_8). Asterisks mark resonances of the starting material Li_2[**4**].

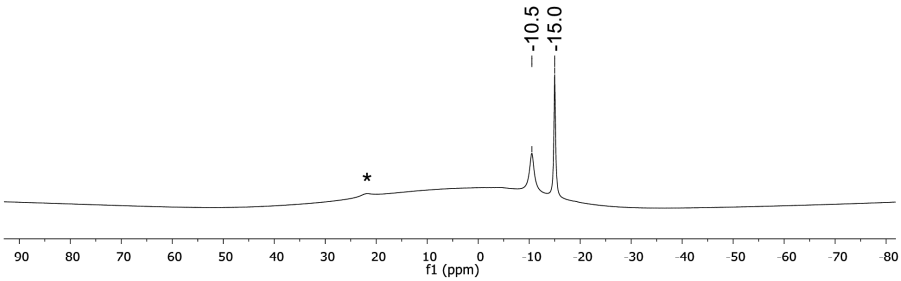

Figure S112. ^{11}B NMR spectrum of Li[**10**] (160.5 MHz, THF-d_8). Asterisk marks resonances of the starting material Li_2[**4**].

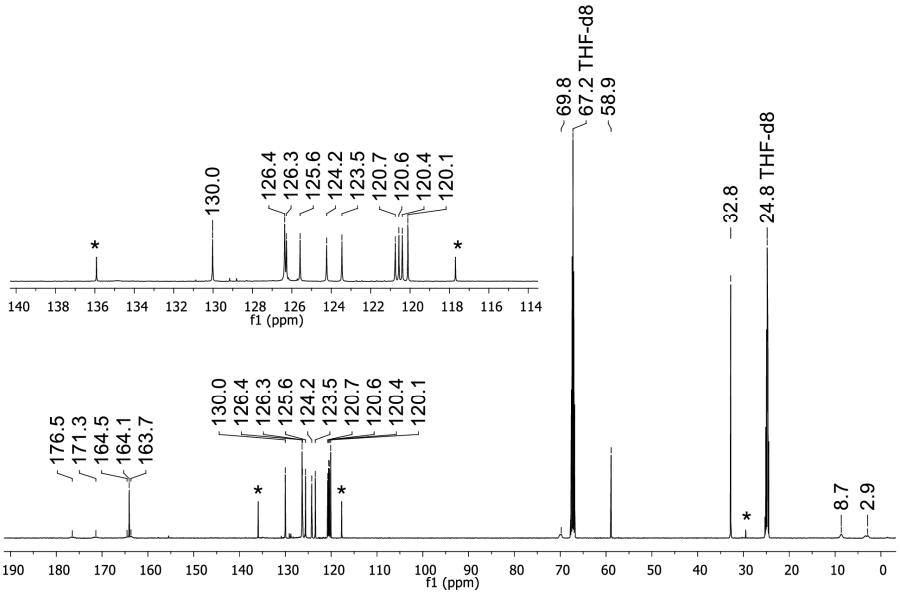

Figure S113. $^{13}C\{^{1}H\}$ NMR spectrum of Li[**10**] (125.8 MHz, THF-d_8). Asterisks mark resonances of the starting material Li_2[**4**].

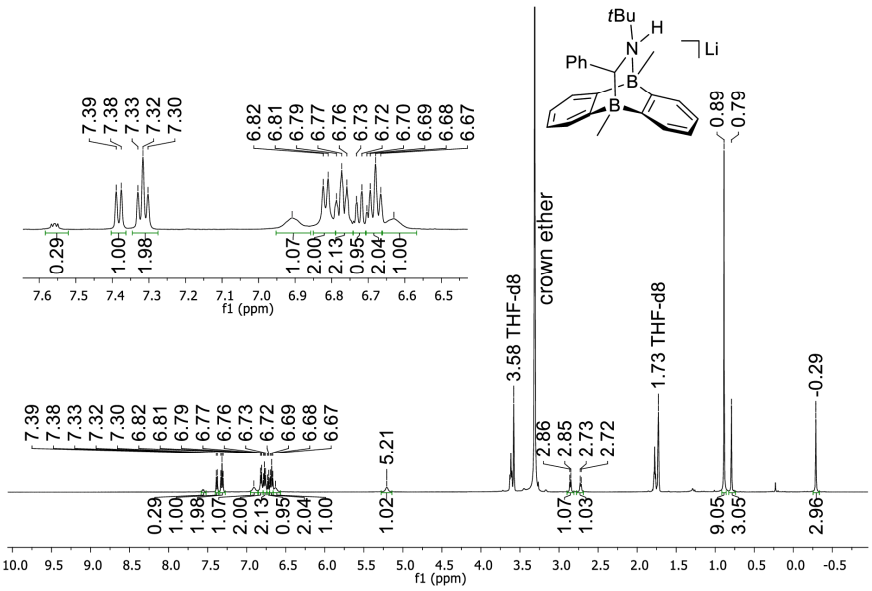

Figure S114. ^{1}H NMR spectrum of crystals of LiH[**10**] (500.2 MHz, THF-d_8).

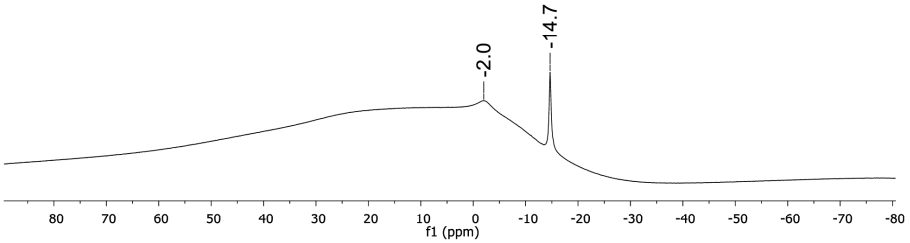

Figure S115. ^{11}B NMR spectrum of crystals of LiH[**10**] (160.5 MHz, THF-d_8).

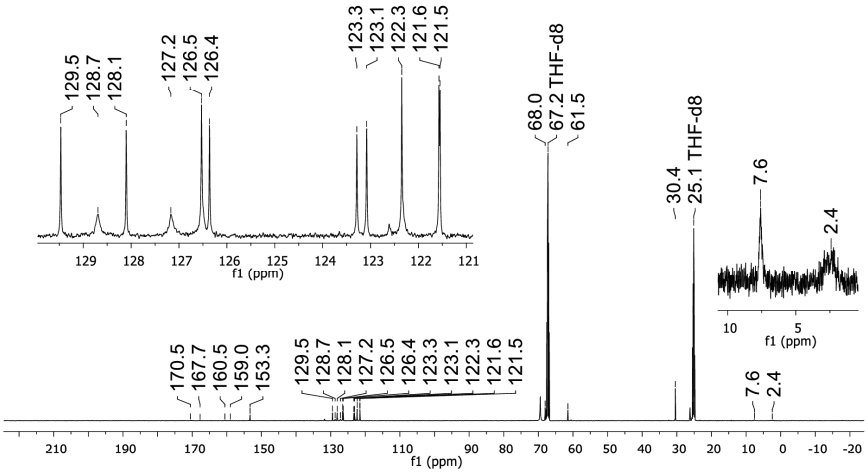

Figure S116. ^{13}C{^{1}H} NMR spectrum of crystals of LiH[**10**] (125.8 MHz, THF-d_8).

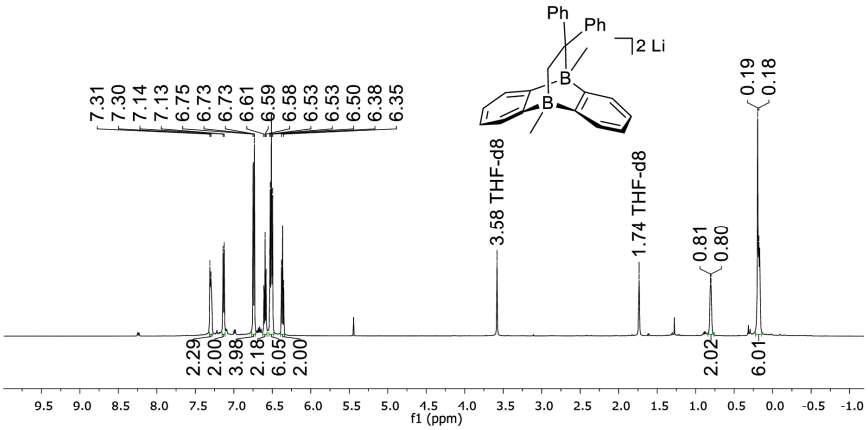

Figure S117. ^{1}H NMR spectrum of the cycloadduct of Li_2[**4**] with 1,1'-diphenylethylene (500.2 MHz, THF-d_8).

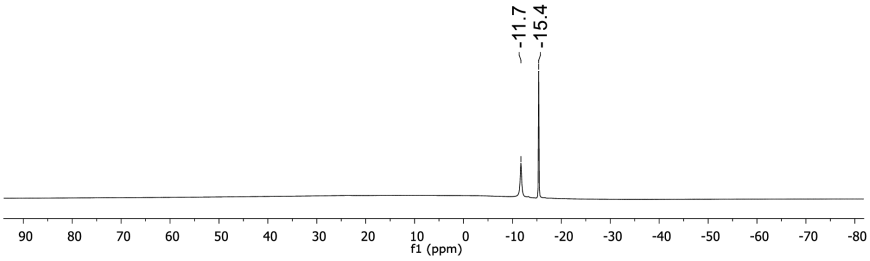

Figure S118. ^{11}B NMR spectrum of the cycloadduct of Li_2[**4**] with 1,1'-diphenylethylene (160.5 MHz, THF-d_8).

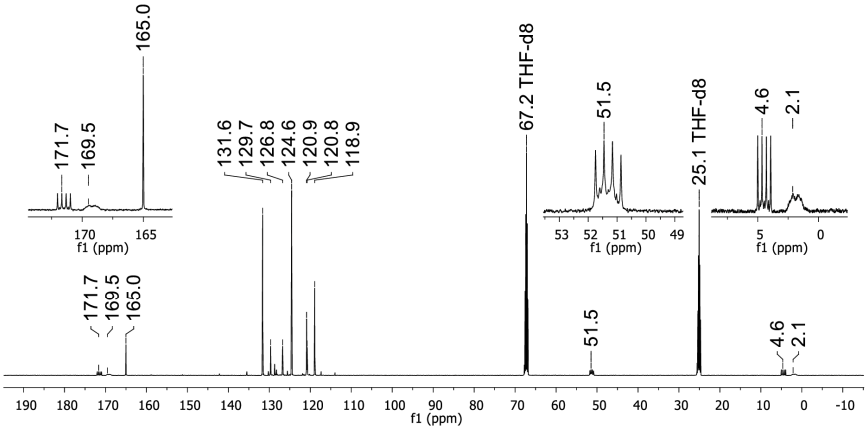

Figure S119. ^{13}C{^{1}H} NMR spectrum of the cycloadduct of Li_2[**4**] with 1,1'-diphenylethylene (125.8 MHz, THF-d_8).

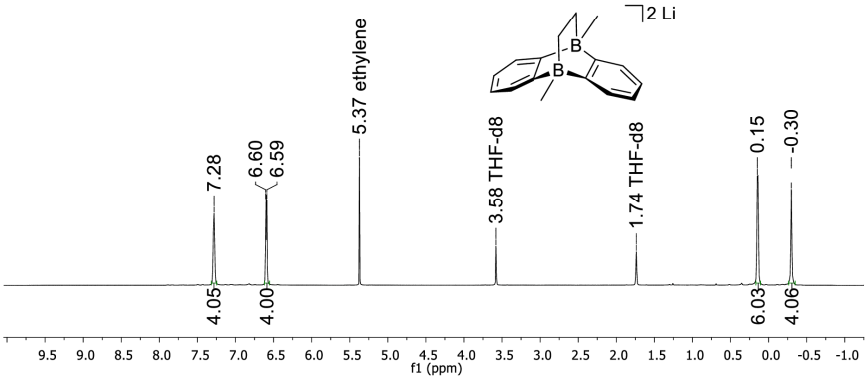

Figure S120. ^{1}H NMR spectrum of Li_2[**11**] (500.2 MHz, THF-d_8).

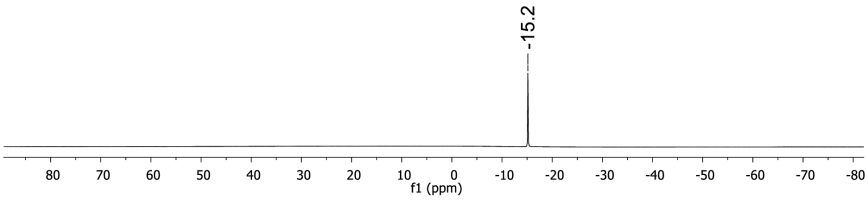

Figure S121. ^{11}B NMR spectrum of Li_2[**11**] (160.5 MHz, THF-d_8).

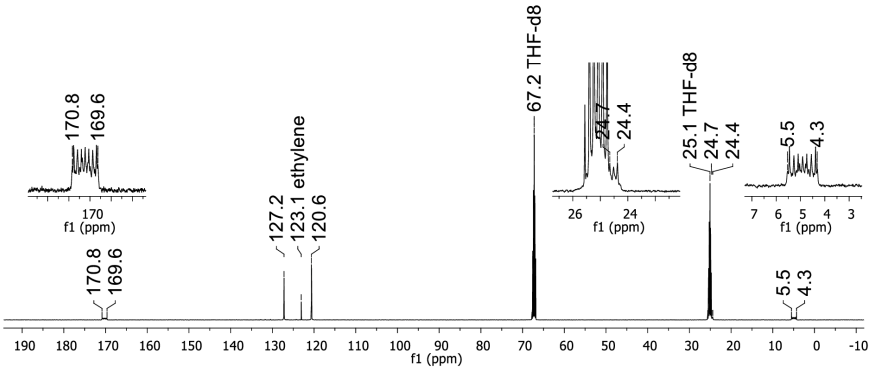

Figure S122. ^{13}C{^{1}H} NMR spectrum of Li_2[**11**] (125.8 MHz, THF-d_8).

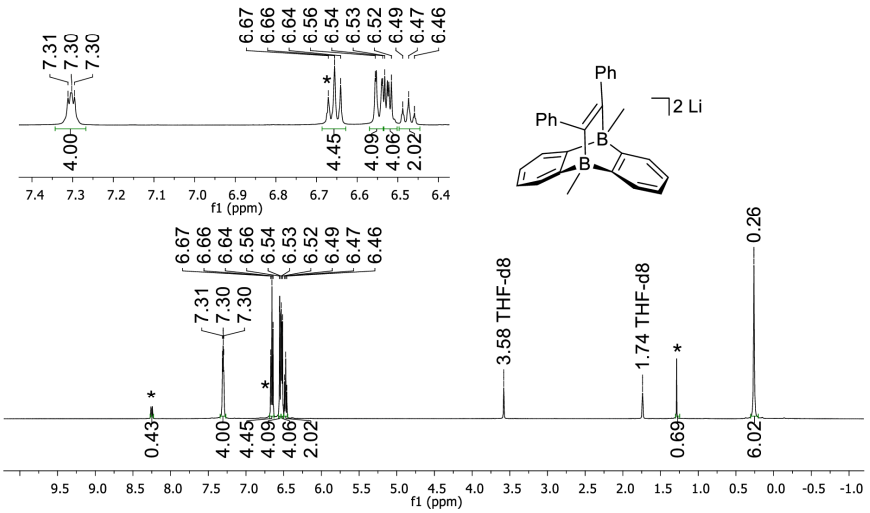

Figure S123. ^{1}H NMR spectrum of the cycloadduct of Li_2[**4**] with diphenylacetylene (500.2 MHz, THF-d_8). Asterisks mark resonances of the starting material Li_2[**4**].

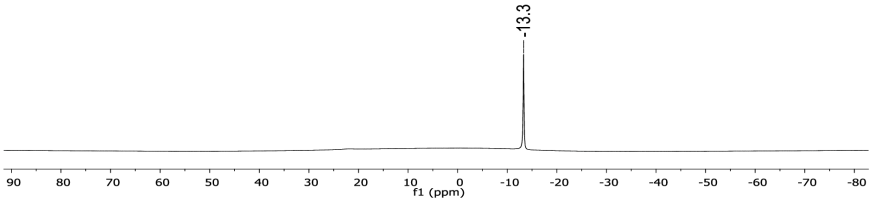

Figure S124. ^{11}B NMR spectrum of the cycloadduct of Li_2[**4**] with diphenylacetylene (160.5 MHz, THF-d_8).

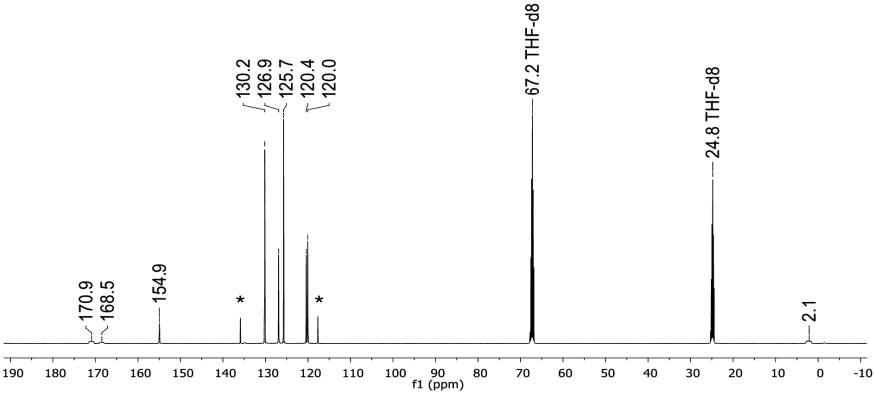

Figure S125. ^{13}C{^{1}H} NMR spectrum of the cycloadduct of Li_2[**4**] with diphenylacetylene (125.8 MHz, THF-d_8). Asterisks mark resonances of the starting material Li_2[**4**].

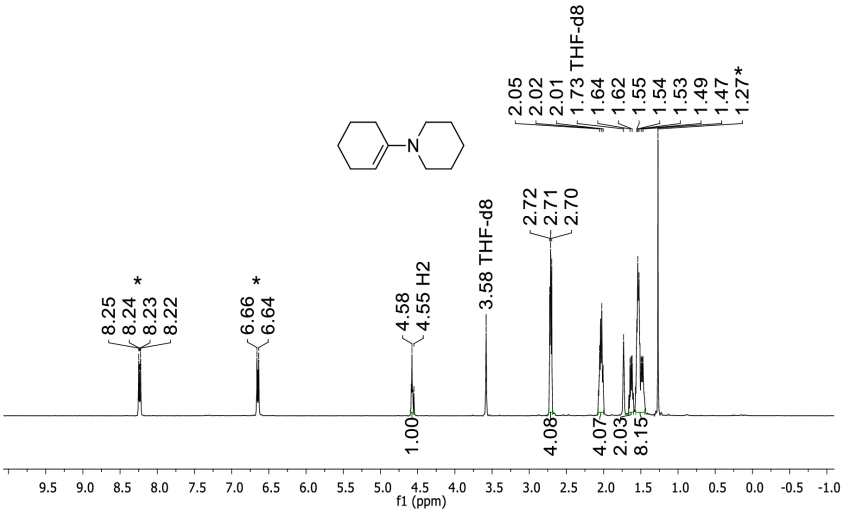

Figure S126. ^{1}H NMR spectrum of 1-(1-piperidinyl)cyclohexene beside Li_2[**4**] (400.1 MHz, THF-d_8).). Asterisks mark resonances of the starting material Li_2[**4**].

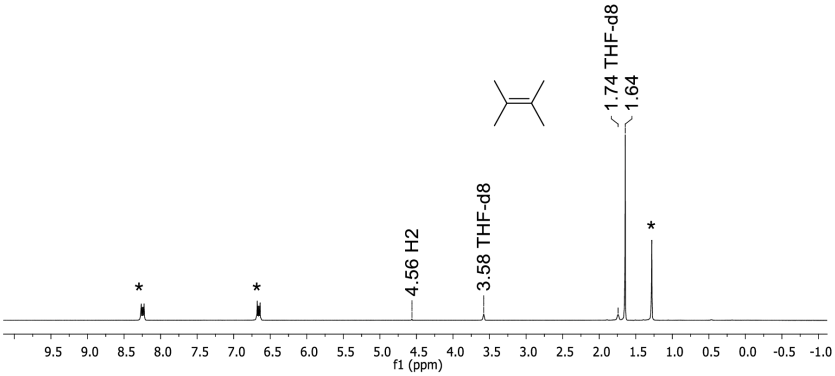

Figure S127. ^{1}H NMR spectrum of 2,3-dimethyl-2-butene beside Li_2[**4**] (250.1 MHz, THF-d_8). Asterisks mark resonances of the starting material Li_2[**4**].

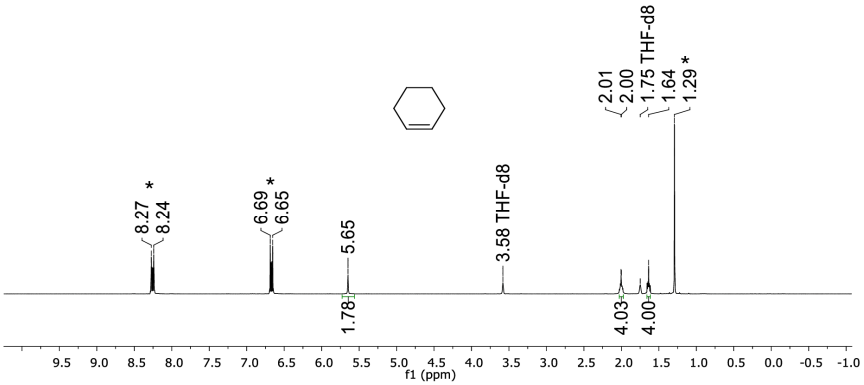

Figure S128. ^{1}H NMR spectrum of cyclohexene beside Li_2[**4**] (300.0 MHz, THF-d_8). Asterisks mark resonances of the starting material Li_2[**4**].

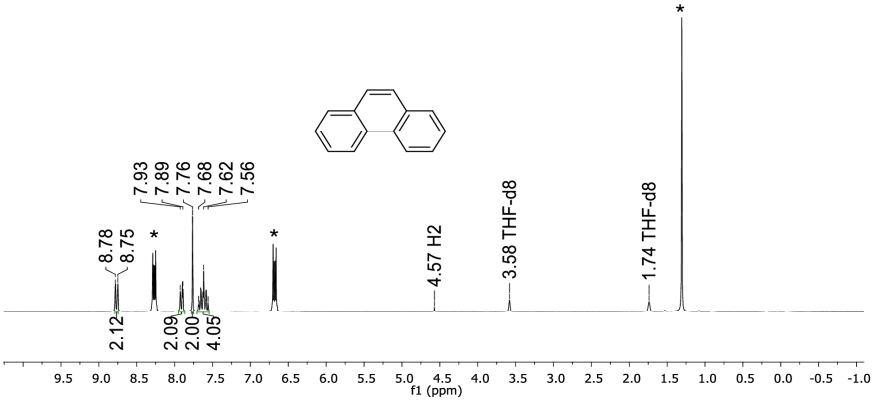

Figure S129. ^{1}H NMR spectrum of phenanthrene beside Li_2[**4**] (250.1 MHz, THF-d_8). Asterisks mark resonances of the starting material Li_2[**4**].

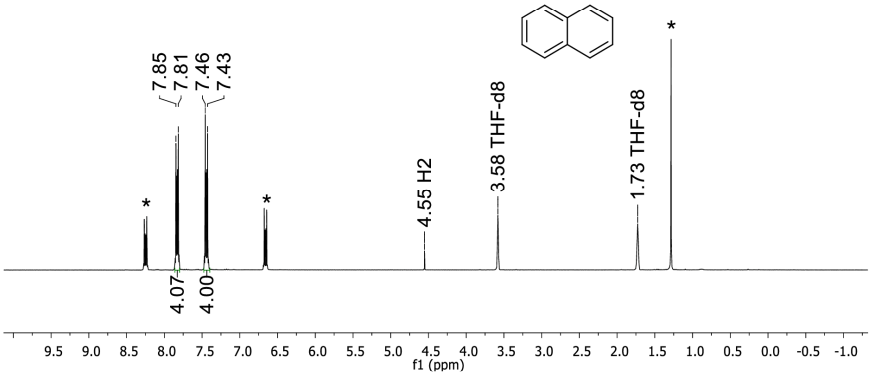

Figure S130. ^{1}H NMR spectrum of naphthalene beside Li_2[**4**] (300.0 MHz, THF-d_8). Asterisks mark resonances of the starting material Li_2[**4**].

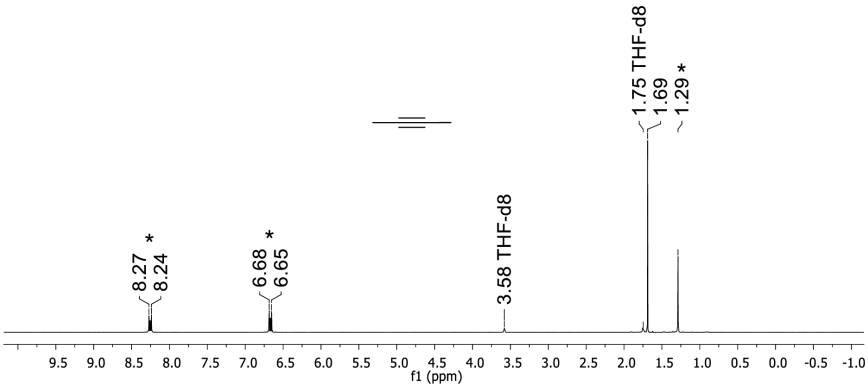

Figure S131. ^{1}H NMR spectrum of 2-butyne beside Li_2[**4**] (300.0 MHz, THF-d_8). Asterisks mark resonances of the starting material Li_2[**4**].

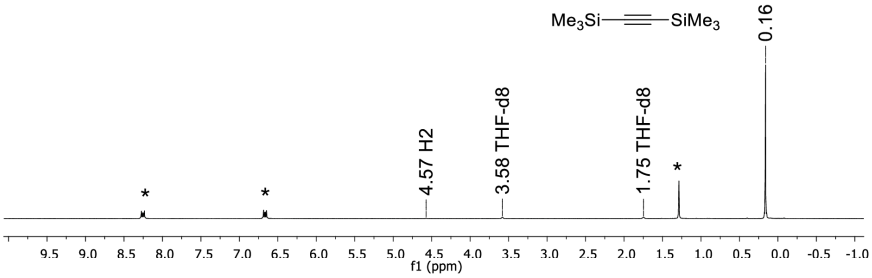

Figure S132. ^{1}H NMR spectrum of bis-(trimethylsilyl)acetylene beside Li_2[**4**] (250.1 MHz, THF-d_8). Asterisks mark resonances of the starting material Li_2[**4**].

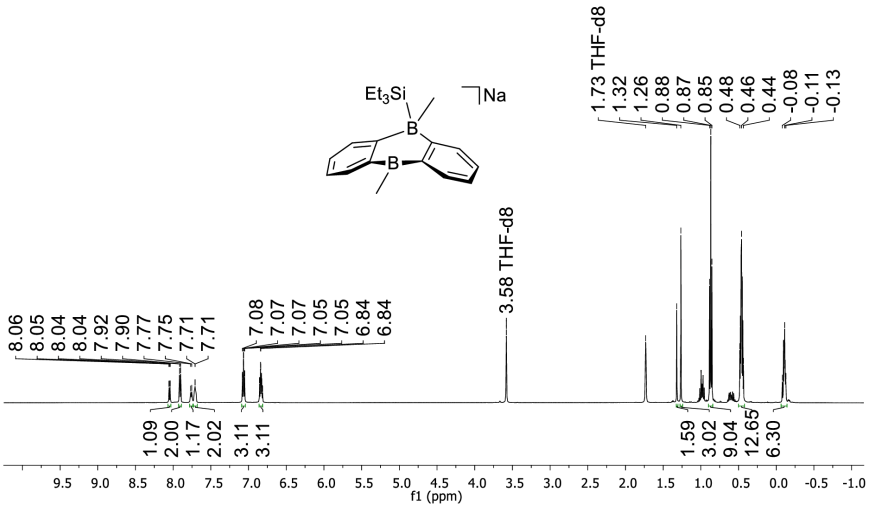

Figure S133. ^{1}H NMR spectrum (500.2 MHz, THF-d_8) recorded 2 d after the addition of Et_3SiCl to a solution of Na_2[**4**] (1:1).

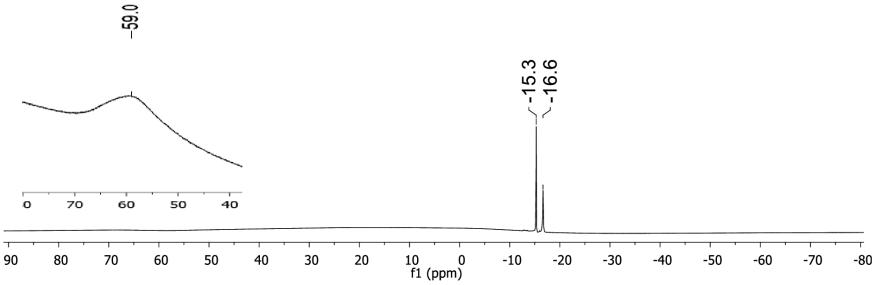

Figure S134. ^{11}B NMR spectrum (160.5 MHz, THF-d_8) recorded 2 d after the addition of Et_3SiCl to a solution of Na_2[**4**] (1:1).

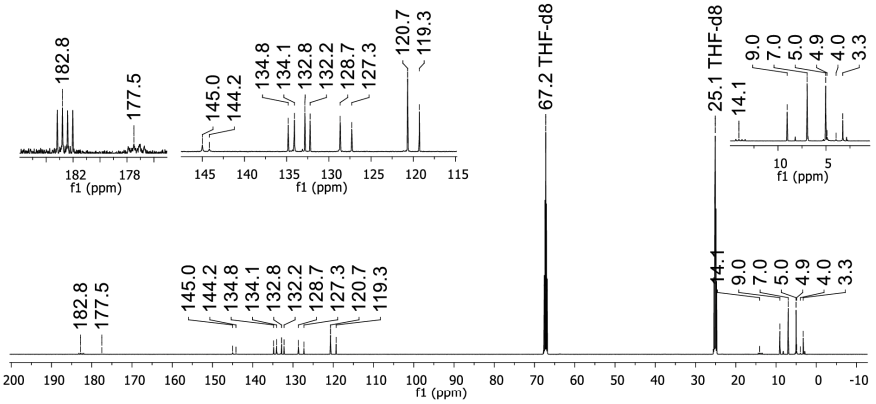

Figure S135. ^{13}C{^{1}H} NMR spectrum (125.8 MHz, THF-d_8) recorded 2 d after the addition of Et_3SiCl to a solution of Na_2[**4**] (1:1).

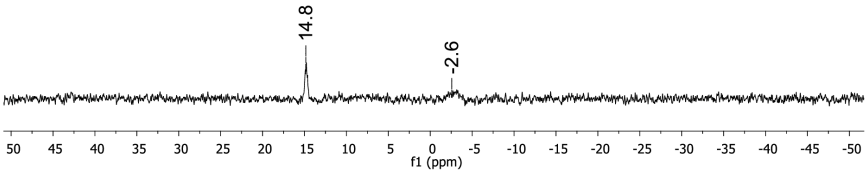

Figure S136. ^{29}Si NMR spectrum (99.4 MHz, THF-d_8) recorded 2 d after the addition of Et_3SiCl to a solution of Na_2[**4**] (1:1).

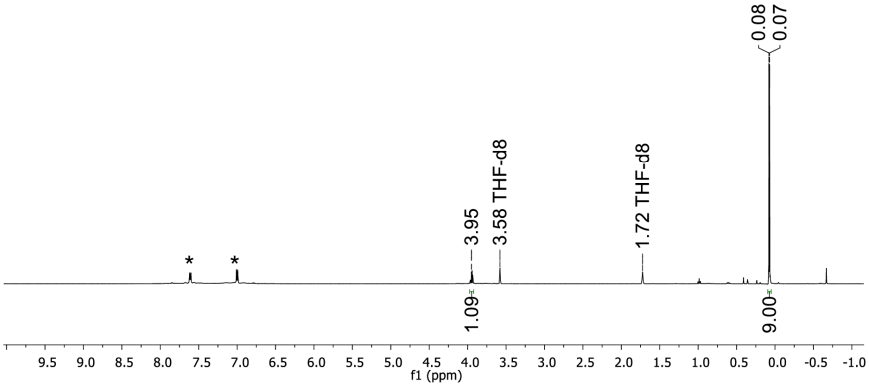

Figure S137. ^{1}H NMR spectrum of the reaction mixture Li_2[**1**-H_2]/Me_3SiCl (500.2 MHz, THF-d_8). Asterisks mark resonances of **1**.

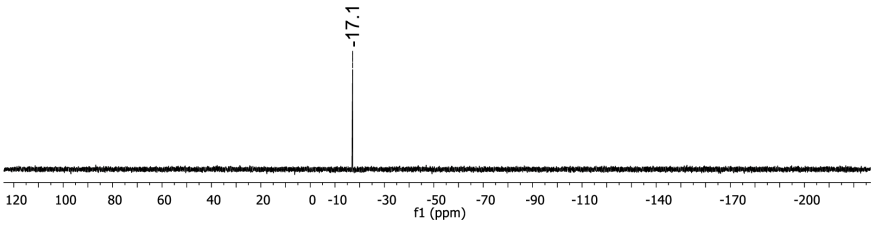

Figure S138. ^{29}Si-INEPT NMR spectrum of the reaction mixture Li_2[**1**-H_2]/Me_3SiCl (99.4 MHz, THF-d_8).

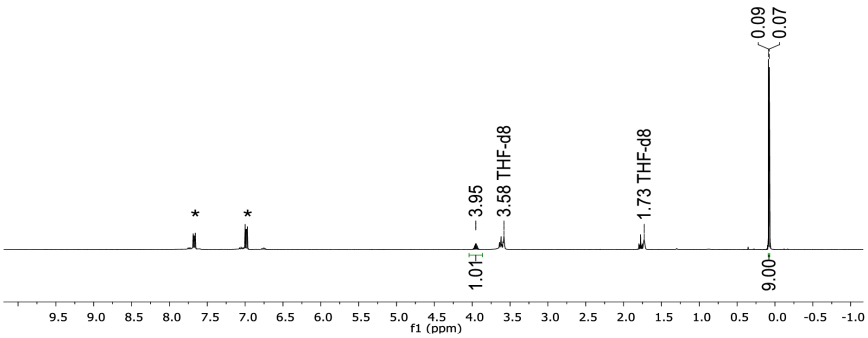

Figure S139. ^{1}H NMR spectrum of the reaction mixture K_2[**1**-H_2]/Me_3SiCl (300.0 MHz, THF-d_8). Asterisks mark resonances of **1**.

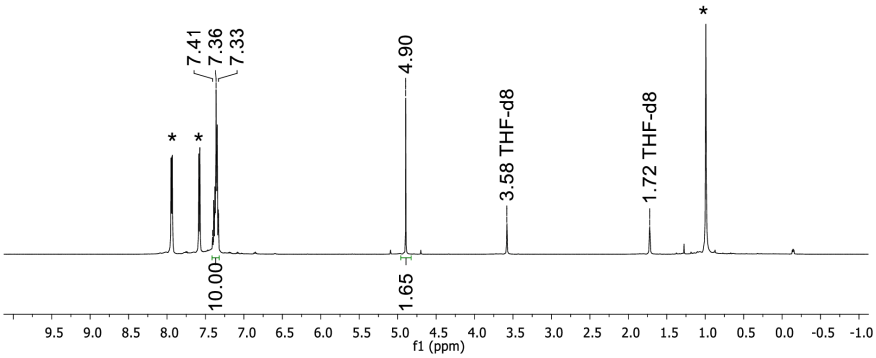

Figure S140. ^{1}H NMR spectrum of the reaction mixture Na_2[**4**-H_2]/Ph_2SiCl_2 (500.2 MHz, THF-d_8). Asterisks mark resonances of **4**.

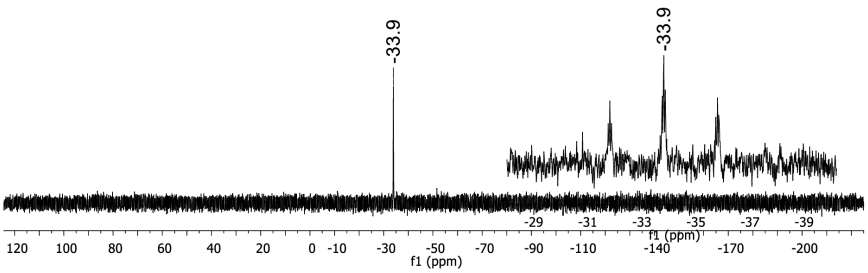

Figure S141. ^{29}Si{^{1}H} NMR spectrum of the reaction mixture Na_2[**4**-H_2]/Ph_2SiCl_2 (99.4 MHz, THF-d_8). The expansion shows the proton-coupled ^{29}Si NMR spectrum.

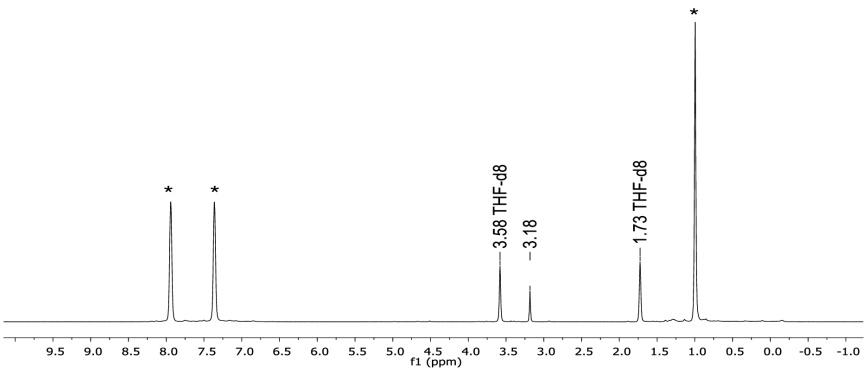

Figure S142. ^{1}H NMR spectrum of the reaction mixture Na_2[**4**-H_2]/$SiCl_4$ (400.1 MHz, THF-d_8). Asterisks mark resonances of **4**.

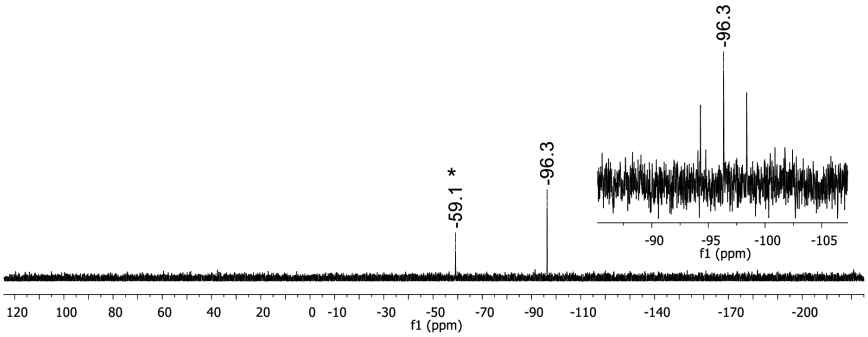

Figure S143. $^{29}Si\{^{1}H\}$ NMR spectrum of the reaction mixture Na_2[**4**-H_2]/$SiCl_4$ (99.4 MHz, THF-d_8). The NMR spectrum was measured several months after the initial reaction so that a second species formed which is marked with an asterisk. The expansion shows the proton-coupled ^{29}Si NMR spectrum.

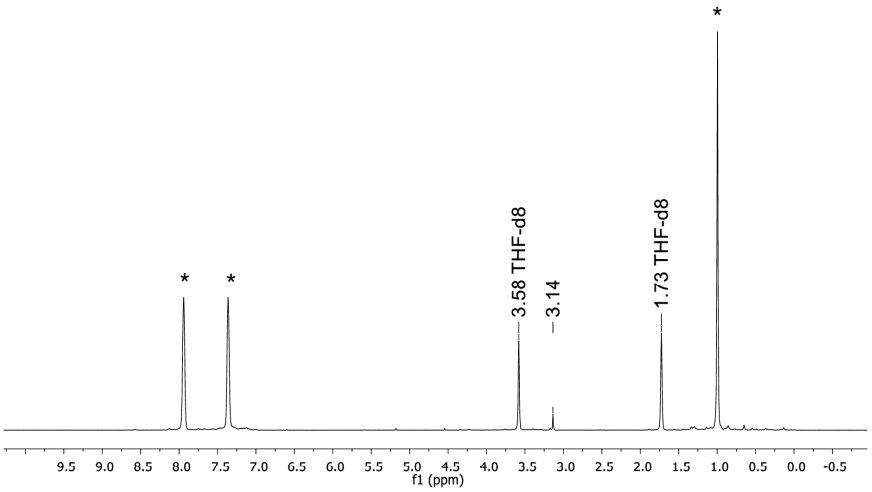

Figure S144. ^{1}H NMR spectrum of the reaction mixture Na_2[**4**-H_2]/$GeCl_4$ (400.1 MHz, THF-d_8). Asterisks mark resonances of **4**.

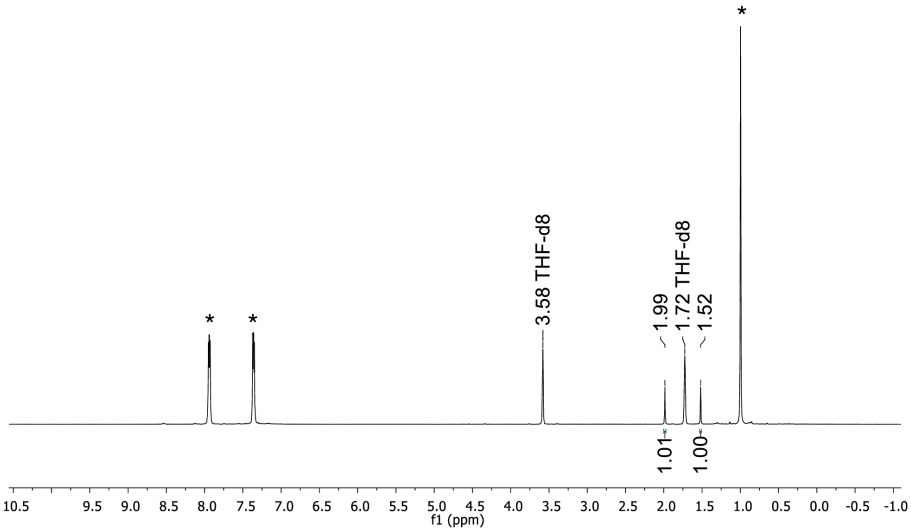

Figure S145. ^{1}H NMR spectrum of the reaction between Na_2[**4**-H_2] and PCl_3 (400.1 MHz, THF-d_8). Asterisks mark resonances of **4**.

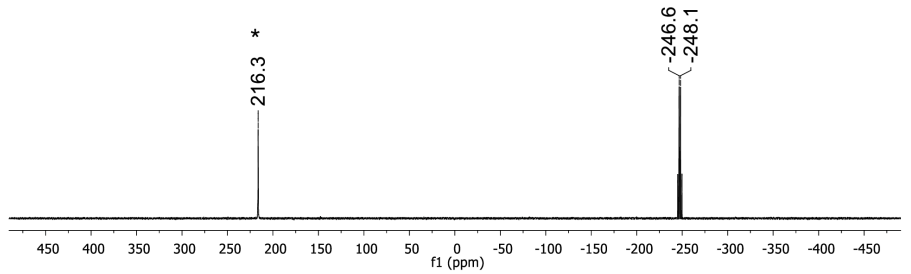

Figure S146. ^{31}P NMR spectrum of the reaction mixture Na_2[**4**-H_2]/PCl_3 (121.5 MHz, THF-d_8). Asterisk marks resonance of the starting material PCl_3 since the stoichiometry of the reaction matched not perfectly.

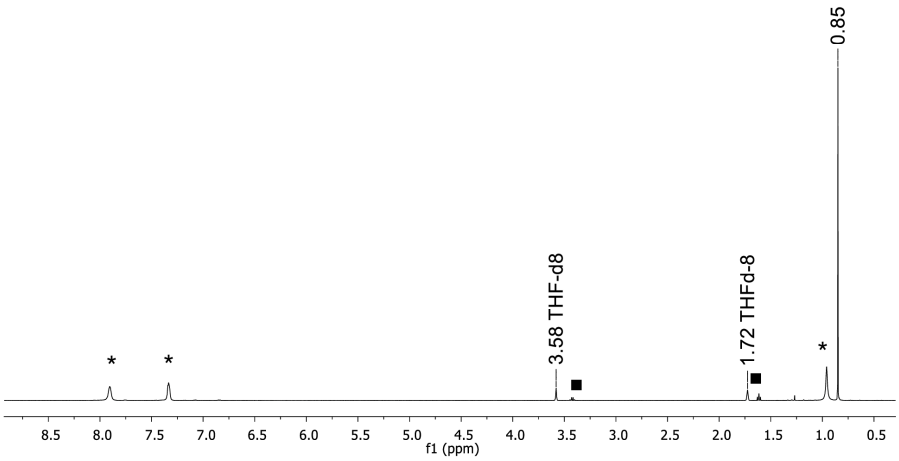

Figure S147. ^{1}H NMR spectrum of the reaction mixture Na_2[**4**-H_2]/EtBr (500.2 MHz, THF-d_8). Asterisks mark resonances of **4** and black squares mark resonances of C_2H_5Br.

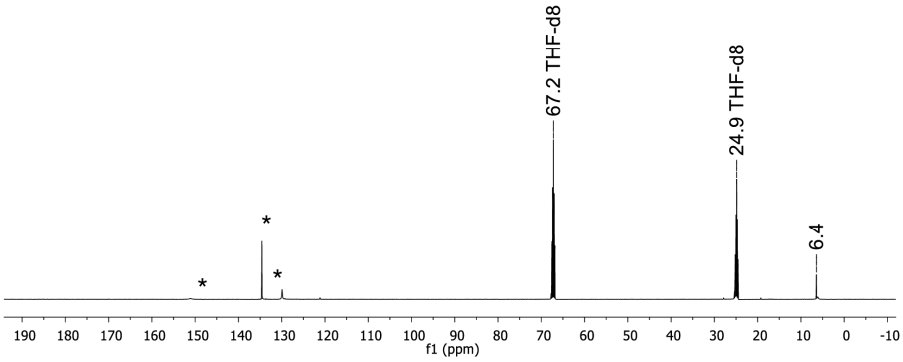

Figure S148. $^{13}C\{^{1}H\}$ NMR spectrum of the reaction mixture Na_2[**4**-H_2]/EtBr (125.8 MHz, THF-d_8). Asterisks mark resonances of **4**.

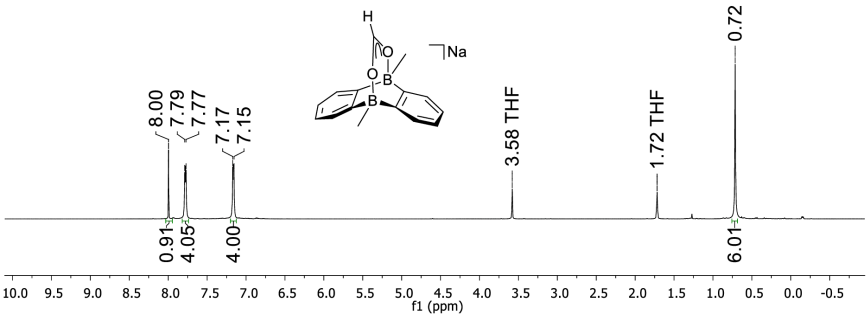

Figure S149. ^{1}H NMR spectrum of the reaction mixture Na_2[**4**-H_2]/CO_2 (500.2 MHz, THF-d_8).

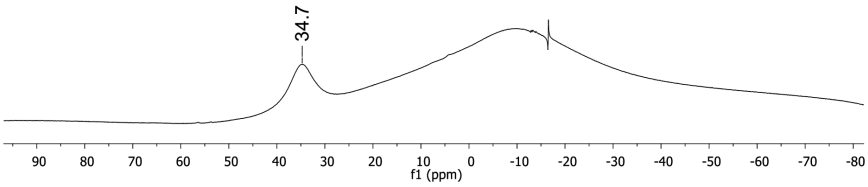

Figure S150. ^{11}B NMR spectrum of the reaction mixture Na_2[**4**-H_2]/CO_2 (160.5 MHz, THF-d_8).

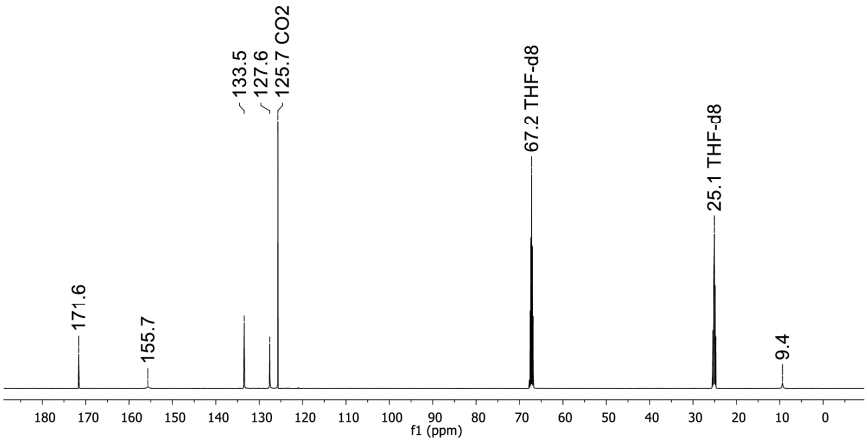

Figure S151. ^{13}C{^{1}H} NMR spectrum of the reaction mixture Na_2[**4**-H_2]/CO_2 (125.8 MHz, THF-d_8).

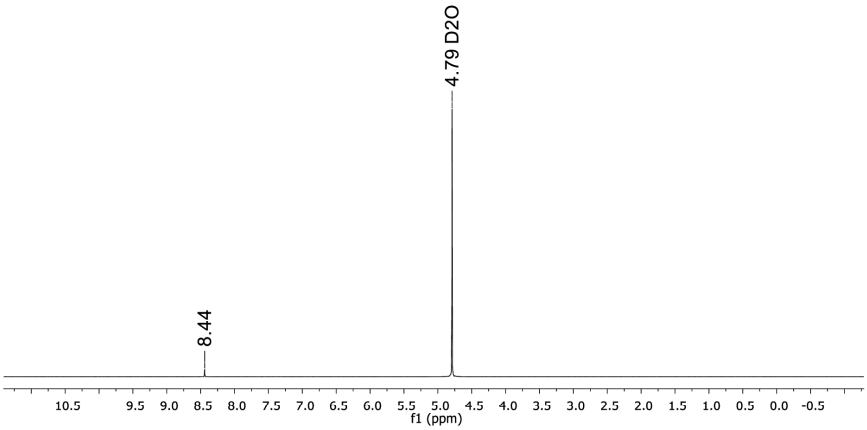

Figure S152. ^{1}H NMR spectrum of sodium formate of the reaction mixture Na_2[**4**-H_2]/CO_2 (500.2 MHz, D_2O).

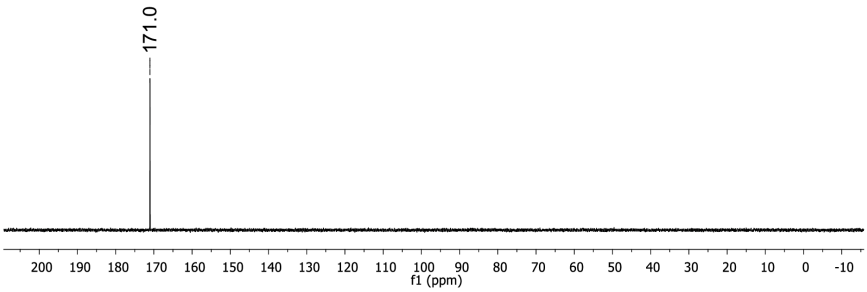

Figure S153. ^{13}C{^{1}H} NMR spectrum of sodium formate of the reaction mixture Na_2[**4**-H_2]/CO_2 (125.8 MHz, D_2O).

8. X-ray crystal structure analyses

Data for all structures were collected on a STOE IPDS II two-circle diffractometer with a Genix Microfocus tube with mirror optics using Mo$K\alpha$ radiation (λ = 0.71073 Å). The data were scaled using the frame-scaling procedure in the X-AREA program system.[23] The structures were solved by direct methods using the program SHELX and refined against F^2 with full-matrix least-squares techniques using the program SHELXL-97.[24]

In **8**, the H atoms of one methyl group in the asymmetric unit are disordered over two positions with a site occupation factor of 0.60(2) for the major occupied sites.

In $[Li(thf)_2]_2$[**7**], two methylene groups of one thf ligand in the asymmetric unit are disordered over two positions with a site occupation factor of 0.576(12) for the major occupied sites. The displacement ellipsoids of the disordered atoms were restrained to an isotropic behavior. The crystal was twinned with a fractional contribution of 0.7830(17) of the major domain.

In $[Na_2(thf)_3]$[**1**], one methylene group of one thf ligand in the asymmetric unit is disordered over two positions with a site occupation factor of 0.527(16) for the major occupied site. The H atom bonded to B was freely refined.

In $[K_2(thf)_4]$[**1**], two methylene groups of one thf ligand in the asymmetric unit are disordered over two positions with a site occupation factor of 0.55(2) for the major occupied sites. The displacement ellipsoids of all atoms of the disordered thf ligand were restrained to an isotropic behavior. The H atom bonded to B was freely refined.

In [Na][Na(thf)$_2$(18-c-6)][Na(thf)$_2$]$_2$(*n*-hexane)[**7**-H$_2$]$_2$, two methylene groups of two thf ligands in the asymmetric unit are disordered over two positions with a site occupation factor of 0.50(3) and 0.54(3), respectively, for the major occupied sites. In two thf ligands one methylene group is disordered over two positions with a site occupation factor of 0.65(3) and 0.63(3), respectively, for the major occupied sites. The displacement ellipsoids of the disordered atoms were restrained to an isotropic behavior. The H atoms bonded to B were freely refined. Bond lengths in the *n*-hexane molecule were restrained to 1.550(1) Å and 1-3 distances were restrained to 2.42(1) Å. The displacement ellipsoids of mutually bonded atoms of the *n*-hexane molecule were restrained to be similar.

In $[K(18\text{-c-}6)]_2[\mathbf{1}\text{-}H_2]$, the H atoms bonded to B were freely refined.
In $[K][K(thf)]_3[\mathbf{4}\text{-}H_2]_2$, two methylene groups of two thf ligands in the asymmetric unit are disordered over two positions with a site occupation factor of 0.664(15) and 0.548(13), respectively, for the major occupied sites. The displacement ellipsoids of all atoms in all thf molecules were restrained to an isotropic behavior. The H atoms bonded to B were freely refined.

In $[K]_2[K(18\text{-c-}6)][K(18\text{-c-}6)(thf)_2][\mathbf{7}\text{-}H_2]_2$, the H atoms bonded to B were freely refined.

In $[Li(12\text{-c-}4)_2](THF)[\mathbf{10}]$, two methylene groups of the co-crystallized THF molecule are disordered over two positions with a site occupation factor of 0.545(16) for the major occupied sites. The displacement ellipsoids of the disordered atoms were restrained to an isotropic behavior. The H atom bonded to N was freely refined.

In [Li(12-c-4)(thf)][Li(12-c-4)][**11**], two methylene groups of the thf ligand are disordered over two positions with a site occupation factor of 0.53(4) for the major occupied sites. One entire crown-ether ring is disordered over two positions with a site occupation factor of 0.697(8) for the major occupied sites. The lower occupied atoms of the disordered crown-ether ring and all disordered atoms of the thf molecule were isotropically refined. The displacement ellipsoids of the higher occupied sites of the disordered crown-ether ring were restrained to an isotropic behavior. The coordinates of the H atoms of the ethylene bridge between the B atoms were refined. Bond lengths and angles of the lower occupied crown-ether ring were restrained to be similar to those of a non-disordered crown-ether ring. Bond lengths and angles of the disordered thf ligand were restrained to be similar to those of a non-disordered thf ligand.

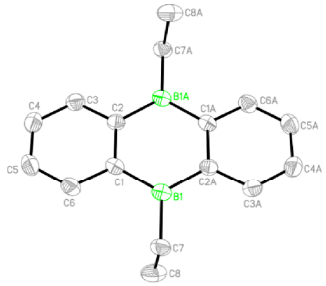

Figure S154. Molecular structure of **5** in the solid state. Displacement ellipsoids are drawn at the 50% probability level; hydrogen atoms are omitted for clarity. Selected bond lengths (Å) and bond angles (°): B1−C1 = 1.577(2), B1−C2A = 1.572(2), B1−C7 = 1.579(2), C1−C2 = 1.425(2), C1−C6 = 1.402(2), C2−C3 = 1.406(2), C3−C4 = 1.393(2), C4−C5 = 1.382(2), C5−C6 = 1.389(2), C7−C8 = 1.539(2); C1−B1−C2A = 118.6(1), C1−B1−C7 = 119.8(1), C2A−B1−C7 = 121.3(1). Symmetry transformation used to generate equivalent atoms: A: −x+1, −y+1, −z+2.

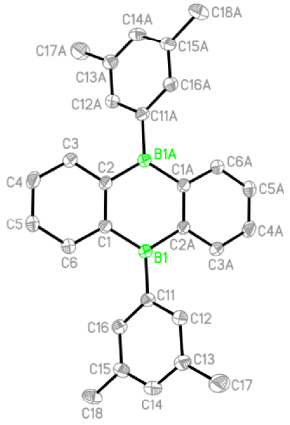

Figure S155. Molecular structure of **8** in the solid state. Displacement ellipsoids are drawn at the 50% probability level; hydrogen atoms are omitted for clarity. Selected bond lengths (Å), bond angles (°), and torsion angle (°): B1−C1 = 1.568(2), B1−C2A = 1.568(2), B1−C11 = 1.572(2), C1−C2 = 1.426(2), C1−C6 = 1.404(2), C2−C3 = 1.409(2), C3−C4 = 1.396(2), C4−C5 = 1.385(2), C5−C6 = 1.396(2); C1−B1−C2A = 119.29(9), C1−B1−C11 = 120.6(1), C2A−B1−C11 = 120.02(10); C1−B1−C11−C12 = −122.4(1). Symmetry transformation used to generate equivalent atoms: A: −x, −y, −z+1.

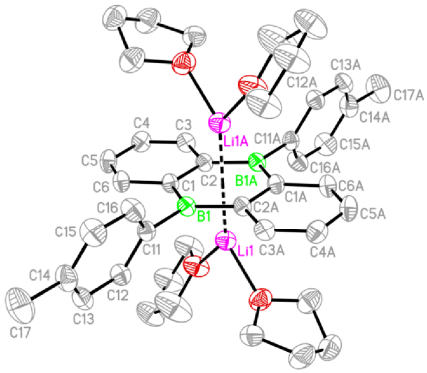

Figure S156. Molecular structure of $[Li(thf)_2]_2$[**7**] in the solid state. Displacement ellipsoids are drawn at the 50% probability level; hydrogen atoms are omitted for clarity. Selected bond lengths (Å), atom···COG distance (Å), bond angles (°), and torsion angle (°): B1−C1 = 1.538(3), B1−C2A = 1.534(3), B1−C11 = 1.605(3), C1−C2 = 1.473(2), C1−C6 = 1.447(3), C2−C3 = 1.447(3), C3−C4 = 1.368(3), C4−C5 = 1.423(3), C5−C6 = 1.366(3); Li···COG = 1.891(4); C1−B1−C2A = 117.4(2), C1−B1−C11 = 121.2(2), C2A−B1−C11 = 121.38(17); C1−B1−C11−C12 = 69.1(3). COG = centroid of the B_2C_4 ring. Symmetry transformation used to generate equivalent atoms: A: −x+1, −y+1, −z+1.

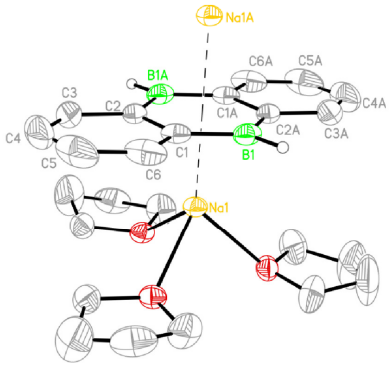

Figure S157. Molecular structure of $[Na_2(thf)_3][\mathbf{1}]$ in the solid state. Displacement ellipsoids are drawn at the 50% probability level; carbon-bonded hydrogen atoms are omitted for clarity. Selected bond lengths (Å), atom···COG distance (Å), and bond angles (°): B1−C1 = 1.527(3), B1−C2A = 1.522(3), B1−H1 = 1.12(3), C1−C2 = 1.468(3), C1−C6 = 1.432(3), C2−C3 = 1.435(3), C3−C4 = 1.354(4), C4−C5 = 1.397(4), C5−C6 = 1.369(4); Na···COG = 2.2394(7); C1−B1−C2A = 118.3(2). COG = centroid of the B_2C_4 ring. Symmetry transformation used to generate equivalent atoms: A: −x+1, −y+1, −z.

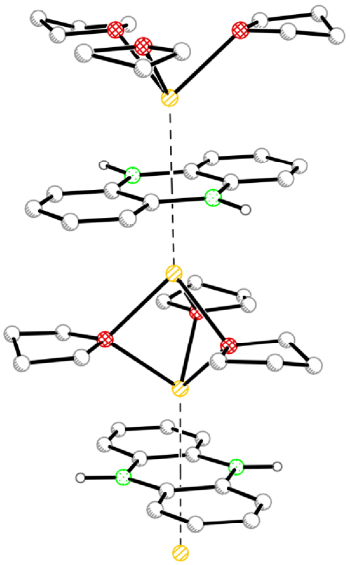

Figure S158. Description of the solid-state structure of $[Na_2(thf)_3][\mathbf{1}]$: Two Na^+ ions are located above and below the B_2C_4 ring. Three thf ligands connect two Na^+ ions of neighboring DBA fragments so that a coordination polymer is formed.

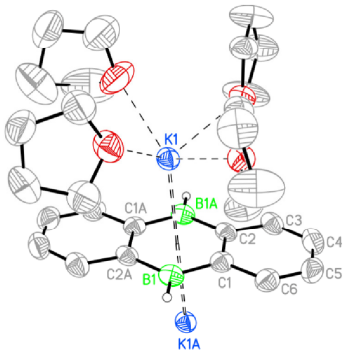

Figure S159. Molecular structure of one of the two crystallographically independent $[\mathbf{1}]^{2-}$ moieties of $[K_2(thf)_4][\mathbf{1}]$ in the solid state. Displacement ellipsoids are drawn at the 50% probability level; carbon-bonded hydrogen atoms are omitted for clarity. Selected bond lengths (Å), atom···COG distances (Å), and bond angles (°) of the two crystallographically independent dianions: B1−C1 = 1.523(4)/1.512(5), B1−C2A = 1.531(4)/1.509(6), B1−H1 = 1.14(3)/1.13(5), C1−C2 = 1.467(4)/1.463(5), C1−C6 = 1.444(4)/1.441(5), C2−C3 = 1.441(4)/1.435(5), C3−C4 = 1.368(5)/1.326(8), C4−C5 = 1.415(5)/1.391(8), C5−C6 = 1.382(5)/1.396(7); K1···COG = 2.7927(6)/2.7165(6); C1−B1−C2A = 118.7(3)/119.1(3). COG = centroid of the B_2C_4 ring. Symmetry transformation used to generate equivalent atoms: A: −x+1, −y+1, −z+1.

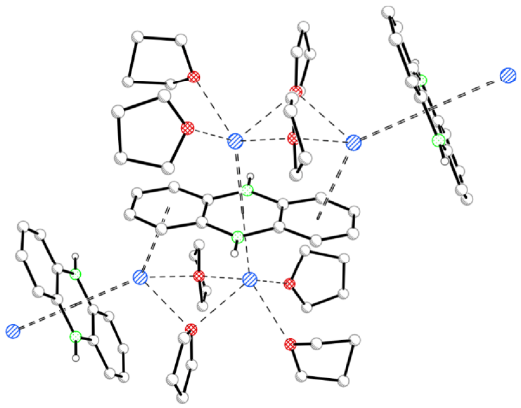

Figure S160. Description of the solid-state structure of $[K_2(thf)_4][\mathbf{1}]$: In the crystal lattice, coordination polymers are formed: Each K^+ ion coordinates one B_2C_4 ring in an η^6 mode, so that two K^+ ions are located above and below each B_2C_4 ring. Half of the K^+ ions connect two $[DBA]^{2-}$ ions because they also coordinate to one phenylene ring (in an η^3 fashion). Two thf ligands are located in bridging positions between two K^+ ions. The coordination sphere of one K^+ ion is completed by two additional thf ligands. Both $[DBA]^{2-}$ units form a dihedral angle of 63.71(9)°.

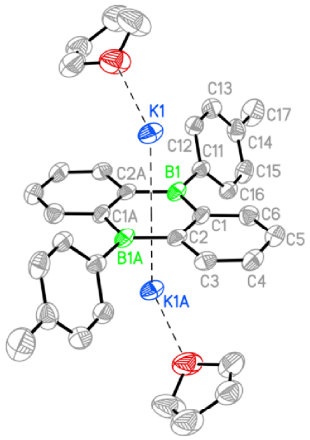

Figure S161. Molecular structure of $[K(thf)]_2$[**7**] in the solid state. Displacement ellipsoids are drawn at the 50% probability level; hydrogen atoms are omitted for clarity. Selected bond lengths (Å), atom···COG distances (Å), bond angles (°), and torsion angle (°): B1−C1 = 1.535(7), B1−C2A = 1.542(7), B1−C11 = 1.583(7), C1−C2 = 1.460(6), C1−C6 = 1.434(6), C2−C3 = 1.444(6), C3−C4 = 1.355(7), C4−C5 = 1.414(7), C5−C6 = 1.374(7); K1···COG = 2.702(1); C1−B1−C2A = 117.4(4), C1−B1−C11 = 122.1(4), C2A−B1−C11 = 120.5(4); C1−B1−C11−C12 = −124.6(5). COG = centroid of the B_2C_4 ring. Symmetry transformation used to generate equivalent atoms: A: −x+1, −y+1, −z+1.

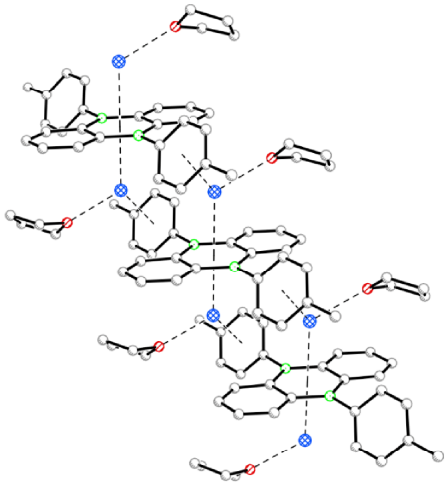

Figure S162. Description of the solid-state structure of $[K(thf)]_2$[**7**]: In the crystal lattice, coordination polymers are formed: Each K^+ ion coordinates one B_2C_4 ring in an η^6 mode, one tolyl ring of a neighboring $[DBA]^{2-}$ unit in an η^3 mode (K1···COG(C11-C16) = 3.201(2)). The coordination sphere is completed by one thf ligand. The $[DBA]^{2-}$ ions and the tolyl groups of the same polymer strand are oriented parallel to each other, respectively.

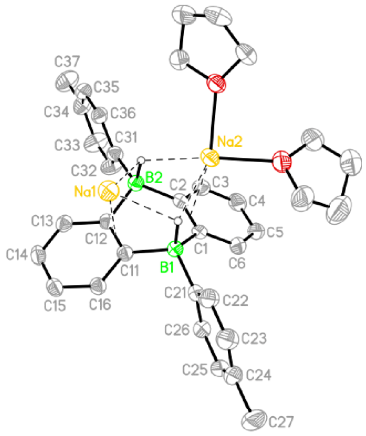

Figure S163. Molecular structure of one of the two crystallographically independent [**7**-H_2]$^{2-}$ moieties of [Na][Na(thf)$_2$(18-c-6)][Na(thf)$_2$]$_2$(*n*-hexane)[**7**-H_2]$_2$ in the solid state. Displacement ellipsoids are drawn at the 30% probability level; carbon-bonded hydrogen atoms, the [Na(thf)$_2$(18-c-6)]$^+$ ion, and the *n*-hexane molecule are omitted for clarity. Selected bond lengths (Å), atom···atom distances (Å), and bond angles (°) of the two crystallographically independent molecules: B1−C1 = 1.624(5)/1.626(5), B1−C11 = 1.620(5)/1.634(5), B1−C21 = 1.625(5)/1.610(5), B1−H1 = 1.26(3)/1.24(3), B2−C2 = 1.627(5)/1.623(5), B2−C12 = 1.630(5)/1.628(5), B2−C31 = 1.626(5)/1.614(4), B2−H2 = 1.27(3)/1.20(3), C1−C2 = 1.424(4)/1.424(4), C11−C12 = 1.424(4)/1.427(4); Na1···C11 = 2.542(3)/2.575(3), Na1···H1 = 2.31(3)/2.46(3), Na1···H2 = 2.29(3)/2.37(3), Na2···C1 = 2.741(3)/2.738(3), Na2···H1 = 2.35(3)/2.31(3), Na2···H2 = 2.28(3)/2.34(3); C1−B1−C11 = 109.1(2)/109.4(2), C2−B2−C12 = 108.7(3)/109.6(3).

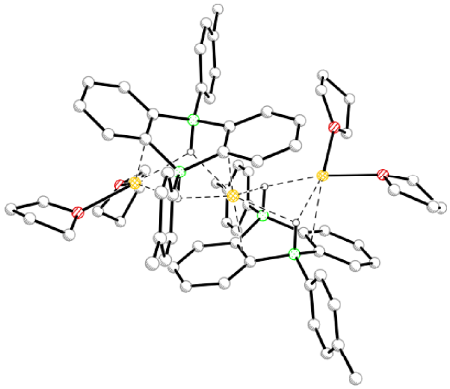

Figure S164. Description of the solid-state structure of [Na][Na(thf)$_2$(18-c-6)][Na(thf)$_2$]$_2$(*n*-hexane)[**7**-H_2]$_2$ (the discrete [Na(thf)$_2$(18-c-6)]$^+$ ion and the *n*-hexane molecule are omitted for clarity): The crystal lattice consists of dimers, in which two [DBA]$^{2-}$ entities are connected by one central Na^+ ion. This cation is coordinated in a chelating manner by the two axial B*H* substituents of each anionic fragment; the octahedral ligand sphere is completed by short contacts to two *trans*-positioned phenylene rings. Two other [Na(thf)$_2$]$^+$ ions are also coordinated in a chelating manner by two axial B*H* substituents of the same [**7**-H_2]$^{2-}$ fragment.

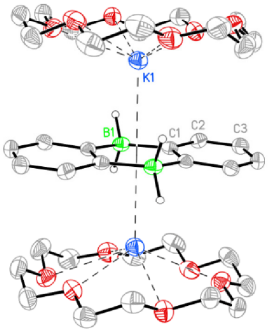

Figure S165: Molecular structure of one of the two crystallographically independent molecules of $[K(18\text{-c-}6)]_2[\mathbf{1}\text{-}H_2]$ in the solid state. Displacement ellipsoids are drawn at the 50% probability level; carbon-bonded hydrogen atoms are omitted for clarity. Selected bond lengths (Å), atom···COG distances (Å), and bond angles (°) of the two crystallographically independent molecules: B1−C1 = 1.619(3)/1.622(3), B1−H1A = 1.16(3)/1.20(3), B1−H1B = 1.13(3)/1.18(4), C1−C1(#1/#2) = 1.431(5)/1.434(4), C1−C2 = 1.408(4)/1.414(4), C2−C3 = 1.383(4)/1.378(4), C3−C3(#1/#2) = 1.399(5)/1.393(5); K1···COG = 2.9165(8)/2.9177(7); C1−B1−C1(#3/#4) = 115.7(3)/116.0(3). COG = centroid of the B_2C_4 ring. Symmetry transformation used to generate equivalent atoms: #1: −x+1, −y+2, z; #2: −x+1, −y+1, z; #3: x, y, −z+1; #4: x, y, −z.

The molecule possesses a high symmetry with a center of inversion, one mirror plane containing the two BH_2 fragments, and one C_2 axis perpendicular to the mirror plane.

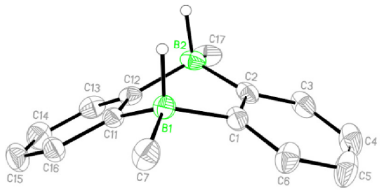

Figure S166. Molecular structure of one of the two crystallographically independent [**4**-H_2]$^{2-}$ moieties of [K][K(thf)]$_3$[**4**-H_2]$_2$ in the solid state. Displacement ellipsoids are drawn at the 30% probability level; carbon-bonded hydrogen atoms and all counter cations are omitted for clarity. Selected bond lengths (Å) and bond angles (°) of the two crystallographically independent molecules: B1−C1 = 1.625(3)/1.638(3), B1−C7 = 1.633(3)/1.645(3), B1−C11 = 1.632(3)/1.632(3), B1−H1 = 1.19(2)/1.18(2), B2−C2 = 1.631(4)/1.630(3), B2−C12 = 1.630(3)/1.628(3), B2−C17 = 1.642(3)/1.627(3), B2−H2 = 1.21(2)/1.220(18), C1−C2 = 1.425(3)/1.426(3), C11−C12 = 1.425(3)/1.432(3); C1−B1−C11 = 107.97(15)/107.15(15), C2−B2−C12 = 108.29(16)/105.87(15).

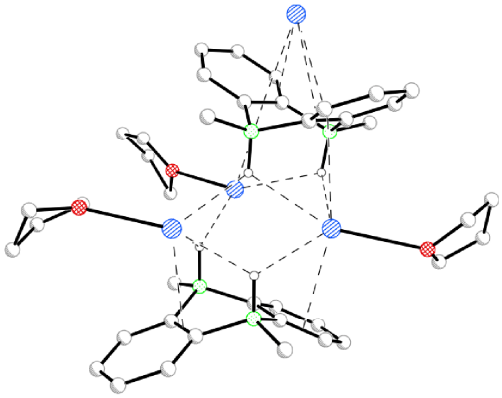

Figure S167. Description of the solid-state structure of [K][K(thf)]$_3$[**4**-H_2]$_2$: In the crystal lattice, coordination polymers are formed. The repeating unit consists of two [DBA]$^{2-}$ entities, which are bridged by three [K(thf)]$^+$ ions, mainly via K···H interactions. The repeating units are connected by K^+ cations embedded between the concave sites of two [**4**-H_2]$^{2-}$ units (contact ion pairs without additional thf ligands).

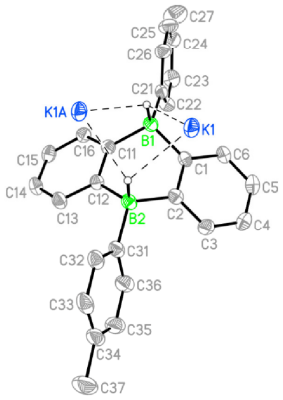

Figure S168. Molecular structure of one $[\mathbf{7}\text{-}H_2]^{2-}$ moiety of $[K]_2[K(18\text{-c-}6)][K(18\text{-c-}6)(thf)_2][\mathbf{7}\text{-}H_2]_2$ in the solid state. Displacement ellipsoids are drawn at the 50% probability level; carbon-bonded hydrogen atoms, the $[K(18\text{-c-}6)]^+$ ion, and the $[K(18\text{-c-}6)(thf)_2]^+$ ion are omitted for clarity. Selected bond lengths (Å), atom···atom distances (Å), and bond angles (°): B1−C1 = 1.628(2), B1−C11 = 1.636(2), B1−C21 = 1.626(2), B1−H1 = 1.217(17), B2−C2 = 1.641(2), B2−C12 = 1.634(2), B2−C31 = 1.631(2), B2−H2 = 1.22(2), C1−C2 = 1.426(2), C11−C12 = 1.427(2); K1···H1 = 2.655(18), $K1^+$···H2 = 2.622(19); C1−B1−C11 = 107.8(1), C2−B2−C12 = 108.3(1).

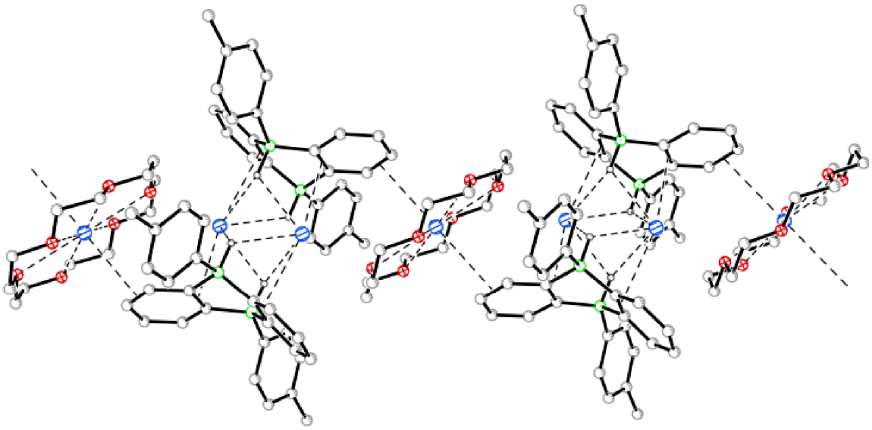

Figure S169. Description of the solid-state structure of $[K]_2[K(18\text{-c-}6)][K(18\text{-c-}6)(thf)_2][\mathbf{7}\text{-}H_2]_2$ (the discrete $[K(18\text{-c-}6)(thf)_2]^+$ ions are omitted for clarity): In the crystal lattice, coordination polymers are formed. The repeating unit consists of two $[\mathbf{7}\text{-}H_2]^{2-}$ entities, which are bridged by two K^+ ions. Each of these cations forms four K···H–B and two K···phenylene short contacts. The repeating units are connected by $[K(18\text{-c-}6)]^+$ ions via K···phenylene and O–K interactions.

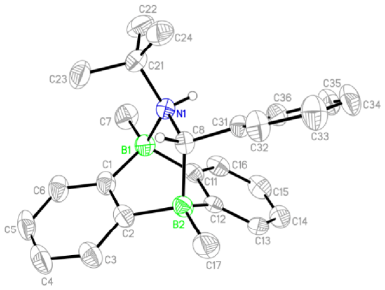

Figure S170. Molecular structure of [Li(12-c-4)$_2$](THF)[**10**] in the solid state. Displacement ellipsoids are drawn at the 50% probability level; carbon-bonded hydrogen atoms, the [Li(12-c-4)$_2$]$^+$ ion, and the co-crystallized THF molecule are omitted for clarity. Selected bond lengths (Å) and bond angles (°): B1−C1 = 1.616(3), B1−C7 = 1.624(3), B1−C11 = 1.629(3), B1−N1 = 1.737(3), B2−C2 = 1.622(3), B2−C8 = 1.693(3), B2−C12 = 1.613(3), B2−C17 = 1.623(3), C1−C2 = 1.408(3), C11−C12 = 1.411(3), C8−N1 = 1.537(3), N1−H1 = 0.90(2), N1−C21 = 1.535(3); C1−B1−C11 = 109.6(2), C2−B2−C12 = 108.3(2).

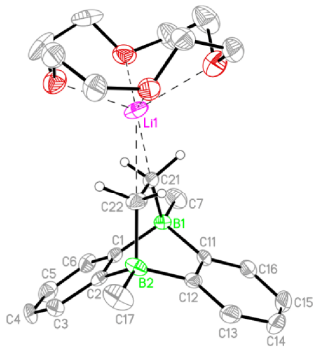

Figure S171. Molecular structure of one of the two crystallographically independent contact-ion pairs [Li(12-c-4)(thf)][Li(12-c-4)][**11**] in the solid state. Displacement ellipsoids are drawn at the 50% probability level; carbon-bonded hydrogen atoms of the DBA scaffold and the [Li(12-c-4)(thf)]$^+$ ion are omitted for clarity. Selected bond lengths (Å), atom···atom distances (Å), bond angles (°), and torsion angles (°) of the two crystallographically independent dianions: B1−C1 = 1.617(7)/1.632(8), B1−C7 = 1.632(8)/1.633(8), B1−C11 = 1.633(8)/1.623(8), B1−C21 = 1.684(7)/1.662(8), B2−C2 = 1.630(8)/1.611(8), B2−C12 = 1.623(9)/1.634(8), B2−C17 = 1.628(9)/1.643(8), B2−C22 = 1.677(8)/1.691(8), C1−C2 = 1.440(7)/1.428(8), C11−C12 = 1.423(8)/1.415(7), C21−C22 = 1.552(8)/1.551(8); Li1$^+$···C21 = 2.334(10)/2.309(11), Li1$^+$···C22 = 2.361(10)/2.420(10); C1−B1−C11 = 104.2(4)/103.5(4), C2−B2−C12 = 105.4(4)/104.3(4); B1−C21−C22−B2 = −1.4(6)/−1.9(6).

Table S6. Selected crystallographic data for **5**, **8**, and $[Li(thf)_2]_2$[**7**].

compound	**5**	**8**	$[Li(thf)_2]_2$[**7**]
CCDC	1888723	1888724	1888725
formula	$C_{16}H_{18}B_2$	$C_{28}H_{26}B_2$	$C_{42}H_{54}B_2Li_2O_4$
M_r	231.92	384.11	658.35
T (K)	173(2)	173(2)	173(2)
radiation, λ (Å)	Mo$K\alpha$, 0.71073	Mo$K\alpha$, 0.71073	Mo$K\alpha$, 0.71073
crystal system	triclinic	monoclinic	triclinic
space group	$P\,\bar{1}$	$P2_1/n$	$P\,\bar{1}$
a (Å)	5.1697(6)	10.3844(7)	9.1549(7)
b (Å)	7.5135(9)	8.6036(4)	9.8159(7)
c (Å)	9.1628(11)	12.5024(8)	11.6092(9)
α (°)	76.716(9)	90	69.862(6)
β (°)	74.826(9)	98.997(5)	79.949(6)
γ (°)	84.882(9)	90	81.811(6)
V (Å^3)	334.15(7)	1103.26(12)	960.60(13)
Z	1	2	1
D_{calcd} (g cm^{-3})	1.153	1.156	1.138
F (000)	124	408	354
μ (mm^{-1})	0.062	0.064	0.069
crystal size (mm)	0.28 × 0.21 × 0.05	0.28 × 0.26 × 0.25	0.19 × 0.18 × 0.09
crystal shape, color	colorless plate	yellow block	red plate
reflections collected	5472	19516	21740
independent reflections	1364	2812	21740
R_{int}	0.0193	0.0287	–
data/restraints/parameters	1364 / 0 / 82	2812 / 0 / 139	21740 / 24 / 247
R_1, wR_2 ($I > 2\,\sigma(I)$)	0.0473, 0.1360	0.0477, 0.1226	0.0604, 0.1410
R_1, wR_2 (all data)	0.0534, 0.1397	0.0562, 0.1282	0.0873, 0.1523
GOF on F^2	1.114	1.059	0.978
largest difference peak and hole (e Å^{-3})	0.265, –0.165	0.317, –0.191	0.243, –0.220

Table S7. Selected crystallographic data for $[Na_2(thf)_3][\mathbf{1}]$, $[K_2(thf)_4][\mathbf{1}]$, and $[K(thf)]_2[\mathbf{7}]$.

compound	$[Na_2(thf)_3][\mathbf{1}]$	$[K_2(thf)_4][\mathbf{1}]$	$[K(thf)]_2[\mathbf{7}]$
CCDC	1888726	1888727	1888728
formula	$C_{24}H_{34}B_2Na_2O_3$	$C_{28}H_{42}B_2K_2O_4$	$C_{34}H_{38}B_2K_2O_2$
M_r	438.11	542.43	578.46
T (K)	173(2)	173(2)	173(2)
radiation, λ (Å)	Mo$K\alpha$, 0.71073	Mo$K\alpha$, 0.71073	Mo$K\alpha$, 0.71073
crystal system	monoclinic	monoclinic	monoclinic
space group	$C2/c$	$P2_1/n$	$P2_1/c$
a (Å)	16.846(2)	14.6657(7)	6.3580(9)
b (Å)	10.2105(8)	10.0154(4)	12.581(2)
c (Å)	15.0325(17)	21.2355(10)	19.691(3)
α (°)	90	90	90
β (°)	106.425(9)	102.926(4)	90.278(12)
γ (°)	90	90	90
V (Å^3)	2480.2(5)	3040.1(2)	1575.1(4)
Z	4	4	2
D_{calcd} (g cm^{-3})	1.173	1.185	1.220
F (000)	936	1160	612
μ (mm^{-1})	0.103	0.341	0.329
crystal size (mm)	0.27 × 0.11 × 0.11	0.28 × 0.12 × 0.12	0.22 × 0.08 × 0.03
crystal shape, color	dark red needle	dark red needle	dark red needle
reflections collected	10625	41456	8870
independent reflections	2316	5727	2778
R_{int}	0.0479	0.0350	0.1002
data/restraints/parameters	2316 / 0 / 155	5727 / 42 / 352	2778 / 0 / 182
R_1, wR_2 ($I > 2\sigma(I)$)	0.0476, 0.1156	0.0597, 0.1597	0.0735, 0.1518
R_1, wR_2 (all data)	0.0689, 0.1238	0.0730, 0.1696	0.1380, 0.1750
GOF on F^2	1.043	1.021	0.971
largest difference peak and hole (e Å^{-3})	0.216, −0.185	0.745, −0.430	0.380, −0.358

Table S8. Selected crystallographic data for [Na][Na(thf)$_2$(18-c-6)][Na(thf)$_2$]$_2$(*n*-hexane)[**7**-H$_2$]$_2$, [K(18-c-6)]$_2$[**1**-H$_2$], and [K][K(thf)]$_3$[**4**-H$_2$]$_2$.

compound	[Na][Na(thf)$_2$(18-c-6)] [Na(thf)$_2$]$_2$(*n*-hexane) [**7**-H$_2$]$_2$	[K(18-c-6)]$_2$[**1**-H$_2$]	[K][K(thf)]$_3$[**4**-H$_2$]$_2$
CCDC	1888729	1888730	1888731
formula	$C_{94}H_{134}B_4Na_4O_{12}$	$C_{36}H_{60}B_2K_2O_{12}$	$C_{40}H_{56}B_4K_4O_3$
M_r	1591.20	784.66	784.48
T (K)	173(2)	173(2)	173(2)
radiation, λ (Å)	Mo$K\alpha$, 0.71073	Mo$K\alpha$, 0.71073	Mo$K\alpha$, 0.71073
crystal system	monoclinic	orthorhombic	monoclinic
space group	$P2_1/c$	$Pbam$	$P2_1/n$
a (Å)	16.0130(8)	22.959(2)	11.1111(3)
b (Å)	17.3067(6)	9.4933(8)	24.7167(5)
c (Å)	34.7821(19)	18.771(2)	16.6417(4)
α (°)	90	90	90
β (°)	101.572(4)	90	107.866(2)
γ (°)	90	90	90
V (Å^3)	9443.3(8)	4091.3(7)	4349.91(19)
Z	4	4	4
D_{calcd} (g cm^{-3})	1.119	1.274	1.198
F (000)	3432	1680	1664
μ (mm^{-1})	0.087	0.289	0.443
crystal size (mm)	0.21 × 0.11 × 0.02	0.17 × 0.17 × 0.08	0.29 × 0.28 × 0.23
crystal shape, color	colorless plate	colorless plate	colorless block
reflections collected	107613	13623	69817
independent reflections	17461	3949	8450
R_{int}	0.0924	0.0558	0.0284
data/restraints/parameters	17461 / 103 / 1105	3949 / 0 / 259	8450 / 90 / 509
R_1, wR_2 ($I > 2\sigma(I)$)	0.0682, 0.1531	0.0422, 0.0586	0.0441, 0.1148
R_1, wR_2 (all data)	0.1432, 0.1844	0.1055, 0.0699	0.0517, 0.1196
GOF on F^2	0.970	0.872	1.059
largest difference peak and hole (e Å^{-3})	0.287, –0.327	0.197, –0.211	0.668, –0.354

Table S9. Selected crystallographic data for and $[K]_2[K(18\text{-c-}6)][K(18\text{-c-}6)(thf)_2][\mathbf{7}\text{-}H_2]_2$, for $[Li(12\text{-c-}4)_2](THF)$[**10**] and [Li(12-c-4)(thf)][Li(12-c-4)][**11**].

compound	$[K]_2[K(18\text{-c-}6)][K(18\text{-c-}6)(thf)_2][\mathbf{7}\text{-}H_2]_2$	$[Li(12\text{-c-}4)_2]$ (THF)[**10**]	[Li(12-c-4)(thf)][Li(12-c-4)][**11**]
CCDC	1888732	1888733	1888734
formula	$C_{84}H_{112}B_4K_4O_{14}$	$C_{45}H_{70}B_2LiNO_9$	$C_{36}H_{58}B_2Li_2O_9$
M_r	1545.37	797.58	670.32
T (K)	173(2)	173(2)	173(2)
radiation, λ (Å)	Mo$K\alpha$, 0.71073	Mo$K\alpha$, 0.71073	Mo$K\alpha$, 0.71073
crystal system	triclinic	monoclinic	monoclinic
space group	$P\bar{1}$	$P2_1/c$	$P2_1$
a (Å)	11.9532(7)	13.8997(6)	14.3173(13)
b (Å)	12.6550(7)	13.1337(5)	12.8231(8)
c (Å)	15.2730(9)	25.5265(12)	20.9241(18)
α (°)	112.470(4)	90	90
β (°)	90.868(5)	104.454(4)	102.873(7)
γ (°)	100.044(5)	90	90
V (Å^3)	2093.7(2)	4512.5(3)	3744.9(5)
Z	1	4	4
D_{calcd} (g cm^{-3})	1.226	1.174	1.189
F (000)	824	1728	1448
μ (mm^{-1})	0.273	0.079	0.081
crystal size (mm)	0.27 × 0.27 × 0.13	0.29 × 0.27 × 0.11	0.14 × 0.11 × 0.04
crystal shape, color	colorless plate	colorless plate	colorless plate
reflections collected	26936	52297	29657
independent reflections	7828	8793	12967
R_{int}	0.0279	0.0622	0.0692
data/restraints/parameters	7828 / 0 / 491	8793 / 24 / 546	12967 / 236 / 955
R_1, wR_2 ($I > 2\sigma(I)$)	0.0367, 0.0902	0.0637, 0.1580	0.0678, 0.1387
R_1, wR_2 (all data)	0.0506, 0.0950	0.0955, 0.1734	0.1072, 0.1541
GOF on F^2	1.048	1.042	0.950
largest difference peak and hole (e Å^{-3})	0.315, –0.302	0.477, –0.183	0.453, –0.210

9. References

(1) Fulmer, G. R.; Miller, A. J. M.; Sherden, N. H.; Gottlieb, H. E.; Nudelman, A.; Stoltz, B. M.; Bercaw, J. E.; Goldberg, K. I., NMR Chemical Shifts of Trace Impurities: Common Laboratory Solvents, Organics, and Gases in Deuterated Solvents Relevant to the Organometallic Chemist. *Organometallics* **2010**, *29*, 2176.

(2) Januszewski, E.; Lorbach, A.; Grewal, R.; Bolte, M.; Bats, J. W.; Lerner, H.-W.; Wagner, M., Unsymmetrically Substituted 9,10-Dihydro-9,10-Diboraanthracenes as Versatile Building Blocks for Boron-Doped π-Conjugated Systems. *Chem. Eur. J.* **2011**, *17*, 12696.

(3) Lorbach, A.; Bolte, M.; Li, H.; Lerner, H.-W.; Holthausen, M. C.; Jäkle, F.; Wagner, M., 9,10-Dihydro-9,10-diboraanthracene: Supramolecular Structure and Use as a Building Block for Luminescent Conjugated Polymers. *Angew. Chem. Int. Ed.* **2009**, *48*, 4584.

(4) von Grotthuss, E.; Diefenbach, M.; Bolte, M.; Lerner, H.-W.; Holthausen, M. C.; Wagner, M., Reversible Dihydrogen Activation by Reduced Aryl Boranes as Main-Group Ambiphiles. *Angew. Chem. Int. Ed.* **2016**, *55*, 14067.

(5) Hoffend, C.; Diefenbach, M.; Januszewski, E.; Bolte, M.; Lerner, H.-W.; Holthausen, M. C.; Wagner, M., Effects of Boron Doping on the Structural and Optoelectronic Properties of 9,10-Diarylanthracenes. *Dalton Trans.* **2013**, *42*, 13826.

(6) Kessler, S. N.; Neuburger, M.; Wegner, H. A., Bidentate Lewis Acids for the Activation of 1,2-Diazines - a New Mode of Catalysis. *Eur. J. Org. Chem.* **2011**, 3238.

(7) von Grotthuss, E.; Prey, S. E.; Bolte, M.; Lerner, H.-W.; Wagner, M., Selective CO_2 Splitting by Doubly Reduced Aryl Boranes to Give CO and $[CO_3]^{2-}$. *Angew. Chem. Int. Ed.* **2018**, *57*, 16491.

(8) Lorbach, A.; Bolte, M.; Lerner, H.-W.; Wagner, M., Dilithio 9,10-Diborataanthracene: Molecular Structure and 1,4-Addition Reactions. *Organometallics* **2010**, *29*, 5762.

(9) Müller; P.; Huck, S. K., H.; Pritzkow, H.; Siebert, W., Synthesis and Structures of 9,10-Dihydro-9,10-diboraanthracene Derivatives. *Z. Naturforsch.* **1995**, *50b*, 1476.

(10) Brunner, E., Solubility of Hydrogen in 10 Organic Solvents at 298.15, 323.15, and 373.15 K. *J. Chem. Eng.Data* **1985**, *30*, 269.

(11) Eisch, J. J.; Kotowicz, B. W., Novel Organoborane Lewis Acids via Selective Boron-Tin Exchange Processes Steric Constraints to Electrophilic Initiation by the Boron Halide. *Eur. J. Inorg. Chem.* **1998**, 761.

(12) Spies, P.; Schwendemann, S.; Lange, S.; Kehr, G.; Fröhlich, R.; Erker, G., Metal-Free Catalytic Hydrogenation of Enamines, Imines, and Conjugated Phosphinoalkenylboranes. *Angew. Chem. Int. Ed.* **2008**, *47*, 7543.

(13) *NMR Basic Principles and Progress - Oxygen-17 and Silicon-29*; Diehl, P.; Fluck, E.; Kosfeld, R., Eds., 17th ed.; Springer-Verlag: Berlin Heidelberg, New York, **1981**.

(14) Thorshaug, K.; Swang, O.; Dahl, I. M.; Olafsen, A., An Experimental and Theoretical Study of Spin-Spin Coupling in Chlorosilanes. *J. Phys. Chem. A* **2006**, *110*, 9801.

(15) *Spectral Database for Organic Compounds (SDBS)*; ^{1}H spectrum; SDBS No.: 9419; RN 7782-65-2; https://sdbs.db.aist.go.jp/sdbs/ (accessed January 14, 2019).

(16) Ebsworth, E. A. V.; Sheldrick, G. M., N.M.R. Spectra of Phosphine, Arsine and Stibine. *Trans. Faraday Soc.* **1967**, *63*, 1071.

(17) *NMR-Spektroskopie von Nichtmetallen - 31P-NMR-Spektroskopie*; Berger, S.; Braun, S.; Kalinowski, H.-O., Eds., 3th ed.; Georg Thieme Verlag: Stuttgart New York, **1993**.

(18) Jana, A.; Tavcar, G.; Roesky, H. W.; John, M., Germanium(II) Hydride Mediated Reduction of Carbon Dioxide to Formic Acid and Methanol with Ammonia Borane as the Hydrogen Source. *Dalton Trans.* **2010**, *39*, 9487.

(19) *Spectral Database for Organic Compounds (SDBS)*; IR spectrum (KBr disc); SDBS No.: 2964; RN 141-53-7; https://sdbs.db.aist.go.jp/sdbs/ (accessed January 14, 2019).

(20) Frisch, M. J.; Trucks, G. W.; Schlegel, H. B.; Scuseria, G. E.; Robb, M. A.; Cheeseman, J. R.; Scalmani, G.; Barone, V.; Mennucci, B.; Petersson, G. A.; Nakatsuji, H.; Caricato, M.; Li, X.; Hratchian, H. P.; Izmaylov, A. F.; Bloino, J.; Zheng, G.; Sonnenberg, J. L.; Hada, M.; Ehara, M.; Toyota, K.; Fukuda, R.; Hasegawa, J.; Ishida, M.; Nakajima, T.; Honda, Y.; Kitao, O.;

Nakai, H.; Vreven, T.; Montgomery, J. A.; Peralta, Jr., J. E.; Ogliaro, F.; Bearpark, M.; Heyd, J. J.; Brothers, E.; Kudin, K. N.; Staroverov, V. N.; Kobayashi, R.; Normand, J.; Raghavachari, K.; Rendell, A.; Burant, J. C.; Iyengar, S. S.; Tomasi, J.; Cossi, M.; Rega, N.; Millam, J. M.; Klene, M.; Knox, J. E.; Cross, J. B.; Bakken, V.; Adamo, C.; Jaramillo, J.; Gomperts, R.; Stratmann, R. E.; Yazyev, O.; Austin, A. J.; Cammi, R.; Pomelli, C.; Ochterski, J. W.; Martin, R. L.; Morokuma, K.; Zakrzewski, V. G.; Voth, G. A.; Salvador, P.; Dannenberg, J. J.; Dapprich, S.; Daniels, A. D.; Farkas, Ö.; Foresman, J. B.; Ortiz, J. V.; Cioslowski J.; Fox, D. J. *Gaussian 09*, Revision D.01, Gaussian, Inc., Wallingford, CT, 2013; http://www.gaussian.com.

(21) Marenich, A. V.; Cramer, C. J.; Truhlar, D. G., Universal Solvation Model Based on Solute Electron Density and on a Continuum Model of the Solvent Defined by the Bulk Dielectric Constant and Atomic Surface Tensions. *J. Phys. Chem. B* **2009**, ***113***, 6378.

(22) Brend'amour, S.; Gilmer, J.; Bolte, M.; Lerner, H.-W.; Wagner, M., C-Halogenated 9,10-Diboraanthracenes: How the Halogen Load and Distribution Influences Key Optoelectronic Properties. *Chem. Eur. J.* **2018**, *24*, 16910.

(23) *X-AREA: Diffractometer Control Program System;* Stoe & Cie: Darmstadt, Germany, **2002**.

(24) Sheldrick, G. M., A Short History of *SHELX*. *Acta Crystallogr. Sect. A* **2008**, *64*, 112.

6.2.2. Chalcogen–Chalcogen-Bond Activation by an Ambiphilic, Doubly Reduced Organoborane

Tetrahedron 75 (2019) 26–30

Contents lists available at ScienceDirect

Tetrahedron

journal homepage: www.elsevier.com/locate/tet

Chalcogen–chalcogen-bond activation by an ambiphilic, doubly reduced organoborane

Esther von Grotthuss, Felix Nawa, Michael Bolte, Hans-Wolfram Lerner, Matthias Wagner*

Institut für Anorganische und Analytische Chemie, Goethe-Universität Frankfurt, Max-von-Laue-Strasse 7, 60438, Frankfurt (Main), Germany

ARTICLE INFO

Article history:
Received 22 October 2018
Received in revised form
30 October 2018
Accepted 7 November 2018
Available online 15 November 2018

Keywords:
Adduct equilibrium
Arylborane
Boron
Dichalcogen activation
Main-group ambiphile

ABSTRACT

The 9,10-dimethyl-9,10-dihydro-9,10-diboraanthracene dianion salt Li_2[**1**] instantaneously reacts with the dichalcogens $O_2(t\text{Bu})_2$, S_2Me_2, $S_2(p\text{Tol})_2$, Se_2Ph_2, and Te_2Ph_2 under reductive cleavage of the chalcogen–chalcogen bonds to give lithium chalcogenides and neutral **1**. In solution, the products are involved in rapid association/dissociation equilibria. In the crystalline state, **1** and Li[O(*t*Bu)] form a diadduct, whereas Li[SMe] gives a B···B-bridged monoadduct. In the three remaining cases, the crystal lattices contain monoadducts of **1** with one tri- and one tetracoordinate boron atom.

1. Introduction

Since the advent of Frustrated Lewis Pairs (FLPs) in 2006 [1], element–element-bond activation is no longer the exclusive domain of transition metal complexes [2]. More recently, it has been shown that also the FLP concept, which relies on sterically crowded Lewis acid/base combinations incapable of adduct formation, can be extended further to encompass doubly reduced ditopic arylboranes [3]. Here, the Lewis base is stripped to its essence: the electron lone pair. Fig. 1 illustrates the formal relationship between a classic FLP and an example of what is nowadays termed a main-group ambiphile (MGA) [4–6]. Notwithstanding the heuristic value of this approach, one has to consider that the excess electrons will in fact be delocalized over the π-electron system and that concerted, transition metal-like activation mechanisms can also be operative [6].

Among the first MGAs introduced in the literature are the dianions $[\mathbf{A}]^{2-}$ of 9,10-dihydro-9,10-diboraanthracenes (DBAs; R = H, Me), which activate H–H and C(sp)–H single bonds as well as C=O double bonds (Scheme 1) [6–8]. Structurally and functionally related systems are Harman's neutral DBA (R = *N*-heterocyclic carbene) [9] and Kinjo's 1,3,2,5- and 1,4,2,5-diazadiborinines [4,5,10].

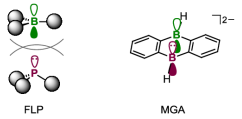

Fig. 1. Formal relationship between a Frustrated Lewis Pair (FLP) and a doubly reduced ditopic arylborane acting as a main-group ambiphile (MGA).

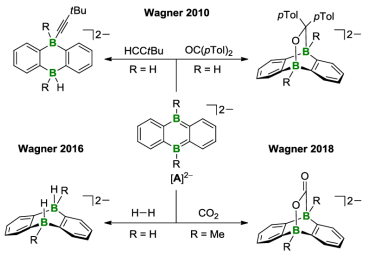

Scheme 1. Doubly reduced 9,10-dihydro-9,10-diboraanthracenes $[\mathbf{A}]^{2-}$ activate C(sp)–H (R = H), H–H (R = H) as well as C–O bonds (R = H, Me) and thus act as formal MGAs. In the presence of excess CO_2, the CO_2 cycloadduct reacts further to afford CO, $[CO_3]^{2-}$, and **A**. *p*Tol = *para*-tolyl.

* Corresponding author.
E-mail address: Matthias.Wagner@chemie.uni-frankfurt.de (M. Wagner).

https://doi.org/10.1016/j.tet.2018.11.012
0040-4020/

A similar concept has also been realized with compounds containing reactive boron–boron single bonds, which can supply the bonding electron pair to suitable substrates [11]. As an example, the diborane(4) (oTol)$_2$B–B(oTol)$_2$ and H_2 furnish the diborane(6) (oTol)$_2$B-(μ-H)$_2$-B(oTol)$_2$ (Lin and Yamashita; oTol = *ortho*-tolyl) [12]. Braunschweig has employed electron-rich species with boron-boron multiple bonds in a similar vein [13]. Particularly important in the context of this paper is the reductive cleavage of elemental selenium and tellurium by *trans*-IMe(Ar)B═B(Ar)IMe to afford three-membered B_2Se- and B_2Te-ring compounds (IMe = 1,3-dimethylimidazol-2-ylidene; Ar = 5-SiMe$_3$-2-thienyl) [14]. Using the triply bonded IDip–B≡B–IDip, his group also achieved the analogous activation of Te_2Ph_2 (Scheme 2: IDip = 1,3-(diisopropylphenyl)imidazol-2-ylidene) [14]. Stephan published the thiolate-adduct salt [Cp*$_2$Fe][(C$_6$F$_5$)$_3$B–SPh], which resulted from an electron-transfer reaction between the redox-active Lewis acid (C$_6$F$_5$)$_3$B, the one-electron donor Cp*$_2$Fe, and 0.5 equiv of S_2Ph_2 (Scheme 2; Cp* = C$_5$Me$_5$) [15]. The activation of dichalcogens is not restricted to electron-rich triel molecules: Streubel observed the 1,4-addition of E_2Ph_2 (E = S, Se) to a 1,4-diphosphinine (Scheme 2) [16]. Given the isoelectronic relationship between this compound and DBA-dianions, we decided to study also the behavior of $[\mathbf{A}]^{2-}$-type molecules in this respect. Herein, we report the reaction between $[\mathbf{1}]^{2-}$ (≙ $[\mathbf{A}]^{2-}$ with R = Me; Scheme 3) and the whole series of compounds $O_2(t\mathrm{Bu})_2$, S_2Me_2, $S_2(p\mathrm{Tol})_2$, Se_2Ph_2, and Te_2Ph_2. The organic substituents were chosen such as to minimize the hazards of the starting materials and to ensure maximum comparability with literature examples.

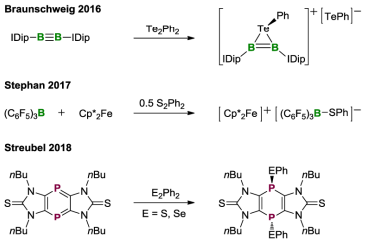

Scheme 2. Selected examples of dichalcogen activation by a diboryne (top), (C$_6$F$_5$)$_3$B/decamethylferrocene (Cp*$_2$Fe; middle), and a 1,4-diphosphinine (bottom). IDip = 1,3-(diisopropylphenyl)imidazol-2-ylidene.

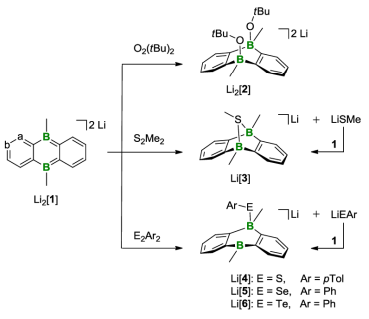

Scheme 3. Dichalcogen-to-chalcogenide reduction by Li$_2$[**1**] to give the *syn*-diadduct Li$_2$[**2**], the bridged monoadduct Li[**3**], and the terminal monoadducts Li[**4**]-Li[**6**].

2. Results and discussion

All five dichalcogens react with Li$_2$[**1**] at room temperature in THF under reductive cleavage of the chalcogen–chalcogen bonds to selectively and quantitatively furnish the corresponding lithium chalcogenides and the neutral DBA **1**. According to X-ray crystallography, both equivalents of Li[O(tBu)] remain coordinated to the two boron atoms of **1**, whereas the heavier analogs form only 1:1 adducts (Scheme 3, Fig. 2).

The single crystals used for X-ray diffraction were obtained directly from the reaction mixtures after treatment of the latter with excess 12-crown-4 (12-c-4) and slow addition of *n*-hexane *via* gas-phase diffusion. Each of the adduct salts [Li(thf)][Li(12-c-4)$_2$][**2**], [Li(12-c-4)$_2$][**4**], and [Li(12-c-4)$_2$][**5**] contains two crystallographically independent, solvent-separated ion pairs in the asymmetric unit. Bond lengths and angles given without an estimated standard deviation (*cf.* Table 1) are the averaged values of all corresponding structural parameters within the same molecule and, where applicable, also within the symmetry-independent congeners.

In the case of [Li(thf)][Li(12-c-4)$_2$][**2**], the central B_2C_4 ring adopts a boat conformation, the two sterically demanding [O(tBu)]$^-$ ligands occupy axial positions in a *syn* fashion with a B–O bond length of 1.560 Å and almost parallel aligned B–O bond vectors (B–B–O angle = 91.9°, O–B–B–O torsion angle = 4.4°). The equatorial positions suffer from steric effects exerted by the *peri*-H atoms. A [Li(thf)]$^+$ cation is chelated by the two oxygen atoms and establishes two additional short contacts to the *ipso*-carbon atoms of one *o*-phenylene ring (Li···C = 2.495 Å). We note in this context that also the neutral SMe_2 diadduct of the parent 9,10-dihydro-9,10-diboraanthracene crystallizes in a boat conformation with axial SMe_2 ligands [17]. The corresponding pyridine diadduct has a perfectly planar DBA scaffold with *anti*-oriented ligands in the solid state. According to quantum-chemical calculations, this structural motif is energetically favored by 2.5 kcal mol^{-1} compared to the respective boat structure with two axial pyridine rings [18].

The small [SMe]$^-$ ligand in [Li(12-c-4)$_2$][**3**] adopts a bridging position between the two boron atoms with B–S bond lengths of 2.089(6) and 2.072(5) Å, a B–S–B bond angle of 79.4(2)°, and a bond-angle sum about the pyramidalized sulfur atom of 295°. [Li(12-c-4)$_2$][**3**] is the first crystallographically characterized example of a compound containing two triorganylborane units and a bridging thiolate ligand. We therefore used the dimeric 9-(methylthio)-9-borabicyclo[3.3.1]nonane for comparison, which has a slightly shorter average B–S bond length of 1.994 Å and a less acute B–S–B bond angle of 84.1° [19].

The sterically demanding [S(pTol)]$^-$ ligand in [Li(12-c-4)$_2$][**4**] is attached to only one boron center (B–S = 1.996 Å), the sulfur atom even points away from the other boron atom, and the pTol substituent is placed above the central B_2C_4 ring. A similar structural motif is also established by the adducts of the heavier chalcogenides [Li(12-c-4)$_2$][**5**] (B–Se = 2.158 Å) and [Li(12-c-4)$_2$][**6**] (B–Te = 2.451(4) Å). Along the series [**4**]$^-$, [**5**]$^-$, and [**6**]$^-$, the B–E–C angles continuously decrease from 112.4° (E = S) to 99.1(2)° (E = Te), in line with the declining proneness of the heavier donor atoms to undergo hybridization (*cf.* [tBu$_3$PS(pTol)]-[(C$_6$F$_5$)$_3$B–S(pTol)] [20]: B–S = 1.991(3) Å, B–S–C = 104.95(13)°) [21,22]. The chalcogen-attached BC_3 moieties become less and less pyramidalized with bond-angle sums Σ(C–B^{tetra}–C) ranging from 335.5° (E = S) up to 347.7° (E = Te; *cf.* 3 × 109.5° = 328.5°) such that the B–B–E angles more and more closely approach a value of 90° (Table 1). These trends reflect the decreasing affinity of the Lewis acidic boron centers to the increasingly softer Lewis bases.

THF-d_8 was used for the NMR spectroscopic characterization of all reaction products. The NMR shift values given in the Experimental section refer to the reaction mixtures; plots of NMR spectra

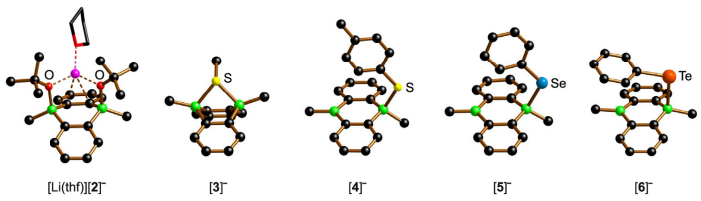

Fig. 2. Molecular structures of [Li(thf)][Li(12-*c*-4)$_2$][**2**], [Li(12-*c*-4)$_2$][**3**], [Li(12-*c*-4)$_2$][**4**], [Li(12-*c*-4)$_2$][**5**], and [Li(12-*c*-4)$_2$][**6**] in the solid state. All [Li(12-*c*-4)$_2$]$^+$ cations and H atoms are omitted for clarity.

Table 1
Selected (averaged) structural parameters of the solid-state structures shown in Fig. 2. In the case of the disordered anion [**6**]$^-$, the data refer to the major occupied sites.

	[**2**]$^{2-}$	[**3**]$^-$	[**4**]$^-$	[**5**]$^-$	[**6**]$^-$
B–E [Å]	1.560	2.081	1.996	2.158	2.451(4)
B–E–C [°]	128.9	107.8	112.4	111.2	99.1(2)
Σ(C–B^{tetra}–C) [°]	329.8	348.0	335.5	338.7	347.7
Σ(C–B^{tri}–C) [°]	–/–	–/–	359.7	359.8	359.4
B–B–E [°]	91.9	50.3	127.9	125.2	97.3

recorded on samples of re-dissolved single crystals are shown in the Supporting Information. The ^{1}H, ^{11}B, and ^{13}C{^{1}H} NMR spectra of [Li(thf)][Li(12-*c*-4)$_2$][**2**] are in agreement with the presence of a diadduct of average C_{2v} symmetry on the NMR timescale (no symmetry breaking by Li$^+$ coordination; free librational motion about the B–O and O–C bonds). The boron resonance appears at δ(^{11}B) = −2.0. The NMR spectra of [Li(12-*c*-4)$_2$][**3**] show signal patterns of a C_{2v}-symmetric monoadduct (proton-integral ratio SMe:BMe = 3:6). The high average symmetry of [**3**]$^-$ in solution requires a fast (formal) inversion of the pyramidalized bridging sulfur atom, which likely proceeds *via* a partially dissociated state [23]. In the case of [Li(12-*c*-4)$_2$][**4**], this process is taken to the extreme and the thiolate ligand rapidly swaps between both boron sites (TolMe:BMe = 3:6; see also Fig. 3 bottom). The ^{11}B NMR shift values of [Li(12-*c*-4)$_2$][**3**] and [Li(12-*c*-4)$_2$][**4**] are 2.3 and 22.0 ppm, respectively, and testify to a significantly lower proportion of free Lewis acid **1** in the association/dissociation equilibrium of [**3**]$^-$ [24]. Even at −30 °C, both adducts retain their dynamic behavior. The amounts of crystalline [Li(12-*c*-4)$_2$][**5**] and [Li(12-*c*-4)$_2$][**6**] were too low to obtain meaningful NMR spectra from their THF-d_8 solutions.

In addition to the isolated products, we have also investigated the crude reaction mixtures of Li[**3**] - Li[**6**] by NMR spectroscopy. The qualitative results were the same, irrespective of the dichalcogen applied and are exemplarily discussed for S$_2$(*p*Tol)$_2$: After the addition of 1 equiv of S$_2$(*p*Tol)$_2$ to Li$_2$[**1**], the *p*Tol substituents give rise to only three ^{1}H NMR signals and the DBA moiety also shows only one BMe, one H-a, and one H-b resonance (Fig. 3 top; Scheme 3). The corresponding integral ratios reveal a 2:1 stoichiometry between the [S(*p*Tol)]$^-$ anions and the organoborane. It is therefore not possible to distinguish between free *vs*. coordinated thiolate ligands, which indicates that intermolecular ligand exchange takes place in addition to the above-mentioned intramolecular dynamic processes (dynamic monoadducts of DBAs with Lewis bases such as H$_3$CCN and F$^-$ have already been described [25]). As a further test, we reduced the amount of free ligand in the mixture by adding 1 equiv of the acceptor molecule **1** to the NMR sample, whereupon the spectrum showed exclusively the already familiar signal pattern of [Li(12-*c*-4)$_2$][**4**] (except for the crown ether resonance; Fig. 3 bottom).

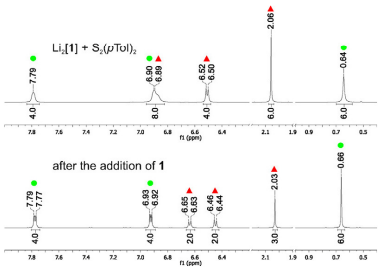

Fig. 3. ^{1}H NMR spectra (500.2 MHz, THF-d_8) of the 1:1 reaction mixture Li$_2$[**1**]/S$_2$(*p*Tol)$_2$ before (top) and after (bottom) the addition of 1 equiv of **1** (● DBA, ▲ [S(*p*Tol)]$^-$ resonances).

3. Conclusion

With this contribution, we have broadened the scope of 9,10-dihydro-9,10-diboraanthracene dianions for small molecule activation to include the reductive cleavage of dichalcogens E$_2$R$_2$ (E = O-Te) [26]. Our results thus indicate that main-group ambiphiles, consisting of just an organoborane and a reducing agent, can not only rival classic FLP reactivity, but even bring about bond-cleavage reactions that have rarely been observed with Lewis acid/base combinations [27].

4. Experimental section

All reactions and manipulations were carried out in an argon-filled glovebox or by applying standard Schlenk techniques under a nitrogen atmosphere. THF was dried over Na/benzophenone; THF-d_8 was dried over Na-K alloy without benzophenone. Prior to use, the solvents were freshly distilled from the drying agent and degassed by applying three freeze-pump-thaw cycles. If not stated otherwise, NMR spectra were recorded at 298 K using Bruker Avance-300 or Avance-500 spectrometers. Chemical shifts are referenced to (residual) solvent signals (^{1}H/^{13}C{^{1}H}; THF-d_8: δ = 3.58/67.21 ppm) [28] or external BF$_3$·Et$_2$O (^{11}B). Abbreviations: s = singlet, d = doublet, t = triplet, m = multiplet, br = broad. The compounds **1** [29] and Li$_2$[**1**] [8] were synthesized according to literature procedures.

Li$_2$[1]: In a glovebox, exc. Li granules were added to a solution of **1** (10 mg, 49 μmol) in THF-d_8 (0.5 mL). The conversion to Li$_2$[**1**] was usually quantitative after 1 h. Non-consumed Li metal was removed and the solution used without further processing.

Li$_2$[2]: Neat O$_2$(*t*Bu)$_2$ (9.1 μL, 7.2 mg, 49 μmol) was added to an

NMR tube containing Li_2[**1**] (49 μmol) in THF-d_8 (0.5 mL), whereupon the initially deep red solution immediately became colorless. The NMR tube was flame-sealed. NMR spectroscopy revealed an essentially quantitative consumption of the starting materials. ^{1}H NMR (500.2 MHz, THF-d_8): $\delta = 7.64–7.62$ (m, 4H; H-a), 6.75–6.74 (m, 4H; H-b), 1.12 (s, 18H; CCH_3), 0.42 (s, 6H; BCH_3). ^{11}B NMR (160.5 MHz, THF-d_8): $\delta = -2.0$ ($h_{1/2} = 290$ Hz). ^{13}C{^{1}H} NMR (125.8 MHz, THF-d_8): $\delta = 164.4$ (br; BC), 132.6 (C-a), 123.0 (C-b), 71.0 (CCH_3), 33.5 (CCH_3), 12.1 (br; BCH_3).

Li[3]: Neat S_2Me_2 (4.4 μL, 4.6 mg, 49 μmol) was added to an NMR tube containing Li_2[**1**] (49 μmol) in THF-d_8 (0.5 mL), whereupon the initially deep red solution immediately became colorless. The NMR tube was flame-sealed. NMR spectroscopy revealed an essentially quantitative consumption of the starting materials. After the addition of **1** (10 mg, 49 μmol) to the sample, only ^{1}H and ^{13}C{^{1}H} resonances assignable to Li[**3**] remained. ^{1}H NMR (500.2 MHz, THF-d_8): $\delta = 7.08–7.07$ (m, 4H; H-a), 6.60–6.58 (m, 4H; H-b), 1.23 (s, 3H; SCH_3), 0.34 (s, 6H; BCH_3). ^{11}B NMR (160.5 MHz, THF-d_8): $\delta = 4.8$ ($h_{1/2} = 390$ Hz). ^{13}C{^{1}H} NMR (125.8 MHz, THF-d_8): $\delta = 164.2$ (br; BC), 126.9 (C-a), 122.1 (C-b), 12.3 (SCH_3), −0.2 (br; BCH_3).

Li[4]: Neat $S_2(p\text{Tol})_2$ (12 mg, 49 μmol) was added to an NMR tube containing Li_2[**1**] (49 μmol) in THF-d_8 (0.5 mL), whereupon the initially deep red solution immediately became pale yellow. The NMR tube was flame-sealed. NMR-spectroscopy revealed an essentially quantitative consumption of the starting materials. After the addition of **1** (10 mg, 49 μmol) to the sample, only ^{1}H and ^{13}C{^{1}H} resonances assignable to Li[**4**] remained. ^{1}H NMR (500.2 MHz, THF-d_8): $\delta = 7.79–7.77$ (m, 4H; H-a), 6.93–6.92 (m, 4H; H-b), 6.64 (d, $^3J_{HH} = 7.9$ Hz, 2H; Tol-H-*o*), 6.45 (d, $^3J_{HH} = 7.9$ Hz, 2H; Tol-H-*m*), 2.03 (s, 3H; Tol-CH_3-*p*), 0.66 (s, 6H; BCH_3). ^{11}B NMR (160.5 MHz. THF-d_8): $\delta = 25.4$ ($h_{1/2} = 650$ Hz). ^{13}C{^{1}H} NMR (125.8 MHz, THF-d_8): $\delta = 159.3$ (br; BC), 142.8 (Tol-C-*i*), 132.6 (C-a), 132.4 (Tol-C-*o*), 130.2 (Tol-C-*p*), 127.6 (Tol-C-*m*), 125.3 (C-b), 20.7 (Tol-CH_3-*p*), 8.3 (BCH_3).

Li[5]: Neat Se_2Ph_2 (15 mg, 48 μmol) was added to an NMR tube containing Li_2[**1**] (49 μmol) in THF-d_8 (0.5 mL), whereupon the initially deep red solution immediately became yellow. The NMR tube was flame-sealed. NMR-spectroscopy revealed an essentially quantitative consumption of the starting materials. After the addition of **1** (10 mg, 49 μmol) to the sample, only ^{1}H and ^{13}C{^{1}H} resonances assignable to Li[**5**] remained. ^{1}H NMR (500.2 MHz, THF-d_8): $\delta = 7.82–7.80$ (m, 4H; H-a), 7.00–6.98 (m, 4H; H-b), 6.86–6.85 (m, 2H; Ph-H-*o*), 6.74–6.71 (m, 1H; Ph-H-*p*), 6.66–6.63 (m, 2H; Ph-H-*m*), 0.79 (s, 6H; BCH_3). ^{11}B NMR (160.5 MHz, THF-d_8): $\delta = 29.5$ ($h_{1/2} = 820$ Hz). ^{13}C{^{1}H} NMR (125.8 MHz, THF-d_8): $\delta = 157.6$ (br; BC), 139.7 (Ph-C-*i*), 136.0 (Ph-C-*o*), 133.6 (C-a), 126.8 (Ph-C-*m*), 125.8 (C-b), 122.8 (Ph-C-*p*), 7.6 (BCH_3).

Li[6]: Neat Te_2Ph_2 (20 mg, 49 μmol) was added to an NMR tube containing Li_2[**1**] (49 μmol) in THF-d_8 (0.5 mL), whereupon the initially deep red solution immediately became orange. The NMR tube was flame-sealed. NMR spectroscopy revealed an essentially quantitative consumption of the starting materials. After the addition of **1** (10 mg, 49 μmol) to the sample, only ^{1}H and ^{13}C{^{1}H} resonances assignable to Li[**6**] remained. ^{1}H NMR (500.2 MHz, THF-d_8): $\delta = 7.85–7.84$ (m, 4H; H-a), 7.23 (d, $^3J_{HH} = 7.0$ Hz, 2H; Ph-H-*o*), 7.02–7.01 (m, 4H; H-b), 6.85 (t, $^3J_{HH} = 7.3$ Hz, 1H; Ph-H-*p*), 6.68–6.65 (m, 2H; Ph-H-*m*), 0.94 (s, 6H; BCH_3). ^{11}B NMR (160.5 MHz, THF-d_8): $\delta = 30.5$ ($h_{1/2} = 900$ Hz). ^{13}C{^{1}H} NMR (125.8 MHz, THF-d_8): $\delta = 156.8$ (br; BC), 141.7 (Ph-C-*o*), 134.0 (C-a), 127.0 (Ph-C-*m*), 126.0 (C-b), 123.7 (Ph-C-*p*), 118.1 (Ph-C-*i*), 7.4 (BCH_3).

X-ray quality crystals of [Li(thf)][Li(12-*c*-4)$_2$][**2**], [Li(12-*c*-4)$_2$][**3**], [Li(12-*c*-4)$_2$][**4**], [Li(12-*c*-4)$_2$][**5**], and [Li(12-*c*-4)$_2$][**6**] were obtained by gas-phase diffusion of *n*-hexane into a THF-d_8/12-crown-4 solution of Li_2[**2**], Li[**3**], Li[**4**], Li[**5**], and Li[**6**], respectively.

Appendix A. Supplementary data

Supplementary data to this article can be found online at https://doi.org/10.1016/j.tet.2018.11.012.

References

[1] G.C. Welch, R.R. San Juan, J.D. Masuda, D.W. Stephan, Science 314 (2006) 1124.
[2] a) G. Erker, D.W. Stephan (Eds.), Frustrated Lewis Pairs I & II, Springer, Heidelberg, 2013;
b) D.W. Stephan, G. Erker, Chem. Sci. 5 (2014) 2625;
c) D.W. Stephan, J. Am. Chem. Soc. 137 (2015) 10018;
d) G. Kehr, G. Erker, Chem. Rec. 17 (2017) 803.
[3] The redox-activity of arylboranes, together with their emitter qualities are also of great current interest in the field of OLED luminophores. *Reviews*:
a) S. Yamaguchi, A. Wakamiya, Pure Appl. Chem. 78 (2006) 1413;
b) Z.M. Hudson, S. Wang, Acc. Chem. Res. 42 (2009) 1584;
c) A. Lorbach, A. Hübner, M. Wagner, Dalton Trans. 41 (2012) 6048;
d) A. Escande, M.J. Ingleson, Chem. Commun. 51 (2015) 6257;
e) L. Ji, S. Griesbeck, T.B. Marder, Chem. Sci. 8 (2017) 846;
f) E. von Grotthuss, A. John, T. Kaese, M. Wagner, Asian J. Org. Chem. 7 (2018) 37.
Original papers:
g) C. Dou, S. Saito, K. Matsuo, I. Hisaki, S. Yamaguchi, Angew. Chem. Int. Ed. 51 (2012) 12206;
h) T. Kushida, Z. Zhou, A. Wakamiya, S. Yamaguchi, Chem. Commun. 48 (2012) 10715;
i) C. Reus, S. Weidlich, M. Bolte, H.-W. Lerner, M. Wagner, J. Am. Chem. Soc. 135 (2013) 12892;
j) C. Reus, F. Guo, A. John, M. Winhold, H.-W. Lerner, F. Jäkle, M. Wagner, Macromolecules 47 (2014) 3727;
k) A.J. Warner, J.R. Lawson, V. Fasano, M.J. Ingleson, Angew. Chem. Int. Ed. 54 (2015) 11245;
l) V.M. Hertz, M. Bolte, H.-W. Lerner, M. Wagner, Angew. Chem. Int. Ed. 54 (2015) 8800;
m) V.M. Hertz, H.-W. Lerner, M. Wagner, Org. Lett. 17 (2015) 5240;
n) K. Schickedanz, T. Trageser, M. Bolte, H.-W. Lerner, M. Wagner, Chem. Commun. 51 (2015) 15808;
o) F. Miyamoto, S. Nakatsuka, K. Yamada, K. Nakayama, T. Hatakeyama, Org. Lett. 17 (2015) 6158;
p) V.M. Hertz, J.G. Massoth, M. Bolte, H.-W. Lerner, M. Wagner, Chem. Eur. J. 22 (2016) 13181;
q) V.M. Hertz, N. Ando, M. Hirai, M. Bolte, H.-W. Lerner, S. Yamaguchi, M. Wagner, Organometallics 36 (2017) 2512;
r) A. John, M. Bolte, H.-W. Lerner, M. Wagner, Angew. Chem. Int. Ed. 56 (2017) 5588;
s) K. Schickedanz, J. Radtke, M. Bolte, H.-W. Lerner, M. Wagner, J. Am. Chem. Soc. 139 (2017) 2842;
t) J. Radtke, S.K. Mellerup, M. Bolte, H.-W. Lerner, S. Wang, M. Wagner, Org. Lett. 20 (2018) 3966;
u) A. John, M. Bolte, H.-W. Lerner, G. Meng, S. Wang, T. Peng, M. Wagner, J. Mater. Chem. C 6 (2018) 10881.
[4] a) D. Wu, L. Kong, Y. Li, R. Ganguly, R. Kinjo, Nat. Commun. 6 (2015) 7340;
b) D. Wu, R. Ganguly, Y. Li, S.N. Hoo, H. Hirao, R. Kinjo, Chem. Sci. 6 (2015) 7150.
[5] B. Wang, Y. Li, R. Ganguly, H. Hirao, R. Kinjo, Nat. Commun. 7 (2016) 11871.
[6] E. von Grotthuss, M. Diefenbach, M. Bolte, H.-W. Lerner, M.C. Holthausen, M. Wagner, Angew. Chem. Int. Ed. 55 (2016) 14067.
[7] A. Lorbach, M. Bolte, H.-W. Lerner, M. Wagner, Organometallics 29 (2010) 5762.
[8] E. von Grotthuss, S.E. Prey, M. Bolte, H.-W. Lerner, M. Wagner, Angew. Chem. Int. Ed. (2018), https://doi.org/10.1002/anie.201811135.
[9] J.W. Taylor, A. McSkimming, C.F. Guzman, W.H. Harman, J. Am. Chem. Soc. 139 (2017) 11032.
[10] a) Y. Su, Y. Li, R. Ganguly, R. Kinjo, Angew. Chem. Int. Ed. 57 (2018) 7846;
b) B. Wang, R. Kinjo, Tetrahedron (2018), https://doi.org/10.1016/j.tet.2018.10.067.
[11] a) A. Hübner, A.M. Diehl, M. Diefenbach, B. Endeward, M. Bolte, H.-W. Lerner, M.C. Holthausen, M. Wagner, Angew. Chem. Int. Ed. 53 (2014) 4832;
b) H. Asakawa, K.-H. Lee, Z. Lin, M. Yamashita, Nat. Commun. 5 (2014) 4245;
c) A. Hübner, T. Kaese, M. Diefenbach, B. Endeward, M. Bolte, H.-W. Lerner, M.C. Holthausen, M. Wagner, J. Am. Chem. Soc. 137 (2015) 3705;
d) Y. Katsuma, H. Asakawa, K.-H. Lee, Z. Lin, M. Yamashita, Organometallics 35 (2016) 2563;
e) T. Araki, M. Hirai, A. Wakamiya, W.E. Piers, S. Yamaguchi, Chem. Lett. 46 (2017) 1714;
f) T. Kaese, H. Budy, M. Bolte, H.-W. Lerner, M. Wagner, Angew. Chem. Int. Ed. 56 (2017) 7546;
g) Y. Katsuma, H. Asakawa, M. Yamashita, Chem. Sci. 9 (2018) 1301;
h) J. Zheng, Z.H. Li, H. Wang, Chem. Sci. 9 (2018) 1433;
i) Y. Katsuma, N. Tsukahara, L. Wu, Z. Lin, M. Yamashita, Angew. Chem. Int. Ed.

57 (2018) 6109.
[12] N. Tsukahara, H. Asakawa, K.-H. Lee, Z. Lin, M. Yamashita, J. Am. Chem. Soc. 139 (2017) 2593.
[13] a) M. Arrowsmith, J. Böhnke, H. Braunschweig, M.A. Celik, T. Dellermann, K. Hammond, Chem. Eur. J. 22 (2016) 17169;
b) A. Stoy, J. Böhnke, J.O.C. Jiménez-Halla, R.D. Dewhurst, T. Thiess, H. Braunschweig, Angew. Chem. Int. Ed. 57 (2018) 5947;
c) see also: T. Kaese, T. Trageser, H. Budy, M. Bolte, H.-W. Lerner, M. Wagner Chem. Sci. 9 (2018) 3881.
[14] H. Braunschweig, P. Constantinidis, T. Dellermann, W.C. Ewing, I. Fischer, M. Hess, F.R. Knight, A. Rempel, C. Schneider, S. Ullrich, A. Vargas, J.D. Woollins, Angew. Chem. Int. Ed. 55 (2016) 5606.
[15] a) L.L. Liu, L.L. Cao, Y. Shao, D.W. Stephan, J. Am. Chem. Soc. 139 (2017) 10062;
b) see also: L. Kaufmann, H. Vitze, M. Bolte, H.-W. Lerner, M. Wagner Organometallics 27 (2008) 6215.
[16] A. Koner, Z. Kelemen, G. Schnakenburg, L. Nyulaszi, R. Streubel, Chem. Commun. 54 (2018) 1182.
[17] A. Lorbach, M. Bolte, H.-W. Lerner, M. Wagner, Chem. Commun. 46 (2010) 3592.
[18] A. Lorbach, M. Bolte, H. Li, H.-W. Lerner, M.C. Holthausen, F. Jäkle, M. Wagner, Angew. Chem. Int. Ed. 48 (2009) 4584.
[19] a) R. Köster, G. Seidel, R. Boese, Chem. Ber. 121 (1988) 1137;
b) M. Yalpani, R. Köster, R. Boese, Chem. Ber. 122 (1989) 19.
[20] M.A. Dureen, G.C. Welch, T.M. Gilbert, D.W. Stephan, Inorg. Chem. 48 (2009) 9910.
[21] W. Kutzelnigg, Angew. Chem. Int. Ed. 23 (1984) 272.
[22] H.B. Wedler, P. Wendelboe, P.P. Power, Organometallics 37 (2018) 2929.
[23] P.C. Turley, P. Haake, J. Am. Chem. Soc. 89 (1967) 4617.
[24] H. Nöth, B. Wrackmeyer, Nuclear magnetic resonance spectroscopy of boron compounds, in: P. Diehl, E. Fluck, R. Kosfeld (Eds.), NMR Basic Principles and Progress, Springer, Berlin, 1978.
[25] a) S. Kirschner, J.-M. Mewes, M. Bolte, H.-W. Lerner, A. Dreuw, M. Wagner, Chem. Eur. J. 23 (2017) 5104;
b) T. Agou, M. Sekine, T. Kawashima, Tetrahedron Lett. 51 (2010) 5013.
[26] This transformation might well follow a concerted mechanism (compare the examples given in Ref. [6], the *syn* configuration of the diadduct Li_2[**2**], and the fact that *in situ* NMR spectroscopy did not provide any hints at the presence of paramagnetic impurities). However, an outer sphere, single-electron transfer process can also not be ruled out, given that the reduction of dichalcogens to the corresponding chalcogenides is also possible through heterogeneous electron transfer from, *e.g.*, alkali metals or a cathodic current:
a) K.J. Irgolic, P.J. Busse, R.A. Grigsby, M.R. Smith, J. Organomet. Chem. 88 (1975) 175;
b) A. Sobkowiak, D.T. Sawyer, Inorg. Chem. 29 (1990) 1248;
c) T.I. Kückmann, M. Hermsen, M. Bolte, M. Wagner, H.-W. Lerner, Inorg. Chem. 44 (2005) 3449.
[27] B. Inés, S. Holle, R. Goddard, M. Alcarazo, Angew. Chem. Int. Ed. 49 (2010) 8389.
[28] G.R. Fulmer, A.J.M. Miller, N.H. Sherden, H.E. Gottlieb, A. Nudelman, B.M. Stoltz, J.E. Bercaw, K.I. Goldberg, Organometallics 29 (2010) 2176.
[29] S.N. Kessler, M. Neuburger, H.A. Wegner, Eur. J. Org. Chem. (2011) 3238.

Supporting Information

Chalcogen–chalcogen-bond activation by an ambiphilic, doubly reduced organoborane

Esther von Grotthuss, Felix Nawa, Michael Bolte, Hans-Wolfram Lerner, and Matthias Wagner*

Institut für Anorganische und Analytische Chemie, Goethe-Universität Frankfurt,
Max-von-Laue-Strasse 7, 60438 Frankfurt (Main), Germany
E-mail: Matthias.Wagner@chemie.uni-frankfurt.de

Table of contents:

1. Comparisons of the ^{1}H NMR spectra of the reactions between Li_2[1] and E_2R_2 before and after the addition of 1

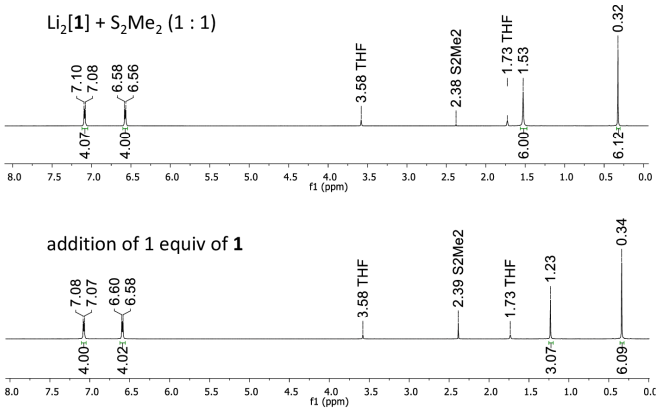

Figure S1. ^{1}H NMR spectrum (500.2 MHz, THF-d_8) of the reaction mixture of S_2Me_2 and 1 equiv of Li_2[**1**] (top). ^{1}H NMR spectrum of the same sample after the addition of 1 equiv of **1** (bottom).

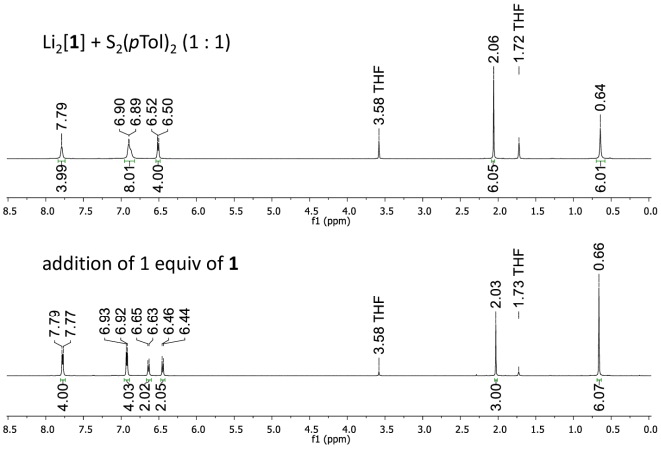

Figure S2. ^{1}H NMR spectrum (500.2 MHz, THF-d_8) of the reaction mixture of S_2(*p*Tol)$_2$ and 1 equiv of Li_2[**1**] (top). ^{1}H NMR spectrum of the same sample after the addition of 1 equiv of **1** (bottom; note the better resolution of the AA'BB' spin system of the *p*Tol substituent as a result of less motional broadening).

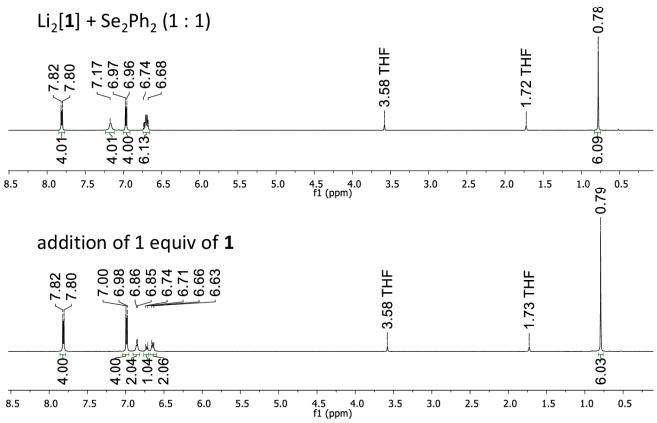

Figure S3. ^{1}H NMR spectrum (500.2 MHz, THF-d_8) of the reaction mixture of Se_2Ph_2 and 1 equiv of Li_2[**1**] (top). ^{1}H NMR spectrum of the same sample after the addition of 1 equiv of **1** (bottom).

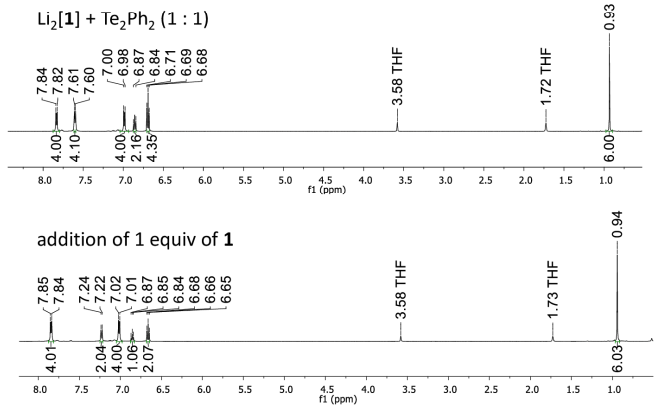

Figure S4. ^{1}H NMR spectrum (500.2 MHz, THF-d_8) of the reaction mixture of Te_2Ph_2 and 1 equiv of Li_2[**1**] (top). ^{1}H NMR spectrum of the same sample after the addition of 1 equiv of **1** (bottom).

2. Plots of the NMR spectra

2.1. NMR spectra of re-dissolved single crystals

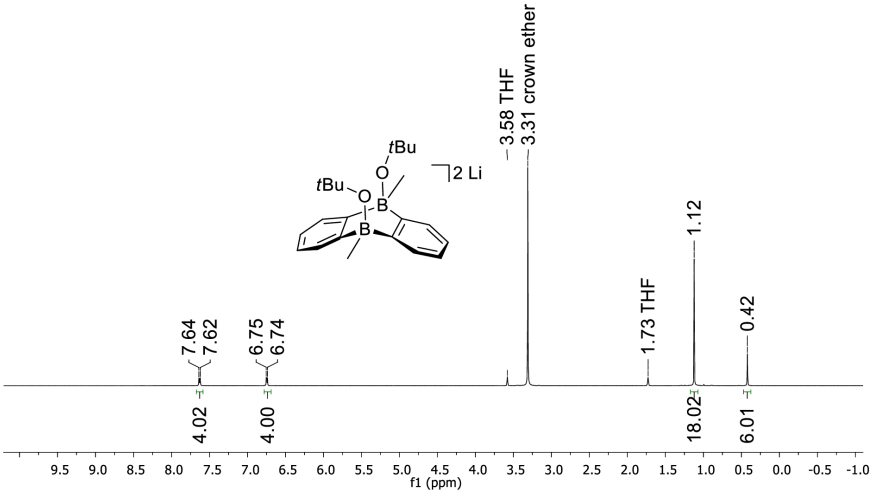

Figure S5. ^{1}H NMR spectrum of [Li(thf)][Li(12-c-4)$_2$][**2**] (500.2 MHz, THF-d_8).

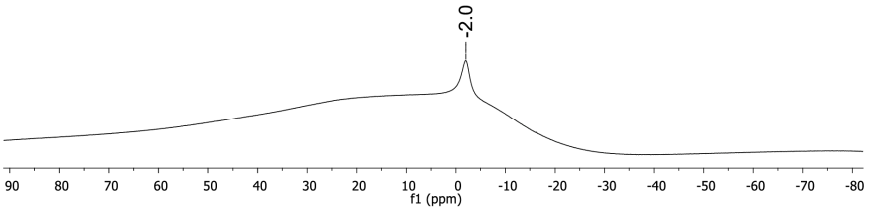

Figure S6. ^{11}B NMR spectrum of [Li(thf)][Li(12-c-4)$_2$][**2**] (160.5 MHz, THF-d_8).

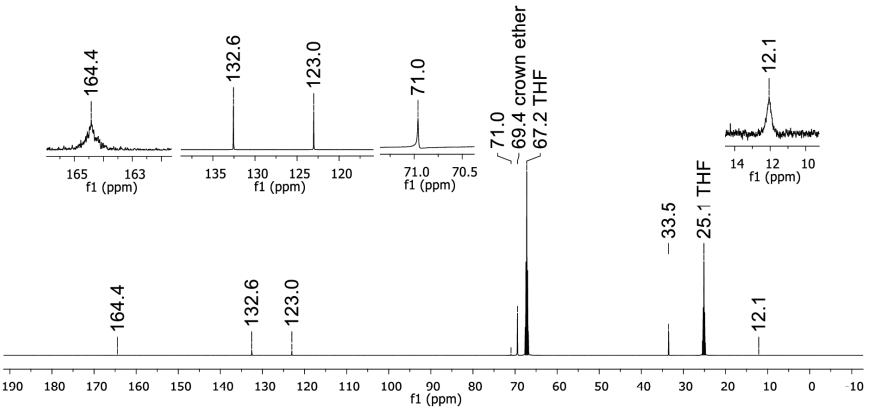

Figure S7. ^{13}C{^{1}H} NMR spectrum of [Li(thf)][Li(12-c-4)$_2$][**2**] (125.8 MHz, THF-d_8).

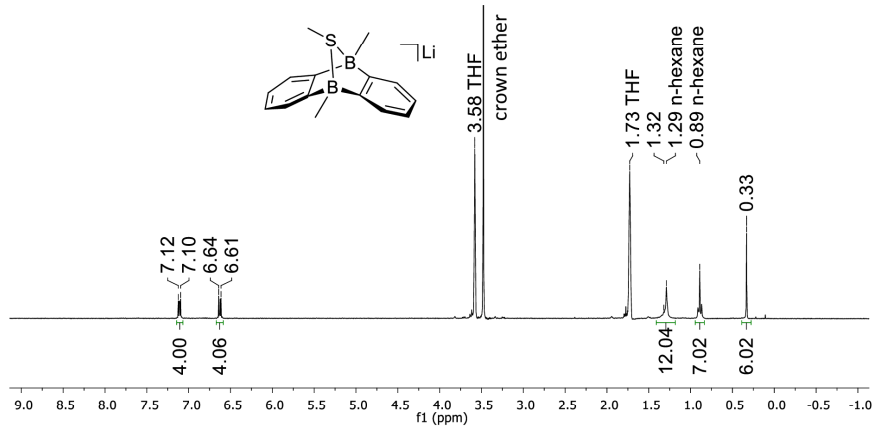

Figure S8. ^{1}H NMR spectrum of [Li(12-c-4)$_2$][**3**] (300.0 MHz, THF-d_8).

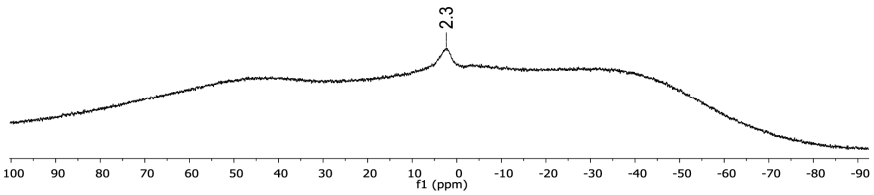

Figure S9. ^{11}B NMR spectrum of [Li(12-c-4)$_2$][**3**] (96.3 MHz, THF-d_8).

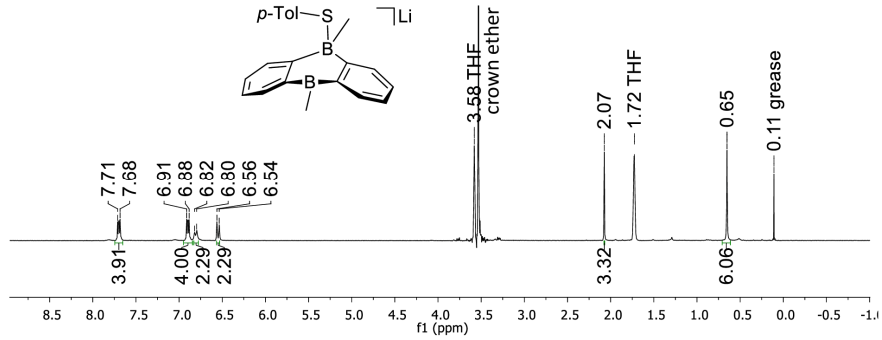

Figure S10. ^{1}H NMR spectrum of [Li(12-c-4)$_2$][**4**] (300.0 MHz, THF-d_8).

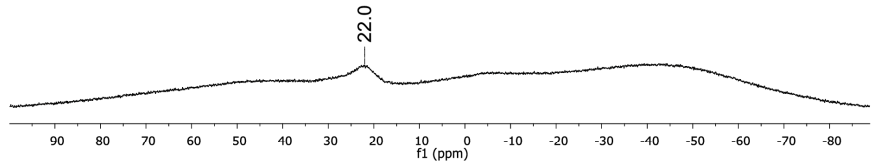

Figure S11. ^{11}B NMR spectrum of [Li(12-c-4)$_2$][**4**] (96.3 MHz, THF-d_8).

2.2. NMR spectra of reaction mixtures

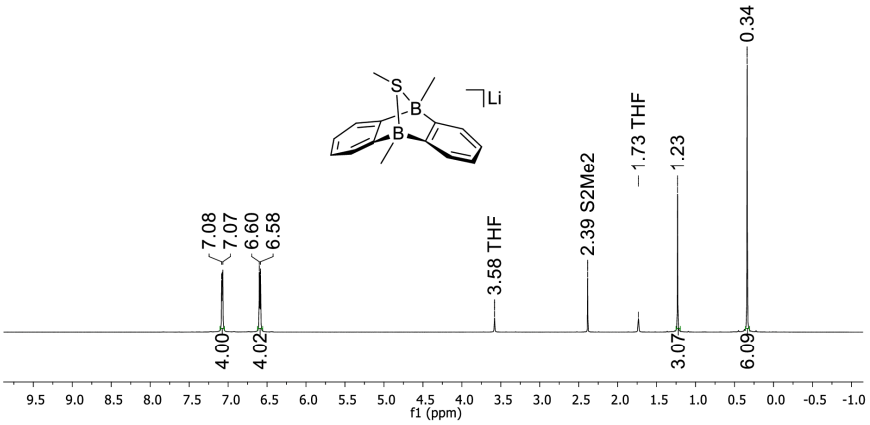

Figure S12. ^{1}H NMR spectrum of Li[**3**] (500.2 MHz, THF-d_8).

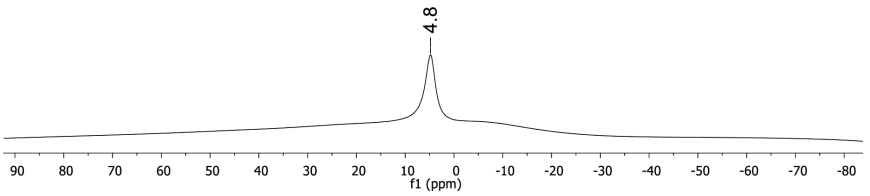

Figure S13. ^{11}B NMR spectrum of Li[**3**] (160.5 MHz, THF-d_8).

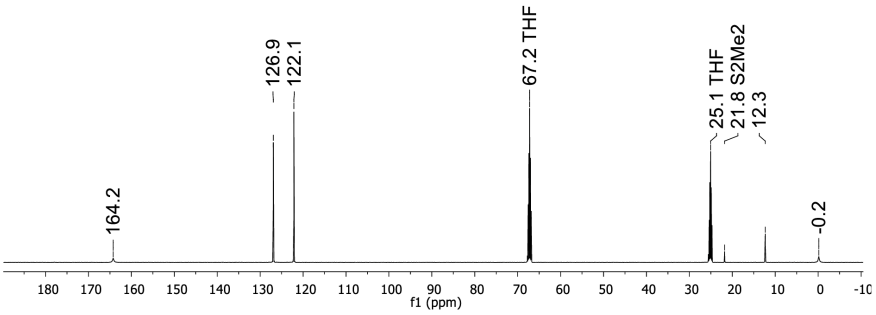

Figure S14. ^{13}C{^{1}H} NMR spectrum of Li[**3**] (125.8 MHz, THF-d_8).

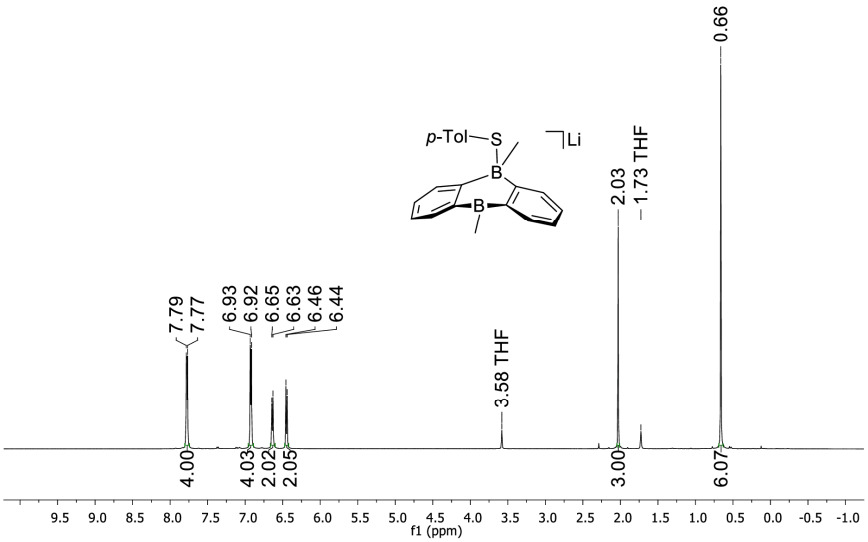

Figure S15. ^{1}H NMR spectrum of Li[**4**] (500.2 MHz, THF-d_8).

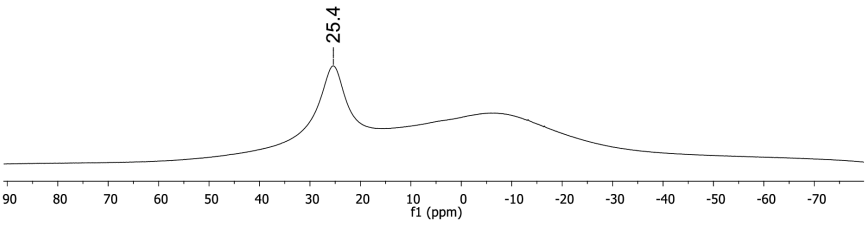

Figure S16. ^{11}B NMR spectrum of Li[**4**] (160.5 MHz, THF-d_8).

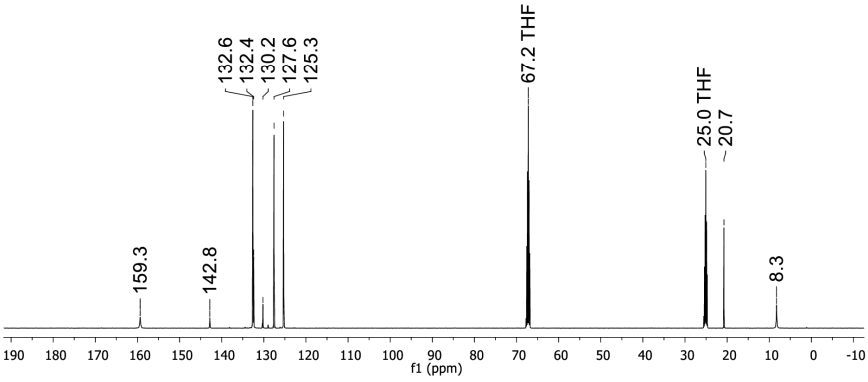

Figure S17. ^{13}C{^{1}H} NMR spectrum of Li[**4**] (125.8 MHz, THF-d_8).

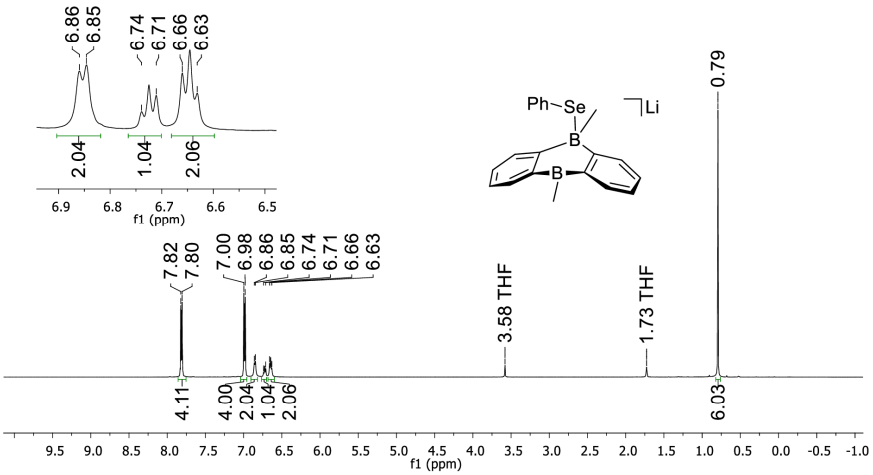

Figure S18. ^{1}H NMR spectrum of Li[**5**] (500.2 MHz, THF-d_8).

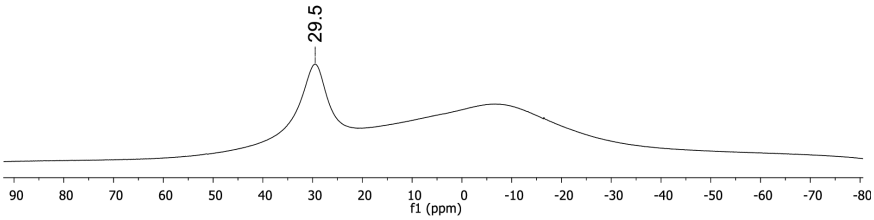

Figure S19. ^{11}B NMR spectrum of Li[**5**] (160.5 MHz, THF-d_8).

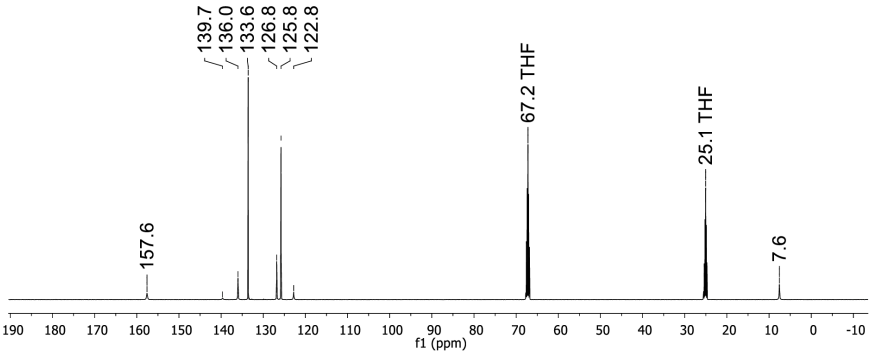

Figure S20. ^{13}C{^{1}H} NMR spectrum of Li[**5**] (125.8 MHz, THF-d_8).

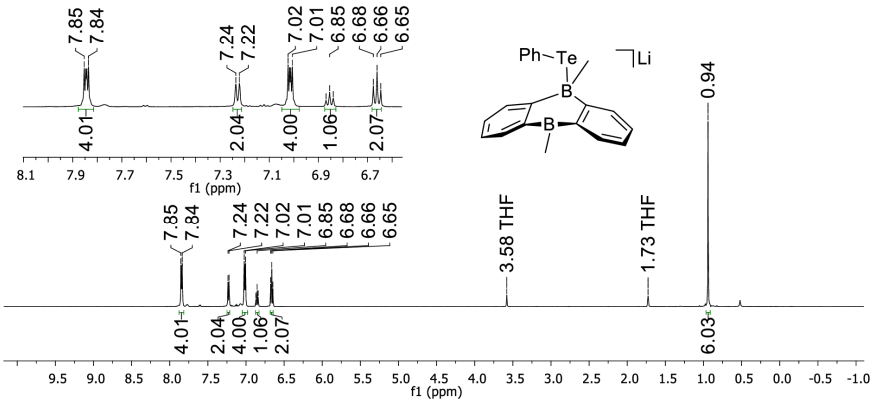

Figure S21. ^{1}H NMR spectrum of Li[**6**] (500.2 MHz, THF-d_8).

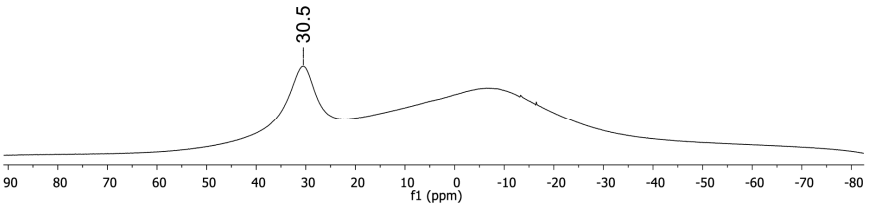

Figure S22. ^{11}B NMR spectrum of Li[**6**] (160.5 MHz, THF-d_8).

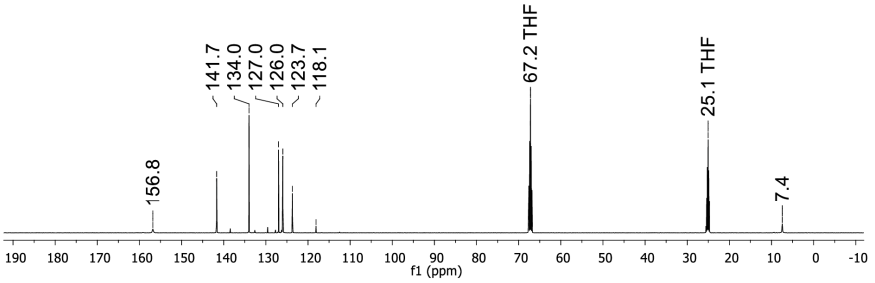

Figure S23. ^{13}C{^{1}H} NMR spectrum of Li[**6**] (125.8 MHz, THF-d_8).

3. X-ray crystal structure analyses

Data for all structures were collected on a STOE IPDS II two-circle diffractometer with a Genix Microfocus tube with mirror optics using Mo$K\alpha$ radiation (λ = 0.71073 Å). The data were scaled using the frame-scaling procedure in the X-AREA program system.[S1] The structures were solved by direct methods using the program SHELX and refined against F^2 with full-matrix least-squares techniques using the program SHELXL-97.[S2]

In [Li(thf)][Li(12-c-4)$_2$][**2**], there are two symmetry-independent formula units in the asymmetric unit. For all atoms of one crown ether ring, the components of the displacement parameters in the direction of the bonds were restrained to be equal.

The absolute structure of [Li(12-c-4)$_2$][**3**] could not be reliably determined; Flack-x-parameter = 0.52(6).

The crystal of [Li(12-c-4)$_2$][**4**] was non-merohedrally twinned with a fractional contribution of 0.628(3) of the major component. There are two symmetry-independent formula units in the asymmetric unit. The anions and the Li^+ cations are related by a non-space group translation (x+1/2, y, z+1/2), whereas the crown ether rings of the two symmetry-independent formula units are rotated by approximately 90^o with respect to each other. The absolute structure could not be reliably determined; Flack-x-parameter = 0.28(7).

The crystal of [Li(12-c-4)$_2$][**5**] was non-merohedrally twinned with a fractional contribution of 0.660(4) of the major component. There are two symmetry-independent formula units in the asymmetric unit. The anions and the Li cations are related by a non-space group translation (x+1/2, y, z+1/2), whereas the crown ether rings of the two symmetry-independent formula units are rotated by approximately 90^o with respect to each other. The absolute structure could not be reliably determined; Flack-x-parameter = 0.314(9). The displacement parameters of all atoms of one crown ether ring were restrained to an isotropic behavior.

[Li(12-c-4)$_2$][**4**] and [Li(12-c-4)$_2$][**5**] are isomorphous and show the same kind of pseudo-symmetry and twinning.

In [Li(12-c-4)$_2$][**6**], the TePh residue is disordered over two positions with a site occupation factor of 0.913(1) for the major occupied sites. The minor occupied C atoms were isotropically refined with a common displacement parameter.

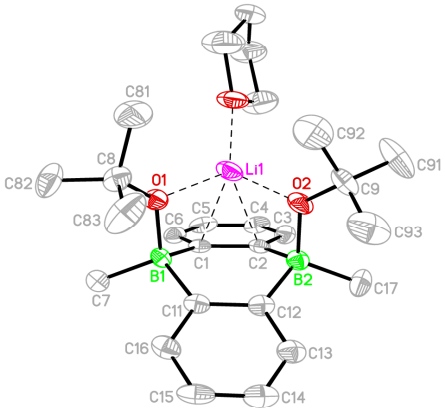

Figure S24. Molecular structure of one of the two crystallographically independent dianions of [Li(thf)][Li(12-c-4)$_2$][**2**] in the solid state. The [Li(12-c-4)$_2$]$^+$ cation and all hydrogen atoms are omitted for clarity. Displacement ellipsoids are drawn at the 50% probability level. Selected bond lengths (Å), atom···atom distances (Å), bond angles (°), and dihedral angles (°) of the two crystallographically independent dianions: B1−C1 = 1.657(7)/1.647(7), B1−C7 = 1.637(7)/1.644(7), B1−C11 = 1.639(7)/1.645(8), B1−O1 = 1.554(6)/1.554(7), B2−C2 = 1.645(7)/1.648(7), B2−C12 = 1.632(8)/1.645(7), B2−C17 = 1.638(7)/1.645(7), B2−O2 = 1.570(6)/1.561(6), C1−C2 = 1.430(7)/1.422(6), C11−C12 = 1.431(7)/1.412(7); Li1···O1 = 1.870(9)/1.869(10), Li1···O2 = 1.872(10)/1.885(9), Li1···C1 = 2.499(10)/2.413(10), Li1···C2 = 2.499(9)/2.570(10); B1−O1−C8 = 128.7(4)/130.7(4), B2−O2−C9 = 128.3(4)/127.8(4) , C1−B1−C11 = 108.1(4)/108.5(4), C2−B2−C12 = 108.6(4)/107.6(4); C1 to C6//C11 to C16 = 39.5(2)/39.0(2).

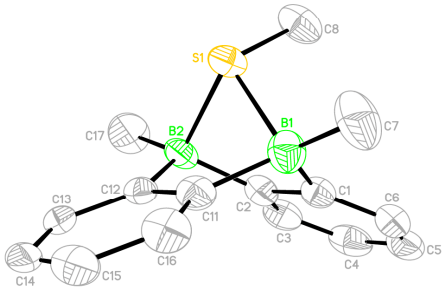

Figure S25. Molecular structure of [Li(12-c-4)$_2$][**3**] in the solid state. The [Li(12-c-4)$_2$]$^+$ cation and all hydrogen atoms are omitted for clarity. Displacement ellipsoids are drawn at the 50% probability level. Selected bond lengths (Å), bond angles (°), and dihedral angle (°): B1−C1 = 1.596(8), B1−C7 = 1.612(7), B1−C11 = 1.618(8), B1−S1 = 2.089(6), B2−C2 = 1.607(7), B2−C12 = 1.610(7), B2−C17 = 1.611(7), B2−S1 = 2.072(5), C1−C2 = 1.429(6), C11−C12 = 1.417(6), S1−C8 = 1.813(6); B1−S1−B2 = 79.4(2), C1−B1−C11 = 109.4(4), C2−B2−C12 = 110.1(4); C1 to C6//C11 to C16 = 51.15(12).

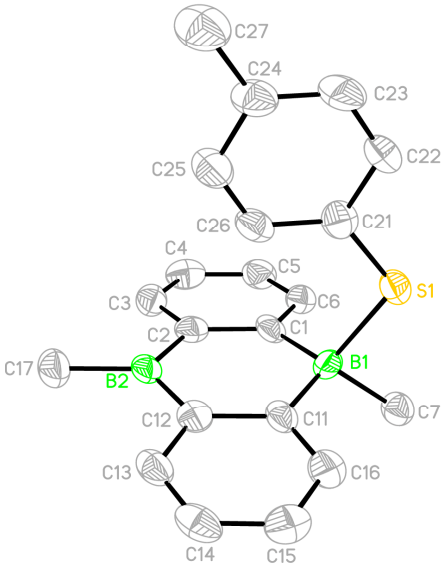

Figure S26. Molecular structure of one of the two crystallographically independent monoanions of $[Li(12\text{-}c\text{-}4)_2][\mathbf{4}]$ in the solid state. The $[Li(12\text{-}c\text{-}4)_2]^+$ cation and all hydrogen atoms are omitted for clarity. Displacement ellipsoids are drawn at the 50% probability level. Selected bond lengths (Å), bond angles (°), and dihedral angles (°) of the two crystallographically independent monoanions: B1−C1 = 1.633(15)/1.639(16), B1−C7 = 1.646(12)/1.629(12), B1−C11 = 1.608(15)/1.588(15), B1−S1 = 1.993(10)/1.999(9), B2−C2 = 1.561(15)/1.529(15), B2−C12 = 1.553(17)/1.572(16), B2−C17 = 1.578(12)/1.587(12), C1−C2 = 1.404(14)/1.413(14), C11−C12 = 1.432(14)/1.406(13), S1−C21 = 1.768(9)/1.763(8); B1−S1−C21 = 113.9(4)/110.9(4), C1−B1−C11 = 113.2(7)/113.6(7), C2−B2−C12 = 118.4(7)/119.9(7); C1 to C6//C11 to C16 = 16.30(18)/1.65(10).

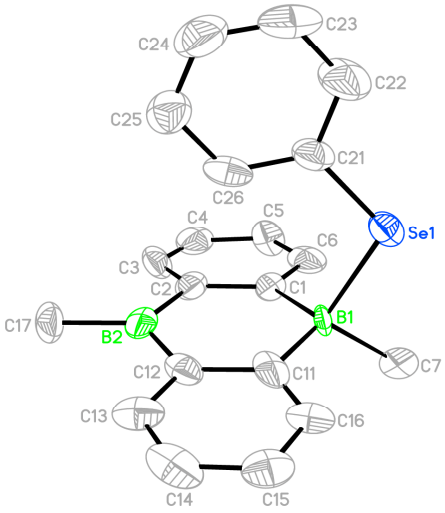

Figure S27. Molecular structure of one of the two crystallographically independent monoanions of $[Li(12\text{-}c\text{-}4)_2][\mathbf{5}]$ in the solid state. The $[Li(12\text{-}c\text{-}4)_2]^+$ cation and all hydrogen atoms are omitted for clarity. Displacement ellipsoids are drawn at the 50% probability level. Selected bond lengths (Å), bond angles (°), and dihedral angles (°) of the two crystallographically independent monoanions: B1−C1 = 1.64(2)/1.64(3), B1−C7 = 1.613(19)/1.611(19), B1−C11 = 1.59(3)/1.60(3), B1−Se1 = 2.161(14)/2.155(14), B2−C2 = 1.56(3)/1.57(3), B2−C12 = 1.58(3)/1.56(3), B2−C17 = 1.58(2)/1.58(2), C1−C2 = 1.41(2)/1.43(2), C11−C12 = 1.43(2)/1.43(2), Se1−C21 = 1.911(14)/1.897(11); B1−Se1−C21 = 113.3(6)/109.0(5), C1−B1−C11 = 113.0(11)/115.5(11), C2−B2−C12 = 119.6(12)/119.8(12); C1 to C6//C11 to C16 = 15.5(3)/2.3(2).

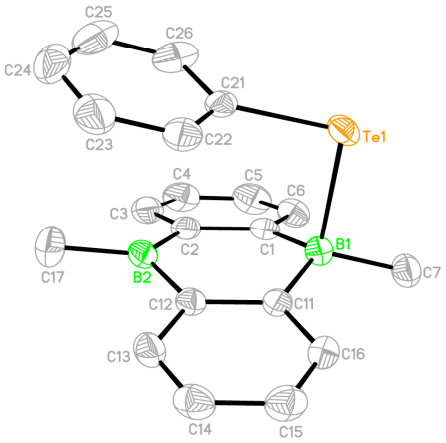

Figure S28. Molecular structure of $[Li(12\text{-}c\text{-}4)_2][\mathbf{6}]$ in the solid state. The minor occupied sites of the TePh group, the $[Li(12\text{-}c\text{-}4)_2]^+$ cation, and all hydrogen atoms are omitted for clarity. Displacement ellipsoids are drawn at the 50% probability level. Selected bond lengths (Å), bond angles (°), and dihedral angle (°) of the major occupied site: B1−C1 = 1.595(6), B1−C7 = 1.608(6), B1−C11 = 1.598(5), B1−Te1 = 2.451(4), B2−C2 = 1.562(6), B2−C12 = 1.556(6), B2−C17 = 1.571(6), C1−C2 = 1.423(5), C11−C12 = 1.422(5), Te1−C21 = 2.113(5); B1−Te1−C21 = 99.14(15), C1−B1−C11 = 114.4(3), C2−B2−C12 = 118.0(3); C1 to C6//C11 to C16 = 23.63(8).

Table S1. Selected crystallographic data for [Li(thf)][Li(12-c-4)$_2$][**2**], [Li(12-c-4)$_2$][**3**], and [Li(12-c-4)$_2$] [**4**].

compound	[Li(thf)][Li(12-c-4)$_2$][**2**]	[Li(12-c-4)$_2$][**3**]	[Li(12-c-4)$_2$][**4**]
CCDC	1873537	1873538	1873539
formula	$C_{42}H_{72}B_2Li_2O_{11}$	$C_{31}H_{49}B_2LiO_8S$	$C_{37}H_{53}B_2LiO_8S$
M_r	788.49	610.32	686.41
T (K)	173(2)	173(2)	173(2)
radiation, λ (Å)	Mo$K\alpha$, 0.71073	Mo$K\alpha$, 0.71073	Mo$K\alpha$, 0.71073
crystal system	monoclinic	orthorhombic	monoclinic
space group	$P2_1/n$	$P2_12_12_1$	$P2_1$
a (Å)	15.9573(10)	9.7517(4)	11.7559(8)
b (Å)	26.7455(10)	13.2986(8)	21.8980(10)
c (Å)	21.3156(12)	25.7368(12)	13.9692(7)
α (°)	90	90	90
β (°)	102.675(5)	90	90.386(5)
γ (°)	90	90	90
V (Å^3)	8875.5(8)	3337.7(3)	3596.0(3)
Z	8	4	4
D_{calcd} (g cm^{-3})	1.180	1.215	1.268
F (000)	3424	1312	1472
μ (mm^{-1})	0.081	0.143	0.141
crystal size (mm)	0.19 × 0.18 × 0.17	0.22 × 0.18 × 0.15	0.21 × 0.11 × 0.06
crystal shape, color	colorless block	colorless block	light yellow plate
reflections collected	74767	25977	35110
independent reflections	15663	6480	13443
R_{int}	0.0986	0.0441	0.0476
data/restraints/parameters	15663 / 72 / 1027	6480 / 0 / 388	13443 / 1 / 886
R_1, wR_2 ($I > 2\sigma(I)$)	0.1195, 0.2787	0.0606, 0.1327	0.0706, 0.1641
R_1, wR_2 (all data)	0.1982, 0.3270	0.0774, 0.1371	0.0940, 0.1878
GOF on F^2	0.981	1.331	1.055
largest difference peak and hole (e Å^{-3})	1.292, –0.345	0.821, –0.231	0.410, –0.366

Table S2. Selected crystallographic data for $[Li(12\text{-c-}4)_2][\mathbf{5}]$ and $[Li(12\text{-c-}4)_2][\mathbf{6}]$.

compound	$[Li(12\text{-c-}4)_2][\mathbf{5}]$	$[Li(12\text{-c-}4)_2][\mathbf{6}]$
CCDC	1873540	1873541
formula	$C_{36}H_{51}B_2LiO_8Se$	$C_{36}H_{51}B_2LiO_8Te$
M_r	719.28	767.92
T (K)	173(2)	173(2)
radiation, λ (Å)	Mo$K\alpha$, 0.71073	Mo$K\alpha$, 0.71073
crystal system	monoclinic	monoclinic
space group	$P2_1$	$P2_1/n$
a (Å)	11.7238(7)	15.3324(4)
b (Å)	22.0401(10)	13.8591(4)
c (Å)	13.8787(7)	18.0259(5)
α (°)	90	90
β (°)	90.675(5)	108.861(2)
γ (°)	90	90
V (Å^3)	3585.9(3)	3624.71(18)
Z	4	4
D_{calcd} (g cm^{-3})	1.332	1.407
F (000)	1512	1584
μ (mm^{-1})	1.097	0.870
crystal size (mm)	0.18 × 0.16× 0.16	0.18 × 0.13 × 0.03
crystal shape, color	yellow block	red plate
reflections collected	52310	48063
independent reflections	13932	6667
R_{int}	0.0606	0.0401
data/restraints/parameters	13932 / 73 / 866	6667 / 0 / 464
R_1, wR_2 ($I > 2\,\sigma(I)$)	0.0804, 0.1975	0.0494, 0.1123
R_1, wR_2 (all data)	0.1049, 0.2154	0.0598, 0.1175
GOF on F^2	1.557	1.091
largest difference peak and hole (e Å^{-3})	2.256, −1.119	0.987, −0.443

4. References

[S1] Stoe & Cie, X.-A. *Diffractometer control program system*; Stoe & Cie: Darmstadt, Germany, **2002**.
[S2] Sheldrick, G. M. *Acta Crystallogr. Sect. A* **2008**, *64*, 112.

6.2.3. Synthesis and Ring Strain of a Benzoborirene-*N*-Heterocyclic Carbene Adduct

ChemPubSoc Europe

DOI: 10.1002/chem.201804629

CHEMISTRY A European Journal Communication

Strained Molecules

Synthesis and Ring Strain of a Benzoborirene-*N*-Heterocyclic Carbene Adduct

Jennifer Hahn,[a] Constanze Keck,[a] Cäcilia Maichle-Mössmer,[b] Esther von Grotthuss,[c] Paul Niklas Ruth,[d] Alexander Paesch,[d] Dietmar Stalke,[d] and Holger F. Bettinger*[a]

Dedicated to Professor W. E. Billups in appreciation of his seminal contributions to strained molecules

Abstract: The reduction of an *N*-heterocyclic carbene (1,3-diisopropyl-4,5-dimethylimidazolin-2-ylidene, l*i*Pr$_{Me_2}$) adduct of dichloro(*ortho*-bromophenyl)borane by *tert*-butyl lithium at low temperature yields the l*i*Pr$_{Me_2}$ adduct **A** of parent benzoborirene, a highly strained boron-containing bicyclic compound. **A** is unstable at room temperature and dimerizes at low temperature to the bis-l*i*Pr$_{Me_2}$ adduct of 9,10-dihydro-9,10-diboraanthracene, characterized by single-crystal X-ray crystallography.

Aromaticity,[1] conjugation,[2] hyperconjugation,[3] and ring strain[4] are classical concepts of organic chemistry. The interplay between strain and aromaticity has attracted quite some attention in efforts to understand the influence of bond-length alternation on the properties of aromatic compounds, and resulted in the synthesis of an impressive array of highly strained annulated aromatic systems.[5] This research was motivated by the Mills–Nixon effect,[6] and culminated in the development of the concept of strain-induced bond localization.[7]

Besides experiment work, theory was also invoked to study the influence of small heterocyclic rings on the aromaticity and bond length alternation in systems that are not accessible experimentally, a case in point being benzoborirene (**1**).[7a,8] This heteroaromatic compound was first observed as a product of the reaction of boron atoms and benzene under single-collision conditions.[9] Later on, the *B*-iodo derivative and parent benzoborirene were detected to result from photoreactions of diiodophenylborane and phenylborylene, respectively, in matrix isolation experiments.[10] Benzoborirene (**1**) is isoelectronic to the benzocyclopropenium ion (**2**). Halton et al. obtained the first NMR spectral evidence for the existence of a derivative of **2** in 1974, but noted its limited stability that made full characterization difficult.[11] The neutral compounds, cycloproparenes, have received considerable attention[12] since Anet and Anet[13] reported the first derivative, and Vogel and Billups described syntheses of the parent benzocyclopropene **3**.[14]

Although the strain of **1** is much smaller than that of known all-carbon scaffolds **2** and **3** (Scheme 1), efforts aimed at the targeted synthesis of benzoborirenes under conventional conditions were unsuccessful. Schacht and Kaufmann reduced (2-bromophenyl)phenylbromoborane **4** with Li and postulated

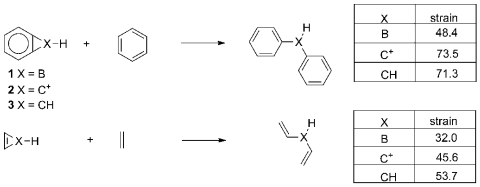

X	strain
B	48.4
C$^+$	73.5
CH	71.3

X	strain
B	32.0
C$^+$	45.6
CH	53.7

Scheme 1. Benzoborirene (**1**), benzocyclopropenium ion (**2**), benzocyclopropene (**3**), and their strain energies (in kcal mol^{-1}) according to homodesmotic equations computed at the CCSD(T)/cc-pVTZ//B3LYP/6–311+G** level of theory.

formation of a benzoboratirene **5** based on degradation experiments (Scheme 2, reaction a).[15] Attempted benzoborirene formation by thermal elimination of trimethylchlorosilane from 2-(dichloroboryl)phenyl trimethylsilane **6** resulted in **7** by HCl elimination (Scheme 2, reaction b) instead. These experiments indicate the resistance towards benzoborirene formation, possibly due to a combination of strain and the inherent reactivity of a planar, sterically unprotected boron center.

On the other hand, monocyclic borirenes are well-known.[16] These are less strained than benzoborirenes (32.0 vs. 48.4 kcal mol^{-1} according to homodesmotic equations, Scheme 1), and were found to undergo coordination to Lewis bases such as *N*-heterocyclic carbenes (NHC).[16i] As interaction with an NHC could protect the boron center by reducing its Lewis acidity

[a] Dr. J. Hahn, C. Keck, Prof. Dr. H. F. Bettinger
Institut für Organische Chemie, Universität Tübingen, Auf der Morgenstelle 18, 72076 Tübingen (Germany)
E-mail: holger.bettinger@uni-tuebingen.de

[b] Dr. C. Maichle-Mössmer
Institut für Anorganische Chemie, Universität Tübingen, Auf der Morgenstelle 18, 72076 Tübingen (Germany)

[c] E. von Grotthuss
Institut für Anorganische und Analytische Chemie
Universität Frankfurt
Max-von-Laue-Str. 7, 60438 Frankfurt (Germany)

[d] P. N. Ruth, A. Paesch, Prof. Dr. D. Stalke
Institut für Anorganische Chemie, Universität Göttingen
Tammannstrasse 4, 37077 Göttingen (Germany)

Supporting information and the ORCID identification number(s) for the author(s) of this article can be found under: https://doi.org/10.1002/chem.201804629.

ChemPubSoc Europe

CHEMISTRY A European Journal Communication

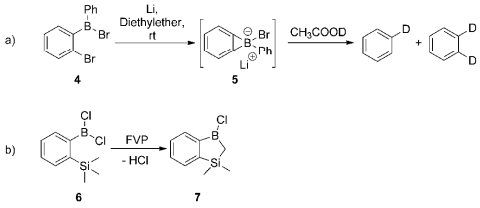

Scheme 2. Attempted benzoborirene syntheses by reductive elimination (reaction a) or flash vacuum pyrolysis (FVP, reaction b) according to Kaufmann et al.[15]

and providing steric shielding, we employed NHC coordination in the synthesis of a benzoborirene. We here report the first synthesis of a benzoborirene-NHC adduct under conventional solution phase conditions and its characterization by multinuclear NMR spectroscopy.

We reasoned that the bromo-lithium exchange of a NHC adduct (**9**) of the known dichloro-2-bromophenylborane **8**[17] might provide access to the benzoborirene scaffold (Scheme 3). The NHC adducts **9** were obtained as colorless

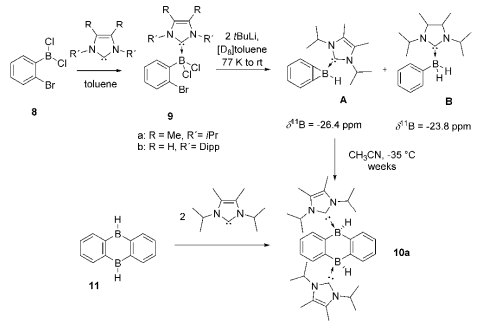

Scheme 3. Synthesis of the benzoborirene-NHC adduct A and its decomposition.

solids in good to moderate yields by treating **8** with the free NHC in toluene and could be fully characterized by multinuclear NMR spectroscopy and single-crystal X-ray crystallography (see Supporting Information, Figure S16, S17).[18] The ^{11}B NMR shifts (1.8 ppm for **9a** and 1.1 ppm for **9b**) are as expected.[19]

Treatment of compound **9a** with two equivalents of *tert*-BuLi in [D_8]toluene at low temperature was monitored by NMR spectroscopy. Two new signals were observed by ^{11}B{^{1}H} NMR at −26.4 ppm (compound **A**) and −23.8 ppm (compound **B**), with the former one showing the highest intensity. After keeping the solution at room temperature for a day, the signal at −26.4 ppm had disappeared completely, whereas the signal for compound **B** was still present. In a proton-coupled ^{11}B NMR spectrum, the signal at −23.8 ppm due to compound **B** splits into a triplet with a $^1J_{BH}$ coupling constant of 87.0 Hz, indicating that two hydrogen atoms are bound to boron. Comparison of the spectral data allows assignment to the known NHC adduct of phenylborane.[20]

Compound **A** is the NHC adduct of benzoborirene based on the following arguments. The proton coupled ^{11}B NMR spectrum results in splitting of the signal at −26.4 ppm into a doublet with a $^1J_{BH}$ coupling constant of 120.5 Hz, showing that a single hydrogen atom is bonded to the boron center. This hydrogen atom can be observed at 3.70 ppm in a ^{1}H{^{11}B} spectrum, and an HETCOR NMR experiment proves that a coupling exists with the boron signal at −26.4 ppm. Both the ^{11}B chemical shift and the $^1J_{BH}$ value are very similar to those reported by Curran et al. for a NHC-borirane.[21] In the ^{1}H NMR spectrum an AA′BB′ spin system with multiplets at 7.97 and 7.51 ppm and the signals of an intact coordinated NHC molecule are observed that integrate in the required ratio and also disappear quickly at room temperature. The aromatic protons of benzocyclopropene (**3**) resonate at 7.12 ppm.[14a] The AA′BB′ spin system in **A** is associated with two ^{13}C NMR signals at 126.6 and 122.4 ppm that each carry a single hydrogen atom according to a DEPT-135 NMR experiment. The boron-bound fusion centers were observed in a low temperature ^{13}C NMR experiment at 149.0 ppm, but the carbene center could not unambiguously be detected. The assignment to **A** is supported by density functional theory computations (Table 1) of the chemical shifts.

Table 1. Comparison of experimental and computed (B3LYP/def2-TZVP//B3LYP/6–311+G**) chemical shifts of **A**.

Molecule **A**	Nucleus	δ_{exp} [ppm]	δ_{calc} [ppm][a]
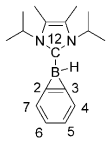	C2/C3	149.0	147.1
	C4/C7	122.4	120.1
	C6/C5	126.6	125.4
	C12	not observed	173.3
	B	−26.4	−26.9

[a] Carbon with reference to benzene and its experimental chemical shift $\delta^{13}C = 128.06$ ppm, boron with reference to compound **B** and its experimental shift $\delta^{11}B = -23.8$ ppm.

Electron impact mass spectrometry shows that compound **A** ionizes with loss of one hydrogen atom. The high resolution measurement of the resulting $[M-H]^+$ mass is in agreement with the assignment to **A**. The formation of borane-NHC adducts from dihaloborane-NHC adducts under reductive conditions has been observed before and was explained to result from reaction with solvent or with an unspecified hydrogen atom source.[22]

Attempted crystallization of **A** at −35 °C in acetonitrile solution resulted in the formation of colorless crystals. Single-crystal X-ray crystallography identified these as **10a**, the formal dimer of **A** (Figure 1). The two NHC ligands are in *syn* orienta-

ChemPubSoc Europe

CHEMISTRY
A European Journal
Communication

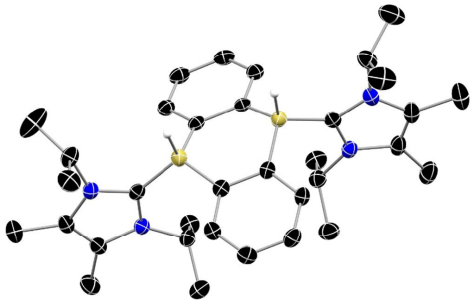

Figure 1. Molecular structure of **10a** in the solid state. Anisotropic displacement parameters are depicted at the 50% probability level. Hydrogen atoms bonded to carbon atoms were omitted for clarity. For bond lengths and angles, see Figure S18 in the Supporting Information.

tion, similar to the bis-dimethylsulfide adduct described previously by Wagner et al.[23] We synthesized **10a** independently by treating 9,10-dihydro-9,10-diboraanthracene[24] **11** in [D_8]THF with two equivalents of the NHC *li*Pr_{Me_2}. The spectral data of the poorly soluble dimer **10a** (^{13}C, ^{11}B = −17.5 ppm, $^1J_{BH} \approx 62$ Hz) differ so strongly from that assigned to **A** (e.g., boron-bound carbon atoms of the diboraanthracene backbone resonate at 156.9 ppm, see the Supporting Information for details) that solvent effects cannot be responsible. Most importantly, dimer **10a** ionizes with the loss of one hydrogen atom, and the high-resolution mass spectrum is in agreement with the $[M-H]^+$ ion of **10a**. These analyses of **10a** confirm that the dimer is not observed initially, but forms slowly during attempted crystallization of monomeric **A**. Formation of dimer **10a** can be considered an indirect proof of the assignment to **A**.

The dimerization of sterically unprotected borirenes is known to be a low-barrier process.[25] Likewise, the dimerization of benzoborirene is associated with a zero-point energy corrected barrier of only $E_0 = 7$ kcal mol^{-1} ($\Delta G^{\ddagger} = 17$ kcal mol^{-1}) and with considerable energy gain ($\Delta G = -84$ kcal mol^{-1}) according to quantum chemical computations (DLPNO-CCSD(T)/cc-pVTZ//B3LYP/6–311 + G**).[26] The transition state for dimerization involves interaction of the three-coordinate boron centers with the ring fusion atoms (see the Supporting Information, Figure S20). A similar transition state is difficult to imagine for **A** as the boron center is electronically saturated and the bulky NHC ligands provide some steric protection. But despite the bulkiness of the NHC ligands, dimerization of **A** to **10a** is a very strongly exergonic process ($\Delta G = -83$ kcal mol^{-1}), similar to that of parent benzoborirene. The interaction of the NHC with the boron center is so strong ($E_0 = 42$ kcal mol^{-1}, $\Delta G = 31$ kcal mol^{-1}) that dissociation of the NHC is not expected to be important at room temperature or below. One conceivable dimerization mechanism may involve the zwitterionic intermediate **12a** (Scheme 4). Similar zwitterions were invoked previously to explain the increased tendency of pyridine-coordinated borirene molecules to undergo ring-opening reactions.[16f,i] Zwitterion **12a** is a minimum on the potential energy surface, which lies 30 kcal mol^{-1} higher in energy than benzoborirene. This energy difference is reduced to 25 kcal mol^{-1} after taking into account acetonitrile solvent effects using a polarizable continuum model (see the Supporting Information). The NHC stabilizes the borenium ion center and, without the NHC, the zwitterion would collapse to benzoborirene according to computations. Hence, the NHC, though providing steric protection, can open a decomposition pathway that is not available to uncoordinated benzoborirenes with bulky boron substitution. Due to the high exothermicity of the dimerization reaction of **A**, the existence of other hitherto unidentified lower energy pathways that avoid the zwitterion intermediate is possible.

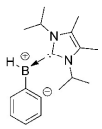

Scheme 4. Zwitterionic isomer **12a** of **A**.

In summary, we could provide for the first time NMR spectroscopic evidence for the existence of the benzoborirene molecular framework in the form of an NHC adduct under conventional solution-phase conditions. The dimerization of the compound is very strongly exothermic despite the coordinating NHC, and this reaction may be facilitated by the NHC through stabilization of a zwitterionic isomer. Future research is aimed at introducing bulky groups on the boron center in benzoborirene as an alternative means of steric protection that avoids Lewis base coordination.

Acknowledgements

We thank Professors Lars Wesemann and Alexey Timoshkin for helpful discussions, Dr. Fabian Uhlemann for providing the *N*-heterocyclic carbenes, and Deutsche Forschungsgemeinschaft for financial support of this research. C. K. thanks the Fonds der chemischen Industrie for a Kekulé fellowship. The computations were performed on the BwForCluster JUSTUS. The authors acknowledge support by the state of Baden-Württemberg through bwHPC and the German Research Foundation (DFG) through grant no INST 40/467-1 FUGG.

Conflict of interest

The authors declare no conflict of interest.

Keywords: boron · fused ring systems · heterocycles · strained molecules · ylides

[1] a) M. Faraday, *Philos. Trans. R. Soc. London* **1825**, *115*, 440–466; b) A. Kekulé, *Lehrbuch der organischen Chemie oder der Chemie der Kohlenstoffverbindungen*, F. Enke, Erlangen, **1866**.
[2] J. Thiele, *Liebigs Ann. Chem.* **1899**, *306*, 87–142.
[3] a) R. S. Mulliken, *J. Chem. Phys.* **1939**, *7*, 339–352; b) R. S. Mulliken, C. A. Rieke, W. G. Brown, *J. Am. Chem. Soc.* **1941**, *63*, 41–56.
[4] A. Baeyer, *Ber. Dtsch. Chem. Ges.* **1885**, *18*, 2269–2281.
[5] a) R. Diercks, K. P. C. Vollhardt, *J. Am. Chem. Soc.* **1986**, *108*, 3150–3152; b) R. Boese, D. Bläser, W. E. Billups, M. M. Haley, A. H. Maulitz, D. L. Mohler, K. P. C. Vollhardt, *Angew. Chem. Int. Ed. Engl.* **1994**, *33*, 313–317;

ChemPubSoc Europe

CHEMISTRY
A European Journal
Communication

Angew. Chem. **1994**, *106*, 321 – 325; c) N. L. Frank, K. K. Baldridge, J. S. Siegel, *J. Am. Chem. Soc.* **1995**, *117*, 2102 – 2103; d) H.-B. Bürgi, K. K. Baldridge, K. Hardcastle, N. L. Frank, P. Gantzel, J. S. Siegel, J. Ziller, *Angew. Chem. Int. Ed. Engl.* **1995**, *34*, 1454 – 1456; *Angew. Chem.* **1995**, *107*, 1575 – 1577; e) N. L. Frank, K. K. Baldridge, P. Gantzel, J. S. Siegel, *Tetrahedron Lett.* **1995**, *36*, 4389 – 4392; f) F. Cardullo, D. Giuffrida, F. H. Kohnke, F. M. Raymo, J. F. Stoddart, D. J. Williams, *Angew. Chem. Int. Ed. Engl.* **1996**, *35*, 339 – 341; *Angew. Chem.* **1996**, *108*, 347 – 349.

[6] a) W. H. Mills, I. G. Nixon, *J. Chem. Soc.* **1930**, 2510 – 2524; b) A. Stanger, *J. Am. Chem. Soc.* **1991**, *113*, 8277 – 8280; c) J. S. Siegel, *Angew. Chem. Int. Ed. Engl.* **1994**, *33*, 1721 – 1723; *Angew. Chem.* **1994**, *106*, 1808 – 1810.

[7] a) A. Stanger, *J. Am. Chem. Soc.* **1998**, *120*, 12034 – 12040; b) A. Stanger, E. Tkachenko, *J. Comput. Chem.* **2001**, *22*, 1377 – 1386; c) S. M. Bachrach, *J. Organomet. Chem.* **2002**, *643 – 644*, 39 – 46; d) A. J. Boydston, M. Laskoski, U. H. F. Bunz, M. M. Haley, *Synlett* **2002**, 981 – 983; e) C. Cohrs, H. Reuchlein, P. W. Musch, C. Selinka, B. Walfort, D. Stalke, M. Christl, *Eur. J. Org. Chem.* **2003**, 901 – 906; f) T. Rosenau, G. Ebner, A. Stanger, S. Perl, L. Nuri, *Chem. Eur. J.* **2005**, *11*, 280 – 287; g) A. Patel, F. Liebner, T. Netscher, K. Mereiter, T. Rosenau, *J. Org. Chem.* **2007**, *72*, 6504 – 6512; h) K. J. Donald, M. Bober, *Chem. Eur. J.* **2011**, *17*, 1936 – 1945; i) A. D. Payne, B. W. Skelton, A. H. White, D. Wege, *ChemistrySelect* **2016**, *1*, 5339 – 5346.

[8] a) M. Eckert-Maksić, Z. Glasovac, Z. B. Maksić, I. Zrinski, *Theochem* **1996**, *366*, 173 – 183; b) Z. B. Maksić, M. Eckert-Maksić, K.-H. Pfeifer, *J. Mol. Struct.* **1993**, *300*, 445 – 453; c) M. R. Molavian, A. Abdolmaleki, K. Eskandari, *Comput. Theor. Chem.* **2017**, *1099*, 102 – 108.

[9] a) R. I. Kaiser, H. F. Bettinger, *Angew. Chem. Int. Ed.* **2002**, *41*, 2350 – 2352; *Angew. Chem.* **2002**, *114*, 2456 – 2458; b) H. F. Bettinger, R. I. Kaiser, *J. Phys. Chem. A* **2004**, *108*, 4576 – 4586; c) F. Zhang, Y. Guo, X. Gu, R. I. Kaiser, *Chem. Phys. Lett.* **2007**, *440*, 56 – 63.

[10] a) H. F. Bettinger, *Chem. Commun.* **2005**, 2756 – 2757; b) H. F. Bettinger, *J. Am. Chem. Soc.* **2006**, *128*, 2534 – 2535.

[11] B. Halton, A. D. Woolhouse, H. M. Hugel, D. P. Kelly, *J. Chem. Soc. Chem. Commun.* **1974**, 247 – 248.

[12] a) B. Halton, *Chem. Rev.* **1973**, *73*, 113 – 126; b) B. Halton, *Chem. Rev.* **1989**, *89*, 1161 – 1185; c) B. Halton, *Chem. Rev.* **2003**, *103*, 1327 – 1369; d) W. E. Billups, *Acc. Chem. Res.* **1978**, *11*, 245 – 251; e) W. E. Billups, W. A. Rodin, M. M. Haley, *Tetrahedron* **1988**, *44*, 1305 – 1338.

[13] R. Anet, F. A. L. Anet, *J. Am. Chem. Soc.* **1964**, *86*, 525 – 526.

[14] a) E. Vogel, W. Grimme, S. Korte, *Tetrahedron Lett.* **1965**, *6*, 3625 – 3631; b) R. Neidlein, D. Christen, V. Poignée, R. Boese, D. Bläser, A. Gieren, C. Ruiz-Pérez, T. Hübner, *Angew. Chem. Int. Ed. Engl.* **1988**, *27*, 294 – 295; *Angew. Chem.* **1988**, *100*, 292 – 293; c) W. E. Billups, A. J. Blakeney, W. Y. Chow, *J. Chem. Soc. D, Chem. Commun.* **1971**, 1461 – 1462; d) W. E. Billups, W. Y. Chow, K. H. Leavell, E. S. Lewis, J. L. Margrave, R. L. Sass, J. J. Shieh, P. G. Werness, J. L. Wood, *J. Am. Chem. Soc.* **1973**, *95*, 7878 – 7880; e) W. E. Billups, A. J. Blakeney, W. Y. Chow, *Org. Synth.* **1976**, *55*, 12 – 15.

[15] a) D. E. Kaufmann, W. Schacht, *Pure Appl. Chem.* **1991**, *63*, 383 – 386; b) W. Schacht, D. Kaufmann, *J. Organomet. Chem.* **1987**, *331*, 139 – 152.

[16] a) J. J. Eisch, F. Shen, K. Tamao, *Heterocycles* **1982**, *18*, 245 – 250; b) C. Habben, A. Meller, *Chem. Ber.* **1984**, *117*, 2531 – 2537; c) C. Pues, A. Berndt, *Angew. Chem. Int. Ed. Engl.* **1984**, *23*, 313 – 314; *Angew. Chem.* **1984**, *96*, 306 – 307; d) B. Pachaly, R. West, *Angew. Chem. Int. Ed. Engl.* **1984**, *23*, 454; *Angew. Chem.* **1984**, *96*, 444; e) J. J. Eisch, B. Shafii, A. L. Rheingold, *J. Am. Chem. Soc.* **1987**, *109*, 2526 – 2528; f) J. J. Eisch, B. Shafii, J. D. Odom, A. L. Rheingold, *J. Am. Chem. Soc.* **1990**, *112*, 1847 – 1853; g) H. Braunschweig, T. Herbst, D. Rais, F. Seeler, *Angew. Chem. Int. Ed.* **2005**, *44*, 7461 – 7463; *Angew. Chem.* **2005**, *117*, 7627 – 7629; h) C. E. Anderson, H. Braunschweig, R. D. Dewhurst, *Organometallics* **2008**, *27*, 6381 – 6389; i) H. Braunschweig, A. Damme, R. D. Dewhurst, S. Ghosh, T. Kramer, B. Pfaffinger, K. Radacki, A. Vargas, *J. Am. Chem. Soc.* **2013**, *135*, 1903 – 1911.

[17] D. Kaufmann, *Chem. Ber.* **1987**, *120*, 901 – 905.

[18] CCDC 1862384, 1862385, and 1862386 contain the supplementary crystallographic data for this paper. These data are provided free of charge by The Cambridge Crystallographic Data Centre.

[19] J. J. Dunsford, I. A. Cade, K. L. Fillman, M. L. Neidig, M. J. Ingleson, *Organometallics* **2014**, *33*, 370 – 377.

[20] J. C. Walton, M. M. Brahmi, J. Monot, L. Fensterbank, M. Malacria, D. P. Curran, E. Lacôte, *J. Am. Chem. Soc.* **2011**, *133*, 10312 – 10321.

[21] T. R. McFadden, C. Fang, S. J. Geib, E. Merling, P. Liu, D. P. Curran, *J. Am. Chem. Soc.* **2017**, *139*, 1726 – 1729.

[22] a) Y. Wang, B. Quillian, P. Wei, C. S. Wannere, Y. Xie, R. B. King, H. F. Schaefer, P. v. R. Schleyer, G. H. Robinson, *J. Am. Chem. Soc.* **2007**, *129*, 12412 – 12413; b) R. Kinjo, B. Donnadieu, M. A. Celik, G. Frenking, G. Bertrand, *Science* **2011**, *333*, 610 – 613.

[23] A. Lorbach, M. Bolte, H.-W. Lerner, M. Wagner, *Chem. Commun.* **2010**, *46*, 3592 – 3594.

[24] A. Lorbach, M. Bolte, H. Li, H.-W. Lerner, M. C. Holthausen, F. Jäkle, M. Wagner, *Angew. Chem. Int. Ed.* **2009**, *48*, 4584 – 4588; *Angew. Chem.* **2009**, *121*, 4654 – 4658.

[25] a) P. H. M. Budzelaar, S. M. Van der Kerk, K. Krogh-Jespersen, P. v. R. Schleyer, *J. Am. Chem. Soc.* **1986**, *108*, 3960 – 3967; b) M. Krasowska, H. F. Bettinger, *Chem. Eur. J.* **2016**, *22*, 10661 – 10670.

[26] a) C. Riplinger, F. Neese, *J. Chem. Phys.* **2013**, *138*, 034106; b) C. Riplinger, B. Sandhoefer, A. Hansen, F. Neese, *J. Chem. Phys.* **2013**, *139*, 134101.

Manuscript received: September 10, 2018
Version of record online: November 16, 2018

CHEMISTRY
A European Journal

Supporting Information

Synthesis and Ring Strain of a Benzoborirene-*N*-Heterocyclic Carbene Adduct

Jennifer Hahn,[a] Constanze Keck,[a] Cäcilia Maichle-Mössmer,[b] Esther von Grotthuss,[c] Paul Niklas Ruth,[d] Alexander Paesch,[d] Dietmar Stalke,[d] and Holger F. Bettinger*[a]

chem_201804629_sm_miscellaneous_information.pdf

Supporting Information

Table of Contents

1. Experimental Methods

General Procedures. All experiments were performed under anhydrous conditions using argon as protective gas. All NMR spectra were referenced to residual solvent signals (^{1}H, ^{13}C) and externally (^{11}B: BF_3•OEt_2). All commercially available compounds and dry solvents were purchased. NMR spectra were recorded on Bruker Avance III HDX 600 and on Bruker Avance III 400 spectrometers. For HR-EI-MS measurements a sector field spectrometer MAT95 (Finnigan MAT) was used. 1,3-Diisopropyl-4,5-dimethylimidazolin-2-ylidene,[1] 1,3-di-(2,6-diisopropylphenyl)-4,5-dimethylimidazolin-2-ylidene,[2] and 9,10-dihydro-9,10-dibora-anthracene[3] were synthesized as described in the literature.

Synthesis

The synthesis started from 1,2-dibromobenzene **I** that we converted to 1,2-bis(trimethylsilyl)benzene **II** following Wagner *et al.*[4] Monoborylation of **II** by reaction with borontrichloride and bromination of the resulting **III** yielded dichloro-2-bromophenylborane **8** as described by Kaufmann.[5] The spectral properties of **II**, **III**, and **8** are in agreement with literature reports.[4-5]

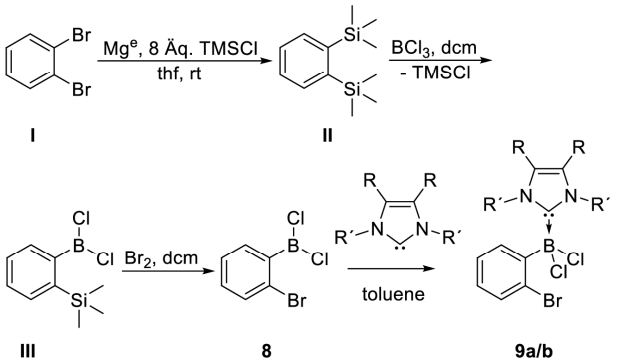

Compound 9a. Dichloro-2-bromophenylborane **8** (100 mg, 0.53 mmol) was dissolved in 1 mL toluene and added dropwise to a to –20 °C cooled solution of 1,3-diisopropyl-4,5-dimethylimidazolin-2-ylidene (76 mg, 0.53 mmol) in 2 mL toluene. After the solution was stirred over night at –20 °C the solvent was evaporated in vacuum at room temperature. The light orange oil was washed three times with n-pentane and the gained white solid is dried in vacuum at room temperature (76 mg, 46 %). ^{1}H (400 MHz, CD_2Cl_2): δ = 8.11 (d, $^{3}J_{HH}$ = 7.7 Hz, 1 H), 7.41 (d, $^{3}J_{HH}$ = 7.9 Hz, 1 H), 7.35 – 7.31 (m, 1 H), 7.08 – 7.04 (m, 1 H), 5.70 (sept, $^{3}J_{HH}$ = 7.1 Hz, 2 H), 2.28 (s, 6 H), 1.30 (d, $^{3}J_{HH}$ = 7.1 Hz, 12 H) ppm; ^{13}C{^{1}H} (100 MHz, CD_2Cl_2): δ = 133.5, 133.3, 128.7, 128.0, 127.5, 126.8, 50.5, 21.0, 11.1 ppm; ^{11}B{^{1}H} (128 MHz, CD_2Cl_2): δ = 1.8 ppm.

Compound 9b. Dichloro-2-bromophenylborane **8** (100 mg, 0.53 mmol) was dissolved in 1 mL toluene and added dropwise to a to –20 °C cooled solution of 1,3-di-(2,6-diisopropylphenyl)-4,5-dimethylimidazolin-2-ylidene (164 mg, 0.53 mmol) in 2 mL toluene. Immediately a white solid precipitated. After the suspension was stirred over night at –20 °C the solvent was decanted. The gained white solid was washed three times with n-pentane and dried under vacuum at room temperature (164 mg, 44 %). ^{1}H (400 MHz, CD_2Cl_2): δ = 7.37 (t, $^{3}J_{HH}$ = 7.8 Hz, 2 H), 7.28 (dd, $^{3}J_{HH}$ = 7.1 Hz, $^{4}J_{HH}$ = 1.2 Hz, 1 H), 7.18 – 7.15 (m, 5 H), 7.14 (s, 2 H), 6.79 – 6.75 (m, 1 H), 6.70 – 6.66 (m, 1 H), 2.93 (sept, $^{3}J_{HH}$ = 6.6 Hz, 4 H), 1.31 (d, $^{3}J_{HH}$ = 6.6 Hz, 12 H), 1.06 (d, $^{3}J_{HH}$ = 6.6 Hz, 12 H) ppm; ^{13}C{^{1}H} (100 MHz, CD_2Cl_2): δ = 146.3, 136.7, 134.8, 133.7, 130.8, 127.9, 125.8, 125.3, 124.0, 29.3, 26.6, 22.6 ppm; ^{11}B{^{1}H} (128 MHz, CD_2Cl_2): δ = 1.1 ppm.

Synthesis of compound A. Adduct **9a** (10 mg, 0.023 mmol) was dissolved in 0.5 mL toluene-d_8 and cooled down with liquid nitrogen. Then precooled *tert*-butyllithium solution (0.025 mL, 0.048 mmol, 1.9 M in pentane, 8 °C) was added and simultaneously the liquid nitrogen Dewar

was removed. Immediately a bright yellow suspension formed which was measured directly by NMR spectroscopy or the solvent was quickly evaporated in vacuum. ^{1}H (400 MHz, C_6D_6, 298 K): δ = 7.97 (m, 2 H), 7.51 (m, 2 H), 6.15 (sept, $^{3}J_{HH}$ = 7.1 Hz, 2 H), 3.70 (q, $^{1}J_{BH}$ = 120.5 Hz, BH, 1H), 1.47 (s, 6 H), 1.10 (d, $^{3}J_{HH}$ = 7.1 Hz, 12 H) ppm; ^{13}C{^{1}H} (151 MHz, Tol-d_8, 273 K): δ = 149.0, 126.6, 124.8, 122.4, 50.5, 20.7, 9.5 ppm; ^{11}B (192 MHz, Tol-d_8, 298 K): δ = –26.4 (d, $^{1}J_{BH}$ = 120.5 Hz) ppm; HR-EI-MS: calc. for $C_{17}H_{24}N_2B$ 267.202706 Da, found 267.20340 Da [*M*-H]$^{\bullet+}$.

Compound 10a. 9,10-Dihydro-9,10-diboraanthracene (4 mg, 0.02 mmol) and 1,3-diisopropyl-4,5-dimethylimidazolin-2-ylidene (8 mg, 0.04 mmol) were dissolved in 0.5 mL thf-d_8 and measured by NMR spectroscopy. For subsequent mass spectrometry analysis, the solvent was removed under vacuum. ^{1}H (600 MHz, THF-d_8, 298 K): δ = 6.82, (bs, 4H), 6.57 (m, 4H), 4.15 (sept, 4H, $^{3}J_{HH}$ = 6.5 Hz), 3.79 (bs, 2H, BH), 2.04 (s, 12H), 1.39 (d, $^{3}J_{HH}$ = 6.6 Hz, 24H) ppm; ^{13}C{^{1}H} (176 MHz, THF-d_8, 298 K): δ = 207.8, 156.9, 133.9, 122.2, 121.7, 48.6, 24.5, 8.7 ppm; ^{11}B (193 MHz, THF-d_8, 298 K): δ = –17.5 (d, $^{1}J_{BH}$ = 61.6 Hz) ppm; HR-EI-MS: calc. for $C_{34}H_{49}N_4B_2$ 535.413786 Da, found 535.41164 Da.

2. Spectra

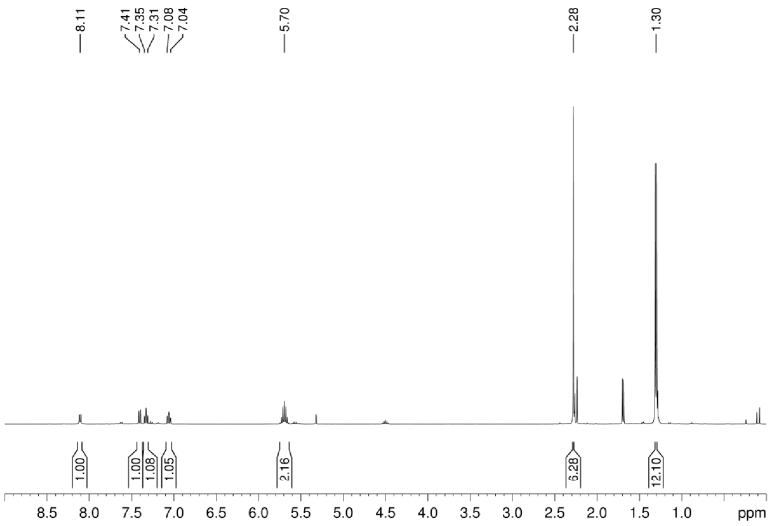

Figure S1. ^{1}H NMR of compound **9a** in CD_2Cl_2.

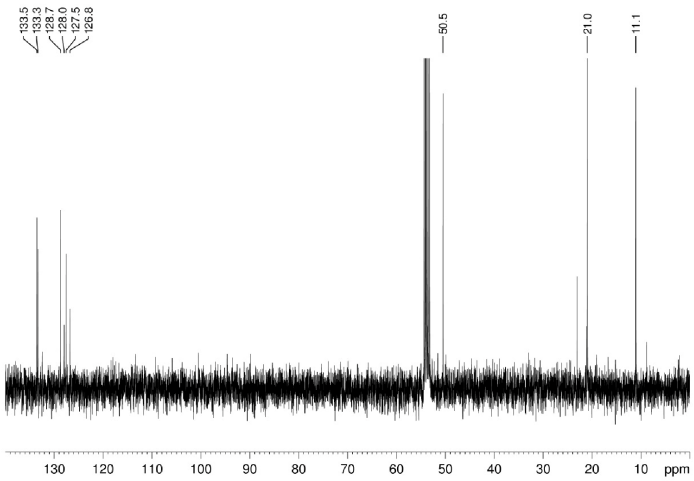

Figure S2. $^{13}C\{^{1}H\}$ NMR spectrum of compound **9a** in CD_2Cl_2.

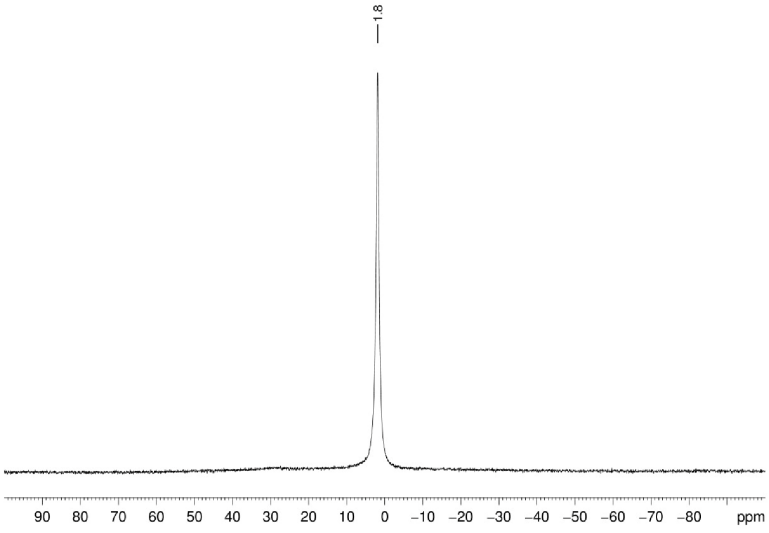

Figure S3. $^{11}B\{^{1}H\}$ NMR spectrum of compound **9a** in CD_2Cl_2.

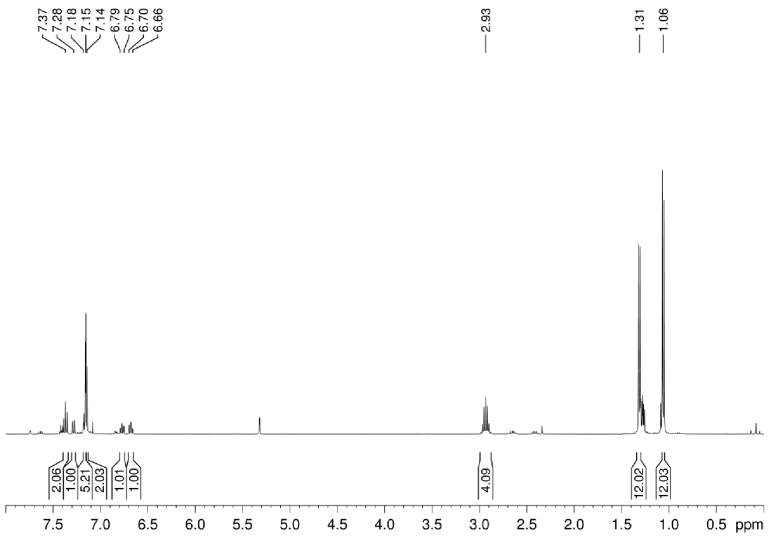

Figure S4. ^{1}H NMR spectrum of compound **9b** in CD_2Cl_2.

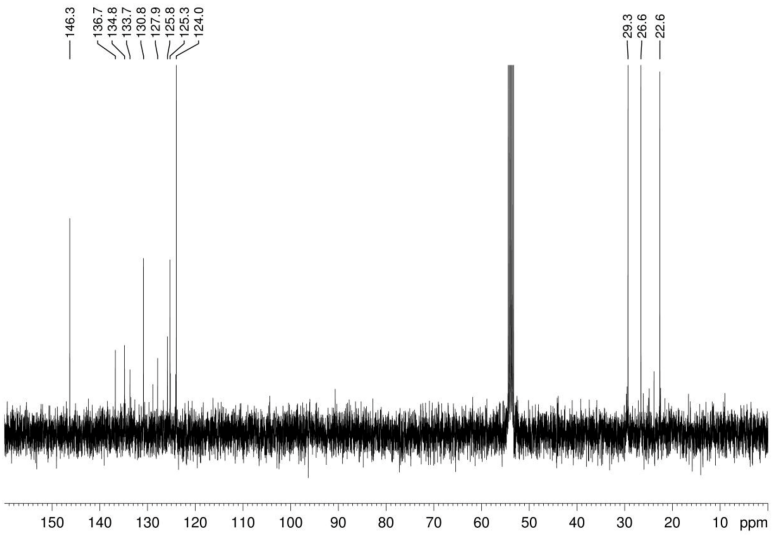

Figure S5. $^{13}C\{^{1}H\}$ NMR spectrum of compound **9b** in CD_2Cl_2.

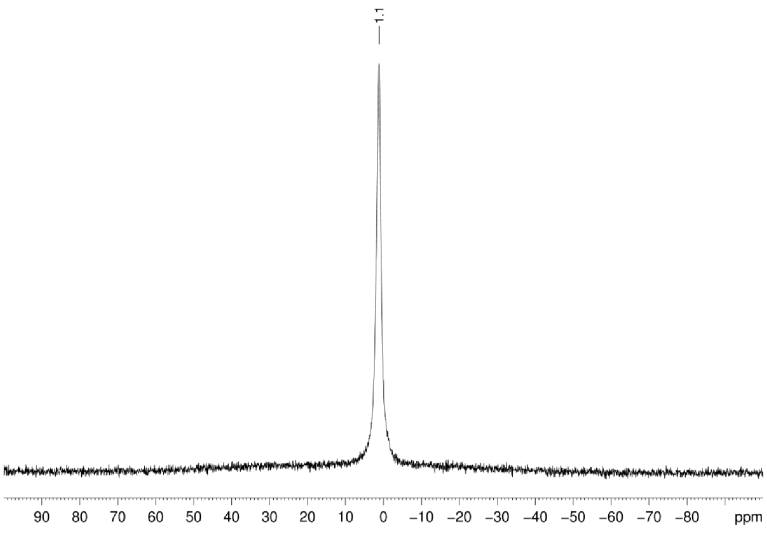

Figure S6. $^{11}B\{^{1}H\}$ NMR spectrum of compound **9b** in CD_2Cl_2.

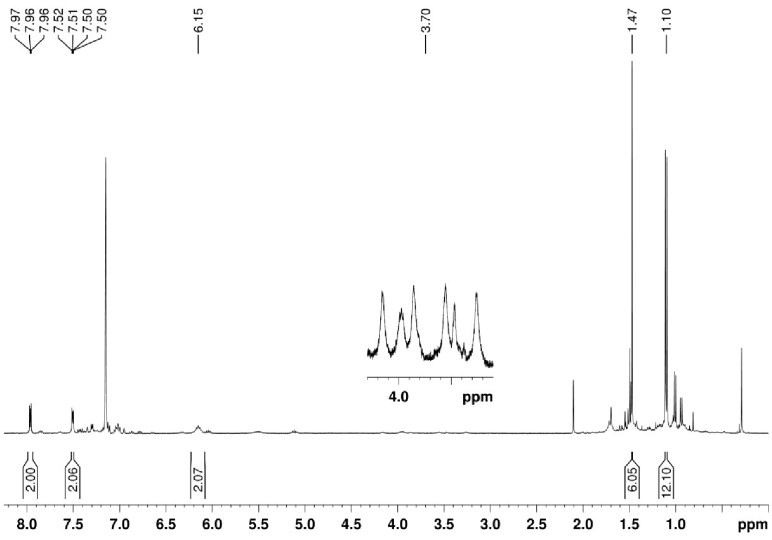

Figure S7. ^{1}H NMR spectrum of compounds **A** and **B** in C_6D_6 at room temperature (BH signal is shown enlarged).

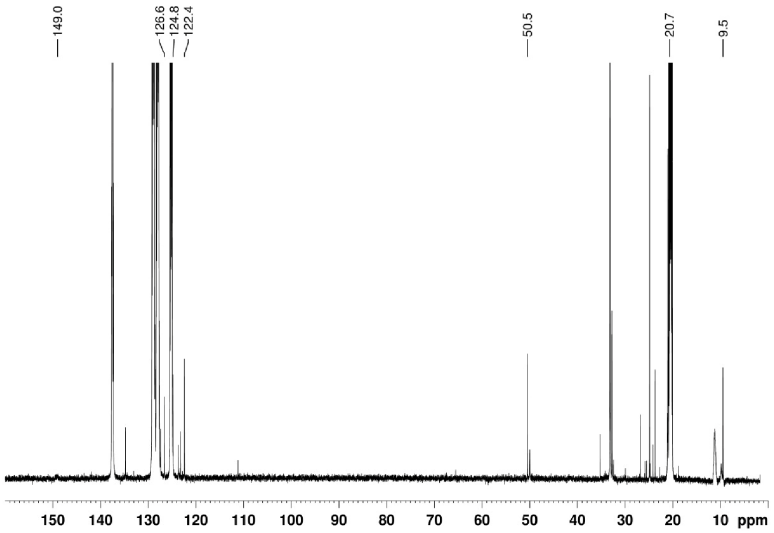

Figure S8. $^{13}C\{^{1}H\}$ NMR spectrum of compounds **A** and **B** in Tol-d_8 at 273 K.

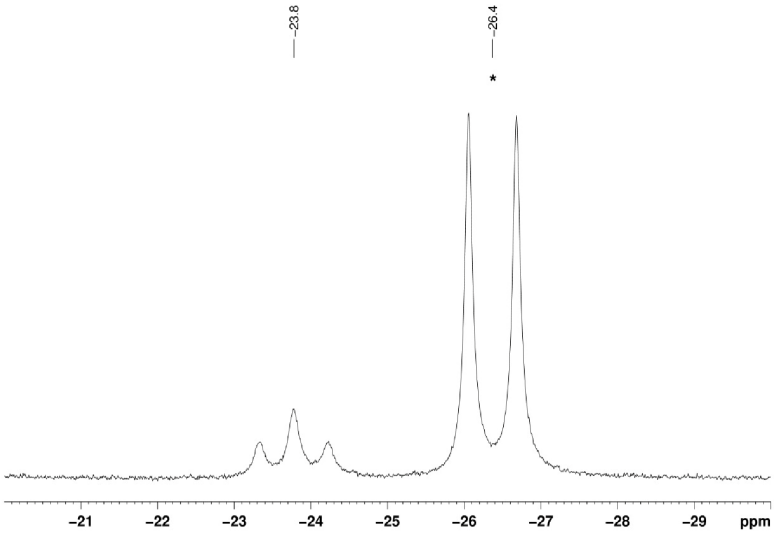

Figure S9. ^{11}B NMR spectrum of compounds **A** (marked with a star) and **B** in Tol-d_8 at room temperature.

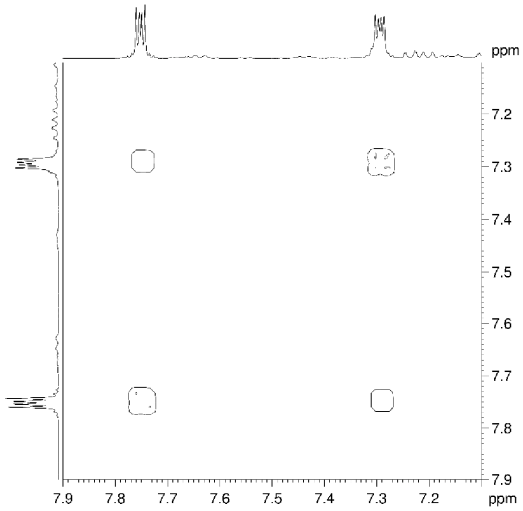

Figure S10. H-H COSY NMR spectrum of compound **A** in the aromatic region.

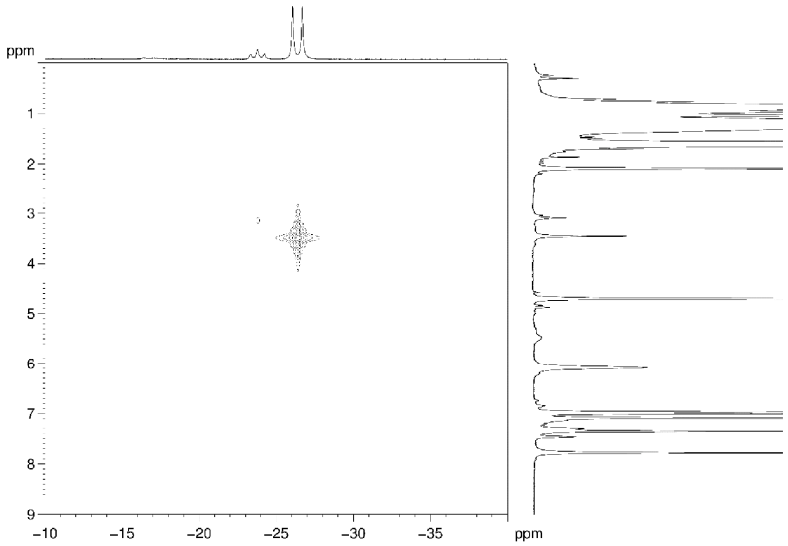

Figure S11. HETCOR NMR spectrum of compound **A** in Tol-d_8 at room temperature.

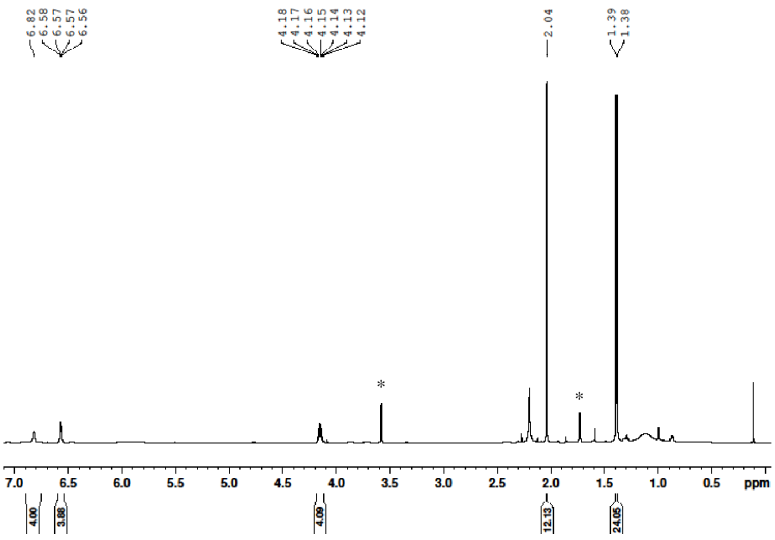

Figure S12. ^{1}H NMR spectrum of compound **10a** in THF-d_8. * marks residual THF signals.

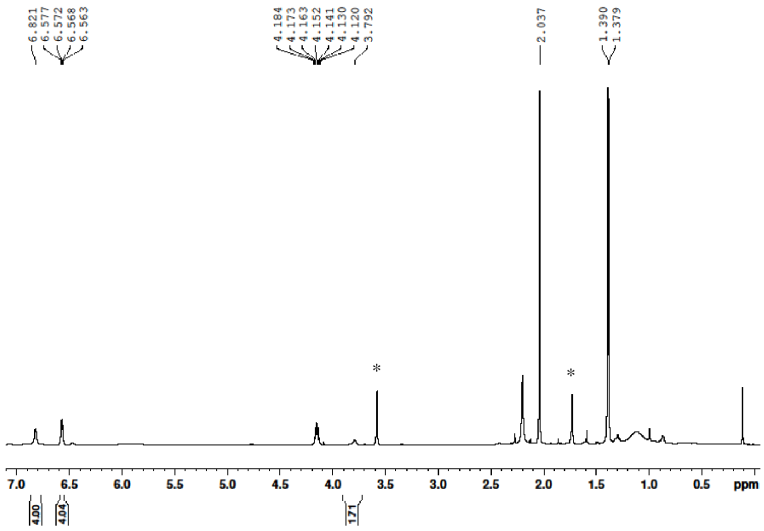

Figure S13. $^{1}H\{^{11}B\}$ NMR spectrum of compound **10a** in THF-d_8. * marks residual THF signals.

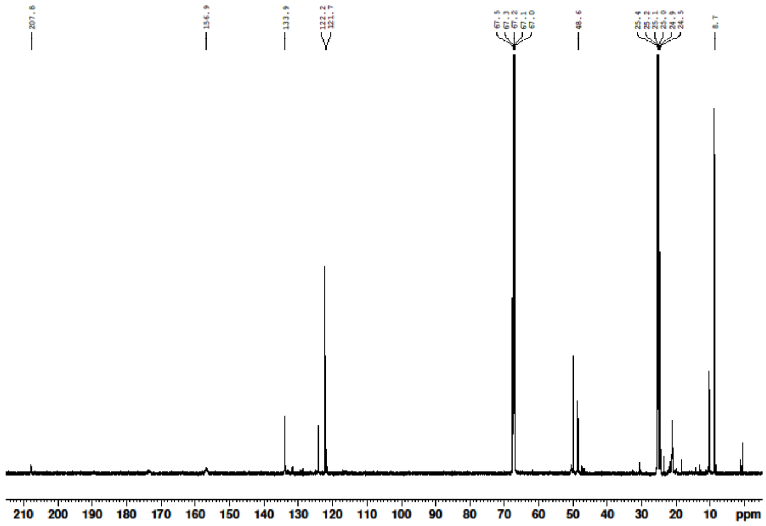

Figure S14. $^{13}C\{^{1}H\}$ NMR spectrum of compound **10a** in THF-d_8.

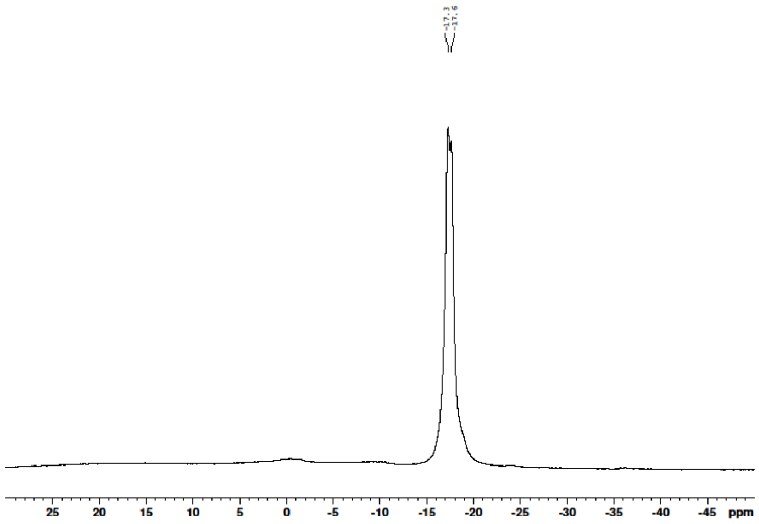

Figure S15. ^{11}B NMR spectrum of compound **10a** in THF-d_8.

3. X-Ray Crystallography

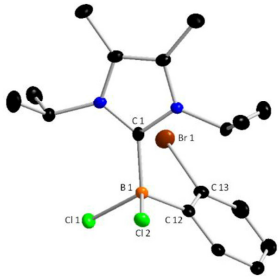

Figure S16. Molecular structures of **9a** in the solid state. Selected bond lengths [Å] and angles [°]: C1-B1 1.649(3), B1-C12 1.611(3), Br1-C13 1.951(2), C13-C12 1.395(3), B1-Cl1 1.882(3), B1-Cl2 1.905(3); C1-B1-C12 115.7(2), C1-B1-Cl1 115.6(2), C1-B1-Cl2 103.8(1), C12-B1-Cl1 104.6(2), C12-B1-Cl2 110.8(2), Cl1-B1-Cl2 106.0(1). Anisotropic displacement parameters are depicted at the 50 % probability level. Hydrogen atoms were omitted for clarity.

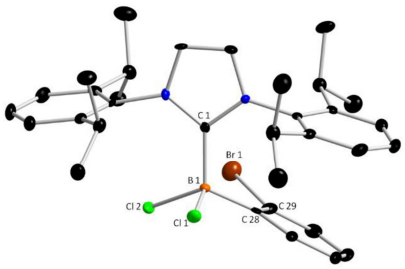

Figure S17. Molecular structures of **9b** in the solid state. Selected bond lengths [Å] and angles [°]: C1-B1 1.637(6), B1-C28 1.621(6), Br1-C29 1.913(4), C28-C29 1.389(4), B1-Cl1 1.882(4), B1-Cl2 1.897(4); C1-B1-C28 115.6(3), C1-B1-Cl1 111.0(3), C1-B1-Cl2 104.4(3), C28-B1-Cl1 110.1(3), C28-B1-Cl2 110.0(3), Cl1-B1-Cl2 105.0(2). Anisotropic displacement parameters are depicted at the 50 % probability level. Hydrogen atoms were omitted for clarity.

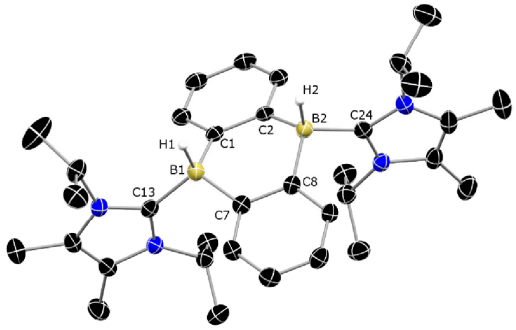

Figure S18. Molecular structures of **10a** in the solid state. Selected bond lengths [Å] and angles [°]: B1-H1 1.105(14), B2-H2 1.126(14) (the two B-H bond lengths were restrained onto each other), B1-C1 1.621(2), B1-C7 1.623(2), B2-C2 1.622(2), B2-C8 1-628(2), B1-C13 1.634(2), B2-C24 1.633(2), H1-B1-C1 104.8(8), H1-B1-C7 104.5(8), H2-B2-C2 108.0(8), H2-B2-C8 104.8(8), H1–B1–C13 112.0(6), H2–B2–C24 111.0(7). Anisotropic displacement parameters are depicted at the 50 % probability level. Hydrogen atoms bonded to carbon atoms were omitted for clarity.

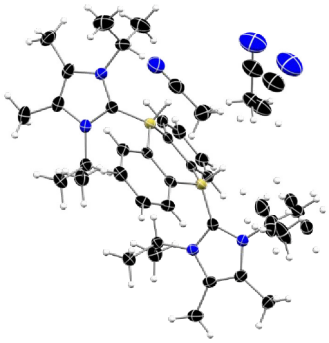

Figure S19. Full asymmetric unit of **10a** in the solid state. Ellipsoids are given at the 50 % probability level. The fractions of the acetonitrile disorder were 82.5(4) % and 17.5(4) % respectively. One of the isopropyl groups at the N-heterocyclic carbene had three disordered positions with fractions of 19.9(9) %, 71.5(8) % and 8.5(7) % respectively.

Table S1. Crystallographic Information for **9a**, **9b** and **10a**.			
	9a	**9b**	**10a**
Empirical formula	$C_{17}H_{24}BBrCl_2N_2$	$C_{34}H_{42}BBrCl_4N_2$	$C_{38}H_{56}B_2N_6$
Formula weight	418.00	711.21	618.50
Temperature [K]	100(2)	100(2)	100(2)
Crystal system	orthorhombic	monoclinic	triclinic
Space group	*P*bca	$P2_1/n$	$P\bar{1}$
Unit cell dimensions	a = 15.420(7) Å	a = 13.6476(18) Å	a = 9.587(2) Å
	b = 15.656(8) Å	b = 15.994(2) Å	b = 11.627(2) Å
	c = 15.891(8) Å	c = 16.158(2) Å	c = 18.798(3) Å
	α = 90°	α = 90°	α = 97.07(2)°
	β = 90°	β = 110.865(3)°	β = 96.36(2)°
	γ = 90°	γ = 90°	γ = 111.73(3)°
Volume [$Å^3$]	3836(3)	3451.7(8)	1903.7(7)
Z	8	4	2
Density (calculated) [Mg/m^3]	1.447	1.369	1.079
Crystal size [mm]	0.243 · 0.045 · 0.027	0.3593 · 0.0823 · 0.032	0.3463 · 0.1373 · 0.078
Theta range for data collection	2.254 to 28.282°	1.987 to 27.100°	1.108 to 25.385°
Index ranges	-20 ≤ h ≤16, -20 ≤ k ≤ 20, -21 ≤ l ≤ 21	-17 ≤ h ≤ 16, -19 ≤ k ≤ 20, -19 ≤ l ≤ 20	-11 ≤ h ≤ 11, -14 ≤ k ≤ 14, -22 ≤ l ≤ 22
Reflections collected	28741	16198	43114
Independent reflections	4755 [R(int) = 0.0734]	7538 [R(int) = 0.0641]	6987 [R(int) = 0.0338]
Goodness-of-fit on F^2	1.012	1.040	1.026
Final R indices [I>2sigma(I)]	R1 = 0.0342, wR2 = 0.0637	R_1 = 0.0571, wR_2 = 0.1414	R1 = 0.0471, wR2 = 0.1115
R indices (all data)	R1 = 0.0635, wR2 = 0.0718	R_1 = 0.0899, wR_2 = 0.1584	R1 = 0.0622, wR2 = 0.1211
CCDC number	1862386	1862384	1862385

Experimental Data

Crystals suitable for X-Ray crystallography were grown by standard techniques from solutions using dichloromethane (**9a** and **9b**) at ambient temperature and acetonitrile (**10a**) at -35 °C. Single crystals were selected, coated with Parabar 10312 (previously known as Paratone N, Hampton Research) and fixed on a microloop.

Data were collected on a Bruker APEX DUO instrument equipped with an IμS microfocus sealed tube and QUAZAR optics for MoK_α radiation (λ = 0.71073 Å). The Data collection strategy was determined using COSMO[6] employing ω-scans. Raw data were processed using APEX[7] and SAINT,[8] corrections for absorption effects were applied using SADABS.[9] The

structure was solved by direct methods and refined against all data by full-matrix least-squares methods on F^2 using SHELXTL[10] and Shelxle.[11]

4. Computational Methods

Geometry optimizations were performed using B3LYP[12] as implemented[13] in Gaussian 09[14] in conjunction with the 6-311+G**[15] basis set. Single point energies required for evaluation of strain energies (Scheme 1) were obtained at the level of coupled-cluster theory with singles, doubles, and a perturbative estimate of triples excitations, CCSD(T),[16] using the cc-pVTZ[17] basis set and the frozen core approximation. The resolution-of-the-identity (RI) approximation was used along with the corresponding fitting basis set.[18] The RI-CCSD(T) computations were performed with the Turbomole program package.[19] Due to the size of the systems, all other CCSD(T) single point energies employed the linear scaling domain based local pair natural orbital approximation, DLPNO-CCSD(T), introduced by Neese et al.[20] The DLPNO-CCSD(T) single point computations also employed the cc-pVTZ and the recommended RI fitting basis sets, and were performed with the Orca 4.0 program developed by the Neese group.[21] The effect of acetonitrile solvent at the DLPNO-CCSD(T)/cc-pVTZ level was modelled using the conductor-like polarizable continuum model.[22]

The isotropic chemical shielding constants of **A** were computed using the GIAO method[23] and the B3LYP functional in conjunction with the def2-TZVP[24] triple-ζ basis set. The chemical shift was computed with reference to the experimental values of **B** (^{11}B: –23.72 ppm) and benzene (^{13}C: 128.06 ppm).

Table S1. Absolute energies (in hartree), zero-point vibrational corrected energies (E+ZPVE, in hartree), and Gibbs energies (in hartree) computed at various levels of theory.

compound	E(B3LYP)[a]	E+ZPVE[b]	G(B3LYP)[b]	E(CCSD(T)[c]	E(DPLNO-CCSD(T)) [c]
1	-256.49824	-256.40806	-256.43601	-255.92461	-255.92017
2	-269.44001	-269.34666	-269.37526	-268.85991	
3	-270.32527	-270.22110	-270.24985	-269.74008	
benzene	-232.31125	-232.21111	-232.23623	-231.80578	
Ph2BH	-488.88236	-488.68839	-488.72567	-487.81117	
Ph2CH+	-501.86775	-501.67137	-501.70775	-500.78565	
Ph2CH2	-502.74346	-502.53466	-502.57393	-501.66403	
borirene	-102.82827	-102.78659	-102.81031	-102.58101	
cyclopropenium	-115.76107	-115.71604	-115.73967	-115.50938	
cyclopropene	-116.65432	-116.59860	-116.62254	-116.39784	
ethene	-78.61551	-78.56472	-78.58559	-78.43868	
(C2H3)2BH	-181.49528	-181.39785	-181.42752	-181.07570	
(C2H3)2CH+	-194.46029	-194.35783	-194.38638	-194.02729	
(C2H3)2CH2	-195.35709	-195.24432	-195.27366	-194.92843	
DBA, **11**	-513.14755	-512.96144	-512.99608	-512.01081	-512.00088
TS dimer. of **1**	-512.97622	-512.79499	-512.83424	-511.83042	-511.84071
A	-797.38972	-797.00202	-797.05358		-795.70098
A (in CH_3CN)	-797.40387	-797.01645	-797.06764		-795.72024
NHC I^iPr_{Me2} a	-540.83671	-540.54248	-540.58439		-539.70981
syn-**10a**	-1594.90901	-1594.12807	-1594.20381		-1591.56733
anti-**10a**	-1594.91393	-1594.13311	-1594.21061		-1591.57400
12a	-797.34588	-796.95940	-797.01011		-795.65288
12a (in CH_3CN)	-797.36700	-796.98065	-797.03259		-795.67860

[a] Using the 6-311+G** basis set. [b] B3LYP/6-311G**. [c] Using the cc-pVTZ basis set and B3LYP/6-311+G** geometries.

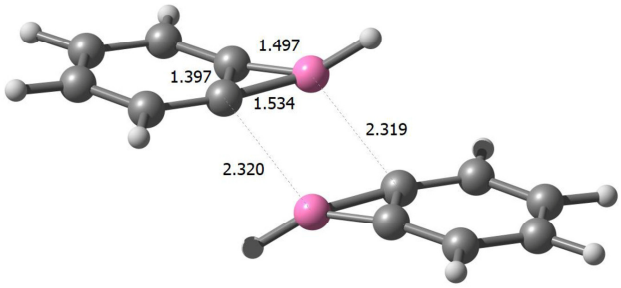

Figure S20. Geometry of the transition state for dimerization of benzoborirene **1** as computed at the B3LYP/6-311+G** level of theory. Interatomic distances involving the three-membered ring are given in Å.

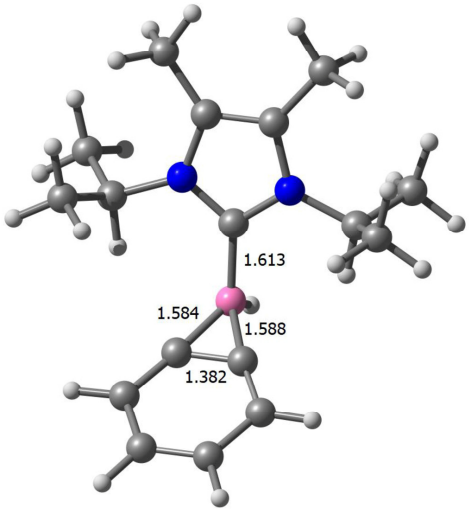

Figure S21. Geometry of the adduct **A** between benzoborirene **1** and 1,3-diisopropyl-4,5-dimethylimidazolin-2-ylidene as computed at the B3LYP/6-311+G** level of theory. Interatomic distances involving the three-membered ring are given in Å.

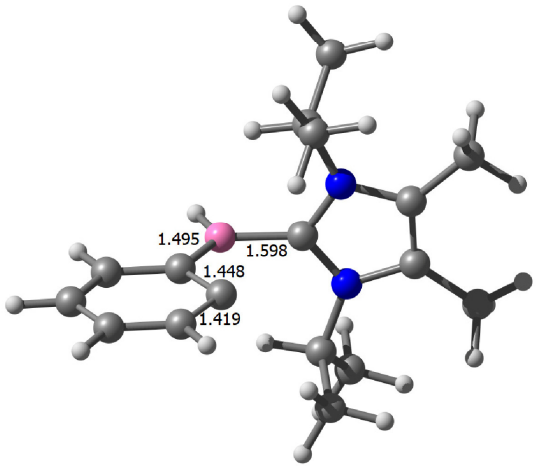

Figure S22. Geometry of the zwitterionic opened isomer of adduct **A**, compound **12a**, as computed at the B3LYP/6-311+G** level of theory. Selected interatomic distances are given in Å.

5. Cartesian Coordinates

Computed at the B3LYP/6-311+G** level of theory and given in Å.

```
12
benzoborirene 1
B      0.000000    0.000000    2.233196
C      0.000000    0.700056    0.929446
C      0.000000    1.445280   -0.263538
C      0.000000   -1.445280   -0.263538
C      0.000000    0.712204   -1.434759
C      0.000000   -0.712204   -1.434759
C      0.000000   -0.700056    0.929446
H      0.000000    1.224635   -2.391488
H      0.000000   -1.224635   -2.391488
H      0.000000    0.000000    3.412473
H      0.000000    2.530315   -0.284633
H      0.000000   -2.530315   -0.284633

12
benzocyclopropenium ion 2
C        0.284099000      1.493721000     -0.000030000
C       -0.876111000      0.702290000     -0.000006000
C       -0.876116000     -0.702285000     -0.000007000
C        0.284091000     -1.493722000     -0.000030000
C        1.428494000     -0.724613000      0.000015000
C        1.428498000      0.724607000      0.000015000
C       -2.047067000      0.000004000      0.000039000
H        2.395519000     -1.215898000      0.000097000
H        2.395526000      1.215887000      0.000097000
H        0.291971000      2.575331000     -0.000105000
H        0.291956000     -2.575332000     -0.000106000
H       -3.130297000      0.000004000      0.000044000

13
benzocyclopropene 3
C       -0.334637000     -1.452304000      0.000327000
C        0.802192000     -0.674236000     -0.000597000
C       -1.527885000     -0.700525000     -0.000056000
H       -2.480185000     -1.219939000     -0.000391000
C        0.802718000      0.673512000     -0.000391000
C       -1.527376000      0.701157000     -0.000044000
H       -2.479200000      1.221459000     -0.000256000
C       -0.333893000      1.452259000      0.000228000
H       -0.348097000      2.536357000      0.001103000
H       -0.349059000     -2.536346000      0.000885000
C        2.146536000     -0.000138000      0.000205000
H        2.745491000      0.000466000     -0.910571000
H        2.745123000     -0.000342000      0.911200000

12
benzene
C      0.000000    1.394737    0.000000
C      0.000000   -1.394737    0.000000
C      1.207878    0.697368    0.000000
C     -1.207878   -0.697368    0.000000
C     -1.207878    0.697368    0.000000
C      1.207878   -0.697369    0.000000
H      0.000000    2.479201    0.000000
H      0.000000   -2.479201    0.000000
H      2.147051    1.239600    0.000000
H     -2.147051   -1.239600    0.000000
H     -2.147051    1.239600    0.000000
H      2.147051   -1.239601    0.000000

24
(C6H5)2BH
B        0.000003000     -1.190411000      0.000200000
C        1.388988000     -0.497519000      0.037383000
C        2.524137000     -1.228618000     -0.372165000
C        3.795902000     -0.663760000     -0.376326000
C        3.972720000      0.646200000      0.068900000
C        2.874982000      1.384912000      0.512168000
C        1.602369000      0.822304000      0.487702000
H        4.649332000     -1.243899000     -0.709833000
```

```
H         4.963896000      1.086651000      0.081551000
H         3.014918000      2.397006000      0.876059000
H         0.763200000      1.405653000      0.040609000
H         2.396394000     -2.256474000     -0.695798000
H        -0.000022000     -2.388697000      0.000467000
C        -1.388991000     -0.497509000     -0.037293000
C        -1.602327000      0.822328000     -0.487588000
C        -2.524210000     -1.228641000      0.372043000
C        -2.874920000      1.384944000     -0.512173000
C        -3.795956000     -0.663747000      0.376169000
C        -3.972705000      0.646240000     -0.068996000
H        -0.763072000      1.405658000     -0.848356000
H        -2.396486000     -2.256548000      0.695515000
H        -3.014846000      2.397049000     -0.876040000
H        -4.649429000     -1.243879000      0.709573000
H        -4.963855000      1.086748000     -0.081699000

24
(C6H5)2CH+
C        -0.000003000     -0.998482000      0.000084000
C        -1.289842000     -0.417364000     -0.038042000
C        -2.390837000     -1.265519000      0.276004000
C        -3.679440000     -0.767899000      0.303708000
C        -3.908459000      0.571001000     -0.029998000
C        -2.848354000      1.412424000     -0.397638000
C        -1.553977000      0.933350000     -0.402470000
H        -4.508431000     -1.412725000      0.567041000
H        -4.921179000      0.957787000     -0.028679000
H        -3.050102000      2.433384000     -0.697206000
H        -0.750836000      1.569331000     -0.747709000
H        -2.203911000     -2.304570000      0.522867000
H        -0.000004000     -2.087013000      0.000030000
C         1.289840000     -0.417369000      0.038125000
C         1.554007000      0.933340000      0.402549000
C         2.390808000     -1.265524000     -0.276013000
C         2.848385000      1.412409000      0.397627000
C         3.679411000     -0.767909000     -0.303806000
C         3.908460000      0.570986000      0.029899000
H         0.750894000      1.569321000      0.747856000
H         2.203860000     -2.304572000     -0.522875000
H         3.050160000      2.433364000      0.697193000
H         4.508380000     -1.412735000     -0.567208000
H         4.921181000      0.957768000      0.028510000

25
(C6H5)2CH2
C         3.663432000      0.174074000      0.857830000
C         2.684450000     -0.665068000      1.392000000
C         1.503764000     -0.898256000      0.693003000
C         1.277829000     -0.302203000     -0.554185000
C         2.265758000      0.535560000     -1.078378000
C         3.450400000      0.774304000     -0.380036000
C        -0.003842000     -0.575053000     -1.322210000
C        -1.279395000     -0.196833000     -0.587549000
C        -2.302725000     -1.129881000     -0.400187000
C        -3.485282000     -0.777993000      0.252198000
C        -3.660699000      0.518576000      0.727901000
C        -2.645649000      1.459230000      0.547806000
C        -1.467148000      1.103172000     -0.101591000
H        -4.266192000     -1.518213000      0.388165000
H        -4.577822000      0.795378000      1.235589000
H        -2.772626000      2.471501000      0.915860000
H        -0.679822000      1.839173000     -0.227377000
H        -2.175245000     -2.142800000     -0.769374000
H         0.035117000     -0.034438000     -2.274068000
H         0.744439000     -1.544421000      1.121380000
H         2.109007000      1.005597000     -2.044307000
H         2.841789000     -1.136991000      2.355754000
H         4.203621000      1.428847000     -0.804782000
H         4.582350000      0.357066000      1.403351000
H        -0.049970000     -1.638475000     -1.579809000

6
borirene
C        -0.000021000     -0.379900000      0.675357000
B        -0.000021000      0.927163000      0.000000000
C        -0.000021000     -0.379900000     -0.675357000
H         0.000375000     -1.090412000      1.490792000
```

```
H        0.000375000     -1.090412000     -1.490792000
H       -0.000385000      2.103812000      0.000000000

6
cyclopropenium ion
C        0.000010000     -0.393248000      0.681258000
C        0.000010000      0.786785000      0.000000000
C        0.000010000     -0.393248000     -0.681258000
H       -0.000054000     -0.935309000      1.617801000
H       -0.000054000     -0.935309000     -1.617801000
H       -0.000064000      1.868882000      0.000000000

7
cyclopropene
C       -0.502035000      0.645144000     -0.000151000
C        0.863930000      0.000448000      0.000125000
C       -0.500998000     -0.645652000      0.000153000
H       -1.044025000      1.574912000      0.000311000
H       -1.041762000     -1.576193000      0.000239000
H        1.459188000      0.000238000     -0.913894000
H        1.461214000      0.001403000      0.912579000

6
ethene
C        0.000000000      0.000000000      0.664266000
C        0.000000000      0.000000000     -0.664266000
H        0.000000000      0.922522000      1.235375000
H        0.000000000     -0.922522000      1.235375000
H        0.000000000      0.922522000     -1.235375000
H        0.000000000     -0.922522000     -1.235375000

12
(C2H3)2BH
B        0.046609000      0.776072000      0.000217000
H        0.474611000      1.894192000      0.000478000
C       -1.490645000      0.563480000     -0.000162000
H       -2.144660000      1.435088000     -0.000622000
C       -2.089241000     -0.639387000      0.000081000
H       -1.518378000     -1.563503000      0.000543000
H       -3.170146000     -0.753831000     -0.000273000
C        1.081035000     -0.372840000      0.000042000
H        0.776090000     -1.419356000     -0.000170000
C        2.402121000     -0.126146000     -0.000078000
H        2.780267000      0.892390000      0.000071000
H        3.149147000     -0.915983000     -0.000414000

12
(C2H3)2CH+
C        0.054865000      0.651668000      0.000357000
H        0.470069000      1.657855000      0.000619000
C       -1.360232000      0.563682000     -0.000086000
H       -1.910314000      1.498129000     -0.000274000
C       -2.049886000     -0.609154000     -0.000289000
H       -1.565481000     -1.579443000     -0.000082000
H       -3.134531000     -0.611488000     -0.000125000
C        0.989319000     -0.404661000      0.000401000
H        0.660612000     -1.437338000      0.001173000
C        2.320820000     -0.121639000     -0.000413000
H        2.683386000      0.901776000     -0.000913000
H        3.066942000     -0.908866000     -0.000217000

13
(C2H3)2CH2
C       -0.000022000      0.297291000      0.671528000
H        0.000150000      1.115600000      1.406805000
C        1.256024000      0.403554000     -0.156458000
H        1.353642000      1.307219000     -0.756389000
C        2.222538000     -0.509655000     -0.200465000
H        2.165713000     -1.427881000      0.376583000
H        3.105140000     -0.372608000     -0.815040000
C       -1.256060000      0.403605000     -0.156493000
H       -1.354068000      1.307543000     -0.755932000
C       -2.222442000     -0.509758000     -0.200512000
H       -2.165351000     -1.428055000      0.376402000
H       -3.105333000     -0.372691000     -0.814663000
H       -0.000126000     -0.639346000      1.236634000

24
```

9,10-dihydro-9,10-diboraanthracene, **11**

H	0.000000000	0.000000000	2.679957000
B	0.000000000	0.000000000	1.483248000
C	0.000000000	1.348024000	0.713450000
C	0.000000000	1.348024000	-0.713450000
C	0.000000000	2.573667000	-1.391667000
C	0.000000000	3.785874000	-0.695960000
C	0.000000000	3.785874000	0.695960000
C	0.000000000	2.573667000	1.391667000
B	0.000000000	0.000000000	-1.483248000
H	0.000000000	0.000000000	-2.679957000
C	0.000000000	-1.348024000	-0.713450000
C	0.000000000	-1.348024000	0.713450000
C	0.000000000	-2.573667000	1.391667000
C	0.000000000	-3.785874000	0.695960000
C	0.000000000	-3.785874000	-0.695960000
C	0.000000000	-2.573667000	-1.391667000
H	0.000000000	2.581144000	2.477134000
H	0.000000000	-4.725158000	1.238521000
H	0.000000000	-2.581144000	2.477134000
H	0.000000000	-2.581144000	-2.477134000
H	0.000000000	-4.725158000	-1.238521000
H	0.000000000	4.725158000	1.238521000
H	0.000000000	4.725158000	-1.238521000
H	0.000000000	2.581144000	-2.477134000

24

TS for dimerization of **1**

C	-1.509041000	-0.397766000	0.401099000
C	-1.802588000	0.958569000	0.239580000
C	-3.085789000	1.397027000	-0.087372000
C	-4.058660000	0.412503000	-0.224515000
C	-3.760375000	-0.958697000	-0.051886000
C	-2.476979000	-1.395307000	0.251207000
H	-3.332807000	2.444421000	-0.226929000
H	-5.078723000	0.695283000	-0.462695000
H	-4.560338000	-1.682819000	-0.165362000
H	-2.254378000	-2.453160000	0.342990000
B	-0.455028000	0.639388000	0.809111000
H	0.269113000	0.888344000	1.703986000
C	1.802776000	-0.958725000	-0.239726000
C	1.508842000	0.397617000	-0.400662000
C	2.476600000	1.395329000	-0.250608000
C	3.760150000	0.958911000	0.052032000
C	4.058806000	-0.412289000	0.224104000
C	3.086156000	-1.396989000	0.086809000
H	2.253709000	2.453161000	-0.341914000
H	4.559966000	1.683180000	0.165596000
H	5.078991000	-0.694906000	0.461958000
H	3.333443000	-2.444377000	0.225927000
B	0.455189000	-0.639717000	-0.809130000
H	-0.269162000	-0.888570000	-1.703838000

45

benzoborirene-1,3-diisopropyl-4,5-dimethylimidazolin-2-ylidene adduct **A**

B	1.101802000	-0.186177000	1.193500000
C	2.387045000	0.488187000	0.558512000
C	2.277495000	-0.877857000	0.381158000
C	3.258778000	-1.615632000	-0.262342000
C	4.380000000	-0.910686000	-0.733150000
C	4.491917000	0.471845000	-0.552404000
C	3.486117000	1.200983000	0.105057000
H	3.199259000	-2.692193000	-0.411234000
H	5.177183000	-1.444443000	-1.242081000
H	5.374008000	0.984915000	-0.923877000
H	3.600414000	2.275476000	0.237214000
C	-0.343116000	-0.012387000	0.498857000
N	-1.192152000	-1.018585000	0.178889000
C	-2.362215000	-0.502160000	-0.387366000
C	-2.223414000	0.855993000	-0.402623000
N	-0.969911000	1.137989000	0.154360000
C	-0.826494000	-2.440946000	0.408183000
H	0.119128000	-2.367734000	0.943358000
C	-1.829593000	-3.162509000	1.312282000
H	-1.402958000	-4.121272000	1.617358000
H	-2.028300000	-2.582518000	2.216392000
H	-2.777855000	-3.370572000	0.813203000
C	-0.548050000	-3.172145000	-0.908421000

H	-0.152642000	-4.167376000	-0.689252000
H	-1.444865000	-3.300892000	-1.518896000
H	0.200666000	-2.633161000	-1.491707000
C	-3.528194000	-1.320597000	-0.840728000
H	-4.211514000	-0.700851000	-1.421629000
H	-3.225639000	-2.153862000	-1.476690000
H	-4.094615000	-1.731255000	-0.000097000
C	-3.205455000	1.880247000	-0.872845000
H	-2.754827000	2.609444000	-1.548022000
H	-4.014516000	1.392113000	-1.416503000
H	-3.656986000	2.429262000	-0.041941000
C	-0.336684000	2.466305000	0.368620000
H	0.587150000	2.213081000	0.886644000
C	0.050100000	3.131818000	-0.955178000
H	0.634828000	4.031387000	-0.746074000
H	0.669782000	2.461395000	-1.553227000
H	-0.817199000	3.433185000	-1.546770000
C	-1.168909000	3.363973000	1.288436000
H	-0.565165000	4.227049000	1.579896000
H	-2.072189000	3.744135000	0.807708000
H	-1.453298000	2.832172000	2.199285000
H	0.979615000	-0.339023000	2.390411000

33
1,3-diisopropyl-4,5-dimethylimidazolin-2-ylidene, **a**

C	-0.000005000	-1.246799000	0.152156000
N	-1.070401000	-0.404790000	0.073053000
C	-0.682602000	0.937613000	-0.059534000
C	0.682614000	0.937605000	-0.059534000
N	1.070400000	-0.404797000	0.073077000
C	-2.434040000	-0.968804000	0.096496000
H	-2.241505000	-2.028046000	0.274234000
C	-3.279080000	-0.441914000	1.261667000
H	-4.191102000	-1.030745000	1.340576000
H	-2.730122000	-0.522660000	2.202681000
H	-3.580757000	0.598547000	1.123558000
C	-3.140520000	-0.843129000	-1.258515000
H	-4.074021000	-1.412805000	-1.241894000
H	-3.391390000	0.191594000	-1.504319000
H	-2.510403000	-1.244300000	-2.055231000
C	-1.611544000	2.107197000	-0.142766000
H	-1.050295000	3.014163000	-0.371781000
H	-2.363633000	1.987194000	-0.926340000
H	-2.141624000	2.283591000	0.798334000
C	1.611585000	2.107190000	-0.142535000
H	2.364637000	1.986616000	-0.925079000
H	1.050590000	3.013954000	-0.372977000
H	2.140506000	2.284326000	0.799089000
C	2.434039000	-0.968813000	0.096519000
H	2.241525000	-2.028020000	0.274491000
C	3.140392000	-0.843434000	-1.258586000
H	4.073873000	-1.413142000	-1.241938000
H	2.510180000	-1.244754000	-2.055152000
H	3.391272000	0.191226000	-1.504648000
C	3.279161000	-0.441666000	1.261510000
H	4.191365000	-1.038350000	1.348370000
H	3.580655000	0.598827000	1.123249000
H	2.730336000	-0.522386000	2.202605000

90
10a, syn isomer

C	3.027846000	0.306319000	-0.037932000
C	5.284374000	0.084791000	-0.009994000
C	4.749299000	-1.168316000	-0.067951000
C	4.290751000	2.462471000	0.093054000
C	5.092087000	3.078664000	-1.057476000
H	6.168101000	2.919260000	-0.967904000
H	4.921086000	4.158232000	-1.063369000
H	4.757368000	2.684044000	-2.019498000
C	4.746990000	2.926756000	1.479925000
H	4.110617000	2.497754000	2.256295000
H	4.659704000	4.014954000	1.538977000
H	5.785751000	2.667504000	1.697543000
C	2.335735000	-2.090140000	-0.124252000
C	2.304600000	-2.906384000	1.171924000
H	2.180493000	-2.253886000	2.036482000
H	3.199201000	-3.517708000	1.308992000
H	1.448537000	-3.585957000	1.139702000

C	2.456379000	-2.957726000	-1.380922000
H	1.567986000	-3.589927000	-1.456831000
H	3.325304000	-3.617990000	-1.357451000
H	2.497905000	-2.338613000	-2.278199000
C	0.730421000	0.543475000	1.354631000
C	-0.689889000	0.544967000	1.376767000
C	-1.335330000	0.335127000	2.608234000
H	-2.423488000	0.354949000	2.650207000
C	-0.638839000	0.122349000	3.798390000
H	-1.175661000	-0.027887000	4.730658000
C	0.753619000	0.117575000	3.776367000
H	1.318776000	-0.038831000	4.690688000
C	1.413105000	0.327528000	2.564755000
H	2.502163000	0.335347000	2.572124000
C	0.689882000	0.545081000	-1.376650000
C	-0.730428000	0.543606000	-1.354514000
C	-1.413114000	0.327777000	-2.564659000
H	-2.502172000	0.335610000	-2.572028000
C	-0.753631000	0.117923000	-3.776289000
H	-1.318791000	-0.038396000	-4.690623000
C	0.638827000	0.122677000	-3.798310000
H	1.175648000	-0.027487000	-4.730590000
C	1.335320000	0.335340000	-2.608135000
H	2.423478000	0.355151000	-2.650107000
C	-3.027849000	0.306320000	0.037995000
C	-5.284373000	0.084777000	0.009872000
C	-4.749293000	-1.168330000	0.067763000
C	-4.290761000	2.462476000	-0.092850000
C	-5.092220000	3.078526000	1.057670000
H	-6.168226000	2.919138000	0.967963000
H	-4.921215000	4.158092000	1.063717000
H	-4.757607000	2.683784000	2.019679000
C	-4.746858000	2.926923000	-1.479714000
H	-4.110390000	2.490023000	-2.256069000
H	-4.659581000	4.015129000	-1.538624000
H	-5.785593000	2.667684000	-1.697474000
C	-2.335724000	-2.090140000	0.124177000
C	-2.456455000	-2.957820000	1.380773000
H	-1.568062000	-3.590018000	1.456701000
H	-3.325452000	-3.618091000	1.357188000
H	-2.498056000	-2.338775000	2.278094000
C	-2.304481000	-2.906286000	-1.172058000
H	-2.180292000	-2.253725000	-2.036556000
H	-3.199075000	-3.517594000	-1.309253000
H	-1.448427000	-3.585870000	-1.139808000
N	3.360796000	-1.011788000	-0.083680000
N	4.209557000	0.980897000	0.004253000
N	-4.209562000	0.980893000	-0.004213000
N	-3.360792000	-1.011794000	0.083611000
B	1.507261000	0.923080000	-0.022804000
H	1.604788000	2.140823000	-0.025337000
B	-1.507266000	0.923090000	0.022956000
H	-1.604798000	2.140833000	0.025598000
C	5.475697000	-2.472590000	-0.153338000
H	5.083818000	-3.215098000	0.542460000
H	5.431370000	-2.901941000	-1.158271000
H	6.528169000	-2.324022000	0.089507000
C	6.730052000	0.467933000	-0.008571000
H	6.959642000	1.226561000	0.740581000
H	7.341502000	-0.405752000	0.218839000
H	7.056919000	0.850221000	-0.980001000
C	-5.475687000	-2.472617000	0.152983000
H	-5.083779000	-3.215048000	-0.542881000
H	-5.431394000	-2.902074000	1.157871000
H	-6.528152000	-2.324028000	-0.089881000
C	-6.730056000	0.467905000	0.008353000
H	-6.959567000	1.226657000	-0.740697000
H	-7.341470000	-0.405748000	-0.219276000
H	-7.057038000	0.850025000	0.979811000
H	-1.399607000	-1.541107000	0.194344000
H	-3.253632000	2.768491000	0.027151000
H	3.253607000	2.768490000	-0.026807000
H	1.399607000	-1.541111000	-0.194306000

90
10a, anti isomer

B	1.408796000	-0.710760000	-0.056803000
B	-1.408918000	0.710943000	0.056746000

C	0.634724000	-0.200987000	-1.396130000
C	-0.649284000	0.394442000	-1.348278000
C	-1.259061000	0.760775000	-2.564944000
C	-0.653232000	0.560496000	-3.802053000
C	0.611617000	-0.028107000	-3.849393000
C	1.230735000	-0.395377000	-2.658228000
H	-2.242560000	1.227525000	-2.542975000
H	-1.155702000	0.860098000	-4.717145000
H	1.104380000	-0.198493000	-4.802166000
H	2.214071000	-0.859379000	-2.711374000
C	0.649201000	-0.394203000	1.348215000
C	-0.634787000	0.201272000	1.396067000
C	-1.230745000	0.395773000	2.658167000
C	-0.611613000	0.028544000	3.849339000
C	0.653204000	-0.560123000	3.801997000
C	1.258993000	-0.760490000	2.564881000
H	-2.214050000	0.859840000	2.711314000
H	-1.104339000	0.199024000	4.802115000
H	1.155686000	-0.859703000	4.717089000
H	2.242478000	-1.227271000	2.542922000
C	2.926054000	-0.074097000	-0.015835000
N	4.125040000	-0.721919000	-0.026854000
C	5.177678000	0.201777000	0.012297000
C	4.608758000	1.440375000	0.051996000
N	3.225496000	1.249956000	0.036464000
C	-2.926105000	0.074091000	0.015839000
N	-4.125184000	0.721748000	0.027134000
C	-5.177700000	-0.202082000	-0.012150000
C	-4.608610000	-1.440596000	-0.052169000
N	-3.225375000	-1.249989000	-0.036713000
C	2.170987000	2.298852000	0.113694000
H	1.246124000	1.740319000	0.015326000
C	2.231090000	3.275015000	-1.064029000
H	1.315153000	3.070697000	-1.065031000
H	3.073898000	3.966846000	-1.004747000
H	2.275767000	2.735173000	-2.011885000
C	2.144289000	2.981868000	1.484212000
H	2.087443000	2.238959000	2.281478000
H	3.009259000	3.626712000	1.656526000
H	1.248903000	3.605002000	1.546547000
C	4.244682000	-2.200323000	-0.096568000
H	3.210950000	-2.531007000	-0.023717000
C	4.781918000	-2.672778000	-1.451693000
H	4.710545000	-3.762536000	-1.504942000
H	4.188409000	-2.257477000	-2.268498000
H	5.828127000	-2.404011000	-1.612434000
C	5.006446000	-2.787596000	1.096020000
H	4.625887000	-2.386686000	2.038107000
H	4.857933000	-3.870536000	1.109547000
H	6.081713000	-2.606666000	1.048625000
C	5.294502000	2.768716000	0.080722000
H	4.927979000	3.406265000	0.886449000
H	6.363588000	2.628955000	0.240542000
H	5.170112000	3.314265000	-0.858326000
C	6.632591000	-0.144440000	0.029385000
H	6.906147000	-0.840037000	-0.765729000
H	7.225171000	0.758406000	-0.118024000
H	6.942693000	-0.587187000	0.980054000
C	-6.632653000	0.143948000	-0.029021000
H	-6.906446000	0.838481000	0.766951000
H	-6.942683000	0.587851000	-0.979166000
H	-7.225110000	-0.759181000	0.117131000
C	-5.294155000	-2.769035000	-0.081147000
H	-4.927389000	-3.406441000	-0.886872000
H	-5.169844000	-3.314663000	0.857870000
H	-6.363237000	-2.629427000	-0.241130000
C	-4.245011000	2.200121000	0.097280000
H	-3.211273000	2.530902000	0.024942000
C	-4.782865000	2.672131000	1.452314000
H	-4.711338000	3.761856000	1.506007000
H	-5.829206000	2.403501000	1.612416000
H	-4.189844000	2.256435000	2.269277000
C	-5.006321000	2.787688000	-1.095448000
H	-4.625311000	2.387115000	-2.037494000
H	-6.081588000	2.606613000	-1.048562000
H	-4.857942000	3.870654000	-1.108582000
C	-2.170719000	-2.298722000	-0.114123000
H	-1.245938000	-1.740067000	-0.015695000

C	-2.143930000	-2.981545000	-1.484739000
H	-1.248360000	-3.604398000	-1.547227000
H	-3.000720000	-3.626625000	-1.657002000
H	-2.087358000	-2.238505000	-2.281904000
C	-2.230648000	-3.275043000	1.063484000
H	-2.275318000	-2.735320000	2.011407000
H	-3.073387000	-3.966955000	1.004176000
H	-1.314647000	-3.870628000	1.065147000
H	-1.529449000	1.924402000	0.146913000
H	1.529200000	-1.924239000	-0.147064000

45
zwitterion isomer of **A**, compound **12a**

B	-1.412508000	0.983559000	0.000000000
C	-0.574923000	2.221767000	0.000000000
C	0.857623000	2.012956000	0.000000000
C	1.606957000	3.217735000	0.000000000
C	1.028573000	4.483684000	0.000000000
C	-0.372034000	4.647538000	0.000000000
C	-1.169108000	3.522850000	0.000000000
H	2.696795000	3.169153000	0.000000000
H	1.660025000	5.370970000	0.000000000
H	-0.805157000	5.642556000	0.000000000
H	-2.252619000	3.626023000	0.000000000
C	-0.650930000	-0.421414000	0.000000000
N	-0.309783000	-1.142328000	1.085836000
C	0.322654000	-2.324025000	0.682674000
C	0.322654000	-2.324025000	-0.682674000
N	-0.309783000	-1.142328000	-1.085836000
C	-0.433670000	-0.570617000	2.453221000
H	-1.040528000	0.324872000	2.299226000
C	-1.200166000	-1.488511000	3.407997000
H	-1.441361000	-0.929840000	4.315655000
H	-2.138028000	-1.829171000	2.962274000
H	-0.617996000	-2.361243000	3.708433000
C	0.927626000	-0.106505000	2.975874000
H	0.785251000	0.471101000	3.893044000
H	1.585312000	-0.947456000	3.210015000
H	1.404669000	0.530694000	2.225736000
C	0.835381000	-3.373239000	1.614402000
H	1.422016000	-4.104550000	1.058464000
H	1.483253000	-2.955421000	2.386790000
H	0.024683000	-3.913461000	2.112232000
C	0.835381000	-3.373239000	-1.614402000
H	1.483253000	-2.955421000	-2.386790000
H	1.422016000	-4.104550000	-1.058464000
H	0.024683000	-3.913461000	-2.112232000
C	-0.433670000	-0.570617000	-2.453221000
H	-1.040528000	0.324872000	-2.299226000
C	0.927626000	-0.106505000	-2.975874000
H	0.785251000	0.471101000	-3.893044000
H	1.404669000	0.530694000	-2.225736000
H	1.585312000	-0.947456000	-3.210015000
C	-1.200166000	-1.488511000	-3.407997000
H	-1.441361000	-0.929840000	-4.315655000
H	-0.617996000	-2.361243000	-3.708433000
H	-2.138028000	-1.829171000	-2.962274000
H	-2.612940000	0.939112000	0.000000000

6. References

[1] N. Kuhn, T. Kratz, *Synthesis* **1993**, *1993*, 561-562.
[2] A. J. Arduengo, R. Krafczyk, R. Schmutzler, H. A. Craig, J. R. Goerlich, W. J. Marshall, M. Unverzagt, *Tetrahedron* **1999**, *55*, 14523-14534.
[3] A. Lorbach, M. Bolte, H. Li, H.-W. Lerner, M. C. Holthausen, F. Jäkle, M. Wagner, *Angew. Chem. Int. Ed.* **2009**, *48*, 4584-4588.
[4] A. Lorbach, C. Reus, M. Bolte, H.-W. Lerner, M. Wagner, *Adv. Synth. Catal.* **2010**, *352*, 3443-3449.
[5] D. Kaufmann, *Chem. Ber.* **1987**, *120*, 901-905.
[6] COSMO v. 1.61, Madison, WI, **2012**.
[7] APEX 3 v. 2016.5-0, Madison, Wi, **2016**.
[8] SAINT v. 8.37A, Madison, Wi, **2015**.
[9] L. Krause, R. Herbst-Irmer, G. M. Sheldrick, D. Stalke, *J. Appl. Cryst.* **2015**, *48*, 3-10.
[10] a) G. Sheldrick, *Acta Cryst.* **2015**, *C71*, 3-8; b) G. Sheldrick, *Acta Cryst.* **2015**, *A71*, 3-8.
[11] C. B. Hübschle, G. M. Sheldrick, B. Dittrich, *J. Appl. Cryst.* **2011**, *44*, 1281-1284.
[12] a) A. D. Becke, *J. Chem. Phys.* **1993**, *98*, 5648-5652; b) C. Lee, W. Yang, R. G. Parr, *Phys. Rev. B* **1988**, *37*, 785-789.
[13] P. J. Stephens, F. J. Devlin, C. F. Chabalowski, M. J. Frisch, *J. Phys. Chem.* **1994**, *98*, 11623-11627.
[14] M. J. Frisch, G. W. Trucks, H. B. Schlegel, G. E. Scuseria, M. A. Robb, J. R. Cheeseman, G. Scalmani, V. Barone, B. Mennucci, G. A. Petersson, H. Nakatsuji, M. Caricato, X. Li, H. P. Hratchian, A. F. Izmaylov, J. Bloino, G. Zheng, J. L. Sonnenberg, M. Hada, M. Ehara, K. Toyota, R. Fukuda, J. Hasegawa, M. Ishida, T. Nakajima, Y. Honda, O. Kitao, H. Nakai, T. Vreven, J. A. Montgomery, J. E. Peralta, F. Ogliaro, M. Bearpark, J. J. Heyd, E. Brothers, K. N. Kudin, V. N. Staroverov, R. Kobayashi, J. Normand, K. Raghavachari, A. Rendell, J. C. Burant, S. S. Iyengar, J. Tomasi, M. Cossi, N. Rega, J. M. Millam, M. Klene, J. E. Knox, J. B. Cross, V. Bakken, C. Adamo, J. Jaramillo, R. Gomperts, R. E. Stratmann, O. Yazyev, A. J. Austin, R. Cammi, C. Pomelli, J. W. Ochterski, R. L. Martin, K. Morokuma, V. G. Zakrzewski, G. A. Voth, P. Salvador, J. J. Dannenberg, S. Dapprich, A. D. Daniels, Ö. Farkas, J. B. Foresman, J. V. Ortiz, J. Cioslowski, D. J. Fox, Gaussian 09, Revision D.01, Wallingford CT, **2009**.
[15] R. Krishnan, J. S. Binkley, R. Seeger, J. A. Pople, *J. Chem. Phys.* **1980**, *72*, 650-654.
[16] K. Raghavachari, G. W. Trucks, J. A. Pople, M. Head-Gordon, *Chem. Phys. Lett.* **1989**, *157*, 479.
[17] T. H. Dunning, *J. Chem. Phys.* **1989**, *90*, 1007-1023.
[18] F. Weigend, A. Köhn, C. Hättig, *J. Chem. Phys.* **2002**, *116*, 3175-3183.
[19] J. Krüger, F. García, F. Eisenhut, D. Skidin, J. M. Alonso, E. Guitián, D. Pérez, G. Cuniberti, F. Moresco, D. Peña, *Angew. Chem. Int. Ed.* **2017**, *56*, 11945-11948.
[20] a) C. Riplinger, F. Neese, *J. Chem. Phys.* **2013**, *138*, 034106; b) C. Riplinger, B. Sandhoefer, A. Hansen, F. Neese, *J. Chem. Phys.* **2013**, *139*, 134101.
[21] F. Neese, *WIREs Comput. Mol. Sci.* **2012**, *2*, 73-78.
[22] V. Barone, M. Cossi, *J. Phys. Chem. A* **1998**, *102*, 1995-2001.
[23] K. Wolinski, J. F. Hinton, P. Pulay, *J. Am. Chem. Soc.* **1990**, *112*, 8251-8260.
[24] F. Weigend, R. Ahlrichs, *Phys. Chem. Chem. Phys.* **2005**, *7*, 3297-3305.

6.2.4. Selective CO_2 Splitting by Doubly Reduced Aryl Boranes to Give CO and $[CO_3]^{2-}$

GDCh Communications Angewandte International Edition Chemie

Electrocatalysis

International Edition: DOI: 10.1002/anie.201811135
German Edition: DOI: 10.1002/ange.201811135

Selective CO_2 Splitting by Doubly Reduced Aryl Boranes to Give CO and $[CO_3]^{2-}$

*Esther von Grotthuss, Sven E. Prey, Michael Bolte, Hans-Wolfram Lerner, and Matthias Wagner**

Abstract: *Alkali metal salts M_2[**1**] (M = Li, Na) of doubly reduced 9,10-dimethyl-9,10-dihydro-9,10-diboraanthracene (**1**) instantaneously add the C=O bond of CO_2 across their boron centers to furnish formal [4+2]-cycloadducts M_2[**2**]. If only 1 equiv of CO_2 is supplied, these products are stable. In the presence of excess CO_2, however, C–O bond cleavage occurs and an O^{2-} equivalent is transferred to CO_2 to furnish CO and $[CO_3]^{2-}$. With M = Li, Li_2CO_3 precipitates and the neutral **1** is liberated such that it can be reduced again to establish a catalytic cycle. With M = Na, $[CO_3]^{2-}$ remains coordinated to both boron atoms in a bridging mode (Na_2[**4**]). A mechanistic scenario is proposed, based on isolated intermediates and model reactions.*

The exhaust gas CO_2 has long been neglected as a ubiquitous and potentially valuable C_1 building block for chemical synthesis. Today, however, this situation is dramatically changing, driven by the general awareness that fossil oil and gas are limited resources and that the accumulation of CO_2 in the earth's atmosphere significantly contributes to climate change.[1] Conversion of the thermodynamically stable CO_2 molecule into useful chemicals requires the input of energy and reduction equivalents. As an additional challenge, high-pressure conditions are only avoidable with the help of carefully designed catalysts.

Prospective technologies for the renewable production of organic compounds from CO_2 are often based on the heterogeneous $CO_2 \rightarrow CO$ electroreduction at metal surfaces and nanoparticles (e.g., Cu, Ag, Au),[2–4] bismuth-modified glassy carbon cathodes,[5] or metal-organic frameworks.[6] Common obstacles include high electrode overpotentials, low energetic efficiencies, rapid deactivation of the systems, and poor product selectivities.[3] The one-electron reduction of CO_2 occurs only at very cathodic potential values, mainly because of the energy penalty associated with bending of the linear molecule upon electron uptake to furnish the $[CO_2]^{\bullet-}$ radical. Correspondingly, the bent $[CO_2]^{\bullet-}$ is predisposed to accept a second electron.[1a] Some transition-metal compounds can act as nucleophiles toward CO_2 molecules and thereby transfer two electrons simultaneously onto the substrate, which is afterwards stabilized through π back-bonding (see below). Indeed, several metal complexes exist that are capable of achieving the $CO_2 \rightarrow CO$ reduction under mild conditions, albeit not always in a catalytic fashion.[7–10]

Since the advent of frustrated Lewis pair (FLP) chemistry, increasing efforts have been devoted to the replacement of transition-metal catalysts by appropriate combinations of main-group Lewis acids and bases. In the context of CO_2 activation, a plethora of capture products such as R_3P-C(O)-O-BR'_3 are nowadays known. Follow-up reactions with various reducing agents have been studied and the palette of obtainable compounds encompasses CO, HC(O)OH, H_3COH, and CH_4.[11] Despite these impressive achievements, examples of catalytic CO_2 reductions with FLPs are still scarce and often require drastic reaction conditions, extended periods of time, as well as rather expensive hydride donors (e.g., $HB(OR)_2$, $HSiR_3$). The reduction products are mainly obtained in the form of organyloxyboranes and -silanes (e.g., H_3CO-$B(OR)_2$) and the released O atoms appear incorporated in dibor- or disiloxanes (e.g., $(RO)_2B$-O-$B(OR)_2$).[11]

In the quest for more atom economic main-group reduction catalysts, arylboranes with two cooperating boron centers and the ability to accept two electrons from an electropositive metal or a negative electrode bear particular promise. In 2010, our group reported the activation of C(sp)–H ($[\mathbf{B}]^{2-}$) and C=O ($[\mathbf{C}]^{2-}$) bonds by the doubly reduced 9,10-dihydro-9,10-diboraanthracene $[\mathbf{A}]^{2-}$ (Scheme 1a).[12,13] Later we also succeeded in the cleavage of H_2 on the $[\mathbf{A}]^{2-}$ platform and proposed a concerted addition of the H_2 molecule to the two boron atoms.[14] In the meantime, related systems have been disclosed by Kinjo[15,16] and Harman[17] and shown to add CO_2 through one of its C=O bonds (**D**–**F**; Scheme 1b). Even under a CO_2 atmosphere no further transformation took place. Braunschweig et al. encountered a different situation when they treated the diborene **G** with CO_2 (Scheme 1c).[18] As a thermally unstable primary intermediate, they observed the dibora-β-lactone **H**, which rearranged with CO_2 splitting to form the isomeric 2,4-diboraoxetan-3-one **I**.

Herein, we report that reactions of CO_2 with alkali metal salts M_2[**1**] (M = Li, Na; cf. Scheme 2) do not stop at the stage of **F**-type cycloadducts, but proceed further to furnish CO and O^{2-} equivalents. Contrary to the stoichiometric system **G**–**I**, however, CO is released and the O^{2-} equivalent transferred to CO_2 with formation of $[CO_3]^{2-}$. The reaction is quantitative and the scaffold of **1** remains fully intact, which renders the system catalytic.

[*] M. Sc. E. von Grotthuss, B. Sc. S. E. Prey, Dr. M. Bolte, Dr. H.-W. Lerner, Prof. Dr. M. Wagner
Institut für Anorganische Chemie, Goethe-Universität Frankfurt
Max-von-Laue-Strasse 7, 60438 Frankfurt (Main) (Germany)
E-mail: Matthias.Wagner@chemie.uni-frankfurt.de

Supporting information (including all experimental procedures together with further spectroscopic, crystallographic, and computational details) and the ORCID identification number(s) for the author(s) of this article can be found under https://doi.org/10.1002/anie.201811135.

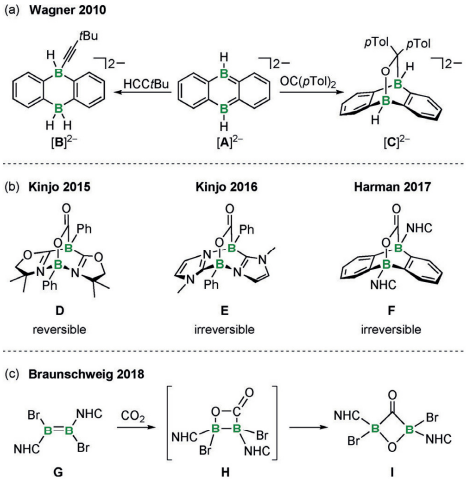

Scheme 1. a) Activation of C(sp)–H and C=O bonds by a doubly reduced 9,10-dihydro-9,10-diboraanthracene ([**A**]$^{2-}$). b) Cycloaddition products of CO_2 with neutral boron-containing heterocycles (**D**–**F**). c) Reaction of the diborene **G** with CO_2 to furnish **I** via **H**. NHC = 1,3-bis(2,6-diisopropylphenyl)imidazol-2-ylidene.

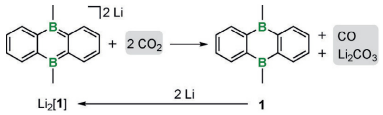

Scheme 2. Highly selective transformation of CO_2 to CO and Li_2CO_3 with lithium metal and **1** as the redox catalyst (THF, room temperature, 1 atm).

Stirring of the known **1**[19] in THF over lithium or sodium metal quantitatively provides the respective M_2[**1**] salts. Exposure of a red solution of Li_2[**1**] in [D_8]THF to excess CO_2 resulted in an immediate decolorization (room temperature, 1 atm). After an induction period of several minutes, gas evolution set in, accompanied by the formation of a colorless precipitate (Scheme 2). An NMR spectroscopic investigation of the supernatant after 30 min revealed the selective and quantitative conversion of Li_2[**1**] to **1**. A solution of the precipitate in D_2O showed only one resonance in the $^{13}C\{^1H\}$ and one in the ^7Li NMR spectrum ($\delta = 167.7$ and 0.11 ppm, respectively). Moreover, the precipitate gave rise to a prominent IR stretch at 1435 cm^{-1} with a shoulder at higher wavenumbers. These values are in accordance with corresponding data recorded on commercial samples of Li_2CO_3. On a preparative scale, Li_2[**1**] and CO_2 gave Li_2CO_3 in yields of 83 %. When the reaction was carried out in a sealed NMR tube, also the resonances of newly formed CO ($\delta(^{13}C) = 184.9$ ppm[20]) and residual CO_2 ($\delta(^{13}C) = 125.7$ ppm[21]) were detected. Further evidence for the formation of CO was gathered from a chemical analysis technique based on the reduction of colorless, aqueous $PdCl_2$ to black Pd metal.[22] In conclusion, 1 equiv of Li_2[**1**] transforms 2 equiv of CO_2 into 1 equiv of CO and 1 equiv of Li_2CO_3. Importantly, the reaction can also be performed in a catalytic fashion: as a proof of principle, we have treated the **1**-containing supernatant first with lithium metal, then with CO_2, and harvested a second crop of Li_2CO_3/CO.

Given that the rate of H_2 activation with M_2[**A**] salts is significantly influenced by the choice of the counter cation M^+,[14] the CO_2 reduction was next repeated with the green-colored Na_2[**1**]. An X-ray crystal-structure analysis of the polymeric inverse sandwich complex [Na_2(thf)$_3$][**1**] is shown in Figure 1 (av. Na···COG = 2.268 Å; COG: centroid of the B_2C_4 ring). Upon addition of CO_2, decolorization of the solution and CO evolution occurred as before, but no Na_2CO_3 precipitated and the reaction mixture also contained no free **1**. Rather, the ^{11}B NMR spectrum was characterized by a broad resonance at 2.7 ppm, indicating tetracoordinate boron nuclei.[23] In line with that, the three signals observed in the ^1H NMR spectrum [7.25 (4H), 6.71 (4H), 0.31 (6H) ppm] and the corresponding ^{13}C resonances were considerably shifted upfield compared to those of **1**. An additional ^{13}C signal appeared at $\delta = 163.5$ ppm and the IR spectrum of the product contained two strong stretches in the carbonyl region (1399, 1523 cm^{-1}). Taken together, the spectroscopic results indicated the presence of a symmetric diadduct of **1**, which was finally identified as the $[CO_3]^{2-}$ complex Na_2[**4**] by X-ray crystallography. The thf-solvated salt forms C_1-symmetric tetramers [Na_8(thf)$_{14}$][**4**]$_4$ in the solid state (see the Supporting Information). The bicyclo[3.2.2] ion [**4**]$^{2-}$ acquires its negative charges from a bridging $[CO_3]^{2-}$ ion (Figure 1). The average lengths of the formal C=O double and C–OB single bonds are 1.252 Å and 1.302 Å, respectively,[24] with an unstrained O-C-O bond angle of 123°. The comparatively large spread of the individual B–O bond lengths (1.600(8)–1.646(8) Å) indicates

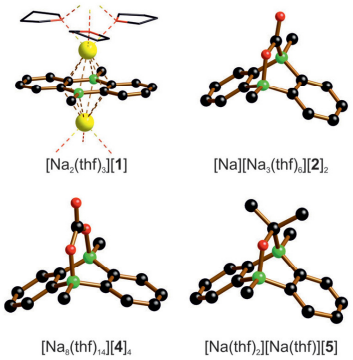

Figure 1. Molecular structures of [Na_2(thf)$_3$][**1**], [Na][Na_3(thf)$_6$][**2**]$_2$, [Na_8(thf)$_{14}$][**4**]$_4$, and [Na(thf)$_2$][Na(thf)][**5**] in the solid state. Na^+ cations and coordinating thf molecules are only shown for [Na_2(thf)$_3$][**1**]; all H atoms are omitted for clarity.

a soft bonding potential. Together with the large average B–O bond length of 1.626 Å,[25] this points toward a weak interaction. Consequently, the extra thermodynamic driving force provided by the higher lattice energy of Li_2CO_3 vs. Na_2CO_3 ($\Delta U_{POT} = 2523$ vs. 2301 kJ mol^{-1})[26] suffices to cause the precipitation of the former while the latter remains coordinated to the ditopic Lewis acid **1**.

We next treated M_2[**1**] (M = Li, Na) with only 1 equiv of CO_2. The bicyclo[2.2.2] adducts M_2[**2**] formed quantitatively (Scheme 3a).[27] Na_2[**2**] gives rise to two ^{11}B NMR signals: a broad one at $\delta = 2.0$ ppm, similar to the $[CO_3]^{2-}$ adduct Na_2[**4**], is assignable to the *B*O atom. A sharp one at $\delta = -14.6$ ppm corresponds to the boron center attached to the carbonyl carbon atom. The carbonyl ^{13}C resonance ($\delta = 219.9$ ppm; cf. **F**: 198.4 ppm) is broadened almost beyond detection due to the effect of the boron quadrupole moment. According to the overall numbers and patterns of the ^{1}H and ^{13}C NMR signals, $[\mathbf{2}]^{2-}$ possesses average C_s symmetry in solution. The NMR data of Li_2[**2**] are essentially the same as those of Na_2[**2**]. Single crystals of $[Na][Na_3(thf)_6][\mathbf{2}]_2$ grew directly from the reaction mixture. Its solid-state structure

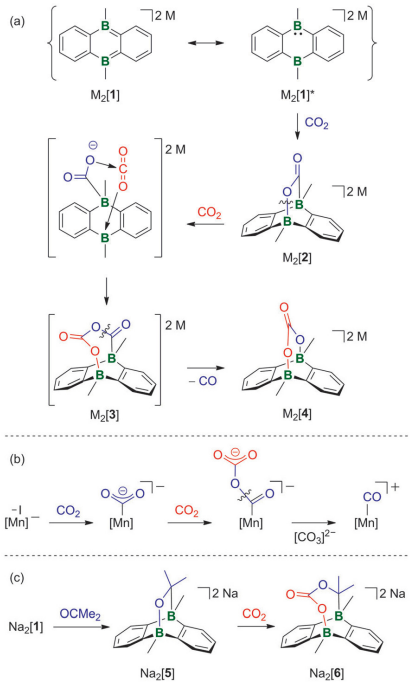

Scheme 3. a) Proposed mechanism for the reaction of M_2[**1**] (M = Li, Na) with CO_2. b) Related transformation mediated by the anionic *fac*-$[Mn^{-I}(CO)_3(bis\text{-}^{Me}NHC)]^-$ complex containing a methylene bis(*N*-methylimidazol-2-ylidene) ligand. c) Stable model complex Na_2[**6**] of the putative intermediate Na_2[**3**], obtained by treatment of Na_2[**1**] with acetone and then with CO_2.

contains two crystallographically independent $[\mathbf{2}]^{2-}$ ions with identical geometric parameters within experimental error (Figure 1). The B–O bond length of $[\mathbf{2}]^{2-}$ (av. 1.589 Å) lies between that of Harman's neutral derivative **F** (1.509(2) Å) and that of the $[CO_3]^{2-}$ adduct $[Na_8(thf)_{14}][\mathbf{4}]_4$ (av. 1.626 Å). The formal C–O single bond of the CO_2 bridge in $[\mathbf{2}]^{2-}$ (av. 1.319 Å) is longer by 0.053 Å than the C=O double bond (av. 1.266 Å). The primary C=O activation step is reminiscent of common [4+2]-cycloaddition reactions across the two central carbon atoms of anthracene,[28] an isoelectronic analog of $[\mathbf{1}]^{2-}$. Alternatively, one can view the $[\mathbf{1}]^{2-}$ ion as containing ambiphilic boron centers, which concertedly act on the substrate as a frustrated B^{+I}/B^{+III} Lewis pair (see the resonance form M_2[**1**]* in Scheme 3a).[16] Analogous to the μ-$[CO_3]^{2-}$ adduct Na_2[**4**], the primary product Na_2[**2**] may be described as featuring a $[CO_2]^{2-}$ dianion, simultaneously bonded to the two boron atoms of neutral **1**.

When M_2[**2**] was put under a blanket of CO_2 ([D_8]THF, room temperature, 1 atm), we obtained the same product mixtures as before when we had treated M_2[**1**] directly with excess CO_2, which confirmed the role of M_2[**2**] as an intermediate in the CO_2 reduction sequence. The elongated B–O bond likely constitutes the weak link of $[\mathbf{2}]^{2-}$ and the site of attack of a second CO_2 molecule, which reacts through the insertion of one C=O bond. A plausible mechanism of this insertion involves an equilibrium in which ring-opening occurs through B–O bond heterolysis. The transient intramolecular B/O-FLP could activate the substrate CO_2 in the usual manner to afford compound M_2[**3**] (Scheme 3a). Its $[R_3B\text{-}O\text{-}C(O)\text{-}O\text{-}C(O)\text{-}BR_3]^{2-}$ fragment has a structural analog in the mixed carboxylic-carbonic anhydrides (MCCAs) $R_3C\text{-}O\text{-}C(O)\text{-}O\text{-}C(O)\text{-}CR_3$,[29] which often suffer from low stability. In the case of $[\mathbf{3}]^{2-}$, decomposition is even too rapid to allow an NMR-spectroscopic characterization. The molecular structure of this putative intermediate was therefore investigated by quantum-chemical calculations. The computed dianion $[\mathbf{3}^c]^{2-}$ represents a local minimum on the energy surface (Figure 2). Regarding the release of CO, the most noteworthy structural peculiarity lies in the pronounced difference between the two C(sp^2)–O bond lengths within the central C-O-C unit: the one belonging to the CO_3 moiety is 1.357 Å, whereas the one belonging to the CO_2 fragment amounts to 1.437 Å. We therefore assume that the latter heterolytically dissociates in the course of the subsequent reaction step, whereupon a species is formed, which contains an η^1-coordinated $[CO_3]^{2-}$ ligand on one boron atom and a CO ligand on the other. Ample precedence exists for R_3B-CO complexes and association/dissociation equilibria with

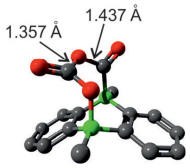

Figure 2. Calculated structure of $[\mathbf{3}^c]^{2-}$ at the PBE0D/TZVP level of theory with the SMD polarized continuum model for solvation in THF.

their free components R_3B/CO.[30] In this vein, loss of CO should readily occur also in the present situation and the generated Lewis-acidic B center can subsequently bind to the $[CO_3]^{2-}$ ligand to give the bridged complex M_2[**4**], which persists in the case of M = Na, but dissociates in the case of M = Li. We note that the mechanistic scenario outlined in Scheme 3a is strikingly similar to the CO_2-activation reaction mediated by the transition-metal complex *fac*-[Mn^{+I}-$(CO)_3$(bis-^{Me}NHC)Br] with a chelating methylene bis(*N*-methylimidazol-2-ylidene) ligand (Scheme 3b):[10] In the course of the catalytic cycle, the metal-centered HOMO of an electrogenerated [Mn ^{I}] intermediate nucleophilically attacks an incoming CO_2 molecule and forms a [Mn^{+I}-CO_2]$^-$ anion, which subsequently chains up with a second equivalent of CO_2. Finally, $[CO_3]^{2-}$ dissociates from the complex to leave a [Mn^{+I}-CO]$^+$ cation behind.

In order to gain further proof for the intermediacy of Na_2[**3**], we decided to replace the carbonyl group marked in blue in Scheme 3a by a CMe_2 group, which should be less easily extricable than CO. The addition of 1 equiv of acetone to Na_2[**1**] gave Na_2[**5**] in a clean reaction (Scheme 3c). X-ray crystallography on [Na(thf)$_2$][Na(thf)][**5**] (Figure 1) revealed a B–O bond length of 1.562(6) Å, which is shorter by 0.027 Å than that of [Na][Na_3(thf)$_6$][**2**]$_2$, but still longer by 0.053 Å than that of Harman's CO_2-inert adduct **F**. Upon exposure to CO_2 (room temperature, 1 atm), Na_2[**5**] was converted further to Na_2[**6**] (Scheme 3c). The NMR spectra of this product are in line with the uptake of 1 equiv of CO_2: i) all ^{1}H, ^{11}B, and ^{13}C resonances were shifted compared to the starting material Na_2[**5**], but the signal patterns remained compatible with a bridged derivative of **1** with average C_s symmetry. ii) A new ^{13}C resonance appeared at $\delta = 159.1$ ppm, which we assign to the carbonyl carbon atom of the activated CO_2 molecule (cf. the $[CO_3]^{2-}$ signal of Na_2[**4**] at $\delta = 163.5$ ppm). iii) The IR spectrum of Na_2[**6**] (but not of Na_2[**5**]) contains strong absorption bands at 1358 and 1397 cm^{-1}, in the typical region of C=O stretches. Notably, even if the reaction was carried out in a sealed NMR tube, no resonance of CO could be detected. This result strongly indicates that the CO released in the course of the reaction between M_2[**1**] and CO_2 indeed originates from the first incorporated molecule of CO_2.

To conclude, the presence of 9,10-dimethyl-9,10-dihydro-9,10-diboraanthracene (**1**) as a redox catalyst enables the clean reduction of CO_2 with lithium metal under ambient conditions and with selective formation of CO and Li_2CO_3 (the main products of the corresponding uncatalyzed reaction are Li_2O and elemental carbon[31]). Notwithstanding the relevance of Li_2CO_3 for the chemical and pharmaceutical industry,[32] it would be desirable to prepare also Na_2CO_3 in the same way. The reaction currently stops at the stage of an isolable Na_2CO_3-**1** aggregate, but our system offers multiple options to promote the release of Na_2CO_3, e.g., by adjusting the steric demand of the boron-bonded substituents.

Conflict of interest

The authors declare no conflict of interest.

Keywords: boron · CO_2 · electrocatalysis · main-group ambiphile · reduction

How to cite: *Angew. Chem. Int. Ed.* **2018**, *57*, 16491 – 16495
Angew. Chem. **2018**, *130*, 16729 – 16733

[1] a) A. M. Appel, J. E. Bercaw, A. B. Bocarsly, H. Dobbek, D. L. DuBois, M. Dupuis, J. G. Ferry, E. Fujita, R. Hille, P. J. A. Kenis, C. A. Kerfeld, R. H. Morris, C. H. F. Peden, A. R. Portis, S. W. Ragsdale, T. B. Rauchfuss, J. N. H. Reek, L. C. Seefeldt, R. K. Thauer, G. L. Waldrop, *Chem. Rev.* **2013**, *113*, 6621 – 6658; b) M. Aresta, A. Dibenedetto, A. Angelini, *Chem. Rev.* **2014**, *114*, 1709 – 1742.

[2] Y. Hori, H. Wakebe, T. Tsukamoto, O. Koga, *Electrochim. Acta* **1994**, *39*, 1833 – 1839.

[3] B. A. Rosen, A. Salehi-Khojin, M. R. Thorson, W. Zhu, D. T. Whipple, P. J. A. Kenis, R. I. Masel, *Science* **2011**, *334*, 643 – 644.

[4] D. Kim, J. Resasco, Y. Yu, A. M. Asiri, P. Yang, *Nat. Commun.* **2014**, *5*, 4948.

[5] J. L. DiMeglio, J. Rosenthal, *J. Am. Chem. Soc.* **2013**, *135*, 8798 – 8801.

[6] N. Kornienko, Y. Zhao, C. S. Kley, C. Zhu, D. Kim, S. Lin, C. J. Chang, O. M. Yaghi, P. Yang, *J. Am. Chem. Soc.* **2015**, *137*, 14129 – 14135.

[7] P. Zimmermann, S. Hoof, B. Braun-Cula, C. Herwig, C. Limberg, *Angew. Chem. Int. Ed.* **2018**, *57*, 7230 – 7233; *Angew. Chem.* **2018**, *130*, 7349 – 7353.

[8] S. Fukuzumi, Y.-M. Lee, H. S. Ahn, W. Nam, *Chem. Sci.* **2018**, *9*, 6017 – 6034.

[9] Z. Cao, J. S. Derrick, J. Xu, R. Gao, M. Gong, E. M. Nichols, P. T. Smith, X. Liu, X. Wen, C. Copéret, C. J. Chang, *Angew. Chem. Int. Ed.* **2018**, *57*, 4981 – 4985; *Angew. Chem.* **2018**, *130*, 5075 – 5079.

[10] F. Franco, M. F. Pinto, B. Royo, J. Lloret-Fillol, *Angew. Chem. Int. Ed.* **2018**, *57*, 4603 – 4606; *Angew. Chem.* **2018**, *130*, 4693 – 4696.

[11] a) A. E. Ashley, A. L. Thompson, D. O'Hare, *Angew. Chem. Int. Ed.* **2009**, *48*, 9839 – 9843; *Angew. Chem.* **2009**, *121*, 10023 – 10027; b) A. Berkefeld, W. E. Piers, M. Parvez, *J. Am. Chem. Soc.* **2010**, *132*, 10660 – 10661; c) D. W. Stephan, G. Erker, *Chem. Sci.* **2014**, *5*, 2625 – 2641; d) D. W. Stephan, *Acc. Chem. Res.* **2015**, *48*, 306 – 316; e) Z. Lu, H. Hausmann, S. Becker, H. A. Wegner, *J. Am. Chem. Soc.* **2015**, *137*, 5332 – 5335; f) R. Declercq, G. Bouhadir, D. Bourissou, M.-A. Légaré, M.-A. Courtemanche, K. S. Nahi, N. Bouchard, F.-G. Fontaine, L. Maron, *ACS Catal.* **2015**, *5*, 2513 – 2520; g) F.-G. Fontaine, D. W. Stephan, *Curr. Opin. Green Sustainable Chem.* **2017**, *3*, 28 – 32; h) F.-G. Fontaine, É. Rochette, *Acc. Chem. Res.* **2018**, *51*, 454 – 464.

[12] A. Lorbach, M. Bolte, H.-W. Lerner, M. Wagner, *Organometallics* **2010**, *29*, 5762 – 5765.

[13] The X-ray crystal structure analysis of a close derivative of [**C**]$^{2-}$ is provided in Figure S49.

[14] E. von Grotthuss, M. Diefenbach, M. Bolte, H.-W. Lerner, M. C. Holthausen, M. Wagner, *Angew. Chem. Int. Ed.* **2016**, *55*, 14067 – 14071; *Angew. Chem.* **2016**, *128*, 14273 – 14277.

[15] D. Wu, L. Kong, Y. Li, R. Ganguly, R. Kinjo, *Nat. Commun.* **2015**, *6*, 7340.

[16] B. Wang, Y. Li, R. Ganguly, H. Hirao, R. Kinjo, *Nat. Commun.* **2016**, *7*, 11871.

[17] J. W. Taylor, A. McSkimming, C. F. Guzman, W. H. Harman, *J. Am. Chem. Soc.* **2017**, *139*, 11032 – 11035.

[18] A. Stoy, J. Böhnke, J. O. C. Jiménez-Halla, R. D. Dewhurst, T. Thiess, H. Braunschweig, *Angew. Chem. Int. Ed.* **2018**, *57*, 5947 – 5951; *Angew. Chem.* **2018**, *130*, 6055 – 6059.

[19] S. N. Kessler, M. Neuburger, H. A. Wegner, *Eur. J. Org. Chem.* **2011**, 3238 – 3245.

[20] B. von Ahsen, C. Bach, G. Balzer, B. Bley, M. Bodenbinder, G. Hägele, H. Willner, F. Aubke, *Magn. Reson. Chem.* **2005**, *43*, 520 – 527.
[21] G. R. Fulmer, A. J. M. Miller, N. H. Sherden, H. E. Gottlieb, A. Nudelman, B. M. Stoltz, J. E. Bercaw, K. I. Goldberg, *Organometallics* **2010**, *29*, 2176 – 2179.
[22] A. F. Holleman, E. Wiberg, N. Wiberg, *Lehrbuch der Anorganischen Chemie*, *Vol. 102*, De Gruyter, Berlin, **2007**.
[23] "Nuclear Magnetic Resonance Spectroscopy of Boron Compounds": H. Nöth, B. Wrackmeyer in *NMR Basic Principles and Progress* (Eds.: P. Diehl, E. Fluck, R. Kosfeld), Springer, Berlin, **1978**.
[24] Compare the C–O bond lengths of $CaCO_3$: 1.280(1), 1.2818(9), and 1.2818(9) Å: B. Pokroy, J. S. Fieramosca, R. B. von Dreele, A. N. Fitch, E. N. Caspi, E. Zolotoyabko, *Chem. Mater.* **2007**, *19*, 3244 – 3251.
[25] B–O bond lengths for comparison are listed in the legend of Figure S45.
[26] L. Glasser, H. D. B. Jenkins, *J. Am. Chem. Soc.* **2000**, *122*, 632 – 638.
[27] The dianion $[\mathbf{2}]^{2-}$ is also comparable to published 9,10-dihydro-9,10-diboraanthracene- and 1,2-diborylbenzene-diazene adducts: a) A. Lorbach, M. Bolte, H.-W. Lerner, M. Wagner, *Chem. Commun.* **2010**, *46*, 3592 – 3594; b) Ö. Seven, S. Popp, M. Bolte, H.-W. Lerner, M. Wagner, *Dalton Trans.* **2014**, *43*, 8241 – 8253; c) Z. Lu, H. Quanz, O. Burghaus, J. Hofmann, C. Logemann, S. Beeck, P. R. Schreiner, H. A. Wegner, *J. Am. Chem. Soc.* **2017**, *139*, 18488 – 18491.
[28] J. C. C. Atherton, S. Jones, *Tetrahedron* **2003**, *59*, 9039 – 9057.
[29] a) D. S. Tarbell, E. J. Longosz, *J. Org. Chem.* **1959**, *24*, 774 – 778; b) D. S. Tarbell, *Acc. Chem. Res.* **1969**, *2*, 296 – 300; c) C.-O. Chan, C. J. Cooksey, D. Crich, *J. Chem. Soc. Perkin Trans. 1* **1992**, 777 – 780.
[30] H. C. Brown, *Acc. Chem. Res.* **1969**, *2*, 65 – 72.
[31] G. Zhuang, Y. Chen, P. N. Ross, Jr., *Surf. Sci.* **1998**, *418*, 139 – 149; at −153 °C, the principal reaction products are Li_2CO_3 and CO (probably formed via an oxalate intermediate), but even at such low temperatures the reaction is far less selective than the one mediated by $Li_2[\mathbf{1}]$.
[32] J. Deberitz, *Lithium: production and application of a fascinating and versatile element*, SZ Scala GmbH, München, **2006**.

Manuscript received: September 27, 2018
Accepted manuscript online: October 15, 2018
Version of record online: November 12, 2018

Angewandte Chemie
Eine Zeitschrift der Gesellschaft Deutscher Chemiker

Supporting Information

Selective CO_2 Splitting by Doubly Reduced Aryl Boranes to Give CO and $[CO_3]^{2-}$

*Esther von Grotthuss, Sven E. Prey, Michael Bolte, Hans-Wolfram Lerner, and Matthias Wagner**

anie_201811135_sm_miscellaneous_information.pdf

Table of contents:

1. Experimental details and characterization data

General considerations. All reactions and manipulations were carried out in an argon-filled glovebox or by applying standard Schlenk techniques under a nitrogen atmosphere. Toluene, Et_2O, and THF were dried over Na/benzophenone; [D_8]THF was dried over Na-K alloy without benzophenone. Prior to use, the solvents were freshly distilled from the drying agent; THF and [D_8]THF were degassed by applying three freeze-pump-thaw cycles.

NMR spectra were recorded at 298 K using the following spectrometers: Bruker Avance-300, Avance-400, or Avance-500.

Chemical shifts are referenced to (residual) solvent signals ($^1H/^{13}C\{^1H\}$; [D_8]THF: δ = 3.58/67.21 ppm[S1]) or external $BF_3{\cdot}Et_2O$ (^{11}B; $^{11}B\{^1H\}$). Abbreviations: s = singlet, d = doublet, t = triplet, q = quartet, m = multiplet, br = broad, n.o. = not observed, n.r. = multiplet expected but not resolved.

Numbering schemes for symmetrically substituted (left) and unsymmetrically substituted (right) DBA cores are as follows:

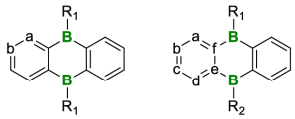

IR spectra were measured on a JASCO FT/IR spectrometer 4200 series by attenuated total reflection (ATR).

The compound 9,10-dibromo-DBA[S2,3] was synthesized according to literature procedures.

Synthesis of 1 (protocol modified from Siebert[S4] and Wegner[S5])

Freshly prepared MeMgI (5.52 mmol, 2.3 equiv) in Et_2O (20 mL) was added dropwise with stirring over 15 min to a cooled (−78 °C) solution of 9,10-dibromo-DBA (800 mg, 2.40 mmol, 1.0 equiv) in toluene (50 mL). The reaction mixture was slowly allowed to warm to room temperature and stirred overnight. All volatiles were removed under reduced pressure, the off-white solid residue was extracted into toluene (3 × 10 mL) and the combined extracts were filtered over a glass frit (G4) covered with Celite (1 cm; pre-dried at 120 °C for several days). After the removal of all volatiles from the filtrate *in vacuo* and the subsequent sublimation of the crude product at 110 °C/10^{-3} mbar, **1** was obtained as a pale yellow solid. Yield: 391 mg (1.92 mmol, 80%).

^{1}H NMR (300.0 MHz, [D$_8$]THF): δ = 7.95–7.93 (m, 4H; H-a), 7.37–7.35 (m, 4H; H-b), 1.00 ppm (s, 6H; CH_3).

^{11}B NMR (96.3 MHz, [D$_8$]THF): δ = 42.6 ppm ($h_{1/2}$ = 420 Hz).

^{13}C{^{1}H} NMR (125.8 MHz, [D$_8$]THF): δ = 150.6 (br; BC), 134.2 (C-a), 129.7 (C-b), 6.7 ppm (CH_3).

^{1}H and ^{11}B NMR data in C_6D_6 are in accordance with the literature.[S5]

^{1}H NMR (400.1 MHz, C_6D_6): δ = 8.03–8.01 (m, 4H; C_6H_4), 7.36–7.33 (m, 4H; C_6H_4), 1.33 ppm (s, 6H; CH_3).

^{11}B NMR (96.3 MHz, C_6D_6): δ = 67.0 ppm ($h_{1/2}$ = 390 Hz).

Synthesis of Li_2[1]

Lithium granules (10 mg, 1.44 mmol) were added at room temperature to a stirred solution of **1** (15 mg, 0.074 mmol) in [D$_8$]THF (0.5 mL), whereupon the reaction mixture immediately adopted a red color. After 30 min, the solution was separated from residual lithium metal with a syringe and used without further treatment. NMR analysis revealed the quantitative conversion to Li_2[**1**]. X-ray-quality crystals of [Li(thf)$_2$]$_2$[**1**] were grown by slow evaporation of a THF solution of Li_2[**1**].

^{1}H NMR (300.0 MHz, [D$_8$]THF): δ = 8.27–8.23 (m, 4H; H-a), 6.68–6.65 (m, 4H; H-b), 1.28 ppm (s, 6H; CH_3).

^{11}B NMR (96.3 MHz, [D$_8$]THF): δ = 21.3 ppm ($h_{1/2}$ = 390 Hz).

^{13}C{^{1}H} NMR (75.4 MHz, [D$_8$]THF): δ = 135.6 (C-a), 134.5 (br; BC), 117.5 (C-b), −1.0 ppm (CH_3).

Synthesis of Na_2[1]

Sodium metal (20 mg, 0.87 mmol) was added at room temperature to a stirred solution of **1** (15 mg, 0.074 mmol) in [D_8]THF (0.5 mL), whereupon the reaction mixture immediately adopted a pink color and turned dark green after 30 min. After 60 min, the solution was separated from residual sodium metal with a syringe and used without further treatment. NMR analysis revealed the quantitative conversion to Na_2[**1**]. X-ray-quality crystals of [Na_2(thf)$_3$][**1**] were grown by slow evaporation of a THF solution of Na_2[**1**].

^{1}H NMR (300.0 MHz, [D_8]THF): δ = 8.27–8.25 (m, 4H; H-a), 6.53–6.50 (m, 4H; H-b), 1.21 ppm (s, 6H; CH_3).

^{11}B NMR (96.3 MHz, [D_8]THF): δ = 21.0 ppm ($h_{1/2}$ = 500 Hz).

^{13}C{^{1}H} NMR (75.4 MHz, [D_8]THF): δ = 137.1 (br; BC), 136.1 (C-a), 115.0 (C-b), –0.4 ppm (CH_3).

General synthesis procedure for reactions with CO_2 (excess or 1 equiv)

Excess CO_2: An NMR tube, charged with a solution of M_2[**1**] (0.074 mmol; M = Li or Na) in [D_8]THF (0.5 mL), was connected to a Schlenk line. The solution was frozen with liquid nitrogen, the system evacuated, and CO_2 (quality grade 4.5; 1 atm) was filled in. The content of the NMR tube was allowed to warm to room temperature and the excess pressure released through a Hg bubbler. After 10 min, the reaction mixture was frozen again, the NMR tube was evacuated, and flame-sealed.

1 Equiv CO_2: A fixed amount of CO_2 was gauged with the help of a special J. Young's valve vessel, the volume of which corresponded to 1.8 mL (≙ 0.074 mmol CO_2 at 25 °C and 1 atm). This amount was deposited onto a frozen solution of M_2[**1**] (0.074 mmol; M = Li or Na) in [D_8]THF (0.5 mL). The NMR tube was flame-sealed while the mixture was still frozen at liquid nitrogen temperature.

NMR spectroscopy proved the quantitative conversions of M_2[**1**] to M_2[**2**] (1 equiv CO_2) or **1**, Li_2CO_3, CO / Na_2[**4**], CO (excess CO_2) within minutes.

X-ray-quality crystals of [Na][Na_3(thf)$_6$][**2**]$_2$ and [Na_8(thf)$_{14}$][**4**]$_4$ were obtained by gas-phase diffusion of hexane into a THF solution of Na_2[**2**] and Na_2[**4**], respectively.

NMR data of Li_2[2]

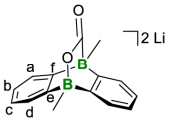

^{1}H NMR (500.2 MHz, [D_8]THF): δ = 7.13–7.12 (m, 2H; H-d), 7.05–7.03 (m, 2H; H-a), 6.53–6.47 (m, 4H; H-b,c), 0.54 (s, 3H; OBCH_3), 0.24 ppm (s, 3H; CBCH_3).

^{11}B NMR (96.3 MHz, [D_8]THF): δ = 1.2 (br; BO), –16.6 ppm (BC).

$^{13}C\{^{1}H\}$ NMR (125.8 MHz, $[D_8]THF$): $\delta = 224.0$* (BC(O)OB), 163.7 (br; C-f), 161.7 (br; C-e), 126.3 (C-a), 125.7 (C-d), 121.4 (C-b), 120.8 (C-c), 1.1 ($OBCH_3$), −1.6 ppm (br; $CBCH_3$); *detected through a cross peak with the resonance at 0.24 ppm in the ^{1}H-^{13}C-HMBC spectrum

NMR data of Na_2[2]

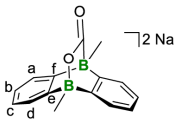

^{1}H NMR (500.2 MHz, $[D_8]THF$): $\delta = 7.18–7.16$ (m, 2H; H-d), 7.12−7.10 (m, 2H; H-a), 6.61−6.55 (m, 4H; H-b,c), 0.39 (s, 3H; $OBCH_3$), 0.22 ppm (s, 3H; $CBCH_3$).

^{11}B NMR (160.5 MHz, $[D_8]THF$): $\delta = 2.0$ (br; BO), −14.6 ppm (BC).

$^{13}C\{^{1}H\}$ NMR (125.8 MHz, $[D_8]THF$): $\delta = 219.9$ (BC(O)OB), 164.8 (br; C-f), 162.9 (C-e), 126.6 (C-a), 125.8 (C-d), 121.7 (C-b), 121.2 (C-c), 1.5 ($OBCH_3$), −1.1 ppm (br; $CBCH_3$).

NMR data of Na_2[4]

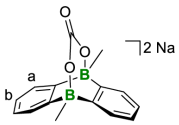

^{1}H NMR (500.2 MHz, $[D_8]THF$): $\delta = 7.25$ (n.r., 4H; H-a), 6.71 (n.r., 4H; H-b), 0.31 ppm (s, 6H; CH_3).

^{11}B NMR (96.3 MHz, $[D_8]THF$): $\delta = 2.7$ ppm (br).

$^{13}C\{^{1}H\}$ NMR (125.8 MHz, $[D_8]THF$): $\delta = 163.5$ (CO_3), 161.0 (br; BC), 127.7 (C-a), 123.1 (C-b), 4.6 ppm (CH_3).

Reaction between Li_2[1] and CO_2 on a preparative scale

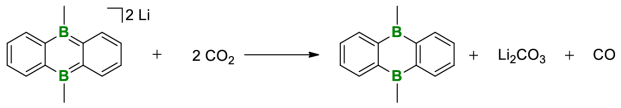

Li_2[**1**], freshly prepared from **1** (50 mg, 0.245 mmol) and lithium granules (30 mg, 4.32 mmol) in THF (5 mL), was transferred into a J. Young's valve vessel. The red solution was put under a blanket of CO_2 (1 atm), whereupon the color of the solution changed from red to colorless, a colorless gas (CO) evolved, and a white precipitate formed (Li_2CO_3). The separation of **1** from Li_2CO_3 was achieved by filtration. Compound **1** (42 mg, 0.206 mmol) was recovered in 84% yield and Li_2CO_3 (15 mg, 0.203 mmol) was isolated in 83% yield.

The reaction was also carried out in a sealed NMR tube {Li_2[**1**] (0.074 mmol); [D_8]THF (0.5 mL)}. A subsequent NMR spectroscopic investigation revealed the presence of neutral **1**, CO, and residual CO_2 as the sole components of the solution (cf. Figures S1-S3). The formation of CO was further confirmed by its characteristic reduction reaction with $PdCl_2$ (see below; cf. Figure S8). According to $^{13}C\{^1H\}$ NMR spectroscopy (D_2O) and IR measurements (cf. Figures S4-S7), the precipitate consisted of Li_2CO_3.

As a proof of principle that the reaction can be performed in a catalytic fashion, the recovered **1** was reduced with lithium again and successfully used for a subsequent reaction with CO_2.

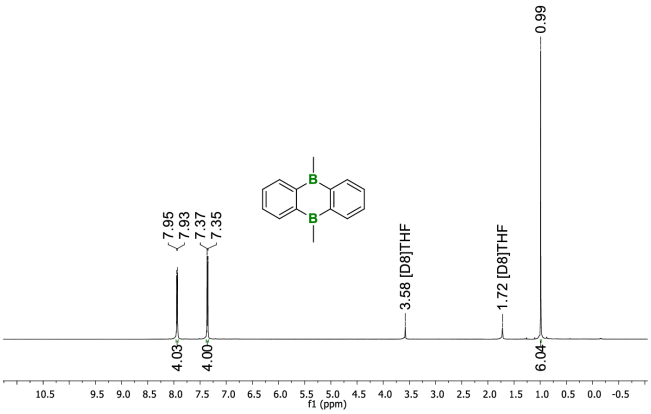

Figure S1. ^1H NMR spectrum recorded after the reaction of Li_2[**1**] and CO_2 (500.2 MHz, [D_8]THF).

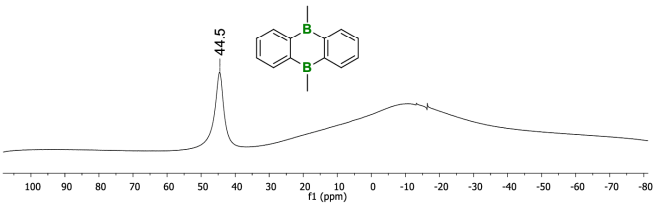

Figure S2. ^{11}B NMR spectrum recorded after the reaction of Li_2[**1**] and CO_2 (160.5 MHz, [D_8]THF).

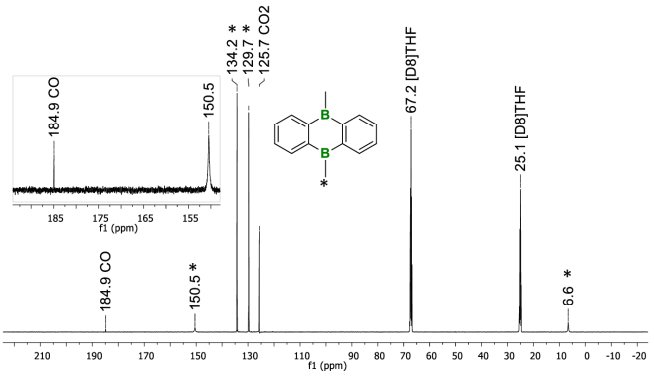

Figure S3. ^{13}C{^{1}H} NMR spectrum recorded after the reaction of Li_2[**1**] and CO_2 (sealed NMR tube; 125.8 MHz, [D_8]THF). The resonances of **1** are marked with asterisks; the reaction mixture contains residual starting material (CO_2) and the product (CO; chemical shift value according to the literature: δ(^{13}C) = 184 ppm[S6]).

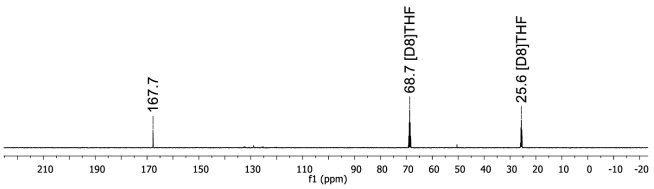

Figure S4. ^{13}C{^{1}H} NMR spectrum recorded after the reaction of Li_2[**1**] and CO_2 (125.8 MHz, D_2O) showing the formation of Li_2CO_3.

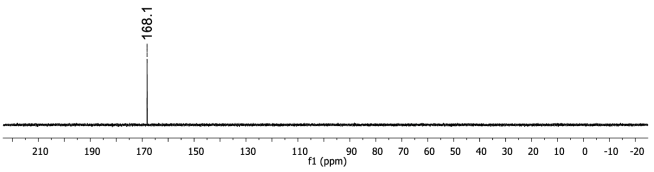

Figure S5. ^{13}C{^{1}H} NMR spectrum of commercial Li_2CO_3 (125.8 MHz, D_2O).

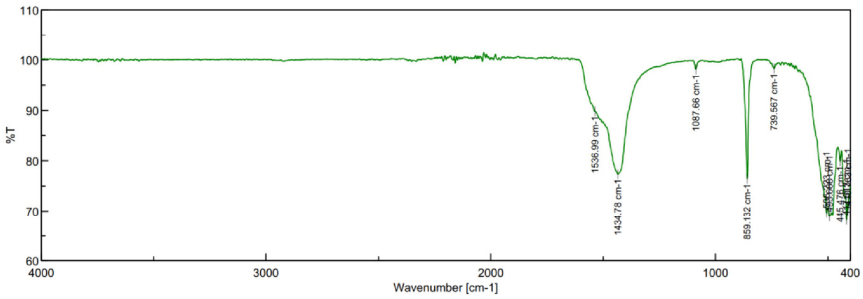

Figure S6. IR spectrum of Li_2CO_3 obtained from the reaction between Li_2[**1**] and CO_2.

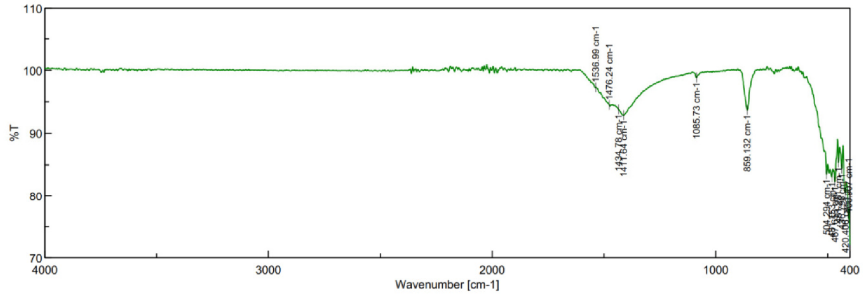

Figure S7. IR spectrum of commercial Li_2CO_3.

Chemical analysis can prove the presence of CO with the help of an aqueous Pd^{2+} salt solution: Pd^{2+} is reduced to elemental Pd, which precipitates as a dark solid.[S7] This test was positive for the described reaction.

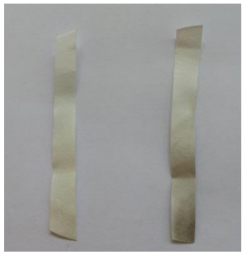

Figure S8. Both filter papers were exposed to an aqueous $PdCl_2$ solution: the left one is air-dried and the right one was brought in contact to CO from the reaction between Li_2[**1**] and CO_2.

2. Synthesis of structural analogs of proposed intermediates for mechanistic discussions

Synthesis of Na_2[5]

Neat acetone (0.791 g mL^{-1}; 5.4 µL, 4.3 mg, 74 µmol) was added at room temperature to Na_2[**1**], prepared as outlined above from **1** (15 mg, 74 µmol) and excess sodium metal, in [D_8]THF (0.5 mL). The mixture was transferred to an NMR tube and the tube was flame-sealed. ^{1}H NMR spectroscopy revealed the immediate and quantitative transformation to Na_2[**5**].

X-ray-quality crystals of [Na(thf)$_2$][Na(thf)][**5**] were obtained by gas-phase diffusion of hexane into a THF solution of Na_2[**5**].

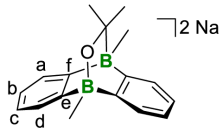

^{1}H NMR (500.2 MHz, [D_8]THF): δ = 7.29 (n.r., 2H; H-a), 7.15–7.14 (m, 2H; H-d), 6.68–6.65 (m, 2H; H-b), 6.62–6.60 (m, 2H; H-c), 0.59 (s, 6H; $OC(CH_3)_2$), 0.19 (s, 3H; $OBCH_3$), 0.08–0.07 ppm (m, 3H; $CBCH_3$).

^{11}B NMR (160.5 MHz, [D_8]THF): δ = –4.4 (br; BO), –13.5 ppm (BC).

^{13}C{^{1}H} NMR (125.8 MHz, [D_8]THF): δ = 172.0 (q, ^1J(C,B) = 44.9 Hz; C-f), 167.5 (br; C-e), 127.5 (C-a), 125.0 (C-d), 122.0 (C-b), 120.9 (C-c), 70.0 (q, ^1J(C,B) = 41.8 Hz; $OC(CH_3)_2$), 30.9 ($OC(CH_3)_2$), 3.2 (br; $OBCH_3$), 1.0 ppm (q, ^1J(C,B) = 45.8 Hz; $CBCH_3$).

Synthesis of Na_2[6]

An NMR tube was charged with a [D_8]THF solution of Na_2[**6**] (74 µmol), the sample was frozen with liquid nitrogen, and CO_2 (1.8 mL, 74 µmol) was deposited onto it as described above. The NMR tube was flame-sealed and NMR spectroscopy revealed the immediate and quantitative conversion to Na_2[**6**].

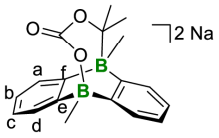

^{1}H NMR (500.2 MHz, [D_8]THF): δ = 7.77−7.73 (m, 4H; H-a,d), 7.17−7.14 (m, 2H; H-b), 6.95−6.93 (m, 2H; H-c), 1.22 (s, 3H; OBCH_3), 0.44 ppm (br, 9H; C(CH_3)$_2$, CBCH_3).

^{11}B NMR (160.5 MHz, [D_8]THF): 1.8 (br; BO); −13.7 ppm (BC).

^{13}C{^{1}H} NMR (125.8 MHz, [D_8]THF): δ = 167.7 (br; C-f), 159.1 (O*C*(O)OC), 144.8 (C-e), 133.2 (C-a), 131.6 (C-d), 128.4 (C-b), 123.0 (C-c), 30.1 (C(*C*H_3)$_2$), 21.3 (*C*(CH_3)$_2$), 4.9 ppm (OBCH_3); n.o. CB*C*H_3.

Synthesis of the BMe analog of $[C]^{2-}$: Li_2[C*]

Benzophenone (13 mg, 74 µmol) was added at room temperature to Li_2[**1**], prepared as outlined above from **1** (15 mg, 74 µmol) and excess lithium, in [D_8]THF (0.5 mL). The mixture was transferred to an NMR tube and the tube was flame-sealed. ^{1}H NMR spectroscopy revealed the immediate and quantitative transformation to Li_2[**C***].

X-ray-quality crystals of [Li(thf)$_2$][Li(thf)(12-c-4)](THF)[**C***] were obtained by gas-phase diffusion of hexane into a THF/12-crown-4 solution of Li_2[**C***].

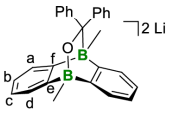

^{1}H NMR (500.2 MHz, [D_8]THF): δ = 7.14–7.12 (m, 4H; H-a,d), 6.99 (d, ^3J(HH) = 7.4 Hz, 4H; Ph-H-*o*), 6.70–6.67 (m, 4H; Ph-H-*m*), 6.58 (tr, ^3J(HH) = 7.1 Hz, 2H; Ph-H-*p*), 6.55–6.51 (m, 4H; H-b,c), 0.33 (s, 3H; OBCH_3), 0.30 ppm (s, 3H; CBCH_3).

^{11}B NMR (160.5 MHz, [D_8]THF): δ = −2.9 (br; BO), −13.3 ppm (BC).

^{13}C{^{1}H} NMR (125.8 MHz, [D_8]THF): δ = 168.7 (br; C-f), 166.3 (br; C-e), 158.7 (Ph-C-*i*), 130.2 (Ph-C-*o*), 128.8 (C-a or C-d), 125.6 (Ph-C-*m*), 125.4 (C-a or C-d), 122.0 (Ph-C-*p*), 121.8 (C-b), 120.4 (C-c), 82.7 (br; O*C*Ph$_2$), 1.9 (br; CB*C*H_3), 1.0 ppm (OBCH_3).

3. Plots of the IR spectra

The highlighted area is characteristic for C=O stretches of carboxylic and carbonic esters.[S8]

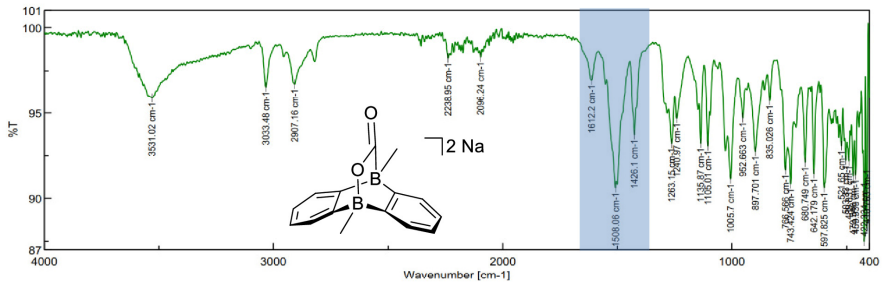

Figure S9. IR spectrum of Na_2[**2**] recorded with an ATR probe.

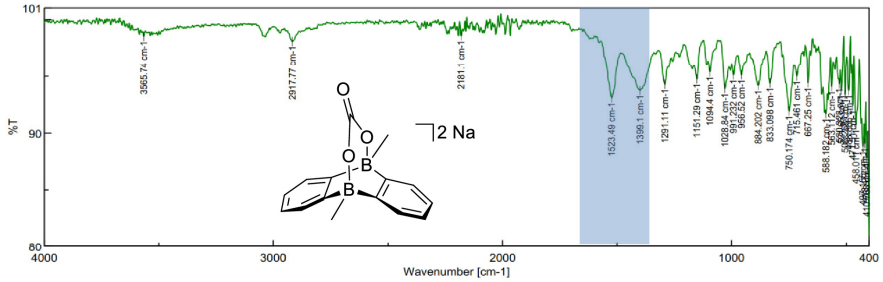

Figure S10. IR spectrum of Na_2[**4**] recorded with an ATR probe.

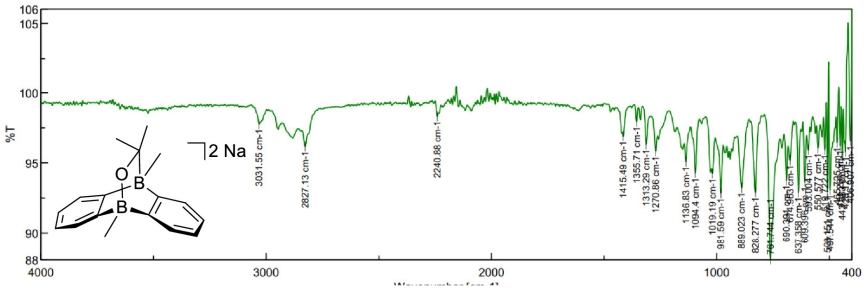

Figure S11. IR spectrum of Na_2[**5**] recorded with an ATR probe.

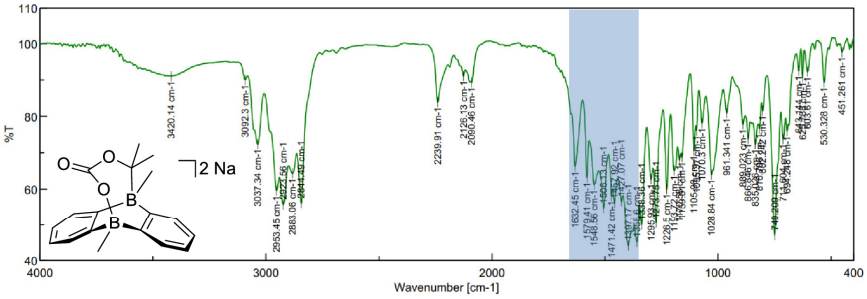

Figure S12. IR spectrum of Na_2[**6**] (KBr pellet).

4. Plots of the NMR spectra

Figure S13. ^{1}H NMR spectrum of **1** (300.0 MHz, [D_8]THF).

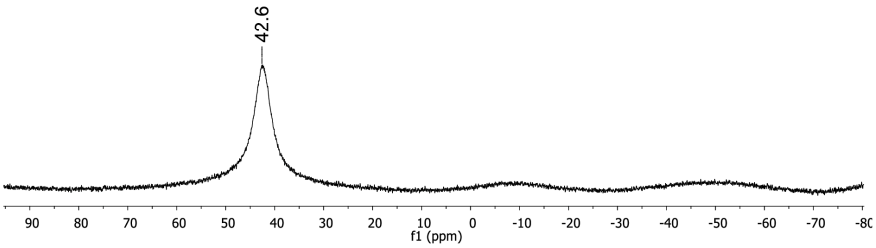

Figure S14. ^{11}B NMR spectrum of **1** (96.3 MHz, [D_8]THF).

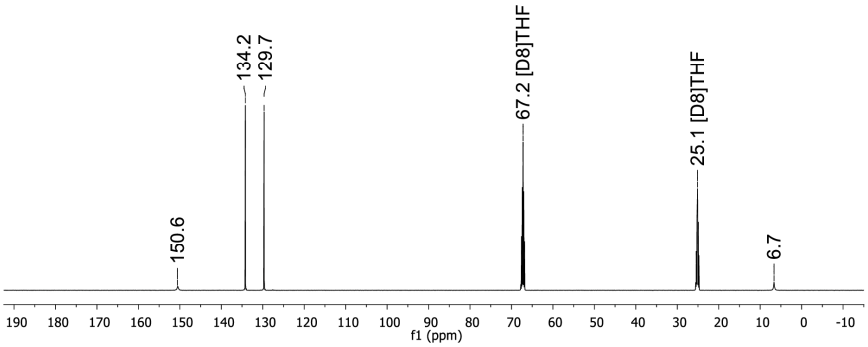

Figure S15. ^{13}C{^{1}H} NMR spectrum of **1** (125.8 MHz, [D_8]THF).

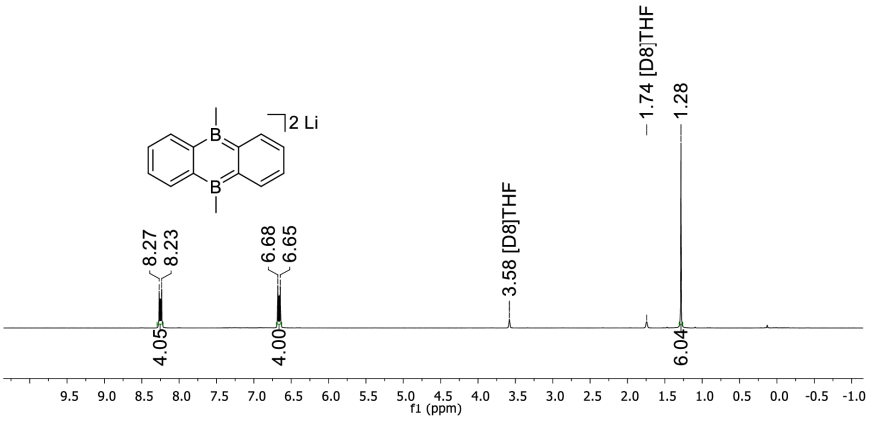

Figure S16. ^{1}H NMR spectrum of Li_2[**1**] (300.0 MHz, [D_8]THF).

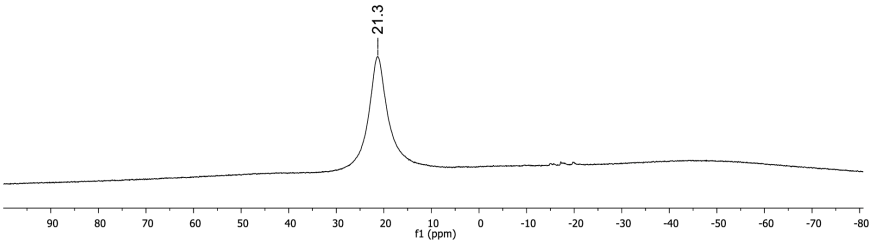

Figure S17. ^{11}B NMR spectrum of Li_2[**1**] (96.3 MHz, [D_8]THF).

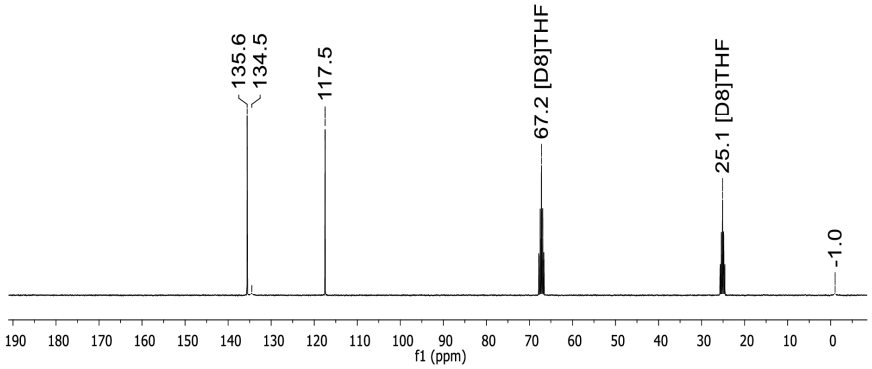

Figure S18. ^{13}C{^{1}H} NMR spectrum of Li_2[**1**] (75.4 MHz, [D_8]THF).

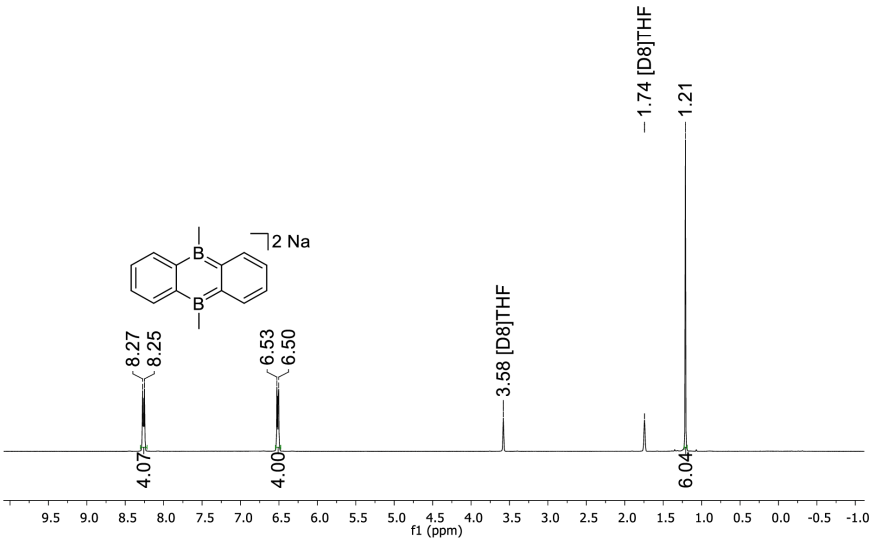

Figure S19. ^{1}H NMR spectrum of Na_2[**1**] (300.0 MHz, [D_8]THF).

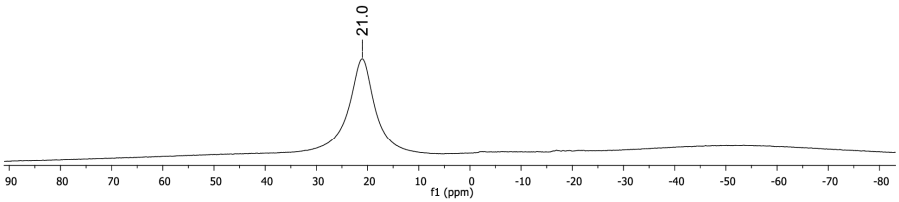

Figure S20. ^{11}B NMR spectrum of Na_2[**1**] (96.3 MHz, [D_8]THF).

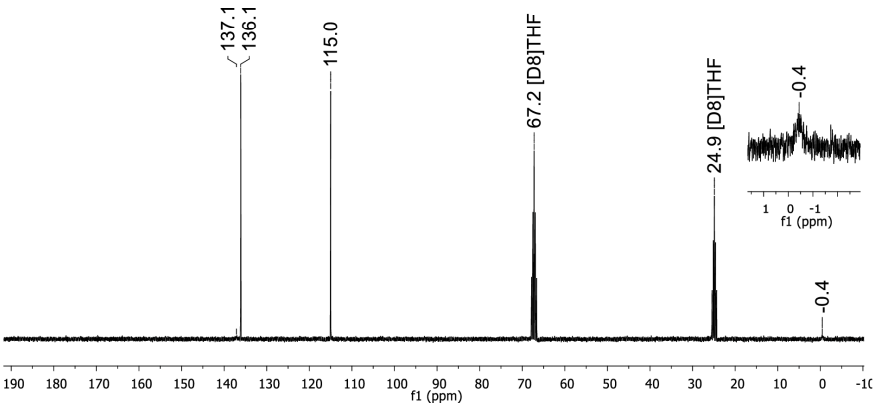

Figure S21. ^{13}C{^{1}H} NMR spectrum of Na_2[**1**] (75.4 MHz, [D_8]THF).

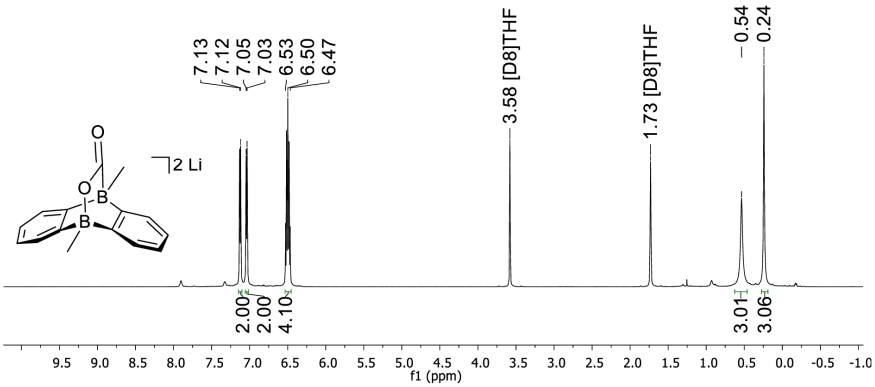

Figure S22. ^{1}H NMR spectrum of Li_2[**2**] (500.2 MHz, [D_8]THF).

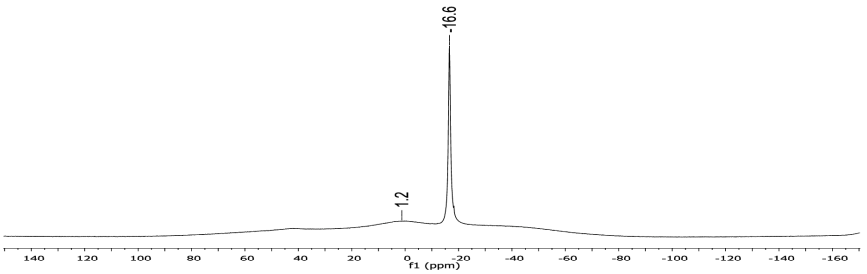

Figure S23. ^{11}B NMR spectrum of Li_2[**2**] (96.3 MHz, [D_8]THF).

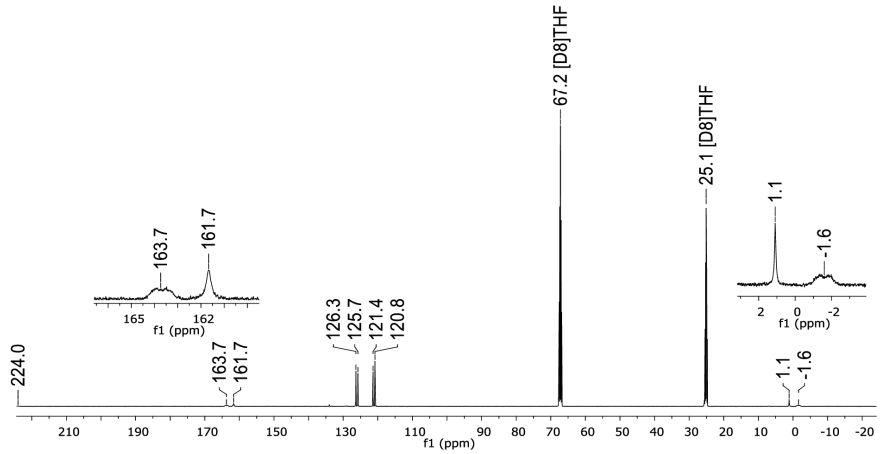

Figure S24. ^{13}C{^{1}H} NMR spectrum of Li_2[**2**] (125.8 MHz, [D_8]THF).

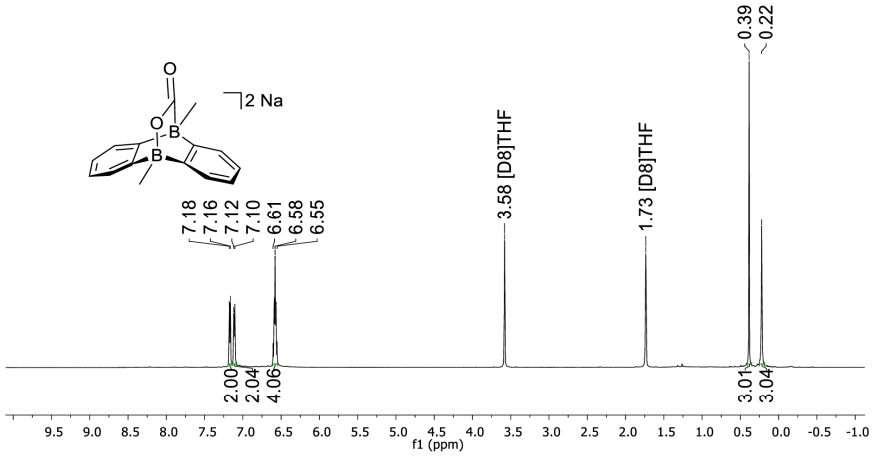

Figure S25. ^{1}H NMR spectrum of Na_2[**2**] (500.2 MHz, [D_8]THF).

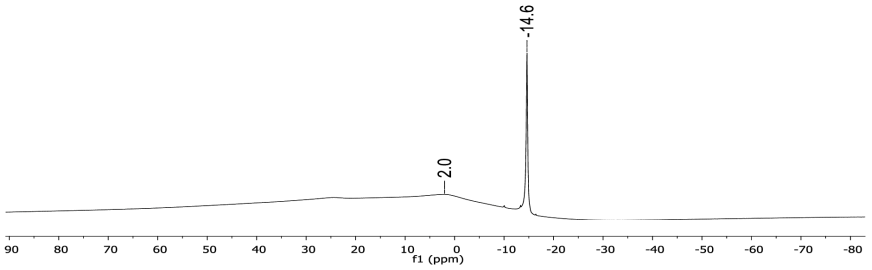

Figure S26. ^{11}B NMR spectrum of Na_2[**2**] (160.5 MHz, [D_8]THF).

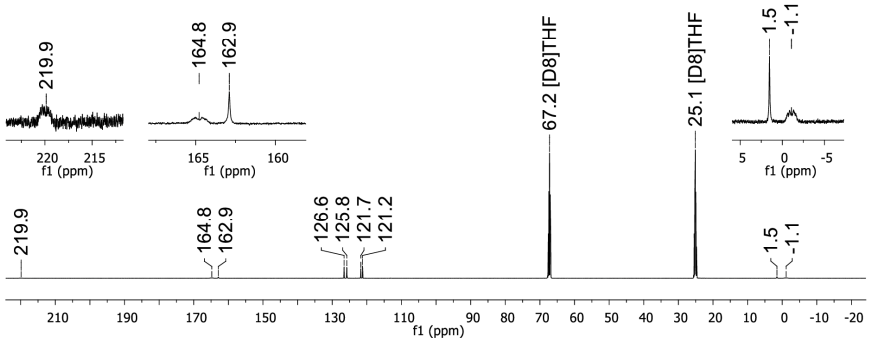

Figure S27. ^{13}C{^{1}H} NMR spectrum of Na_2[**2**] (125.8 MHz, [D_8]THF).

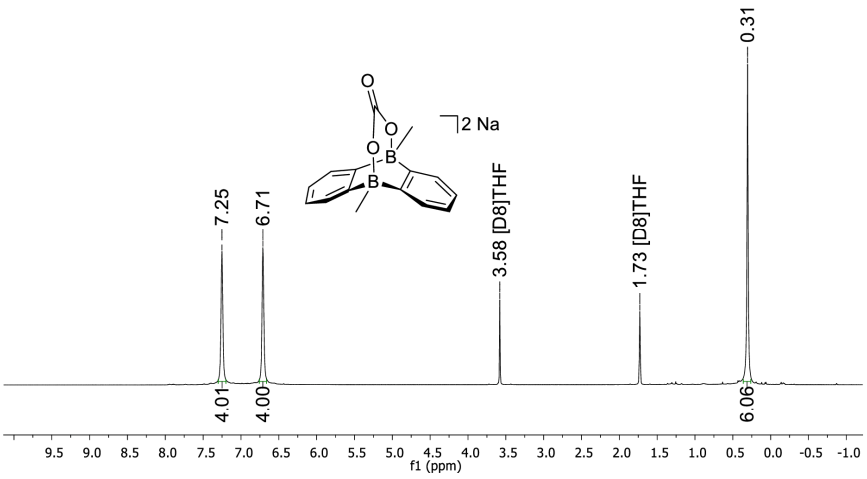

Figure S28. ^{1}H NMR spectrum of Na_2[**4**] (500.2 MHz, [D_8]THF).

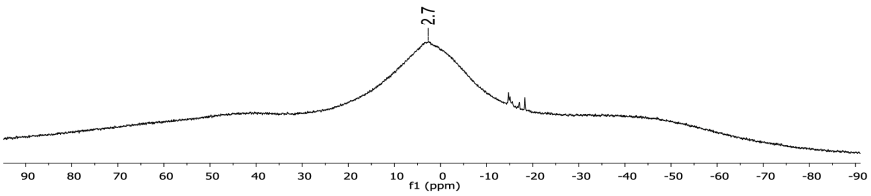

Figure S29. ^{11}B NMR spectrum of Na_2[**4**] (96.3 MHz, [D_8]THF).

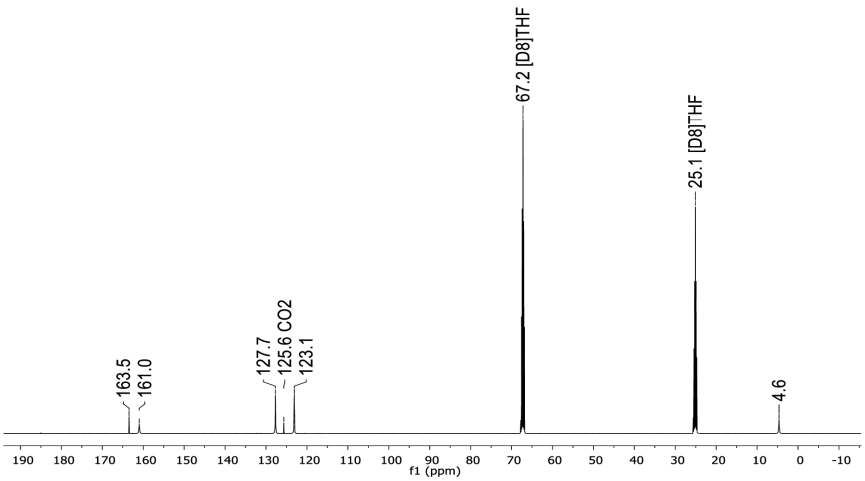

Figure S30. ^{13}C{^{1}H} NMR spectrum of Na_2[**4**] (125.8 MHz, [D_8]THF).

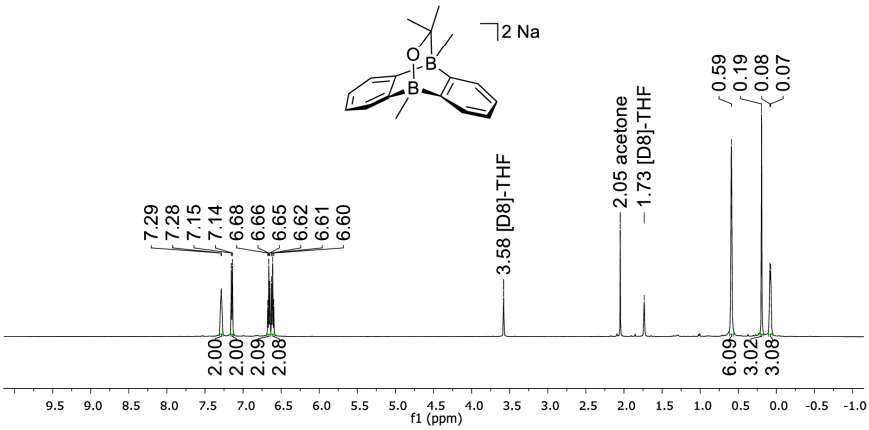

Figure S31. ^{1}H NMR spectrum of Na_2[**5**] (500.2 MHz, [D_8]THF).

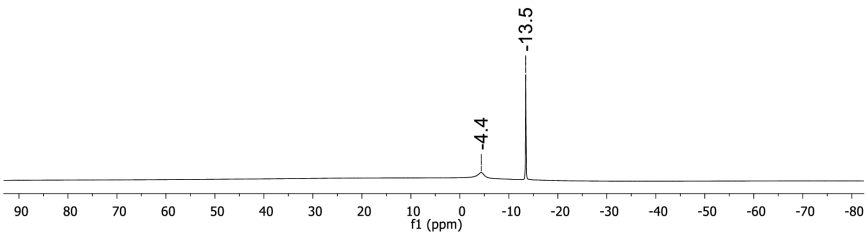

Figure S32. ^{11}B NMR spectrum of Na_2[**5**] (160.5 MHz, [D_8]THF).

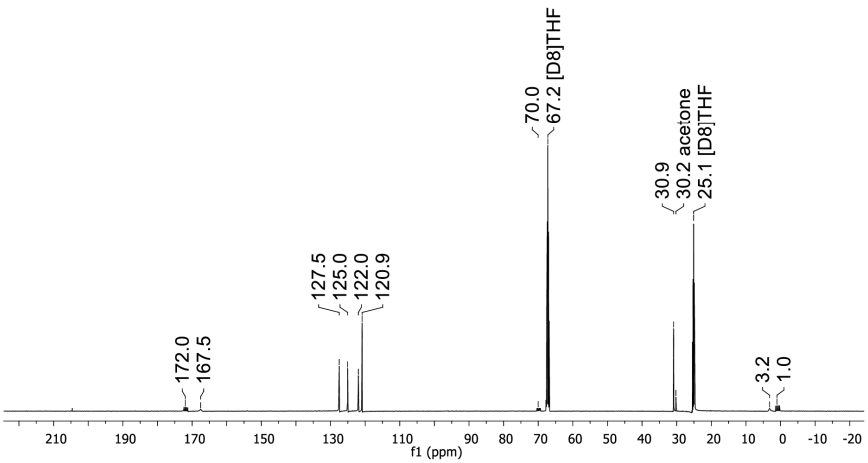

Figure S33. ^{13}C{^{1}H} NMR spectrum of Na_2[**5**] (125.8 MHz, [D_8]THF).

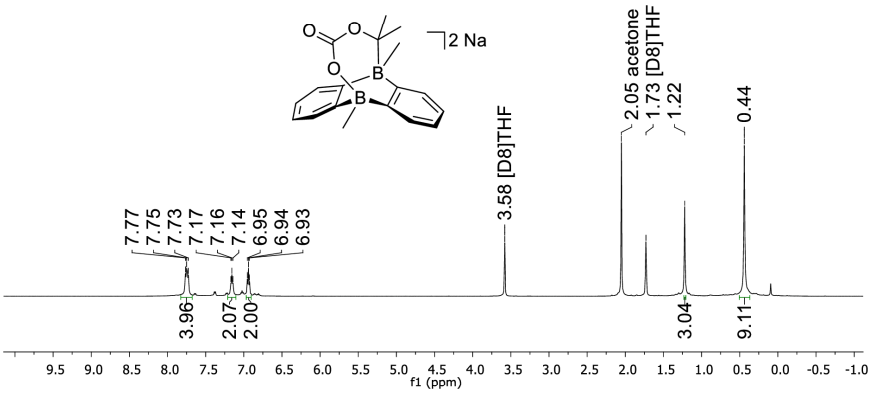

Figure S34. ^{1}H NMR spectrum of Na_2[**6**] (500.2 MHz, [D_8]THF).

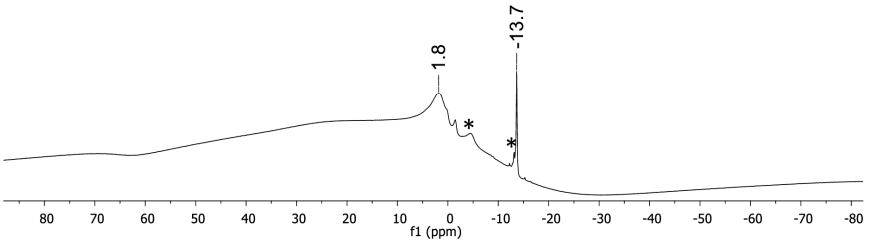

Figure S35. ^{11}B NMR spectrum of Na_2[**6**] (160.5 MHz, [D_8]THF). Residual resonances of the starting material Na_2[**5**] are marked with asterisks.

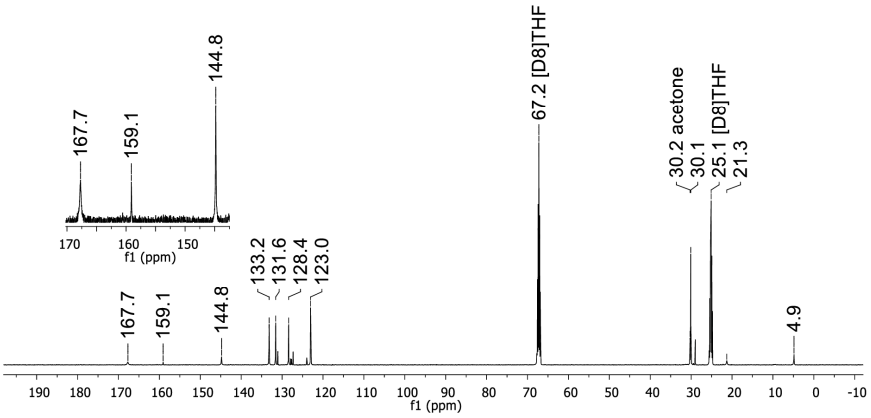

Figure S36. ^{13}C{^{1}H} NMR spectrum of Na_2[**6**] (125.8 MHz, [D_8]THF).

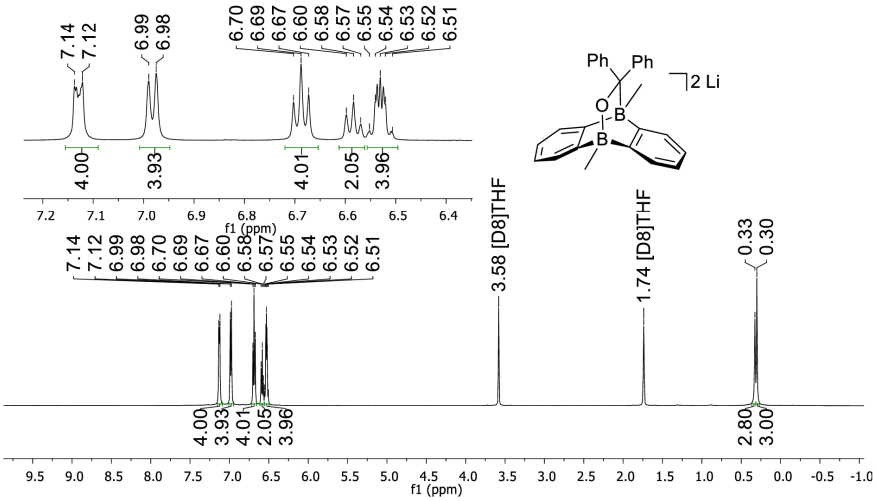

Figure S37. ^{1}H NMR spectrum of Li_2[**C***] (500.2 MHz, [D_8]THF).

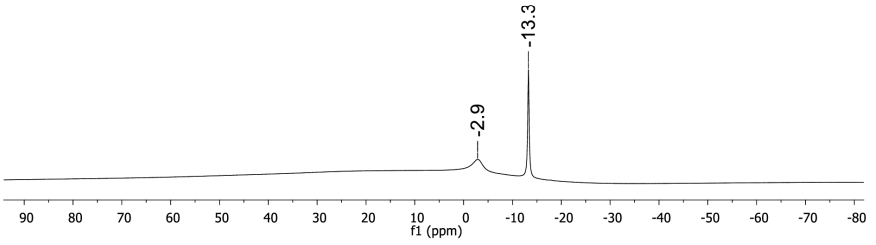

Figure S38. ^{11}B NMR spectrum of Li_2[**C***] (160.5 MHz, [D_8]THF).

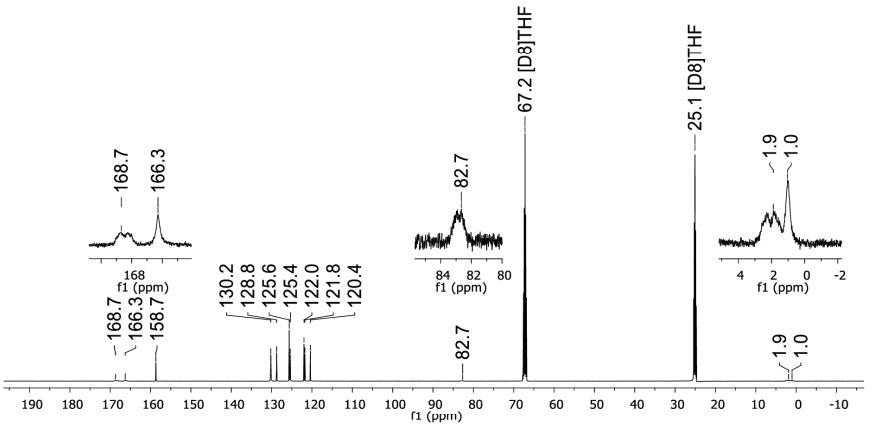

Figure S39. ^{13}C{^{1}H} NMR spectrum of Li_2[**C***] (125.8 MHz, [D_8]THF).

5. X-ray crystal structure analyses

Data for all structures were collected on a STOE IPDS II two-circle diffractometer with a Genix Microfocus tube with mirror optics using Mo$K\alpha$ radiation (λ = 0.71073 Å). The data were scaled using the frame-scaling procedure in the X-AREA program system.[S9] The structures were solved by direct methods using the program SHELXS[S10] and refined against F^2 with full-matrix least-squares techniques using the program SHELXL-97.[S10]

In $[Li(thf)_2]_2$[**1**], three CH_2 groups of one thf ligand are disordered over two positions with a site occupation factor of 0.53(1) for the major occupied sites. In another thf ligand, one CH_2 group is disordered over two positions with a site occupation factor of 0.73(1) for the major occupied site. The displacement parameters of the disordered atoms were restrained to an isotropic behavior.

In $[Na_2(thf)_3]$[**1**], two CH_2 groups of one thf ligand are disordered over two positions with a site occupation factor of 0.51(2) for the major occupied sites. In three thf ligands, one CH_2 group is disordered over two positions with site occupation factors of 0.57(2), 0.58(2), and 0.53(3) for each major occupied site. The displacement parameters of the disordered atoms were restrained to an isotropic behavior. In addition, the components of the displacement parameters in the direction of the bonds were restrained to be equal for all thf atoms. The structure features a polymeric chain with two symmetry-independent formula units in the asymmetric unit.

In $[Na][Na_3(thf)_6][\mathbf{2}]_2$, the displacement parameters of all thf atoms were restrained to an isotropic behavior. The structure features a polymeric chain with two symmetry-independent dianions, four sodium cations and six thf ligands in the asymmetric unit.

In $[Na_8(thf)_{14}][\mathbf{4}]_4$, three CH_2 groups of one thf ligand are disordered over two positions with a site occupation factor of 0.55(1) for the major occupied sites. The components of the displacement parameters of mutually bonded atoms of all thf ligands were restrained to be equal. The absolute structure could not be reliably determined, Flack-x-parameter 0.2(3). The asymmetric unit contains non-polymeric aggregates of four symmetry-independent dianions, eight sodium cations and 14 thf ligands.

In $[Na(thf)_2][Na(thf)]$[**5**], the displacement parameters of all thf atoms were restrained to an isotropic behavior. The contribution of the solvent to the structure factors was treated using the *SQUEEZE* option in the program *PLATON*.[11]

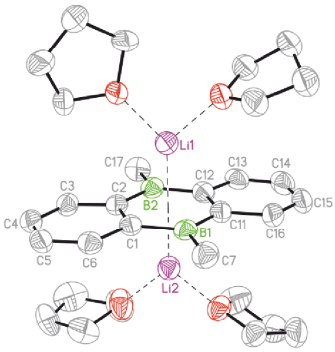

Figure S40. Molecular structure of $[Li(thf)_2]_2$[**1**] in the solid state. Displacement ellipsoids are drawn at the 50% probability level; hydrogen atoms are omitted for clarity. Selected bond lengths (Å), $Li^+\cdots$COG distances (Å), and bond angles (°): B1−C1 = 1.544(4), B1−C7 = 1.600(5), B1−C11 = 1.542(4), B2−C2 = 1.535(4), B2−C12 = 1.541(4), B2−C17 = 1.602(5), C1−C2 = 1.468(4), C11−C12 = 1.463(4); $Li1^+\cdots$COG = 1.925(5), $Li2^+\cdots$COG = 1.897(5); C1−B1−C11 = 115.0(3), C2−B2−C12 = 115.3(3); COG = centroid of the B_2C_4 ring.

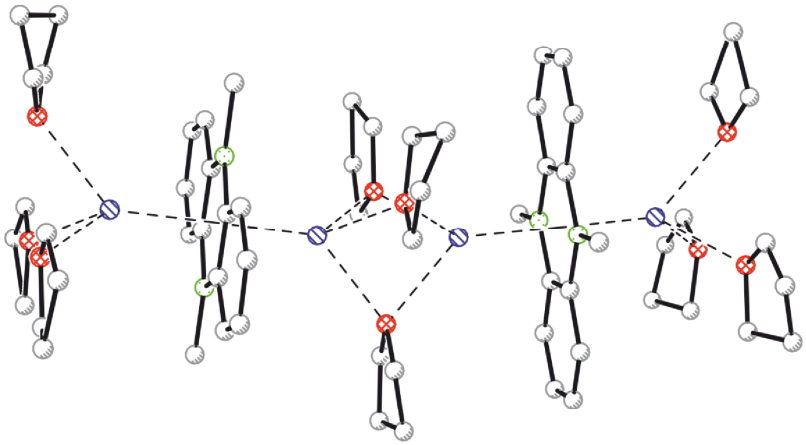

Figure S41. *Description of the crystal structure of [Na$_2$(thf)$_3$][**1**]:* Each side of the B_2C_4 ring is coordinated to one Na^+ ion. Three thf ligands connect two Na^+ ions of neighboring DBA fragments so that a coordination polymer is formed.

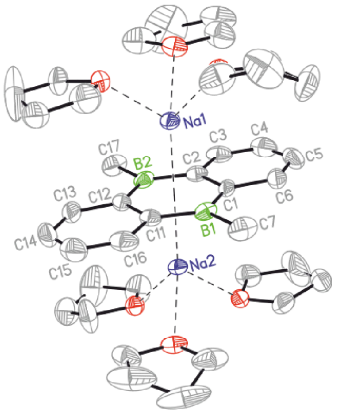

Figure S42. Molecular structure of a section of the coordination polymer [$Na_2(thf)_3$][**1**]. Displacement ellipsoids are drawn at the 50% probability level; hydrogen atoms are omitted for clarity. Selected bond lengths (Å), $Na^+\cdots$COG distances (Å), and bond angles (°) of the two crystallographically independent dianions: B1−C1 = 1.515(4)/1.537(4), B1−C7 = 1.630(4)/1.624(4), B1−C11 = 1.517(4)/1.525(4), B2−C2 = 1.540(4)/1.537(4), B2−C12 = 1.534(4)/1.529(4), B2−C17 = 1.607(4)/1.620(4), C1−C2 = 1.475(4)/1.489(4), C11−C12 = 1.475(4)/1.466(4); $Na1^+\cdots$COG = 2.265(2)/2.268(1), $Na2^+\cdots$COG = 2.271(2)/2.269(1); C1−B1−C11 = 118.2(2)/116.8(2), C2−B2−C12 = 115.9(2)/116.0(2); COG = centroid of the B_2C_4 ring.

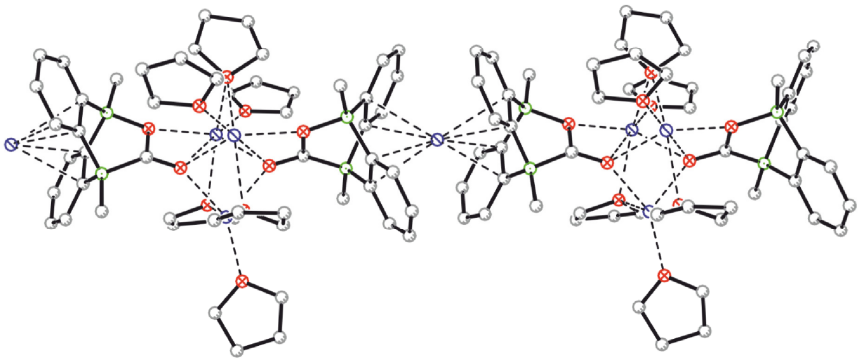

Figure S43. *Description of the crystal structure of [Na][Na$_3$(thf)$_6$][**2**]$_2$:* The asymmetric unit contains two crystallographically independent Na$_2$[**2**] moieties. The structural parameters of both [**2**]$^{2-}$ ions are identical within experimental error. Their CO_2 bridges are pointing toward each other with an almost orthogonal mutual orientation (dihedral angle O1C8O2//O1AC8AO2A = 81.7(3)°). Three Na^+ ions, located between the two [**2**]$^{2-}$ ions, are residing at the corners of an equilateral triangle, which is completed to a trigonal bipyramid by two apical, μ^3-coordinating carbonyl oxygen atoms. Each BOC-oxygen atom binds to one of the three Na^+ ions. Three of the six thf ligands are coordinated to the corners of the Na_3 triangle and the other three are bridging its edges. The supramolecular aggregates are connected to coordination polymers by the fourth Na^+ ion, which is encapsulated by the concave sides of two DBA adducts.

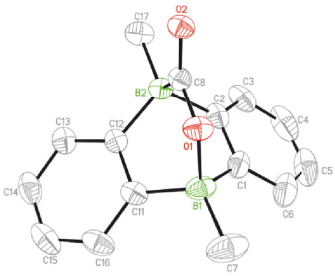

Figure S44. Molecular structure of one of the two crystallographically independent dianions [**2**]$^{2-}$ of [Na][Na$_3$(thf)$_6$][**2**]$_2$ in the solid state. Hydrogen atoms are omitted for clarity. Displacement ellipsoids are drawn at the 30% probability level. Selected bond lengths (Å) and bond angles (°) of the two crystallographically independent dianions: B1−C1 = 1.621(8)/1.626(6), B1−C7 = 1.614(7)/1.608(6), B1−C11 = 1.618(7)/1.618(7), B1−O1 = 1.591(6)/1.586(5), B2−C2 = 1.633(6)/1.630(7), B2−C8 = 1.615(6)/1.614(6), B2−C12 = 1.629(6)/1.631(6), B2−C17 = 1.614(6)/1.625(6), C1−C2 = 1.409(7)/1.420(6), C11−C12 = 1.415(6)/1.416(6), C8−O1 = 1.319(5)/1.318(5), C8−O2 = 1.267(5)/1.265(4); C1−B1−C11 = 106.1(4)/105.9(3), C2−B2−C12 = 104.6(3)/105.3(3), O1−C8−O2 = 115.2(3)/115.4(3).

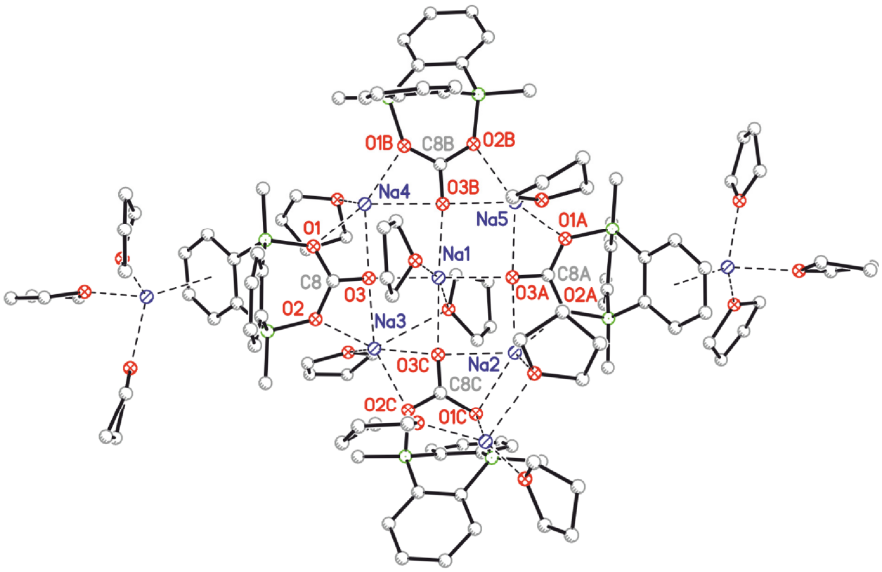

Figure S45. *Description of the crystal structure of [$Na_8(thf)_{14}$][**4**]$_4$:* The [**4**]$^{2-}$ ions are tricyclic entities featuring a carbonate bridge between the two boron centers. The salt Na_2[**4**] forms C_1-symmetric tetramers in the solid state, which are solvated by overall 14 thf ligands. The planar core of the tetrameric cluster consists of five Na^+ ions, four of them (Na2-Na5) residing at the corners of an approximate square and the fifth at its center (Na1). This cation substructure is held together by the carbonate moieties of the four [**4**]$^{2-}$ ions: the carbonyl-oxygen atoms (O3-O3C) reside at the approximate midpoints of the edges of the square and simultaneously coordinate to the central $Na1^+$ ion and two Na^+ ions at adjacent corners. Two carbonate bridges occupying opposite edges of the Na_5 aggregate are almost coplanar to the central square, the other two deviate by dihedral angles CO_3//(Na2-Na5) of 45.4(2)° and 46.6(2)° into opposite directions. Two $[Na(thf)_3]^+$ ions coordinate to the phenylene rings of two DBA fragments in an η^6 mode. The final $[Na(thf)_2]^+$ ion, which is mainly responsible for breaking the cluster symmetry, is connected to one DBA-phenylene ring (η^2) and one boron-bonded carbonate-oxygen atom (O1C). Of the remaining six thf ligands, four are coordinated to the corners of the Na_5 core and two to its centroid.

The [**4**]$^{2-}$ ions possess a large average B–O bond length of 1.626 Å. The B–O bond lengths of $[Me_4N][(C_6F_5)_3B–OC(O)Me]$ (1.514(2) Å) and $[(\eta^3\text{-allyl})Pd][(Ph_2PC_6H_4)_2PhB–OC(O)Me]$ (1.527(3) Å) are drastically shorter; even the B–O bond in the neutral adduct Ph_3B–thf (1.6500(17) Å), which possesses a tri- rather than dicoordinate oxygen atom, is only slightly longer: a) S. Mitu, M. C. Baird, *Can. J. Chem.* **2006**, *84*, 225-232; b) T. Schindler, M. Lux, M. Peters, L. T. Scharf, H. Osseili, L. Maron, M. E. Tauchert, *Organometallics* **2015**, *34*, 1978-1984; c) M. Niehues, G. Erker, O. Meyer, R. Fröhlich, *Organometallics* **2000**, *19*, 2813-2815.

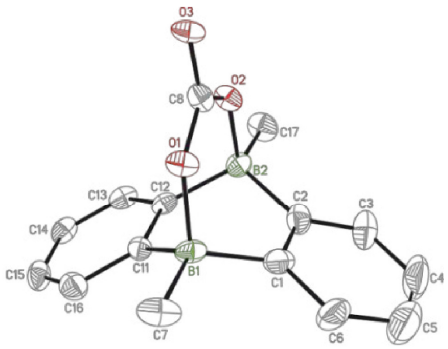

Figure S46. Molecular structure of one of the four crystallographically independent dianions $[\mathbf{4}]^{2-}$ of $[Na_8(thf)_{14}][\mathbf{4}]_4$. Hydrogen atoms are omitted for clarity. Displacement ellipsoids are drawn at the 50% probability level. Selected bond lengths (Å) and bond angles (°):

	I	II	III	IV	average
bond lengths					
B1–O1	1.614(8)	1.646(8)	1.644(8)	1.617(9)	1.630
B2–O2	1.600(8)	1.628(8)	1.614(8)	1.642(8)	1.621
C8–O1	1.296(8)	1.279(7)	1.295(7)	1.321(7)	1.298
C8–O2	1.325(8)	1.304(7)	1.284(8)	1.308(7)	1.305
C8–O3	1.238(8)	1.268(7)	1.260(8)	1.241(7)	1.252
bond angles					
O1–C8–O2	122.0(6)	124.6(5)	123.3(6)	121.5(5)	122.9
O1–C8–O3	119.9(6)	119.1(5)	117.4(6)	119.2(5)	118.9
O2–C8–O3	118.0(6)	116.3(5)	119.3(5)	119.2(5)	118.2

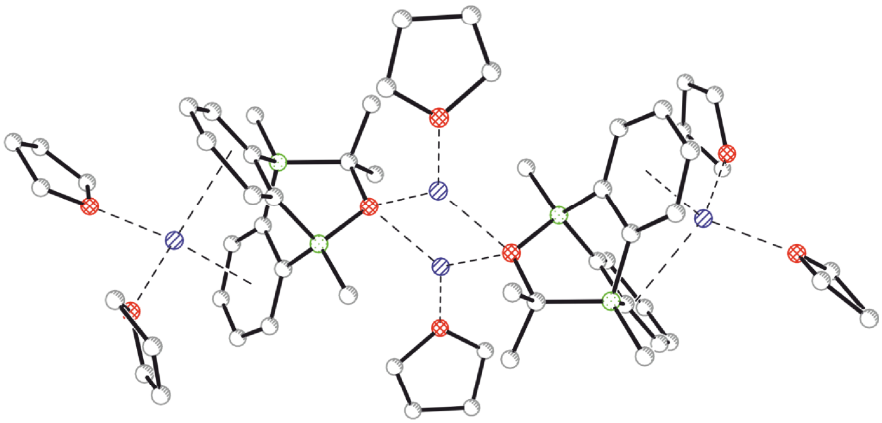

Figure S47. *Description of the crystal structure of [Na(thf)$_2$][Na(thf)][**5**]:* The [**5**]$^{2-}$ ions form centrosymmetric dimers, which are connected by an exactly planar Na_2O_2 diamond. Each of these Na^+ ions carries one thf ligand. Each DBA fragment binds to one $[Na(thf)_2]^+$ ion *via* both phenylene rings (η^6).

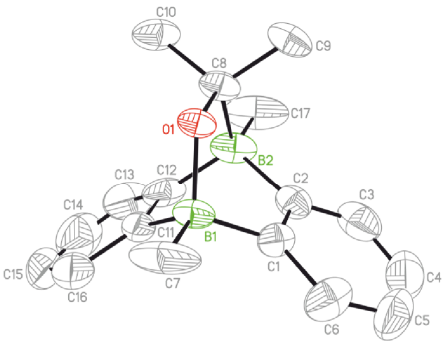

Figure S48. Molecular structure of [Na(thf)$_2$][Na(thf)][**5**] in the solid state. Counter cations and hydrogen atoms are omitted for clarity. Displacement ellipsoids are drawn at the 30% probability level. Selected bond lengths (Å) and bond angles (°): B1−C1 = 1.589(8), B1−C7 = 1.622(7), B1−C11 = 1.637(8), B1−O1 = 1.562(6), B2−C2 = 1.615(9), B2−C8 = 1.664(7), B2−C12 = 1.583(10), B2−C17 = 1.653(8), C1−C2 = 1.421(7), C11−C12 = 1.407(9), C8−O1 = 1.478(5); C1−B1−C11 = 105.3(4), C2−B2−C12 = 105.1(4), B1−O1−C8 = 114.1(3).

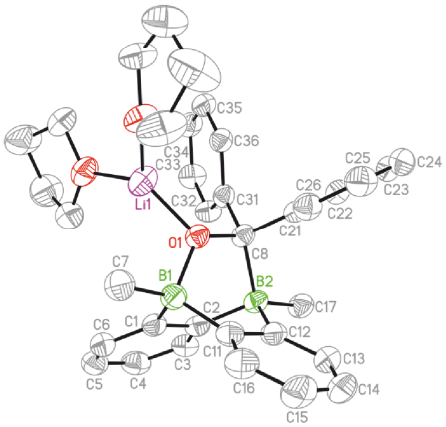

Figure S49. Molecular structure of $[Li(thf)_2][Li(thf)(12\text{-}c\text{-}4)](THF)$[**C***] in the solid state. The separated counter cation $[Li(thf)(12\text{-}c\text{-}4)]^+$, an isolated THF molecule, and all hydrogen atoms are omitted for clarity. Displacement ellipsoids are drawn at the 50% probability level. Selected bond lengths (Å) and bond angles (°): B1−C1 = 1.618(4), B1−C7 = 1.627(4), B1−C11 = 1.613(4), B1−O1 = 1.566(3), B2−C2 = 1.626(4), B2−C8 = 1.717(4), B2−C12 = 1.634(4), B2−C17 = 1.632(4), C1−C2 = 1.429(4), C11−C12 = 1.426(4), C8−O1 = 1.460(3); C1−B1−C11 = 106.7(2), C2−B2−C12 = 106.2(2), B1−O1−C8 = 117.91(17).

Table S1. Selected crystallographic data for $[Li(thf)_2]_2$[**1**], $[Na_2(thf)_3]$[**1**], and $[Na][Na_3(thf)_6]$[**2**]$_2$.

compound	$[Li(thf)_2]_2$[**1**]	$[Na_2(thf)_3]$[**1**]	$[Na][Na_3(thf)_6]$[**2**]$_2$
CCDC	1867029	1867030	1867031
formula	$C_{30}H_{46}B_2Li_2O_4$	$C_{26}H_{38}B_2Na_2O_3$	$C_{54}H_{76}B_4Na_4O_{10}$
M_r	506.17	466.16	1020.34
T (K)	173(2)	173(2)	173(2)
radiation, λ (Å)	Mo$K\alpha$, 0.71073	Mo$K\alpha$, 0.71073	Mo$K\alpha$, 0.71073
crystal system	monoclinic	monoclinic	monoclinic
space group	$C2/c$	$C2/c$	$P2_1/c$
a (Å)	27.127(3)	30.6776(9)	14.1264(10)
b (Å)	14.0500(19)	20.8983(7)	35.2976(18)
c (Å)	19.664(2)	19.8308(6)	12.8498(8)
α (°)	90	90	90
β (°)	127.905(6)	125.212(2)	116.796(5)
γ (°)	90	90	90
V (Å^3)	5913.5(13)	10387.4(6)	5719.2(7)
Z	8	16	4
D_{calcd} (g cm^{-3})	1.137	1.192	1.185
F (000)	2192	4000	2176
μ (mm^{-1})	0.071	0.102	0.104
crystal size (mm)	0.28 × 0.25 × 0.22	0.28 × 0.27 × 0.16	0.26 × 0.22 × 0.21
crystal shape, color	red block	black block	colorless block
reflections collected	11115	70808	43471
independent reflections	5201	9162	10533
R_{int}	0.0529	0.0443	0.0566
data/restraints/parameters	5201 / 109 / 383	9162 / 163 / 667	10533 / 180 / 649
R_1, wR_2 ($I > 2\sigma(I)$)	0.0614, 0.1433	0.0612, 0.1674	0.0800, 0.2094
R_1, wR_2 (all data)	0.1259, 0.1680	0.0996, 0.1897	0.1402, 0.2415
GOF on F^2	0.904	1.075	1.051
largest difference peak and hole (e Å^{-3})	0.201, −0.227	0.411, −0.195	0.681, −0.491

Table S2. Selected crystallographic data for $[Na_8(thf)_{14}][\mathbf{4}]_4$, $[Na(thf)_2][Na(thf)][\mathbf{5}]$, and $[Li(thf)_2][Li(thf)(12\text{-}c\text{-}4)](THF)[\mathbf{C}^*]$.

compound	$[Na_8(thf)_{14}][\mathbf{4}]_4$	$[Na(thf)_2][Na(thf)][\mathbf{5}]$	$[Li(thf)_2][Li(thf)(12\text{-}c\text{-}4)](THF)[\mathbf{C}^*]$
CCDC	1867032	1867033	1867034
formula	$C_{116}H_{168}B_8Na_8O_{26}$	$C_{29}H_{44}B_2Na_2O_4$	$C_{51}H_{72}B_2Li_2O_9$
M_r	2248.89	524.24	864.58
T (K)	173(2)	173(2)	173(2)
radiation, λ (Å)	Mo$K\alpha$, 0.71073	Mo$K\alpha$, 0.71073	Mo$K\alpha$, 0.71073
crystal system	monoclinic	triclinic	orthorhombic
space group	$P2_1$	$P\bar{1}$	$Pbca$
a (Å)	16.0082(6)	9.6787(9)	15.0404(4)
b (Å)	14.2523(6)	9.6915(9)	17.1238(5)
c (Å)	27.6914(11)	18.7353(18)	37.4437(13)
α (°)	90	81.523(8)	90
β (°)	105.208(3)	75.929(8)	90
γ (°)	90	75.936(7)	90
V (Å^3)	6096.6(4)	1646.3(3)	9643.6(5)
Z	2	2	8
D_{calcd} (g cm^{-3})	1.225	1.058	1.191
F (000)	2400	564	3728
μ (mm^{-1})	0.107	0.089	0.078
crystal size (mm)	0.25 × 0.24 × 0.22	0.21 × 0.18 × 0.15	0.25 × 0.25 × 0.22
crystal shape, color	colorless block	colorless block	colorless block
reflections collected	62830	16590	59137
independent reflections	21067	5801	8496
R_{int}	0.0454	0.0369	0.0628
data/restraints/parameters	21067 / 487 / 1451	5801 / 222 / 334	8496 / 0 / 577
R_1, wR_2 ($I > 2\sigma(I)$)	0.0627, 0.1383	0.1143, 0.3249	0.0665, 0.1741
R_1, wR_2 (all data)	0.0924, 0.1490	0.1598, 0.3578	0.0924, 0.1886
GOF on F^2	1.172	1.180	1.046
largest difference peak and hole (e Å^{-3})	0.520, –0.421	0.753, –0.353	0.577, –0.370

6. Computational details

DFT calculations were carried out with the Gaussian program package.[S12] The PBE0[S13-16] hybrid functional was used and combined with the D3BJ atom-pairwise dispersion correction with Becke-Johnson damping as devised by Grimme.[S17-18] Geometry optimizations and harmonic frequency calculations were computed under gas-phase conditions with the TZVP basis set.[S19] All stationary points reported were characterized as minima by eigenvalue analysis of the diagonalized Hessians. Gibbs energies reported correspond to the total energies of single point calculations with the SMD solvation model[S20] (to account for effects of the THF solvent), corrected by thermal contributions from the gas-phase frequency analyses. The computed dianion is denoted with a superscript 'c' (*i.e.*, $[\mathbf{3}^{c}]^{2-}$ represents $[\mathbf{3}]^{2-}$).

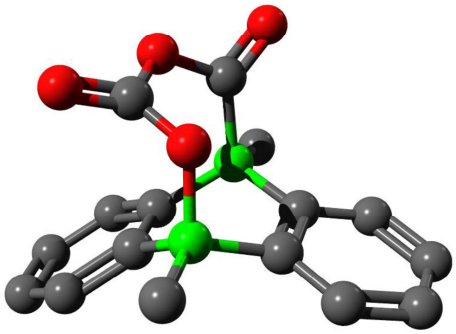

$[\mathbf{3}^{c}]^{2-}$

O	2.272237	-0.290797	2.520407	C	3.036025	0.260659	-2.256484
C	1.214473	0.102373	2.075122	C	3.156554	-1.069041	-1.878795
O	1.034556	1.438079	1.918487	C	-0.071366	1.899609	1.124720
O	0.156926	-0.606946	1.824666	O	-0.674616	2.801885	1.644751
C	-1.587482	0.346768	-0.424649	H	-2.997258	1.808445	-1.134447
C	-2.850376	0.771161	-0.843086	H	-4.909769	0.270317	-1.244101
C	-3.941363	-0.095471	-0.912092	H	-4.617393	-2.116602	-0.611845
C	-3.778899	-1.426806	-0.559942	H	-2.409961	-2.911413	0.150243
B	-0.286231	1.340199	-0.409898	H	-0.722096	2.452511	-2.359041
C	-1.429352	-1.009724	-0.049694	H	0.317787	3.379574	-1.278518
C	-2.526185	-1.866925	-0.132872	H	-1.395009	3.264658	-0.941270
C	1.001091	0.481970	-0.921664	H	1.886338	2.053250	-2.095511
C	-0.535951	2.689161	-1.302709	H	0.036197	-3.684571	0.014480
B	0.027097	-1.458596	0.492306	H	-0.541035	-3.326768	1.641612
C	1.135212	-0.872695	-0.530519	H	1.179070	-3.241819	1.283240
C	1.967078	1.015939	-1.779087	H	2.315148	-2.659263	-0.720462
C	0.184235	-3.020172	0.876554	H	3.767806	0.709448	-2.923622
C	2.207933	-1.618747	-1.020351	H	3.983266	-1.671899	-2.245996

6. References

[S1] G. R. Fulmer, A. J. M. Miller, N. H. Sherden, H. E. Gottlieb, A. Nudelman, B. M. Stoltz, J. E. Bercaw, K. I. Goldberg, *Organometallics* **2010**, *29*, 2176-2179.

[S2] E. Januszewski, A. Lorbach, R. Grewal, M. Bolte, J. W. Bats, H.-W. Lerner, M. Wagner, *Chem. Eur. J.* **2011**, *17*, 12696-12705.

[S3] C. Reus, S. Weidlich, M. Bolte, H.-W. Lerner, M. Wagner, *J. Am. Chem. Soc.* **2013**, *135*, 12892-12907.

[S4] S. K. Müller, P. Huck, H. Köppel, H. Pritzkow, H. W. Siebert, *Z. Naturforsch.* **1995**, *50b*, 1476-1484.

[S5] S. N. Kessler, M. Neuburger, H. A. Wegner, *Eur. J. Org. Chem.* **2011**, 3238-3245.

[S6] B. von Ahsen, C. Bach, G. Balzer, B. Bley, M. Bodenbinder, G. Hägele, H. Willner, F. Aubke, *Magn. Reson. Chem.* **2005**, *43*, 520-527.

[S7] A. F. Holleman, E. Wiberg, N. Wiberg, *Lehrbuch der Anorganischen Chemie, Vol. 102*, De Gruyter, Berlin, New York, **2007**.

[S8] M. Hesse, H. Meier, B. Zeeh, *Spektroskopische Methoden in der organischen Chemie, 5th edition*, G. Thieme Verlag, Stuttgart, New York, **2005**.

[S9] Stoe & Cie, *X-AREA., Diffractometer control program system*, Stoe & Cie, Darmstadt, Germany, **2002**.

[S10] G. M. Sheldrick, *Acta Crystallogr. Sect. A* **2008**, *64*, 112-122.

[S11] A. L. Spek, *Acta Crystallogr. Sect. D* **2009**, *65*, 148−155.

[S12] M. J. Frisch, G. W. Trucks, H. B. Schlegel, G. E. Scuseria, M. A. Robb, J. R. Cheeseman, G. Scalmani, V. Barone, B. Mennucci, G. A. Petersson, H. Nakatsuji, M. Caricato, X. Li, H. P. Hratchian, A. F. Izmaylov, J. Bloino, G. Zheng, J. L. Sonnenberg, M. Hada, M. Ehara, K. Toyota, R. Fukuda, J. Hasegawa, M. Ishida, T. Nakajima, Y. Honda, O. Kitao, H. Nakai, T. Vreven, J. A. Montgomery, Jr., J. E. Peralta, F. Ogliaro, M. Bearpark, J. J. Heyd, E. Brothers, K. N. Kudin, V. N. Staroverov, R. Kobayashi, J. Normand, K. Raghavachari, A. Rendell, J. C. Burant, S. S. Iyengar, J. Tomasi, M. Cossi, N. Rega, J. M. Millam, M. Klene, J. E. Knox, J. B. Cross, V. Bakken, C. Adamo, J. Jaramillo, R. Gomperts, R. E. Stratmann, O. Yazyev, A. J. Austin, R. Cammi, C. Pomelli, J. W. Ochterski, R. L. Martin, K. Morokuma, V. G. Zakrzewski, G. A. Voth, P. Salvador, J. J. Dannenberg, S. Dapprich, A. D. Daniels, Ö. Farkas, J. B. Foresman, J. V. Ortiz, J. Cioslowski, D. J. Fox, *Gaussian 09*, Revision D.01, Gaussian, Inc., Wallingford, CT, 2013; http://www.gaussian.com.

[S13] J. P. Perdew, K. Burke, M. Ernzerhof, *Phys. Rev. Lett.* **1996**, *77*, 3865-3868.

[S14] J. P. Perdew, K. Burke, M. Ernzerhof, *Phys. Rev. Lett.* **1997**, *78*, 1396-1396.

[S15] J. P. Perdew, M. Ernzerhof, K. Burke, *J. Chem. Phys.* **1996**, *105*, 9982-9985.

[S16] C. Adamo, V. Barone, *J. Chem. Phys.* **1999**, *110*, 6158-6170.

[S17] L. Goerigk, S. Grimme, *J. Chem. Theory Comput.* **2011**, *7*, 291-309.

[S18] S. Grimme, S. Ehrlich, L. Goerigk, *J. Comput. Chem.* **2011**, *32*, 1456-1465.

[S19] A. Schäfer, C. Huber, R. Ahlrichs, *J. Chem. Phys.* **1994**, *100*, 5829-5835.

[S20] A. V. Marenich, C. J. Cramer, D. G. Truhlar, *J. Phys. Chem. B* **2009**, *113*, 6378-6396.

6.2.5. Doping Polycyclic Aromatics with Boron for Superior Performance in Materials Science and Catalysis

ACES Asian Chemical Editorial Society
DOI: 10.1002/ajoc.201700495
ASIAN JOURNAL OF ORGANIC CHEMISTRY
Focus Review

Polycyclic Aromatic Hydrocarbons

Doping Polycyclic Aromatics with Boron for Superior Performance in Materials Science and Catalysis

Esther von Grotthuss[+], Alexandra John[+], Thomas Kaese[+], and Matthias Wagner*[a]

Dedicated to Professor Wolfgang A. Herrmann on the occasion of his 70th birthday

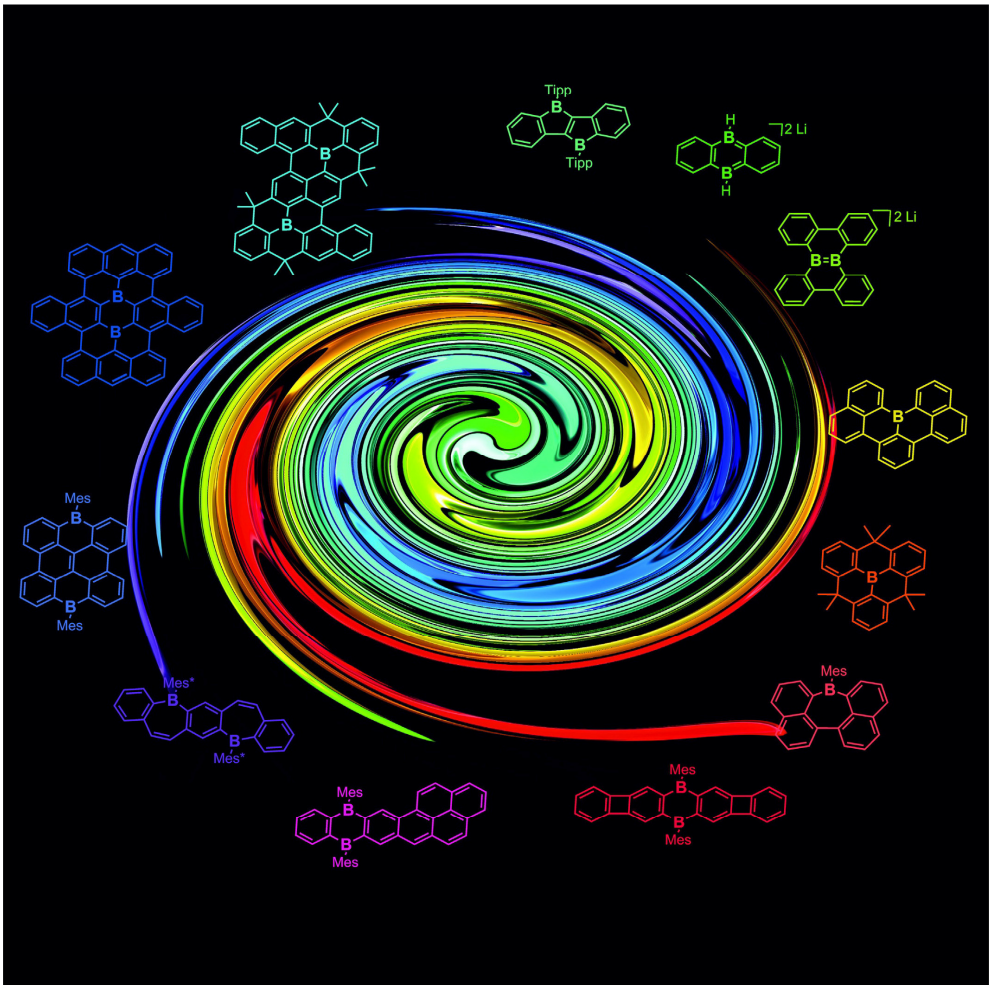

ACES Asian Chemical Editorial Society

ASIAN JOURNAL OF ORGANIC CHEMISTRY
Focus Review

Abstract: Boron has one valence electron less than a carbon atom and an available vacant p_z orbital. The incorporation of sp^2-hybridized boron atoms into the host lattice of a polycyclic aromatic hydrocarbon (PAH) is formally related to oxidative doping. A boron-containing B-PAH has an energetically low-lying LUMO and a narrow HOMO–LUMO gap, which renders it a strong Lewis acid/electron acceptor and promotes fluorescence in the visible range of the electromagnetic spectrum. Many methods have been developed to access B-PAHs that are deliberately designed for specific tasks. Herein, we highlight recent breakthroughs in the field of B-PAH synthesis and the scope of their applications, which range from Lewis acid and redox catalysis to device fabrication. We will also report on the dynamic covalent chemistry of neutral and anionic B-PAHs, as it is a potential limitation in the design of catalyst systems but can also provide a powerful synthetic tool for the preparation of otherwise inaccessible B-PAHs.

1. Introduction

Extended, conjugated organic π-electron systems are not only fundamentally interesting but also provide the basis of materials for optoelectronic devices, such as organic light-emitting diodes (OLEDs), organic field-effect transistors (OFETs), and organic photovoltaic cells (OPVs), as well as the materials for electrodes in lithium batteries.[1] Among compounds currently considered as most relevant for future development, polycyclic aromatic hydrocarbons (PAHs) are particularly promising, as they allow for the controlled design of their molecular structures and often show predictable supramolecular arrangements.[2] In the past few years, the atomically precise synthesis of nanoscale PAHs with customized edge configurations[3] has witnessed rapid development.[4] It has also become more and more obvious that the performance of parent all-carbon compounds can often be improved if selected carbon atoms are replaced by other main group elements. Nitrogen, phosphorus, or sulfur atoms have been employed as dopant atoms for decades.[4,5] Boron has only recently entered the center stage of PAH development, but since its introduction, it has turned out to be among the most effective electronically perturbative elements to be incorporated into PAH core structures. As a key feature, the three-coordinate, sp^2-hybridized boron centers have vacant p_z orbitals (rendering them formally equivalent to carbenium ions) and low Pauling electronegativities [EN(B) = 2.0, EN(C) = 2.6]. As a consequence, they act simultaneously as π-electron acceptors and σ-electron donors.

This review presents the most efficient strategies for the synthesis of boron-containing PAHs (B-PAHs), including approaches that rely on electrons as catalysts[6] and on dynamic covalent chemistry. It further highlights unusual bonding situations that have been encountered in this context and describes the impact of incorporated boron atoms on the overall electronic structures of B-PAHs. Recent advances in optoelectronic applications and B-PAH-catalyzed molecular transformations will be summarized. We will conclude with an outlook on boron-doped nanographenes and nanoribbons. To maintain a focus on species that exclusively contain boron heteroatoms, which are integral parts of rigid, π-delocalized scaffolds,[7] we omit compounds with dangling boryl substituents, borylene-bridged polymers, and B–N/O isosteres of PAHs. For an overview of these compound classes, we refer the reader to earlier review articles.[4,8–16]

[a] *E. von Grotthuss,[+] A. John,[+] T. Kaese,[+] Prof. Dr. M. Wagner*
Institut für Anorganische Chemie
Goethe-Universität Frankfurt
Max-von-Laue-Strasse 7, 60438
Frankfurt a. M. (Germany)
E-mail: Matthias.Wagner@chemie.uni-frankfurt.de

[+] *These authors contributed equally to this work.*

The ORCID identification number(s) for the author(s) of this article can be found under https://doi.org/10.1002/ajoc.201700495.

2. Electronic Structures and Classification of Boron-Doped PAHs (B-PAHs)

To illustrate the effects of the incorporation of boron atoms on the electronic structures of PAH frameworks, Figure 1 compares the calculated relative energies and nodal structures of the frontier orbitals of three prototypical compounds, that is, benzene, 9,10-dihydro-9,10-diboraanthracene (DBA), and anthracene.[17] DBA can be regarded as either a doubly borylated benzene or doubly boron-doped anthracene. Relative to the HOMO energy level of benzene, that of DBA remains unchanged, as the two boron atoms do not contribute to this molecular orbital. In stark contrast, the vacant boron p_z orbitals do participate in the LUMO of DBA, which is thus more energetically favored than that of benzene. Both the HOMO and LUMO of DBA are lower in energy relative to those of anthra-

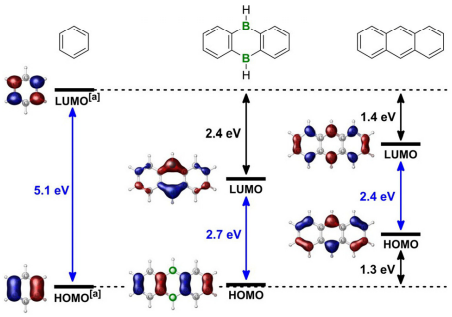

Figure 1. Comparison of the calculated energy levels and nodal structures of the frontier orbitals of benzene, 9,10-dihydro-9,10-diboraanthracene, and anthracene. [a] Only one orbital of the doubly degenerate set is shown.

ACES Asian Chemical Editorial Society

ASIAN JOURNAL OF ORGANIC CHEMISTRY
Focus Review

cene, but the orbital energy gaps are similar in both species. These specific observations can be generalized to two useful rules of thumb: (1) B-PAHs tend to be excellent electron acceptors and (2) the HOMO–LUMO transitions of B-PAHs are in an ideal range to bring about visible light emission.

Because of their vacant p_z orbitals, boron atoms are well-suited to facilitate electronic communication between adjacent aryl substituents. With the addition of a Lewis base, there is the possible formation of a Lewis acid-base adduct, which results in pyramidalization of the trigonal planar boron center, a shutdown of the conjugation pathway at this position, and a concomitant change in the absorption and emission characteristics of the molecule. With respect to chemical sensing, this can be a desirable effect, given the adduct formation is specific for a certain Lewis basic analyte.[18] The Lewis acidity of the boron atom is also a decisive asset in terms of B-PAH catalysis, as adduct formation influences the frontier orbitals of the Lewis base substrate.

Unfortunately, water is a ubiquitous Lewis base, and the readiness of boron to expand its coordination number from three to four provides a pathway for subsequent hydrolytic degradation. Benchtop-stable B-PAHs, of which a considerable number already exist, are usually designed in one of three ways (Figure 2): (1) The introduction of a π-donor substituent

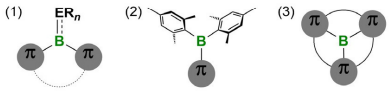

Figure 2. Three strategies to generate benchtop-stable arylboranes: (1) the introduction of a π-donor substituent ER_n, (2) steric shielding by the attachment of bulky groups, and (3) structural constraint by incorporation of the boron atom at a central site.

ER_n, such as an alkoxy group, to reduce the electron deficiency at the boron site through partial double-bond formation. As a downside, this can lead to a loss in the unique character of the boron center. (2) The attachment of bulky groups, such as mesityl (Mes) rings, onto the boron site, which leads to kinetic protection but can also hinder the dense π-stacking of the molecules in the solid state and thus be detrimental to the charge-carrier properties of the bulk material in optoelectronic devices. (3) Incorporation at the central position, rather than at the perimeter, of the PAH to provide full structural constraint of the boron atom within the rigid PAH framework. As a result, boron pyramidalization in the course of the formation of a water adduct is now associated with a considerable energy penalty and thus becomes unfavorable. B–C bond cleavage is also prevented by the chelating effect. B-PAHs with centrally located boron atoms, however, are challenging to prepare. Thus, for each specific application, the most viable and cost-efficient method must be carefully considered to alleviate the problem of hydrolysis.

For a classification of B-PAH structures, it is helpful to first consider the two simplest, uncharged, and completely conjugated cyclic hydrocarbons, namely, antiaromatic cyclobutadiene and aromatic benzene (Figure 3). The formal insertion of borylene units into the former leads to borole (**A**) and 1,4-diboracyclohexa-2,5-diene (**B**). As the number of π-electrons remains unchanged, both boron heterocycles are still antiaromatic species.[19–21] An analogous ring expansion transforms benzene into the aromatic borepin (**E**). Conjugated six-mem-

Esther von Grotthuss, born in 1991, received her B.Sc. degree from the Philipps-Universität Marburg (Germany) and her M.Sc. degree from the Goethe-Universität Frankfurt/Main (Germany). She was supported by a grant from the "Studienstiftung des deutschen Volkes". Since 2015, she has been pursuing her Ph.D. in Prof. Dr. M. Wagner's research group. Focusing on the reactivity of reduced 9,10-dihydro-9,10-diboraanthracene derivatives, she seeks to establish their use in catalysis.

Alexandra John, born in 1991, studied chemistry (B.Sc., M.Sc.) at the Goethe-Universität Frankfurt/Main (Germany). During her master's studies, she stayed for 6 months with Prof. Dr. F. Jäkle and afterwards joined Prof. Dr. M. Wagner's research group for her Ph.D. thesis. Her current research interests include the synthesis of π-conjugated arylboranes for potential applications in organic electronics.

Thomas Kaese, born in 1990, obtained his B.Sc. and M.Sc. degrees from the Goethe-Universität Frankfurt/Main (Germany). He is currently working on his Ph.D. thesis in the group of Prof. Dr. M. Wagner and focuses on the reactivity of reduced boranes to elucidate their dynamic covalent chemistry and unusual bonding situations. He was supported by grants from the "Studienstiftung des deutschen Volkes" and the "Fonds der Chemischen Industrie".

Prof. Dr. Matthias Wagner obtained his Ph.D. with Prof. Dr. H. Nöth at the Ludwig-Maximilians-Universität München (Germany). He stayed for a postdoc position with Prof. M. L. H. Green, FRS, at Oxford University (UK) and finished his Habilitation in 1997 at the Technische Universität München in the group of Prof. Dr. W. A. Herrmann. Since 1999, he holds the chair of Organometallic Chemistry at the Goethe-Universität Frankfurt/Main (Germany). His current research interests are general boron and silicon chemistry, the investigation of reactive intermediates, and organometallic catalysis directed toward materials synthesis.

ACES Asian Chemical Editorial Society
ASIAN JOURNAL OF ORGANIC CHEMISTRY
Focus Review

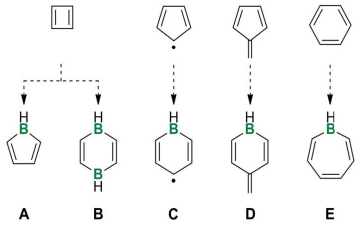

Figure 3. Formal borylene insertion into cyclobutadiene, the cyclopentadienyl radical, fulvene, and benzene to furnish neutral boron heterocycles **A**–**E**.

bered heterocycles that contain only one boron atom require either a carbon radical (i.e., **C**) or an exocyclic double bond (i.e., **D**) at the 4-position and are formally derived through borylene insertion into the cyclopentadienyl radical or fulvene, respectively.[22] Although the extreme reactivity of parent compounds **A**–**E** has precluded their isolation, a number of derivatives that have dangling substituents, especially from the borole family, have been reported.[23–29] Another mode of stabilization is provided by benzannulation, and the vast majority of B-PAHs can be regarded as derivatives of **A**–**E**, in which an increasing number of benzene rings are grouped around the heterocyclic core.

3. Syntheses of B-PAHs

3.1. General Synthetic Approaches to Arylboranes

B–C(aryl) bonds can be formed in numerous ways. A selection of particularly versatile and/or atom-economic protocols are shown in Figure 4. One of the most well-known synthetic methods involves the reaction of aryllithium (ArLi) or aryl Grignard (ArMgBr) reagents with haloboranes (XBR_2) or alkoxyboranes ($ROBR_2$).[30] Fluoroboranes are the reagent of choice if

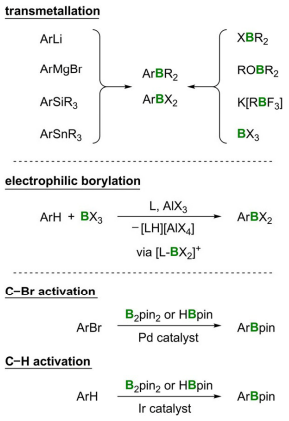

Figure 4. Common synthetic strategies for the preparation of arylboranes [B_2pin_2 = bis(pinacolato)diboron, HBpin = pinacolatoborane].

the more reactive higher haloboranes undergo unselective transformations. Nucleophilic substitution reactions that involve $ROBR_2$ often stop at the stage of the adducts $[Ar(RO)BR_2]^-$, from which the three-coordinate target products $ArBR_2$ have to be liberated by aqueous workup under acidic conditions.[30] Alkoxyboranes are thus particularly valuable starting materials to prevent the formation of unwanted ate complexes $[Ar_2BR_2]^-$. Recently, the Molander salts $K[RBF_3]$, which are conveniently accessible from arylboronates and $K[HF_2]$,[31,32] have been successfully employed in cases in which haloboranes or alkoxyboranes failed to provide the desired products.[29,33–35]

In addition to varying the leaving groups at the electrophilic boron sites, it can also be beneficial to modify the transmetalation agents. Arylsilanes ($ArSiR_3$) and arylstannanes ($ArSnR_3$) are classic starting materials for the preparation of aryldihaloboranes through electrophilic Si/B or Sn/B exchange reactions with BX_3 (X = Cl, Br).[30] By using multiply silylated arenes, multiply borylated arenes are conveniently accessible. However, the first Si/B exchange generally proceeds under milder conditions than that needed to introduce a second or third BX_2 group, especially if the electron-withdrawing boryl substituents are introduced in mutual *ortho* or *para* positions.[36]

Parent arenes can undergo electrophilic borylation reactions in a manner reminiscent of a Friedel–Crafts transformation. Highly electrophilic borenium cation intermediates $[L\text{-}BX_2]^+$ are generated from BX_3, a bulky amine ligand (L), and AlX_3 to attach BX_2 groups to the organic scaffold.[37,38] In addition to its role as a stabilizing ligand for the cationic boron intermediate, the amine ligand also acts as a Brønsted base to trap liberated HX. Electrophilic aryl borylations can also be conducted with dihalo(aryl)boranes as borylation reagents, which make them highly versatile synthetic tools.

Further synthetic strategies increasingly rely on Pd-mediated C–Br or Ir-catalyzed C–H activation/borylation reactions.[39,40] Bis(pinacolato)diboron (B_2pin_2) and pinacolatoborane (HBpin) act as the boron sources. C–H activation/borylation reactions are mainly governed by steric factors and thus usually occur *meta* and *para* to a preexisting substituent in statistical ratios of 2:1.

A less common, but potentially powerful approach, takes advantage of substituent redistribution reactions. Dihydro(aryl)boranes ($ArBH_2$) tend to engage in exchange equilibria, in which all four conceivable species Ar_nBH_{3-n} (n = 0–3) are present.[13] However, under carefully controlled conditions (i.e., the removal of the volatile B_2H_6 from the reaction mixture and proper choice of the steric demand of the aryl substituent), the equilibrium can be shifted toward either Ar_2BH or Ar_3B.[41] Even condensation polymerization protocols that lead to the formation of main-chain boron-containing macromolecules have been elaborated by comparable dismutation reactions.[42–45]

3.2. Specific Synthetic Approaches to B-PAHs

Boron-halogenated dibenzo[*b*,*d*]boroles (borafluorenes) **G**[46,47] and dibenzo[*b*,*f*]borepins (DBBs) **I**[48,49] are commonly synthe-

ACES Asian Chemical Editorial Society
ASIAN JOURNAL OF ORGANIC CHEMISTRY
Focus Review

sized by the treatment of corresponding silacycles or stannacycles, **F** or **H**, with BX_3 (X = Cl, Br; Scheme 1). 9,10-Dihydro-9,10-diboraanthracenes (DBAs) **K** are not usually prepared from 9,10-dihydro-9,10-disilaanthracenes but rather by a cyclocondensation reaction between 1,2-bis(trimethylsilyl)benzenes **J**[50–52] and BX_3.[52–56] As a general feature, substituents may be located *meta* to the boron atoms, but not at the sterically more encumbered *ortho* positions of **K**.

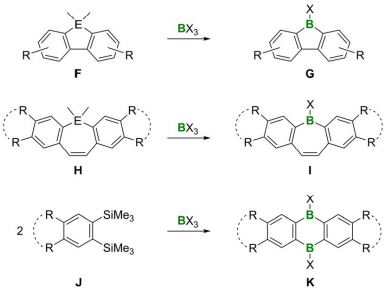

Scheme 1. Syntheses of dibenzo[*b*,*d*]boroles **G** and dibenzo[*b*,*f*]borepins **I** by E/B exchange reactions of the corresponding silacycles or stannacycles, **F** or **H**. Formation of DBAs **K** by cyclocondensation reactions between **J** and BX_3 (R = unspecified substituent; E = Si, Sn; X = halogen atom).

ortho-Substituted DBAs are accessible through Li/Br exchange of appropriately functionalized (2-bromophenyl)boronates **L**, which afford dianionic DBA derivatives **M** through twofold B–C adduct formation (Scheme 2).[57] Upon aqueous workup, the corresponding borinic acids **N** are generated, which can readily be transformed into the 9,10-dibromo-DBAs **O** for further derivatization.[55,58]

Recently, a widely applicable synthetic strategy towards unsymmetrical annulated DBAs was developed. The reaction between 4,5-dichloro-1,2-bis(trimethylsilyl)benzene (**1**), BBr_3, and various PAHs furnished the vicinally borylated compounds **2a–i**, which were easily converted into benchtop-stable derivatives **3a–i** by a mesitylation reaction (Scheme 3).[59] With one exception (i.e., **3g**), the preferred sites of electrophilic attack have

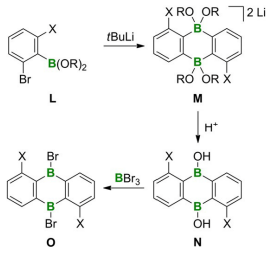

Scheme 2. Preparation of 1,5-dihalogenated DBAs **N** and **O** from **L** by Li/Br exchange and twofold B–C adduct formation (X = F, Cl, Br).

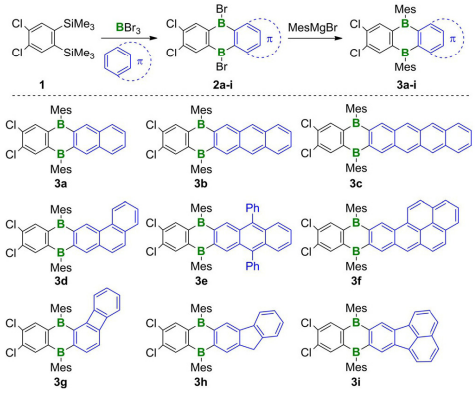

Scheme 3. Three-component reactions to furnish unsymmetrical benzannulated B-PAHs **3a–i** by electrophilic vicinal diborylation of commercial PAHs (shown in blue).

hydrogen atoms in their *ortho* positions, which minimizes unfavorable steric congestion in the transition states of the borylation reactions. To achieve decent yields, the sterically induced selectivity preferences need to be compatible with the nodal structure of the HOMO of the respective PAH, that is, the atomic orbitals of the carbon atoms at the sites of attack need to significantly contribute to this frontier molecular orbital. The two electron-withdrawing Cl atoms in **1** are needed to accomplish efficient PAH borylation. After the borylation step, these Cl substituents can either be removed through a Pd-catalyzed reduction with Et_3SiH or employed in a Stille-type derivatization reaction.[59]

In all of the B-PAH syntheses described so far, the closure of the boron-containing ring occurred through B–C bond formation in the final stages of the reaction sequence. In the past few years, however, transition-metal-mediated C–C coupling protocols that are compatible with preexisting B–C bonds in a substrate have been identified and are applicable to late-stage cyclization reactions of appropriately functionalized triarylboranes. For example, the benchtop-stable quadruply benzannulated borepin **6a** was prepared by starting from bis(8-bromonaphth-1-yl)mesitylborane (**4a**) under Yamamoto conditions (Scheme 4).[35] The reaction is also applicable to the corresponding acenaphthene and acenaphthylene precursors **4b** and **4c** to yield borepin derivatives **6b** and **6c**.

Only in the case of **4b**, which contains the most electron-rich naphthyl fragment, the Yamamoto dehalogenation reaction was accompanied by dehydrohalogenation and led to C–H activation product **9** (Scheme 5). The local concentration of the Ni^0 reagent was the determining factor that governed the relative ratio of **6b**/**9**, which could be varied from 3:1 to 1:2.5.[35] The Yamamoto approach to B-PAHs is highly modular and also applicable to the synthesis of B-doped [4]helicenes. The replacement of the chemically inert mesityl group in **4a–c** by a 2,6-dibromophenyl ring (i.e., **5**) allowed for the formation

ACES Asian Chemical Editorial Society
ASIAN JOURNAL OF ORGANIC CHEMISTRY
Focus Review

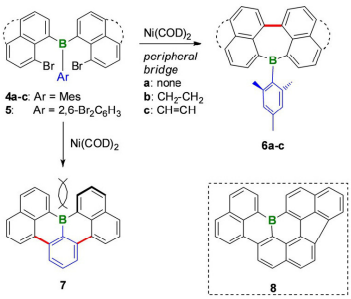

Scheme 4. Modular synthesis of the benzannulated borepins **6a–c** and the B-doped [4]helicene **7** by Yamamoto C–C coupling starting from triarylborane precursors **4a–c** and **5** [bottom right: B-PAH **8** (structurally related to **7**); COD = 1,5-cyclooctadiene].

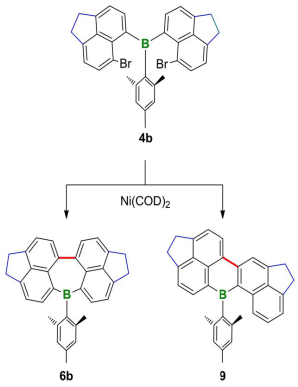

Scheme 5. Formation of isomers **6b** and **9** by competing dehalogenation and dehydrohalogention reactions upon treatment of **4b** with $Ni(COD)_2$.

of two C–C bonds to afford compound **7** (Scheme 4).[34] X-ray crystallography reveals a slight helical distortion to the molecular scaffold of **7**, which renders it soluble even in hexane despite the absence of solubilizing side groups. As it is structurally constrained, compound **7** is inert towards air and moisture, although it still forms weak adducts with pyridine bases.[34] An alternative approach to helicene **7** involves the tandem intramolecular electrophilic arene borylation reaction of 1-dibromoboryl-2,6-bis(naphth-1-yl)benzene.[60] The relevance of the helical distortion to the pronounced solubility of **7** is evident by examining the structurally related but poorly soluble B-PAH **8** (Scheme 4), which was prepared from tris(8-bromonaphth-1-yl)borane through an intramolecular radical cyclization [$(Me_3Si)_3SiH$, ABCN = 1,1′-azobis(cyclohexanecarbonitrile)].[61] Because of its peripheral bridge, the cove region[3] of **8** is widened, which leads to fewer intramolecular steric repulsions and an essentially planar molecular framework.

In addition to the dehalogenation (to give **6** or **7**) and dehydrohalogenation C–C coupling protocols (to give **9**), various dehydrogenation reactions have also been employed for the preparation of extended B-PAHs. Under Scholl reaction conditions, 6,13-bis(anthr-9-yl)-6,13-dihydro-6,13-diborapentacenes **10a–c** underwent an eightfold C–H activation and fourfold C–C coupling reaction to furnish the doubly boron-doped nanographenes **11a–c** (Scheme 6).[62,63] The bulky organyloxy substituents at the 4,5-positions of the anthryl substituents are required to accomplish the regioselective C–C bond formation at their *para* positions. By the same token, the diborapentacene core seems essential for a successful cyclization reaction, as related 9,10-bis(anthr-9-yl)-9,10-dihydro-9,10-diboraanthracenes (e.g., **12**) have failed to proceed through a comparable transformation.[64,65] The purple graphene flake **11a** represents another prototypical example of an air-stable arylborane because of the structural constraint of its rigid molecular framework.

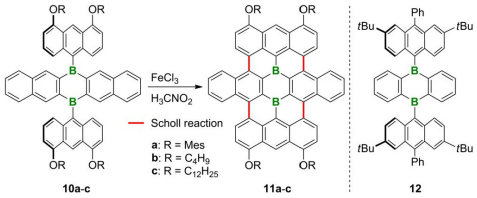

Scheme 6. Preparation of doubly B-doped nanographenes **11a–c** through the Scholl cyclization of 6,13-dihydro-6,13-diborapentacenes **10a–c**. 9,10-Dihydro-9,10-diboraanthracene **12** does not undergo an analogous planarization reaction.

Friedel–Crafts-type reactions are well-suited to generate further planarized triarylboranes, which are configurationally constrained by multiple methylene tethers (Scheme 7).[66,67] Compound **14** was obtained by the treatment of 2,6-di(2-propenyl)-phenyl-substituted precursor **13** with scandium(III) triflate. The doubly boron-doped species **17** was generated in a similar manner by starting from the corresponding doubly 2,6-di(2-propenyl)phenyl-substituted DBA. The use of $Sc(OTf)_3$ has been shown as crucial to the success of the cyclization reaction, as a broad selection of other Lewis (and Brønsted) acids failed in this respect. The oxidation of monoborane **14** at the CH_2 bridge by treatment with CrO_3 yields carbonyl derivative **15**, which can be readily transformed into the fully methylated, D_{3h}-symmetric congener **16**. Ketone **15** is also the key precursor to the unique radical species **18** (Scheme 7), which is a representative example of a **C**-type species (Figure 3). Radical **18** is accessible by a four-step sequence that involves the addition of 2,6-di(2-propenyl)phenyllithium to **15**, the reduction of the resulting tertiary alcohol, a Friedel–Crafts cyclization, and an H-atom abstraction. Because of the (moderate) π-conjugation of the odd electron with the boron center, **18** exhibits outstanding thermal stability and resistance toward atmospheric conditions.[68]

Only a few doubly boron-doped PAHs that do not have a DBA framework currently exist. Examples include dibenzodi-

ACES Asian Chemical Editorial Society
ASIAN JOURNAL OF ORGANIC CHEMISTRY
Focus Review

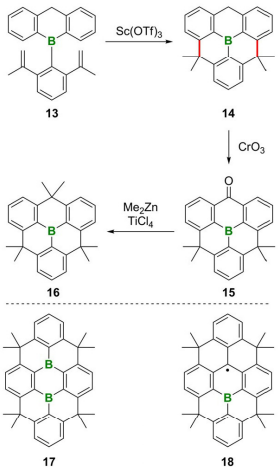

Scheme 7. Synthesis of methylene-tethered B-PAHs **14** and **16** along with structurally related planarized DBA **17** and radical **18** (OTf = trifluoromethanesulfonate).

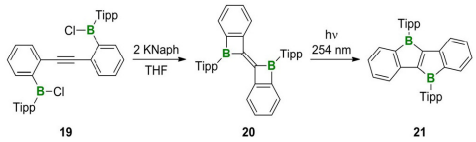

Scheme 8. Photorearrangement of **20** to afford the doubly boron-bridged stilbene **21** (Tipp = 2,4,6-triisopropylphenyl, Naph = naphthalenide).

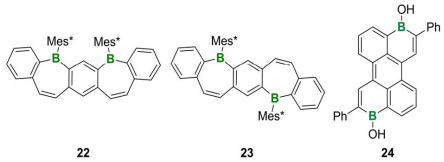

Figure 5. Conjugated *meta*- and *para*-*B*-entacenes (i.e., **22** and **23**) and the 3,9-boron-doped perylene **24** (Mes* = 2,4,6-tri-*tert*-butylphenyl).

borapentalene **21** (synthesized by reduction of **19** and photoisomerization of the resulting **20**; Scheme 8),[69,70] fused benzoborepin isomers **22** and **23** (synthesized by Sn/B exchange; Figure 5),[71,72] and 3,9-diboraperylene **24** (one-pot synthesis through alkene hydroboration, electrophilic borylation, dehydrogenation, and hydrolysis to furnish the borinic acid; Figure 5).[73] Another example is diborabisanthene **28** (Scheme 9),[74] in which the structural motif of a six-membered bora-heterocycle with exocyclic C=C bond has been realized (see also **D**; Figure 3). The synthesis of **28** starts with sila-heterocycles **25** and **26** and proceeds through a Peterson olefination, a stilbene-type photocyclization, and an Si/B exchange reaction. After mesitylation, the resulting compound **28** is stable towards air and moisture over the long term.

This general approach for the preparation of **28** is compatible with a variety of aryl ketones and aryl aldehydes.[74] If the Peterson olefination between **25** and suitable alkynyl carbonyl compounds such as **27** is carried out, then a subsequent Ru-catalyzed ene–yne benzannulation step expands the range of readily accessible B-PAHs further (e.g., **33**).[75] The proper sequences of these four synthetic modules thus provide access to a complete series of mutually related B-PAHs **28**–**33** as shown in Scheme 9.[76]

An alternative approach affords 1,6-diborapyrenes **37** and **38** (Scheme 10). The sequence of linear steps[77] involves a two-fold borylative-cyclization reaction[78] followed by an intramolecular electrophilic C–H borylation, which converts diyne **34** into double boracycle compound **35**. Then, **35** is oxidized to give fully conjugated B-PAH **36**, which is stabilized either by incorporation into a planarized structurally constrained framework (i.e., **37**) or by the introduction of bulky 2,4,6-triisopropylphenyl rings at the boron sites (i.e., **38**). A detailed comparison

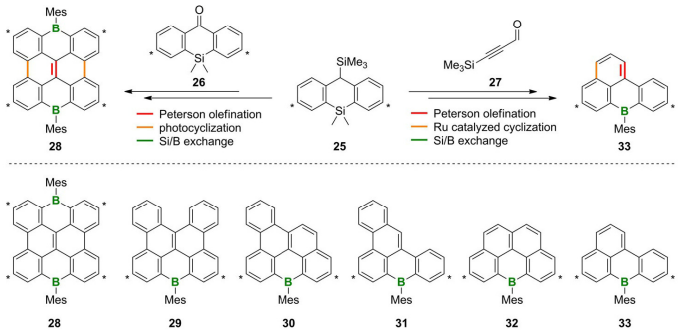

Scheme 9. Modular route to B-PAHs **28**–**33** with π-systems of different sizes and shapes by combining Peterson olefination, photocyclization, Ru-catalyzed cyclization, and Si/B exchange reactions (* = *tert*-butyl).

ACES Asian Chemical Editorial Society
ASIAN JOURNAL OF ORGANIC CHEMISTRY
Focus Review

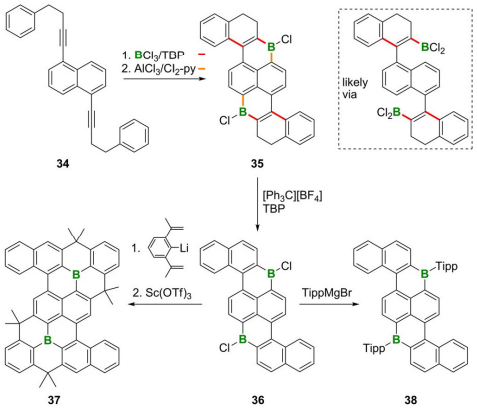

Scheme 10. Sequential borylative cyclization/electrophilic C–H borylation/oxidation reaction to form B-PAH **36** with a 1,6-diborapyrene core along with the stabilization of **36** through structural constraint (i.e., **37**) and steric shielding (i.e., **38**; TBP = 2,4,6-tri-*tert*-butylpyridine and Cl_2-py = 2,6-dichloropyridine).

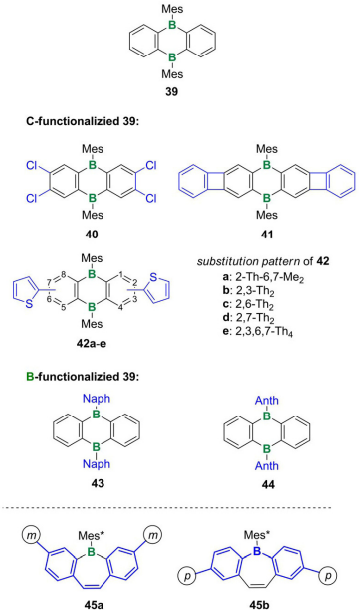

Figure 6. Derivatives of **39** substituted on either the organic scaffold or the boron atom (top); *meta*- and *para*-substituted borepins (bottom; Th = 2-thienyl, Np = naphth-1-yl derivative, Anth = anthr-9-yl derivative).

of mutually related B-PAHs, such as **37** and **38**, provides essential information about the influence of the different stabilization modes on key optoelectronic and bulk structural parameters.[77,79]

4. Specific Reactivities and Applications of B-PAHs

4.1. B-PAHs in Organic Optoelectronic Materials

Until now, the development of B-PAHs has mainly focused on their potential applications as future organic optoelectronic materials.[7,15] On the basis of available experimental data, some general trends are beginning to emerge.

B-PAHs have energetically low-lying LUMOs and thus are good electron acceptors (see Figure 1). More specifically, a majority of PAHs that contain one boron atom show one reversible reduction wave in their cyclic voltammograms (e.g., **29**–**33**; Scheme 9). A significant number of compounds that contain two incorporated boron atoms are able to accept a second electron in a reversible manner (e.g., **28** and members of the DBA family of compounds).

If boron doping is applied to extended PAH frameworks, even ambipolar species that are capable of undergoing reversible reduction as well as oxidation become available (e.g., **11a**, **28**, and **29**; Schemes 6 and 9). Especially the latter are of recent interest, as they have the potential to simultaneously act as electron- and hole-transporting materials in organic optoelectronic devices. The influence of substitution patterns on the redox potentials of B-PAHs has been thoroughly evaluated for DBA-based systems. In tetrahydrofuran (THF), 9,10-dimesityl-9,10-dihydro-9,10-diboraanthracene (**39**; Figure 6) has redox potentials of $E_{1/2} = -1.84$, -2.73 V relative to the ferrocene/ferrocenium couple.[17] Three strategies turned out to effectively improve the electron affinity of the parent system: (1) The introduction of electronegative substituents (tetrachlorinated **40**: $E_{1/2} = -1.38$ V; the compound decomposes at potential values more cathodic than approximately -2.5 V).[56] (2) The incorporation of antiaromatic moieties (biphenylene derivative **41**: $E_{1/2} = -1.52$, -2.30 V).[52] (3) The extension of the π-conjugated scaffold (nanographene **11a** in Scheme 6: $E_{1/2} = -1.45$, -1.66 V).[62]

To date, three types of systematically varied series of related B-PAH derivatives are available, which allows for the assessment of the relationship between their molecular structures and photoemission properties. The first series includes the vicinally diborylated PAHs **3a–f** (Scheme 3), which show bathochromically shifted emission wavelengths (λ_{em}) compared with their respective PAH moieties (drawn in blue in Scheme 3).[59] Nevertheless, the order of the λ_{em} values determined for the B-PAHs still reflects the sequence measured for the corresponding PAHs. These observations agree with the computed orbital scheme for the model pair DBA-benzene as outlined in Figure 1.

The second series begins with the singly boron-doped 7*H*-benzo[*de*]anthracene **33** and ends with the doubly boron-doped bisanthene **28** (Scheme 9).[74,75] All members emit in the

ACES Asian Chemical Editorial Society
ASIAN JOURNAL OF ORGANIC CHEMISTRY
Focus Review

blue spectral region, and the number and position of the annulated benzene rings have only a minor influence on the emission wavelengths. However, compared with 7,14-di(mesityl)bisanthene (λ_{em} = 705 nm), the fluorescence band of **28** is dramatically blueshifted (λ_{em} = 449 nm). Relative to dibenzo[*g*,*p*]chrysene (λ_{em} = 395 nm), the emission maxima of **28** and **29** undergo bathochromic shifts to λ_{em} = 449 and 439 nm, respectively. Most importantly, the boron-bridged molecules **28** and **29** exhibit fourfold higher photoluminescence quantum yields (Φ_{PL}) than dibenzo[*g*,*p*]chrysene.

In the third series of compounds, the number and positional arrangement of the peripheral substituents are varied, as the central B-PAH scaffold of DBA remains unchanged. Compounds **42a**–**e** have significant charge-transfer character because of the electron-donating effect of the 2-thienyl rings and the electron-accepting nature of the DBA core (Figure 6).[56,80] Increasing the number of attached 2-thienyl groups results in a continuous redshift of the emission wavelengths from λ_{em} = 469 (for **42a**) to 540 nm (for **42e**). The fluorescence maxima of the 2,3- (i.e., **42b**) and 2,6-disubstituted isomer (i.e., **42c**) also differ by as much as 38 nm. Changing the positions of the pendant substituents thus provides a tool to modify the emission properties of DBA fluorophores. The positional arrangement of the 2-thienyl rings also has a marked influence on the photoluminescence quantum efficiencies. The highest values were achieved by gathering all of the substituents on the same half of the molecule, thereby generating donor-acceptor dyads as opposed to donor-acceptor-donor triads.[56]

Noticeable substituent effects are also obvious for the three DBA derivatives **39**, **43**, and **44** (Figure 6), which contain phenyl, naphth-1-yl, and anthr-9-yl groups on the boron atoms. These compounds give rise to blue (**39**), green (**43**), and red (**44**) emissions that emanate from a twisted internal charge-transfer (TICT) state. In contrast, their three all-carbon congeners are characterized by the local π–π^* photoexcitation of their 9,10-anthrylene cores and corresponding blue fluorescence.[17,64]

From an inspection of the series of *meta*- and *para*-substituted dibenzo[*b*,*f*]borepins **45a** and **45b** (Figure 6),[81] it was concluded that the installation of *meta* substituents decreases the HOMO–LUMO gap relative to that of the unsubstituted system and that charge delocalization should occur mainly through the stilbene backbone without the participation of the boron atom (**45a**). The installation of *para* substituents increases the electron affinities of the compounds, as the electron-deficient boron center becomes an integral part of the conjugation pathway (**45b**).

A comparison of (pseudo)isomeric B-PAHs provides further insight into key structure-property relationships (Figure 7). Similar to the PAH biphenylene, the deep red, vicinally boron-bridged species **41** is nonfluorescent, whereas the yellow 6,13-dihydro-6,13-diborapentacene **46** shows blue luminescence (λ_{em} = 412 nm; Φ_{PL} = 47%).[52] Its isomer **47**, in which the two central boron atoms have been formally shifted to an adjacent ring, features a lower energy emission band and an almost doubled quantum yield (λ_{em} = 456 nm; Φ_{PL} = 87%).[52,59] Fundamental differences in key optical properties are also apparent

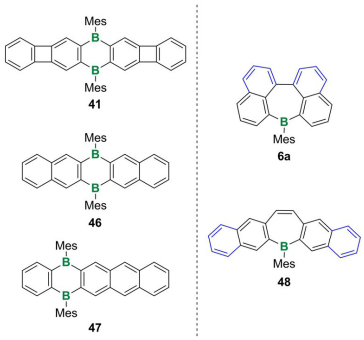

Figure 7. Comparison of (pseudo)isomers of benzannulated DBAs (left) and borepins (right).

for the borepin pair **6a**[35] and **48**.[49] The linear annulation scheme of **48** results in a bathochromically shifted fluorescence [λ_{em}(**6a** vs. **48**) = 432 vs. 477 nm] but at the expense of the Φ_{PL}, which precipitously drops from 38 to 1%, respectively.[35]

Finally, the pair of planarized B-PAHs **8** and **16** (Schemes 4 and 7) demonstrate that structural constraints can impart unique flexibility to molecules, which is immediately relevant to their optical behavior. Because of their compressed B–C bonds, these compounds readily interconvert between planar and bowl-shaped conformations. As a result, the molecular frameworks are compatible with both three- and four-coordinate boron centers. Consequently, trinaphthylborane **8** still retains a sufficiently high Lewis acidity to form isolable adducts with pyridine (i.e., **8**·Py).[61] Acid-base pairing is reversible, and the nitrogen ligand can be released quantitatively upon thermal treatment. Moreover, when **8**·Py is photoexcited, a partial dissociation of the adduct occurs in the lowest singlet excited state (S_1). As a result, dual emission is observed with the higher energy band originating from the residual adduct and the bathochromic band from the fraction of liberated borane.[61] Methylene-tethered triphenylborane **16** shows related excited state dynamics, even in the absence of Lewis bases. Two local minimum structures (i.e., planar and bowl-shaped) exist in the S_1 state, and their respective relaxations to the ground state (S_0) again give rise to dual fluorescence.[66,67]

As outlined above, B-PAHs combine exceptional redox properties with unique UV/vis emission characteristics and offer ample opportunities to customize their molecular and electronic structures. They are, therefore, widely regarded as promising building blocks for next-generation organic optoelectronic materials, and a number of proof of concept devices have already been fabricated. For example, ambipolar compounds **49a** and **49b** (Figure 8) have successfully been incorporated into the electron-transporting layer of organic light-emitting diodes (OLEDs).[82] These compounds are based on the planarized triphenylborane **14** (Scheme 7), which is readily deprotonable[83] and therefore constitutes an ideal functional group to

ACES Asian Chemical Editorial Society
ASIAN JOURNAL OF ORGANIC CHEMISTRY
Focus Review

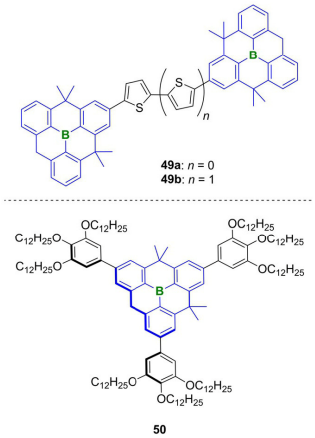

Figure 8. Ambipolar species **49a** and **49b** as building blocks for electron-transporting layers in OLEDs (top). The trigonally π-extended compound **50** forms liquid-crystalline aggregates with significant electron and hole mobilities (bottom).

host negative charges (permethylated **16** is also reducible to give a stable anionic radical[84]). The structural constraint exerted by the rigid organic scaffold gives **49a** and **49b** sufficient stability for subsequent processing by vacuum vapor deposition. Moreover, the absence of kinetically protecting side groups enables a dense packing of the molecules in the solid state and, thus, promotes charge-carrier mobility.

The use of **14** (Scheme 7) in charge-transport materials is not restricted to solid-state applications.[85] The trigonally π-extended derivative **50** (Figure 8) is a discotic liquid-crystalline mesogen that forms a hexagonal columnar phase with short vertical disc-to-disc distances of 3.6 Å, indicative of close π-stacking (see also Ref. [61]). Electron and hole mobilities of 10^{-3} and 3×10^{-5} $cm^2V^{-1}s^{-1}$ have been determined for these liquid crystals at ambient temperature.[85]

The applicability of B-PAHs goes beyond their use in charge-transporting devices. An OLED that generates green electroluminescence and shows good performance in terms of driving voltage and luminous efficiencies has been fabricated with B-doped [4]helicene **7**[34,60] (Scheme 4) as an emissive component.[60] Spin-coated thin films of **7** are also promising semiconducting materials. The transfer and output curves of a corresponding organic field-effect transistor are indicative of p-type modulation.[60] One particularly remarkable example of a p-type OFET has been found, in which the peculiar features of its boron dopant atom have not only been used to imprint the desired electronic properties on the parent PAH, but also to facilitate the fabrication of the device by cost-efficient spin-coating from precursor solutions:[86] trinaphthylborane **8** (Scheme 4)[61] is poorly soluble in common organic solvents as a result of its planar molecular structure, which promotes the formation of densely π-stacked columnar aggregates. As mentioned above, the addition of pyridine generates the four-coordinate boron-nitrogen adduct **8**·Py and induces a plane-to-bowl conversion of the B-PAH skeleton, thereby disfavoring intermolecular π-interactions. Importantly, upon moderate heating, the nitrogen ligand is released to regenerate the tricoordinate B-PAH. Thus, spin-coating solutions of **8**·Py on glass substrates first gives amorphous thin films. After briefly annealing at 180 °C, the coated adduct film is converted into a polycrystalline film of parent **8**. The solution-processed layer exhibits electronic characteristics that are identical to those of a thin film that was prepared by the laborious vacuum vapor deposition of **8**. The neutral π-monoradical **18** (Scheme 7) provides the materials basis for another OFET and an organic Mott-insulator transistor.[68] The thermally and hydrolytically stable compound shows well-balanced ambipolar charge-transport abilities that result from virtually identical spatial distributions of its singly occupied and unoccupied molecular orbitals.

The electron-acceptor capacity of B-PAHs suggests their possible use as active electrode materials in lithium-ion batteries. In this context, the utility of **11**-type nanographenes (Scheme 6) was assessed with the help of a half cell coupled to a counter electrode made of Li metal.[63] When electrodes that consist of carbon black blended with **11a** (R = Mes) or **11b** ($R = C_4H_9$) are compared, a higher specific capacity is observed for the nanographene compound that contains the smaller substituents, as they allow for a more densely packed supramolecular structure. The battery with **11b** shows a stable performance over 10 charge/discharge cycles. In this context, the poor solubility of **11b** in the electrolyte is essential, given that dianion $[\mathbf{11a}]^{2-}$, which has a triplet biradical ground state, degrades rapidly in solution at room temperature.

Finally, we note reports of OLEDs and organic solar cells (OSCs) that contain borafluorene or DBA moieties with four-coordinate boron atoms and chelating 2-(2-hydroxyphenyl)benzimidazole, 8-hydroxyquinoline, and aza-dipyrromethene ligands.[87–89]

4.2. Dynamic Covalent Chemistry of B-PAHs

Under inert conditions, 9,10-dihydro-9,10-diboraanthracene (DBA) derivatives retain their structural integrity regardless of which substituents are chosen for installation at the boron centers (e.g., H, alkyl, aryl, halogen, NR_2, OR). This is also true for the smallest possible substituent, namely, the hydrogen atom. Parent **52**, which is accessible from 9,10-dibromo-DBA **51** and Et_3SiH, forms coordination polymer $(\mathbf{52})_n$ in the solid state, in which individual DBA monomers are linked by B–H–B two-electron three-center bonds (Scheme 11).[90] Me_2S cleanly splits this polymer into its monomeric building blocks to furnish *syn*-Me_2S–B diadduct **52**·$(SMe_2)_2$ (Scheme 11).[91,92]

The borafluorene scaffold is also compatible with a wide variety of substituents at the boron atom.[93] Contrary to parent DBA **52**, however, parent 9*H*-9-borafluorene **54** exhibits extensive dynamic covalent behavior. Its central borole ring remains intact only if coordinating Lewis bases, such as pyridine,[94] THF,[95] or SMe_2,[96] are available.[97] In the absence of the appropriate ligands, **54** forms partly ring-opened, C_1-symmetric dimers $(\mathbf{54})_2$, in which the boron atoms are bridged by one hy-

ACES Asian Chemical Editorial Society
ASIAN JOURNAL OF ORGANIC CHEMISTRY
Focus Review

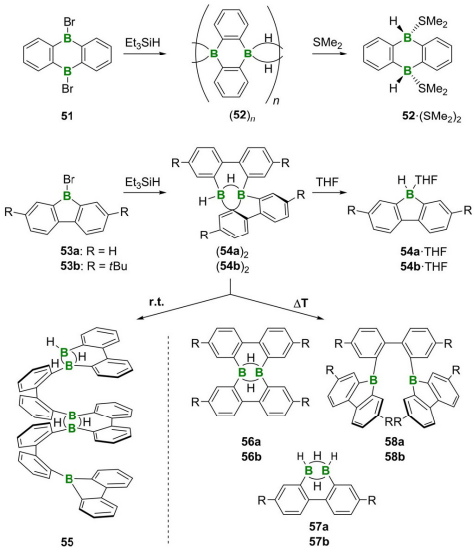

Scheme 11. The comparison between polymeric parent DBA $(\mathbf{52})_n$ to dimeric parent borafluorene $(\mathbf{54a})_2$. At ambient temperature, $(\mathbf{54a})_2$ undergoes a ring-opening oligomerization to furnish **55**. At elevated temperatures, $(\mathbf{54a})_2$ and $(\mathbf{54b})_2$ form the lower molecular weight products **56a**–**58a** and **56b**–**58b** (**a**: R = H; **b**: R = *t*Bu).

drogen atom and one of the aryl rings.[94] A crystal structure has been reported for *t*Bu-substituted derivative $(\mathbf{54b})_2$ (Scheme 11).[47] Without the kinetically stabilizing *t*Bu substituents, the ring-opening reaction proceeds further, already at ambient temperature, to afford main-chain boron-containing oligophenylenes, such as **55**. The oligomer main chain of **55** is reinforced and conformationally constrained by intrastrand B–H–B bonds (Scheme 11).[94]

At elevated temperatures of 120 °C, entropy comes into play, and $(\mathbf{54a})_2$ and $(\mathbf{54b})_2$ are converted into the lower molecular weight species **56a**–**58a** and **56b**–**58b**, respectively (Scheme 11).[98] Alternative rational and high-yielding syntheses have been developed for **57a** and **58a**,[96,98] whereas the thermolysis of $(\mathbf{54a})_2$ and $(\mathbf{54b})_2$ still provides the only route to 1,2:1,2-bis(2,2′-biphenylylen)diborane(6) derivatives, which are isomers of $(\mathbf{54a})_2$ and $(\mathbf{54b})_2$ (yields of **56a** and **56b**: 34%). With respect to the synthetic utility of $(\mathbf{54a})_2$, it is important to note that the partial ring-opening reaction is reversible in the presence of Lewis bases[95] or unsaturated hydrocarbons. For example, the reaction of freshly prepared solutions of $(\mathbf{54a})_2$ with *tert*-butylacetylene cleanly affords diborylmethane **59** through the twofold hydroboration of the C≡C bond (Scheme 12).[94]

Rearrangement reactions not only are observed for the neutral 9*H*-9-borafluorenes $(\mathbf{54a})_2$ and $(\mathbf{54b})_2$ but also can be induced by electron injection. Contrary to the readily reducible DBA polymer $(\mathbf{52})_n$ and its resultant discrete dianion

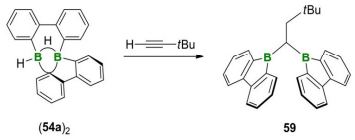

Scheme 12. Synthesis of diborylmethane **59** by twofold hydroboration of *tert*-butylacetylene with $(\mathbf{54a})_2$.

$[\mathbf{52}]^{2-}$,[99,100] the C_1-dimer $(\mathbf{54b})_2$ furnishes the doubly boron-doped dibenzo[*g*,*p*]chrysene $[\mathbf{60}]^{2-}$ in yields of 43% when treated with an excess amount of Li granules in THF (Scheme 13; the reaction likely proceeds through adduct **54b**·THF).[101] Doubly boron-doped $[\mathbf{60}]^{2-}$ is interesting not only because of its use in PAH chemistry but also because of its localized B=B bond, which likely has unique reactivity (four Clar sextets can be drawn for the dianion, which leaves an isolated B=B fragment behind).

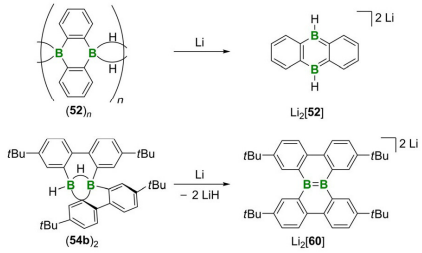

Scheme 13. Lithium reduction of $(\mathbf{52})_n$ produces discrete dianions $[\mathbf{52}]^{2-}$, whereas $(\mathbf{54b})_2$ loses hydrogen atoms and rearranges to the B=B bonded species $[\mathbf{60}]^{2-}$.

As the B_2H_2 core is ideally preorganized for reductive B–B coupling, the redox behavior of **56b** was also investigated.[95] The reaction outcome is strongly dependent on the number of redox equivalents employed and on the nature of the reducing agent, that is, lithium metal or lithium naphtalenide versus potassium graphite (KC_8). The treatment of **56b** with increasing amounts of lithium napthalenide furnishes Li_2[**61**], Li_2[**62**], and Li_2[**60**] as the major products, respectively (Scheme 14). In the case of isomers Li_2[**61**] and Li_2[**62**], B–B bond formation is accompanied by skeletal rearrangement. The use of an excess amount of KC_8 did not provide any $[\mathbf{60}]^{2-}$ but led to the formation of $[\mathbf{63}]^{2-}$, the nonrearranged isomer of Li_2[**61**] and Li_2[**62**]. From this reactivity study, it was concluded that (1) more reducing agent leads to less rearrangement and (2) hydride abstraction with concomitant overreduction (to afford $[\mathbf{60}]^{2-}$) takes place only in the presence of Li^+ counterions. These experimental findings were rationalized by assuming that the rearrangement cascade is triggered by the addition of the first electron, which acts as a catalyst, and is terminated immediate-

ACES Asian Chemical Editorial Society
ASIAN JOURNAL OF ORGANIC CHEMISTRY
Focus Review

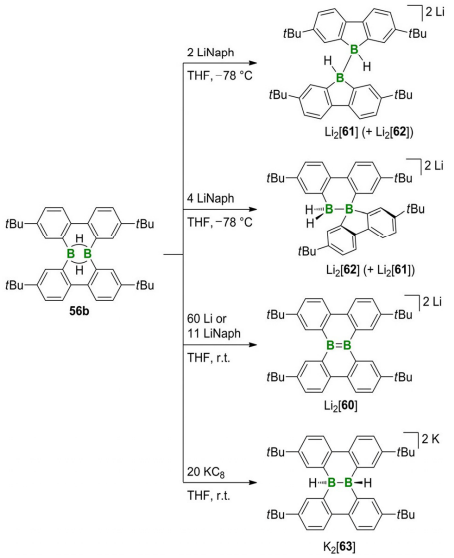

Scheme 14. Degree of skeletal rearrangement upon reduction of **56b** as a function of the amount and nature of the reducing agent. In all cases, B–B bonds are formed (minor side products are listed in brackets).

ly after the second electron has been accepted by the system.[95]

Organo(hydro)boranes are generally regarded as hydridic species. As a fundamental change of paradigm, the successful deprotonation of **56b** with concomitant formation of $[\mathbf{64}]^-$ has been reported (Scheme 15). In the presence of $[(Me_3Si)_3C]^-$ or

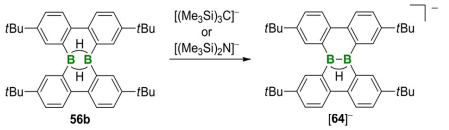

Scheme 15. Deprotonation of **56b** by using bulky bases to generate the B–B bond in $[\mathbf{64}]^-$ (note that B*H* atoms are generally regarded as hydridic).

$[(Me_3Si)_2N]^-$ as a base, one of the B–H–B bridges is transformed into a B–B bond, which is a unique strategy for the coupling of two boron atoms.[102]

The rich dynamic covalent chemistry of parent **54a** and **54b** clearly correlates with their boron-bonded hydrogen atoms. For instance, Tipp-substituted borafluorene **65** is electrochemically well-behaved, as it undergoes a reversible first reduction ($E_{1/2} = -2.11$ V in THF vs. FcH/FcH$^+$; FcH = ferrocene), and electron injection results in no significant structural modifications (Figure 9).[103] The less sterically shielded ditopic arylboranes **58a** and **59** also undergo reversible reductions, already at markedly more anodic potential values of $E_{1/2} = -1.49$, -1.75 V

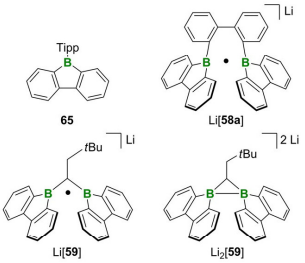

Figure 9. Borafluorene **65** undergoes reversible electrochemical reduction. Compounds containing one-electron two-center bonds (i.e., Li[**58a**], Li[**59**]) and two-electron two-center bonds (i.e., Li_2[**59**]) are accessible by reduction of the structurally preorganized ditopic boranes **58a** and **59**.

(**58a**)[104] and $E_{1/2} = -1.76$, -2.17 V (**59**).[105] In both compounds, the organyl bridges impose a face-to-face arrangement of the borafluorenyl units, thereby promoting an overlap of the vacant boron p_z orbitals. The resulting cooperativity between the two boron atoms greatly increases the electron affinities of both systems. Arylboranes **58a** and **59** have also been chemically reduced on a preparative scale by using lithium napthalenide or Li metal. In the case of **58a**, it was possible to isolate monoanion radical $[\mathbf{58a}]^{\bullet-}$, which represents the first example of a fully characterized compound featuring a B·B one-electron two-center bond (EPR spectroscopic data exists for a comparable bonding situation in the 1,8-bis(diphenylboryl)naphthalene radical anion[106]).[104] Upon reduction of the diborylmethane derivative **59**, both the B·B-bonded radical anion $[\mathbf{59}]^{\bullet-}$ and the B–B bonded dianion $[\mathbf{59}]^{2-}$ became accessible, the latter of which is isoelectronic to highly strained cyclopropanes. The B···B distance continuously decreases along the sequence **59** → $[\mathbf{59}]^{\bullet-}$ → $[\mathbf{59}]^{2-}$, which is in accordance with an increasing B···B bond order.

Borafluorenes tend to engage in B–C insertion reactions, thereby expanding their antiaromatic[103] central borole rings. For example, 9-amino-9-borafluorene **66** undergoes a rearrangement well below ambient temperature to give heteroaromatic, benzannulated 1,2-dihydro-1,2-azaborine **67** (Scheme 16).[12, 107] By the same token, the thermolysis of

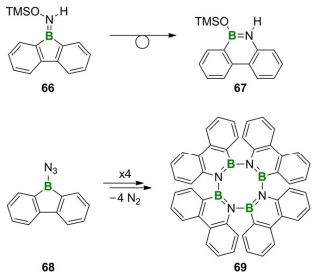

Scheme 16. Nitrogen atom insertion into the central borole rings of **66** and **68** to give azaborine motifs (TMS = trimethylsilyl).

ACES Asian Chemical Editorial Society
ASIAN JOURNAL OF ORGANIC CHEMISTRY
Focus Review

9-azido-9-borafluorene **68**[108] at reflux in heptane generates the tetramer (i.e., **69**) of a 9,10-*B*,*N* analogue of 9,10-phenanthryne (Scheme 16).[109,110] This chemistry has further been exploited for the on-surface synthesis of large B,N-doped aromatic networks.[111]

A wide variety of alkynes readily insert into 9-chloro-9-borafluorene **70** by a 1,2-carboboration reaction to furnish vicinally substituted, doubly benzannulated borepins (e.g., **71**; Scheme 17). The subsequent one-electron oxidation by using

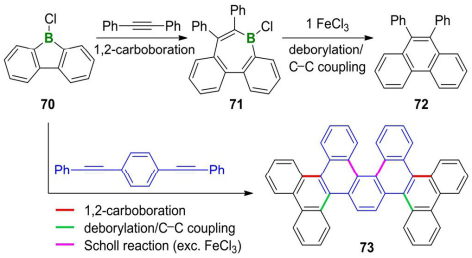

Scheme 17. Synthesis of highly substituted borepins (e.g., **71**) by the 1,2-carboboration of diarylacetylenes with 9-chloro-9-borafluorene (**70**). The oxidation by treatment with $FeCl_3$ results in the deborylation/C–C coupling reaction sequence to give **72**. An excess amount of $FeCl_3$ can be employed to perform an additional Scholl dehydrogenation reaction to give **73**.

atmospheric O_2, $FeCl_3$, or MnO_2 results in a deborylation/C–C coupling reaction sequence to afford 9,10-disubstituted phenanthrenes (e.g., **72**).[112] It should be noted that the $FeCl_3$-promoted variant is related to the dehydrogenative Scholl reaction. Thus, by using an excess amount of $FeCl_3$ and suitably designed substrates, it is possible to perform the deborylation/C–C coupling and Scholl coupling reactions as one-pot protocols to conveniently assemble sophisticated molecular structures. The reaction sequence is extremely versatile and substrates that contain multiple alkyne moieties have already been used for the preparation of high-molecular weight PAHs (e.g., **73**; Scheme 17) and helicenes.[112]

In summary, the high reactivity of the antiaromatic borole is still echoed by its benzannulated congener 9-borafluorene.[113] If the kinetically shielding boron-bonded substituents are missing, as in the cases of 9*H*- and 9-chloro-9-borafluorene, the compounds have a pronounced tendency to undergo B–C bond cleavage, which is increasingly recognized as a potentially useful reactivity pattern.

4.3. B-PAHs in Organocatalysis

In the preceding chapter, we have reviewed reactions that ultimately result in structural modifications of B-PAHs. Yet, B-PAHs also serve an essential role in the transformation of external substrates, sometimes in a catalytic manner. Lewis acid catalysis is a well-developed synthetic tool in organic chemistry, and several reports have been published about ditopic boranes, especially derivatives of 9,10-dihydro-9,10-diboraanthracene (DBA). DBA can serve as a structurally well-defined, bidentate Lewis acid that is capable of interacting simultaneously with two Lewis basic sites of the same substrate molecule. When equipped with small substituents (e.g., H and Me) at the boron centers, DBA readily coordinates with 1,2-diazines (e.g., pyrazolides and phthalazines) to generate tricyclic paddle-wheel structures, such as **74** (Figure 10).[91,114] As a consequence, the electron density of the respective 1,2-diazine is reduced, and its LUMO energy level is lowered, which facilitates inverse electron-demand Diels–Alder (IEDDA) reactions with electron-rich dienophiles.[115] The primary cycloadducts release N_2 and in turn DBA, which can subsequently coordinate to the next 1,2-diazine molecule. DBA is thus required only in catalytic amounts. As a model reaction, phthalazine **75** is converted into naphthalene derivative **78** in the presence of oxazolidine **76** (1.5 equiv) and 9,10-dimethyl-DBA **77** (5 mol%). An oxazolidine ring-opening occurs in the course of a final H-atom shift to aromatize the naphthalene moiety (Scheme 18).[116]

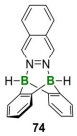

Figure 10. Paddle-wheel structure of the phthalazine adduct of **52** (i.e., **74**).

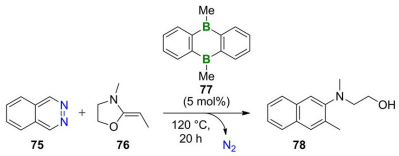

Scheme 18. Model IEDDA reaction between phthalazine **75** and dienophile **76** in the presence of **77** as the catalyst.

This general catalytic scheme has been further developed to include one-pot domino processes that merge IEDDAs and (1) cyclopropanation reactions to prepare benzonorcaradienes[117] or (2) normal electron-demand Diels–Alder reactions to produce bridged tri- and tetracyclic 1,2,3,4-tetrahydronaphthalenes.[118] In addition to varying the dienophile, it is also possible to expand the substrate scope with regard to the diene. To this end, DBA catalysis has been elegantly exploited twice: (1) for the synthesis of 2,3-diazaanthraquinones (e.g., **81**) from 1,4-naphthoquinones (e.g., **79**) and 1,2,4,5-tetrazine **80** and (2) for the IEDDA of 2,3-diazaanthraquinones with an alkene or alkyne to furnish substituted anthraquinones (e.g., **82**; Scheme 19).[119] The products of the reaction are relevant as building blocks for organic optoelectronic materials and substructures of pharmacologically active molecules.

The efficient catalytic dehydrogenation of ammonia-borane (NH_3BH_3, **83**) is a topic of continuing interest in terms of both hydrogen storage and ceramic materials production (e.g., hexagonal boron nitride). As one of only four metal-free systems capable of releasing H_2 from **83** at moderate temperatures, 9,10-dichloro-DBA **84** mediates the evolution of up to 2.5 equiv of H_2 by starting from 1 equiv of **83** (Scheme 20).[120] Borazine **85** and its cross-linked oligomers $(\mathbf{85})_n$ have been

ACES Asian Chemical Editorial Society
ASIAN JOURNAL OF ORGANIC CHEMISTRY
Focus Review

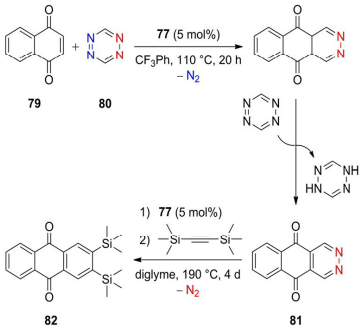

Scheme 19. Model IEDDA reaction of 1,4-naphthoquinone **79** and 1,2,4,5-tetrazine **80** as both the diene and oxidant to afford **81**. The subsequent synthesis of anthraquinone **82** through the IEDDA reaction of **81**.

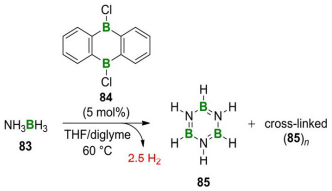

Scheme 20. Dehydrogenation of ammonia-borane **83** in the presence of catalytic amounts of 9,10-dichloro-DBA **84**.

identified as the main dehydrogenation products. Under the employed conditions (5 mol% **84**, THF/diglyme, 60 °C, 7 h), the DBA catalyst could be used 15 times without substantial loss of activity.

The activation of element-element bonds has long been regarded as the exclusive domain of transition-metal complexes. This view has changed since "frustrated Lewis pairs" (FLPs) have proven their potential in the transformation of many substrate molecules through the concerted action of main-group Lewis acids (e.g., boranes) and bases (e.g., phosphines).[121] As shown above, uncharged DBA **84** promotes B–H and N–H activation reactions without the addition of a Lewis base. Moreover, DBAs readily accept two electrons, and the resulting dianions can formally be viewed as FLPs in which the Lewis base is broken down to its absolute essence, the electron lone pair. Doubly reduced DBAs are capable of activating even C–H bonds and H_2.[99,100] For example, the treatment of Li_2[**52**] with *tert*-butylacetylene does not result in the hydroboration of the C≡C bond but rather in the splitting of the terminal C–H bond to form the mixed acetylide/hydride adduct Li_2[**86**] (Scheme 21).[99] In the presence of an excess amount of the alkyne, a subsequent acid-base reaction (hydridic B*H*, protic C≡C*H*) leads to the formation of double acetylide adduct Li_2[**87**] with the concomitant liberation of H_2. 1,4-B_2C_4 heterocycles with four-coordinate boron centers prefer to adopt boat conformations. In the case of Li_2[**87**], the small hydrogen substituents will occupy both axial positions and, thus, are ideally prearranged to liberate H_2. In a closed system at moderately elevated temperatures, a dynamic equilibrium is established between Li_2[**87**] and Li_2[**88**]/H_2 (Scheme 21).[100] At 100 °C, the equilibrium is shifted to the thermolysis products, whereas at 50 °C, Li_2[**87**] and Li_2[**88**] are equally abundant. Rapid cooling from either 100 or 50 °C to room temperature largely freezes the respective equilibria. The doubly reduced parent DBA Li_2[**52**] activates H_2 quantitatively to furnish Li_2[**89**] at a temperature of 100 °C and a pressure of 1 atm. Although the boron substituents (alkynyl vs. H) determine the position of the H_2-activation equilibrium at a given temperature, the counter cations influence the reaction rate. As a general rule, cations with a high tendency to bind to the electron-rich B_2C_4 ring of the DBA dianion (e.g., Li^+) inhibit the access of H_2 to the reactive boron sites, thereby slowing down the reaction rate. Conversely, less strongly coordinating cations (e.g., K^+) help to achieve faster H_2 activation.

In summary, DBA-based Lewis acids can bring about enhanced reactivities relative to monotopic arylboranes. After a twofold reduction, the compounds lose their Lewis acidity, but, in line with the nodal structures of their frontier orbitals, acquire metal-like behavior instead (e.g., the ability to activate C–H and H–H bonds).

5. Growing Even Bigger: Boron-Doped Graphene Flakes and Nanoribbons

Future developments will continue to go beyond B-PAHs with the goal to customize nanosized boron-doped substructures of graphene. The associated challenges are formidable if starting from soluble precursors and performing multiple C–C coupling reactions in the liquid phase to obtain monodisperse, defect-free, atomically precise graphene flakes or ribbons.[122] Fortunately, the fabrication process can be facilitated by an on-sur-

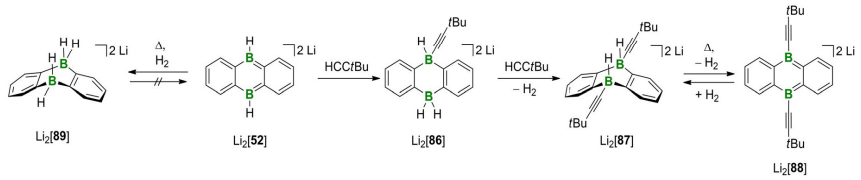

Scheme 21. C–H activation of *tert*-butylacetylene by Li_2[**52**] to form Li_2[**86**]. An excess amount of the alkyne furnishes Li_2[**87**] along with the release of H_2. Both DBA salts Li_2[**52**] and Li_2[**88**] add H_2 across their boron centers, the latter of them in a reversible fashion.

ACES Asian Chemical Editorial Society

ASIAN JOURNAL OF ORGANIC CHEMISTRY
Focus Review

face approach, thereby confining the reaction space from three to two dimensions.[123,124] The ideal surface fulfills two purposes, including: (1) the minimization of the possible number of mutual orientations of the adsorbed precursor molecules and (2) the catalysis of the required C–C coupling steps.

Encouraging results have been obtained by vacuum deposition of the bromine-functionalized 9,10-bis(anthr-9-yl)-DBA **90** onto an Au(111) surface and the thermal annealing of the resulting adsorbate (Scheme 22). At approximately 200 °C, the

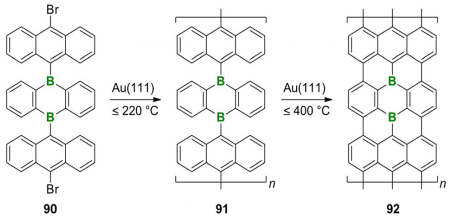

Scheme 22. Temperature-induced dehalogenation of DBA derivative **90** on an Au(111) surface to give polymer **91**. Further heating leads to cyclodehydrogenation and the formation of boron-doped nanoribbon **92**.

precursor molecules undergo surface catalytic dehalogenation to form linear polymer **91**. Subsequent heating up to 400 °C results in a clean cyclodehydrogenation to furnish the target nanoribbon **92**. The armchair-edged structure has a uniform width of seven carbon atoms and features boron sites at its center row with a fixed doping density of 4.8 atom-%.[125,126]

6. Conclusions

Plastic electronics are a key future technology given that organic materials are mechanically flexible, lightweight, film-forming species that can be easily tailored for specific tasks using the broad and sophisticated toolbox of organic reactions. Among potential organic building blocks, polycyclic aromatic hydrocarbons (PAHs) already hold a dominant position but are still the subject of intense development. Boron doping provides a means to endow PAH materials with superior optoelectronic properties relative to their all-carbon congeners. Many of the resulting B-PAHs are excellent electron acceptors as well as visible-light emitters and have therefore been applied as materials for organic light-emitting diodes (OLEDs) and organic field-effect transistors (OFETs) as well as components of next-generation battery electrodes. However, challenging questions remain, among which include: (1) how to simplify the syntheses of B-PAHs by exploiting atom- and step-economic domino reactions, (2) how to impart chemical inertness without sacrificing the chance for the optimal π-stacking of the molecules in deposited thin films, and (3) how to transfer surface-generated, boron-containing nanoribbons to the actual device (e.g., by stamping techniques).

Recently, the range of applications has been expanded to the field of organocatalysis, which takes advantage of the Lewis acidity and pronounced electron affinity of suitably designed B-PAHs. Especially 9,10-dihydro-9,10-diboraanthracenes serve as proper catalysts to promote electrocyclic reactions and activate B–H and N–H bonds. After a twofold reduction, dianionic DBAs are capable of splitting C–H bonds and H_2 molecules. Desirable improvements in the years to come would include: (1) the development of electroreduction methods in place of a chemical B-PAH reduction with hazardous alkali metals and (2) the design of chiral B-PAH catalysts, e.g., derived from configurationally stable boron-doped helicenes.

Finally, certain B-PAHs exhibit rich dynamic covalent chemistry, which so far has little practical implications but is fundamentally important for a deeper understanding of the specificities of the B–C bond. Given vigorous advances in B-PAH chemistry and the interesting questions that arise from it, we expect that exciting results will likely continue to emerge from this fruitful area.

Acknowledgements

T.K. thanks the Fonds der Chemischen Industrie for a Ph.D. grant. This work was partially funded by the Bundesministerium für Wirtschaft und Energie through the WIPANO (Wissens- und Technologietransfer durch Patente und Normen) grant number 03THW10F04. We are grateful to Soren K. Mellerup (honored B.Sc.), Queen's University, Kingston (Canada) for helpful discussions.

Conflict of interest

The authors declare no conflict of interest.

Keywords: boron · dynamic covalent chemistry · luminescence · organocatalysis · polycycles

[1] F. So, *Organic Electronics: Materials, Processing, Devices and Applications*, CRC Press, Boca Raton, **2010**.
[2] J. Wu, W. Pisula, K. Müllen, *Chem. Rev.* **2007**, *107*, 718–747.
[3] R. Rieger, K. Müllen, *J. Phys. Org. Chem.* **2010**, *23*, 315–325.
[4] A. Narita, X.-Y. Wang, X. Feng, K. Müllen, *Chem. Soc. Rev.* **2015**, *44*, 6616–6643.
[5] M. Stępień, E. Gońka, M. Żyła, N. Sprutta, *Chem. Rev.* **2017**, *117*, 3479–3716.
[6] A. Studer, D. P. Curran, *Nature Chem.* **2014**, *6*, 765–773.
[7] A. Escande, M. J. Ingleson, *Chem. Commun.* **2015**, *51*, 6257–6274.
[8] C. D. Entwistle, T. B. Marder, *Angew. Chem. Int. Ed.* **2002**, *41*, 2927–2931; *Angew. Chem.* **2002**, *114*, 3051–3056.
[9] F. Jäkle, *Coord. Chem. Rev.* **2006**, *250*, 1107–1121.
[10] S. Yamaguchi, A. Wakamiya, *Pure Appl. Chem.* **2006**, *78*, 1413–1424.
[11] F. Jäkle, *Chem. Rev.* **2010**, *110*, 3985–4022.
[12] P. G. Campbell, A. J. V. Marwitz, S.-Y. Liu, *Angew. Chem. Int. Ed.* **2012**, *51*, 6074–6092; *Angew. Chem.* **2012**, *124*, 6178–6197.
[13] A. Lorbach, A. Hübner, M. Wagner, *Dalton Trans.* **2012**, *41*, 6048–6063.
[14] A. Wakamiya, S. Yamaguchi, *Bull. Chem. Soc. Jpn.* **2015**, *88*, 1357–1377.
[15] L. Ji, S. Griesbeck, T. B. Marder, *Chem. Sci.* **2017**, *8*, 846–863.
[16] Z. M. Hudson, S. Wang, *Acc. Chem. Res.* **2009**, *42*, 1584–1596.
[17] C. Hoffend, M. Diefenbach, E. Januszewski, M. Bolte, H.-W. Lerner, M. C. Holthausen, M. Wagner, *Dalton Trans.* **2013**, *42*, 13826–13837.
[18] C. R. Wade, A. E. J. Broomsgrove, S. Aldridge, F. P. Gabbaï, *Chem. Rev.* **2010**, *110*, 3958–3984.

ACES Asian Chemical Editorial Society

ASIAN JOURNAL OF ORGANIC CHEMISTRY
Focus Review

[19] J. J. Eisch, J. E. Galle, S. Kozima, *J. Am. Chem. Soc.* **1986**, *108*, 379 – 385.
[20] H. Braunschweig, I. Fernández, G. Frenking, T. Kupfer, *Angew. Chem. Int. Ed.* **2008**, *47*, 1951 – 1954; *Angew. Chem.* **2008**, *120*, 1977 – 1980.
[21] H. Braunschweig, C. Hörl, L. Mailänder, K. Radacki, J. Wahler, *Chem. Eur. J.* **2014**, *20*, 9858 – 9861.
[22] Further stabilization is provided with the help of N-hetereocyclic carbene (NHC) ligands. For details, see: T. K. Wood, W. E. Piers, B. A. Keay, M. Parvez, *Angew. Chem. Int. Ed.* **2009**, *48*, 4009 – 4012; *Angew. Chem.* **2009**, *121*, 4069 – 4072.
[23] C.-W. So, D. Watanabe, A. Wakamiya, S. Yamaguchi, *Organometallics* **2008**, *27*, 3496 – 3501.
[24] C. Fan, L. G. Mercier, W. E. Piers, H. M. Tuononen, M. Parvez, *J. Am. Chem. Soc.* **2010**, *132*, 9604 – 9606.
[25] H. Braunschweig, T. Kupfer, *Chem. Commun.* **2011**, *47*, 10903 – 10914.
[26] H. Braunschweig, V. Dyakonov, J. O. C. Jimenez-Halla, K. Kraft, I. Krummenacher, K. Radacki, A. Sperlich, J. Wahler, *Angew. Chem. Int. Ed.* **2012**, *51*, 2977 – 2980; *Angew. Chem.* **2012**, *124*, 3031 – 3034.
[27] R. Bertermann, H. Braunschweig, R. D. Dewhurst, C. Hörl, T. Kramer, I. Krummenacher, *Angew. Chem. Int. Ed.* **2014**, *53*, 5453 – 5457; *Angew. Chem.* **2014**, *126*, 5557 – 5561.
[28] J. H. Barnard, S. Yruegas, K. Huang, C. D. Martin, *Chem. Commun.* **2016**, *52*, 9985 – 9991.
[29] Z. Zhang, R. M. Edkins, M. Haehnel, M. Wehner, A. Eichhorn, L. Mailänder, M. Meier, J. Brand, F. Brede, K. Müller-Buschbaum, H. Braunschweig, T. B. Marder, *Chem. Sci.* **2015**, *6*, 5922 – 5927.
[30] T. Onak, *Organoborane Chemistry*, Academic Press, New York, **1975**.
[31] G. A. Molander, N. Ellis, *Acc. Chem. Res.* **2007**, *40*, 275 – 286.
[32] G. A. Molander, *J. Org. Chem.* **2015**, *80*, 7837 – 7848.
[33] K. Samigullin, M. Bolte, H.-W. Lerner, M. Wagner, *Organometallics* **2014**, *33*, 3564 – 3569.
[34] K. Schickedanz, T. Trageser, M. Bolte, H.-W. Lerner, M. Wagner, *Chem. Commun.* **2015**, *51*, 15808 – 15810.
[35] K. Schickedanz, J. Radtke, M. Bolte, H.-W. Lerner, M. Wagner, *J. Am. Chem. Soc.* **2017**, *139*, 2842 – 2851.
[36] M. C. Haberecht, J. B. Heilmann, A. Haghiri, M. Bolte, J. W. Bats, H.-W. Lerner, M. C. Holthausen, M. Wagner, *Z. Anorg. Allg. Chem.* **2004**, *630*, 904 – 913.
[37] T. S. De Vries, A. Prokofjevs, E. Vedejs, *Chem. Rev.* **2012**, *112*, 4246 – 4282.
[38] M. J. Ingleson, *Synlett* **2012**, *23*, 1411 – 1415.
[39] T. Ishiyama, N. Miyaura, *Chem. Rec.* **2004**, *3*, 271 – 280.
[40] I. A. I. Mkhalid, J. H. Barnard, T. B. Marder, J. M. Murphy, J. F. Hartwig, *Chem. Rev.* **2010**, *110*, 890 – 931.
[41] A. Schnurr, K. Samigullin, J. M. Breunig, M. Bolte, H.-W. Lerner, M. Wagner, *Organometallics* **2011**, *30*, 2838 – 2843.
[42] J. B. Heilmann, Y. Qin, F. Jäkle, H.-W. Lerner, M. Wagner, *Inorg. Chim. Acta* **2006**, *359*, 4802 – 4806.
[43] J. B. Heilmann, M. Scheibitz, Y. Qin, A. Sundararaman, F. Jäkle, T. Kretz, M. Bolte, H.-W. Lerner, M. C. Holthausen, M. Wagner, *Angew. Chem. Int. Ed.* **2006**, *45*, 920 – 925; *Angew. Chem.* **2006**, *118*, 934 – 939.
[44] C. Cui, J. Heilmann-Brohl, A. Sánchez Perucha, M. D. Thomson, H. G. Roskos, M. Wagner, F. Jäkle, *Macromolecules* **2010**, *43*, 5256 – 5261.
[45] M. Scheibitz, H. Li, J. Schnorr, A. Sánchez Perucha, M. Bolte, H.-W. Lerner, F. Jäkle, M. Wagner, *J. Am. Chem. Soc.* **2009**, *131*, 16319 – 16329.
[46] U. Gross, D. Kaufmann, *Chem. Ber.* **1987**, *120*, 991 – 994.
[47] A. Hübner, M. Diefenbach, M. Bolte, H.-W. Lerner, M. C. Holthausen, M. Wagner, *Angew. Chem. Int. Ed.* **2012**, *51*, 12514 – 12518; *Angew. Chem.* **2012**, *124*, 12682 – 12686.
[48] A. J. Ashe III, W. Klein, R. Rousseau, *Organometallics* **1993**, *12*, 3225 – 3231.
[49] L. G. Mercier, W. E. Piers, M. Parvez, *Angew. Chem. Int. Ed.* **2009**, *48*, 6108 – 6111; *Angew. Chem.* **2009**, *121*, 6224 – 6227.
[50] A. Lorbach, C. Reus, M. Bolte, H.-W. Lerner, M. Wagner, *Adv. Synth. Catal.* **2010**, *352*, 3443 – 3449.
[51] C. Reus, N.-W. Liu, M. Bolte, H.-W. Lerner, M. Wagner, *J. Org. Chem.* **2012**, *77*, 3518 – 3523.
[52] S. Kirschner, J.-M. Mewes, M. Bolte, H.-W. Lerner, A. Dreuw, M. Wagner, *Chem. Eur. J.* **2017**, *23*, 5104 – 5116.
[53] W. Schacht, D. Kaufmann, *J. Organomet. Chem.* **1987**, *331*, 139 – 152.
[54] J. Chen, J. W. Kampf, A. J. Ashe III, *Organometallics* **2008**, *27*, 3639 – 3641.
[55] E. Januszewski, A. Lorbach, R. Grewal, M. Bolte, J. W. Bats, H.-W. Lerner, M. Wagner, *Chem. Eur. J.* **2011**, *17*, 12696 – 12705.
[56] C. Reus, S. Weidlich, M. Bolte, H.-W. Lerner, M. Wagner, *J. Am. Chem. Soc.* **2013**, *135*, 12892 – 12907.
[57] S. Luliński, J. Smętek, K. Durka, J. Serwatowski, *Eur. J. Org. Chem.* **2013**, 8315 – 8322.
[58] K. Schickedanz, Dissertation, Goethe Universität (Frankfurt/Main), **2017**.
[59] A. John, M. Bolte, H.-W. Lerner, M. Wagner, *Angew. Chem. Int. Ed.* **2017**, *56*, 5588 – 5592; *Angew. Chem.* **2017**, *129*, 5680 – 5684.
[60] F. Miyamoto, S. Nakatsuka, K. Yamada, K. Nakayama, T. Hatakeyama, *Org. Lett.* **2015**, *17*, 6158 – 6161.
[61] K. Matsuo, S. Saito, S. Yamaguchi, *J. Am. Chem. Soc.* **2014**, *136*, 12580 – 12583.
[62] C. Dou, S. Saito, K. Matsuo, I. Hisaki, S. Yamaguchi, *Angew. Chem. Int. Ed.* **2012**, *51*, 12206 – 12210; *Angew. Chem.* **2012**, *124*, 12372 – 12376.
[63] S. Osumi, S. Saito, C. Dou, K. Matsuo, K. Kume, H. Yoshikawa, K. Awaga, S. Yamaguchi, *Chem. Sci.* **2016**, *7*, 219 – 227.
[64] C. Hoffend, F. Schödel, M. Bolte, H.-W. Lerner, M. Wagner, *Chem. Eur. J.* **2012**, *18*, 15394 – 15405.
[65] C. Dou, S. Saito, S. Yamaguchi, *J. Am. Chem. Soc.* **2013**, *135*, 9346 – 9349.
[66] Z. Zhou, A. Wakamiya, T. Kushida, S. Yamaguchi, *J. Am. Chem. Soc.* **2012**, *134*, 4529 – 4532.
[67] T. Kushida, C. Camacho, A. Shuto, S. Irle, M. Muramatsu, T. Katayama, S. Ito, Y. Nagasawa, H. Miyasaka, E. Sakuda, N. Kitamura, Z. Zhou, A. Wakamiya, S. Yamaguchi, *Chem. Sci.* **2014**, *5*, 1296 – 1304.
[68] T. Kushida, S. Shirai, N. Ando, T. Okamoto, H. Ishii, H. Matsui, M. Yamagishi, T. Uemura, J. Tsurumi, S. Watanabe, J. Takeya, S. Yamaguchi, *J. Am. Chem. Soc.* **2017**, *139*, 14336 – 14339.
[69] J. F. Araneda, B. Neue, W. E. Piers, M. Parvez, *Angew. Chem. Int. Ed.* **2012**, *51*, 8546 – 8550; *Angew. Chem.* **2012**, *124*, 8674 – 8678.
[70] J. F. Araneda, W. E. Piers, M. J. Sgro, M. Parvez, *Chem. Sci.* **2014**, *5*, 3189 – 3196.
[71] A. Caruso, Jr., J. D. Tovar, *Org. Lett.* **2011**, *13*, 3106 – 3109.
[72] D. R. Levine, A. Caruso, Jr., M. A. Siegler, J. D. Tovar, *Chem. Commun.* **2012**, *48*, 6256 – 6258.
[73] J. M. Farrell, D. Schmidt, V. Grande, F. Würthner, *Angew. Chem. Int. Ed.* **2017**, *56*, 11846 – 11850; *Angew. Chem.* **2017**, *129*, 12008 – 12012.
[74] V. M. Hertz, M. Bolte, H.-W. Lerner, M. Wagner, *Angew. Chem. Int. Ed.* **2015**, *54*, 8800 – 8804; *Angew. Chem.* **2015**, *127*, 8924 – 8928.
[75] V. M. Hertz, H.-W. Lerner, M. Wagner, *Org. Lett.* **2015**, *17*, 5240 – 5243.
[76] V. M. Hertz, J. G. Massoth, M. Bolte, H.-W. Lerner, M. Wagner, *Chem. Eur. J.* **2016**, *22*, 13181 – 13188.
[77] D. Crossley, R. Kahan, S. Endres, A. Warner, R. A. Smith, J. Cid, J. Dunsford, J. E. Jones, I. Vitorica-Yrzebal, M. J. Ingleson, *Chem. Sci.* **2017** https://doi.org/10.1039/C7SC02793A.
[78] A. J. Warner, J. R. Lawson, V. Fasano, M. J. Ingleson, *Angew. Chem. Int. Ed.* **2015**, *54*, 11245 – 11249; *Angew. Chem.* **2015**, *127*, 11397 – 11401.
[79] V. M. Hertz, N. Ando, M. Hirai, M. Bolte, H.-W. Lerner, S. Yamaguchi, M. Wagner, *Organometallics* **2017**, *36*, 2512 – 2519.
[80] C. Reus, F. Guo, A. John, M. Winhold, H.-W. Lerner, F. Jäkle, M. Wagner, *Macromolecules* **2014**, *47*, 3727 – 3735.
[81] A. Caruso, Jr., J. D. Tovar, *J. Org. Chem.* **2011**, *76*, 2227 – 2239.
[82] A. Shuto, T. Kushida, T. Fukushima, H. Kaji, S. Yamaguchi, *Org. Lett.* **2013**, *15*, 6234 – 6237.
[83] T. Kushida, Z. Zhou, A. Wakamiya, S. Yamaguchi, *Chem. Commun.* **2012**, *48*, 10715 – 10717.
[84] T. Kushida, S. Yamaguchi, *Organometallics* **2013**, *32*, 6654 – 6657.
[85] T. Kushida, A. Shuto, M. Yoshio, T. Kato, S. Yamaguchi, *Angew. Chem. Int. Ed.* **2015**, *54*, 6922 – 6925; *Angew. Chem.* **2015**, *127*, 7026 – 7029.
[86] K. Matsuo, S. Saito, S. Yamaguchi, *Angew. Chem. Int. Ed.* **2016**, *55*, 11984 – 11988; *Angew. Chem.* **2016**, *128*, 12163 – 12167.
[87] Z. Zhang, H. Zhang, C. Jiao, K. Ye, H. Zhang, J. Zhang, Y. Wang, *Inorg. Chem.* **2015**, *54*, 2652 – 2659.
[88] K. Durka, I. Głowacki, S. Luliński, B. Łuszczyńska, J. Smętek, P. Szczepanik, J. Serwatowski, U. E. Wawrzyniak, G. Wesela-Bauman, E. Witkowska, G. Wiosna-Sałyga, K. Woźniak, *J. Mater. Chem. C* **2015**, *3*, 1354 – 1364.
[89] M. Lorenz-Rothe, K. S. Schellhammer, T. Jägeler-Hoheisel, R. Meerheim, S. Kraner, M. P. Hein, C. Schünemann, M. L. Tietze, M. Hummert, F. Ort-

ACES Asian Chemical Editorial Society

ASIAN JOURNAL OF ORGANIC CHEMISTRY
Focus Review

mann, G. Cuniberti, C. Körner, K. Leo, *Adv. Electron. Mater.* **2016**, *2*, 1600152.
[90] A. Lorbach, M. Bolte, H. Li, H.-W. Lerner, M. C. Holthausen, F. Jäkle, M. Wagner, *Angew. Chem. Int. Ed.* **2009**, *48*, 4584 – 4588; *Angew. Chem.* **2009**, *121*, 4654 – 4658.
[91] A. Lorbach, M. Bolte, H.-W. Lerner, M. Wagner, *Chem. Commun.* **2010**, *46*, 3592 – 3594.
[92] Ö. Seven, Z.-W. Qu, H. Zhu, M. Bolte, H.-W. Lerner, M. C. Holthausen, M. Wagner, *Chem. Eur. J.* **2012**, *18*, 11284 – 11295.
[93] M. F. Smith, S. J. Cassidy, I. A. Adams, M. Vasiliu, D. L. Gerlach, D. A. Dixon, P. A. Rupar, *Organometallics* **2016**, *35*, 3182 – 3191.
[94] A. Hübner, Z.-W. Qu, U. Englert, M. Bolte, H.-W. Lerner, M. C. Holthausen, M. Wagner, *J. Am. Chem. Soc.* **2011**, *133*, 4596 – 4609.
[95] T. Kaese, A. Hübner, M. Bolte, H.-W. Lerner, M. Wagner, *J. Am. Chem. Soc.* **2016**, *138*, 6224 – 6233.
[96] A. Das, A. Hübner, M. Weber, M. Bolte, H.-W. Lerner, M. Wagner, *Chem. Commun.* **2011**, *47*, 11339 – 11341.
[97] For examples of luminescent 9-borafluorene base adducts, see: C. J. Berger, G. He, C. Merten, R. McDonald, M. J. Ferguson, E. Rivard, *Inorg. Chem.* **2014**, *53*, 1475 – 1486.
[98] A. Hübner, A. M. Diehl, M. Bolte, H.-W. Lerner, M. Wagner, *Organometallics* **2013**, *32*, 6827 – 6833.
[99] A. Lorbach, M. Bolte, H. W. Lerner, M. Wagner, *Organometallics* **2010**, *29*, 5762 – 5765.
[100] E. von Grotthuss, M. Diefenbach, M. Bolte, H.-W. Lerner, M. C. Holthausen, M. Wagner, *Angew. Chem. Int. Ed.* **2016**, *55*, 14067 – 14071; *Angew. Chem.* **2016**, *128*, 14273 – 14277.
[101] A. Hübner, M. Bolte, H.-W. Lerner, M. Wagner, *Angew. Chem. Int. Ed.* **2014**, *53*, 10408 – 10411; *Angew. Chem.* **2014**, *126*, 10576 – 10579.
[102] T. Kaese, H. Budy, M. Bolte, H.-W. Lerner, M. Wagner, *Angew. Chem. Int. Ed.* **2017**, *56*, 7546 – 7550; *Angew. Chem.* **2017**, *129*, 7654 – 7658.
[103] A. Iida, S. Yamaguchi, *J. Am. Chem. Soc.* **2011**, *133*, 6952 – 6955.
[104] A. Hübner, A. M. Diehl, M. Diefenbach, B. Endeward, M. Bolte, H.-W. Lerner, M. C. Holthausen, M. Wagner, *Angew. Chem. Int. Ed.* **2014**, *53*, 4832 – 4835; *Angew. Chem.* **2014**, *126*, 4932 – 4935.
[105] A. Hübner, T. Kaese, M. Diefenbach, B. Endeward, M. Bolte, H.-W. Lerner, M. C. Holthausen, M. Wagner, *J. Am. Chem. Soc.* **2015**, *137*, 3705 – 3714.
[106] J. D. Hoefelmeyer, F. P. Gabbaï, *J. Am. Chem. Soc.* **2000**, *122*, 9054 – 9055.
[107] S. Biswas, C. Maichle-Mössmer, H. F. Bettinger, *Chem. Commun.* **2012**, *48*, 4564 – 4566.
[108] S. Biswas, I. M. Oppel, H. F. Bettinger, *Inorg. Chem.* **2010**, *49*, 4499 – 4506.
[109] M. Müller, C. Maichle-Mössmer, H. F. Bettinger, *Angew. Chem. Int. Ed.* **2014**, *53*, 9380 – 9383; *Angew. Chem.* **2014**, *126*, 9534 – 9537.
[110] H. F. Bettinger, M. Müller, *J. Phys. Org. Chem.* **2015**, *28*, 97 – 103.
[111] C. Sánchez-Sánchez, S. Brüller, H. Sachdev, K. Müllen, M. Krieg, H. F. Bettinger, A. Nicolaï, V. Meunier, L. Talirz, R. Fasel, P. Ruffieux, *ACS Nano* **2015**, *9*, 9228 – 9235.
[112] Y. Shoji, N. Tanaka, S. Muranaka, N. Shigeno, H. Sugiyama, K. Takenouchi, F. Hajjaj, T. Fukushima, *Nat. Commun.* **2016**, *7*, 12704.
[113] A. Iida, A. Sekioka, S. Yamaguchi, *Chem. Sci.* **2012**, *3*, 1461 – 1466.
[114] Ö. Seven, S. Popp, M. Bolte, H.-W. Lerner, M. Wagner, *Dalton Trans.* **2014**, *43*, 8241 – 8253.
[115] L. Schweighauser, H. A. Wegner, *Chem. Eur. J.* **2016**, *22*, 14094 – 14103.
[116] S. N. Kessler, H. A. Wegner, *Org. Lett.* **2010**, *12*, 4062 – 4065.
[117] S. N. Kessler, M. Neuburger, H. A. Wegner, *J. Am. Chem. Soc.* **2012**, *134*, 17885 – 17888.
[118] L. Schweighauser, I. Bodoky, S. N. Kessler, D. Häussinger, C. Donsbach, H. A. Wegner, *Org. Lett.* **2016**, *18*, 1330 – 1333.
[119] L. Hong, S. Ahles, M. A. Strauss, C. Logemann, H. A. Wegner, *Org. Chem. Front.* **2017**, *4*, 871 – 875.
[120] Z. Lu, L. Schweighauser, H. Hausmann, H. A. Wegner, *Angew. Chem. Int. Ed.* **2015**, *54*, 15556 – 15559; *Angew. Chem.* **2015**, *127*, 15777 – 15780.
[121] D. W. Stephan, *Science* **2016**, *354*, 1248 – 1255.
[122] S. Agnoli, M. Favaro, *J. Mater. Chem. A* **2016**, *4*, 5002 – 5025.
[123] J. Cai, P. Ruffieux, R. Jaafar, M. Bieri, T. Braun, S. Blankenburg, M. Muoth, A. P. Seitsonen, M. Saleh, X. Feng, K. Müllen, R. Fasel, *Nature* **2010**, *466*, 470 – 473.
[124] M. Treier, C. A. Pignedoli, T. Laino, R. Rieger, K. Müllen, D. Passerone, R. Fasel, *Nature Chem.* **2011**, *3*, 61 – 67.
[125] S. Kawai, S. Saito, S. Osumi, S. Yamaguchi, A. S. Foster, P. Spijker, E. Meyer, *Nat. Commun.* **2015**, *6*, 8098.
[126] R. R. Cloke, T. Marangoni, G. D. Nguyen, T. Joshi, D. J. Rizzo, C. Bronner, T. Cao, S. G. Louie, M. F. Crommie, F. R. Fischer, *J. Am. Chem. Soc.* **2015**, *137*, 8872 – 8875.

Manuscript received: September 4, 2017
Revised manuscript received: October 5, 2017
Version of record online: November 24, 2017

6.2.6. Reversible Dihydrogen Activation by Reduced Aryl Boranes as Main-Group Ambiphiles

GDCh Communications Angewandte International Edition Chemie

H_2 Activation

International Edition: DOI: 10.1002/anie.201608324
German Edition: DOI: 10.1002/ange.201608324

Reversible Dihydrogen Activation by Reduced Aryl Boranes as Main-Group Ambiphiles

Esther von Grotthuss, Martin Diefenbach, Michael Bolte, Hans-Wolfram Lerner, Max C. Holthausen, and Matthias Wagner**

Dedicated to Professor Gerhard Erker on the occasion of his 70th birthday

Abstract: *A new approach to main-group H_2 activation combining concepts of transition-metal and frustrated Lewis pair chemistry is reported. Ambiphilic, metal-like reactivity toward H_2 can be conferred to 9,10-dihydro-9,10-diboraanthracene (DBA) acceptors by the injection of two electrons. The resulting $[DBA]^{2-}$ ions cleave the H–H bond with the formation of hydridoborates under moderate conditions (T = 50–100 °C; p < 1 atm). Depending on the boron-bonded substituents R, the addition is either reversible (R = C≡CtBu) or irreversible (R = H). The reaction rate is strongly influenced by the nature and the coordination behavior of the countercation (Li^+ slower than K^+). Quantum-chemical calculations support the experimental observations and suggest a concerted, homolytic addition of H_2 across both boron atoms. As proven by the successful conversion of Me_3SiCl into Me_3SiH, the system $Li_2[DBA]/H_2$ appears generally relevant for the hydrogenation of element–halide bonds.*

Reversible activation of dihydrogen (H_2) is a common reaction of various transition-metal complexes, the most prominent example being the Wilkinson catalyst ([Rh(PPh_3)$_3$Cl]).[1] According to the generally accepted transition-state model, H_2 splitting results from the interaction between a vacant metal d orbital with the H_2 σ-MO augmented by back-bonding from a filled d orbital into the H_2 σ*-MO (Figure 1, middle; MO = molecular orbital). It was a change of paradigm when Stephan and co-workers disclosed that H_2 activation is not unique to transition metals, but is also possible with suitable combinations of main-group Lewis acids and bases.[2] For example, sterically demanding organoboranes and -phosphanes, incapable of stabilization through adduct formation (frustrated Lewis pairs, FLPs), retain their reactivity and can cooperatively act on an H_2 molecule to heterolytically cleave its covalent bond.[3] In such cases, the boron center provides the acceptor orbital, and the phosphorus lone pair takes the role of the filled metal d orbital to accomplish back donation. Moreover, optimal orbital interactions in the transition state demand a stereochemical arrangement of the two Lewis sites as shown in Figure 1, left.[3] Conceptually, a comparison of the modes of action of FLPs and transition-metal centers raises the question: Do we really need the Lewis base, or can we simplify the system to just a main-group acceptor and evoke ambiphilic, metal-like behavior toward H_2 by injecting two electrons?

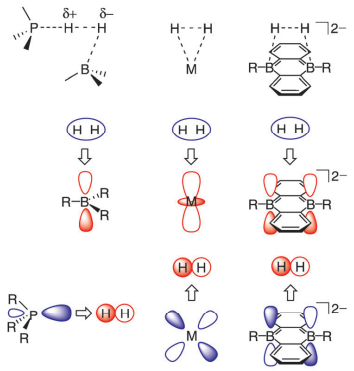

Figure 1. Transition-state orbital interactions relevant for H_2 activation: Heterolytic cleavage by FLPs (left) versus homolytic cleavage at a transition-metal center (middle) and at $[DBA]^{2-}$ (right). HOMOs and LUMOs are shown in blue and red, respectively.

Numerous aryl boranes are redox active.[4] Among them, derivatives of 9,10-dihydro-9,10-diboraanthracene (DBA) stand out for their ability to accept two electrons in a reversible manner ($[DBA]^{2-}$).[5–7] Both boron atoms are also ideally prearranged within the rigid scaffold for cooperative action.[8] Notably, the HOMO and the LUMO of $[DBA]^{2-}$ have the same local symmetries at the boron atoms as the corresponding frontier orbitals involved in metal-mediated H_2 splitting (Figure 1, right).[6] As a related case, we have previously demonstrated that the derivative Li_2[**1**] reacts with terminal alkynes, such as HC≡CtBu, through C–H splitting to give an addition product of the type Li_2[**2**] (Scheme 1).[7] Herein, we show that $[DBA]^{2-}$ is actually capable of adding H_2 across the two boron atoms

[*] M. Sc. E. von Grotthuss, Dr. M. Diefenbach, Dr. M. Bolte, Dr. H.-W. Lerner, Prof. Dr. M. C. Holthausen, Prof. Dr. M. Wagner
Institut für Anorganische Chemie, Goethe-Universität Frankfurt
Max-von-Laue-Strasse 7, 60438 Frankfurt (Main) (Germany)
E-mail: Max.Holthausen@chemie.uni-frankfurt.de
Matthias.Wagner@chemie.uni-frankfurt.de

Supporting information for this article can be found under: http://dx.doi.org/10.1002/anie.201608324.

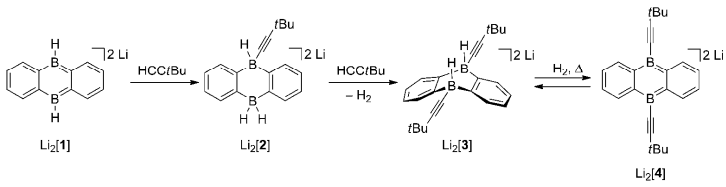

Scheme 1. The $[DBA]^{2-}$ derivative Li$_2$[**1**] reacts with HC≡C*t*Bu to form Li$_2$[**2**] or Li$_2$[**3**]. At elevated temperatures, a dynamic equilibrium exists between Li$_2$[**3**] and Li$_2$[**4**]/H_2.

under mild conditions. The ability to undergo this prototypical reaction renders our system unique among main-group ambiphiles (MGAs).[9]

We first revisited and optimized the reaction between Li$_2$[**1**] and HC≡C*t*Bu: An equimolar mixture of both compounds furnished the monoalkynyl derivative Li$_2$[**2**] together with Li$_2$[**3**] (Scheme 1). In contrast, selective formation of Li$_2$[**3**] was observed upon the treatment of Li$_2$[**1**] with excess HC≡C*t*Bu (4 equiv) at 50 °C for 3 days. Remarkably, the crude product gave rise to only one set of signals in the ^{1}H and ^{13}C{^{1}H} NMR spectra, thus ruling out the presence of *syn*/*anti* isomers. In the majority of crystallographically characterized DBA derivatives with tetracoordinated boron atoms, the central B_2C_4 ring adopts a boat conformation in the solid state (the same is true for Li$_2$[**5**]; Figure 5b; see below).[10] If this preferred conformation prevails also in solution, the sterically more demanding alkynyl substituents of Li$_2$[**3**] should occupy both equatorial positions, which would not only explain the observed NMR spectral features, but also place the two hydrogen substituents in the axial positions and thereby render them ideally preoriented for the concerted elimination of H_2. Given this background, we continued our investigations with the thermolysis of Li$_2$[**3**] in a closed system.

A solution of Li$_2$[**3**] in [D$_8$]THF in a vacuum-sealed NMR tube was heated to 100 °C over a period of several days, and the reaction progress was monitored by ^{1}H NMR spectroscopy at room temperature (see Figure S1 in the Supporting Information). We observed a successive decrease in the amount of Li$_2$[**3**] with the concomitant formation of H_2 ($\delta(^1H) = 4.55$ ppm[11]) and a new symmetrical $[DBA]^{2-}$ derivative, identified as Li$_2$[**4**] ($\delta(^{11}B) = 13.7$ ppm). After 8 days at 100 °C, a stationary state was reached (Li$_2$[**3**]/Li$_2$[**4**] ≈ 1:2). The relative proportion of Li$_2$[**3**] in the reaction mixture increased again (Li$_2$[**3**]/Li$_2$[**4**] ≈ 1:1) when the temperature was subsequently lowered to 50 °C, which corresponds to the conditions initially applied for the synthesis of Li$_2$[**3**]. X-ray crystallography on [Li(thf)$_2$]$_2$[**4**] revealed an essentially planar tricylic core structure ($\Sigma B^{CCC} = 360°$; Figure 5a); no residual electron density attributable to BH hydrogen atoms was present in the electron-density map. Similar to the solid-state structure of Li$_2$[**1**],[6,7] two $[Li(thf)_2]^+$ cations are located above and below the centroid (COG) of the B_2C_4 ring (Li^+···COG distance: 1.942(5) Å).

The experimental data acquired so far indicate that the conversion of Li$_2$[**3**] into Li$_2$[**4**] is a reversible thermolysis reaction. In a closed system from which H_2 can not escape, a dynamic equilibrium between Li$_2$[**3**] and Li$_2$[**4**]/H_2 exists: At 100 °C, the equilibrium is shifted to the side of Li$_2$[**4**], at 50 °C, both organoboron species are equally abundant, and at room temperature, the equilibrium is largely frozen in (see the Supporting Information). To further confirm this conclusion, we prepared an authentic sample of Li$_2$[**4**] through the reduction of **4** with lithium metal in [D$_8$]THF. The solution was transferred to an NMR tube, covered with a blanket of H_2 (< 1 atm), and flame-sealed. At this stage, exclusively Li$_2$[**4**] was detectable in the ^{1}H NMR spectrum (Figure 2). Upon heating to 100 °C,

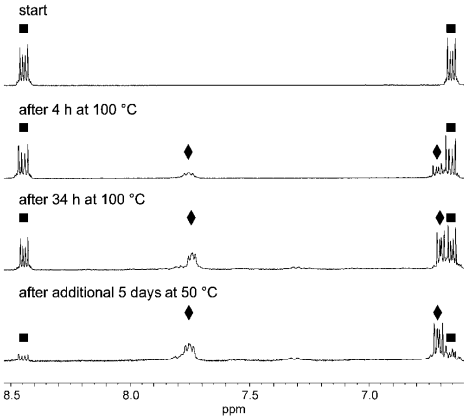

Figure 2. Changes in the ^{1}H NMR spectrum (500.2 MHz, [D$_8$]THF) of a solution of Li$_2$[**4**] under an H_2 atmosphere (< 1 atm) upon heat treatment. The spectra were recorded at room temperature in a flame-sealed NMR tube; ■ Li$_2$[**4**], ◆ Li$_2$[**3**].

the signals belonging to Li$_2$[**4**] lost intensity, whereas resonances assignable to Li$_2$[**3**] gradually evolved. After 34 h, the ratio between Li$_2$[**4**] and Li$_2$[**3**] approached 1:1. The largest fraction of Li$_2$[**3**] was again generated after further heating of the sample at 50 °C. Since the amount of H_2 was significantly higher in the H_2-activation experiment as compared to the thermolysis reaction, the equilibrium was reached faster, and the equilibrating mixture contained a higher relative proportion of Li$_2$[**3**]. However, irrespective of the conditions applied, the conversion of Li$_2$[**4**] into Li$_2$[**3**] could never be driven to completion. This finding agrees with the assumption of a dynamic equilibrium between Li$_2$[**3**] and Li$_2$[**4**]/H_2.

We next attempted H_2 activation by the parent system Li$_2$[**1**]. In the presence of excess H_2 (< 1 atm) and at 100 °C, solutions of Li$_2$[**1**] in [D$_8$]THF afforded the hydrogen-addition

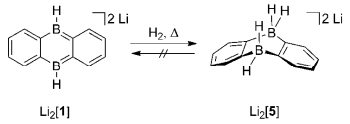

Scheme 2. Irreversible H_2 addition to Li_2[**1**] to afford Li_2[**5**].

product Li_2[**5**] in quantitative yield after 2 days (Scheme 2). Contrary to Li_2[**3**], vacuum-sealed solutions of Li_2[**5**] in THF showed no tendency to liberate H_2 at temperatures up to 100 °C. The chemical composition of Li_2[**5**] was confirmed by a comparison of its NMR data with those of a sample independently prepared from 9,10-dihydroxy-DBA and $LiAlH_4$.[12] According to X-ray crystal-structure analysis of [Li(thf)$_2$][Li(thf)][**5**], the central B_2C_4 heterocycle of the dianionic moiety [**5**]$^{2-}$ adopts a boat conformation with a dihedral angle C1B1C11//C2B2C12 of 56.2(3)° (Figure 5b). All four BH hydrogen atoms were isotropically refined. As a blind test, we also heated solutions of Li_2[**1**] in THF in the absence of H_2 to 100 °C, but observed no formation of Li_2[**5**]. Moreover, the deuterium analogue Li_2[**1**-D_2] of Li_2[**1**] was prepared by two-electron reduction of 9,10-dideuterio-DBA with lithium metal. Subsequent H_2 activation in [D_8]THF afforded Li_2[**5**-D_2], which exhibited a signal for boron-bonded deuterium atoms at 2.29 ppm in the $^2H\{^{11}B\}$ NMR spectrum and a BH resonance, which integrated to 2H (instead of 4H), at the same chemical-shift value in the ^1H NMR spectrum (see the Supporting Information).

For future applications of MGAs as hydrogenation catalysts, it would be desirable to further accelerate the H_2-activation reaction and to lower the required temperatures. For this goal to be achieved, a largely unhindered interaction of the H_2 molecule with the B_2C_4 ring has to be ensured. The solid-state structure of Li_2[**1**] shows two [Li(thf)$_2$]$^+$ ions coordinated to both sides of the heterocyclic core, thereby blocking access to the boron centers. A prominent resonance at −9.0 ppm in the room-temperature ^7Li NMR spectrum of Li_2[**1**] proves that the compound forms contact-ion pairs also in [D_8]THF solution (similar observations hold for Li_2[**4**]).[1] We therefore assumed that heating is (at least in part) required to break up ion pairing and create the necessary space for the incoming H_2 substrate. Cation dissociation can alternatively be promoted by an exchange of Li^+ for K^+, because K^+ tends to bind organic π-electron systems less tightly than Li^+.[13] K_2[**1**] was synthesized by the reduction of **1** with KC_8 (2 equiv). A comparison of the ^1H NMR spectra of K_2[**1**] and Li_2[**1**] revealed a close relationship between both species. Small but significant shifts of their NMR signals are probably due to the aimed-for differences in cation coordination. This assumption is supported by the observation that the addition of 12-crown-4 to a solution of Li_2[**1**] in [D_8]THF had a similar qualitative effect on the proton resonances of [**1**]$^{2-}$ as the replacement of Li^+ with K^+ (see Figure S4).

To compare the reactivities of Li_2[**1**], Li_2[**1**]/12-crown-4, and K_2[**1**], equimolar solutions of the three salts in [D_8]THF were prepared in NMR tubes under an atmosphere of H_2 (< 1 atm) and flame-sealed. After heating at 50 °C for 24 h, the sample with Li_2[**1**] contained only 25 % of the dihydride adduct Li_2[**5**]. In contrast, Li_2[**5**] already constituted the major component (75 %) of the second sample. H_2 activation by K_2[**1**] was quantitative in less than 15 h (Figure 3; see also the Supporting Information).

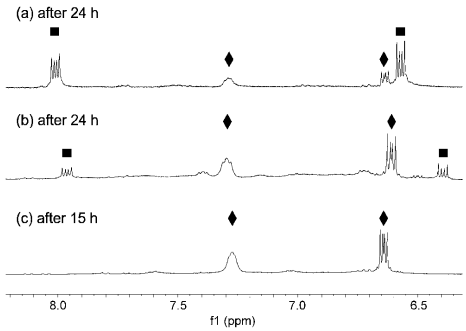

Figure 3. ^1H NMR spectra (300.0 MHz, [D_8]THF) showing the progress of H_2 activation (< 1 atm) at 50 °C by a) Li_2[**1**], b) Li_2[**1**]/12-crown-4, and c) K_2[**1**]. ■ M_2[**1**], ◆ M_2[**5**].

Mechanistically, two scenarios for the H_2 activation appear plausible: i) On the basis of the nodal structures of the frontier orbitals of [**1**]$^{2-}$ discussed above (see Figure 1 and the Supporting Information), a metal-like, concerted addition of H_2 to both boron atoms is conceivable; ii) on the basis of the mesomeric resonance structures of [**1**]$^{2-}$ shown in Figure 4, an FLP-like, heterolytic addition of H_2 to one boron atom and to its electronegative *ipso* carbon neighbor could also take place,[14] followed by hydrogen-atom migration from the carbon atom to the second boron atom. For further insight, we performed quantum-chemical calculations on both pathways (Figure 4). Commencing with the bare dianion [**1**]$^{2-}$, H_2 activation by concerted 9,10-addition

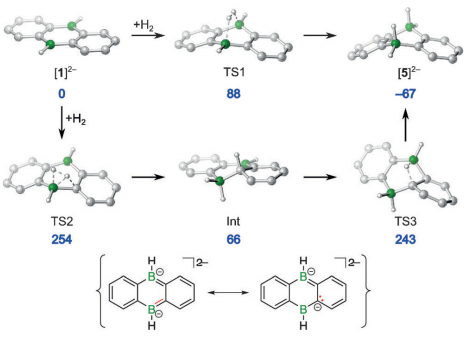

Figure 4. Reaction paths for the addition of H_2 to [**1**]$^{2-}$ (ΔG^{298} in kJ mol^{-1}, B2GP-PLYP-D/CBS(T,Q)//SMD-PBE0D/6-31 + G(d,p) calculations). The barrier for the inversion of [**5**]$^{2-}$ via a planar transition structure is $\Delta G^{\ddagger}_{inv} = 9$ kJ mol^{-1}.

requires passage of a moderate activation barrier ($\Delta G^{\ddagger} = 88\ kJ\ mol^{-1}$), and the formation of $[\mathbf{5}]^{2-}$ is exergonic by $\Delta_r G = -67\ kJ\ mol^{-1}$. Alternative 1,2-addition across the B–C bond (**TS2**) as well as subsequent [1,3]-H migration (**TS3**) are kinetically strongly disfavored and can safely be discarded in this case.[15] The presence of alkynyl substituents in $[\mathbf{4}]^{2-}$ hardly affects the computed activation barrier, but leads to a significantly less stable dihydride adduct (Table 1), consistent with the experimentally observed reversibility of the H_2 addition only for $[\mathbf{3}]^{2-}$. To assess the influence of coordinating counterions, we computed the H_2-activation paths for $[M(thf)_2]_2[\mathbf{1}]$ (M = Li, K; Figure 5c). In the optimized reactant structure $\mathbf{A_{Li}}$, both $Li(thf)_2$ groups assume an η^6 coordination mode above and below the central B_2C_4 ring, in agreement with the published X-ray data for $[Li(thf)_2]_2[\mathbf{1}]$.[7] In the transition state $\mathbf{TS_{Li}}$, one of the $Li(thf)_2$ groups slips into an η^2 coordination mode, thereby vacating space for the incoming H_2. As compared to the bare dianion, a moderately increased activation barrier results, and the transition state $\mathbf{TS_{Li}}$ is directly connected to $\mathbf{B_{Li}}$ (a slightly less stable minimum, more closely resembling the solid-state structure of $[Li(thf)_2][Li(thf)][\mathbf{5}]$, was also identified; see the Supporting Information). The same reaction path computed for M = K results in a lower activation barrier and higher product stability (Table 1), in line with the experimental observation of faster H_2 addition (see above). These differences are accompanied by a change in the metal coordination in $\mathbf{TS_K}$ and a planarized central B_2C_4 ring in $\mathbf{B_K}$.

Table 1: Activation barriers and product stabilities computed for the addition of H_2 to selected substrates (ΔG^{298} in kJ mol^{-1}, B2GP-PLYP-D/CBS(T,Q)//SMD-PBE0D/6-31+G(d,p) level of theory).

	$[\mathbf{1}]^{2-}$	$[\mathbf{4}]^{2-}$	$[Li(thf)_2]_2[\mathbf{1}]$	$[K(thf)_2]_2[\mathbf{1}]$	anthracene[15]
reactants	0	0	0	0	0
transition state	88	92	112	101	191
product	−67	−33	−28	−63	−33

To conclude, MGAs, such as $M_2[\mathbf{1}]$, must be conceptually distinguished from FLPs, such as R_3B/PR'_3: In the latter, the H_2 molecule undergoes heterolytic cleavage with a proton ending up at the Lewis base and a hydride ion at the Lewis acid. $M_2[\mathbf{1}]$ salts, however, generate two hydride ions from one H_2 molecule. $Li_2[\mathbf{4}]$ apparently adopts an intermediate position, because, similar to certain B/P FLPs, H_2 can be released again from the addition product $Li_2[\mathbf{3}]$. Given this overall background, $M_2[\mathbf{1}]$ salts are ideally suited for such reduction reactions, during which a hydride ion substitutes an appropriate leaving group. We are particularly interested in the economic conversion of chlorosilanes into hydrosilanes owing to their widespread application potential.[16] As a proof-of-principle experiment, $Li_2[\mathbf{5}]$ in $[D_8]$THF was treated with Me_3SiCl (2 equiv). In addition to quantitatively affording Me_3SiH, the reaction left the DBA skeleton (largely) intact. This result opens the perspective of converting element halides into element hydrides by use of a reducing agent and H_2 in the presence of suitably chosen 9,10-dihydro-9,10-diboraanthracenes as redox catalysts.

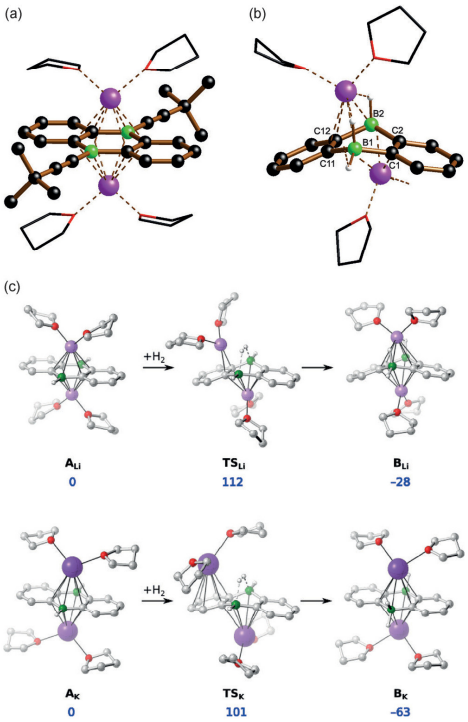

Figure 5. a,b) Solid-state structures of $[Li(thf)_2]_2[\mathbf{4}]$ (a) and $[Li(thf)_2][Li(thf)][\mathbf{5}]$ (b); H atoms bonded to carbon atoms are omitted for clarity. $[Li(thf)_2][Li(thf)][\mathbf{5}]$ forms coordination polymers in the crystal lattice. c) Reaction paths for the addition of H_2 to $[M(thf)_2]_2[\mathbf{1}]$ (M = Li, K; ΔG^{298} in kJ mol^{-1}, B2GP-PLYP-D/CBS(T,Q)//SMD-PBE0D/6-31+G-(d,p) calculations).

Acknowledgements

We gratefully acknowledge the help of Dr. C. Richter with ^2H NMR spectroscopy.

Keywords: boron · H_2 activation · main-group ambiphiles · quantum-chemical calculations · reduction

How to cite: *Angew. Chem. Int. Ed.* **2016**, *55*, 14067–14071
Angew. Chem. **2016**, *128*, 14273–14277

[1] C. Elschenbroich, *Organometallics*, Wiley-VCH, Weinheim, **2006**.
[2] G. C. Welch, R. R. San Juan, J. D. Masuda, D. W. Stephan, *Science* **2006**, *314*, 1124–1126.
[3] a) *Frustrated Lewis Pairs I & II* (Eds.: G. Erker, D. W. Stephan), Springer, Heidelberg, **2013**; b) D. W. Stephan, G. Erker, *Chem. Sci.* **2014**, *5*, 2625–2641; c) D. W. Stephan, *J. Am. Chem. Soc.* **2015**, *137*, 10018–10032.

[4] a) F. Jäkle, *Chem. Rev.* **2010**, *110*, 3985 – 4022; b) V. M. Hertz, M. Bolte, H.-W. Lerner, M. Wagner, *Angew. Chem. Int. Ed.* **2015**, *54*, 8800 – 8804; *Angew. Chem.* **2015**, *127*, 8924 – 8928.

[5] C. Reus, S. Weidlich, M. Bolte, H. W. Lerner, M. Wagner, *J. Am. Chem. Soc.* **2013**, *135*, 12892 – 12907.

[6] C. Hoffend, M. Diefenbach, E. Januszewski, M. Bolte, H.-W. Lerner, M. C. Holthausen, M. Wagner, *Dalton Trans.* **2013**, *42*, 13826 – 13837.

[7] A. Lorbach, M. Bolte, H.-W. Lerner, M. Wagner, *Organometallics* **2010**, *29*, 5762 – 5765.

[8] a) A. Lorbach, M. Bolte, H.-W. Lerner, M. Wagner, *Chem. Commun.* **2010**, *46*, 3592 – 3594; b) Ö. Seven, S. Popp, M. Bolte, H.-W. Lerner, M. Wagner, *Dalton Trans.* **2014**, *43*, 8241 – 8253; c) L. Schweighauser, H. A. Wegner, *Chem. Eur. J.* **2016**, *22*, 14094 – 14103.

[9] The uncharged 1,4,2,5-diazadiborinine FLP analogue described by Kinjo and co-workers possesses an ambiphilic nature; however, H_2 activation has not been reported: B. Wang, Y. Li, R. Ganguly, H. Hirao, R. Kinjo, *Nat. Commun.* **2016**, *7*, 11871. There is precedent for H_2 splitting by ambiphilic cyclic alkyl amino carbenes (CAACs) and aromatic triphosphabenzenes: G. D. Frey, V. Lavallo, B. Donnadieu, W. W. Schoeller, G. Bertrand, *Science* **2007**, *316*, 439 – 441; L. E. Longobardi, C. A. Russell, M. Green, N. S. Townsend, K. Wang, A. J. Holmes, S. B. Duckett, J. E. McGrady, D. W. Stephan, *J. Am. Chem. Soc.* **2014**, *136*, 13453 – 13457.

[10] CSD (Version 5.37, November 2015, plus three updates): C. R. Groom, I. J. Bruno, M. P. Lightfoot, S. C. Ward, *Acta Crystallogr. Sect. B* **2016**, *72*, 171 – 179).

[11] G. R. Fulmer, A. J. M. Miller, N. H. Sherden, H. E. Gottlieb, A. Nudelman, B. M. Stoltz, J. E. Bercaw, K. I. Goldberg, *Organometallics* **2010**, *29*, 2176 – 2179.

[12] E. Januszewski, A. Lorbach, R. Grewal, M. Bolte, J. W. Bats, H.-W. Lerner, M. Wagner, *Chem. Eur. J.* **2011**, *17*, 12696 – 12705.

[13] a) M. Ichikawa, K. Tamaru, *J. Am. Chem. Soc.* **1971**, *93*, 2079 – 2080; b) A. H. Ilkhechi, J. M. Mercero, I. Silanes, M. Bolte, M. Scheibitz, H.-W. Lerner, J. M. Ugalde, M. Wagner, *J. Am. Chem. Soc.* **2005**, *127*, 10656 – 10666.

[14] a) C. Fan, L. G. Mercier, W. E. Piers, H. M. Tuononen, M. Parvez, *J. Am. Chem. Soc.* **2010**, *132*, 9604 – 9606; b) A. Y. Houghton, V. A. Karttunen, C. Fan, W. E. Piers, H. M. Tuononen, *J. Am. Chem. Soc.* **2013**, *135*, 941 – 947; c) Z.-W. Qu, H. Zhu, *J. Phys. Chem. C* **2013**, *117*, 11989 – 11993.

[15] Remarkably, anthracene, an isoelectronic congener of $[\mathbf{1}]^{2-}$, shows no tendency to add H_2 under comparable conditions. Correspondingly, our quantum-chemical results for this system reveal an activation barrier more than twice as high as that in the $[\mathbf{1}]^{2-}/H_2$ system (Table 1; see also the Supporting Information). Concerted H_2 elimination from 9,10-dihydroanthracene upon UV irradiation has been reported: Y. Fu, J. Szczepanski, N. C. Polfer, *Astrophys. J.* **2012**, *744*, 61.

[16] a) M. A. Brook, *Silicon in Organic, Organometallic, and Polymer Chemistry*, Wiley, Weinheim, **1999**; b) J. B. Grande, T. Urlich, T. Dickie, M. A. Brook, *Polym. Chem.* **2014**, *5*, 6728 – 6739.

Received: August 25, 2016
Published online: October 6, 2016

Angewandte Chemie
Eine Zeitschrift der Gesellschaft Deutscher Chemiker

Supporting Information

Reversible Dihydrogen Activation by Reduced Aryl Boranes as Main-Group Ambiphiles

Esther von Grotthuss, Martin Diefenbach, Michael Bolte, Hans-Wolfram Lerner, Max C. Holthausen, and Matthias Wagner**

anie_201608324_sm_miscellaneous_information.pdf

Table of contents:

1. Experimental details and characterization data

General Considerations. All reactions, manipulations and analyses were carried out in an argon-filled glovebox or by applying standard Schlenk techniques under a nitrogen atmosphere. Toluene, C_6H_6, Et_2O, and THF were dried over Na/benzophenone; [D_8]THF was dried over Na-K alloy without benzophenone. Prior to use, the solvents were distilled from the drying agent; THF/[D_8]THF were degassed by applying three freeze-pump-thaw cycles when used for reduction reactions.

NMR spectra were recorded at 298 K using the following spectrometers: Bruker Avance-300, Avance-400, or Avance-500.

Chemical shifts are referenced to (residual) solvent signals (^{1}H/^{13}C{^{1}H}; [D_8]THF: δ = 3.58/67.2 ppm[11]) or external $BF_3{\cdot}Et_2O$ (^{11}B; ^{11}B{^{1}H}). Abbreviations: s = singlet, d = doublet, t = triplet, q = quartet, m = multiplet, br = broad, n.o. = not observed.

Combustion analyses were performed by the Microanalytical Laboratory Pascher (Remagen, Germany).

All H_2 activation reactions were carried out in flame-sealed NMR tubes. The experimental set-up was as follows: An NMR tube connected to a Schlenk line was charged with a solution of the respective doubly reduced 9,10-dihydro-9,10-diboraanthracene (DBA). The solution was frozen with liquid nitrogen and the system was evacuated before H_2 (5.0) was filled in through a condensation trap cooled with liquid nitrogen. The content of the NMR tube was allowed to unfreeze whereby H_2 dissolved in [D_8]THF.[2] The mixture was frozen again, the partial pressure of H_2 was adjusted such that it remained slightly below 1 atm, and the NMR tube was flame-sealed.

The compounds 9,10-dibromo-DBA[3] and **1**[4] were synthesized according to literature procedures. 9,10-Dideuterio-DBA was prepared in a similar way as **1**, using Et_3SiD instead of Et_3SiH; subsequent reduction to Li_2[**1**-D_2] was achieved following the protocol for the synthesis of Li_2[**1**] (see below). The targeted hydrolysis of 9,10-dibromo-DBA furnishes 9,10-dihydroxy-DBA, the analytical data of which are published.[3]

Synthesis of Li_2[1]: A modified literature protocol was used for the chemical reduction of **1**.[5] **1** (20 mg, 0.11 mmol) was dissolved in [D_8]THF (0.6 mL). Two lithium granules (10 mg) were added at room temperature to the pale yellow solution, whereupon the reaction mixture immediately adopted a red color. The reduction reaction was complete after 30 min of stirring. For further use, the solution was separated from residual Li metal with a syringe (we recommend to generally use freshly synthesized Li_2[**1**] for the subsequent experiments).

^{1}H{^{11}B} NMR (500.2 MHz, [D_8]THF): δ = 8.02 (m, 4H; C_6H_4), 6.58 (m, 4H; C_6H_4), 5.55 ppm (br, 2H; BH).

^{11}B NMR (160.5 MHz, [D_8]THF): δ = 20.6 ppm ($h_{1/2}$ = 320 Hz).

^{13}C{^{1}H} NMR (125.8 MHz, [D_8]THF): δ = 139.6 (C_6H_4), 118.3 ppm (C_6H_4); n.o. (BC).

Synthesis of Li_2[3]: A red solution of Li_2[**1**] (0.11 mmol; see above) in [D_8]THF (0.6 mL) was placed in an NMR tube. Excess neat HC≡C*t*Bu (0.05 mL, 0.41 mmol) was added, the NMR tube was flame-sealed, and stored at 50 °C for 3 d. Afterwards, the color of the mixture was yellow-orange, and NMR spectroscopy revealed the quantitative formation of Li_2[**3**]. The NMR tube was opened and its content evaporated to dryness under a dynamic vacuum in order to remove unreacted HC≡C*t*Bu. Yield: 55 mg (0.11 mmol, quant.; calcd. as [Li(thf)]$_2$[**3**]).

^{1}H{^{11}B} NMR (500.2 MHz, [D_8]THF): δ = 7.73 (m, 4H; C_6H_4), 6.69 (m, 4H; C_6H_4), 1.91 (br, 2H; BH), 1.33 ppm (s, 18H; CH_3).

^{11}B NMR (96.3 MHz, [D_8]THF): δ = −23.4 ppm (d, ^1J(B,H) = 67 Hz).

^{13}C{^{1}H} NMR (125.8 MHz, [D_8]THF): δ = 131.7 (C_6H_4), 122.0 (C_6H_4), 33.1 (C*C*H$_3$), 28.6 ppm (*C*CH$_3$); n.o. (BC, *C*≡*C*t*Bu).

Synthesis of 4: A solution of 9,10-dibromo-DBA (200 mg, 0.60 mmol) in toluene (20 mL) was added dropwise at room temperature to a toluene (10 mL) suspension of LiC≡C*t*Bu (111 mg, 1.26 mmol; prepared from HC≡C*t*Bu and *n*BuLi in hexane). The reaction mixture was stirred for 2 d to yield a yellow suspension. After filtration, the filtrate was evaporated to dryness under reduced pressure to afford **4** as an analytically pure orange-brown solid (130 mg, 0.39 mmol, 65%). Sublimation of **4** is possible at 140 °C/10^{-3} torr, albeit with substantial yield loss (130 mg → 27 mg). The sublimed compound formed colorless crystals, some of them were suitable for X-ray analysis.

^{1}H NMR (500.2 MHz, [D_8]THF): δ = 8.10 (m, 4H; C_6H_4), 7.37 (m, 4H; C_6H_4), 1.40 ppm (s, 18H; CH_3).

^{11}B NMR (160.5 MHz, [D_8]THF): δ = 32.7 ppm ($h_{1/2}$ = 660 Hz).

^{13}C{^{1}H} NMR (125.8 MHz, [D_8]THF): δ = 149.3 (BC), 137.2 (C_6H_4), 130.6 (C_6H_4), 122.4 (C≡*C*t*Bu), 31.3 (C*C*H$_3$), 29.0 ppm (*C*CH$_3$); n.o. (*C*≡C*t*Bu).

EA (%): calculated for $C_{24}H_{26}B_2$ [336.09]: C 85.77, H 7.80; found: C 85.02, H 7.62.

Synthesis of Li_2[4]:

*Method A (chemical reduction of **4**)*: Two lithium granules (10 mg) were added at room temperature to a solution of **4** (10 mg, 0.03 mmol) in [D_8]THF (0.6 mL), whereupon the reaction mixture immediately adopted a red color. The reduction reaction was complete after 30 min of stirring. For further use, the solution was separated from residual Li metal with a syringe (we recommend to generally use freshly synthesized Li_2[**4**] for the subsequent experiments).

Method B (thermolysis of Li_2[3]): An NMR tube was charged with Li_2[**3**] (55 mg, 0.11 mmol) and [D_8]THF (0.6 mL). After the tube had been flame-sealed, it was repeatedly heated at 100 °C for several hours. NMR spectroscopy at room temperature revealed a continuous decrease of the amount of Li_2[**3**] with a concomitant formation of Li_2[**4**] and liberation of H_2. After 8 d, a stationary point was reached at which the stoichiometric ratios of the components remained constant (Li_2[**3**]:Li_2[**4**] ≈ 1:2).

Note: The single crystal of Li_2[**4**] used for X-ray analysis was obtained from the thermolysis reaction of Li_2[**3**].

^{1}H NMR (300.0 MHz, [D_8]THF): δ = 8.46 (m, 4H; C_6H_4), 6.67 (m, 4H; C_6H_4), 1.42 ppm (s, 18H; CH_3).

^{11}B NMR (96.3 MHz, [D_8]THF): δ = 13.7 ppm ($h_{1/2}$ = 370 Hz).

^{13}C{^{1}H} NMR (75.4 MHz, [D_8]THF): δ = 137.5 (C_6H_4), 118.4 (C_6H_4), 115.1 (C≡*C*t Bu), 32.7 (C*C*H_3), 29.2 ppm (*C*CH_3); n.o. (BC, *C*≡C*t*Bu).

Synthesis of Li_2[5]:

Method A (reaction of 9,10-dihydroxy-DBA with $LiAlH_4$): A modified literature protocol was used for the synthesis of an authentic sample of Li_2[**5**].[3] 9,10-Dihydroxy-DBA was kept at room temperature under a dynamic vacuum for several hours. A sample of this pretreated 9,10-dihydroxy-DBA (30 mg, 0.14 mmol) was suspended in a mixture of Et_2O (8 mL) and C_6H_6 (2 mL). $LiAlH_4$ in THF (1 M, 0.5 mL, 0.50 mmol) was added at 0 °C, the mixture was stirred for 30 min, and allowed to warm to room temperature within 1 h. All volatiles were removed from the resulting clear solution at room temperature under reduced pressure, and the colorless solid residue was extracted into THF (0.6 mL). X-ray quality crystals of [$Li(thf)_2$][Li(thf)][**5**] were grown by slow evaporation of this solution.

Method B (hydrogenation of Li_2[1]): Following the general procedure described above, a solution of Li_2[**1**] (0.11 mmol, see above) in [D_8]THF (0.6 mL) was prepared in an NMR tube under an atmosphere of H_2. Storage of the flame-sealed NMR tube at 120 °C for 15 h resulted in the quantitative conversion of Li_2[**1**] to Li_2[**5**], accompanied by a color change of the solution from red to orange. The conversion rate is strongly temperature dependent: At 50 °C and 100 °C, 30 d and 2 d, respectively, are required.

^{1}H NMR (500.2 MHz, [D_8]THF): δ = 7.29 (m, 4H; C_6H_4), 6.64 (m, 4H; C_6H_4), 2.31 ppm (q, ^1J(B,H) = 76 Hz, 4H; BH_2).

^{11}B NMR (160.5 MHz, [D_8]THF): δ = −18.0 ppm (t, ^1J(B,H) = 76 Hz).

^{13}C{^{1}H} NMR (125.8 MHz, [D_8]THF): δ = 133.8 (C_6H_4), 122.0 ppm (C_6H_4); n.o. (BC).

Synthesis of K_2[1]: Neat solid KC_8 (20 mg, 0.148 mmol) was added at room temperature to a solution of **1** (13 mg, 0.074 mmol) in THF (1.5 mL). The mixture turned dark green within a few minutes. After stirring had been continued for 30 min, insoluble graphite was removed by filtration. The filtrate was evaporated to dryness under reduced pressure and the dark red residue was extracted into [D_8]THF (0.6 mL).

^{1}H{^{11}B} NMR (500.2 MHz, [D_8]THF): δ = 8.03 (m, 4H; C_6H_4), 6.41 (m, 4H; C_6H_4), 5.54 ppm (br, 2H; BH).

^{11}B NMR (160.5 MHz, [D_8]THF): δ = 23.5 ppm ($h_{1/2}$ = 280 Hz).

^{13}C{^{1}H} NMR (125.8 MHz, [D_8]THF): δ = 139.4 (C_6H_4), 115.1 ppm (C_6H_4); n.o. (BC).

Synthesis of K_2[5]: Following the general procedure described earlier, a solution of K_2[**1**] (0.074 mmol, see above) in [D_8]THF (0.6 mL) was prepared in an NMR tube under an atmosphere of H_2. Storage of the flame-sealed NMR tube at 50 °C for 15 h resulted in the quantitative conversion of K_2[**1**] to K_2[**5**].

^{1}H NMR (300.0 MHz, [D_8]THF): δ = 7.27 (m, 4H; C_6H_4), 6.66 (m, 4H; C_6H_4), 2.53 ppm (q, ^1J(B,H) = 76 Hz, 4H; BH_2).

^{11}B NMR (96.3 MHz, [D_8]THF): δ = −20.7 ppm (t, ^1J(B,H) = 76 Hz).

^{13}C{^{1}H} NMR (75.4 MHz, [D_8]THF): δ = 134.9 (C_6H_4), 122.4 ppm (C_6H_4); n.o. (BC).

2. Reversible addition of H_2 to Li_2[4] with formation of Li_2[3]

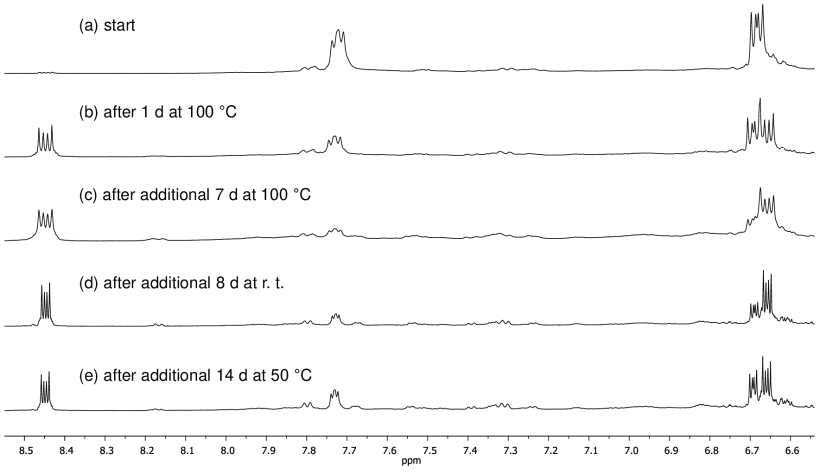

Figure S1: ^{1}H NMR spectra of a sample of Li_2[**3**] following heat treatment {(a) – (c): 300.0 MHz, (d) – (e): 500.2 MHz; [D_8]THF; recorded at room temperature in a vacuum-sealed NMR tube}. Minor resonances correspond to the monosubstituted Li_2[**2**].[5]

At the starting point, only Li_2[**3**] and no Li_2[**4**] was detectable in the ^{1}H NMR spectrum (Figure S1a). Heating at 100 °C leads to a successive decrease of the amount of Li_2[**3**] with concomitant formation of Li_2[**4**] (Figure S1b,c). After 8 d at 100 °C, the ratio between Li_2[**3**] and Li_2[**4**] was approximately 1:2 and remained essentially unchanged when the sample was stored at room temperature for additional 8 d (Figure S1d/Figure S2). Further heating to 50 °C for 14 d resulted in the partial recovery of the starting material (Li_2[**3**]:Li_2[**4**] ≈ 1:1; Figure S1e/Figure S2).

These experimental data are in line with the following interpretation: The conversion of Li_2[**3**] to Li_2[**4**] at 100 °C is not an irreversible thermolysis reaction. Rather, in a closed system from which H_2 cannot escape, a dynamic equilibrium between Li_2[**3**] and Li_2[**4**]/H_2 exists. At 100 °C, the equilibrium is shifted to the side of Li_2[**4**], at 50 °C, both organoboron species are equally abundant, and at room temperature, the equilibrium is largely frozen in.

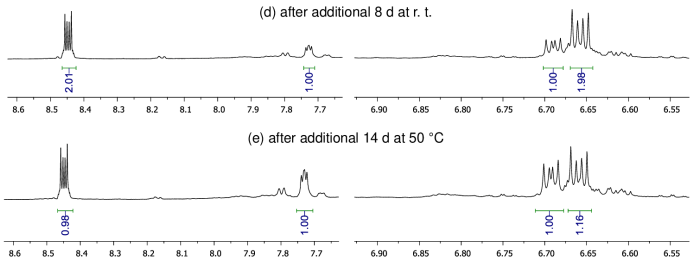

Figure S2: Details of the ^{1}H NMR spectra plotted in Figures S1d and S1e to show the relative distributions of Li_2[**3**] and Li_2[**4**].

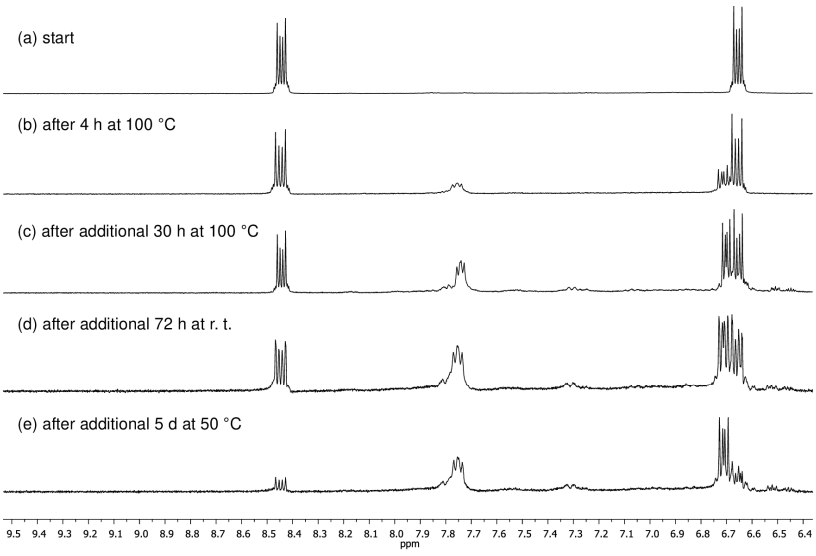

Figure S3: ^{1}H NMR spectra of a solution of Li_2[**4**] under an atmosphere of H_2 following heat treatment {500.2 MHz; [D_8]THF; recorded at room temperature in a flame-sealed NMR tube}. Minor resonances correspond to the monosubstituted Li_2[**2**].[5]

At the starting point, only Li_2[**4**] and no Li_2[**3**] was detectable in the ^{1}H NMR spectrum (Figure S3a). Heating at 100 °C leads to a successive decrease of the amount of Li_2[**4**] with concomitant formation of Li_2[**3**] (Figure S3b,c). After 34 h at 100 °C, the ratio between Li_2[**4**] and Li_2[**3**] was approximately 1:1. Subsequent storage of the sample at room temperature for 72 h resulted in a further minor increase in the amount of Li_2[**3**] (Figure S3d). The highest relative proportion of Li_2[**3**] was obtained after further heating of the sample at 50 °C for 5 d (Figure S3e). Irrespective of the reaction conditions applied, the conversion of Li_2[**4**] to Li_2[**3**] was never quantitative. This observation nicely agrees with the assumption of a dynamic equilibrium between Li_2[**3**] and Li_2[**4**]/H_2; cf. Figure S1. It is important to note at this point that the amount of H_2 was significantly smaller in the thermolysis experiment outlined in Figure S1 compared to the H_2-activation experiment outlined in Figure S3.

The NMR spectra compiled in Figure S3 unequivocally show activation of H_2 by a doubly reduced 9,10-dihyro-9,10-diboraanthracene.

3. Counterion effects on the ^{1}H NMR resonances of M_2[1] (M = Li, K)

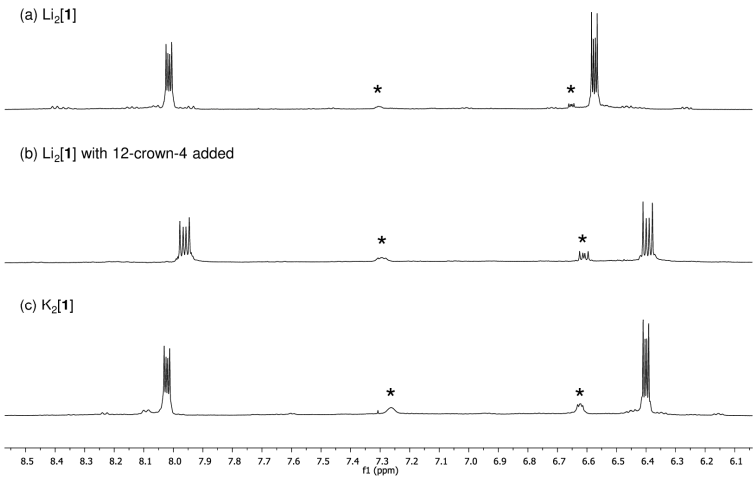

Figure S4: ^{1}H NMR spectra of DBA-dianions with different counter cations {(a) and (c): 500.2 MHz, (b): 300.0 MHz; [D_8]THF; recorded at room temperature in vacuum-sealed NMR tubes}. Signals marked with an asterisk correspond to trace amounts of M_2[**5**] (M = Li, K).

A comparison of the ^{1}H NMR spectra of Li_2[**1**] (Figure S4a) and K_2[**1**] (Figure S4c) reveals a dependence of the chemical shift values from the natures of the metal cations; the differences are particularly pronounced for the respective upfield signal. Addition of 12-crown-4 to the solution of Li_2[**1**] (Figure S3b) has a similar effect on the proton resonances as the replacement of Li^+ by K^+.

We therefore propose that a different coordination behavior of Li^+ vs. K^+ is the likely reason for the observed proton-shift differences: Even in THF solution, Li^+ tends to form contact ion pairs with the organic dianion (Figure S5 below), while K^+ is less likely to do so.[6, 7]

The minor signals marked with (*) can be assigned to the hydride adducts M_2[**5**]. The intensity of the resonances remained unchanged even after prolonged heating to 100 °C. In the case of the corresponding alkynyl-substituted dianion Li_2[**4**], which also activates H_2, analogous signals were absent unless H_2 was added. We assume that the trace amounts of M_2[**5**] detected in the NMR spectra of Figure S4 were generated during alkali metal reduction of the starting material **1**. **1** forms B–H–B-bridged polymers in the solid state;[4] oligomeric fragments are likely to prevail in THF solution.[8] We have recently shown that the reduction of related diborane(6) derivatives indeed leads to hydridoborate species.[9]

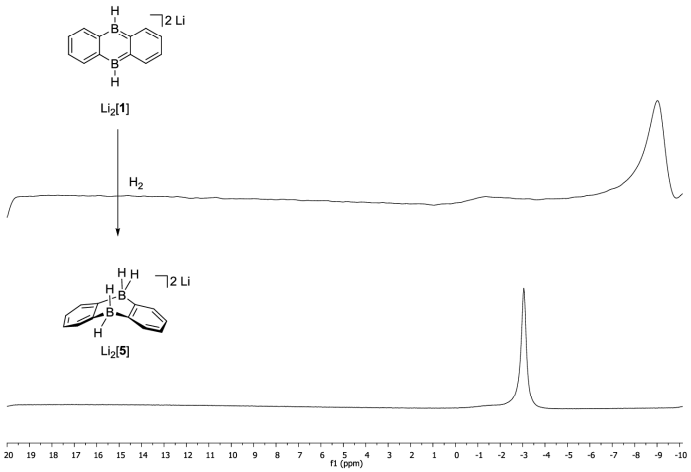

Figure S5: ^{7}Li NMR spectra (116.0 MHz, [D$_8$]THF) comparing Li$_2$[**1**] with its H$_2$ addition product Li$_2$[**5**].

The ^{7}Li NMR spectrum of Li$_2$[**1**] in [D$_8$]THF shows one major resonance at –9.0 ppm, a value typical for "structures in which the Li$^+$ cation resides above the plane of the cyclic carbanion, that is, in the shielding region of the aromatic ring current".[6] For comparison, Li$^+$C$_5$H$_5^-$ forms a contact ion pair showing a resonance at –8.37 ppm in THF solution.[6]

Upon H$_2$ activation, which generates Li$_2$[**5**], the ^{7}Li NMR signal experiences a downfield shift to $\delta(^{7}\mathrm{Li}) = -2.9$ ppm. This value is still significantly different from that of free [Li(thf)$_4$]$^+$ ($\delta(^{7}\mathrm{Li}) = -1.10$ ppm[6]), thereby indicating that the Li$^+$···HB interactions present in the solid state (cf. Figure S34) are still non-negligible in solution.

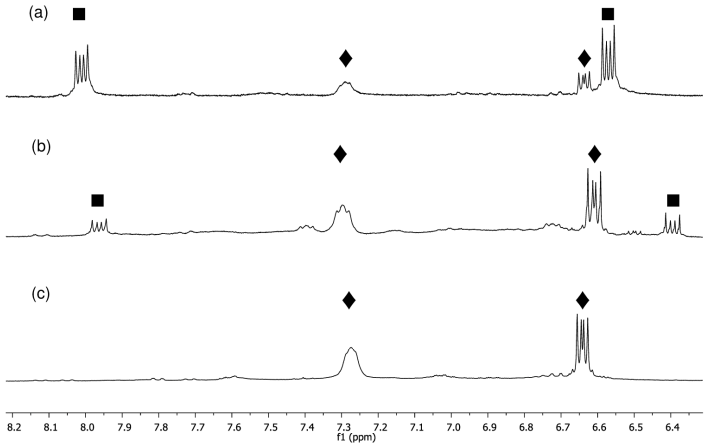

Figure S6: ^{1}H NMR spectra (300.0 MHz, [D_8]THF) showing the progress of H_2 activation at 50 °C by Li_2[**1**] (24 h; Figure S6a), Li_2[**1**]/12-crown-4 (24 h; Figure S6b), and K_2[**1**] (15 h; Figure S6c). M_2[**1**] (■), M_2[**5**] (♦).

The three systems Li_2[**1**], Li_2[**1**]/12-crown-4, and K_2[**1**] add H_2 at considerably different rates: The contact-ion pair Li_2[**1**] is the least reactive compound, while the potassium salt K_2[**1**] possesses the highest reactivity. Addition of 1 equiv 12-crown-4 to Li_2[**1**], which should weaken the cation/anion interactions, leads to a system of intermediate activity.

Contrary to the situation encountered with Li_2[**1**] and K_2[**1**] (Figure S4), the C*H* resonances of the H_2 activation products Li_2[**5**] and K_2[**5**] are essentially the same (Figure S6a vs. Figure S6c). In agreement with our interpretation of the ^{7}Li NMR spectra of Li_2[**1**] vs. Li_2[**5**] (Figure S5), this again indicates the loss of any appreciable Li^+···phenylene contacts in Li_2[**5**]. On the other hand, the B*H* signal appears at 2.31 ppm for Li_2[**5**], but at 2.53 ppm for K_2[**5**]. Thus, the preferred site of Li^+ interaction with its dianion has apparently changed to the (potentially chelating) BH moieties.

4. Deuteration experiment to prove the reactivity of H_2 with Li_2[1-D_2]

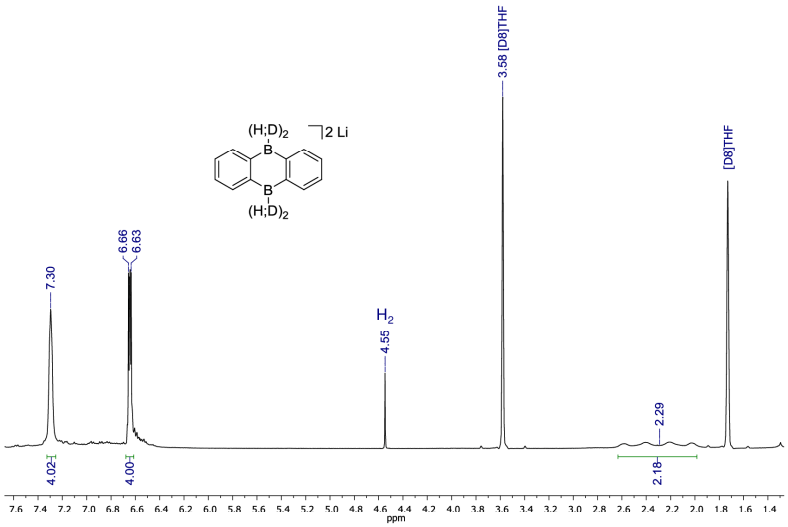

Figure S7: ^{1}H NMR spectrum after H_2 activation by Li_2[**1**-D_2] (400.1 MHz, [D_8]THF). All chemical shift values are identical to those of Li_2[**1**]. Importantly, however, the integral value of the B*H* signals corresponds to only two protons.

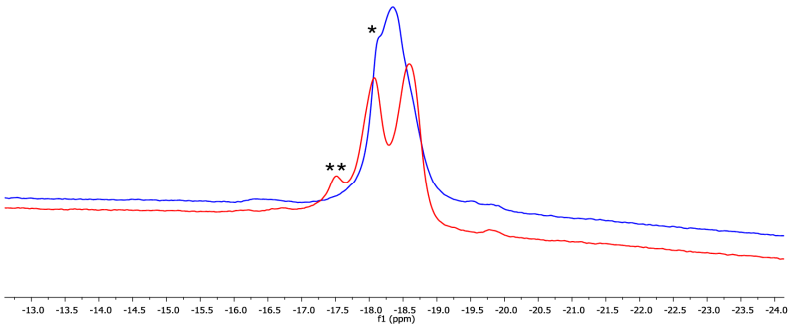

Figure S8: ^{11}B NMR spectrum (red) and ^{11}B{^{1}H} NMR spectrum (blue) of the H_2-activation product of Li_2[**1**-D_2] (128.4 MHz, [D_8]THF). The major doublet in the red spectrum (^1J(B,H) = 70 Hz) is assignable to BHD moieties. The shoulder (*) in the blue spectrum likely originates from a substituent-scrambling product containing BH_2 units. This species should give rise to a 1:2:1 ^{11}B triplet resonance; most of this triplet (**) is likely hidden underneath the major doublet in the red spectrum. The smaller ^1J(B,D) coupling is not resolved in the spectra.[10]

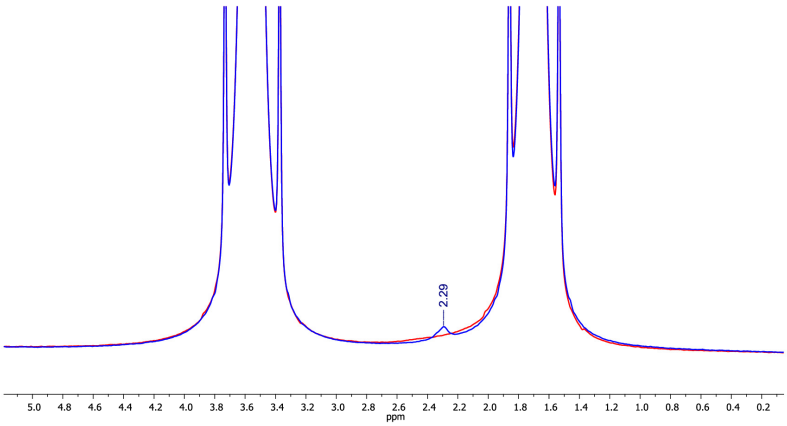

Figure S9: ^{2}H NMR spectrum (red) and ^{2}H{^{11}B} NMR spectrum (blue) of the H_2-activation product of Li_2[**1**-D_2] (61.4 MHz, [D_8]THF). Importantly, the signal at 2.29 ppm is only detectable after ^{11}B decoupling, which strongly points toward the presence of boron-bonded deuterium atoms. The chemical shift values of the B*D* nuclei are the same as those of corresponding B*H* nuclei (cf. Figure S7).

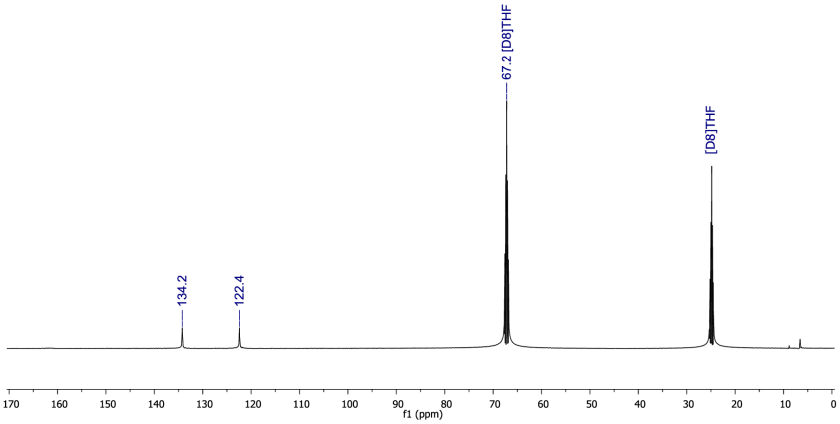

Figure S10: ^{13}C{^{1}H} NMR spectrum after H_2 activation by Li_2[**1**-D_2] (125.8 MHz, [D_8]THF).

5. Plots of the NMR spectra of Li_2[1], Li_2[3], 4, Li_2[4], Li_2[5], K_2[1], and K_2[5]

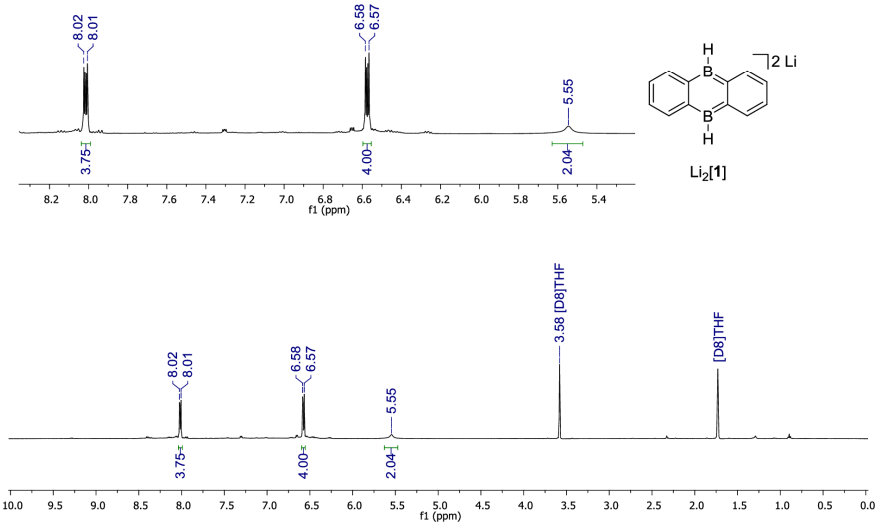

Figure S11: $^{1}H\{^{11}B\}$ NMR spectrum of Li_2[**1**] (500.2 MHz, [D_8]THF).

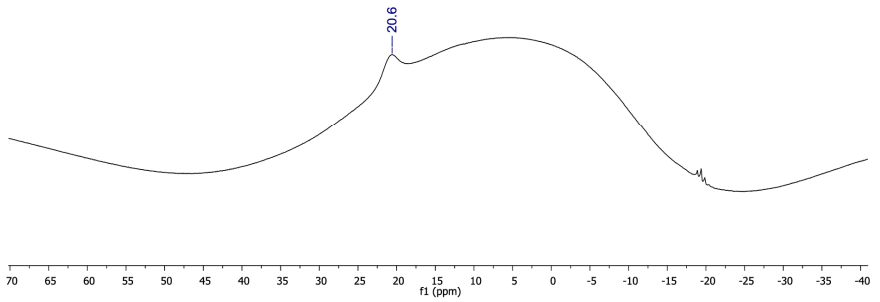

Figure S12: ^{11}B NMR spectrum of Li_2[**1**] (160.5 MHz, [D_8]THF).

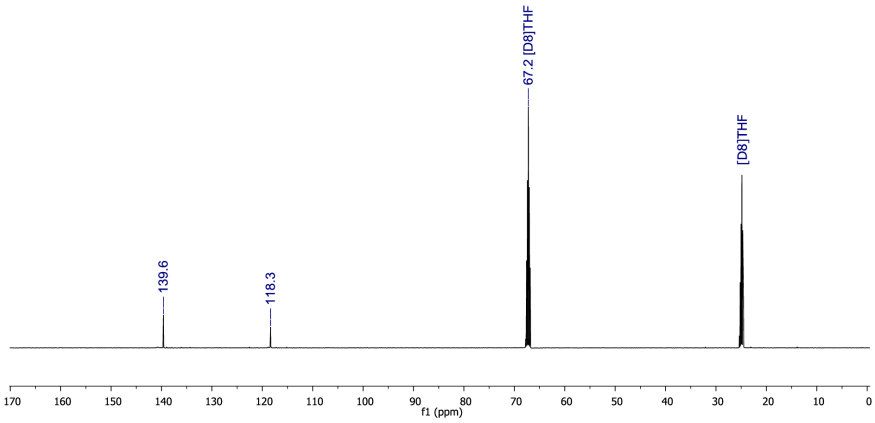

Figure S13: $^{13}C\{^{1}H\}$ NMR spectrum of Li_2[**1**] (125.8 MHz, $[D_8]$THF).

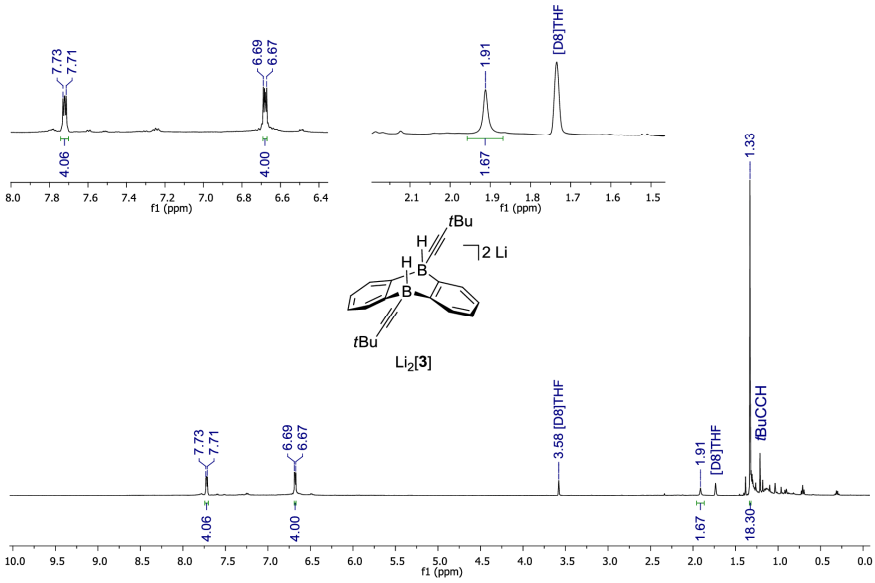

Figure S14: $^{1}H\{^{11}B\}$ NMR spectrum of Li_2[**3**] (500.2 MHz, $[D_8]$THF).

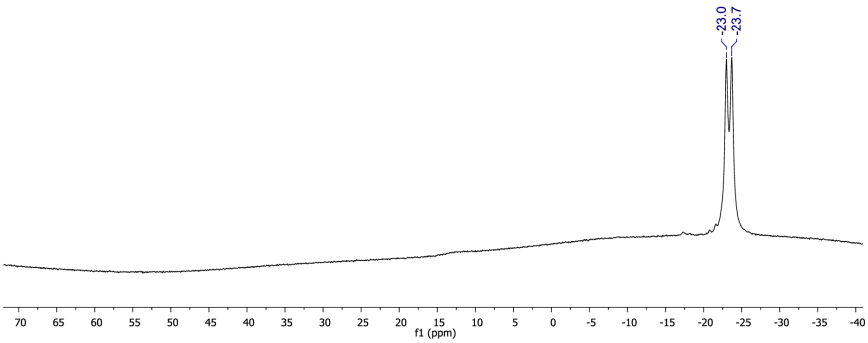

Figure S15: ^{11}B NMR spectrum of Li_2[**3**] (96.3 MHz, [D_8]THF).

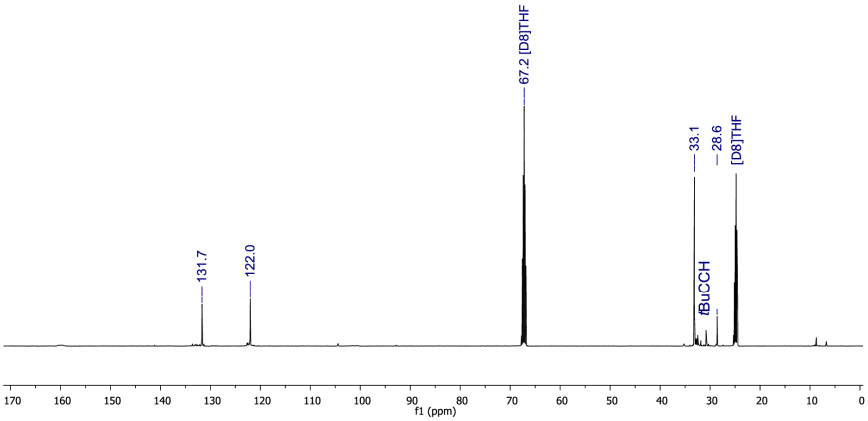

Figure S16: ^{13}C{^{1}H} NMR spectrum of Li_2[**3**] (125.8 MHz, [D_8]THF).

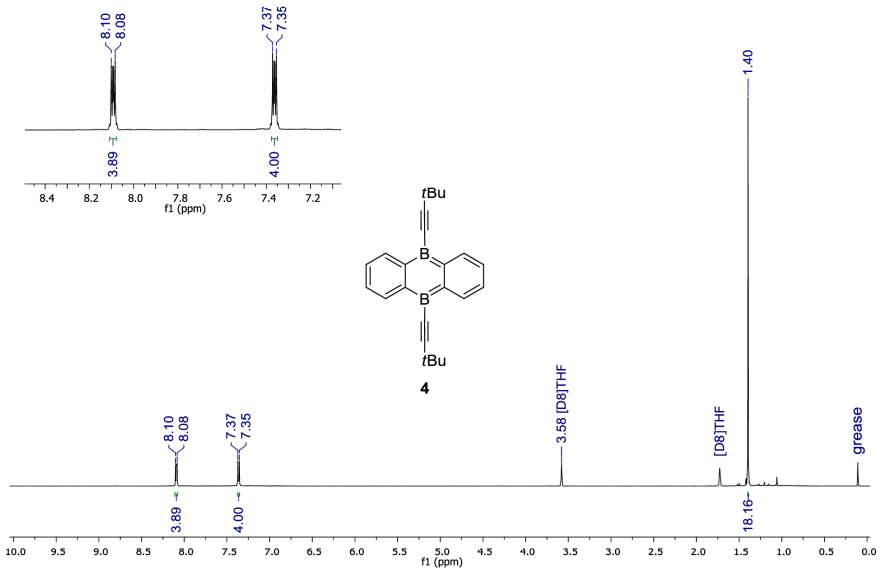

Figure S17: ^{1}H NMR spectrum of **4** (500.2 MHz, [D_8]THF).

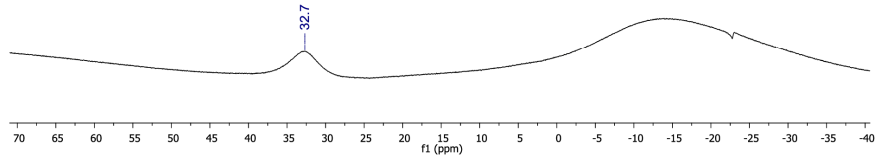

Figure S18: ^{11}B NMR spectrum of **4** (160.5 MHz, [D_8]THF).

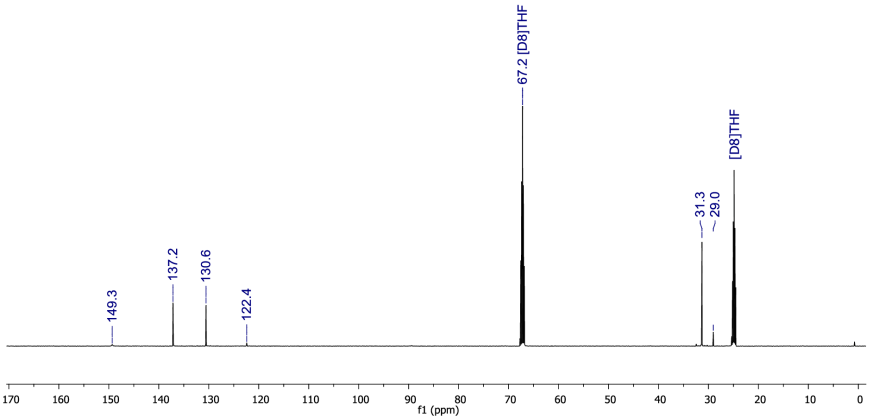

Figure S19: $^{13}C\{^{1}H\}$ NMR spectrum of **4** (125.8 MHz, $[D_8]$THF).

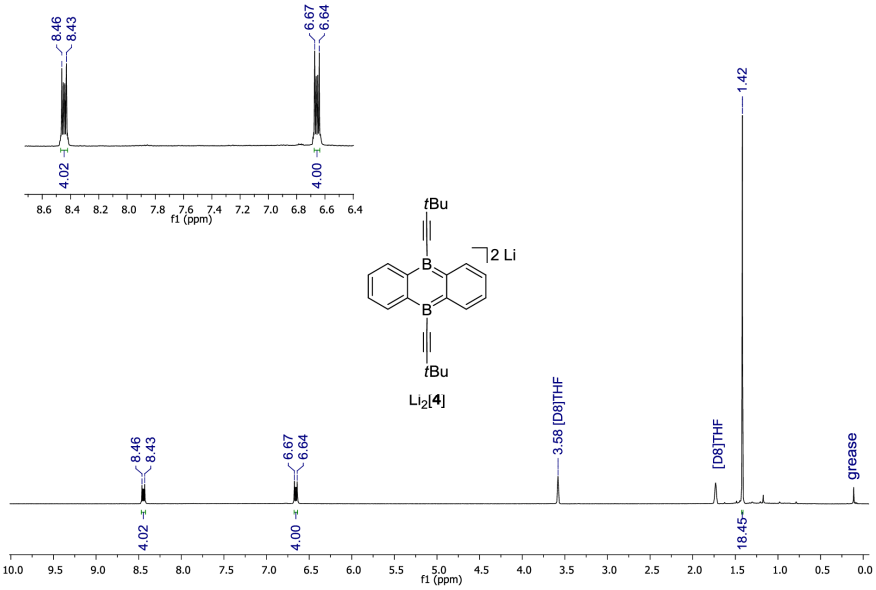

Figure S20: ^{1}H NMR spectrum of Li_2[**4**] (300.0 MHz, $[D_8]$THF; obtained via method A).

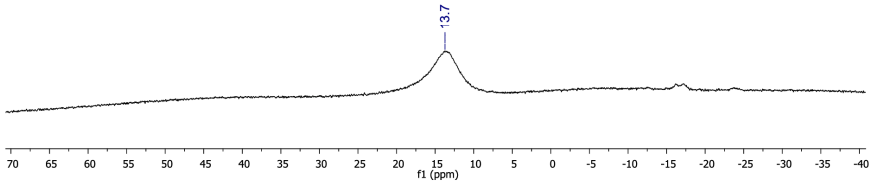

Figure S21: ^{11}B NMR spectrum of Li_2[**4**] (96.3 MHz, [D_8]THF; obtained via method A).

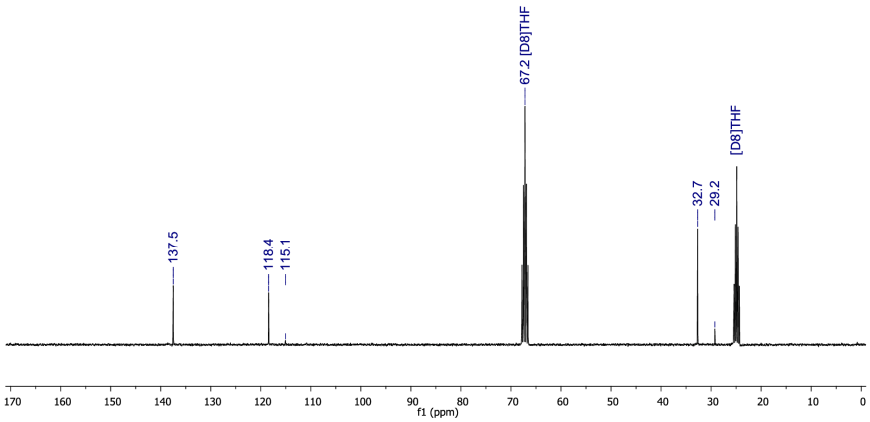

Figure S22: ^{13}C{^{1}H} NMR spectrum of Li_2[**4**] (75.4 MHz, [D_8]THF; obtained via method A).

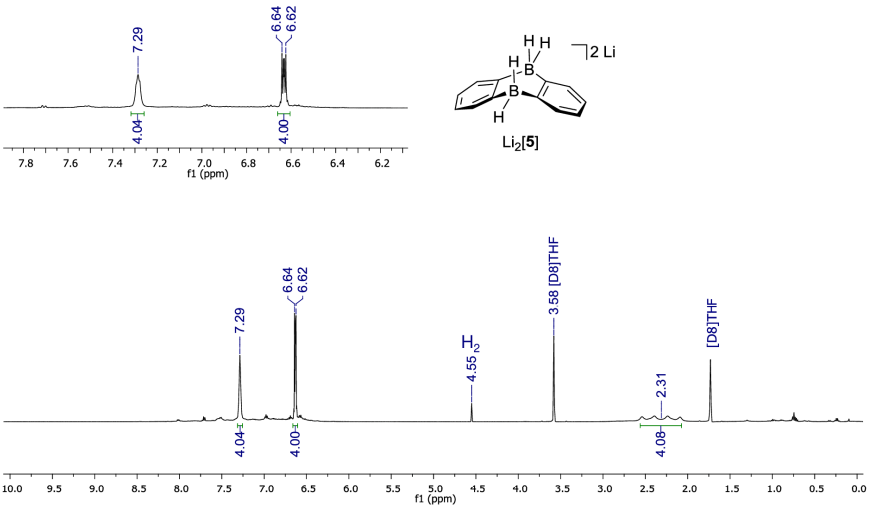

Figure S23: ^{1}H NMR spectrum of Li_2[**5**] (500.2 MHz, [D_8]THF; obtained via method B).

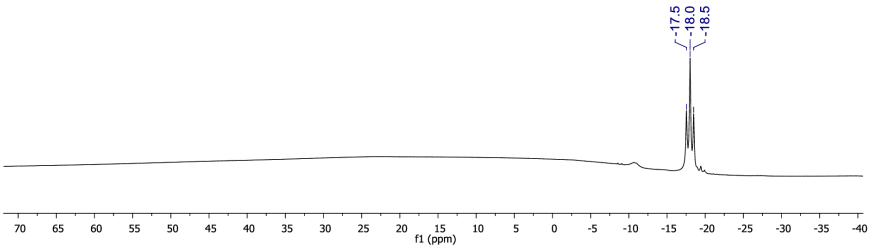

Figure S24: ^{11}B NMR spectrum of Li_2[**5**] (160.5 MHz, [D_8]THF; obtained via method B).

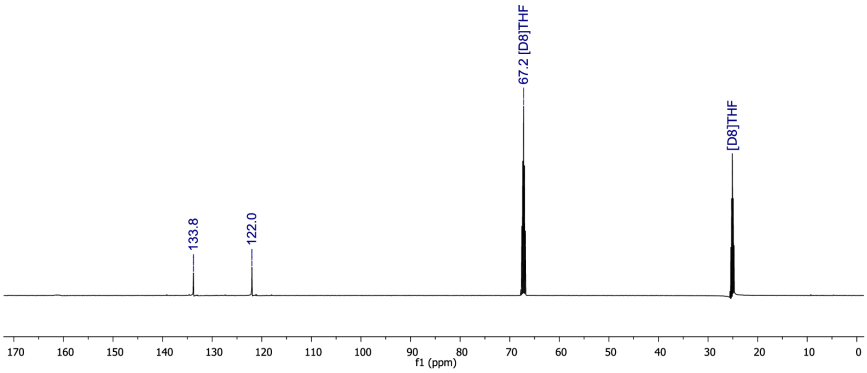

Figure S25: $^{13}C\{^{1}H\}$ NMR spectrum of Li_2[**5**] (125.8 MHz, [D_8]THF; obtained via method B).

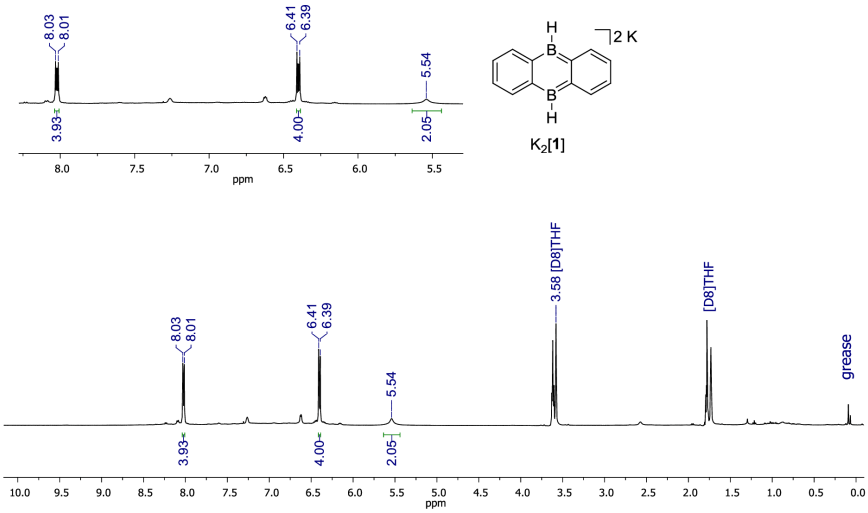

Figure S26: $^{1}H\{^{11}B\}$ NMR spectrum of K_2[**1**] (500.2 MHz, [D_8]THF).

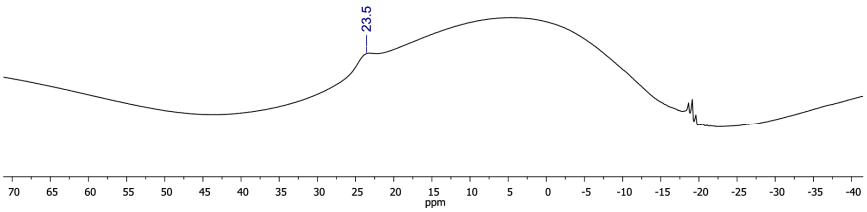

Figure S27: ^{11}B NMR spectrum of K_2[**1**] (160.5 MHz, [D_8]THF).

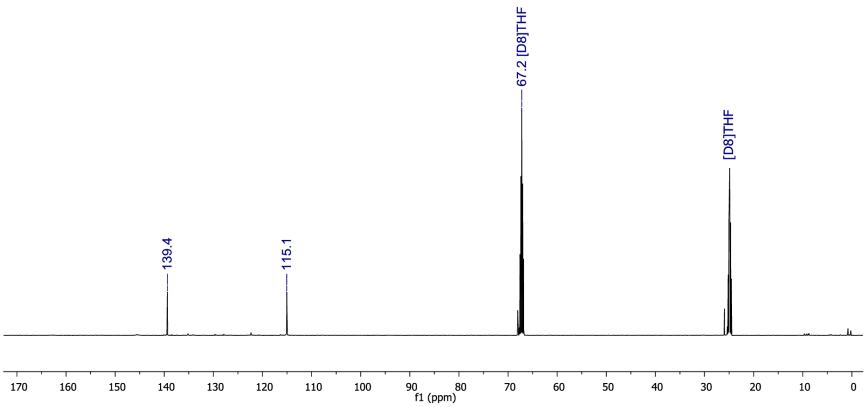

Figure S28: ^{13}C{^{1}H} NMR spectrum of K_2[**1**] (125.8 MHz, [D_8]THF).

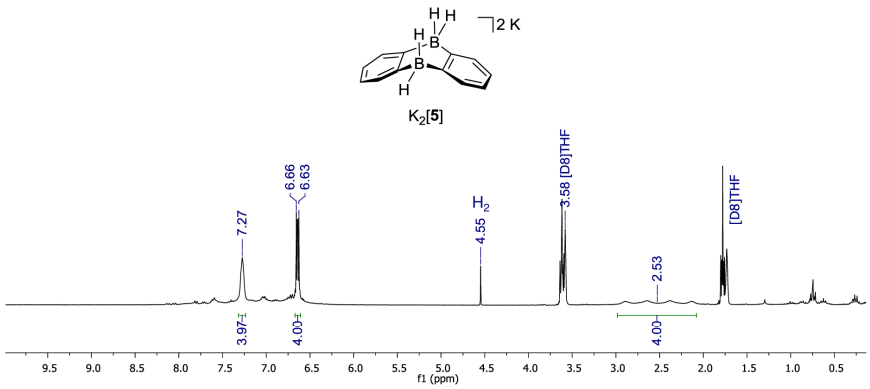

Figure S29: ^{1}H NMR spectrum of K_2[**5**] (300.0 MHz, [D_8]THF).

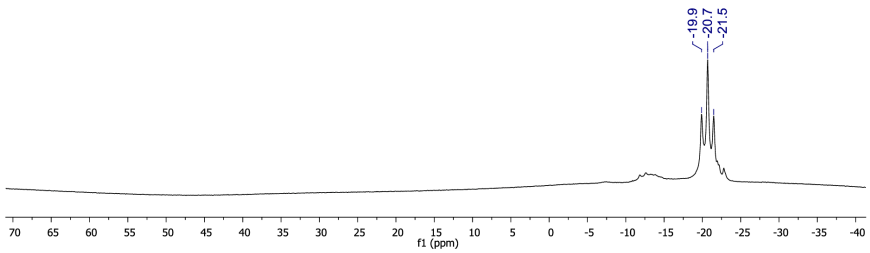

Figure S30: ^{11}B NMR spectrum of K_2[**5**] (96.3 MHz, [D_8]THF).

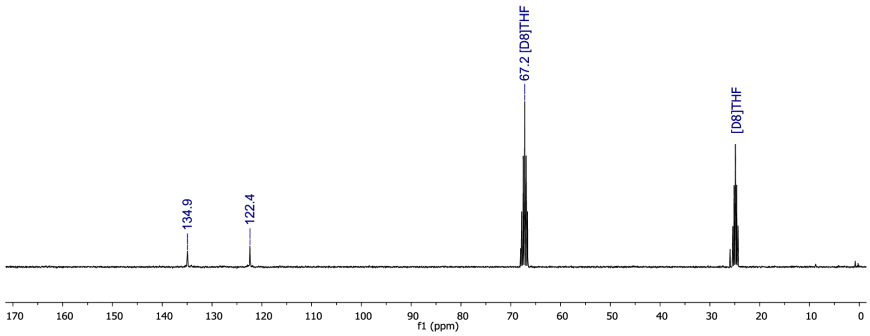

Figure S31: ^{13}C{^{1}H} NMR spectrum of K_2[**5**] (75.4 MHz, [D_8]THF).

6. X-ray crystal structure analyses of 4, $[Li(thf)_2]_2$[4], and $[Li(thf)_2][Li(thf)]$[5]

Data for all structures were collected on a STOE IPDS II two circle diffractometer with a Genix Microfocus tube with mirror optics using Mo$K\alpha$ radiation (λ = 0.71073 Å). The data were scaled using the frame-scaling procedure in the X-AREA program system.[11] The structures were solved by direct methods using the program SHELX and refined against F^2 with full-matrix least-squares techniques using the program SHELXL-97.[12]

In **Li_2[4]**, the displacement parameters of two atoms (C12 and C14) in one of the thf molecules were restrained to an isotropic behavior.

In **Li_2[5]**, the H atoms bonded to B were isotropically refined. In one thf molecule, three methylene groups are disordered over two positions with a site occupation factor of 0.56(1) for the major occupied site. In another thf molecule, two methylene groups are disordered over two positions with a site occupation factor of 0.71(1) for the major occupied site. The displacement parameters of four atoms (C24, C35', C43, and C44') in the thf molecules were restrained to an isotropic behavior.

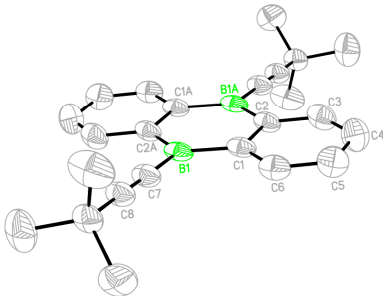

Figure S32: Molecular structure of **4** in the solid state (C_i symmetry). Displacement ellipsoids are drawn at the 50% probability level; hydrogen atoms are omitted for clarity. Selected bond lengths (Å) and bond angles (°): B1−C1 = 1.558(4), B1−C2A = 1.564(4), B1−C7 = 1.534(3), C1−C2 = 1.434(3), C1−C6 = 1.401(3), C2−C3 = 1.395(4), C3−C4 = 1.390(4), C4−C5 = 1.384(4), C5−C6 = 1.387(4), C7−C8 = 1.208(3); C1−B1−C2A = 120.6(2), C1−B1−C7 = 119.4(2), C2A−B1−C7 = 120.0(2), B1−C7−C8 = 176.3(2). Symmetry transformation used to generate equivalent atoms: A: −x+1, −y+1, −z+1.

The tricyclic core of **4** is essentially planar (sum of bond angles about boron = 360°). A C7−C8 distance of 1.208(3) Å proves the presence of a C≡C triple bond.

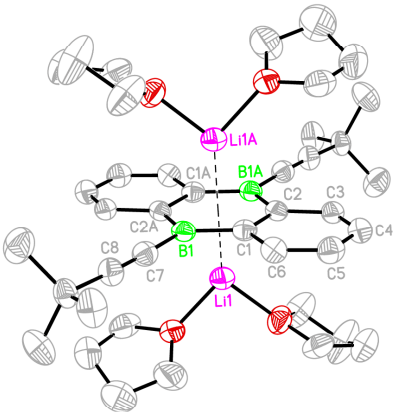

Figure S33: Molecular structure of $[Li(thf)_2]_2$[**4**] in the solid state (C_i symmetry). Displacement ellipsoids are drawn at the 50% probability level; hydrogen atoms are omitted for clarity. Selected bond lengths (Å), atom···atom distance (Å), and bond angles (°): B1−C1 = 1.529(4), B1−C2A = 1.534(4), B1−C7 = 1.557(4), C1−C2 = 1.465(4), C1−C6 = 1.444(4), C2−C3 = 1.435(4), C3−C4 = 1.368(4), C4−C5 = 1.416(4), C5−C6 = 1.370(4), C7−C8 = 1.212(4); Li^+···COG = 1.942(5); C1–B1–C2A = 118.0(2), C1–B1–C7 = 122.0(3), C2A–B1–C7 = 120.0(3), B1–C7–C8 = 176.5(3). COG = centroid of the B_2C_4 ring. Symmetry transformation used to generate equivalent atoms: A: −x+1, −y+1, −z+1.

Upon two-electron reduction, the tricyclic core of **4** retains its planar configuration, however, distinct changes are evident for individual atom···atom distances. For example, the average endocyclic B−C bond length is contracted from 1.561 Å (**4**) to 1.532 Å ($[Li(thf)_2]_2$[**4**]), whereas the C1–C2 bond is simultaneously elongated from 1.434(**3**) Å to 1.465(4) Å. These effects nicely reflect the nodal structure of the LUMO of **4**/HOMO of Li_2[**4**].[13] Two $[Li(thf)_2]^+$ cations are located above and below the centroid (COG) of the B_2C_4 ring (Li^+···COG = 1.942(5) Å).

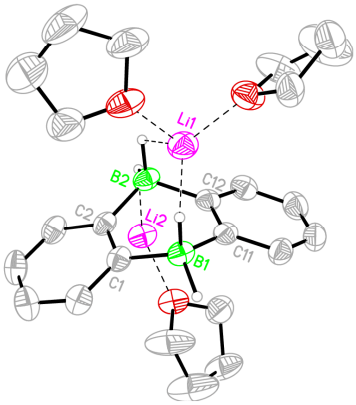

Figure S34: Asymmetric unit of the coordination polymer formed by $[Li(thf)_2][Li(thf)][\mathbf{5}]$ in the solid state. Displacement ellipsoids are drawn at the 50% probability level; hydrogen atoms, except on boron, are omitted for clarity. Selected bond lengths (Å), atom···atom distances (Å), bond angles (°), and dihedral angles (°): B1−C1 = 1.611(4), B1−C11 = 1.619(4), B2−C2 = 1.618(4), B2−C12 = 1.625(4), C1−C2 = 1.421(3), B1−H1A = 1.16(2), B1−H1B = 1.21(3), B2−H2A = 1.17(3), B2−H2B = 1.14(3), Li1···H1B = 1.91(3), Li1···H2B = 1.88(3), Li2···H2A = 1.88(3); Li1−B1 = 2.541(5), Li1−B2 = 2.497(6), Li2−B2 = 2.330(5). C1B1C11//C2B2C12 = 56.2(3), Ar(C1)//Ar(C11) = 36.4(1). Ar (C1), Ar(C11) = phenylene rings containing C1 and C11, respectively.

The central B_2C_4 heterocycle of the dianionic moiety $[\mathbf{5}]^{2-}$ adopts a boat conformation with a dihedral angle C1B1C11//C2B2C12 of 56.2(3)°. Correspondingly, an angle of Ar(C1)//Ar(C11) = 36.4(1)° is found between the planes of the two phenylene rings. The average B−C bond length in $[\mathbf{5}]^{2-}$ amounts to 1.618 Å, which can be compared to an average B−C bond length of only 1.520 Å in $Li_2[\mathbf{1}]$.[5] The difference of almost 0.1 Å between both values clearly testifies to the presence of sp^3-hybridized boron atoms in $[\mathbf{5}]^{2-}$ and all four B*H* hydrogen atoms have been located in the difference Fourier map and isotropically refined. The lithium ion $Li1^+$ is coordinated in a chelating manner by the two axial B*H* substituents of the anionic fragment; the ligand sphere is completed by two thf ligands. The $Li2^+$ ion binds to one thf ligand and the equatorial hydrogen substituent of B2. In addition, $Li2^+$ establishes an η^2 complex with the $B1H_2$ unit of a neighboring $[\mathbf{5}]^{2-}$ ion to ultimately form a polymer chain.

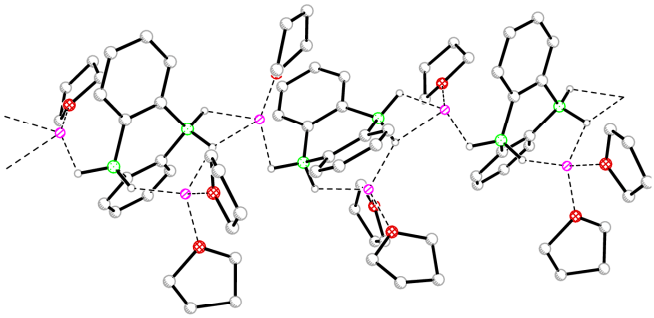

Table S1. Selected crystallographic data for **4**, $[Li(thf)_2]_2$[**4**], and $[Li(thf)_2][Li(thf)]$[**5**].

compound	**4**	$[Li(thf)_2]_2$[**4**]	$[Li(thf)_2][Li(thf)]$[**5**]
CCDC	1497837	1497838	1497839
formula	$C_{24}H_{26}B_2$	$C_{40}H_{58}B_2Li_2O_4$	$C_{24}H_{36}B_2Li_2O_3$
M_r	336.07	638.36	408.03
T (K)	173(2)	173(2)	173(2)
radiation, λ (Å)	Mo$K\alpha$, 0.71073	Mo$K\alpha$, 0.71073	Mo$K\alpha$, 0.71073
crystal system	orthorhombic	monoclinic	monoclinic
space group	*Pbca*	$P2_1/c$	$P2_1/c$
a (Å)	11.5562(16)	12.2379(18)	10.1474(10)
b (Å)	10.8803(15)	13.6613(11)	17.9279(12)
c (Å)	17.1317(19)	11.8734(16)	13.4047(14)
α (°)	90	90	90
β (°)	90	100.057(11)	95.056(8)
γ (°)	90	90	90
V (Å^3)	2154.1(5)	1954.6(4)	2429.1(4)
Z	4	2	4
D_{calcd} (g cm^{-3})	1.036	1.085	1.116
F (000)	720	692	880
μ (mm^{-1})	0.057	0.066	0.068
crystal size (mm)	0.19 × 0.17 × 0.13	0.22 × 0.22 × 0.05	0.21 × 0.12 × 0.09
crystal shape, color	light brown block	orange-red plate	colorless needle
reflections collected	5735	13162	40988
independent reflections	1999	3462	4603
R_{int}	0.0591	0.0653	0.0924
data/restraints/parameters	1999 / 0 / 118	3462 / 12 / 217	4603 / 24 / 343
R_1, wR_2 ($I > 2\sigma(I)$)	0.0595, 0.1377	0.0753, 0.1646	0.0809, 0.1675
R_1, wR_2 (all data)	0.1058, 0.1554	0.1420, 0.1955	0.1143, 0.1820
GOF on F^2	0.962	1.003	1.161
largest difference peak and hole (e Å^{-3})	0.147, –0.127	0.355, –0.166	0.295, –0.320

7 Quantum-Chemical Results

Computational Details. Molecular geometries were optimized with the Gaussian program[14] employing the PBE0 hybrid density functional[15] in conjunction with Grimme's atom-pairwise dispersion correction D3BJ[16,17] and the 6-31+G(d,p) orbital basis set.[18–21] Solvent effects on equilibrium geometries and energies were accounted for by the SMD polarized continuum model[22] (solvent tetrahydrofuran). This level of density functional theory (DFT) is dubbed SMD-PBE0D/6-31+G(d,p). Stationary points were characterized as minima or first order saddle points by eigenvalue analysis of the computed Hessians. Connectivities between minima and transition states implied in figures and schemes were validated either by intrinsic reaction coordinate (IRC) following calculations[23] or by displacing the transition-state geometries along both directions of the transition mode, followed by unconstrained optimizations to the respective minima. Energies of solvation ΔE_{solv} were estimated from total energy differences of SMD-PBE0D/6-31+G(d,p) results and PBE0D/6-31+G(d,p) single-point energy calculations under gas-phase conditions.

Improved relative energies for selected structures were obtained from single-point energy calculations on SMD-PBE0D/6-31+G(d,p) geometries employing the double-hybrid functionals B2GP-PLYP-D[24] and DSD-PBEP86-D,[25] and the domain based local pair-natural orbital coupled cluster method with single and double excitations and perturbative triple contributions, DLPNO-CCSD(T),[26,27] all carried out using the Orca program package.[28,29] Furthermore, the explicitly correlated coupled cluster ansatz with single and double excitations and connected triples, CCSD(T)-F12,[30,31] was employed using the Molpro quantum chemistry code.[32]

The double-hybrid functionals include the D3BJ dispersion correction[16,17] and were utilized either as implemented in the Orca program package (B2GP-PLYP-D) or as devised by Kozuch and Martin[25] (DSD-PBEP86-D). The def2-TZVP and def2-QZVP[33] orbital basis sets were used together with the RI-JK scheme[34] and the corresponding Coulomb and exchange fitting basis sets,[35] and supplemented with the auxiliary correlation fit basis sets.[36] For the DLPNO-CCSD(T) calculations the standard cutoff settings were adopted, and the def2-TZVPP and def2-QZVPP[33] orbital basis sets were employed along with the corresponding correlation fitting basis sets,[36] without further Coulomb and exchange fitting schemes. Extrapolation to the complete basis set (CBS) limit was accomplished according to

$$E_{\mathrm{SCF}}^{\infty} = E_{\mathrm{SCF}}^{Y} + \frac{E_{\mathrm{SCF}}^{Y} - E_{\mathrm{SCF}}^{X}}{e^{\alpha(\sqrt{Y}-\sqrt{X})} - 1} \tag{1}$$

for the DFT or Hartree–Fock reference energy part, with $\alpha = 7.88$, and

$$E_{\mathrm{corr}}^{\infty} = \frac{X^{\beta} E_{\mathrm{corr}}^{X} - Y^{\beta} E_{\mathrm{corr}}^{Y}}{X^{\beta} - Y^{\beta}} \tag{2}$$

for the MP2 correlation energy, with $\beta = 3.00$, as is also implemented in Orca. Here, X and

Y correspond to the cardinal numbers, i.e. $X = 3$ for triple-zeta and $Y = 4$ for quadruple-zeta basis sets, and E^X_{SCF} and E^Y_{SCF} correspond to total energies from triple and quadruple-zeta calculations, respectively.

In the CCSD(T)-F12 calculations the fixed-amplitude F12b ansatz was chosen and the cc-pVnZ-F12 (n = D, T) orbital basis sets[37,38] complemented with the corresponding standard auxiliary sets were applied. Due to the inavailability of correlation consistent basis sets, for potassium the def2-SVP and def2-TZVPP orbital basis sets[33] were used together with the corresponding auxiliary basis sets.[34,36] Extrapolation to the CBS(D,T) limit was conducted according to the formula of Hill *et al.*,[39]

$$E^{\infty}_{\mathrm{corr}} = (E^Y_{\mathrm{corr}} - E^X_{\mathrm{corr}}) \times F + E^X_{\mathrm{corr}}, \tag{3}$$

where E^X_{corr} and E^Y_{corr} correspond to the correlation energies from double- and triple-zeta calculations, respectively, and $F = 1.387\,834$ for the CCSD-F12b correlation energies and $F = 1.529\,817$ for the (canonical) triples contributions. For all single-point calculations, which use the frozen-core ansatz (DSD-PBEP86-D, DLPNO-CCSD(T), CCSD(T)-F12), the semi-core 3s and 3p electrons of potassium were included in the correlation treatment, and Gibbs energy corrections as well as solvation energy corrections ΔE_{solv} were taken from the PBE0D calculations as described above.

Frontier Orbital Interactions. The frontier molecular orbitals (FMOs) for the $[\mathbf{1}]^{2-}/H_2$ system are shown in Figure S35. The nodal structure of the highest occupied molecular orbital (HOMO) in $[\mathbf{1}]^{2-}$ matches the lowest unoccupied molecular orbital (LUMO) of H_2 and vice versa. This nodal structure is also mirrored in the FMOs of the H_2 addition product $[\mathbf{5}]^{2-}$, in which the two resulting B–H bonds are represented by the two occupied orbitals HOMO−2 and HOMO.

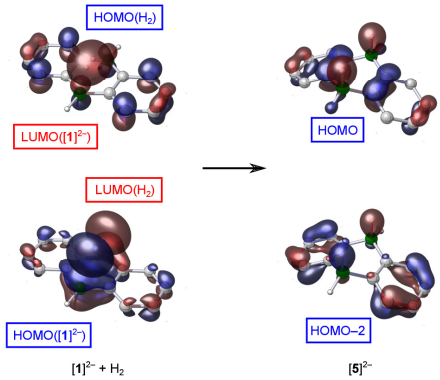

Figure S35: Frontier molecular orbitals for the addition of dihydrogen to the $[\mathbf{1}]^{2-}$ dianion, computed from SMD-PBE0D/6-31+G(d,p) wavefunctions (isovalue = $0.05\,a_0^{-3/2}$)

Benchmark Calculations. To identify a correlation treatment further applicable to a realistic molecular system resembling the experimental conditions, selected model systems relevant for the addition of dihydrogen towards $[\mathbf{1}]^{2-}$ were computed with the double-hybrid DFT, pair natural orbital based local coupled cluster and explicitly correlated coupled cluster methods at the SMD-PBE0D/6-31+G(d,p) geometries (Table S2 and Figures S36–S38).

Table S2: Relative Gibbs energies at 298 K for the concerted addition of dihydrogen to anthracene (ant) to yield 9,10-dihydroanthracene (H_2-ant), and to the DBA-related systems $[\mathbf{1}]^{2-}$, $\mathbf{a_{Li}}$ and $\mathbf{a_K}$, computed at the DFT, correlated double-hybrid DFT and coupled-cluster levels of theory. Geometries, Gibbs energy contributions and solvation energy corrections are taken from SMD-PBE0D/6-31+G(d,p) results.

	ΔG^{298} (kJ mol^{-1})				
	PBE0D[a]	B2GP-PLYP-D[b][e]	DSD-PBEP86-D[b][f]	DLPNO-CCSD(T)[c][f]	CCSD(T)-F12[d][f]
ant + H_2	0	0	0	0	0
$\mathbf{TS1_{ant}}$	171	191	185	193	193
H_2-ant	−51	−33	−38	−43	−38
$[\mathbf{1}]^{2-}$ + H_2	0	0	0	0	0
TS	69	88	82	83	91
$[\mathbf{5}]^{2-}$	−80	−67	−70	−84	−70
$\mathbf{a_{Li}}$ + H_2	0	0	0	0	0
$\mathbf{ts_{Li}}$	112	128	122	126	128
$\mathbf{b_{Li}}$	−29	−12	−16	−23	−16
$\mathbf{a_K}$ + H_2	0	0	0	0	0
$\mathbf{ts_K}$	85	98	93	94	100
$\mathbf{b_K}$	−68	−57	−59	−58	−54

[a] SMD-PBE0D/6-31+G(d,p)
[b] Extrapolation to the complete basis set limit using the def2-TZVP/def2-QZVP basis sets.
[c] Extrapolation to the complete basis set limit using the def2-TZVPP/def2-QZVPP basis sets.
[d] CCSD(T)-F12b ansatz extrapolated to the complete basis set limit in conjunction with cc-pVnZ-F12 (n = D, T) basis sets for H, B, C, Li, and def2-SVP and def2-TZVPP basis sets for K.
[e] Full MP2 correlation treatment.
[f] Frozen-core treatment with semi-core correlation of 3s and 3p electrons for K.

With reference to the explicitly correlated CCSD(T)-F12/CBS(D,T) level of theory the B2GP-PLYP-D/CBS(T,Q) approach does perform best. Relative energies given in the following correspond to Gibbs free energies at 298 K corrected by solvation energy contributions, i.e., $\Delta G^{298} + \Delta E_{\mathrm{solv}}$, obtained at the B2GP-PLYP-D/CBS(T,Q) // SMD-PBE0D/6-31+G(d,p) level of theory.

Anthracene. Reaction of dihydrogen with anthracene (Figure S36) may proceed via routes equivalent to those of the dianionic $[\mathbf{1}]^{2-}/H_2$ system, but is energetically much more demanding. Formation of 9,10-dihydroanthracene is exergonic by $\Delta_r G = -33\,\mathrm{kJ\,mol^{-1}}$. The H_2-adduct adopts a bent geometry with a boat-shape conformation in the central ring, and interconversion via a planar transition structure is facile with a barrier of $14\,\mathrm{kJ\,mol^{-1}}$. A direct and concerted 9,10-addition, however, is associated with a considerable barrier of $\Delta G^{\ddagger} = 191\,\mathrm{kJ\,mol^{-1}}$. The alternative stepwise route via a 1,2-addition requires more than twice the amount ($\Delta G^{\ddagger} = 391\,\mathrm{kJ\,mol^{-1}}$), the subsequent intermediate and the [1,3]-hydrogen shift are located $85\,\mathrm{kJ\,mol^{-1}}$ and $297\,\mathrm{kJ\,mol^{-1}}$ above the reactants, respectively.

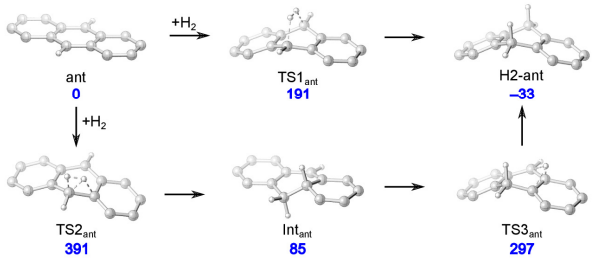

Figure S36: Reaction paths for the addition of dihydrogen to anthracene. Relative energies correspond to $\Delta G^{298} + \Delta E_{solv}$ in $\mathrm{kJ\,mol^{-1}}$ computed at the B2GP-PLYP-D/CBS(T,Q)//SMD-PBE0D/6-31+G(d,p) level of theory. The barrier for inversion of 9,10-dihydroanthracene through a planar transition structure is $\Delta^{\ddagger}G_{inv}$(H2-ant) = $14\,\mathrm{kJ\,mol^{-1}}$

M_2DBA Model Systems. To inspect the effect of metal counter ions on the dianionic $[\mathbf{1}]^{2-}/H_2$ system towards the addition of dihydrogen, the metal-coordinated model systems M_2DBA (M = Li, K; Figures S37 and S38) were investigated. Commencing with the symmetric structures $\mathbf{a_M}$, in both systems the metal ions assume an η^6 coordination above and below the central B_2C_4 ring, following the solid state structure of $[Li(thf)_2]_2[\mathbf{1}]$. In the transition structures $\mathbf{ts_M}$, the incoming dihydrogen moiety coordinates above the two boron atoms while one of the metal ions vacates space: in the lithiated system, one Li-ion slips into an η^2 coordination mode, whereas in $\mathbf{ts_K}$ the potassium acquires an η^6 coordination above one peripheral C_6 ring yielding somewhat more room for the incoming dihydrogen. Several product isomers were considered, the four most stable of which are $\mathbf{b_{Li}}$, $\mathbf{c_{Li}}$, $\mathbf{b_K}$, and $\mathbf{c_K}$. Compared to the activation barrier in the bare dianionic $[\mathbf{1}]^{2-}/H_2$ system ($\Delta G^{\ddagger} = 88\,\mathrm{kJ\,mol^{-1}}$), addition of H_2 requires $128\,\mathrm{kJ\,mol^{-1}}$ in the Li-model system, while the activation barrier is only moderately raised for the potassium analog ($\Delta G^{\ddagger} = 98\,\mathrm{kJ\,mol^{-1}}$). The overall reaction is also less exergonic in the Li-model system as compared to the potassium analog ($\Delta_r G = -21\,\mathrm{kJ\,mol^{-1}}$ for $\mathbf{c_{Li}}$ and $-57\,\mathrm{kJ\,mol^{-1}}$ for $\mathbf{b_K}$), which is above $\Delta_r G = -67\,\mathrm{kJ\,mol^{-1}}$ for $[\mathbf{5}]^{2-}$.

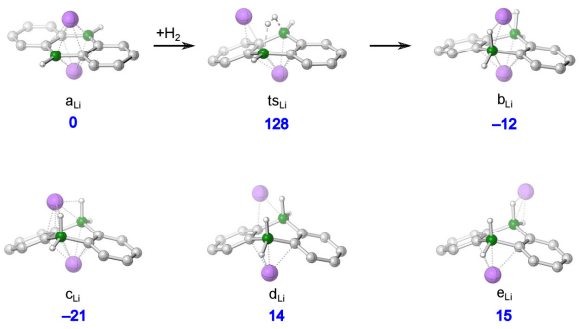

Figure S37: Reaction path and product isomers for the Li_2DBA/H_2 model system without THF ligands. Relative energies correspond to $\Delta G^{298} + \Delta E_{solv}$ in kJ mol^{-1} computed at the B2GP-PLYP-D/CBS(T,Q) // SMD-PBE0D/6-31+G(d,p) level of theory

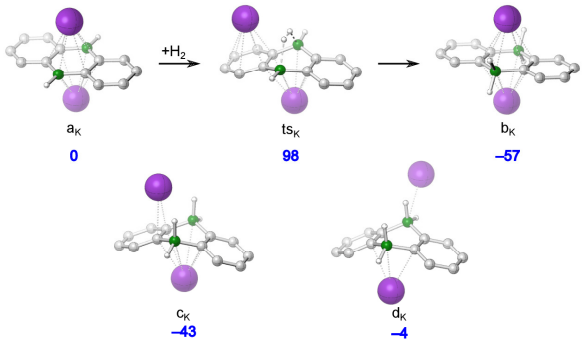

Figure S38: Reaction path and product isomers for the K_2DBA/H_2 model system without THF ligands. Relative energies correspond to $\Delta G^{298} + \Delta E_{solv}$ in kJ mol^{-1} computed at the B2GP-PLYP-D/CBS(T,Q) // SMD-PBE0D/6-31+G(d,p) level of theory

[M(thf)$_2$]$_2$DBA Systems. Compared to the lowest-energy minima $\mathbf{B_M}$, which are exergonic by $\Delta_r G = -28\,\mathrm{kJ\,mol^{-1}}$ (M = Li) and $\Delta_r G = -63\,\mathrm{kJ\,mol^{-1}}$ (M = K), respectively, two slightly less stable minima $\mathbf{C_{Li}}$ and $\mathbf{C_K}$, which resemble the solid-state structure of [Li(thf)$_2$][Li(thf)][**5**] more closely, have also been identified (Figure S39). They are $8\,\mathrm{kJ\,mol^{-1}}$ (M = Li) and $23\,\mathrm{kJ\,mol^{-1}}$ (M = K) less stable than their corresponding lowest-energy isomers.

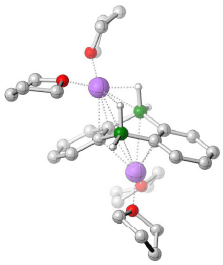

$\mathbf{C_{Li}}$
$\Delta_r G = -20\,\mathrm{kJ\,mol^{-1}}$

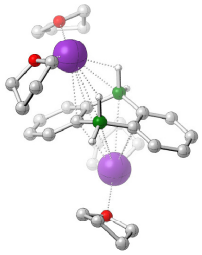

$\mathbf{C_K}$
$\Delta_r G = -40\,\mathrm{kJ\,mol^{-1}}$

Figure S39: Product isomers for [M(thf)$_2$]$_2$[**5**]. Relative energies correspond to $\Delta G^{298} + \Delta E_{solv}$ in $\mathrm{kJ\,mol^{-1}}$ computed at the B2GP-PLYP-D/CBS(T,Q)//SMD-PBE0D/6-31+G(d,p) level of theory

7.1 Total Energies

For all computed species the total energies calculated at the geometries optimized with the SMD-PBE0D/6-31+G(d,p) level of DFT are compiled in Tables S3–S8 together with solvation energy corrections, Gibbs energy contributions, dispersion corrections and correlation energy contributions, where applicable.

Table S3: Total energies E_{tot}, solvation energy corrections E_{solv}, Gibbs energy contributions G_{corr}^{298} in Hartree, and imaginary frequencies ν_{imag} in cm^{-1} for the computed species, along with term symbols and point groups, all obtained at the SMD-PBE0D/6-31+G(d,p) level of DFT.

Species	State / PG	E_{tot}	E_{solv}	G_{corr}^{298}	ν_{imag}
H_2[a]	$^1\Sigma_g^+$ / $D_{\infty h}$	−1.166 583	0.000 532	−0.001 365	
			$[\mathbf{1}]^{2-}/H_2$		
$[\mathbf{1}]^{2-}$	^1A_g / D_{2h}	−512.639 825	−0.241 604	0.147 522	
TS1	$^1A_1$ / C_{2v}	−513.796 103	−0.241 154	0.162 252	617 i
$[\mathbf{5}]^{2-}$	$^1A_1$ / C_{2v}	−513.855 682	−0.244 723	0.165 116	
TS2	^1A / C_1	−513.736 134	−0.236 243	0.159 890	1447 i
Int	^1A / C_1	−513.806 863	−0.241 089	0.165 047	
TS3	^1A / C_1	−513.738 676	−0.241 572	0.159 767	790 i
$TS_{inv}([\mathbf{5}]^{2-})$	^1A_g / D_{2h}	−513.851 611	−0.243 537	0.164 942	79 i
			anthracene/H_2		
ant	^1A_g / D_{2h}	−538.964 739	−0.016 823	0.161 959	
$TS1_{ant}$	$^1A_1$ / C_{2v}	−540.082 054	−0.016 395	0.176 528	1145 i
H2-ant	$^1A_1$ / C_{2v}	−540.172 864	−0.017 061	0.182 762	
$TS2_{ant}$	^1A / C_1	−540.008 230	−0.031 623	0.174 450	1298 i
Int_{ant}	^1A / C_1	−540.128 234	−0.016 421	0.181 719	
$TS3_{ant}$	^1A / C_1	−540.044 365	−0.021 074	0.176 138	838 i
TS_{inv}(H2-ant)	^1A_g / D_{2h}	−540.169 836	−0.017 117	0.184 756	55 i
			$[\mathbf{4}]^{2-}/H_2$		
$[\mathbf{4}]^{2-}$	^1A / C_1	−979.015 580	−0.228 074	0.374 912	
TS_{4-3}	^1A / C_1	−980.169 190	−0.228 444	0.388 885	592 i
$[\mathbf{3}]^{2-}$	^1A / C_1	−980.220 262	−0.228 982	0.395 072	7 i[b]
			Li_2DBA/H_2		
$\mathbf{a_{Li}}$	^1A_g / D_{2h}	−527.584 638	−0.026 119	0.155 423	
$\mathbf{ts_{Li}}$	$^1A'$ / C_s	−528.720 376	−0.030 896	0.165 784	872 i
$\mathbf{b_{Li}}$	$^1A_1$ / C_{2v}	−528.778 136	−0.027 789	0.170 062	
$\mathbf{c_{Li}}$	$^1A'$ / C_s	−528.779 141	−0.031 135	0.169 275	
$\mathbf{d_{Li}}$	^1A / C_1	−528.764 653	−0.041 565	0.168 514	
$\mathbf{e_{Li}}$	$^1A'$ / C_s	−528.761 519	−0.050 736	0.166 947	
			K_2DBA/H_2		
$\mathbf{a_K}$	^1A_g / D_{2h}	−1712.014 060	−0.028 846	0.145 381	
$\mathbf{ts_K}$	$^1A'$ / C_s	−1713.161 500	−0.033 090	0.157 224	762 i
$\mathbf{b_K}$	$^1A'$ / C_s	−1713.225 442	−0.028 007	0.163 021	
$\mathbf{c_K}$	$^1A'$ / C_s	−1713.220 448	−0.034 074	0.162 195	12 i[b]
$\mathbf{d_K}$	$^1A'$ / C_s	−1713.205 689	−0.049 783	0.159 053	
			$[Li(thf)_2]_2DBA/H_2$		
$\mathbf{A_{Li}}$	^1A / C_1	−1456.531 871	−0.029 192	0.589 330	
$\mathbf{TS_{Li}}$	^1A / C_1	−1457.676 248	−0.037 214	0.601 009	749 i
$\mathbf{B_{Li}}$	^1A / C_1	−1457.736 573	−0.036 168	0.609 964	
$\mathbf{C_{Li}}$	^1A / C_1	−1457.733 655	−0.038 123	0.609 262	
			$[K(thf)_2]_2DBA/H_2$		
$\mathbf{A_K}$	^1A_g / C_i	−2640.931 120	−0.034 864	0.572 761	
$\mathbf{TS_K}$	^1A / C_1	−2642.078 501	−0.038 010	0.585 163	741 i
$\mathbf{B_K}$	^1A_g / C_i	−2642.144 067	−0.035 839	0.589 887	
$\mathbf{C_K}$	^1A / C_1	−2642.137 311	−0.041 263	0.589 557	

[a] Optimized interatomic distance r_{H-H} = 0.7447 Å.
[b] Artifact—no imaginary mode if integration grid is increased to Int=(Ultra).

Table S4: Total energies in Hartree from the benchmark calculations (see above) utilizing the B2GP-PLYP-D double-hybrid DFT functional. Tabulated values comprise the DFT reference energy E_{ref} and the MP2 correlation energy E_{corr} obtained from triple-zeta (def2-TZVP) and quadruple-zeta (def2-QZVP) basis sets, as well as CBS-extrapolated energies according to equations 1 and 2. D3BJ dispersion correction energies E_{disp} are also given.

	E_{ref}			E_{corr}			E_{disp}	E_{tot}
	def2-TZVP	def2-QZVP	CBS(T,Q)	def2-TZVP	def2-QZVP	CBS(T,Q)		CBS
H_2	−1.156 177	−1.157 169	−1.157 306	−0.011 347	−0.013 447	−0.014 979	−0.000 031	−1.172 316
ant	−538.221 443	−538.248 433	−538.252 151	−0.996 765	−1.093 380	−1.163 882	−0.019 269	−539.435 302
TS1$_{ant}$	−539.301 941	−539.329 806	−539.333 644	−1.023 631	−1.123 046	−1.195 592	−0.021 434	−540.550 670
H$_2$-ant	−539.412 487	−539.440 626	−539.444 502	−1.004 798	−1.104 356	−1.177 006	−0.019 954	−540.641 462
$[\mathbf{1}]^{2-}$	−511.667 914	−511.697 467	−511.701 538	−0.982 439	−1.077 419	−1.146 729	−0.019 420	−512.867 687
TS	−512.793 305	−512.823 341	−512.827 478	−1.004 130	−1.101 986	−1.173 395	−0.021 805	−514.022 677
$[\mathbf{5}]^{2-}$	−512.871 290	−512.900 649	−512.904 693	−0.986 109	−1.084 043	−1.155 509	−0.020 529	−514.080 731
a$_{Li}$	−526.831 917	−526.860 250	−526.864 152	−1.002 357	−1.098 153	−1.168 057	−0.027 440	−528.059 650
ts$_{Li}$	−527.931 183	−527.960 699	−527.964 764	−1.025 567	−1.124 407	−1.196 534	−0.028 516	−529.189 813
b$_{Li}$	−528.006 516	−528.036 061	−528.040 131	−1.011 012	−1.109 665	−1.181 654	−0.028 681	−529.250 466
a$_K$	−1711.133 221	−1711.184 179	−1711.191 198	−1.118 666	−1.279 454	−1.396 785	−0.032 189	−1712.620 172
ts$_K$	−1712.247 743	−1712.299 401	−1712.306 516	−1.140 801	−1.304 751	−1.424 391	−0.032 737	−1713.763 645
b$_K$	−1712.332 718	−1712.384 081	−1712.391 156	−1.123 914	−1.287 998	−1.407 734	−0.034 621	−1713.833 511

Table S5: Total energies in Hartree from the benchmark calculations (see above) utilizing the DSD-PBEP86-D double-hybrid DFT functional. Tabulated values comprise the DFT reference energy E_{ref} and the MP2 correlation energy E_{corr} obtained from triple-zeta (def2-TZVP) and quadruple-zeta (def2-QZVP) basis sets, as well as CBS-extrapolated energies according to equations 1 and 2. D3BJ dispersion correction energies E_{disp} are also given.

	E_{ref}			E_{corr}			E_{disp}	E_{tot}
	def2-TZVP	def2-QZVP	CBS(T,Q)	def2-TZVP	def2-QZVP	CBS(T,Q)		CBS
H_2	−1.149 755	−1.150 697	−1.150 826	−0.016 106	−0.019 112	−0.021 307	−0.000 049	−1.172 182
ant	−537.560 580	−537.586 206	−537.589 735	−1.078 910	−1.161 419	−1.221 628	−0.022 467	−538.833 830
TS1$_{ant}$	−538.637 096	−538.663 554	−538.667 199	−1.110 501	−1.196 495	−1.259 247	−0.025 083	−539.951 529
H$_2$-ant	−538.747 967	−538.774 668	−538.778 345	−1.091 400	−1.177 539	−1.240 397	−0.023 278	−540.042 020
$[1]^{2-}$	−511.023 567	−511.051 708	−511.055 584	−1.062 404	−1.143 758	−1.203 125	−0.022 245	−512.280 954
TS	−512.144 965	−512.173 536	−512.177 471	−1.088 427	−1.173 353	−1.235 326	−0.025 070	−513.437 867
$[5]^{2-}$	−512.222 384	−512.250 251	−512.254 089	−1.070 930	−1.155 634	−1.217 445	−0.023 515	−513.495 049
a$_{Li}$	−526.153 167	−526.180 019	−526.183 718	−1.056 771	−1.137 909	−1.197 118	−0.028 935	−527.409 770
ts$_{Li}$	−527.248 209	−527.276 307	−527.280 177	−1.084 638	−1.169 557	−1.231 525	−0.030 247	−528.541 949
b$_{Li}$	−527.322 835	−527.350 860	−527.354 720	−1.070 709	−1.155 203	−1.216 862	−0.030 352	−528.601 934
a$_K$	−1710.126 750	−1710.176 098	−1710.182 895	−1.217 624	−1.350 635	−1.447 697	−0.029 300	−1711.659 892
ts$_K$	−1711.237 062	−1711.287 100	−1711.293 992	−1.244 044	−1.381 009	−1.480 957	−0.030 210	−1712.805 159
b$_K$	−1711.321 467	−1711.371 177	−1711.378 024	−1.227 861	−1.364 464	−1.464 147	−0.031 694	−1712.873 865

Table S6: Total energies in Hartree from the benchmark calculations (see above) utilizing the DLPNO-CCSD(T) method. Tabulated values comprise the SCF reference energy E_{ref} and the CCSD(T) correlation energy E_{corr} obtained from triple-zeta (def2-TZVPP) and quadruple-zeta (def2-QZVPP) basis sets, as well as CBS-extrapolated energies according to equations 1 and 2.

	E_{ref}			E_{corr}			E_{tot}
	def2-TZVPP	def2-QZVPP	CBS(T,Q)	def2-TZVPP	def2-QZVPP	CBS(T,Q)	CBS
H_2	−1.132 920	−1.133 506	−1.133 586	−0.039 464	−0.040 398	−0.041 080	−1.174 666
ant	−536.178 291	−536.199 559	−536.202 489	−2.323 844	−2.445 323	−2.533 970	−538.736 459
$\mathbf{TS1_{ant}}$	−537.221 466	−537.243 162	−537.246 150	−2.395 145	−2.517 739	−2.607 200	−539.853 350
$\mathbf{H_2}$**-ant**	−537.348 112	−537.369 865	−537.372 861	−2.365 259	−2.487 129	−2.576 062	−539.948 923
$[\mathbf{1}]^{2-}$	−509.662 695	−509.686 782	−509.690 100	−2.285 743	−2.400 348	−2.483 978	−512.174 078
TS	−510.755 199	−510.779 178	−510.782 480	−2.347 090	−2.464 824	−2.550 738	−513.333 219
$[\mathbf{5}]^{2-}$	−510.848 377	−510.871 697	−510.874 909	−2.319 011	−2.435 913	−2.521 220	−513.396 130
$\mathbf{a_{Li}}$	−524.765 683	−524.787 867	−524.790 922	−2.279 221	−2.395 677	−2.480 658	−527.271 580
$\mathbf{ts_{Li}}$	−525.831 387	−525.853 870	−525.856 966	−2.343 229	−2.461 542	−2.547 879	−528.404 845
$\mathbf{b_{Li}}$	−525.919 252	−525.941 722	−525.944 817	−2.321 026	−2.438 442	−2.524 124	−528.468 941
$\mathbf{a_K}$	−1708.159 002	−1708.203 582	−1708.209 722	−2.634 086	−2.870 254	−3.042 594	−1711.252 316
$\mathbf{ts_K}$	−1709.240 192	−1709.285 030	−1709.291 206	−2.694 359	−2.933 837	−3.108 592	−1712.399 798
$\mathbf{b_K}$	−1709.339 554	−1709.384 154	−1709.390 297	−2.670 228	−2.906 063	−3.078 160	−1712.468 457

Table S7: Total energies in Hartree from the benchmark calculations (see above) utilizing the CCSD(T)-F12 method. Tabulated values comprise the F12 reference energy $E_{\mathrm{ref}}^{\mathrm{F12}}$, the CCSD-F12 correlation energy $E_{\mathrm{corr}}^{\mathrm{F12}}$ and the canonical triples correlation energy $E_{\mathrm{corr}}^{(\mathrm{T})}$ obtained from double-zeta (VDZ-F12) and triple-zeta (VTZ-F12) basis sets, as well as CBS-extrapolated energies according to equation 3.

	$E_{\mathrm{ref}}^{\mathrm{F12}}$			$E_{\mathrm{corr}}^{\mathrm{F12}}$			$E_{\mathrm{corr}}^{(\mathrm{T})}$			E_{tot}
	VDZ-F12	VTZ-F12	CBS(D,T)	VDZ-F12	VTZ-F12	CBS(D,T)	VDZ-F12	VTZ-F12	CBS(D,T)	CBS
H_2	−1.133 088	−1.133 440	−1.133 440	−0.040 370	−0.040 599	−0.040 688	0.000 000	0.000 000	0.000 000	−1.174 128
ant	−536.172 891	−536.197 529	−536.197 529	−2.346 661	−2.377 171	−2.389 003	−0.116 656	−0.134 584	−0.144 083	−538.730 616
TS1$_{\mathrm{ant}}$	−537.216 311	−537.241 106	−537.241 106	−2.414 177	−2.445 012	−2.456 970	−0.120 668	−0.139 100	−0.148 866	−539.846 942
H$_2$-ant	−537.342 972	−537.367 780	−537.367 780	−2.389 898	−2.421 174	−2.433 304	−0.112 278	−0.130 159	−0.139 632	−539.940 716
[1]$^{2-}$	−509.664 881	−509.688 292	−509.688 292	−2.297 894	−2.327 917	−2.339 562	−0.118 766	−0.136 788	−0.146 337	−512.174 191
TS	−510.755 794	−510.779 275	−510.779 275	−2.358 945	−2.389 313	−2.401 090	−0.121 193	−0.139 514	−0.149 221	−513.329 586
[5]$^{2-}$	−510.847 461	−510.870 841	−510.870 841	−2.336 063	−2.366 504	−2.378 310	−0.113 850	−0.131 575	−0.140 966	−513.390 116
a$_{\mathrm{Li}}$	−524.763 342	−524.786 278	−524.786 278	−2.296 984	−2.327 259	−2.339 000	−0.115 328	−0.133 115	−0.142 538	−527.267 817
ts$_{\mathrm{Li}}$	−525.829 102	−525.852 272	−525.852 272	−2.358 236	−2.388 765	−2.400 605	−0.119 013	−0.137 201	−0.146 837	−528.399 714
b$_{\mathrm{Li}}$	−525.916 853	−525.940 079	−525.940 079	−2.339 333	−2.369 747	−2.381 543	−0.113 167	−0.130 800	−0.140 142	−528.461 765
a$_{\mathrm{K}}$	−1708.007 570	−1708.180 314	−1708.180 314	−2.788 494	−2.832 629	−2.849 746	−0.119 466	−0.140 287	−0.151 319	−1711.181 379
ts$_{\mathrm{K}}$	−1709.088 990	−1709.261 666	−1709.261 666	−2.848 588	−2.892 622	−2.909 700	−0.122 300	−0.143 453	−0.154 660	−1712.326 025
b$_{\mathrm{K}}$	−1709.188 770	−1709.360 813	−1709.360 813	−2.826 668	−2.870 763	−2.887 865	−0.115 412	−0.135 870	−0.146 709	−1712.395 388

Table S8: Total energies in Hartree for the systems $[\mathbf{4}]^{2-}/H_2$, $[Li(thf)_2]_2[\mathbf{1}]/H_2$, and $[K(thf)_2]_2[\mathbf{1}]/H_2$, computed with the B2GP-PLYP-D double-hybrid DFT functional on SMD-PBE0D/6-31+G(d,p) geometries. Tabulated values comprise the DFT reference energy E_{ref} and the MP2 correlation energy E_{corr} obtained from triple-zeta (def2-TZVP) and quadruple-zeta (def2-QZVP) basis sets, as well as the CBS-extrapolated energies according to equations 1 and 2. D3BJ dispersion correction energies E_{disp} are also given.

	E_{ref}		E_{corr}		E_{disp}	E_{tot}
	def2-TZVP	def2-QZVP	def2-TZVP	def2-QZVP		CBS
$[\mathbf{4}]^{2-}$	−977.379 484	−977.435 535	−1.881 254	−2.070 325	−0.038 945	−979.690 496
$\mathbf{TS}_{4-3}$	−978.501 968	−978.558 630	−1.902 620	−2.094 275	−0.041 568	−980.842 134
$[\mathbf{3}]^{2-}$	−978.576 802	−978.633 035	−1.882 729	−2.074 329	−0.040 542	−980.895 468
$\mathbf{A_{Li}}$	−1454.567 169	−1454.650 970	−2.653 713	−2.930 390	−0.068 315	−1457.863 116
$\mathbf{TS_{Li}}$	−1455.677 116	−1455.762 165	−2.671 788	−2.951 396	−0.068 129	−1458.997 443
$\mathbf{B_{Li}}$	−1455.757 100	−1455.842 006	−2.655 079	−2.934 579	−0.068 339	−1459.060 579
$\mathbf{C_{Li}}$	−1455.748 374	−1455.833 285	−2.657 285	−2.936 870	−0.069 013	−1459.054 885
$\mathbf{A_K}$	−2638.850 405	−2638.956 028	−2.761 030	−3.104 131	−0.070 106	−2642.395 185
$\mathbf{TS_K}$	−2639.965 119	−2640.071 755	−2.782 864	−3.129 401	−0.070 494	−2643.539 216
$\mathbf{B_K}$	−2640.047 953	−2640.154 057	−2.766 155	−3.113 028	−0.073 513	−2643.608 337
$\mathbf{C_K}$	−2640.040 376	−2640.146 684	−2.763 774	−3.109 695	−0.070 321	−2643.593 772

7.2 Cartesian coordinates of optimized geometries (Å)

24
[1]$^{2-}$

H	0.000000000000	4.728744658751	1.257040026131
C	0.000000000000	3.785032576984	0.712989313990
H	0.000000000000	2.594538327246	2.481621595753
C	0.000000000000	2.584155021640	1.389417578129
C	0.000000000000	2.584155021640	-1.389417578129
C	0.000000000000	1.313814786947	0.732021917923
C	0.000000000000	3.785032576984	-0.712989313990
C	0.000000000000	1.313814786947	-0.732021917923
B	0.000000000000	0.000000000000	1.497055204394
H	0.000000000000	4.728744658751	-1.257040026131
H	0.000000000000	0.000000000000	-2.725204932067
H	0.000000000000	2.594538327246	-2.481621595753
C	0.000000000000	-1.313814786947	0.732021917923
H	0.000000000000	0.000000000000	2.725204932067
C	0.000000000000	-2.584155021640	1.389417578129
C	0.000000000000	-1.313814786947	-0.732021917923
H	0.000000000000	-2.594538327246	-2.481621595753
B	0.000000000000	0.000000000000	-1.497055204394
C	0.000000000000	-3.785032576984	0.712989313990
H	0.000000000000	-2.594538327246	2.481621595753
H	0.000000000000	-4.728744658751	1.257040026131
C	0.000000000000	-3.785032576984	-0.712989313990
H	0.000000000000	-4.728744658751	-1.257040026131
C	0.000000000000	-2.584155021640	-1.389417578129

26
TS1

H	-4.641276215863	1.251913123805	-0.591788534879
C	-3.723055689401	0.705567236266	-0.379307167111
H	-2.558639355645	2.480095365102	-0.096449133985
C	-2.546639750641	1.388356917813	-0.103967616999
C	-2.546639750641	-1.388356917813	-0.103967616999
C	-1.324823216858	0.721585418697	0.161366879963
C	-3.723055689401	-0.705567236266	-0.379307167111
C	-1.324823216858	-0.721585418697	0.161366879963
B	0.000000000000	1.438755633650	0.520643884284
H	-4.641276215863	-1.251913123805	-0.591788534879
H	0.000000000000	-2.660109993844	0.648080856124
H	-2.558639355645	-2.480095365102	-0.096449133985
C	1.324823216858	0.721585418697	0.161366879963
H	0.000000000000	2.660109993844	0.648080856124
C	2.546639750641	1.388356917813	-0.103967616999
C	1.324823216858	-0.721585418697	0.161366879963
H	2.558639355645	-2.480095365102	-0.096449133985
B	0.000000000000	-1.438755633650	0.520643884284
C	3.723055689401	0.705567236266	-0.379307167111
H	2.558639355645	2.480095365102	-0.096449133985
H	4.641276215863	1.251913123805	-0.591788534879
C	3.723055689401	-0.705567236266	-0.379307167111
H	4.641276215863	-1.251913123805	-0.591788534879
C	2.546639750641	-1.388356917813	-0.103967616999
H	0.000000000000	0.465610680303	1.988069909951
H	0.000000000000	-0.465610680303	1.988069909951

26
[5]$^{2-}$
H -4.516452801151 1.248707609467 -0.871676107251
C -3.635926618300 0.697282902677 -0.543882332801
H -2.490407280787 2.470932770436 -0.145957555916
C -2.486243244690 1.379407283272 -0.129972249604
C -2.486243244690 -1.379407283272 -0.129972249604
C -1.328330414199 0.712362741205 0.303352468122
C -3.635926618300 -0.697282902677 -0.543882332801
C -1.328330414199 -0.712362741205 0.303352468122
B 0.000000000000 1.485960292051 0.798743881166
H -4.516452801151 -1.248707609467 -0.871676107251
H 0.000000000000 -2.677142124628 0.436280036420
H -2.490407280787 -2.470932770436 -0.145957555916
C 1.328330414199 0.712362741205 0.303352468122
H 0.000000000000 2.677142124628 0.436280036420
C 2.486243244690 1.379407283272 -0.129972249604
C 1.328330414199 -0.712362741205 0.303352468122
H 2.490407280787 -2.470932770436 -0.145957555916
B 0.000000000000 -1.485960292051 0.798743881166
C 3.635926618300 0.697282902677 -0.543882332801
H 2.490407280787 2.470932770436 -0.145957555916
H 4.516452801151 1.248707609467 -0.871676107251
C 3.635926618300 -0.697282902677 -0.543882332801
H 4.516452801151 -1.248707609467 -0.871676107251
C 2.486243244690 -1.379407283272 -0.129972249604
H 0.000000000000 1.492277765401 2.051293255482
H 0.000000000000 -1.492277765401 2.051293255482

26
TS2
H 4.610550561938 -1.226860473888 -0.723988619234
C 3.704041753319 -0.688345685392 -0.456778549772
H 2.530810632889 -2.456433871057 -0.134246120476
C 2.533911584125 -1.364740246027 -0.138488864443
C 2.544183915486 1.423018782709 -0.066152358381
C 1.342777233151 -0.688989039866 0.193047334936
C 3.690743305540 0.738046404997 -0.399078627064
C 1.293404790202 0.775336544506 0.237270015724
B -0.042665290231 -1.464051281626 0.617360021030
H 4.602441559274 1.291443542001 -0.625406590172
H -0.013565523575 2.734007935958 0.531402422835
H 2.574457171854 2.514069149939 -0.039176977567
C -1.347242240771 -0.689907266427 0.192457959208
H 0.030912765857 -2.672708156718 0.551828540594
C -2.505155207429 -1.364336198218 -0.197112634759
C -1.335469865546 0.751823989369 0.275097461013
H -2.614997132511 2.489858614419 0.035724217884
B -0.007968481372 1.503568264525 0.509455756766
C -3.710017361334 -0.695830506316 -0.468977880153
H -2.480742197245 -2.454193428630 -0.263022944534
H -4.609184736522 -1.247527185115 -0.736185827836
C -3.727218913845 0.705157915335 -0.356860053980
H -4.649008612212 1.253298959718 -0.554138497239
C -2.575174812872 1.399980062335 -0.010705856578
H -0.025587022329 -1.233160906151 2.029920356494
H 0.844376310435 -0.996667637005 1.470903475785

26
Int
H 4.711729298600 -1.170041694351 -0.299829705076
C 3.772104856119 -0.662504262740 -0.073680649058
H 2.648716827504 -2.457028492627 -0.085605651388
C 2.625470985342 -1.372373081996 0.046594332753
C 2.556095322975 1.439097400650 0.003856192480
C 1.306776315966 -0.726601680658 0.391585252929
C 3.768149653564 0.786210142573 0.022603466215
C 1.295764115235 0.767696405077 0.033934161910
B 0.024841757647 -1.522796525770 -0.242136786651
H 4.705101179520 1.336296180824 -0.045046134446
H -0.012670383316 2.702855951932 -0.279109927179
H 2.549595826800 2.528964425433 -0.094705618672
C -1.364903185839 -0.707808570673 -0.087884419141
H 0.232193951785 -1.695667365029 -1.467415111149
C -2.610427622308 -1.354184602283 -0.026738968614
C -1.358519191845 0.722565780894 -0.071656871148
H -2.582948981631 2.497534258494 0.012825435271
B 0.009177720098 1.484078223497 -0.139829560798
C -3.821879347553 -0.658629199403 0.054328573692
H -2.635410992644 -2.445323500090 -0.039344459090
H -4.764555202794 -1.201387426582 0.111143724688
C -3.812385112982 0.737607352103 0.070381320195
H -4.745617957154 1.294874919667 0.135794229434
C -2.589455003475 1.406369978199 0.003875045610
H -0.084059957351 -2.663666795605 0.255088460811
H 1.207078290766 -0.798492921160 1.502851867099

26
TS3
H -4.656032677111 1.014378660738 0.303151716899
C -3.695940634249 0.524489222602 0.121783543744
H -2.703333425519 1.815732999215 1.537039812677
C -2.588803132741 0.999780689809 0.822663836665
C -2.424704230311 -1.296201213671 -0.808885032751
C -1.245401276703 0.540330547453 0.435730329769
C -3.650169368968 -0.542554427105 -0.792200567287
C -1.299389533403 -0.798333617703 -0.225364752509
B -0.061502619302 1.556430446849 -0.081369840730
H -4.538779248092 -0.873531274040 -1.324636575200
H -0.300810099255 -1.909899119976 1.663019480957
H -2.427673513900 -2.316649220234 -1.204809712930
C 1.344676732158 0.755188294744 -0.112165711873
H -0.382382596245 1.970356791862 -1.205348070441
C 2.581088039012 1.285450332315 -0.508132488741
C 1.318944053411 -0.590299758962 0.356750298777
H 2.486856762097 -2.357966222734 0.778178147029
B -0.121971940004 -1.091244886273 0.780690780273
C 3.760388314328 0.533379271391 -0.465742374467
H 2.630164975130 2.316917627539 -0.861020021592
H 4.702918862428 0.974106804444 -0.787506995905
C 3.725459270815 -0.782880076330 -0.003404068443
H 4.638001151208 -1.375386587774 0.037259771529
C 2.507262154651 -1.330948792622 0.411483406648
H 0.015015457256 2.553058412734 0.665288399345
H -0.547035179466 0.078550493822 1.507680832721

26
$TS_{inv}([5]^{2-})$

B	0.000000000000	1.578880602016	0.000000000000
H	0.000000000000	2.345875332600	0.988973375678
C	1.364773267600	0.710177532571	0.000000000000
C	1.364773267600	-0.710177532571	0.000000000000
C	2.609491647684	-1.372991536857	0.000000000000
H	2.617990347449	-2.465189952299	0.000000000000
C	3.830015886372	-0.698993748080	0.000000000000
H	4.768718337640	-1.251686090264	0.000000000000
C	3.830015886372	0.698993748080	0.000000000000
H	4.768718337640	1.251686090264	0.000000000000
C	2.609491647684	1.372991536857	0.000000000000
H	2.617990347449	2.465189952299	0.000000000000
B	0.000000000000	-1.578880602016	0.000000000000
H	0.000000000000	-2.345875332600	0.988973375678
C	-1.364773267600	-0.710177532571	0.000000000000
C	-1.364773267600	0.710177532571	0.000000000000
C	-2.609491647684	1.372991536857	0.000000000000
H	-2.617990347449	2.465189952299	0.000000000000
C	-3.830015886372	0.698993748080	0.000000000000
H	-4.768718337640	1.251686090264	0.000000000000
C	-3.830015886372	-0.698993748080	0.000000000000
H	-4.768718337640	-1.251686090264	0.000000000000
C	-2.609491647684	-1.372991536857	0.000000000000
H	-2.617990347449	-2.465189952299	0.000000000000
H	0.000000000000	2.345875332600	-0.988973375678
H	0.000000000000	-2.345875332600	-0.988973375678

24
ant

H	0.000000000000	4.597848283613	1.245891762682
C	0.000000000000	3.651203368027	0.712396179209
H	0.000000000000	2.467401824754	2.494058146910
C	0.000000000000	2.471738624931	1.406536645793
C	0.000000000000	2.471738624931	-1.406536645793
C	0.000000000000	1.219509178965	0.720282707747
C	0.000000000000	3.651203368027	-0.712396179209
C	0.000000000000	1.219509178965	-0.720282707747
C	0.000000000000	0.000000000000	1.403858697523
H	0.000000000000	4.597848283613	-1.245891762682
H	0.000000000000	0.000000000000	-2.492156892256
H	0.000000000000	2.467401824754	-2.494058146910
C	0.000000000000	-1.219509178965	0.720282707747
H	0.000000000000	0.000000000000	2.492156892256
C	0.000000000000	-2.471738624931	1.406536645793
C	0.000000000000	-1.219509178965	-0.720282707747
H	0.000000000000	-2.467401824754	-2.494058146910
C	0.000000000000	0.000000000000	-1.403858697523
C	0.000000000000	-3.651203368027	0.712396179209
H	0.000000000000	-2.467401824754	2.494058146910
H	0.000000000000	-4.597848283613	1.245891762682
C	0.000000000000	-3.651203368027	-0.712396179209
H	0.000000000000	-4.597848283613	-1.245891762682
C	0.000000000000	-2.471738624931	-1.406536645793

26
TS1$_{ant}$

H	-4.500980738975	1.242057667679	-0.633019203997
C	-3.583754991595	0.705026561517	-0.406766048060
H	-2.430055222409	2.492769826007	-0.097073150992
C	-2.429712787877	1.405699315972	-0.114390174601
C	-2.429712787877	-1.405699315972	-0.114390174601
C	-1.232090197228	0.709076894113	0.144991622987
C	-3.583754991595	-0.705026561517	-0.406766048060
C	-1.232090197228	-0.709076894113	0.144991622987
C	0.000000000000	1.328282738118	0.553925351404
H	-4.500980738975	-1.242057667679	-0.633019203997
H	0.000000000000	-2.402138355953	0.735068247039
H	-2.430055222409	-2.492769826007	-0.097073150992
C	1.232090197228	0.709076894113	0.144991622987
H	0.000000000000	2.402138355953	0.735068247039
C	2.429712787877	1.405699315972	-0.114390174601
C	1.232090197228	-0.709076894113	0.144991622987
H	2.430055222409	-2.492769826007	-0.097073150992
C	0.000000000000	-1.328282738118	0.553925351404
C	3.583754991595	0.705026561517	-0.406766048060
H	2.430055222409	2.492769826007	-0.097073150992
H	4.500980738975	1.242057667679	-0.633019203997
C	3.583754991595	-0.705026561517	-0.406766048060
H	4.500980738975	-1.242057667679	-0.633019203997
C	2.429712787877	-1.405699315972	-0.114390174601
H	0.000000000000	0.465302586641	1.915539550602
H	0.000000000000	-0.465302586641	1.915539550602

26
H2$_{ant}$

H	-4.408110505981	1.244317812771	-0.859360591475
C	-3.525873021113	0.697138835339	-0.537877211264
H	-2.378553457601	2.478231432630	-0.141783482175
C	-2.385667418458	1.390328062890	-0.133290759125
C	-2.385667418458	-1.390328062890	-0.133290759125
C	-1.245251405798	0.701257438279	0.282307546786
C	-3.525873021113	-0.697138835339	-0.537877211264
C	-1.245251405798	-0.701257438279	0.282307546786
C	0.000000000000	1.415736897210	0.739025385244
H	-4.408110505981	-1.244317812771	-0.859360591475
H	0.000000000000	-2.454001182468	0.394002733319
H	-2.378553457601	-2.478231432630	-0.141783482175
C	1.245251405798	0.701257438279	0.282307546786
H	0.000000000000	2.454001182468	0.394002733319
C	2.385667418458	1.390328062890	-0.133290759125
C	1.245251405798	-0.701257438279	0.282307546786
H	2.378553457601	-2.478231432630	-0.141783482175
C	0.000000000000	-1.415736897210	0.739025385244
C	3.525873021113	0.697138835339	-0.537877211264
H	2.378553457601	2.478231432630	-0.141783482175
H	4.408110505981	1.244317812771	-0.859360591475
C	3.525873021113	-0.697138835339	-0.537877211264
H	4.408110505981	-1.244317812771	-0.859360591475
C	2.385667418458	-1.390328062890	-0.133290759125
H	0.000000000000	1.453750790213	1.840458185757
H	0.000000000000	-1.453750790213	1.840458185757

26
TS2$_{ant}$
H 4.527004044968 -1.219985020630 -0.658538295529
C 3.615319255622 -0.683892684787 -0.415311490618
H 2.417206103974 -2.455886356000 -0.174246514977
C 2.440591049827 -1.368112467499 -0.155767893341
C 2.456261047471 1.428457181250 -0.039281770463
C 1.266845113306 -0.663835593118 0.144430711526
C 3.604638519498 0.727621028756 -0.335809663405
C 1.213447555055 0.766510208356 0.204711521407
C -0.032827258761 -1.409771391869 0.533219129347
H 4.525032934244 1.276898413163 -0.521448939972
H -0.006183909656 2.525683456071 0.429682138956
H 2.476511693449 2.515271452508 -0.004120574373
C -1.268872868156 -0.668864734329 0.149814171463
H 0.037820712731 -2.465203458113 0.267368123179
C -2.430586483987 -1.365991482273 -0.170577700637
C -1.233948561705 0.751740272077 0.215023743099
H -2.486762144440 2.503174597885 0.025096204179
C -0.003536080367 1.438862136347 0.423038336164
C -3.619579249371 -0.684108311090 -0.418392412865
H -2.405373706788 -2.453603935387 -0.206528478992
H -4.527995468867 -1.227144525379 -0.660464644797
C -3.622009796273 0.715921139957 -0.321007640279
H -4.544550932466 1.264925070114 -0.496324919269
C -2.465898125250 1.416470747717 -0.018516187501
H -0.187392793599 -1.584486154129 1.737972529053
H 0.655618764998 -1.085679837070 1.488116249161

26
Int$_{ant}$
H 4.591443629983 -1.208939976948 -0.127535607231
C 3.643261117293 -0.690790149546 -0.007538590511
H 2.513421086091 -2.472476665289 0.189860792752
C 2.504157873312 -1.384365930671 0.162231271915
C 2.467221698127 1.453093290209 -0.042834309844
C 1.185345903571 -0.705301721865 0.385274841395
C 3.633083508957 0.763190148342 -0.052446040771
C 1.195862275898 0.772074160588 0.040296456915
C 0.034145031048 -1.416619213807 -0.321784427016
H 4.578887328410 1.290720175738 -0.143187132275
H -0.001470985289 2.494857244495 -0.275087145398
H 2.462724242171 2.536062582548 -0.148223354993
C -1.271168915498 -0.695266795674 -0.119619038370
H 0.254467014908 -1.461380765504 -1.400826479008
C -2.489147221562 -1.369037760120 -0.072773143418
C -1.257545593161 0.716671703845 -0.051828779664
H -2.459366370943 2.496321874696 0.103004000732
C 0.012476445958 1.417441576108 -0.119017346360
C -3.691860068632 -0.670670149584 0.050238287008
H -2.497462763655 -2.455528053952 -0.129794857218
H -4.631847089659 -1.213759441883 0.098373407999
C -3.681974120414 0.723128088276 0.112945999312
H -4.614857022671 1.272645693920 0.206153110853
C -2.473065256724 1.409563413845 0.057573184278
H -0.041326181463 -2.450887462541 0.029640466085
H 0.980631043083 -0.766299164958 1.473312608489

26
TS3$_{ant}$
H 4.364353878756 -1.291262244159 -0.879167938008
C 3.489383088927 -0.735141015937 -0.557640247057
H 2.297379482315 -2.490670087061 -0.224947875948
C 2.340328640070 -1.405069802651 -0.183779998103
C 2.454417105360 1.415904716771 -0.106686570313
C 1.210069151302 -0.714969297618 0.276772751960
C 3.539255158638 0.684080654705 -0.491921969548
C 1.215851422994 0.762726300511 0.336071297171
C -0.028170207591 -1.361550526572 0.818298802009
H 4.449578157825 1.197992671762 -0.788874144932
H -0.022907409016 2.533329223114 0.532185419761
H 2.482302777873 2.501963100487 -0.108749744578
C -1.242210032511 -0.681115185048 0.242845949608
H -0.019628001480 -2.435577054723 0.610619408000
C -2.364860767602 -1.381437956125 -0.185444335505
C -1.240439911985 0.744620460409 0.264090968527
H -2.486925269339 2.489609556204 -0.032816748811
C -0.030813354621 1.447567213120 0.518969259532
C -3.540527258742 -0.712764076847 -0.533330800935
H -2.332330752729 -2.469527129549 -0.206370791664
H -4.420858933028 -1.270936980362 -0.839118162635
C -3.576960071122 0.685570306002 -0.447235902055
H -4.490911478223 1.219086125617 -0.698596448176
C -2.454983519335 1.402397151163 -0.060432701689
H -0.040482658318 -1.242234592640 1.917402196623
H 1.598393542679 0.353313760022 1.374975808748

26
TS$_{inv}$(H2-ant)
C 0.000000000000 1.499090426022 0.000000000000
H 0.000000000000 2.167227774847 0.871726817786
C 1.274677228070 0.699096796525 0.000000000000
C 1.274677228070 -0.699096796525 0.000000000000
C 2.499358435139 -1.382174949786 0.000000000000
H 2.494689379793 -2.470656211004 0.000000000000
C 3.708446401595 -0.698575317574 0.000000000000
H 4.645815799090 -1.248408243123 0.000000000000
C 3.708446401595 0.698575317574 0.000000000000
H 4.645815799090 1.248408243123 0.000000000000
C 2.499358435139 1.382174949786 0.000000000000
H 2.494689379793 2.470656211004 0.000000000000
C 0.000000000000 -1.499090426022 0.000000000000
H 0.000000000000 -2.167227774847 0.871726817786
C -1.274677228070 -0.699096796525 0.000000000000
C -1.274677228070 0.699096796525 0.000000000000
C -2.499358435139 1.382174949786 0.000000000000
H -2.494689379793 2.470656211004 0.000000000000
C -3.708446401595 0.698575317574 0.000000000000
H -4.645815799090 1.248408243123 0.000000000000
C -3.708446401595 -0.698575317574 0.000000000000
H -4.645815799090 -1.248408243123 0.000000000000
C -2.499358435139 -1.382174949786 0.000000000000
H -2.494689379793 -2.470656211004 0.000000000000
H 0.000000000000 2.167227774847 -0.871726817786
H 0.000000000000 -2.167227774847 -0.871726817786

52
[**4**]$^{2-}$

B	-1.504487271611	0.076219710545	-0.042752936399
C	-0.680600020943	1.362373121068	-0.046788994105
C	0.775270745449	1.307609608748	-0.048279274365
C	1.480583612500	2.549074441978	-0.051447667894
H	2.570847389383	2.517020327402	-0.052496736102
C	0.849283852170	3.774446924897	-0.053608804164
H	1.429569444018	4.696144347962	-0.056780948365
C	-0.571843718334	3.827601761543	-0.051670692330
H	-1.081903177153	4.790087603668	-0.053232132464
C	-1.292959819550	2.652490489815	-0.048152956408
H	-2.382868233458	2.702642924646	-0.046808688483
B	1.503351741666	-0.035577879678	-0.043862602885
C	0.679479932154	-1.322012408372	-0.048580539064
C	-0.776300827318	-1.267380755848	-0.048967420807
C	-1.481079559317	-2.509182914034	-0.052546484122
H	-2.571283842799	-2.477884675151	-0.052930736765
C	-0.849570188514	-3.734429610773	-0.055607444712
H	-1.429783179089	-4.656178379469	-0.058717011033
C	0.571484453846	-3.787347249845	-0.054763691172
H	1.081841022981	-4.749674145914	-0.057085535894
C	1.292140347714	-2.611996058784	-0.051237321315
H	2.382017882537	-2.661787186645	-0.050918414566
C	3.049606774716	-0.075209021348	-0.021142668261
C	4.278262626395	-0.078277824019	0.008297788618
C	-3.051006414632	0.108215424193	-0.019684506183
C	-4.279541240579	0.087540907762	0.009133935607
C	5.748902202384	-0.061968840566	0.055815073870
C	6.224857120671	-0.246768509282	1.506382946787
C	6.266094137188	1.283411996497	-0.478291824584
H	5.943316194208	1.442317388056	-1.512544915352
H	5.887530340095	2.114623351173	0.125951390931
H	7.362669917767	1.306961403138	-0.450499147406
H	5.842225912875	0.554412556940	2.147028197990
H	7.321330345381	-0.232544320170	1.553379479017
H	5.874884991601	-1.201703791852	1.912210698708
C	-5.748638530468	0.018675488813	0.055509771253
C	-6.213604919402	-0.162597705376	1.510141209662
C	-6.230161950258	-1.179036698120	-0.779315258279
H	-5.917518022676	-1.078059997299	-1.823853999472
H	-5.815540660765	-2.115289927415	-0.390958715113
H	-7.324850446088	-1.248114582926	-0.750658506290
H	-5.796686498882	-1.079536440898	1.939664808216
H	-7.308375689766	-0.225820895185	1.555869129167
H	-5.891359661436	0.679774090270	2.130835873580
C	-6.354164902711	1.310706156141	-0.513642253322
H	-6.041850880774	1.463476285968	-1.551986894498
H	-7.449940362752	1.261289877576	-0.486082332070
H	-6.034424383273	2.181629508746	0.068395864951
C	6.311824696286	-1.200438862166	-0.809198147426
H	5.995340138189	-1.091339379674	-1.851761620661
H	7.408632169585	-1.194893997281	-0.777944885734
H	5.961946483340	-2.173760277540	-0.449125189572

54
$TS_{4\rightarrow3}$

B	1.437764697859	0.016419564115	-0.010625630632
C	0.709170683293	1.335877851468	-0.401344404452
C	-0.728352979939	1.324431481289	-0.410070230222
C	-1.405517195075	2.530274655539	-0.705071914149
H	-2.496435263979	2.529605104933	-0.705161828802
C	-0.729379564866	3.706807050598	-0.999304965742
H	-1.282189920702	4.615311974079	-1.235096283891
C	0.679405527285	3.718707976717	-0.987950931482
H	1.220547976596	4.636455878939	-1.214826638368
C	1.370587285091	2.553064427832	-0.685428625788
H	2.461272872154	2.570767542909	-0.669086026307
B	-1.440774731033	-0.004870150153	-0.022407733279
C	-0.709407091127	-1.323017993450	-0.412058787675
C	0.728081901097	-1.312008208365	-0.407255498438
C	1.407189490755	-2.517758438771	-0.698200544397
H	2.498028506498	-2.517865389603	-0.687797129820
C	0.733265457253	-3.693434841306	-1.000695930647
H	1.287904233460	-4.601841732457	-1.232558596630
C	-0.675571084655	-3.704440879318	-1.003922999733
H	-1.214924805729	-4.621436577695	-1.237984205061
C	-1.368903476839	-2.539101136024	-0.705272004137
H	-2.459709618718	-2.556024415112	-0.699441159810
H	0.457398236940	0.006815353406	1.417066933898
H	-0.472300898691	0.000117167421	1.412868902285
C	-2.977100640505	-0.013584366746	0.201530806854
C	-4.189195016163	-0.015764182999	0.393347986442
C	2.973657115070	0.022248959652	0.217144098328
C	4.186200210853	0.018041559541	0.406029920012
C	-5.637706709538	-0.015007800490	0.652417343375
C	-6.292902827353	1.170792350963	-0.072821601550
C	-5.893896661604	0.111614696909	2.163134348484
H	-5.440041479801	-0.723758745755	2.706483065932
H	-5.467456019752	1.041469255829	2.553751603547
H	-6.972101837658	0.113016111814	2.367356506165
H	-5.873221323824	2.120598059789	0.274977135989
H	-7.373728437031	1.180700256519	0.115940184987
H	-6.131633384193	1.104494933986	-1.153896811557
C	5.636957246012	0.000510786631	0.650575868004
C	6.333532084221	-0.837818640475	-0.432820159496
C	5.922185440072	-0.616179787690	2.029455601861
H	5.440041171071	-0.035905736324	2.823026296339
H	5.544831666827	-1.642668705276	2.082722539059
H	7.002376783000	-0.634383423172	2.221921459558
H	5.962206338875	-1.868030963653	-0.427467879007
H	7.416678863415	-0.860163886868	-0.258630509353
H	6.153018045308	-0.417094354567	-1.427481759559
C	6.185374966304	1.435043982349	0.613621877701
H	5.704235008948	2.055788948936	1.376686644265
H	7.266415319448	1.432716201789	0.800900261326
H	6.006049575367	1.896917380809	-0.362982373102
C	-6.255180650932	-1.325782145488	0.141919543617
H	-5.806409707043	-2.189647972184	0.643520877901
H	-7.335273168298	-1.336696626230	0.334152581070
H	-6.095489618880	-1.438106862257	-0.935549752116

54
[3]$^{2-}$

B	-1.480412473277	0.000000070955	-0.885010088755
C	-0.710776033685	1.325907546080	-0.354791816575
C	0.710753116123	1.325898708147	-0.354639773032
C	1.379312538995	2.474457027966	0.095592564577
H	2.469688186360	2.476864503535	0.106206578849
C	0.696812205396	3.614641275395	0.532630007262
H	1.249124323207	4.489007787289	0.874967729371
C	-0.696975527287	3.614660259983	0.532464613628
H	-1.249344854779	4.489042694760	0.874669120925
C	-1.379404593038	2.474488862946	0.095281284833
H	-2.469782005382	2.476926276637	0.105656445586
B	1.480450614844	0.000000130460	-0.884769495418
C	0.710753173624	-1.325898443441	-0.354639684646
C	-0.710775976314	-1.325907338912	-0.354791729690
C	-1.379404486366	-2.474488659071	0.095281434841
H	-2.469781898419	-2.476926116731	0.105656592921
C	-0.696975373947	-3.614660002745	0.532464830174
H	-1.249344666472	-4.489042440980	0.874669385521
C	0.696812358950	-3.614640961320	0.532630223340
H	1.249124512831	-4.489007431558	0.874967993535
C	1.379312644996	-2.474456710027	0.095592716753
H	2.469688292848	-2.476864140369	0.106206727398
H	-1.372309305918	0.000000033062	-2.128857649111
H	1.372417774595	0.000000121982	-2.128625682739
C	3.030447480226	0.000000208351	-0.541151709232
C	4.224952902870	-0.000000019348	-0.268169605673
C	-3.030419845756	0.000000033022	-0.541416942775
C	-4.224902096613	-0.000000041744	-0.268333502640
C	5.657093089209	-0.000000185856	0.077565265932
C	5.817620034592	-0.000000329838	1.605580687107
C	6.331177792284	1.253269443269	-0.501727823129
H	6.236678381787	1.278895698301	-1.592351433246
H	5.872409829571	2.162915751488	-0.099971756226
H	7.398477340851	1.263266607755	-0.247359641246
H	5.348372897748	0.885881761667	2.046198948369
H	6.880688992053	-0.000000438064	1.877750773750
H	5.348372752952	-0.885882419425	2.046198798650
C	-5.657005804702	-0.000000127859	0.077558242233
C	-5.817363803979	-0.000000151658	1.605592997985
C	-6.331158416183	-1.253270252334	-0.501655315332
H	-6.236780084253	-1.278903347817	-1.592289171247
H	-5.872350658149	-2.162915758934	-0.099943036037
H	-7.398429968790	-1.263261585774	-0.247169013624
H	-5.348068375086	-0.885881496227	2.046160737992
H	-6.880403417586	-0.000000218661	1.877878049895
H	-5.348068482014	0.885881241549	2.046160754349
C	-6.331158571458	1.253269920928	-0.501655298395
H	-6.236780244224	1.278903041618	-1.592289154177
H	-7.398430125027	1.263261119506	-0.247168995210
H	-5.872350925034	2.162915479072	-0.099943008103
C	6.331177573353	-1.253269818910	-0.501728070073
H	6.236678158671	-1.278895841857	-1.592351685445
H	7.398477120396	-1.263267220338	-0.247359890858
H	5.872409451694	-2.162916126702	-0.099972183800

26
a_{Li}
Li 0.000000000000 0.000000000000 1.670727516267
B 0.000000000000 1.523784769680 0.000000000000
H 0.000000000000 2.730864782009 0.000000000000
C -1.310055059896 0.733853752974 0.000000000000
C -1.310055059896 -0.733853752974 0.000000000000
C -2.583805063838 -1.399652102426 0.000000000000
H -2.590586225533 -2.488411487895 0.000000000000
C -3.767768280794 -0.713110215519 0.000000000000
H -4.713972318891 -1.249059379835 0.000000000000
C -3.767768280794 0.713110215519 0.000000000000
H -4.713972318891 1.249059379835 0.000000000000
C -2.583805063838 1.399652102426 0.000000000000
H -2.590586225533 2.488411487895 0.000000000000
B 0.000000000000 -1.523784769680 0.000000000000
H 0.000000000000 -2.730864782009 0.000000000000
C 1.310055059896 -0.733853752974 0.000000000000
C 1.310055059896 0.733853752974 0.000000000000
C 2.583805063838 1.399652102426 0.000000000000
H 2.590586225533 2.488411487895 0.000000000000
C 3.767768280794 0.713110215519 0.000000000000
H 4.713972318891 1.249059379835 0.000000000000
C 3.767768280794 -0.713110215519 0.000000000000
H 4.713972318891 -1.249059379835 0.000000000000
C 2.583805063838 -1.399652102426 0.000000000000
H 2.590586225533 -2.488411487895 0.000000000000
Li 0.000000000000 0.000000000000 -1.670727516267

28
ts_{Li}
Li -2.137180365499 -1.569695301643 0.000000000000
B -0.508483094805 0.039336196218 1.443777722368
H -0.645038949583 0.031994749090 2.647748949375
C -0.161810588558 1.382277220498 0.718421054846
C -0.161810588558 1.382277220498 -0.718421054846
C 0.091697541224 2.601653030715 -1.395760161592
H 0.087340059114 2.610069045045 -2.484917524416
C 0.337126154948 3.774617704852 -0.704890060286
H 0.529135448487 4.698624675346 -1.245790699977
C 0.337126154948 3.774617704852 0.704890060286
H 0.529135448487 4.698624675346 1.245790699977
C 0.091697541224 2.601653030715 1.395760161592
H 0.087340059114 2.610069045045 2.484917524416
B -0.508483094805 0.039336196218 -1.443777722368
H -0.645038949583 0.031994749090 -2.647748949375
C -0.109271854563 -1.287224626350 -0.726506891794
C -0.109271854563 -1.287224626350 0.726506891794
C 0.173891914475 -2.515753286314 1.401081313261
H 0.169316335420 -2.524590061150 2.489877264554
C 0.452448815484 -3.673973517598 0.709196083780
H 0.673986958326 -4.592694528432 1.247071239486
C 0.452448815484 -3.673973517598 -0.709196083780
H 0.673986958326 -4.592694528432 -1.247071239486
C 0.173891914475 -2.515753286314 -1.401081313261
H 0.169316335420 -2.524590061150 -2.489877264554
Li 1.443239797478 0.079188054668 0.000000000000
H -1.935905423772 0.126096854651 0.480386177489
H -1.935905423772 0.126096854651 -0.480386177489

28
b_{Li}
Li 0.000000000000 0.000000000000 -1.458877155980
B 0.000000000000 1.563641824000 0.483603684020
H 0.000000000000 1.838361706000 1.706448782020
C 1.358125830000 0.711946559000 0.166039563020
C 1.358125830000 -0.711946559000 0.166039563020
C 2.567943374000 -1.386066181000 -0.105636893980
H 2.570908451000 -2.474914876000 -0.118865292980
C 3.748556568000 -0.700067986000 -0.356703131980
H 4.666367291000 -1.245789756000 -0.563265234980
C 3.748556568000 0.700067986000 -0.356703131980
H 4.666367291000 1.245789756000 -0.563265234980
C 2.567943374000 1.386066181000 -0.105636893980
H 2.570908451000 2.474914876000 -0.118865292980
B 0.000000000000 -1.563641824000 0.483603684020
H 0.000000000000 -1.838361706000 1.706448782020
C -1.358125830000 -0.711946559000 0.166039563020
C -1.358125830000 0.711946559000 0.166039563020
C -2.567943374000 1.386066181000 -0.105636893980
H -2.570908451000 2.474914876000 -0.118865292980
C -3.748556568000 0.700067986000 -0.356703131980
H -4.666367291000 1.245789756000 -0.563265234980
C -3.748556568000 -0.700067986000 -0.356703131980
H -4.666367291000 -1.245789756000 -0.563265234980
C -2.567943374000 -1.386066181000 -0.105636893980
H -2.570908451000 -2.474914876000 -0.118865292980
H 0.000000000000 2.647057096000 -0.076235947980
H 0.000000000000 -2.647057096000 -0.076235947980
Li 0.000000000000 0.000000000000 2.039967394020

28
c_{Li}
Li -2.313800324937 -0.937209758672 0.000000000000
B -0.769611264675 0.024930921399 1.493108387802
H -0.452671217671 0.008923332776 2.672896911418
C -0.287069538925 1.365483086891 0.711877115660
C -0.287069538925 1.365483086891 -0.711877115660
C 0.138743654705 2.523184203417 -1.387165610149
H 0.154297037757 2.525877727028 -2.476384201603
C 0.532955808783 3.669694028294 -0.698012517030
H 0.849260731360 4.555329105076 -1.244660735815
C 0.532955808783 3.669694028294 0.698012517030
H 0.849260731360 4.555329105076 1.244660735815
C 0.138743654705 2.523184203417 1.387165610149
H 0.154297037757 2.525877727028 2.476384201603
B -0.769611264675 0.024930921399 -1.493108387802
H -0.452671217671 0.008923332776 -2.672896911418
C -0.260410167255 -1.320030803024 -0.714419157301
C -0.260410167255 -1.320030803024 0.714419157301
C 0.188534309103 -2.473128887442 1.391419885037
H 0.199430368046 -2.476061535181 2.480059443821
C 0.619408590095 -3.599725672265 0.699744870497
H 0.962529455212 -4.476982915487 1.243130274821
C 0.619408590095 -3.599725672265 -0.699744870497
H 0.962529455212 -4.476982915487 -1.243130274821
C 0.188534309103 -2.473128887442 -1.391419885037
H 0.199430368046 -2.476061535181 -2.480059443821
Li 1.360141376369 0.064649098945 0.000000000000
H -2.027277567512 0.054244933152 1.491407174191
H -2.027277567512 0.054244933152 -1.491407174191

28
d_{Li}
Li	-1.623976488295	2.436859055989	1.539901154437
B	0.068137555324	-1.374349765094	1.044782157276
H	0.100169106660	-2.587180531485	0.747420587488
C	1.389218555916	-0.639124069388	0.429971829837
C	1.354972027450	0.766651785464	0.217231532790
C	2.486248557636	1.397258089760	-0.318932372330
H	2.466780414961	2.473756924093	-0.486072435003
C	3.641000133031	0.682085556570	-0.647174087648
H	4.503762995868	1.198061011024	-1.063225184145
C	3.679114342606	-0.696227477676	-0.446055620769
H	4.571369997106	-1.264750275268	-0.699025097918
C	2.557856844763	-1.341961580265	0.083713630466
H	2.596204010846	-2.420783204332	0.243752681006
B	0.014559262545	1.534938716176	0.619112789619
H	-0.071165502798	2.704998228619	0.212600190343
C	-1.296049950337	0.690157434679	0.171795121169
C	-1.277579454491	-0.714602998372	0.406326808828
C	-2.403692204966	-1.465752078175	0.035527688436
H	-2.397502566078	-2.544491443257	0.197193160631
C	-3.544557219739	-0.873833051056	-0.521222881153
H	-4.404598827320	-1.485213588918	-0.784521657000
C	-3.563427499780	0.497440048689	-0.747378402981
H	-4.432189624949	0.970033769007	-1.199536011163
C	-2.438932888598	1.262131137693	-0.411789860185
H	-2.446640748240	2.329151829404	-0.656283000459
Li	0.140841342195	-1.732597607634	-1.034517520297
H	0.051847851959	-1.285610123618	2.266270133781
H	-0.007143220006	1.610961516720	1.873720676789

28
e_{Li}
Li	3.489512189863	1.573544740875	0.000000000000
B	-1.366052967348	1.084562647694	0.000000000000
H	-2.587694628453	0.818092791240	0.000000000000
C	-0.688689278023	0.437160862941	1.335341558438
C	0.704792445973	0.153944406410	1.328530873750
C	1.281107724239	-0.418969964994	2.471693349977
H	2.346868545147	-0.649629226271	2.472614328280
C	0.527758722490	-0.713650505909	3.610877964782
H	1.003121896909	-1.161077375427	4.481386413035
C	-0.838934196791	-0.440516188457	3.621286342152
H	-1.438575053041	-0.668236512316	4.499949545287
C	-1.432432173249	0.123166650894	2.488176460696
H	-2.502919102182	0.333930056313	2.502210740514
B	1.529733010123	0.514096113037	0.000000000000
H	2.650687047429	-0.042456476185	0.000000000000
C	0.704792445973	0.153944406410	-1.328530873750
C	-0.688689278023	0.437160862941	-1.335341558438
C	-1.432432173249	0.123166650894	-2.488176460696
H	-2.502919102182	0.333930056313	-2.502210740514
C	-0.838934196791	-0.440516188457	-3.621286342152
H	-1.438575053041	-0.668236512316	-4.499949545287
C	0.527758722490	-0.713650505909	-3.610877964782
H	1.003121896909	-1.161077375427	-4.481386413035
C	1.281107724239	-0.418969964994	-2.471693349977
H	2.346868545147	-0.649629226271	-2.472614328280
Li	-1.755250359074	-0.985993682012	0.000000000000
H	-1.249011726966	2.304651773192	0.000000000000
H	1.704602092410	1.760167916291	0.000000000000

26
a_K
K	0.000000000000	2.650044018614	0.000000000000
B	0.000000000000	0.000000000000	-1.508822534392
H	0.000000000000	0.000000000000	-2.727533938573
C	-1.310935612850	0.000000000000	-0.733253650924
C	-1.310935612850	0.000000000000	0.733253650924
C	-2.584084691254	0.000000000000	1.394051067020
H	-2.593665994174	0.000000000000	2.484670775533
C	-3.777583179493	0.000000000000	0.712585487936
H	-4.722146220564	0.000000000000	1.252982201912
C	-3.777583179493	0.000000000000	-0.712585487936
H	-4.722146220564	0.000000000000	-1.252982201912
C	-2.584084691254	0.000000000000	-1.394051067020
H	-2.593665994174	0.000000000000	-2.484670775533
B	0.000000000000	0.000000000000	1.508822534392
H	0.000000000000	0.000000000000	2.727533938573
C	1.310935612850	0.000000000000	0.733253650924
C	1.310935612850	0.000000000000	-0.733253650924
C	2.584084691254	0.000000000000	-1.394051067020
H	2.593665994174	0.000000000000	-2.484670775533
C	3.777583179493	0.000000000000	-0.712585487936
H	4.722146220564	0.000000000000	-1.252982201912
C	3.777583179493	0.000000000000	0.712585487936
H	4.722146220564	0.000000000000	1.252982201912
C	2.584084691254	0.000000000000	1.394051067020
H	2.593665994174	0.000000000000	2.484670775533
K	0.000000000000	-2.650044018614	0.000000000000

28
ts_K
K	-2.063094540798	-2.711360424981	0.000000000000
B	-0.541973651007	0.215620625710	1.440416256206
H	-0.669928772940	0.177494713863	2.653265550507
C	-0.541850598811	1.595184273335	0.719998882419
C	-0.541850598811	1.595184273335	-0.719998882419
C	-0.574727586086	2.841956032587	-1.391961228982
H	-0.584132976131	2.851188458258	-2.482360654715
C	-0.586465406744	4.046897183597	-0.704431956195
H	-0.600602116221	4.989666793772	-1.247952892454
C	-0.586465406744	4.046897183597	0.704431956195
H	-0.600602116221	4.989666793772	1.247952892454
C	-0.574727586086	2.841956032587	1.391961228982
H	-0.584132976131	2.851188458258	2.482360654715
B	-0.541973651007	0.215620625710	-1.440416256206
H	-0.669928772940	0.177494713863	-2.653265550507
C	0.163216984252	-0.964882911935	-0.725345488528
C	0.163216984252	-0.964882911935	0.725345488528
C	0.696650565783	-2.101986272088	1.394408933531
H	0.694565196589	-2.114576196249	2.484725347512
C	1.203947296035	-3.194683474633	0.708025388347
H	1.605825250932	-4.047520442958	1.251003094850
C	1.203947296035	-3.194683474633	-0.708025388347
H	1.605825250932	-4.047520442958	-1.251003094850
C	0.696650565783	-2.101986272088	-1.394408933531
H	0.694565196589	-2.114576196249	-2.484725347512
K	2.276195725177	1.014579646481	0.000000000000
H	-1.924947105368	-0.149848044677	0.470277840560
H	-1.924947105368	-0.149848044677	-0.470277840560

28
b_K
K	0.000000000000	2.577648944406	0.000000000000
B	0.000000000000	0.000000000000	1.584786742290
H	0.000000000000	-0.986282670569	2.343039291817
C	1.369192005766	0.000000000000	0.710177903734
C	1.369192005766	0.000000000000	-0.710177903734
C	2.612801131393	0.000000000000	-1.379430955236
H	2.619540933952	0.000000000000	-2.470096151239
C	3.825977980416	0.000000000000	-0.699864197932
H	4.765639752823	0.000000000000	-1.248647127699
C	3.825977980416	0.000000000000	0.699864197932
H	4.765639752823	0.000000000000	1.248647127699
C	2.612801131393	0.000000000000	1.379430955236
H	2.619540933952	0.000000000000	2.470096151239
B	0.000000000000	0.000000000000	-1.584786742290
H	0.000000000000	-0.986282670569	-2.343039291817
C	-1.369192005766	0.000000000000	-0.710177903734
C	-1.369192005766	0.000000000000	0.710177903734
C	-2.612801131393	0.000000000000	1.379430955236
H	-2.619540933952	0.000000000000	2.470096151239
C	-3.825977980416	0.000000000000	0.699864197932
H	-4.765639752823	0.000000000000	1.248647127699
C	-3.825977980416	0.000000000000	-0.699864197932
H	-4.765639752823	0.000000000000	-1.248647127699
C	-2.612801131393	0.000000000000	-1.379430955236
H	-2.619540933952	0.000000000000	-2.470096151239
H	0.000000000000	0.986282670569	2.343039291817
H	0.000000000000	0.986282670569	-2.343039291817
K	0.000000000000	-2.577648944406	0.000000000000

28
c_K
K	-2.604821195932	-2.057951646004	0.000000000000
B	-0.672710499814	0.054914879794	1.509548422729
H	-0.256471317037	0.153961299957	2.667994552717
C	-0.570060693845	1.459172877058	0.712490101271
C	-0.570060693845	1.459172877058	-0.712490101271
C	-0.428562137824	2.687918980503	-1.382376592484
H	-0.412622010906	2.695239677193	-2.472805684074
C	-0.300448639897	3.899892990524	-0.697628150559
H	-0.192664791466	4.833187355631	-1.247046163724
C	-0.300448639897	3.899892990524	0.697628150559
H	-0.192664791466	4.833187355631	1.247046163724
C	-0.428562137824	2.687918980503	1.382376592484
H	-0.412622010906	2.695239677193	2.472805684074
B	-0.672710499814	0.054914879794	-1.509548422729
H	-0.256471317037	0.153961299957	-2.667994552717
C	0.109313606421	-1.124892016735	-0.713977233981
C	0.109313606421	-1.124892016735	0.713977233981
C	0.804759079739	-2.150410252970	1.383929170320
H	0.818328989902	-2.151643052042	2.474139114849
C	1.479708406459	-3.163408369165	0.698005085349
H	2.006491989777	-3.941667745028	1.246483870846
C	1.479708406459	-3.163408369165	-0.698005085349
H	2.006491989777	-3.941667745028	-1.246483870846
C	0.804759079739	-2.150410252970	-1.383929170320
H	0.818328989902	-2.151643052042	-2.474139114849
K	2.259281250699	0.871238146989	0.000000000000
H	-1.885138607801	-0.239518949321	1.614394117728
H	-1.885138607801	-0.239518949321	-1.614394117728

28
$\mathbf{d}_K$
K 0.184311106782 -4.367812464165 0.000000000000
B 1.672080963967 1.057302689526 0.000000000000
H 1.985232242406 2.264285239098 0.000000000000
C 0.820399685329 0.700408247183 1.334746057079
C -0.033236840189 -0.439737335092 1.325977187649
C -0.815584306582 -0.701433448878 2.462179312864
H -1.485728070850 -1.562737024023 2.457507397347
C -0.774253098717 0.109817024880 3.600593820579
H -1.395719044361 -0.120935362499 4.463908218305
C 0.067895749501 1.220956152874 3.616164506412
H 0.115799803287 1.863519410323 4.493427603970
C 0.845477874482 1.505367305753 2.488163611346
H 1.497662350341 2.380863347906 2.508004770633
B -0.052264366422 -1.353675371150 0.000000000000
H -1.021546824730 -2.139308682577 0.000000000000
C -0.033236840189 -0.439737335092 -1.325977187649
C 0.820399685329 0.700408247183 -1.334746057079
C 0.845477874482 1.505367305753 -2.488163611346
H 1.497662350341 2.380863347906 -2.508004770633
C 0.067895749501 1.220956152874 -3.616164506412
H 0.115799803287 1.863519410323 -4.493427603970
C -0.774253098717 0.109817024880 -3.600593820579
H -1.395719044361 -0.120935362499 -4.463908218305
C -0.815584306582 -0.701433448878 -2.462179312864
H -1.485728070850 -1.562737024023 -2.457507397347
K -0.793994362885 2.742230816690 0.000000000000
H 2.724163852399 0.403605342274 0.000000000000
H 1.004630765445 -2.026623292691 0.000000000000

78
A_{Li}

Li	1.883997402409	-0.019047538539	-0.054084743233
B	0.042943804697	0.085129876462	1.507514813556
H	0.079254137199	0.155602298353	2.719389598519
C	0.009317559444	-1.265291328457	0.803049252545
C	-0.033472149439	-1.346452337595	-0.654773450027
C	-0.067704734818	-2.651877345619	-1.246709430309
H	-0.100771402029	-2.719425445629	-2.334198179546
C	-0.060557783156	-3.802239798194	-0.500624161714
H	-0.087523115869	-4.775427183774	-0.986798392627
C	-0.013311095937	-3.723749194943	0.921879651172
H	-0.004778364373	-4.637830369888	1.512376203634
C	0.019738706520	-2.498257512159	1.536438920256
H	0.054414676644	-2.445966755526	2.624750566571
O	3.211783440867	1.419937534230	0.059187633640
C	3.651569801807	2.082159446906	-1.137451506266
H	2.767747548561	2.432312664878	-1.684990453324
H	4.188606471716	1.354779430636	-1.754855368164
C	4.517841315732	3.241334150973	-0.668905537639
H	5.553610113336	2.912980060303	-0.523981251945
H	4.515299214878	4.071077792161	-1.380871473524
C	3.876893580877	3.590652414224	0.672852715490
H	2.969283786642	4.184753024410	0.520183347513
H	4.544178744417	4.138369292644	1.344033581048
C	3.516875963418	2.217014022326	1.211604777114
H	4.362568408480	1.758098913655	1.742352277081
H	2.642316915994	2.216438142128	1.868349834943
O	3.191530856422	-1.475610786592	-0.165834202083
C	3.421183552659	-2.384719964488	-1.249974976092
H	4.263685392792	-2.012859350547	-1.850114875659
H	2.522475265738	-2.405383139740	-1.872337573845
C	3.747136568236	-3.715030495560	-0.596112919692
H	2.821661377262	-4.238565374803	-0.332899195916
H	4.345264897396	-4.362447660534	-1.243334094615
C	4.485625838090	-3.267097664949	0.663576470090
H	5.525388298167	-3.014735617798	0.426241234440
H	4.485598378676	-4.018820548747	1.457659081792
C	3.710397141091	-2.018133124320	1.059251535005
H	2.864238876579	-2.254598986437	1.716380460934
H	4.330282767458	-1.254274776410	1.539985973448
B	-0.043446739036	-0.085263561206	-1.507934385437
H	-0.079741590825	-0.155733930055	-2.719810294114
C	-0.009514446223	1.265157598432	-0.803472897780
C	0.032868812084	1.346315297618	0.654360978482
C	0.066981500363	2.651724164436	1.246328327283
H	0.099598022666	2.719248212684	2.333832587338
C	0.060342813338	3.802094485619	0.500256194602
H	0.087245191573	4.775274996547	0.986448167317
C	0.013777826480	3.723616682153	-0.922269325743
H	0.005738147054	4.637700918082	-1.512768501292
C	-0.019315475726	2.498136141795	-1.536853576134
H	-0.053547968595	2.445868767876	-2.625180710035
Li	-1.884496176124	0.019039481686	0.053552511909
O	-3.212253321785	-1.420216179964	-0.057115987789
C	-3.650849053247	-2.082033442990	1.140200814166
H	-2.766463386427	-2.431456420215	1.687286197973
H	-4.187821049355	-1.354614962789	1.757619113808

C	-4.516861359780	-3.241918157129	0.672921694422
H	-5.552937737289	-2.914227586216	0.528683551367
H	-4.513264044644	-4.071301736562	1.385304829008
C	-3.876809180776	-3.591538578737	-0.669179043331
H	-2.968718114222	-4.185015265695	-0.516964761031
H	-4.544319283797	-4.139998453040	-1.339526972265
C	-3.518061714604	-2.217952455786	-1.208897221137
H	-4.364547221309	-1.759766651457	-1.739008832586
H	-2.644147804547	-2.217193835610	-1.866507511523
O	-3.191520183402	1.476206058316	0.163257368518
C	-3.422221400594	2.384784354876	1.247609454687
H	-4.265467572802	2.012787082990	1.846623494720
H	-2.524198430920	2.404957626664	1.870987438278
C	-3.747196012978	3.715472808030	0.594034068067
H	-2.821330126798	4.238894963415	0.331968311131
H	-4.345808026636	4.362748420783	1.240950625459
C	-4.484560956889	3.268289529066	-0.666581602341
H	-5.524639546629	3.016183793999	-0.430378176699
H	-4.483497928327	4.020349179241	-1.460346154329
C	-3.709359527681	2.019220306877	-1.062038000262
H	-2.862648532445	2.255596509843	-1.718469643298
H	-4.329137259115	1.255701532091	-1.543455234355

80

TS$_{Li}$

Li	2.347836197330	-0.153830689556	-0.306959837112
B	-0.115777450532	-1.453088811570	-0.946534084334
H	-0.077537319909	-2.669111720156	-0.987765339256
C	-1.033521640184	-0.685518025743	-1.938546192544
C	-0.951079580669	0.750389726589	-1.953277661466
C	-1.771975224470	1.462154075949	-2.866237850185
H	-1.714505593356	2.550669487545	-2.884792298810
C	-2.643595576190	0.814401853644	-3.723815632383
H	-3.269508186716	1.386200587605	-4.406116141758
C	-2.718865473519	-0.594965054252	-3.713520531906
H	-3.401715567894	-1.106788046625	-4.388905953702
C	-1.923435698137	-1.318723464897	-2.842976311311
H	-1.984956894005	-2.407098468244	-2.842636926656
O	3.492700155634	-1.646935673250	0.086045948684
C	4.323473516188	-1.566645971252	1.258674797018
H	3.901943327997	-0.815134257377	1.932840817998
H	5.326775687506	-1.244418164097	0.952288759073
C	4.338822936857	-2.968744826709	1.843747186884
H	5.250470431792	-3.168215854840	2.413496872979
H	3.477365207336	-3.115223307029	2.504785602639
C	4.201156825988	-3.832683433404	0.591837456512
H	3.833521854801	-4.841507725789	0.797721101915
H	5.163966837914	-3.913711190251	0.074261551820
C	3.216842639449	-3.022820022176	-0.234277611179
H	3.331466731499	-3.147853504198	-1.314703257499
H	2.178473564330	-3.245928485023	0.036028702442
O	3.740341123876	1.183314363219	-0.428760802538
C	4.656119766956	0.996826152134	-1.524076475071
H	4.235626225024	0.250209401574	-2.204695204722
H	5.605645697342	0.616268946857	-1.125602367124
C	4.818938467269	2.369170989958	-2.152727976306
H	5.773546313578	2.474682892571	-2.675359388486
H	4.008306124203	2.558142496310	-2.865183863244

C	4.684696163281	3.284842296300	-0.938170932339
H	4.410151060534	4.310985589545	-1.196898537537
H	5.623094161310	3.310200842742	-0.372268746151
C	3.594922125339	2.587271644111	-0.140286427020
H	3.685972585755	2.722834520775	0.941379451686
H	2.594708019543	2.902585995014	-0.457862420835
B	0.067911713670	1.427670372193	-0.992882809312
H	0.261533795819	2.626689195557	-1.077473471139
C	0.339950634258	0.713024706168	0.355916203604
C	0.230191869130	-0.732395551197	0.384247891539
C	0.499664637246	-1.401680030154	1.614466849495
H	0.415094311192	-2.487686440399	1.645686215455
C	0.858488062304	-0.717782936414	2.757790192551
H	1.048074196692	-1.256823242405	3.683691820013
C	0.985757490556	0.693000383391	2.724463540162
H	1.272164484472	1.232081272678	3.625186734005
C	0.736848981336	1.378338562482	1.552848966159
H	0.833355664083	2.463620310188	1.537639271200
Li	-1.921512073661	0.095449365245	0.065847291969
O	-3.322398236213	-1.184481182598	0.498131374967
C	-3.166208315942	-2.614074021754	0.526875157872
H	-2.186108005181	-2.856391712112	0.107728540255
H	-3.200183556462	-2.944305565290	1.573667327275
C	-4.331325444370	-3.169006509184	-0.273862629797
H	-4.599431002932	-4.183862507019	0.032420434446
H	-4.086187371327	-3.180589531767	-1.341572547844
C	-5.422574055834	-2.139097814365	0.008869927689
H	-6.220589222357	-2.134461544572	-0.738585348676
H	-5.870965112104	-2.316408107519	0.993317944929
C	-4.633672797117	-0.840352777711	0.010681861659
H	-5.050370620368	-0.069907976211	0.665186244748
H	-4.534509989092	-0.427878604903	-1.001913801787
O	-2.797345975626	1.549108561999	1.002890713061
C	-2.742542032493	2.945938699470	0.671722031536
H	-1.710460970097	3.208799836635	0.408057417770
H	-3.381307136092	3.109160835360	-0.201152426864
C	-3.206702859824	3.669029188940	1.923359568390
H	-4.301798914627	3.696358808826	1.966240468139
H	-2.831982298967	4.694932940174	1.972639689857
C	-2.650984458025	2.765049533518	3.021904688494
H	-1.581545289687	2.954274204439	3.165858883547
H	-3.156256217182	2.886088343340	3.983993578009
C	-2.868007333261	1.380684759327	2.431451121511
H	-3.859271228005	0.982242879708	2.681867755125
H	-2.108798925480	0.653662376595	2.736852783631
H	1.183851246224	-0.566059502078	-1.723087390507
H	1.238559908090	0.369068512127	-1.734785563513

80

B_{Li}

Li	0.000000000000	0.000000000000	2.274312986796
B	1.356474824566	-0.718902743673	0.424398888722
H	2.353604802063	-1.241378158417	-0.063785324772
C	1.259078370124	0.856051412058	0.042471754331
C	0.000000000000	1.517775537626	0.024865284397
C	-0.036701789100	2.881674271518	-0.328073968587
H	-0.999711430607	3.391034723008	-0.355633789002
C	1.115528885101	3.598712665520	-0.636310177271

H	1.053849509050	4.652255262188	-0.901638468154
C	2.354542741008	2.950218765227	-0.610481165177
H	3.263845506234	3.495579824968	-0.855458977069
C	2.411621731741	1.598478711999	-0.283008434119
H	3.378263620447	1.094945480541	-0.280913571916
O	-0.758071291796	-1.284331442680	3.494857693733
C	-1.791967489183	-0.796976656276	4.370355086332
H	-2.143450548172	0.166656275878	3.989092743785
H	-1.359349734899	-0.646739787644	5.367909926152
C	-2.861622825118	-1.875894665038	4.378343043695
H	-3.445269073712	-1.873094460767	5.302931255067
H	-3.546203543298	-1.738930234624	3.533766027888
C	-2.029155754409	-3.141267873789	4.184200591601
H	-2.608746696072	-3.989399095669	3.809926996079
H	-1.551390694404	-3.435294495030	5.126034323182
C	-0.993287624028	-2.670773561458	3.178580866317
H	-0.036397281589	-3.196677801372	3.240083023829
H	-1.371694873302	-2.737914415216	2.152757655366
O	0.758071291796	1.284331442680	3.494857693733
C	1.791967489183	0.796976656276	4.370355086332
H	2.143450548172	-0.166656275878	3.989092743785
H	1.359349734899	0.646739787644	5.367909926152
C	2.861622825118	1.875894665038	4.378343043695
H	3.445269073712	1.873094460767	5.302931255067
H	3.546203543298	1.738930234624	3.533766027888
C	2.029155754409	3.141267873789	4.184200591601
H	2.608746696072	3.989399095669	3.809926996079
H	1.551390694404	3.435294495030	5.126034323183
C	0.993287624028	2.670773561458	3.178580866317
H	0.036397281589	3.196677801372	3.240083023829
H	1.371694873302	2.737914415216	2.152757655366
B	-1.356474824566	0.718902743673	0.424398888722
H	-2.353604802063	1.241378158417	-0.063785324772
C	-1.259078370124	-0.856051412058	0.042471754331
C	0.000000000000	-1.517775537626	0.024865284397
C	0.036701789100	-2.881674271518	-0.328073968587
H	0.999711430607	-3.391034723008	-0.355633789002
C	-1.115528885101	-3.598712665520	-0.636310177271
H	-1.053849509050	-4.652255262188	-0.901638468154
C	-2.354542741008	-2.950218765227	-0.610481165177
H	-3.263845506234	-3.495579824968	-0.855458977069
C	-2.411621731741	-1.598478711999	-0.283008434119
H	-3.378263620447	-1.094945480541	-0.280913571916
Li	0.000000000000	0.000000000000	-1.783262712326
O	-1.266573844118	0.627926038234	-3.077425875336
C	-2.092782904040	1.805773049558	-3.132166355311
H	-2.575006275003	1.932210940401	-2.156774703149
H	-1.446435749389	2.667142613466	-3.325214275598
C	-3.105426499434	1.541692347550	-4.235390732116
H	-2.701636661104	1.837897851210	-5.210417056317
H	-4.041481998601	2.082301392810	-4.071620907957
C	-3.260378057229	0.024026364619	-4.163782943719
H	-3.911325561639	-0.254965662796	-3.327584251939
H	-3.661765441497	-0.417533849538	-5.079965803068
C	-1.834207421832	-0.415725527914	-3.888441510288
H	-1.249405931241	-0.500599287676	-4.813824851277
H	-1.762673697166	-1.359055156157	-3.338274488629
H	1.541609873888	-0.834937111431	1.653612074506

H	-1.541609873888	0.834937111431	1.653612074506
O	1.266573844118	-0.627926038234	-3.077425875336
C	1.834207421832	0.415725527914	-3.888441510288
H	1.249405931241	0.500599287676	-4.813824851277
H	1.762673697166	1.359055156157	-3.338274488629
C	3.260378057229	-0.024026364619	-4.163782943719
H	3.911325561639	0.254965662796	-3.327584251939
H	3.661765441497	0.417533849538	-5.079965803068
C	3.105426499434	-1.541692347550	-4.235390732116
H	2.701636661104	-1.837897851210	-5.210417056317
H	4.041481998601	-2.082301392810	-4.071620907957
C	2.092782904040	-1.805773049558	-3.132166355311
H	2.575006275003	-1.932210940401	-2.156774703149
H	1.446435749389	-2.667142613466	-3.325214275598

80

C_{Li}

Li	2.338969981017	-0.165791862870	-0.639373824700
B	0.163580869265	-1.419390320432	-1.211741250760
H	-0.091254896062	-2.622077593422	-1.215340439069
C	-0.900547200839	-0.529599372357	-2.040627268857
C	-0.817166499272	0.884006271142	-1.901442667179
C	-1.750139621882	1.684436908120	-2.583196466281
H	-1.700373395435	2.767825838371	-2.473564640974
C	-2.736866931983	1.130211141571	-3.400842174825
H	-3.446320209456	1.773377645119	-3.917954874447
C	-2.811870521014	-0.256589894445	-3.544270144381
H	-3.579560971914	-0.700881569952	-4.175018976020
C	-1.902987844333	-1.068565309053	-2.863896130177
H	-1.975518899260	-2.150779997330	-2.972036359396
O	3.460794942506	-1.666565761828	-0.082189689652
C	4.063371582504	-1.536399070787	1.218836635793
H	3.490383399970	-0.807518015879	1.800240905370
H	5.084333627811	-1.157391164607	1.088567542362
C	4.051489818014	-2.932163469882	1.823063362324
H	4.876441396794	-3.084202422804	2.524403356407
H	3.109505936413	-3.110063376141	2.353714780087
C	4.134521357980	-3.816460739619	0.580662863408
H	3.780879747543	-4.837506599778	0.747829352233
H	5.164955824685	-3.861653031605	0.209515122109
C	3.251495809480	-3.054017533764	-0.390667997657
H	3.507608112216	-3.207883784737	-1.442766613489
H	2.191360063992	-3.295869405716	-0.249827512498
O	3.817256632765	1.108162822472	-0.422255503332
C	4.667698228226	1.136150622553	-1.582032337209
H	4.210783699145	0.521547379655	-2.365101673967
H	5.639205243760	0.699049287468	-1.316054121647
C	4.794024048352	2.601836438354	-1.958248248157
H	5.716210534909	2.810657723965	-2.507364895742
H	3.941991318565	2.909203119713	-2.574533678197
C	4.731318877475	3.276505289627	-0.589593640256
H	4.446896803802	4.331039762160	-0.637885419114
H	5.700126167251	3.201131830777	-0.082279237435
C	3.685221022245	2.433846472900	0.123069532225
H	3.833761963296	2.371606764959	1.205555574594
H	2.669382494756	2.791111684135	-0.080146106568
B	0.359881311535	1.467787010631	-0.956641829732
H	0.258780206915	2.672970551808	-0.733422947872

C	0.447901520621	0.594722846071	0.411114944958
C	0.319624738846	-0.820731889624	0.288913793923
C	0.350758907033	-1.605162869863	1.458485808594
H	0.237434961480	-2.685592355669	1.374490479591
C	0.527604440675	-1.036237192982	2.717125066755
H	0.549082867952	-1.664237947583	3.605471981876
C	0.678313822974	0.349584859561	2.834716750774
H	0.817902733781	0.801992554578	3.814496609887
C	0.633402751164	1.146767776646	1.693734360852
H	0.734654481607	2.226851743281	1.795199975363
Li	-1.879652547921	0.117014892106	0.029281601428
O	-3.212189602894	-1.223662537611	0.374660735573
C	-3.005968139707	-2.645548359218	0.266201125181
H	-2.038954887393	-2.813921834034	-0.213439360538
H	-2.983391429498	-3.068370567173	1.279091169994
C	-4.187135948129	-3.167745686790	-0.531990870442
H	-4.404366298143	-4.216391031868	-0.311663849068
H	-3.991639052018	-3.070238746441	-1.605406505595
C	-5.299788000719	-2.213538115651	-0.105202185642
H	-6.131497555372	-2.169818897945	-0.813526460228
H	-5.695161197917	-2.501731513443	0.875519857667
C	-4.560193241043	-0.889370518169	-0.013377439389
H	-4.972242891493	-0.205163611152	0.733272203287
H	-4.528279834526	-0.377477390384	-0.983334350011
O	-2.746816133109	1.540106128472	0.977079885357
C	-2.715962256763	2.949372599512	0.680975891087
H	-1.690621943417	3.224654484813	0.409745061837
H	-3.370523534771	3.129357461578	-0.176507961417
C	-3.172736629854	3.641500856719	1.954508573545
H	-4.266467860812	3.704527669595	1.987569440386
H	-2.766167721937	4.652678443220	2.040666754179
C	-2.662817564291	2.687029650330	3.032087831632
H	-1.589776645284	2.833570825625	3.197456477567
H	-3.180025734872	2.794454008465	3.989442789524
C	-2.917168157220	1.334236468800	2.391709578051
H	-3.943219716530	0.988435882206	2.573430934403
H	-2.219077620829	0.556561268018	2.714576664883
H	1.263153410583	-1.287447935945	-1.799414683741
H	1.419587171051	1.305166035158	-1.598749009762

78

A_K

K	2.707913524449	0.115013016667	-0.235031923701
B	0.121732865684	0.020769786003	1.500149117047
H	0.220569421176	0.037382298738	2.717094277090
C	0.154399139352	-1.297592818395	0.740550252149
C	0.038076507915	-1.317719392665	-0.720159105616
C	0.100806544806	-2.593396636910	-1.369579433498
H	0.016563768692	-2.617716771980	-2.457077845500
C	0.267561632804	-3.774111049740	-0.684480295396
H	0.314369328424	-4.721395212395	-1.218823897821
C	0.375362371256	-3.755061571110	0.736134864887
H	0.503017462669	-4.687847830507	1.282443202788
C	0.316128661702	-2.555875610499	1.406758165284
H	0.400383057572	-2.551715292860	2.494591144318
O	4.011978458660	2.330046448197	0.516570415017
C	3.432151005195	3.495041274394	-0.099109722070
H	2.372740676801	3.297642846742	-0.309945372148

H	3.953415682040	3.680620957786	-1.043989822142
C	3.587288344338	4.622981336308	0.908879432575
H	4.562845501411	5.109714804307	0.795065881568
H	2.806498707293	5.380577834501	0.799319622854
C	3.517052102242	3.869747879209	2.235425750344
H	2.475963187361	3.641940712531	2.487621400200
H	3.969342782208	4.413164397716	3.069640069072
C	4.271190483914	2.592182384176	1.904023122179
H	5.353924771636	2.715651511910	2.044414287857
H	3.941877414959	1.727727103490	2.491110366851
O	4.150315656356	-2.119578288738	0.025998174816
C	4.089924108805	-3.154484227619	-0.970827486780
H	4.965795572505	-3.052635103713	-1.624806042461
H	3.182591746631	-3.015853701947	-1.568841966091
C	4.101822778132	-4.474779270240	-0.213517406271
H	3.078639719928	-4.776635676619	0.033331744690
H	4.572589417017	-5.277061207058	-0.788144756278
C	4.865104484635	-4.108326968979	1.058048102983
H	5.944960945304	-4.092974446651	0.869972563781
H	4.666986878843	-4.786154647566	1.892838803650
C	4.353554801084	-2.702472667560	1.321402982374
H	3.398014325382	-2.723295909900	1.863607551930
H	5.059688331921	-2.072146471838	1.871144226003
B	-0.121732865684	-0.020769786003	-1.500149117047
H	-0.220569421176	-0.037382298738	-2.717094277090
C	-0.154399139352	1.297592818395	-0.740550252149
C	-0.038076507915	1.317719392665	0.720159105616
C	-0.100806544806	2.593396636910	1.369579433498
H	-0.016563768692	2.617716771980	2.457077845500
C	-0.267561632804	3.774111049740	0.684480295396
H	-0.314369328424	4.721395212395	1.218823897821
C	-0.375362371256	3.755061571110	-0.736134864887
H	-0.503017462669	4.687847830507	-1.282443202788
C	-0.316128661702	2.555875610499	-1.406758165284
H	-0.400383057572	2.551715292860	-2.494591144318
K	-2.707913524449	-0.115013016667	0.235031923701
O	-4.011978458660	-2.330046448197	-0.516570415017
C	-3.432151005195	-3.495041274394	0.099109722070
H	-2.372740676801	-3.297642846742	0.309945372148
H	-3.953415682040	-3.680620957786	1.043989822142
C	-3.587288344338	-4.622981336308	-0.908879432575
H	-4.562845501411	-5.109714804307	-0.795065881568
H	-2.806498707293	-5.380577834501	-0.799319622854
C	-3.517052102242	-3.869747879209	-2.235425750344
H	-2.475963187361	-3.641940712531	-2.487621400200
H	-3.969342782208	-4.413164397716	-3.069640069072
C	-4.271190483914	-2.592182384176	-1.904023122179
H	-5.353924771636	-2.715651511910	-2.044414287857
H	-3.941877414959	-1.727727103490	-2.491110366851
O	-4.150315656356	2.119578288738	-0.025998174816
C	-4.089924108805	3.154484227619	0.970827486780
H	-4.965795572505	3.052635103713	1.624806042461
H	-3.182591746631	3.015853701947	1.568841966091
C	-4.101822778132	4.474779270240	0.213517406271
H	-3.078639719928	4.776635676619	-0.033331744690
H	-4.572589417017	5.277061207058	0.788144756278
C	-4.865104484635	4.108326968979	-1.058048102983
H	-5.944960945304	4.092974446651	-0.869972563781

S60

H	-4.666986878843	4.786154647566	-1.892838803650
C	-4.353554801084	2.702472667560	-1.321402982374
H	-3.398014325382	2.723295909900	-1.863607551930
H	-5.059688331921	2.072146471838	-1.871144226003

80

TS$_K$

K	2.993055475906	0.603343730558	1.272424017495
B	0.288635063458	-1.138978599438	-0.546015777149
H	0.581346900107	-2.320075751166	-0.658950216836
C	-0.537393757776	-0.453527564321	-1.670089788432
C	-0.738839997670	0.970229242522	-1.576679864050
C	-1.453823299754	1.615958331448	-2.615377781682
H	-1.599497013351	2.695678929820	-2.559562980056
C	-1.979112464913	0.918515051261	-3.693820318937
H	-2.534763703670	1.441962656547	-4.469827284881
C	-1.782855153258	-0.474553540099	-3.784695976302
H	-2.187556597377	-1.027428115562	-4.630617598843
C	-1.067159618585	-1.132462096091	-2.794794027276
H	-0.911943674862	-2.208862398654	-2.878809434994
O	4.279817539918	-1.721570625642	0.961920263062
C	3.976780176571	-2.812193033852	1.843100087936
H	3.317825566606	-2.442200081843	2.636074452828
H	4.907739799602	-3.173097728132	2.303179669024
C	3.342670402289	-3.878160741841	0.968189946267
H	3.434236260275	-4.879862064097	1.397224096511
H	2.281724030326	-3.656261575818	0.809485045304
C	4.120118201133	-3.700808031753	-0.334422895475
H	3.593909039331	-4.092682708835	-1.208867848468
H	5.096373592799	-4.194522007844	-0.266764867315
C	4.286520419292	-2.188489707244	-0.401673544595
H	5.225063874356	-1.876277337603	-0.871455003676
H	3.447339203369	-1.720426620660	-0.933021506961
O	4.191230453347	2.329468564549	-0.401802979796
C	4.352323706779	1.825842702256	-1.738670586998
H	4.052083563261	0.772489227914	-1.755730069467
H	5.414099179793	1.891109798076	-2.013651008260
C	3.487150799548	2.706839724322	-2.623753011803
H	3.849615233124	2.742434144976	-3.654794350352
H	2.454702277952	2.340883976199	-2.625451691910
C	3.572620571545	4.050159439104	-1.902564238487
H	2.743642038181	4.721794136049	-2.141364845814
H	4.513281835925	4.558848373428	-2.143791684303
C	3.556157308261	3.620015548126	-0.443928670872
H	4.107168662335	4.295663861198	0.218465046990
H	2.524806999025	3.521049869321	-0.077931007493
B	-0.106801503577	1.706061703905	-0.363227190912
H	-0.138506431078	2.927509790413	-0.322982185145
C	0.026408687127	0.917473936855	0.962452997589
C	0.225680532353	-0.515321597839	0.870987505965
C	0.443828091777	-1.235679905484	2.076308293163
H	0.603048868019	-2.313074333365	2.018145662224
C	0.471035366889	-0.618073634077	3.318333925098
H	0.634974374052	-1.203484545883	4.221054227262
C	0.284933630205	0.782009247585	3.406329029699
H	0.304674399326	1.274382720525	4.376727097572
C	0.072491001428	1.518366217773	2.249591113760
H	-0.063525305337	2.598028657210	2.326718988417

K	-2.742830200980	-0.244361500074	0.392547533957
O	-3.488878245814	-2.812358857723	0.203140243621
C	-2.503051003033	-3.779925654383	0.600857117377
H	-1.637213127275	-3.246100896946	1.006222006177
H	-2.928548573570	-4.415187480617	1.390019833610
C	-2.184750552457	-4.580144269579	-0.649657788087
H	-1.808711003257	-5.580569294320	-0.418495544345
H	-1.433643972260	-4.054453899083	-1.249337562058
C	-3.535988759317	-4.587799472017	-1.361007249998
H	-3.461903632595	-4.780838405729	-2.434620675649
H	-4.196139772696	-5.342401140925	-0.918326111012
C	-4.054260246527	-3.188004476684	-1.065032023055
H	-5.145179680079	-3.134288867934	-0.988426205938
H	-3.719076070720	-2.472660328863	-1.828943066769
O	-4.170722605483	1.920790195201	1.067362272568
C	-4.228777767779	2.936933392070	0.054937999118
H	-3.856024157926	2.510759726350	-0.882523808705
H	-5.274644580297	3.242587010382	-0.091333512078
C	-3.383718037779	4.080011292052	0.584654580221
H	-3.644019398894	5.038842805842	0.127986386575
H	-2.322940942364	3.877731641406	0.400027804473
C	-3.694303624655	4.015490581547	2.078905072140
H	-2.926091268783	4.481668290122	2.701793886423
H	-4.652129662334	4.504056533898	2.290442663261
C	-3.793972093370	2.513913014659	2.323997222678
H	-4.544327806972	2.248453576457	3.076373078759
H	-2.826735734804	2.093832453998	2.630821310805
H	1.511454494725	0.044708843603	-0.897366845633
H	1.374711649315	0.963882469644	-0.835880121951

80

B_K

K	-2.353869620432	-0.448611730038	-1.138086104004
B	-0.618452515954	-0.165758235514	1.447963182148
H	-0.053588125442	-0.067673448829	2.553663852273
C	-0.556996866472	1.264428491098	0.683228337877
C	-0.022902458400	1.408962685418	-0.625228993113
C	-0.054467484435	2.687722706140	-1.221305868934
H	0.343973316417	2.802400222416	-2.230331829295
C	-0.570672241427	3.805526508704	-0.572597738705
H	-0.574753063386	4.776623342936	-1.064376133526
C	-1.078888885852	3.666809657688	0.723586280002
H	-1.481791491165	4.529391099388	1.251090610224
C	-1.068467285053	2.412323632310	1.325720774327
H	-1.476434621807	2.309119261007	2.332332994043
O	-3.633439313481	-2.747102621436	-0.646148529643
C	-2.903664395496	-3.925568982214	-1.029020626086
H	-1.827234506309	-3.711389960901	-0.984904984693
H	-3.174156798069	-4.175111057401	-2.060084584817
C	-3.287751976269	-4.998368938103	-0.022491710238
H	-4.209836182191	-5.503816382443	-0.331715950439
H	-2.503512380164	-5.751070742469	0.096693960195
C	-3.526829696590	-4.169972759621	1.238001730642
H	-2.573169703566	-3.918259309551	1.713194358553
H	-4.161828554343	-4.670559024398	1.974137651479
C	-4.178457785740	-2.917650702082	0.672137714455
H	-5.267962979560	-3.029627305732	0.588881696738
H	-3.962812592132	-2.019603306121	1.261314806708

O	-4.413568409358	1.174417325630	-0.631970841035
C	-4.346067668490	2.559436775216	-1.017266970088
H	-4.957614167350	2.689389250820	-1.918976351990
H	-3.307357252359	2.814716166308	-1.255499072799
C	-4.891683768132	3.360490700743	0.159216020290
H	-4.076074405386	3.651903514783	0.829389430693
H	-5.411386503319	4.266146617504	-0.165084791486
C	-5.805199415104	2.348768078953	0.848585550198
H	-6.770015952533	2.282060649406	0.332480985863
H	-5.988629609441	2.578276476150	1.901825806933
C	-5.019352848979	1.063197759092	0.662937394385
H	-4.235249892659	0.963692161820	1.427585636201
H	-5.637732748405	0.160365730259	0.669907802325
B	0.618452515954	0.165758235514	-1.447963182148
H	1.804830887968	0.428427562202	-1.716560031336
C	0.556996866472	-1.264428491098	-0.683228337877
C	0.022902458400	-1.408962685418	0.625228993113
C	0.054467484435	-2.687722706140	1.221305868934
H	-0.343973316417	-2.802400222416	2.230331829295
C	0.570672241427	-3.805526508704	0.572597738705
H	0.574753063386	-4.776623342936	1.064376133526
C	1.078888885852	-3.666809657688	-0.723586280002
H	1.481791491165	-4.529391099388	-1.251090610224
C	1.068467285053	-2.412323632310	-1.325720774327
H	1.476434621807	-2.309119261007	-2.332332994043
K	2.353869620432	0.448611730038	1.138086104004
O	3.633439313481	2.747102621436	0.646148529643
C	2.903664395496	3.925568982214	1.029020626086
H	1.827234506309	3.711389960901	0.984904984693
H	3.174156798069	4.175111057401	2.060084584817
C	3.287751976269	4.998368938103	0.022491710238
H	4.209836182191	5.503816382443	0.331715950439
H	2.503512380164	5.751070742469	-0.096693960195
C	3.526829696590	4.169972759621	-1.238001730642
H	2.573169703566	3.918259309551	-1.713194358553
H	4.161828554343	4.670559024398	-1.974137651479
C	4.178457785740	2.917650702082	-0.672137714455
H	5.267962979560	3.029627305732	-0.588881696738
H	3.962812592132	2.019603306121	-1.261314806708
O	4.413568409358	-1.174417325630	0.631970841035
C	4.346067668490	-2.559436775216	1.017266970088
H	4.957614167350	-2.689389250820	1.918976351990
H	3.307357252359	-2.814716166308	1.255499072799
C	4.891683768132	-3.360490700743	-0.159216020290
H	4.076074405386	-3.651903514783	-0.829389430693
H	5.411386503319	-4.266146617504	0.165084791486
C	5.805199415104	-2.348768078953	-0.848585550198
H	6.770015952533	-2.282060649406	-0.332480985863
H	5.988629609441	-2.578276476150	-1.901825806933
C	5.019352848979	-1.063197759092	-0.662937394385
H	4.235249892659	-0.963692161820	-1.427585636201
H	5.637732748405	-0.160365730259	-0.669907802325
H	-1.804830887968	-0.428427562202	1.716560031336
H	0.053588125442	0.067673448829	-2.553663852273

80

C_K

K	2.948523816719	1.128984259138	0.762372913539
B	-0.347367330376	1.665082495902	0.755786589332
H	-0.989307174454	2.620772336508	0.304033377367
C	-1.203394390159	0.810120370336	1.827962181227
C	-0.767965795159	-0.505174736498	2.162568179932
C	-1.542622871866	-1.257947064660	3.062119907350
H	-1.222847363509	-2.269274655916	3.317133270823
C	-2.716226143681	-0.757777275751	3.636694363609
H	-3.294307338947	-1.369087503572	4.327435418521
C	-3.141460849093	0.529942422292	3.309497494626
H	-4.055518874025	0.933729495450	3.741638216375
C	-2.385712404152	1.293440901241	2.413660126638
H	-2.732525642752	2.294102659873	2.152537321150
O	3.277191875718	3.659484807748	-0.097444282365
C	2.788164501215	3.940620362897	-1.417061294065
H	2.534973834059	2.991858413011	-1.902052992083
H	3.582855447993	4.429090264232	-1.998900801907
C	1.597541428461	4.860809478011	-1.221200702284
H	1.383026482953	5.462172314093	-2.109068629761
H	0.706809773946	4.276571788637	-0.965125943213
C	2.053404928790	5.689149303712	-0.021410726677
H	1.227554681823	6.154956400502	0.522713413117
H	2.745335549570	6.476378539784	-0.342061538388
C	2.778260885852	4.648888789890	0.822518914926
H	3.623376194662	5.058689458076	1.385482979161
H	2.088537012365	4.158490660632	1.522300437181
O	4.738358145985	-0.858559539795	0.518630414135
C	4.726860237424	-1.869662634972	1.533699979387
H	4.114941095242	-1.509247339352	2.366242652347
H	5.752083204667	-2.038794208625	1.894716551939
C	4.167177934125	-3.103865133687	0.853644784735
H	4.434232120572	-4.027183122910	1.375244643451
H	3.075630563913	-3.034654880458	0.800767100033
C	4.795587035789	-2.993587626468	-0.535582621702
H	4.226405134061	-3.516369049583	-1.309249264391
H	5.811203013627	-3.403932925700	-0.525053794355
C	4.830648884536	-1.483532060820	-0.774147950588
H	5.753847398946	-1.153684480527	-1.263998285769
H	3.977023222434	-1.147180337960	-1.375007155045
B	0.561663743938	-1.091680041829	1.451355991501
H	0.633700798665	-2.322199404193	1.551933360372
C	0.623700968977	-0.618607254689	-0.098429042397
C	0.188736945475	0.700099639212	-0.430670487898
C	0.226963364404	1.097358824036	-1.780392441287
H	-0.111411800275	2.099735099043	-2.044316032203
C	0.678650406540	0.249265557078	-2.796147585462
H	0.692683350570	0.588281320715	-3.830350716347
C	1.102167636475	-1.040330904205	-2.471142979664
H	1.449685278058	-1.717275472552	-3.249735140765
C	1.066731018876	-1.457444594686	-1.137337484112
H	1.387975032785	-2.470502425880	-0.895414441130
K	-2.442489428515	-0.965456158603	-0.324618532662
O	-4.217024378072	0.853506743641	-1.147693496562
C	-3.684583631284	2.047806815239	-1.744575928521
H	-2.591782781546	1.993540779508	-1.715445977130
H	-4.009063343879	2.093963211466	-2.793526146694

C	-4.250502997675	3.199672788065	-0.933959394659
H	-4.293357716139	4.129902088672	-1.507210244023
H	-3.637008945945	3.367878130878	-0.041984462901
C	-5.626015980671	2.658502183497	-0.549633241439
H	-6.057216118449	3.148886438798	0.327341141777
H	-6.326474301748	2.767441752731	-1.385520166569
C	-5.325648288797	1.188187345902	-0.294784597077
H	-6.162905430593	0.525514686190	-0.537480116940
H	-5.031013596312	1.016216445532	0.749157510302
O	-2.292550922695	-3.597743083056	-0.747991882982
C	-1.834321874884	-4.427748274065	0.329461683365
H	-1.683297655264	-3.794920802799	1.209512588228
H	-2.603878050482	-5.178131006448	0.560512565989
C	-0.560219731197	-5.076558800702	-0.177104671981
H	-0.325100656215	-6.004058427130	0.352105776367
H	0.280754116355	-4.384868792000	-0.060059372361
C	-0.892241960057	-5.289849485770	-1.652953409365
H	-0.006955882396	-5.374811925066	-2.289121053975
H	-1.492471019651	-6.197758311236	-1.779448846267
C	-1.718880562765	-4.051792894183	-1.986729344024
H	-2.528286849269	-4.256882112368	-2.695881073460
H	-1.093199688254	-3.246191576372	-2.392229182080
H	0.629115754288	2.156852582012	1.359059781834
H	1.553455784383	-0.635489956067	2.059938837230

8. References

[1] G. R. Fulmer, A. J. M. Miller, N. H. Sherden, H. E. Gottlieb, A. Nudelman, B. M. Stoltz, J. E. Bercaw, K. I. Goldberg, *Organometallics* **2010**, *29*, 2176−2179.

[2] E. Brunner, *J. Chem. Eng. Data* **1985**, *30*, 269−273.

[3] E. Januszewski, A. Lorbach, R. Grewal, M. Bolte, J. W. Bats, H.-W. Lerner, M. Wagner, *Chem. Eur. J.* **2011**, *17*, 12696−12705.

[4] A. Lorbach, M. Bolte, H. Li, H.-W. Lerner, M. C. Holthausen, F. Jäkle, M. Wagner, *Angew. Chem. Int. Ed.* **2009**, *48*, 4584−4588; *Angew. Chem.* **2009**, *121*, 4654−4658.

[5] A. Lorbach, M. Bolte, H.-W. Lerner, M. Wagner, *Organometallics* **2010**, *29*, 5762−5765.

[6] C. Elschenbroich, *Organometallics*, *3rd, completely revised and extended ed.*, Wiley-VCH, Weinheim, **2006**.

[7] A. H. Ilkhechi, J. M. Mercero, I. Silanes, M. Bolte, M. Scheibitz, H.-W. Lerner, J. M. Ugalde, M. Wagner, *J. Am. Chem. Soc.* **2005**, *127*, 10656−10666.

[8] Ö. Seven, Z.-W. Qu, H. Zhu, M. Bolte, H.-W. Lerner, M. C. Holthausen, M. Wagner, *Chem. Eur. J.* **2012**, *18*, 11284−11295.

[9] a) A. Hübner, M. Bolte, H.-W. Lerner, M. Wagner, *Angew. Chem. Int. Ed.* **2014**, *53*, 10408−10411; *Angew. Chem.* **2014**, *126*, 10576-10579; b) T. Kaese, A. Hübner, M. Bolte, H.-W. Lerner, M. Wagner, *J. Am. Chem. Soc.* **2016**, *138*, 6224−6233.

[10] R. E. Williams, H. D. Fisher, C. O. Wilson, *J. Phys. Chem.* **1960**, *64*, 1583−1584.

[11] X.-A. Stoe & Cie, *Diffractometer control program system*, Stoe & Cie, Darmstadt, Germany, **2002**.

[12] G. M. Sheldrick, *Acta Crystallogr. Sect. A* **2008**, *64*, 112−122.

[13] C. Hoffend, M. Diefenbach, E. Januszewski, M. Bolte, H.-W. Lerner, M. C. Holthausen, M. Wagner, *Dalton Trans.* **2013**, *42*, 13826−13837.

[14] *Gaussian 09, Revision D.01*, M. J. Frisch, G. W. Trucks, H. B. Schlegel, G. E. Scuseria, M. A. Robb, J. R. Cheeseman, G. Scalmani, V. Barone, B. Mennucci, G. A. Petersson, H. Nakatsuji, M. Caricato, X. Li, H. P. Hratchian, A. F. Izmaylov, J. Bloino, G. Zheng, J. L. Sonnenberg, M. Hada, M. Ehara, K. Toyota, R. Fukuda, J. Hasegawa, M. Ishida, T. Nakajima, Y. Honda, O. Kitao, H. Nakai, T. Vreven, J. A. Montgomery, Jr., J. E. Peralta, F. Ogliaro, M. Bearpark, J. J. Heyd, E. Brothers, K. N. Kudin, V. N. Staroverov, T. Keith, R. Kobayashi, J. Normand, K. Raghavachari, A. Rendell, J. C. Burant, S. S. Iyengar, J. Tomasi, M. Cossi, N. Rega, J. M. Millam, M. Klene, J. E. Knox, J. B. Cross, V. Bakken, C. Adamo, J. Jaramillo, R. Gomperts, R. E. Stratmann, O. Yazyev, A. J. Austin, R. Cammi, C. Pomelli, J. W. Ochterski, R. L. Martin, K. Morokuma, V. G. Zakrzewski, G. A. Voth, P. Salvador, J. J. Dannenberg, S. Dapprich, A. D. Daniels, Ö. Farkas, J. B. Foresman, J. V. Ortiz, J. Cioslowski, D. J. Fox (Gaussian, Inc., Wallingford, CT), **2013**, see http://www.gaussian.com.

[15] C. Adamo, V. Barone, *J. Chem. Phys.* **1999**, *110*, 6158-6170.

[16] L. Goerigk, S. Grimme, *J. Chem. Theory Comput.* **2011**, *7*, 291-309.

[17] S. Grimme, S. Ehrlich, L. Goerigk, *J. Comput. Chem.* **2011**, *32*, 1456-1465.

[18] W. J. Hehre, R. Ditchfield, J. A. Pople, *J. Chem. Phys.* **1972**, *56*, 2257-2261.

[19] J. D. Dill, J. A. Pople, *J. Chem. Phys.* **1975**, *62*, 2921-2923.

[20] T. Clark, J. Chandrasekhar, G. W. Spitznagel, P. v. R. Schleyer, *J. Comput. Chem.* **1983**, *4*, 294-301.

[21] M. J. Frisch, J. A. Pople, J. S. Binkley, *J. Chem. Phys.* **1984**, *80*, 3265-3269.

[22] A. V. Marenich, C. J. Cramer, D. G. Truhlar, *J. Phys. Chem. B* **2009**, *113*, 6378-6396.

[23] K. Fukui, *Accounts of Chemical Research* **1981**, *14*, 363-368.

[24] A. Karton, A. Tarnopolsky, J.-F. Lamère, G. C. Schatz, J. M. L. Martin, *J. Phys. Chem. A* **2008**, *112*, 12868-12886.

[25] S. Kozuch, J. M. L. Martin, *J. Comput. Chem.* **2013**, *34*, 2327-2344, see also http://www.compchem.me/dsd-pbep86-functional.

[26] C. Riplinger, F. Neese, *J. Chem. Phys.* **2013**, *138*, 034106/1-034106/18.

[27] C. Riplinger, B. Sandhoefer, A. Hansen, F. Neese, *J. Chem. Phys.* **2013**, *139*, 134101/1-134101/13.

[28] *ORCA version 3.0.3, an ab initio, DFT and semiempirical SCF-MO package*, F. Neese, F. Wennmohs, U. Becker, D. Bykov, D. Ganyushin, A. Hansen, R. Izsák, D. G. Liakos, C. Kollmar, S. Kossmann, D. A. Pantazis, T. Petrenko, C. Reimann, C. Riplinger, M. Roemelt, B. Sandhöfer, I. Schapiro, K. Sivalingam, B. Wezisla, *with contributions from* M. Kállay, S. Grimme, E. Valeev, G. Chan (Max-Planck-Institut für Chemische Energiekonversion, Mülheim a. d. Ruhr, Germany), **2014**, see https://orcaforum.cec.mpg.de/.

[29] F. Neese, *WIREs Comput. Mol. Sci.* **2012**, *2*, 73–78.
[30] S. Ten-no, *Chem. Phys. Lett.* **2004**, *398*, 56–61.
[31] T. B. Adler, G. Knizia, H.-J. Werner, *J. Chem. Phys.* **2007**, *127*, 221106/1–221106/4.
[32] *MOLPRO, version 2015.1, a package of ab initio programs*, H.-J. Werner, P. J. Knowles, G. Knizia, F. R. Manby, M. Schütz, P. Celani, W. Györffy, D. Kats, T. Korona, R. Lindh, A. Mitrushenkov, G. Rauhut, K. R. Shamasundar, T. B. Adler, R. D. Amos, A. Bernhardsson, A. Berning, D. L. Cooper, M. J. O. Deegan, A. J. Dobbyn, F. Eckert, E. Goll, C. Hampel, A. Hesselmann, G. Hetzer, T. Hrenar, G. Jansen, C. Köppl, Y. Liu, A. W. Lloyd, R. A. Mata, A. J. May, S. J. McNicholas, W. Meyer, M. E. Mura, A. Nicklass, D. P. O'Neill, P. Palmieri, D. Peng, K. Pflüger, R. Pitzer, M. Reiher, T. Shiozaki, H. Stoll, A. J. Stone, R. Tarroni, T. Thorsteinsson, M. Wang (University College Cardiff Consultants Ltd., Cardiff, UK), **2015**, see http://www.molpro.net.
[33] F. Weigend, R. Ahlrichs, *Phys. Chem. Chem. Phys.* **2005**, *7*, 3297–3305.
[34] F. Weigend, *Phys. Chem. Chem. Phys.* **2002**, *4*, 4285–4291.
[35] F. Weigend, *J. Comput. Chem.* **2008**, *29*, 167–175.
[36] F. Weigend, A. Köhn, C. Hättig, *J. Chem. Phys.* **2002**, *116*, 3175–3183.
[37] K. A. Peterson, T. B. Adler, H.-J. Werner, *J. Chem. Phys.* **2008**, *128*, 084102/1–084102/12.
[38] J. G. Hill, K. A. Peterson, *Phys. Chem. Chem. Phys.* **2010**, *12*, 10460–10468.
[39] J. G. Hill, K. A. Peterson, G. Knizia, H.-J. Werner, *J. Chem. Phys.* **2009**, *131*, 194105/1–194105/13.

6.2.7. 10,9-Oxaboraphenanthrenes as Luminescent Fluorophores

Tetrahedron 72 (2016) 1477–1484

Contents lists available at ScienceDirect

Tetrahedron

journal homepage: www.elsevier.com/locate/tet

10,9-Oxaboraphenanthrenes as luminescent fluorophores

Alexandra Budanow, Esther von Grotthuss, Michael Bolte, Matthias Wagner, Hans-Wolfram Lerner *

Institut für Anorganische Chemie der Goethe-Universität, Max-von-Laue-Str. 7, D-60438 Frankfurt, Germany

ARTICLE INFO

Article history:
Received 14 December 2015
Received in revised form 26 January 2016
Accepted 27 January 2016
Available online 30 January 2016

Keywords:
Oxaboraphenanthrene
Fluorophores
Luminescence
X-ray structure analysis

ABSTRACT

Reactions of 9-chloro-10,9-oxaboraphenanthrene (**1**) with the phenyl-, *p*-tolyl-, *m*-xylyl-, mesityl-, 2,4,6-tri-*iso*-propylphenyl-, 3,5-bis(trifluoromethyl)phenyl-, and pentafluorophenyl-Grignard reagents resulted in the formation of the corresponding oxaboraphenanthrene derivatives namely 9-phenyl- (**2**), 9-*p*-tolyl- (**3**), 9-(3,5-dimethylphenyl)- (9-*m*-xylyl-) (**4**), 9-mesityl- (**5**), 9-(2,4,6-tri-*iso*-propylphenyl)- (**6**), 9-(3,5-bis(trifluoromethyl)phenyl)- (**7**), and 9-(pentafluorophenyl)-10,9-oxaboraphenanthrene (**8**). 9-Trisyl- (**9**) and 9-supersilyl-10,9-oxaboraphenanthrene (**10**) were obtained selectively employing **1** and $Li[C(SiMe_3)_3]$ or $Na[SitBu_3]$ as reactants. The compounds **4**–**9** were characterized by X-ray crystallography. The fluorescence measurements of **5**–**9** embedded in PMMA show emission bands with λ_{max} from 341 to 373 nm.

1. Introduction

10,9-oxaboraphenanthrenes (Fig. 1) are versatile compounds which were first published in 1960 by Dewar and Dietz[1] and since then haven been used as antioxidant additives in lubricants,[2] as Lewis acids for use in aldol condensations[3] or as fungicides.[4] Later the interest in oxaboraphenanthrenes roses continually since they can be used as precursors for *ortho*-phenylenes which are studied for multiple applications in organic electronics.[5]

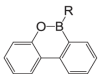

Fig. 1. 10,9-oxaboraphenanthrene derivatives (oxaboraphenanthrene).

When regarding oxaboraphenanthrene as a derivative of *ortho*-phenylene, the additional B–O bond leads to a planar and rigid structure (Fig. 1).[1] In the heterocyclic ring the electron density is predominantly situated on the electron-rich oxygen atom, explaining why this part of the oxaboraphenanthrene shows no distinct aromaticity.[1,5]

Due to its structural motif the oxaboraphenanthrene is an asymmetrically-linked donor-acceptor system, whose acceptor properties can be influenced by the substituent R (Fig. 1). Along with the variation of this donor-acceptor system, a control of the HOMO-LUMO gap is envisioned which is crucial for optoelectronic applications.[6] Dewar and Dietz's UV/vis investigations of 9-substituted oxaboraphenanthrenes in solution showed several absorption bands, with maxima from the phenyl-substituted oxaboraphenanthrene shifted bathochromically compared to those of a hydroxyl-substituted one.[1] While 9-hydroxy-oxaboraphenanthrene (Fig. 1, R=OH)[7] is very stable and therefore has found several applications,[2–4] it shows only an insignificant fluorescence, whereas 9-phenyl-10,9-oxaboraphenanthrene (**2a**) (Fig. 1, R=Ph) fluoresces strongly.[1] Unfortunately **2a** was sensitive to hydrolysis due to the Lewis acidic boron center. Nevertheless, it showed that the fluorescence is tunable depending on the substituent of the oxaboraphenanthrene core.

As the oxaboraphenanthrene unit shows interesting optoelectronic properties we synthesized various 9-substituted BOP derivatives and investigated their stability and luminescence behavior. The emission area would be suitable to use our compounds in UV-OLEDs.[8,9] Equally an incorporation of them in OLEDs as a host material is conceivable in order to suppress luminescence quenching effects.[10,11] Recently Hirai et al. published a boron-containing polycyclic aromatic compound comparable to ours for this purpose.[12]

2. Results and discussion

In this study the 9-substituted oxaboraphenanthrenes were synthesized following a route published by Dewar and Dietz[1] and optimized by Zhou et al.:[13] By reacting 2-phenylphenol with an

* Corresponding author. Fax: +49 69 79829260; e-mail address: lerner@chemie.uni-frankfurt.de (H.-W. Lerner).

http://dx.doi.org/10.1016/j.tet.2016.01.054
0040-4020/

excess of BCl_3 and catalytic amounts of $AlCl_3$ in hexane, 9-chloro-10,9-oxaboraphenanthrene (Scheme 1) was obtained for use as the starting compound for further derivatization reactions.

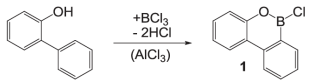

Scheme 1. Synthesis of 9-chloro-10,9-oxaboraphenanthrene (**1**) in the reaction of 2-phenylphenol with BCl_3 and catalytic amounts of $AlCl_3$.

2.1. Synthesis of 9-substituted 10,9-oxaboraphenanthrenes

The substitution with bulky groups at the 9-position should on the one hand lead to (hydrolysis-) stable products and on the other enhance their emission. Therefore we synthesized a series of aryl- and silyl-substituted oxaboraphenanthrenes and investigated their steric shielding effect on the boron atom. As the insertion of an aryl substituent can change the electronic properties of the oxaboraphenanthrene, we tested if there is any effect of electron withdrawing and donating aryl groups on the emission characteristics of the oxaboraphenanthrene (Scheme 2).

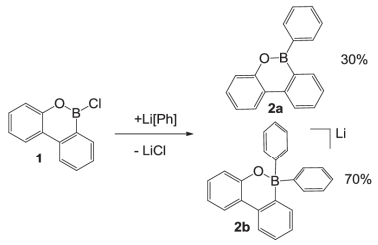

Scheme 2. Reaction of 9-chloro-oxaboraphenanthrene (**1**) with phenyl lithium in THF.

For the substitution reactions on 9-chloro-10,9-oxaboraphenanthrene (**1**) both organolithium as well as Grignard reagents are suitable. Nevertheless, we investigated the case of sterically less demanding aryl substituents, up to *m*-xylyl, and found that the corresponding organolithium species lead to double addition and therefore to product mixtures. For instance, treatment of **1** with 1.1 equiv of Li[Ph] in THF at −78 °C afforded a mixture of 9-phenyl-10,9-oxaboraphenanthrene (**2a**) and the related lithium borate **2b**, as shown in Scheme 2. We identified the borate **2b** by its spectral characteristics and by X-ray structure analysis of single crystals.

By contrast the reactions of **1** with the phenyl-, *p*-tolyl-, *m*-xylyl-, mesityl-, 2,4,6-tri-*iso*-propylphenyl-, 3,5-bis(trifluoromethyl)phenyl-, and pentafluorophenyl-Grignard reagent gave only the corresponding oxaboraphenanthrene derivatives, as shown in Scheme 3.

In addition we also investigated the reaction of **1** with the bulky carbanionic reagent $Li[C(SiMe_3)_3]$ (trisyl lithium)[14,15] and the sterically crowded silanide $Na[SitBu_3]$ (supersilyl sodium),[16,17] respectively. In both reactions the corresponding 9-substituted-oxaboraphenanthrenes **9** and **10** were formed in good yields (see Scheme 4).

In particular 9-mesityl-oxaboraphenanthrene (**5**), 9-(2,4,6-tris-*iso*-propylphenyl)-oxaboraphenanthrene (**6**), and 9-trisyl-oxaboraphenanthrene (**9**) show an extraordinary stability towards nucleophiles like water. This can be explained using the crystal structure of **5**, **6**, and **9**: in all these compounds the substituents shield the boron center from nucleophilic attacks (see Figs. 2–5).

The oxaboraphenanthrene **4** was crystallized from a concentrated THF solution at −30 °C, whereas crystals of **5** and **6** were obtained by slow evaporation of hexane solutions at room temperature (see Fig. 2). The compound **4** crystallizes in the orthorhombic space group *Pba*2 and **5** in the orthorhombic space group $P2_12_12_1$. Both compounds contain two crystallographically independent molecules in the asymmetric unit. Since most structural parameters of molecules **4** as well as **5** are closely similar, in each case the structure of only one molecule of **4** and **5** is shown in Fig. 2. The oxaboraphenanthrene **6** crystallizes in the monoclinic space group $P2_1/c$.

The molecular structures of the oxaboraphenanthrenes **7** and **8**, which bear electron withdrawing groups on the B center, are shown in Fig. 3 below. Crystals of **7** (see Fig. 3) were grown from hexane at room temperature and belong to the monoclinic space group $P2_1/c$. X-ray quality crystals of **8** (monoclinic, $P2_1/c$ space group) were obtained from a hexane/diethyl ether solution at room temperature (see Fig. 3).

By slow evaporation of the solvent of a saturated benzene solution, single crystals of **9** were grown, which were suitable for an investigation by X-ray crystallography. The compound **9** crystallizes in the monoclinic space group $P2_1/c$ with two crystallographically independent molecules in the asymmetric unit. Fig. 4 represents the structure of one of two crystallographically independent molecules of **9** (selected bond lengths in caption of Fig. 4).

Conformation of the aryl-substituted oxaboraphenanthrene derivatives **4**–**8** are shown in Fig. 5. In contrast to the structures of **5**, **6**, and **8** (top) the aryl substituent in **4** and **7** (bottom) lies in the plane of the oxaboraphenanthrene units.

While in the oxaboraphenanthrene derivatives **5**, **6**, **8**, and **9** the boron atoms are shielded (Figs. 2–5), in 9-(3,5-bis(trifluoromethyl) phenyl)-oxaboraphenanthrene (**7**) as well as in the moisture-sensitive 9-(*m*-xylyl)-oxaboraphenanthrene (**4**) the boron center is more accessible (Fig. 5). Nevertheless, **5**, **6**, **8**, and **9** as well as **7** turned out to be relatively stable towards hydrolysis and could be stored for some weeks under air.

2.2. Luminescence investigations of the oxaboraphenanthrene-derivatives 5–9

In general, for application in OLEDs, compounds are preferred which fluoresce with high quantum yields and are oxygen- and moisture-insensitive. Furthermore, they have to form homogeneous layers either alone or in a matrix material, e.g. polymethyl methacrylate (PMMA).[18,19]

As the oxaboraphenanthrene derivatives **5**–**9** proved to be air- and moisture-stable these compounds were tested for their suitability as emitters for organic electronics. The oxaboraphenanthrenes form homogeneous layers when embedded in PMMA and show an emission in the near-UV area with moderate quantum yields (see the experimental section for more details).

The spectra of **5**–**9** possess almost identical absorption maxima (see Table 1 and Fig. 6). However, the oxaboraphenanthrenes **5**, **6** and **9** with electron donating groups reveal an additional absorption band (see Fig. 6). Even the emission maxima of the oxaboraphenanthrenes **5** and **6** with electron donating groups differ slightly from those of the oxaboraphenanthrenes **7** and **8** with electron withdrawing groups (see Table 2 and Fig. 7). Interestingly, the compounds **5**–**9** emit light of short wavelengths in the range of the near-UV area.

This indicates that electron withdrawing substituents in oxaboraphenanthrenes **7** and **8** effect a bathochromic shift of the emission maximum up to 25 nm compared with these of oxaboraphenanthrenes with electron donating substituents (**5** and **6**). In consequence the oxaboraphenanthrenes **7** and **8** reveal marginally larger Stokes shifts than do **5** and **6**.

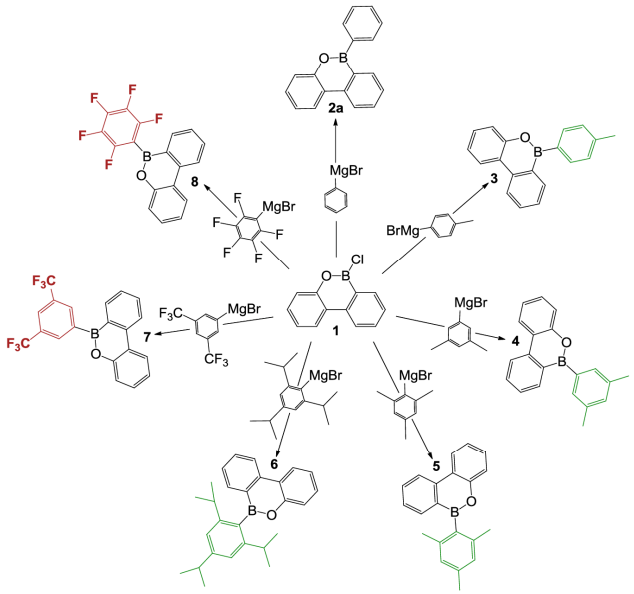

Scheme 3. 9-Aryl-substituted oxaboraphenanthrenes synthesized starting from 9-chloro-oxaboraphenanthrene (**1**) and Grignard-reagents (red: electron withdrawing groups, green: electron donating groups). For the synthesis of 9-phenyl-10,9-oxaboraphenanthrene (**2**), see Ref. 1.

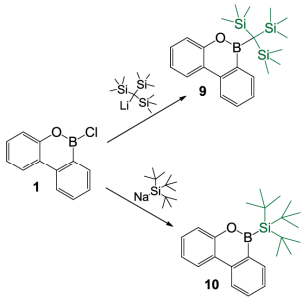

Scheme 4. 9-Alkyl- and 9-silyl-substituted oxaboraphenanthrenes synthesized starting from 9-chloro-oxaboraphenanthrene (**1**) and trisilyl lithium and supersilyl sodium.

Additionally, these results show that oxaboraphenanthrenes with sterically demanding groups show a higher quantum yield even when the concentrations used were lower.[20] This effect may be explained with a higher stability of their molecular scaffolds.

3. Conclusion

In summary, convenient access to oxaboraphenanthrenes with sophisticated substituents on the boron center was established. Reactions of 9-chloro-10,9-oxaboraphenanthrene (**1**) with the *p*-tolyl-, *m*-xylyl-, mesityl-, 2,4,6-tri-*iso*-propylphenyl-, 3,5-bis(trifluoromethyl)phenyl-, and penta-fluorophenyl-Grignard reagent resulted in the formation of the corresponding oxaboraphenanthrene derivatives **3**–**8**. Under the same conditions, **9** and **10** were obtained by selectively employing **1** and Li[C(SiMe$_3$)$_3$] or Na[Si*t*Bu$_3$] as reactants. The oxaboraphenanthrene derivatives **4**–**9** were characterized by X-ray crystallography. The UV/vis measurements of **5**–**9** embedded in PMMA show four to five absorption bands. Interestingly, the compounds **5**–**9** emit light of short wavelengths in the range of the near-UV area. In addition to that we observed a dependency between the quantum yields and the steric bulkiness of the substituent. Thus, oxaboraphenanthrenes are considered to be promising candidates for UV-OLED material.

4. Experimental section

4.1. General materials and methods

All reactions and manipulations were carried out under dry, oxygen-free nitrogen by using standard Schlenk ware or in an argon-filled M. Braun glovebox. The solvents THF, Et$_2$O, Bu$_2$O, pentane, toluene, benzene and [D$_6$]-benzene were stirred over sodium/benzophenone and distilled prior to use. $CHCl_3$ and CH_2Cl_2 were dried over CaH_2 and distilled before use.

The NMR spectra were recorded on *Bruker DPX 250, Avance 300, Avance 400*, and *Avance 500* spectrometers. Elemental analyses were performed at the microanalytical laboratories of the University Frankfurt. The UV/Vis absorption spectra measurements were carried out at a *Varian Cary 500* UV/Vis spectrophotometer, the fluorescence spectra as well as the quantum yields at a *Jasco FP-8300*.

For the luminescence investigations a parent solution was prepared consisting of a mixture of 10 weight percent of the analyte in PMMA, dissolved in methylene chloride (spectrophotometric grade). The results described above are based on parent solutions of 8 mg of the analyte, 72 mg PMMA in 3.6 mL methylene chloride.

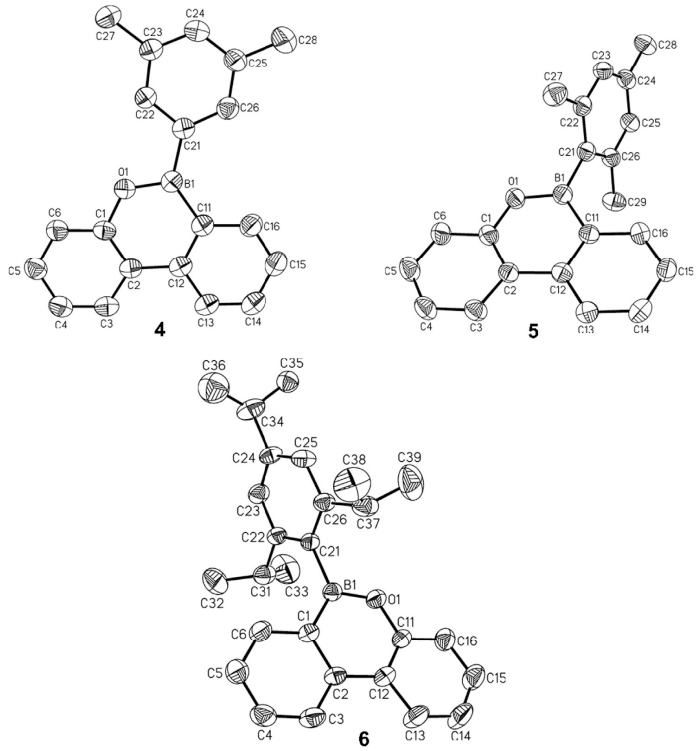

Fig. 2. Solid-state structures of **4** (orthorhombic space group *Pba2*; one of two crystallographically independent molecules), **5** (orthorhombic space group $P2_12_12_1$; one of two crystallographically independent molecules), and **6** (monoclinic space group $P2_1/c$). Displacement ellipsoids are drawn at the 50% probability level. H atoms have been omitted for clarity. Selected bond lengths (Å) and bond angles (deg) **4**: B(1)–O(1) 1.377(2), B(1)–C(11) 1.562(2), B(1)–C(21) 1.569(3), O(1)–C(1) 1.375(2), C–$C_{biphenyl}$ 1.373(3)–1.416(2), C(2)–C(12) 1.469(2), C–$C_{xylyl/aryl}$ 1.386(3)–1.402(2), O(1)–B(1)–C(11) 115.95(15), O(1)–B(1)–C(21) 111.39(14), C(11)–B(1)–C(21) 132.66(14), C(1)–O(1)–B(1) 124.97(13), O(1)–C(1)–C(6) 116.05(14), O(1)–C(1)–C(2) 121.19(14), C–C–$C_{biphenyl}$ 115.78(14) −124.54(15), C(16)–C(11)–B(1) 124.31(15), C(12)–C(11)–B(1) 118.21(14), C–C–$C_{xylyl/aryl}$ 116.31(15)–122.95(15), C(26)–C(21)–B(1) 126.57(15), C(22)–C(21)–B(1) 117.11(14). **5**: B(1)–O(1) 1.375(4), B(1)–C(11) 1.540(4), B(1)–C(21) 1.568(4), O(1)–C(1) 1.375(3), C–$C_{biphenyl}$ 1.377(4)–1.408(4), C(2)–C(12) 1.475(4), C–$C_{mesityl/aryl}$ 1.384(4)–1.409(4); O(1)–B(1)–C(11) 117.9(3), O(1)–B(1)–C(21) 117.2(2), C(11)–B(1)–C(21) 124.9(3), B(1)–O(1)–C(1) 122.3(2), O(1)–C(1)–C(6) 115.8(2), O(1)–C(1)–C(2) 122.4(2), C–C–$C_{biphenyl}$ 116.9(2)–123.1(2), C(16)–C(11)–B(1) 121.8(2), C(12)–C(11)–B(1) 119.6(2), C–C–$C_{mesityl/aryl}$ 118.1(3)–121.8(3), C(22)–C(21)–B(1) 120.6(3). **6**: B(1)–O(1) 1.380(4), B(1)–C(1) 1.533(5), B(1)–C(21) 1.582(4), O(1)–C(11) 1.379(3), C–$C_{biphenyl}$ 1.366(5)–1.419(4), C(2)–C(12) 1.468(5), C–$C_{tip/aryl}$ 1.378(3)–1.406(4); O(1)–B(1)–C(1) 118.2(3), O(1)–B(1)–C(21) 116.5(3), C(1)–B(1)–C(21) 125.3(3), C(11)–O(1)–B(1) 122.1(5), C–C–$C_{biphenyl}$ 116.2(3)–123.6(5), O(1)–C(11)–C(12) 121.7(3), O(1)–C(11)–C(16) 116.0(3), C–C–$C_{tip/aryl}$ 117.8(3)–122.3(3), C(26)–C(21)–B(1) 119.6(3), C(22)–C(21)–B(1) 121.6(3).

Into a lying quartz cuvette ($39\times11\times11$ mm^3) 100 μL of methylene chloride and 10 μL of the parent solution were filled. After evaporation of the solvent a homogeneous layer of PMMA and the luminophore was formed which was analyzed in regard to its luminescence behavior.

By adding the parent solution in 10 μL steps dissolved in methylene chloride onto the existing layer and evaporating the solvent thicker layers can be formed and analyzed.

9-Chloro-10,9-oxaboraphenanthrene,[8] $Li[C(SiMe_3)_3]\cdot 2$ THF,[14,15] and $Na[SitBu_3]$[16,17] were synthesized following literature known methods.

4.2. Synthesis protocols and characterization data

*4.2.1. Synthesis of the lithium borate of **2**.* To a solution of (0.541 g, 2.52 mmol, 1.0 equiv) 9-chloro-oxaboraphenanthrene (**1**) in THF (20 mL) a phenyl lithium solution (1.8 mL, 1.52 M in Bu_2O; 2.77 mmol, 1.1 equiv) was added (90 min) at −90 °C and the resulting reacting mixture was additionally stirred for 1 h at −90 °C. After warming to room temperature, the yellow suspension was filtered and the white precipitate was washed with hexane (3×2 mL). All volatiles were removed from the combined organic layers in vacuo. According to the ^{11}B NMR spectrum 9-phenyl-10,9-oxaboraphenanthrene (**2a**) and the borate **2b** were thereby formed (integral ratio of the signals: **2a**: **2b**=3: 7). The residue was a yellow oil from which X-ray quality crystals were obtained at room-temperature after approx. 3 weeks under nitrogen atmosphere (yield: 34%, 0.482 g, 0.85 mmol).[21]

^{1}H NMR (300.0 MHz, C_6D_6): δ=8.06 (m, 5H), 7.95 (m, 1H), 7.55 (m, 2H), 7.50 (m, 4H), 7.27 (m, 4H), 7.10 (m, 2H), 3.46 (m, 12H, OCH_2), 1.10 (m, 12H, CH_2); ^{11}B NMR (96.3 MHz, C_6D_6): δ=3.3; elemental Anal. Calcd (%) for $C_{38}H_{40}BLiO_3$ (562.45): 81.14, H, 7.17; found: C 81.04, H 7.24.

*4.2.2. Synthesis of 9-p-tolyl-10,9-oxaboraphenanthrene (**3**).* To a solution of (0.523 g, 2.43 mmol, 1.0 equiv) 9-chloro-

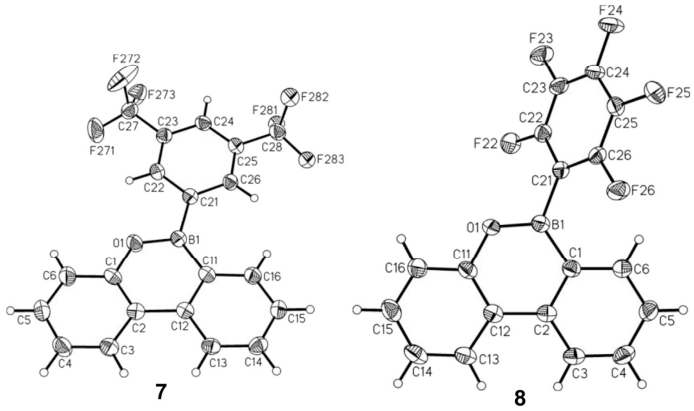

Fig. 3. Solid-state structures of **7** (monoclinic space group $P2_1/c$) and **8** (monoclinic space group $P2_1/c$). Displacement ellipsoids are drawn at the 50% probability level. Selected bond lengths (Å) and bond angles (deg) **7**: O(1)–C(1) 1.370(3), O(1)–B(1) 1.377(4), B(1)–C(11) 1.549(4), B(1)–C(21) 1.585(4), C–$C_{biphenyl}$ 1.376(4)–1.424(4), C(2)–C(12) 1.475(4), C–C_{phenyl} 1.383(4)–1.402(4); C(1)–O(1)–B(1) 124.6(2), O(1)–B(1)–C(11) 117.2(2), O(1)–B(1)–C(21) 110.7(2), C(11)–B(1)–C(21) 132.0(2), O(1)–C(1)–C(6) 116.5(2), O(1)–C(1)–C(2) 121.0(2), C–C–$C_{biphenyl}$ 116.2(3)–124.0(2). **8**: O(1)–B(1) 1.361(2), O(1)–C(11) 1.383(2), B(1)–C(1) 1.533(3), B(1)–C(21) 1.585(2), C–$C_{biphenyl}$ 1.373(3)–1.419(2), C(2)–C(12) 1.472(3), C–C_{phenyl} 1.374(3)–1.397(2), B(1)–O(1)–C(11) 122.26(14), O(1)–B(1)–C(1) 119.60(15), O(1)–B(1)–C(21) 114.60(15), C(1)–B(1)–C(21) 125.77(16), C–C–$C_{biphenyl}$ 116.38(17)–123.36(16), C(6)–C(1)–B(1) 123.75(16), C(2)–C(1)–B(1) 117.55(16), O(1)–C(11)–C(16) 115.96(16), O(1)–C(11)–C(12) 121.45(16).

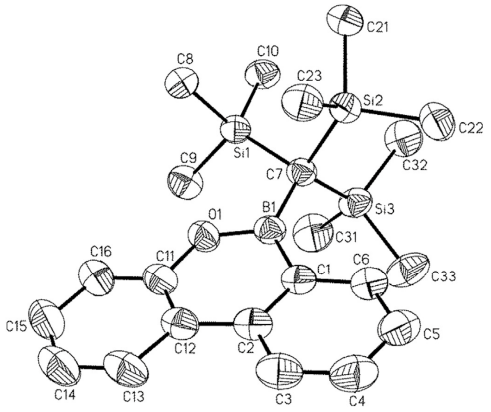

Fig. 4. Solid-state structure of **9** (monoclinic space group $P2_1/c$). Displacement ellipsoids are drawn at the 50% probability level. Selected bond lengths (Å) and bond angles (deg) of one of two crystallographically independent molecules: Si–C_{Me} 1.867(4) –1.886(3), Si–C(7) 1.919–1.933(3), B(1)–O(1) 1.384(4), B(1)–C(1) 1.561(4), B(1)–C(7) 1.580(4), O(1)–C(11) 1.373(4), C(1)–C(6) 1.403(4), C–$C_{biphenyl}$ 1.366(5)–1.424(4), C(2)–C(12) 1.457(5); C–Si–C 102.21(16)–107.22(16), C–Si–C(7) 109.96(14) –117.17(16), O(1)–B(1)–C(1) 114.3(3), O(1)–B(1)–C(7) 114.0(3), C(1)–B(1)–C(7) 131.4(3), C(11)–O(1)–B(1) 126.0(2), C–C–$C_{biphenyl}$ 115.7(3)–122.7(3), C(6)–C(1)–B(1) 123.5(3), C(2)–C(1)–B(1) 119.1(3), B(1)–C(7)–Si 106.6(2)–114.4(2), Si–C(7)–Si 107.77 (14)–111.60(14), O(1)–C(11)–C(16) 116.4(3), O(1)–C(11)–C(12) 120.9(3).

oxaboraphenanthrene (**1**) in THF (5 mL) a *p*-tolyl-Grignard solution (0.8 mL, 0.30 M in THF; 2.80 mmol, 1.1 equiv) was added (10 min) at room temperature and the resulting reacting mixture was stirred for 1 h at 60 °C. After cooling to room temperature, the colorless suspension was filtered and the white precipitate was washed with hexane (3×2 mL). All volatiles were removed from the combined organic layers in vacuo. The product was obtained as a yellowish, hydrolysis-sensitive powder in 88% (0.580 g, 2.15 mmol) yield.

^{1}H NMR (300.0 MHz, C_6D_6): δ=8.10 (d, $^3J_{HH}$=7.8 Hz, 1H), 8.31 (d, $^3J_{HH}$=7.4 Hz, 4H), 7.79 (d, $^3J_{HH}$=7.4 Hz, 1H), 7.64 (m, 2H), 7.34 (m, 2H), 7.04 (m, 2H), 2.10 (s, 3H, CH_3); ^{11}B NMR (96.3 MHz, C_6D_6): δ=42.6 (br, $h_{1/2}$=530 Hz); ^{13}C NMR (75.5 MHz, C_6D_6): δ=141.5, 135.4, 135.1, 130.2, 129.2, 128.9, 128.4, 125.8, 125.3, 123.7, 123.2, 122.7, 112.35, 21.2; elemental Anal. Calcd (%) for $C_{19}H_{15}BO$ (270.13): 84.48, H 5.60; found: C 84.45, H 5.47.

*4.2.3. Synthesis of 9-m-xylyl-10,9-oxaboraphenanthrene (**4**).* To a solution of (0.723 g, 3.36 mmol, 1.0 equiv) 9-chloro-oxaboraphenanthrene (1) in THF (15 mL) 10.0 mL (0.27 m in THF; 4.00 mmol, 1.2 equiv) of an *m*-xylyl-Grignard solution were added (5 min) at room temperature. The resulting yellow reaction mixture was heated for 2.5 h at −70 °C and was filtered after cooling to room temperature over Celite using Schlenk technique. The filtrate was concentrated whereupon colorless plates appropriate for X-ray crystallography were obtained by storing the saturated THF solution of the product at −30 °C overnight. After evaporation of the solvent under reduced pressure the product was obtained as a colorless powder in a yield of 52% (0.521 g, 1.75 mmol).

^{1}H NMR (300.0 MHz, C_6D_6): δ=8.44 (m, 1H), 7.74 (m, 2H), 7.55 (m, 1H), 7.45 (m, 1H), 7.23 (m, 3H), 7.10 (m, 2H), 7.04 (m, 1H), 2.26 (m, 6H, 2 CH_3); ^{11}B NMR (96.3 MHz, C_6D_6): δ=44.3 (br, $h_{1/2}$=780 Hz); ^{13}C NMR (75.5 MHz, C_6D_6): δ=152.1, 139.8, 137.8, 137.2, 133.0, 132.8, 132.2, 130.2, 129.3, 128.5, 127.3, 126.4, 123.9, 123.7, 123.5, 122.1, 120.8, 21.5 (2 CH_3); elemental Anal. Calcd (%) for $C_{20}H_{17}BO$ (284.16): C 84.53; H, 6.03; found: C 84.55, H 6.87.

*4.2.4. Synthesis of 9-mesityl-10,9-oxaboraphenanthrene (**5**).* To a solution of (0.526 g, 2.45 mmol, 1.0 equiv) 9-chloro-oxaboraphenanthrene (**1**) in THF (10 mL) 3.8 mL (0.67 M in THF; 2.55 mmol, 1.2 equiv) of a mesityl-Grignard solution were added (2 min) at room temperature. The resulting colorless suspension was stirred for 30 min at room temperature, mixed with water (50 mL) and the layers were separated. The aqueous layer was treated with diethyl ether (3×20 mL), the combined organic layers

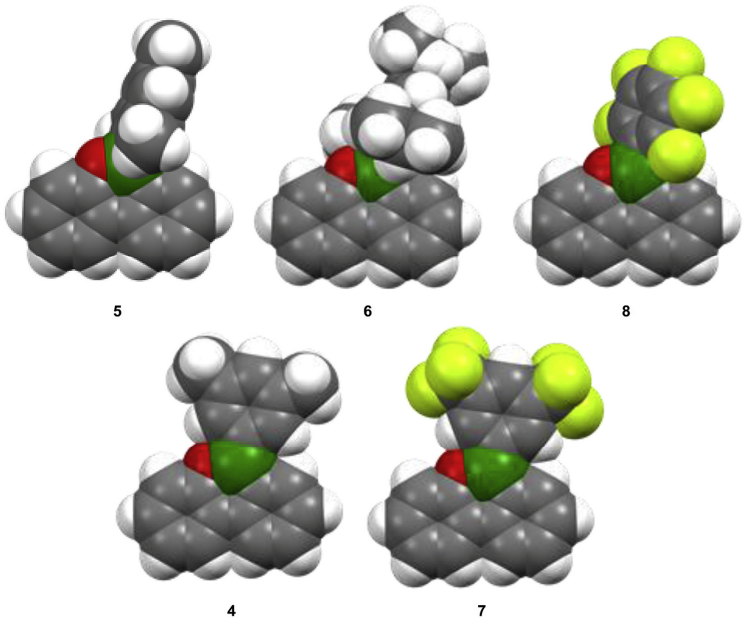

Fig. 5. Conformation of aryl-substituted oxaboraphenanthrene derivatives **4**–**8**.

Table 1
Absorption data of **5**–**9** in PMMA films

	5	6	7	8	9
Wavelengths/nm	262	262	259	260	262
	271	272	269	269	271
	293	293	295	296	295
	309	308	308	307	309
	321	319			322

Table 2
Data for the emission measurements of **5**–**9** in PMMA films which showed no emission itself in the observed wavelengths area

	Excitation λ_{ext} nm	Emission λ_{em} nm	Concentration mmol/L	Substance 10^{-6} mmol	ϕ_{max} %
5	268	348	7.4	0.148	25.2
6	262	341	5.8	0.058	34.8
7	266	373	5.6	0.224	29.5
8	266	361	6.4	0.064	16.1
9	260	344	5.4	0.011	47.3

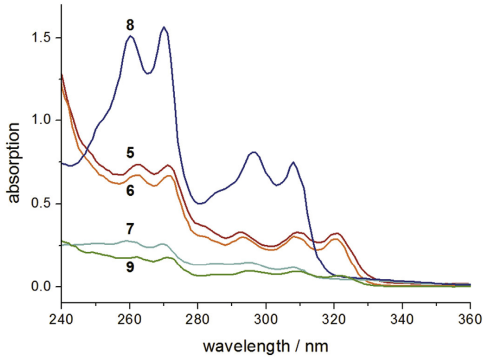

Fig. 6. Absorption spectra of **5**–**9** from PMMA layers of same thickness and same weight percent content of the analyte see Table 1.

dried over $MgSO_4$ and the solvent evaporated under reduced pressure. The oxaboraphenanthrene **5** was obtained as a colorless powder with a yield of 92% (0.678 g, 2.27 mmol). Slow evaporation of a saturated hexane solution of **5** over *Granopent* lead to colorless crystal blocks which were suitable for an investigation by X-ray crystallography.

^{1}H NMR (300.0 MHz, C_6D_6): δ=8.03 (m, 2H), 7.86 (d, $^3J_{HH}$=6.8 Hz, 1H), 7.55 (dd, $^3J_{HH}$=8.1 Hz, $^4J_{HH}$=1.1 Hz, 1H), 7.42 (m, 1H), 7.20–7.07 (m, 3H), 6.87 (s, 2H), 2.26 (s, 3H, CH_3), 2.18 (s, 6H, 2 CH_3); ^{11}B NMR (96.3 MHz, C_6D_6): δ=46.1 (br, $h_{1/2}$=730 Hz); ^{13}C NMR (75.5 MHz, C_6D_6): δ=152.4, 140.3, 139.1, 138.1, 137.7, 133.5, 129.3, 127.8, 127.7, 124.9, 123.7, 123.7, 121.9, 121.0, 22.6 (2 CH_3), 21.4 (1 CH_3); elemental Anal. Calcd (%) for $C_{21}H_{19}BO$ (298.15): C 84.59, H 6.42; found: C 84.55, H 6.87.

*4.2.5. Synthesis of 9-(2,4,6-tri-iso-propylphenyl)-10,9-oxaboraphenanthrene (**6**).* To a solution of (0.522 g, 2.43 mmol, 1.0 equiv) 9-chloro-oxaboraphenanthrene (**1**) in THF (10 mL) a 2,4,6-tri-*iso*-propylphenyl-Grignard solution (0.20 M in THF;

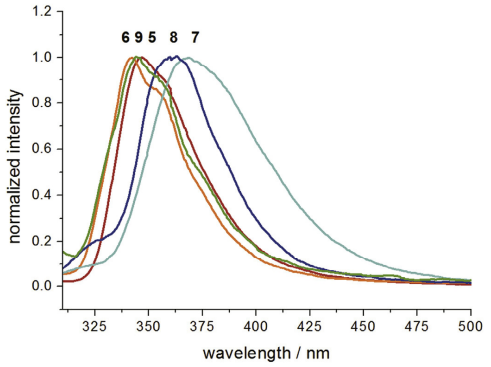

Fig. 7. Emission spectra of **5**–**9**. Measurement with the highest obtained quantum yield with normalized intensities see Table 2.

2.93 mmol, 1.2 equiv) was added (1 h) at room temperature and stirred for 2 h at 60 °C. After cooling to room temperature, the reaction solution was quenched with water (30 mL) and the layers were separated. The aqueous layer was treated with diethyl ether (3×20 mL) and the combined organic layers were dried with $MgSO_4$. After evaporation of the solvent in vacuo, the product was obtained as a colorless powder with a yield of 79% (0.737 g, 1.93 mmol). By slow evaporation colorless crystal blocks which were suitable for an investigation by X-ray crystallography were grown from a saturated hexane solution of **6**.

^{1}H NMR (300.0 MHz, C_6D_6): δ=8.02 (m, 2H), 7.86 (d, $^3J_{HH}$=7.4 Hz, 1H), 7.58 (d, $^3J_{HH}$=8.0 Hz,1H), 7.41 (t, $^3J_{HH}$=7.6 Hz, 1H), 7.24 (s, 2H, *m*-PhH), 7.20–7.07 (m, 3H), 2.93 (m, 1H, CH-*i*Pr), 2.77 (m, 2H, CH-*i*Pr), 1.34 (d, 6H, CH_3-*i*Pr), 1.22 (d, 6H, CH_3-*i*Pr) 1.16 (d, 6H, CH_3-*i*Pr); ^{11}B NMR (96.3 MHz, C_6D_6): δ=46.7 (br, $h_{1/2}$=1700 Hz); ^{13}C NMR (75.5 MHz, C_6D_6): δ=152.4, 140.3, 139.1, 138.1, 137.7, 133.5, 129.3, 127.8, 127.7, 124.9, 123.7, 123.7, 121.9, 121.0, 22.6 (2 *C*H$_3$), 21.4 (1 *C*H$_3$); elemental Anal. Calcd (%) for $C_{27}H_{31}BO$ (382.35): C 84.82, H 8.17; found: C 84.66, H 8.14.

*4.2.6. Synthesis of 9-(3,5-bis(trifluoromethyl)phenyl)-10,9-oxaboraphenanthrene (**7**).* To a solution of (0.824 g, 3.84 mmol, 1.0 equiv) 9-chloro-oxaboraphenanthrene (**1**) in toluene (40 mL) 20.0 mL (0.23 M in THF; 4.52 mmol, 1.2 equiv) of a 3,5-bis(trifluoromethyl)phenyl-Grignard solution were added (30 min) at room temperature, whereby the reddish solution of 9-chloro-oxaboraphenanthrene (**1**) immediately turned yellow. After adding the entire dose of the Grignard solution the brown reaction mixture was stirred for 2.5 h at 70 °C. The now clear yellow reacting solution was cooled to room temperature and quenched with water (50 mL). The separated aqueous layer was treated with diethyl ether (3×20 mL), the combined organic layers were dried over $MgSO_4$ and the solvent removed in vacuo which resulted in a brownish oil. After some hours at room temperature colorless crystal needles of **7** could be obtained from the oil which were suitable for X-ray crystallography. Analytically pure **7** was obtained by crystallization in hexane at room temperature in a yield of 93% (1.401 g, 3.57 mmol).

^{1}H NMR (300.0 MHz, C_6D_6): δ=8.0 (s, 2H), 7.77–7.67 (m, 4H), 7.22–7.13 (m, 2H), 7.01–6.86 (m, 3H); ^{11}B NMR (96.3 MHz, C_6D_6): δ=40.4 (br., $h_{1/2}$=590 Hz); ^{13}C NMR (75.5 MHz, C_6D_6): δ=151.3, 140.0, 136.6, 134.4 (br.), 133.7, 131.4, 131.0, 129.6, 127.7, 126.1, 124.1, 123.9, 123.7, 123.7, 123.6, 123.5, 122.5, 122.3, 120.8; ^{19}F NMR (282.3 MHz, C_6D_6): δ= −62.5 (2CF_3); elemental Anal. Calcd (%) for $C_{20}H_{11}BF_6O$ (392.10): C 61.26, H 2.83; found: C 61.26, H 3.00.

*4.2.7. Synthesis of 9-(pentafluorophenyl)-10,9-oxaboraphenanthrene (**8**).* To a solution of (0.701 g, 3.27 mmol, 1.0 equiv) 9-chloro-oxaboraphenanthrene (**1**) in toluene (20 mL) 20.0 mL (0.18 M in THF; 3.59 mmol, 1.1 equiv) of a pentafluorophenyl-Grignard solution were added (30 min) at room temperature, whereby the reddish 9-chloro-oxaboraphenanthrene (**1**) solution turned immediately yellow. After the entire dose of the Grignard reagent the mixture was stirred for 2 h at room temperature and quenched with water (50 mL). The layers were separated, the aqueous layer was treated with diethyl ether (3×20 mL) and the combined organic layers were dried over $MgSO_4$. Removing the solvent under reduced pressure the crude product was obtained as a brownish crystalline solid. By elution of the solid in hexane (20 mL) and the dropwise addition of diethyl ether (ca. 2 mL) until the solid was completely dissolved and after slow evaporation of the solvent at room temperature colorless crystal blocks of **8** were obtained in a yield of 85% (0.961 g, 2.77 mmol) which were suitable for X-ray crystallography.

^{1}H NMR (300.0 MHz, C_6D_6): δ=7.92–7.89 (m, 2H), 7.78–7.75 (m, 1H), 7.47–7.38 (m, 2H), 7.20 (td, $^3J_{HH}$=7.4 Hz, $^4J_{HH}$=1.0 Hz, 1H), 7.17–7.03 (m, 2H); ^{11}B NMR (96.3 MHz, C_6D_6): δ=41.1 (br., $h_{1/2}$=450 Hz); ^{13}C NMR (75.5 MHz, C_6D_6): δ=151.5, 139.7, 137.1, 134.4, 133.9, 132.6, 129.6, 129.1, 127.7, 124.4, 124.0, 123.4, 122.8, 123.7, 122.1, 121.8, 120.8, 120.0; ^{19}F NMR (282.3 MHz, C_6D_6): δ=−131.30 (m, 2 *o*-Ph*F*), −151.93 (*p*-Ph*F*), −161.53 (2 *m*-Ph*F*); elemental Anal. Calcd (%) for $C_{18}H_8BF_5O$ (346.06): C 62.47, H, 2.33; found: C 62.43, H 2.58.

*4.2.8. Synthesis of 9-trisyl-10,9-oxaboraphenanthrene (**9**).* To a slurry of (1.357 g, 2.87 mmol) Li[C(SiMe$_3$)$_3$]·2 THF in toluene at −78 °C (0.502 g, 2.34 mmol) **1** in toluene (20 mL) was added over a period of 1.5 h and the colorless suspension was warmed to room temperature overnight. The solvent was removed under reduced pressure, the precipitate eluted with hexane (20 mL) and the resulted slurry filtered over Celite. After removal of the solvent **9** was obtained as a colorless powder 65% (0.624 g, 1.52 mmol). By slow evaporation of a saturated benzene solution colorless crystal blocks were grown, which were suitable for X-ray crystallography.

^{1}H NMR (300.0 MHz, C_6D_6): δ=8.54 (dd, $^3J_{HH}$=7.7 Hz, $^4J_{HH}$=1.1 Hz, 1H)), 7.94 (t, $^3J_{HH}$=8.3 Hz, 2H), 7.48 (dd, $^3J_{HH}$=8.1 Hz, $^4J_{HH}$=1.1 Hz, 1H), 7.41–7.31 (m, 1H), 7.30–7.22 (m, 1H), 7.20–7.11 (m, 1H), 7.06–6.99 (m, 1H), 0.40 (s, 27H, 9 *C*H$_3$); ^{11}B NMR (96.3 MHz, C_6D_6): δ=45.1 (br., $h_{1/2}$=550 Hz); ^{13}C NMR (75.5 MHz, C_6D_6): δ=151.3, 138.9, 138.6, 132.4, 129.3, 129.3, 128.6, 125.7, 123.9, 123.3, 123.0, 122.3, 119.7, 6.6 (9 *C*H$_3$); ^{29}Si NMR (59.6 MHz, C_6D_6): δ= −1.4 (3 $SiMe_3$) elemental Anal. Calcd (%) for $C_{22}H_{35}BOSi_3$ (410.58): C 64.36; H, 8.59, found: C 64.03, H 8.51.

*4.2.9. Synthesis of 9-supersilyl-10,9-oxaboraphenanthrene (**10**).* To a solution of (2.67 mmol, 1.1 equiv) Na[Si*t*Bu$_3$]·2 THF in 7 mL toluene at −78 °C (0.520 g, 2.42 mmol, 1.0 equiv) **1** in toluene (20 mL) was added over a period of 1.5 h and the yellow solution was warmed to room temperature overnight. The solvent was removed under reduced pressure, the precipitate eluted with benzene (15 mL) and the resulted slurry filtered over Celite. By concentrating the filtrate **10** was obtained as colorless, dendritic crystals (yield: 90%, g, 2.18 mmol).

^{1}H NMR (300.0 MHz, C_6D_6): δ=8.74 (d, $^3J_{HH}$=7.6 Hz, 1H), 7.99 (t, $^3J_{HH}$=9.1 Hz, 2H), 7.58 (dd, $^3J_{HH}$=8.1 Hz, 1H), 7.40 (t, $^3J_{HH}$=7.5 Hz, 1H), 7.32 (t, $^3J_{HH}$=7.3 Hz, 1H), 7.20–7.13 (m, 1H), 7.07 (t, $^3J_{HH}$=7.6 Hz, 1H), 1.42 (s, 27H, 9 *C*H$_3$); ^{11}B NMR (96.3 MHz, C_6D_6): δ=54.0 (br, $h_{1/2}$=500 Hz); ^{13}C NMR (75.5 MHz, C_6D_6): δ=151.6, 139.9 (2C), 137.1, 132.9, 129.2, 126.8, 123.0, 123.8, 123.0, 122.2, 120.3, 32.6 (9 *C*H$_3$), 23.1 (3 *C*Me$_3$); ^{29}Si NMR (59.6 MHz, C_6D_6): n.b; elemental

Table 3
Crystal data and refinement details for oxaboraphenanthrenes **4**–**9**

	4	5	6	7	8	9
Empirical formula	$C_{20}H_{17}BO$	$C_{21}H_{19}BO$	$C_{27}H_{31}BO$	$C_{20}H_{11}BF_8O$	$C_{18}H_8BF_5O$	$C_{22}H_{35}BOSi_3$
Formula weight	284.15	298.17	382.33	392.10	346.05	410.58
T/K	173(2)	173(2)	293(2)	173(2)	173(2)	173(2)
Wavelength	MoK$_\alpha$, 0.71073 Å	MoK$_\alpha$, 0.71073 Å	MoK$_\alpha$, 0.71073 Å	MoK$_\alpha$, 0.71073 Å	MoK$_\alpha$, 0.71073 Å	MoK$_\alpha$, 0.71073 Å
Crystal system	Orthorhombic	Orthorhombic	Monoclinic	Monoclinic	Monoclinic	Monoclinic
Space group	*Pba*2	$P2_12_12_1$	$P2_1/c$	$P2_1/c$	$P2_1/c$	$P\,2_1/n$
a/Å	15.2162(5)	9.4804(5)	9.0884(7)	12.1297(12)	15.7080(11)	16.5118(8)
b/Å	35.4853(14)	13.7252(6)	32.123(2)	5.4293(4)	7.2722(4)	8.7803(4)
c/Å	5.5091(2)	25.3586(11)	8.5689(6)	25.144(3)	12.5481(10)	33.5288(16)
α/°	90	90	90	90	90	90
β/°	90	90	110.9690(10)	96.922(8)	96.140(6)	99.209(4)
γ/°	90	90	90	90	90	90
V/Å^3	2974.65(19)	3299.7(3)	2336.0(3)	1643.8(3)	1425.17(17)	4798.3(4)
Z	8	8	4	4	4	8
Density calculated g cm^{-3}	1.269	1.200	1.087	1.584	1.613	1.137
F(000)	1200	1264	824	792	696	1776
Index ranges	$-16\le h\le 18$ $-42\le k\le 42$ $-6\le l\le 6$	$-11\le h\le 11$ $-16\le k\le 13$ $-25\le l\le 30$	$-10\le h\le 10$ $-38\le k\le 38$ $-10\le l\le 10$	$-14\le h\le 14$ $-6\le k\le 6$ $-29\le l\le 30$	$-19\le h\le 16$ $-8\le k\le 8$ $-15\le l\le 15$	$-20\le h\le 20$ $-10\le k\le 10$ $-31\le l\le 41$
Crystal size/mm^3	0.23×0.15×0.10	0.48×0.46×0.46	0.65×0.50×0.15	0.35×0.32×0.27	0.28×0.15×0.02	0.42×0.27×0.13
No. of reflections collected	32,715	12,830	22,779	8072	10,868	35,581
$R1$, $wR2$ [$I>2\sigma(I)$]	0.0387, 0.0943	0.0487, 0.1298	0.0878, 0.2010	0.0638, 0.1509	0.0422, 0.0992	0.0620, 0.1570
Data/restraints/parameter	5518/1/402	5765/0/421	4119/9/261	3016/37/265	2664/0/226	9108/0/515
GOOF on F^2	0.990	1.027	1.114	1.051	0.946	1.033
$R1$, $wR2$ (all data)	0.0455, 0.0976	0.0513, 0.1320	0.1168, 0.2165	0.0801, 0.1603	0.0616, 0.1067	0.0791, 0.1665
largest diff peak and hole/eÅ^{-3}	0.168, −0.140	0.0167, −0.220	0.0255, −0.283	0.602, −0.547	0.254, −0.253	0.322, −0.507

Anal. Calcd (%) for $C_{24}H_{35}BOSi$ (378.43): 76.17, H, 9.32, found: C 76.09, H 9.57.

4.3. X-ray structure determination

The data for **6** were collected on a Siemens SMART three-circle diffractometer using MoK_α radiation (λ=0.71073 Å) and were scaled using the program SADABS.[22]

The data for the remaining structures were collected on a STOE IPDS II two-circle diffractometer with a Genix Microfocus tube with mirror optics using MoK_α radiation (λ=0.71073 Å) and were scaled using the frame scaling procedure in the *X-AREA* program system.[23]

The structures were solved by direct methods using the program *SHELXS* and refined against F^2 with full-matrix least-squares techniques using the program *SHELXL-97* (see Table 3).[24]

Due to the absence of anomalous scatterers, the absolute structure of **4** and **5** could not be determined.

The crystal of **6** was measured at room temperature, because the crystals did not survive being cooled. One isopropyl group is disordered over two positions with a site occupation factor of 0.570 (15) for the major occupied site. The disordered atoms were isotropically refined.

One trifluoromethyl group in **7** is disordered over three positions with site occupation factors of 0.447(3), 0.303(3), and 0.250(3). Bond lengths and angles of the disordered atoms were restrained to be equal to those of the non-disordered trifluoromethyl group. The disordered atoms were isotropically refined.

One trimethylsilyl group in **9** is disordered over two positions with a site occupation factor of 0.644(8) for the major occupied site. The disordered atoms were isotropically refined.

CCDC deposition numbers: 1410266 (lithium borate **2b**×**3** THF), 1403456 (**4**), 1403457 (**5**), 1403458 (**6**), 1403459 (**7**), 1403460 (**8**), 1403461 (**9**).

References and notes

1. Dewar, M. J. S.; Dietz, R. *J. Chem. Soc.* **1960**, 1344.
2. Braid, M. U.S. Patent 4 353 807, **1982**.
3. Davis, F. A.; Dewar, M. J. S. *J. Org. Chem.* **1968**, *8*, 3324.
4. Kohn, G. K; McMurtry, R. J. U.S. Patent 3 686 398, **1972**.
5. He, J.; Crase, J. L.; Wadumethrige, S. H.; Thakur, K.; Dai, L.; Zou, S.; Rathore, R.; Hartley, C. S. *J. Am. Chem. Soc.* **2010**, *132*, 13848.
6. Crossley, D. L.; Cade, I. A.; Clark, E. R.; Escande, A.; Humphries, M. J.; King, S. M.; Vitorica-Yrezabal, I.; Ingleson, M. J.; Turner, M. L. *Chem. Sci.* **2015**, *6*, 5144.
7. Budanow, A.; Sinke, T.; Lerner, H.-W.; Bolte, M. *Acta Crystallogr.* **2014**, *C70*, 662.
8. Zou, L.; Savvate'ev, V.; Booher, J.; Kim, C.-H.; Shinarb, J. *Appl. Phys. Lett.* **2001**, *79*, 2282.
9. Qiu, C. F.; Wang, L. D.; Chen, H. Y.; Wong, M.; Kwok, H. S. *Appl. Phys. Lett.* **2001**, *79*, 2276.
10. Liu, H.; Bai, Q.; Yao, L.; Zhang, H.; Xu, H.; Zhang, S.; Li, W.; Gao, Y.; Li, J.; Lu, P.; Wang, H.; Yang, B.; Mac, Y. *Chem. Sci.* **2015**, *6*, 3797.
11. Chao, T.-C.; Lin, Y.-T.; Yang, C.-Y.; Hung, T. S.; Chou, H.-C.; Wu, C.-C.; Wong, K.-T. *Adv. Mater.* **2005**, *17*, 992.
12. Hirai, H.; Nakajima, K.; Nakatsuka, S.; Shiren, K.; Ni, J.; Nomura, S.; Ikuta, T.; Hatakeyama, T. *Angew. Chem., Int. Ed.* **2015**, *54*, 13581.
13. Zhou, Q. J.; Worm, K.; Dolle, R. E. *J. Org. Chem.* **2004**, *69*, 5147.
14. Cowley, A. H.; Norman, N. C.; Pakulski, M.; Becker, G.; Layh, M.; Kirchner, E.; Schmidt, M. *Inorg. Synth.* **1990**, *27*, 235.
15. Eaborn, C.; Hitchcock, P. B.; Smith, J. D.; Sullivan, A. C. *Chem. Commun.* **1983**, 827.
16. Lerner, H.-W. *Coord. Chem. Rev.* **2005**, *249*, 781.
17. Wiberg, N.; Amelunxen, K.; Lerner, H.-W.; Schuster, H.; Nöth, H.; Krossing, I.; Schmidt-Amelunxen, M.; Seifert, T. *J. Organomet. Chem.* **1997**, *542*, 1.
18. Tang, C. W.; VanSlyke, S. A. *Appl. Phys. Lett.* **1987**, *51*, 913.
19. SooKim, H.; Moon, S. I.; Hwang, D. E.; Jeong, K. W.; Kim, C. K.; Moon, D.-G.; Hong, C. *Opt. Laser Technol.* **2016**, *77*, 104.
20. Bahirwar, B. M.; Atram, R. G.; Pode, R. B.; Moharil, S. V. *Mater. Chem. Phys.* **2007**, *106*, 364.
21. **2b**×3 THF ($C_{38}H_{48}BLiO_3$) crystallizes in the 'monoclinic' system, space group '$P\,2_1/n$' with a=9.7010(8) Å, b=19.0850(11) Å, c=17.7489(15) Å, α=90°, β=101.416(7)°, γ=90°, V=3221.1(4), M=562.45, Z=4, and Dc=1.160 g cm^{-3}. 24799 reflections (6030 unique) were collected in the range of 3.393–25.703° at 173 K giving a final residual value of $R1$=0.1021 (all data) $wR2$=0.1721 ([I>2σ(I)]); CCDC 1410266.
22. Sheldrick, G. M. *SADABS, A Program for the Scaling of Area Detector Data, Göttingen, Germany*, 1996.
23. Stoe, C. *X-AREA. Diffractometer Control Program System*; Stoe & Cie: Darmstadt, Germany, 2002.
24. Sheldrick, G. M. *Acta Crystallogr., Sect. A* **2008**, *64*, 112.

6.3. Lebenslauf

Die persönlichen Daten wurden aus der digitalen Version entfernt.

Fachartikel

04/2019 **Dual Role of Doubly Reduced Arylboranes as Dihydrogen- and Hydride-Transfer Catalysts**
E. von Grotthuss, S. E. Prey, M. Bolte, H.-W. Lerner und M. Wagner
J. Am. Chem. Soc. **2019**, *141*, 6082-6091.

01/2019 **Chalcogen–Chalcogen-Bond Activation by an Ambiphilic, Doubly Reduced Organoborane**
E. von Grotthuss, F. Nawa, M. Bolte, H.-W. Lerner und M. Wagner,
Tetrahedron **2019**, *75*, 26-30.

10/2018 **Selective CO_2 Splitting by Doubly Reduced Aryl Boranes to Give CO and $[CO_3]^{2-}$**
E. von Grotthuss, S. E. Prey, M. Bolte, H.-W. Lerner und M. Wagner,
Angew. Chem. Int. Ed. **2018**, *57*, 16491-16495.

09/2018 **Synthesis and Ring Strain of a Benzoborirene-*N*-Heterocyclic Carbene Adduct**
J. Hahn, C. Keck, C. Maichle-Mössmer, E. von Grotthuss, P. N. Ruth, A. Paesch, D. Stalke und H. Bettinger,
Chem. Eur. J. **2018**, *24*, 18634-18637.

01/2018 **Doping Polycyclic Aromatics with Boron for Superior Performance in Materials Science and Catalysis**
E. von Grotthuss,[a] A. John,[a] T. Kaese[a] und M. Wagner,
([a] Diese Autoren haben zu gleichen Teilen an der Arbeit beigetragen)
Asian J. Org. Chem. **2018**, *7*, 37-53.

10/2016 **Reversible Dihydrogen Activation by Reduced Aryl Boranes as Main-Group Ambiphiles**
E. von Grotthuss, M. Diefenbach, M. Bolte, H.-W. Lerner, M. C. Holthausen und M. Wagner,
Angew. Chem. Int. Ed. **2016**, *55*, 14067-14071.

03/2016 **10,9-Oxaboraphenanthrenes as Luminescent Fluorophores**
A. Budanow, E. von Grotthuss, M. Bolte, M. Wagner und H.-W. Lerner,
Tetrahedron **2016**, *72*, 1477-1484.

Tagung

03/2018 **255th ACS National Meeting and Exposition, New Orleans, Louisiana**
Vortrag: “9,10-Dihydro-9,10-diboraanthracene salts as versatile catalysts”

6.4. Erklärung über frühere Promotionsverfahren und Versicherung

Erklärung

Ich erkläre hiermit, dass ich mich bisher keiner Doktorprüfung im mathematisch-naturwissenschaftlichen Bereich unterzogen habe.

_____

Ort, Datum

_____

Esther von Grotthuss

Versicherung

Ich erkläre hiermit, dass ich die vorliegende Dissertation mit dem Titel

Zweifach reduzierte 9,10-Dihydro-9,10-diboraanthracene:

Von der Aktivierung kleiner Moleküle bis zum Einsatz als Katalysatoren

selbstständig angefertigt und mich anderer Hilfsmittel als der in ihr angegebenen nicht bedient habe, insbesondere, dass alle Entlehnungen aus anderen Schriften mit Angabe der betreffenden Schrift gekennzeichnet sind.

Ich versichere, die Grundsätze der guten wissenschaftlichen Praxis beachtet und keine Hilfe einer kommerziellen Promotionsvermittlung in Anspruch genommen zu haben.

_____

Ort, Datum

_____

Esther von Grotthuss